SOLAR CELLS – NEW ASPECTS AND SOLUTIONS

Edited by **Leonid A. Kosyachenko**

INTECHWEB.ORG

Solar Cells – New Aspects and Solutions
Edited by Leonid A. Kosyachenko

Published by InTech
Janeza Trdine 9, 51000 Rijeka, Croatia

Publishing Process Manager Sandra Bakic
Technical Editor Teodora Smiljanic
Cover Designer Jan Hyrat
Image Copyright Carsten Reisinger, 2011. Used under license from Shutterstock.com

First published October, 2011
Printed in Croatia

A free online edition of this book is available at www.intechopen.com
Additional hard copies can be obtained from orders@intechweb.org

Solar Cells – New Aspects and Solutions, Edited by Leonid A. Kosyachenko
p. cm.
ISBN 978-953-307-761-1

Contents

Preface

Photovoltaics covers an extremely wide range of different fields of science and technology that are in a state of continuous development and improvement for decades. Solar cells and models that have been developed to the level of industrial production or prototype samples, as well as the devices of exploratory types are divided into the so-called generations of photovoltaics. Chapters, which concern the problems of the first, second and third generations of solar cells are included in the relevant three books of this edition. Chapters that are general in nature or not related specifically to these generations, some novel scientific ideas and technical solutions, which has not properly approved, new methods of research and testing of solar cells and modules have been collected in the fourth book of the four-volume edition of "Solar cells". General issues of the efficiency of a direct conversion of solar radiation into electrical energy in solar cell and through hydrogen production in photoelectrochemical solar cell are discussed in several chapters of the book. Considerable attention is paid to the quantum-size effects in solar cells both in general and on specific examples of AlGaAs superlattices, CdSe quantum dots, etc. New materials, such as cuprous oxide as an active material for solar cells, AlSb for use as an absorber layer in p-i-n junction solar cells, InGaAsN as a promising material for high efficiency multi-junction tandem solar cells, InP in solar cells with semiconductor-insulator-semiconductor structures are discussed in several chapters. Other chapters are devoted to the analysis of both status and perspective of organic photovoltaics as well as specific issues, such as polymer/fullerene solar cells, poly(p-phenylene-vinylene) derivatives, photovoltaic textiles, photovoltaic fibers, etc.

It appears that the fourth book of the edition of "Solar Cells" will find many interested readers.

The editor addresses special thanks to the contributors for their initiative and high quality work, and to the technical editors that conveyed the text into a qualitative and pleasant presentation.

Professor, Doctor of Sciences, Leonid A. Kosyachenko
National University of Chernivtsi
Ukraine

1

Effects of Optical Interference and Annealing on the Performance of Polymer/Fullerene Bulk Heterojunction Solar Cells

Chunfu Zhang[1], Hailong You[1], Yue Hao[1],
Zhenhua Lin[2] and Chunxiang Zhu[2]
[1]*School Of Microelectronics, Xidian University,*
[2]*ECE, National University of Singapore,*
[1]*China*
[2]*Singapore*

1. Introduction

Polymer solar cells are of tremendous interests due to their attractive properties such as flexibility, ease of fabrication, low materials and energy budget. However, organic materials have short exciton diffusion length and poor charge mobility, which can greatly decrease the performance of polymer solar cells. These challenges can be effectively overcome through the use of the bulk heterojunction (HJ) structure because it can guarantee the effective exciton dissociation and carrier transport simultaneously if a proper bicontinuous interpenetrating network is formed in the active layer. Based on this structure, the performance of polymer solar cells has been improved steadily in the past decade.

The performance of a polymer solar cell is mainly determined by the short-circuit current density (J_{SC}), the open circuit voltage (V_{OC}), and the fill factor (*FF*), given that $\eta=J_{SC}V_{OC}FF/P_{in}$ (where η is power conversion efficiency, *PCE*, and P_{in} is the incident optical power density). V_{OC} has a direct relationship with the offset energies between the highest occupied molecular orbital of Donor (*D*) material and the lowest unoccupied molecular orbital of Acceptor (*A*) material (Cheyns et al., 2008). Since the *D* and *A* materials are intimately mixed together in the bulk HJ structure and their interfaces distribute everywhere in the active layer, it is difficult to increase V_{OC} by changing *D*/*A* interface property for a given material system (such as poly(3-hexylthiophene-2,5-diyl):[6,6]-phenyl C_{61} butyric acid methyl ester, P3HT:PCBM). Thus the usually used optimization method is to improve J_{SC} and *FF*.

J_{SC} greatly depends on the optical interference effect in polymer solar cells. Because of the very high optical absorption ability of organic materials, the active layer is very thin and typically from several ten to several hundred nanometers. This thickness is so thin compared to the incident light wavelength that the optical interference effect has to be carefully considered. Depending on the thicknesses and optical constants of the materials, the optical interference causes distinct distributions of the electric field and energy absorption density. Due to this effect, J_{SC} shows an obvious oscillatory behavior with the variation of active layer thickness. In order to gain a high *PCE*, the active layer thickness needs to be well optimized according to the optical interference.

Besides the serious optical interference effect, J_{SC} also suffers from the non-ideal free carrier generation, low mobility and short carrier lifetime. In order to reduce the exciton loss and guarantee the efficient carrier transport, the optimal interpenetrating network, or to say, the optimal morphology is desired in the bulk HJ structure. In order to achieve an optimal morphology, a thermal treatment is usually utilized in the device fabrication, especially for the widely used P3HT:PCBM solar devices. It is found that the sequence of the thermal treatment is critical for the device performance (Zhang et al., 2011). The polymer solar cells with the cathode confinement in the thermal treatment (post-annealed) show better performance than the solar cells without the cathode confinement in the thermal treatment (pre-annealed). The functions of the cathode confinement are investigated in this chapter by using X-ray photoelectron spectroscopy (XPS), atomic force microscopy (AFM), optical absorption analysis, and X-ray diffraction (XRD) analysis. It is found that the cathode confinement in the thermal treatment strengthens the contact between the active layer and the cathode by forming Al–O–C bonds and P3HT-Al complexes. The improved contact effectively improves the device charge collection ability. More importantly, it is found that the cathode confinement in the thermal treatment greatly improves the active layer morphology. The capped cathode effectively prevents the overgrowth of the PCBM molecules and, at the same time, increases the crystallization of P3HT during the thermal treatment. Thus, a better bicontinuous interpenetrating network is formed, which greatly reduces the exciton loss and improves the charge transport capability. Meanwhile, the enhanced crystallites of P3HT improve the absorption property of the active layer. All these aforementioned effects together can lead to the great performance improvement of polymer solar cells. Besides the thermal treatment sequence, temperature is another very important parameter in the annealing process. Various annealing temperatures have also been tested to find the optimized annealing condition in this chapter.

The contents of this chapter are arranged as the following: Section 2 introduces the effects of the optical interference on J_{SC} in polymer solar cells by considering the non-ideal free carrier generation, low mobility and short carrier lifetime at the same time; Section 3 investigates the influence of the sequence of the thermal treatment on the device performance with emphasis on the cathode confinement in the thermal treatment; based on the optical interference study and the proper thermal treatment sequence, the overall device optimization is presented in Section 4. At last, a short conclusion is given in Section 5.

2. Effects of optical interference on J_{SC}

J_{SC} is directly related to the absorption ability of organic materials. It is believed that increasing the light harvesting ability of the active layer is an effective method to increase J_{SC}. In order to increase J_{SC}, some optical models (Pettersson, 1999; Peumans et al., 2003) have been built to optimize the active layer thickness. However, only optimizing the thickness for better light absorption is difficult to improve J_{SC}. This is because that *PCE* depends not only on the light absorption, but also on exciton dissociation and charge collection. In polymer solar cells, a blend layer consisting of conjugated polymer as the electron donor and fullerene as the electron acceptor is always used as the active layer. For a well blended layer, the length scale of *D* and *A* phases is smaller than the exciton diffusion length (typically less than 10 nm), so that most of the generated excitons can diffuse to the *D/A* interface before they decay. Even if all the excitons can reach the *D/A* interface, not all of them can be dissociated into free carriers. The exciton-to-free-carrier

dissociation probability is not 1 and depends on some factors such as electric field and temperature. When the active layer thickness is increased to optimize the light absorption, the electric field in the blend layer decreases, which lowers down the exciton-to-free-carrier probability and makes charge collection less effective simultaneously. As a result, J_{SC} may become low, although the thickness has been optimized for better light absorption. Thus to obtain a higher J_{SC}, both the optical and the electric properties should be considered at the same time.

Some previous works (Lacic et al., 2005; Monestier et al., 2007) studied the characteristic of J_{SC}. However, they neglected the influence of exciton-to-free-carrier probability, which is important for polymer solar cells. Another study (Koster et al., 2005) considered this factor, but they neglected the optical interference effect, which is a basic property for the very thin organic film. All the above studies are based on the numerical method, and it is not easy to solve the equations and understand the direct influence of various parameters on J_{SC}. In this part, a model predicting J_{SC} is presented by using very simple analytical equations. Based on this model, the effects of optical interference on J_{SC} is investigated. Besides, the carrier lifetime is also found to be an important factor. By considering the optical interference effect and the the carrier lifetime, it is found that when the lifetimes of both electrons and holes are long enough, the exciton-to-free-carrier dissociation probability plays a very important role for a thick active layer and J_{SC} behaves wavelike with the variation of the active layer thickness; when the lifetime of one type of carrier is too short, the accumulation of charges appears near the electrode and J_{SC} increases at the initial stage and then decreases rapidly with the increase of the active layer thickness.

2.1 Theory

2.1.1 Exciton generation

The active layer in polymer solar cells absorbs the light energy when it is propagating through this layer. How much energy can be absorbed depends on the complex index of refraction $\bar{n} = n + i\kappa$ of the materials. At the position z in the organic film (Fig. 1 (a)), the time average of the energy dissipated per second for a given wavelength λ of incident light can be calculated by

$$Q(z,\lambda) = \frac{1}{2} c\varepsilon_0 \alpha_j n \left|\bar{E}(z)\right|^2 \tag{1}$$

where c is the vacuum speed of light, ε_0 the permittivity of vacuum, n the real index of refraction, α the absorption coefficient, $\alpha = 4\pi\kappa / \lambda$, and $E(z)$ the electrical optical field at point z. $Q(z,\lambda)$ have the unit of W / m^3 . Assuming that every photon generates one exciton, the exciton generation rate at position z in the material is given by

$$G(z,\lambda) = \frac{Q(z,\lambda)}{h\gamma} = \frac{\lambda}{hc} Q(z,\lambda) \tag{2}$$

where h is Planck constant, and γ is the frequency of incident light. The total excitons generated by the material at position z in solar spectrum are calculated by

$$G(z) = \int_{300}^{800} G(z,\lambda) d\lambda \tag{3}$$

Here the integration is performed from 300 nm to 800 nm, which is because that beyond this range, only very weak light can be absorbed by P3HT: PCBM active layer. In inorganic solar cells, $Q(z,\lambda)$ is usually modeled by

$$Q(z,\lambda) = \alpha I_0 e^{-\alpha z} \tag{4}$$

I_0 is the incident light intensity. Here, the optical interference effect of the materials is neglected. But in polymer solar cells, the active layers are so thin compared to the wavelength that the optical interference effect cannot be neglected.

2.1.2 Optical model

In order to obtain the distribution of electromagnetic field in a multilayer structure, the optical transfer-matrix theory (TMF) is one of the most elegant methods. In this method, the light is treated as a propagating plane wave, which is transmitted and reflected on the interface. As shown in Fig. 1 (a), a polymer solar cell usually consists of a stack of several layers. Each layer can be treated to be smooth, homogenous and described by the same complex index of refraction $\bar{n} = n + i\kappa$. The optical electric field at any position in the stack is decomposed into two parts: an upstream component E^+ and a downstream component E^-, as shown in Fig. 1 (a). According to Fresnel theory, the complex reflection and transmission coefficients for a propagating plane wave along the surface normal between two adjacent layers *j* and *k* are

$$r_{jk} = \frac{\overline{n_j} - \overline{n_k}}{\overline{n_j} + \overline{n_k}} \tag{5a}$$

$$t_{jk} = \frac{2\overline{n_j}}{\overline{n_j} + \overline{n_k}} \tag{5b}$$

where r_{jk} and t_{jk} are the reflection coefficient and the transmission coefficient, $\overline{n_j}$ and $\overline{n_k}$ the complex index of refraction for layer *j* and layer *k*. So the interface matrix between the two adjacent layers is simply described as

$$I_{jk} = \frac{1}{t_{jk}}\begin{bmatrix} 1 & r_{jk} \\ r_{jk} & 1 \end{bmatrix} = \begin{bmatrix} \dfrac{\overline{n_j} + \overline{n_k}}{2\overline{n_j}} & \dfrac{\overline{n_j} - \overline{n_k}}{2\overline{n_j}} \\ \dfrac{\overline{n_j} - \overline{n_k}}{2\overline{n_j}} & \dfrac{\overline{n_j} + \overline{n_k}}{2\overline{n_j}} \end{bmatrix} \tag{6}$$

When light travels in layer *j* with the thickness *d*, the phase change can be described by the layer matrix (phase matrix)

$$L_j = \begin{bmatrix} e^{-i\beta_j} & 0 \\ 0 & e^{i\beta_j} \end{bmatrix} \tag{7}$$

where $\beta_j = 2\pi\overline{n}_j d_j / \lambda$ is phase change the wave experiences as it traverses in layer *j*. The optical electric fields in the substrate (subscript *0*) and the final layer (subscript *m+1*) have the relationship as

$$\begin{bmatrix} \overline{E_0^+} \\ \overline{E_0^-} \end{bmatrix} = S \begin{bmatrix} \overline{E_{m+1}^+} \\ \overline{E_{m+1}^-} \end{bmatrix} = \begin{bmatrix} S_{11} & S_{12} \\ S_{12} & S_{22} \end{bmatrix} \begin{bmatrix} \overline{E_{m+1}^+} \\ \overline{E_{m+1}^-} \end{bmatrix} = \left(\prod_{v=1}^{m} I_{(v-1)v} L_v \right) \bullet I_{m(m+1)} \tag{8}$$

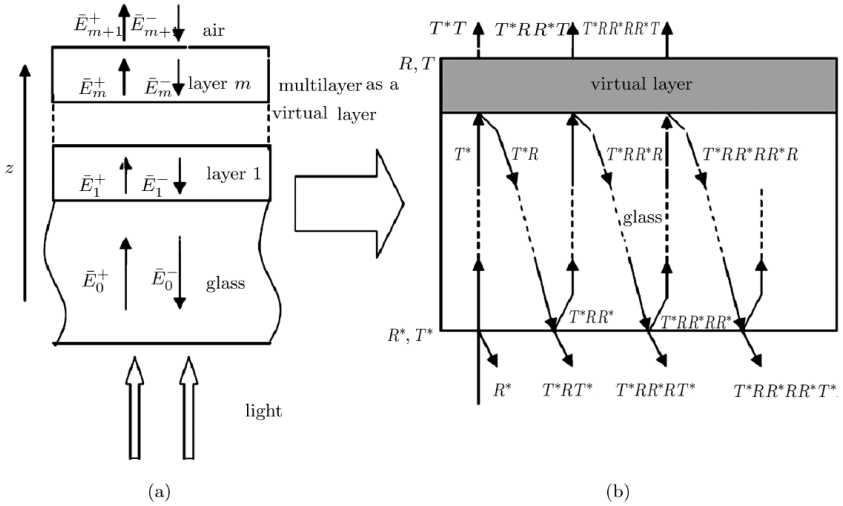

Fig. 1. Multilayer structure in a polymer solar cell. (a) the optical electric field in each layer and (b) treating the multilayer as a virtual layer.

Because in the final layer, $\overline{E_{m+1}^-}$ is 0, it can be derived that the complex reflection and transmission coefficients for the whole multilayer are:

$$r = \frac{\overline{E_0^-}}{\overline{E_0^+}} = \frac{S_{21}}{S_{11}} \tag{9a}$$

$$t = \frac{\overline{E_{m+1}^+}}{\overline{E_0^+}} = \frac{1}{S_{11}} \tag{9b}$$

In order to get the optical electric field E_j (z) in layer *j*, *S* is divided into two parts,

$$S = S_j^{'} L_j S_j^{''} \tag{10}$$

Where

$$S_j^{'} = \left(\prod_{v=1}^{j-1} I_{(v-1)v} L_v \right) \bullet I_{j(j-1)} \tag{11a}$$

$$S_j^{''} = \left(\prod_{v=j+1}^{m} I_{(v-1)v} L_v \right) \bullet I_{m(m+1)} \tag{11b}$$

At the down interface in layer *j*, the upstream optical electric field is denoted as

$$\overline{E_j^+} = t_j^+ \bullet \overline{E_0^+} = \frac{S_{j11}^{''}}{S_{j11}^{'} S_{j11}^{''} + S_{j12}^{'} S_{j21}^{''} e^{i2\beta_j}} \overline{E_0^+} \tag{12}$$

Similarly, at the up interface in layer *j*, the downstream optical electric field is

$$\overline{E_j^-} = t_j^- \bullet \overline{E_0^+} = \frac{S_{j21}^{''}}{S_{j11}^{''}} e^{i2\beta_j} \overline{E_j^+} \tag{13}$$

The optical electric field $\overline{E_j}(z)$ at any position z in layer j is the sum of upstream part $\overline{E_j^+}(z)$ and downstream part $\overline{E_j^-}(z)$

$$\overline{E_j}(z) = \overline{E_j^+}(z) + \overline{E_j^-}(z) = (t_j^+ e^{i\beta_j} + t_j^- e^{-i\beta_j}) \overline{E_0^+} \tag{14}$$

2.1.3 Light loss due to the substrate

Because the glass substrate is very thick compared to wavelength (usually 1mm>> wavelength), the optical interference effect in the substrate can be neglected. Here only the correction of the light intensity at the air/substrate and substrate/multilayer interfaces is made. As shown in Fig. 1 (b), the multilayer can be treated as a virtual layer whose complex reflection and transmission coefficients can be calculated using above equations. Then the irradiance to the multilayer is

$$I_g = T \left(\sum_{i=0}^{\infty} (R^* R)^i \right) I_0 = \frac{1 - R^*}{1 - RR^*} I_0 \tag{15}$$

I_g is described as

$$I_g = \frac{1}{2} c \varepsilon_0 n_g \left| E_0^+ \right|^2 \tag{16}$$

It can be derived that

$$\left| E_0^+ \right| = \sqrt{\frac{2(1 - R^*) * I_0}{\varepsilon_0 c n_g (1 - RR^*)}} \tag{17}$$

2.1.4 Free carrier generation

When the excitons are generated, not all of them can be dissociated into free carriers. The dissociation probability depends on the electric field and temperature. Recently, the

dissociation probability has been taken into consideration in polymer solar cells [13, 16]. The geminate recombination theory, first introduced by Onsager and refined by Brau later, gives the probability of electron-hole pair dissociation,

$$P(F,T) = \frac{k_D(F)}{k_D(F) + k_X} \tag{18}$$

where k_X is the decay rate to the ground state and k_D the dissociation rate of a bound pair. Braun gives the simplified form for dissociation rate

$$k_D(F) = k_R e^{-U_B/k_B T}\left[1 + b + \frac{b^2}{3} + \cdots\right] \tag{19}$$

where a is the initial separation distance of a given electron-hole pair, U_B is electron-hole pair binding energy described as $U_B = q^2/(4\pi\varepsilon_0\varepsilon_r a)$ and $b = q^3F/(8\pi\varepsilon_0\varepsilon_r k_B T^2)$. T is the temperature, F the electric field and ε_r the dielectric constant of the material. In equation (19), k_R is a function of the carrier recombination. For simplification, we treat k_R as a constant. Thus, the dissociation probability P only depends on the electric field F when the temperature keeps constant.

2.1.5 J_{SC} expression equations

J_{SC} is determined by the number of carriers collected by the electrodes in the period of their lifetime τ under short circuit condition. If the active layer thickness L is shorter than the electron and hole drift lengths (which is the product of carrier mobility μ, the electric field F and the carrier lifetime τ) or in other word, the lifetimes of both types of carriers exceed their transit time (case I as in Fig 2 (a)), all generated free carriers can be collected by the electrodes. Considering the exciton-to-free-carrier dissociation probability P, J_{SC} is

$$J_{SC} = qP(F,T)GL \tag{20}$$

where G is the average exciton generation rate in the active layer.

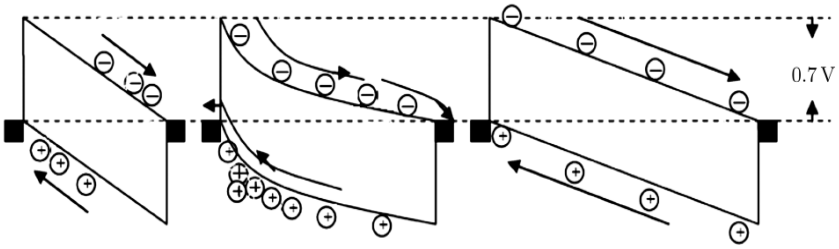

Fig. 2. Energy band diagrams under short circuit condition. (a) Case I: thickness is shorter than both drift lengths, (b) Case II: thickness is longer than hole drift length but shorter than electron drift length, c) Case III: thickness is longer than both hole and electron drift lengths.

If L is longer than drift lengths of electrons and holes, that is to say that the lifetimes of both types of carriers are smaller than their transit time, the carriers are accumulated in the active layer. At steady state, J_{SC} follows Ohm's law. Considering the exciton-to-free-carrier dissociation probability P, J_{SC} is

$$J_{SC} = qP(F,T)G(\mu_e\tau_e + \mu_h\tau_h)F = qP(F,T)G(\mu_e\tau_e + \mu_h\tau_h)V_{bi} / L \tag{21}$$

where V_{bi} is the built-in potential which is usually determined by the difference between cathode and anode work functions. This is case III as described in Fig. 2 (c).

Between case I and case III, it is case II as described in Fig. 2 (b). In this case, L is only longer than the drift length of one type of carrier. For P3HT:PCBM based polymer solar cells, the mobilities of holes and electrons in P3HT:PCBM (1:1 by weight) layer are $2\times10^{-8}\,m^2V^{-1}s^{-1}$ and $3\times10^{-7}\,m^2V^{-1}s^{-1}$, respectively [Mihailetchi et al., 2006]. Because the hole mobility is one order lower than the electron mobility, holes are easy to accumulate in the active layer, which makes the electric field non-uniform. In order to enhance the extraction of holes, the electric field increases near the anode. On the other hand, in order to diminish the extraction of electrons, the electric field decreases near the cathode. The electric field is modified until the extraction of holes equal to the extraction of electrons. Goodman and Rose studied this case and gave an equation for the photocurrent [Goodman & Rose, 1971]. Considering the exciton-to-free-carrier dissociation probability P, J_{SC} is

$$J_{sc} = qP(F,T)GL(1+c)\frac{-c + (c^2 + 4(1-c)V\mu_h\tau_h / L^2)^{\frac{1}{2}}}{2(1-c)} \tag{22}$$

where $c = \mu_h\tau_h / (\mu_e\tau_e)$ is the drift length ratio of holes and electrons. When $c<<1$, the equation is simplified to

$$J_{sc} = qP(F,T)G(\mu_h\tau_h)^{1/2}V^{1/2} \tag{23}$$

2.2 Results and discussion

2.2.1 Exciton generation profile in the active layer

For the studied bulk HJ cell, the D and A materials are well blended and form the active layer. Because the D and A domains are very small, we can neglect the complex reflection and transmission at D/A interfaces, and treat the whole active layer as one homogenous material. All the optical constants (n, k) of the indium tin oxide (ITO), poly(3, 4-ethylenedioxythiophene):poly (styrene sulfonate) (PEDOT:PSS), P3HT:PCBM and the Al electrode are input into our program, and the exciton generation rate in polymer solar cells is calculated. If the interference effect is neglected, the exciton generation rate decreases with the increasing thickness of the active layer as described in equation (4) which makes the corresponding average exciton generation rate (total exciton generation rate divided by the thickness) become smaller. However, when the optical interference effect is considered, the modulation effect of average exciton generation rate with the thickness variation is very clear as shown in Fig. 3. At the initial stage, the average exciton generation rate increases with the increasing thickness of the active layer. This is because the first light peak does not appear in the active layer when the active layer is thin due to the interference effect. With the increase of the active layer, the first light peak approaches and enters the active layer

such that the average generation rate becomes larger. With the further increase of the active layer, the average generation rate decreases although other light peaks enter the active layer. This is because for a thicker film, the thickness of the active layer dominates the generation rate. This evolution of exciton generation is plotted in Fig. 4 for the 500 nm wavelength.

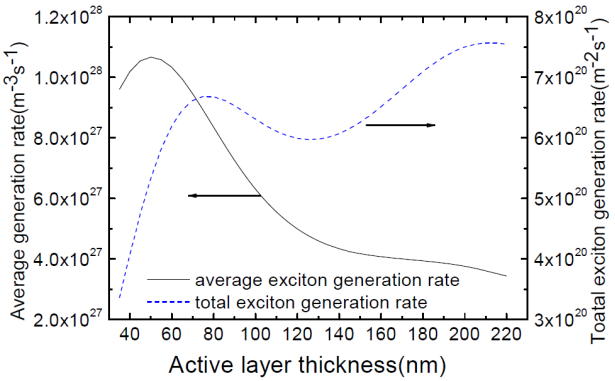

Fig. 3. The calculated exciton generation rate in the active layer when the optical interference effect is considered.

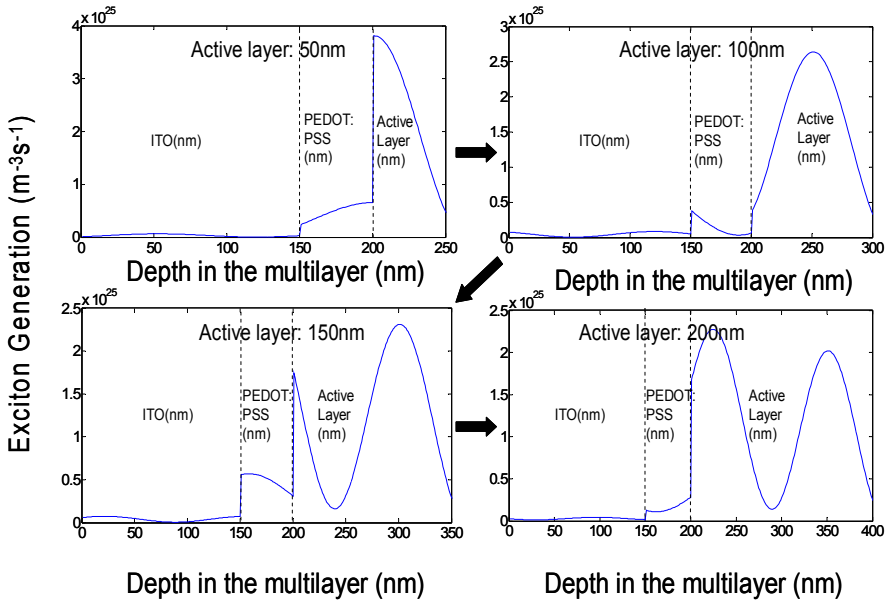

Fig. 4. Evolution of exciton generation in the active layer. The light wavelength is 500 nm. It can be seen that with the increase of the active layer thickness, the first peak enters the active layer, which makes the average exciton generation rate become large. For very thick film, although other peaks can enter the active layer, the absolute values for the peaks become small, which leads to the corresponding decrease of average exciton generation rate.

2.2.2 J_{SC} and the active layer thickness

Based on the calculated exciton generation rate, it is easy to predict J_{SC} when the drift lengths of both carriers are larger than the blend layer thickness. If all the generated excitons can be dissociated into free carriers, and then collected by the electrodes, J_{SC} should be proportional to the total exciton generation rate and behave wavelike as shown in Fig. 5 (solid line). Monestier [Monestier et al., 2007] have found this trend based on P3HT:PCBM systems. In their experiments, the active layer thickness is varied from a few tens nanometer to 215 nm. When the thickness is 70 nm, J_{SC} reaches the maximum value, and followed by a little decrease until 140 nm. When the thickness increases further, J_{SC} increases again. Unfortunately, there is obvious deviation between the prediction and the experiment results, especially in the thick film as shown in Fig. 5 (solid line). Obviously, the assumption that the exciton-to-free-carrier dissociation probability is unity is not correct. The influence of dissociation probability on J_{SC} must be considered.

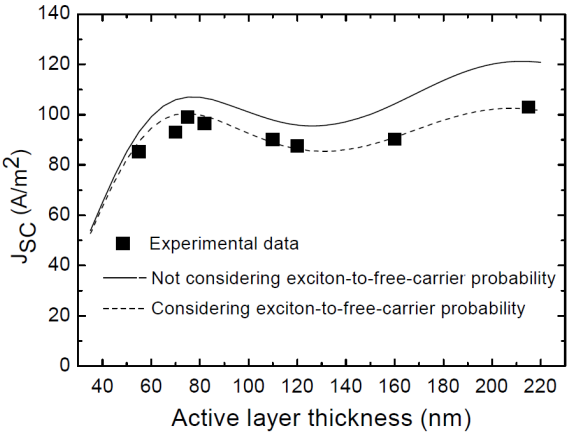

Fig. 5. Long carrier lifetime condition: the lifetimes of both carriers are always longer than their transient time. Experimental data are extracted from the work (Monestier et al. 2007).

In the previous work, Mihailetchi [Mihailetchi et al., 2006] exactly predicted photocurrent of P3HT:PCBM solar cells by assuming the same e-h separation distance (a) and decay rate (k_X). By fitting the experimental data, they obtained e-h separation distance of a=1.8 nm, room temperature bound pair decay rate of $k_X \approx 2\times10^4\,s^{-1}$ for a 120 nm active layer, and the dissociation probability is close to 90%. We use the same data and derive the parameter $k_R = 3.9662\times10^8\,S^{-1}$ (equation 19). The dissociation probability is calculated according to section 2.1.4. The results are shown in Fig. 6. Obviously, the exciton-to-free-carrier probability becomes lower with the increase of the active layer thickness. Using the results to correct J_{SC}, another J_{SC} curve is obtained and also shown in Fig. 5 (dash line). It can be seen that the predicted J_{SC} is exactly in accordance with the experimental results. This confirms the validity of our model. In the previous work, Monestier [Monestier et al., 2007]] modeled J_{SC} and found that the predicted J_{SC} is larger than the experimental data, especially for the thickness larger than 180 nm. They attributed this to the thickness dependence of optical constants. Here, according to our model, it is found that the deviation should come from the low exciton-to-free-carrier probability for thick active layers.

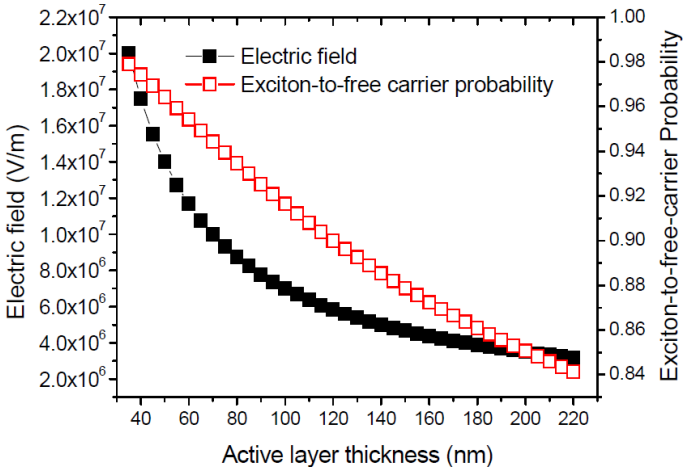

Fig. 6. Relations of electric field and exciton-to-free-carrier probability with layer thickness.

We have predicted J_{SC} precisely for the long enough carrier lifetime case. However, for polymer solar cells, the performance is sensitive to the process and experimental conditions. This may make the carrier lifetime relatively short. For P3HT:PCBM system, because the hole mobility is one order of magnitude lower than the electron mobility, holes are easy to accumulate in the active layer and limit the photocurrent. This is the case II as described in section 2.1.5. By tuning the parameters to fit the experimental data, the best fitting curve is obtained (Fig. 7) when the average hole lifetime τ is $6.2\times10^{-7}\,s$ and exciton-to-free-carrier dissociation probability is unity. A short lifetime τ may imply that there are many defects.

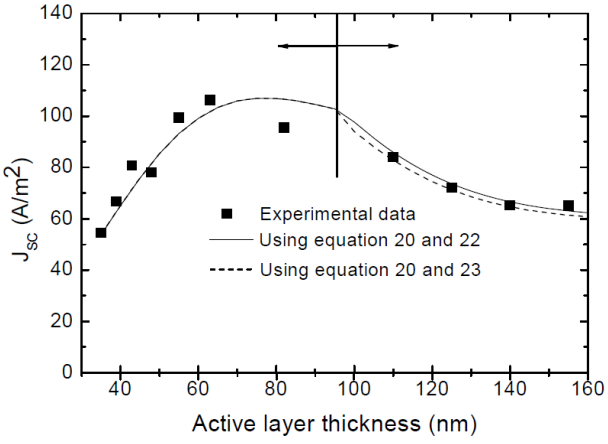

Fig. 7. Short hole carrier lifetime condition. Left arrow: hole lifetime is longer than its transient time; right arrow: hole lifetime is shorter than its transient time, and hole lifetime is $6.2\times10^{-7}\,s$, and electron lifetime is $1\times10^{-6}\,s$. Experimental data are from [Li et al., 2005].

These defects increase the exciton-to-free-carrier probability. More important, the transport process becomes the dominant limiting factor for J_{SC}, and the exciton-to-free-carrier process becomes relatively unimportant. Then it seems that the assumption of exciton-to-free-carrier probability as unity can satisfy the need of the prediction. In Fig. 7, we can see that there are two regions in the fitting curve. The left region is determined by equation (20). In this region, the lifetimes of both carriers are longer than their transient time. The solid line in the right region is determined by equation (22). In this region, hole lifetime is shorter than its transit time and electron lifetime is longer than its transit time.
If it is assumed that the drift length ratio of hole and electron is very small, then the equation (23) can be used to predict J_{SC}. As shown in Fig. 7 (dash line), it can predict J_{SC} very well, which means $c<<1$.

2.3 Summary

In this part, the exciton generation rate was calculated by taking the optical interference effect into account. Based on the calculated exciton generation rate, the dependence of J_{SC} on the active layer thickness was analyzed and compared with experimental data. Because of the optical interference effect, the total exciton generation rate does not monotonously increase with the increase of the active layer thickness, but behaves wavelike which induces the corresponding variation of J_{SC}. The carrier lifetimes also influence J_{SC} greatly. When the lifetimes of both electrons and holes are long enough, dissociation probability plays an important role for the thick active layer. J_{SC} behaves wavelike with the variation of the active layer thickness. When the hole lifetime is too short (drift length is smaller than device thickness), accumulation of charges appears near the electrode and J_{SC} increases at the initial stage and then decreases rapidly with the increase of the active layer thickness. The accordance between the predictions and the experimental results confirms the validity of the proposed model. These results give a guideline to optimize J_{SC}.

3. Effects of annealing sequence on J_{SC}

The detail of the interpenetrating network, or to say, the morphology is essentially important for the performance of polymer solar cells. In order to achieve an optimal morphology, a thermal treatment is usually utilized in the device fabrication. The thermal treatment can be carried out after and before the electrode deposition. Both the methods can greatly improve the device performance. The functions of the thermal treatment have been extensively investigated, and it has been shown that the morphology will be rearranged through the nanoscale phase separation between donor and acceptor components during the thermal treatment. By carefully optimizing the thermal treatment condition, an optimal interpenetrating network can be formed, which greatly improves the charge transport property. Besides, the thermal treatment can also effectively enhance the crystallization of P3HT, which will increase the hole mobility and the optical absorption capability. Due to the importance of the thermal treatment for P3HT:PCBM solar devices, great efforts have been devoted into the study of the thermal annealing process in the past few years. How the thermal annealing ambient, thermal annealing temperature and thermal annealing time affect the device performance has been well studied. However, only very few studies paid attention to the role of cathode in the thermal treatment. As is known, the thermal treatment can be done before and after the cathode deposition and both methods can greatly improve the device performance. The unique difference between them is whether there is cathode confinement in the thermal treatment or not. Although most of the previous studies have

tended to use the cathode confinement and carry out the thermal treatment after the cathode deposition, what are the functions of the cathode confinement in the thermal treatment and how they affect the device performance are still not well studied.

In this part, the effects of cathode confinement on the performance of polymer solar cells are investigated. It is shown that a better device performance can be achieved by using the cathode confinement in the thermal treatment. The experimental analysis indicates that by capping the cathode before the thermal treatment, the Al-O-C bonds and P3HT-Al complexes are formed at the interface between the P3HT:PCBM active layer and the cathode, which leads to a better contact and thus improves the charge collection capability. More importantly, the cathode confinement in the thermal treatment greatly improves the active layer morphology. It is shown that the cathode confinement in the thermal treatment can effectively inhibit the overgrowth of the PCBM molecules, and at the same time increase the crystallization of P3HT. Thus, a better morphology is achieved, which effectively reduces the exciton loss and improves the charge transport capability. Meanwhile, the enhanced P3HT crystallites improve the absorption property of the active layer. All these effects contribute to improve the device performance.

3.1 Experimental

Fig. 8 shows the layer structure of our polymer solar cells and the chemical structures of P3HT and PCBM. All the devices were fabricated on the ITO-coated glass substrates. Briefly, after being cleaned sequentially with detergent, de-ionized water, acetone, and isopropanol in an ultrasonic bath for about 15 mins, the dried ITO glass substrates were treated with oxygen plasma for about 3 mins. Then the filtered PEDOT:PSS (Baytron P VP AI 4083) suspension (through 0.45 μm filter) was spun coated on top of the ITO surface to form a ~50 nm layer under ambient condition, and dried at 120^{o}C in an oven for about one hour.

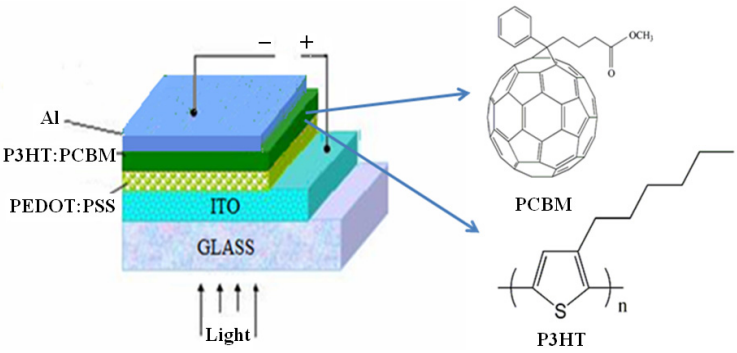

Fig. 8. Layer structure of the polymer solar cells investigated in this work.

P3HT:PCBM solution dissolved in 1,2-dichlorobenzene with a weight ratio of 1:0.8 was then spun coated on the PEDOT:PSS layer in the glove box to form a 100 nm blend layer. A 100 nm Al cathode was further thermally evaporated through a shadow mask giving an active device area of 20 mm^2. In order to investigate the effects of the cathode confinement on the device performance in the thermal treatment, two different types of devices were investigated: the devices without the cathode confinement in the thermal treatment (anneal the devices before the cathode deposition, pre-anneal) and the devices with the cathode confinement in the thermal treatment (anneal the devices after the cathode deposition, post-

anneal). The thermal treatment was carried out by annealing the devices in the glove box at the optimized temperature of 160 °C for about 10 mins as our previous report [Zhang et al., 2008]. For reference, the devices without any thermal treatment were also fabricated.
The current-voltage (*J-V*) characteristics were measured by a Keithley 2400 source-measure unit under AM 1.5 solar illumination at intensity of 100 mW/cm² calibrated by a Thorlabs optical power meter. The XPS samples were consisted of an identical sandwiched structure: ITO coated glass/P3HT:PCBM(100 nm)/Al (3 nm). Because XPS is a surface chemical analysis technique (top 1-10 nm usually), here only a very thin metal layer is used as others [39]. The XPS spectra were measured by transferring the samples to the chamber of a Kratos AXIS HSi spectrometer at once. The operating pressure of the analysis chamber was maintained at $8x10^{-9}$ Torr. A 1486.71 eV monochromatic Al Kα x-ray gun source was used to achieve the Al 2p, O 1s, C 1s and S 2p spectra. Tapping mode AFM measurements were taken with a Nanoscope III A (Digital Instruments) scanning probe microscope. The samples were prepared in the same sequence as the XPS samples. The phase images and the line scanning profiles of the samples were then recorded under air operation. For both the optical absorption study and x-ray diffraction measurement, the thin films of P3HT:PCBM in the same thickness of 100 nm were spun cast on the microscope slides. The optical absorption study was recorded by a Shimadzu UV-3101 PC UV-VIS-NIR scanning spectrophotometer. The XRD measurement was carried out by the θ-2θ scan method with CuKα radiation (λ = 0.1542 nm) using a Shimadu X-Ray diffractometer.

3.2 Results and discussion

Fig. 9 shows the *J-V* characteristics of the devices with the same configuration of ITO/PEDOT:PSS/P3HT:PCBM/Al. For the device without any thermal treatment, it shows the solar response with J_{SC} of 5.12 mA/cm², V_{OC} of 0.58 V, *FF* of 47.63% and *PCE* of 1.41%. The device performance is greatly improved by the thermal treatment. However, there are obvious differences for the devices with and without the cathode confinement in the thermal treatment as shown in Fig. 9 and Table 1. For the device without the cathode confinement in the thermal treatment, it shows the performance of J_{SC}=7.50 mA/cm², V_{OC}=0.58 V, *FF*=57.13% and *PCE*=2.49%. However, a further performance improvement is observed for the device with the cathode confinement in the thermal treatment, which shows a better performance of J_{SC}=8.34 mA/cm², V_{OC}=0.60 V, *FF*=62.57% and *PCE*=3.12%. It can be seen that the cathode confinement in the thermal treatment effectively increases J_{SC} and *FF*, which makes the overall *PCE* improved by 25%. This trend was found for a series of cells. Similar results are reported recently [Kim et al, 2009] where they also observed that the device with thermal treatment after cathode deposition could show a better performance. This further confirms our experimental results.

Samples	V_{OC}	J_{SC}	FF	PCE	J_0	J_{ph}	n	R_{sh}	R_s
Without thermal treatment	0.58	5.13	47.64	1.42	2.75e-4	5.32	2.32	778.25	29.00
Without cathode confinement	0.58	7.50	57.13	2.49	4.80e-5	7.62	1.89	575.19	9.34
With cathode confinement	0.60	8.34	62.25	3.12	3.03e-5	8.40	1.88	617.28	4.43

Units of parameters, V_{OC}: V; J_{SC}, J_0 and J_{ph}: mA/cm²; FF and PCE: %; $R_{sh}$and R_s: Ω cm².

Table 1. Summary of the Parameters Extracted from the J-V Curves Shown in Fig. 9

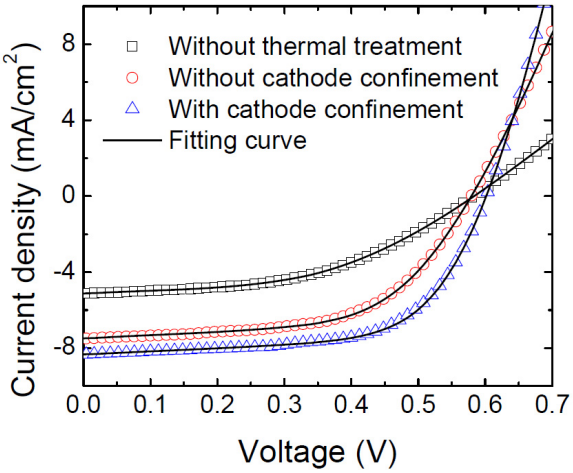

Fig. 9. *J-V* characteristics of the solar cells under the AM 1.5 illumination with the light intensity of 100 mW/cm². The devices without (circle) and with (triangle) the cathode confinement in the thermal treatment and the device without any thermal treatment (squire) are shown in the graph. Solid lines are the fitting curves according to equation (24).

In order to understand the functions of the cathode confinement in the thermal treatment, the electrical parameters need to be extracted. The *J-V* characteristics of organic solar cells can be described approximated by the Shockley equation

$$J = J_0 \left(e^{\frac{q(V - R_S J)}{n k_B T}} - 1 \right) + \frac{V - R_S J}{R_{Sh}} - J_{ph} \tag{24}$$

Where J_0, J_{ph}, R_s, R_{sh}, q, n, k_B and T are the saturation current density, the photocurrent density, the series resistance, the shunt resistance, the electron charge, the ideality factor, the Boltzmann constant and the temperature, respectively. By fitting the Shockley equation (Fig. 9), the estimated parameters are extracted and listed in Table 1. It is shown that R_s of the device with the cathode confinement in the thermal treatment is greatly reduced compared to the device without the cathode confinement in the thermal treatment (from 9.34 Ωcm² to 4.43 Ωcm²). R_s can significantly affect the device performance and reducing the value of R_s is an efficient method to increase *PCE*. The reduced R_s by using the cathode confinement plays one main role for the significant performance improvement of polymer solar cells. R_s is directly related to the contacts between the cathode and the active layer. Thus, these contacts were addressed by the XPS measurement.

The interfacial analysis results obtained by XPS measurement are shown in Fig. 10. Each top curve and bottom curve in the Al 2p, C 1s, O 1s and S 2p core level spectra graphs are corresponding to the samples with and without cathode confinement in the thermal treatment. As shown in Fig. 10, both samples show the Al 2p spectrum peaks located at the binding energy (BE) of 74.95 eV and 74.6 eV, which are corresponding to the Al oxide and Al-O-C bond, respectively, by referring to Table 2. The Al-O-C bond is also confirmed by the peaks located at the BE of 286.2 eV in the C 1s spectrum and 531 eV in the O 1s spectrum as

shown in Fig. 10. It has indicated that the Al-O-C bond is formed by the reaction of Al atoms and the carbonyl groups in PCBM and its existence will improve the contact between the polymer and the metal for both samples. However, by using the cathode confinement in thermal treatment, there is an additional shoulder peak at the BE of 76 eV in the Al 2p spectrum, which means that there forms an additional chemical bond. The additional chemical bond signal can also be seen from the S 2p spectrum. Although the typical peaks of P3HT appeared at the BE of 164.1 eV ($2p_{3/2}$) and 165.3 eV ($2p_{1/2}$) due to the spin-orbit coupling are observed for both samples in S 2p spectrum, there is an extra shoulder peak at the BE of 162.4 eV for the sample by using the cathode confinement. Considering the donation of electron density from the Al metal to the thiophene ring of P3HT, these additional peaks suggest that the interaction between P3HT and the Al metal occurs by using the cathode confinement in the thermal treatment.

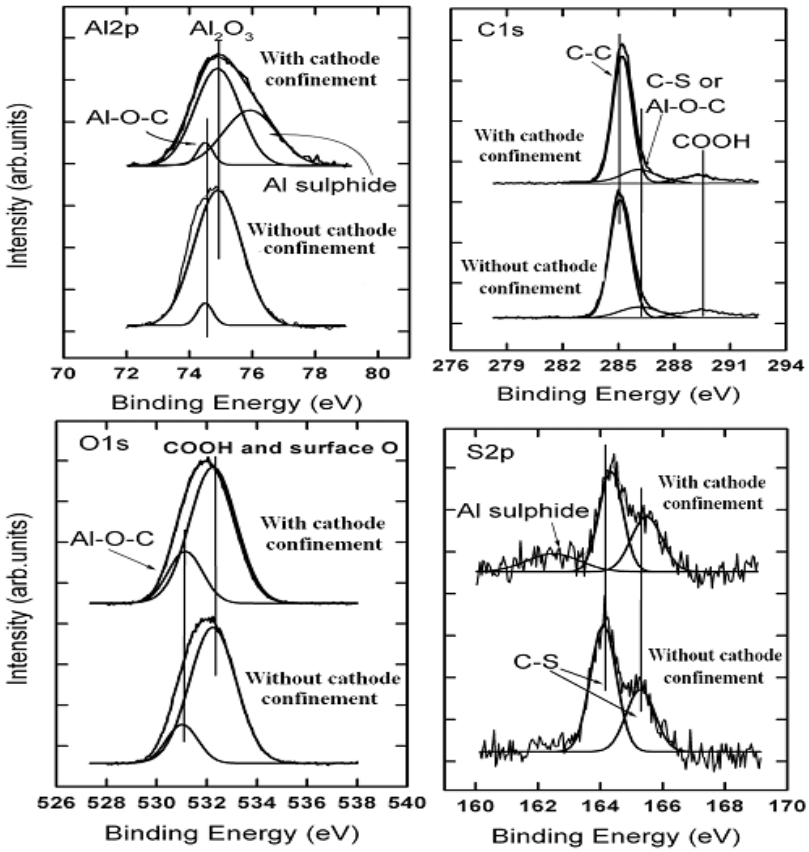

Fig. 10. High-resolution Al 2p, C 1s, O 1s and S 2p XPS spectra of the samples without (bottom curve) and with (top curve) the cathode confinement in the thermal treatment. The samples have the configuration of ITO/P3HT:PCBM (100 nm)/ Al(3 nm). By using the cathode confinement, there is an additional shoulder peak at the BE of 76 eV in the Al 2p spectrum and an additional shoulder peak at the BE of 162.4 eV in the S 2p spectrum.

Bonding states	Al 2p (eV)	C 1s (eV)	O 1s (eV)	S 2p (eV)
Al-O-C	74.6	286.2	531	
Al_2O_3	74.95		532.3	
Al-S	76			162.4
COOH		289.5		
C-C		285.1		
C-S		285.7		164.1, 165.3

Table 2. Summary of the XPS Binding Energies of Different Bonding States

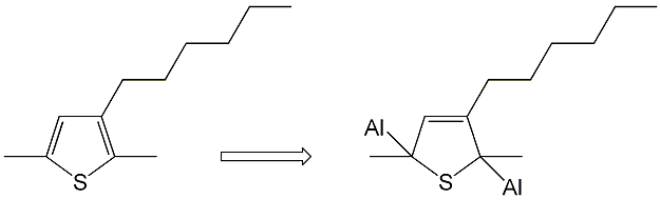

Fig. 11. The proposed molecular structure transits from P3HT to P3HT-Al complex.

Since the direct reaction between the Al atoms and the sulfur atoms is unlikely to occur because of the inherently high electron density on these sites, it is suggested that the Al atoms form bonds with the carbon atoms on the thiophene ring in the positions adjacent to the sulfur atom and form the P3HT-Al complex. One possible structure of the P3HT-Al complex is proposed in Fig. 11. The formation of the P3HT-Al complex will change the electron density of the sulfur atoms. In the P3HT-Al complex, the overall charge density of the sulfur atoms is smaller than that of the pristine P3HT. Thus the S 2p peaks located at the BE of 164.1 eV and 165.3 eV are shifted to the higher BE side at 164.3 eV and 165.5 eV, respectively, for the sample with the cathode confinement in the thermal treatment. Although the P3HT-Al complex is formed, there is only a slight energy difference (~0.1 eV shift in BE) in the C 1s spectrum for both samples as shown in Fig. 10. This is because the C 1s peak is dominated by the aliphatic carbon atoms while the Al atoms preferentially react with the carbon atoms in the conjugated system (thiophene ring of P3HT in this case). The signal arose from the interaction between P3HT and Al is too weak to affect the C 1s spectrum of the sample with cathode confinement. This explains why only very small energy difference in the C 1s spectrum is observed. The exact structure of P3HT-Al complex needs to be ascertained by further experiments.

It has been reported that Al metal can effectively transfer the electron to the conjugated polymer with the sulfide species and this feature makes it as a potential cathode for polymer electronics [Ling et al., 2002]. Another study [Reeja-Jayan et al., 2010] also has reported that Cu can react with P3HT and form sulfide-like species. The formed sulfide-like species can improve the solar cell performance. It is believed that the formation of the P3HT-Al complexes will play the same role. With the help of P3HT-Al complexes and the Al-O-C bonds, there is a better contact between the electrode and the active layer. This improved contact effectively reduces R_s and results in the improvement of the device performance.

How R_s affects the device performance is clearly shown in Fig. 12. It is shown that a large R_s will induce the decrease of *FF* and J_{SC}. By reducing R_s, *FF* and J_{SC} are increased and thus the

device performance is improved. At the same time, it is also noted that although both *FF* and J_{SC} can be affected by R_s, their dependences on R_s are different. From Fig. 12, it can be seen that *FF* can be greatly adjusted by R_s when the value of R_s is just larger than 1.0 Ωcm². The decrease of R_s from 9.34 Ωcm² to 4.43 Ωcm² (Table 1) should be the main reason for the increase of *FF* from 57.13% to 62.25% (Table 1) for the sample by using the cathode confinement. However, there is no obvious change of J_{SC} observed until R_s is larger than 25 Ωcm² (Fig. 12). Since R_s of the two devices are relative low (9.34 Ωcm² and 4.43 Ωcm² respectively, Table 1), it seems that the decrease of R_s is not the main reason for the obvious increase of J_{SC} (from 7.50 mA/cm² to 8.34 mA/cm², Table 1) by using the cathode confinement. This conclusion is also confirmed by the extracted parameter of J_{ph}. J_{ph} is mainly determined by the properties of the active layer and only slightly depends on R_s (independent parameters in equation (24)). If the cathode confinement in the thermal treatment is only to improve the contact and reduce R_s, there should be no such obvious change of J_{ph} (from 7.62 mA/cm² to 8.40 mA/cm², Tabel I). Thus, there must be other more important factors besides R_s which lead to the obvious increase of J_{ph}. It is well known that J_{ph} is very sensitive to the device morphology and material absorption, and thus these aspects should be well addressed.

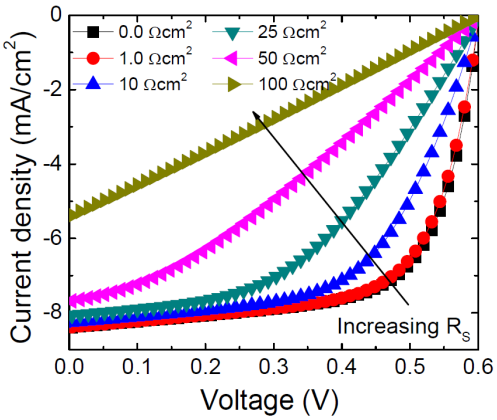

Fig. 12. Effect of R_s variation on *J–V* characteristics of the P3HT:PCBM solar cells according to (1). Only the value of R_s is changed while keep J_0=3.03e-5 mA/cm², J_{ph} =8.40 mA/cm², R_{sh} =617.28Ω cm² and n= 1.88. R_s greatly affects *FF* and thus the overall *PCE*. J_0, R_{sh} and n only slightly affect J_{SC} in the value range shown in Table 1.

The effects of cathode confinement on the device morphology are firstly investigated by the AFM measurement. Because the interface between the active layer and the cathode is mainly enriched by PCBM upon thermal treatment, the evolution of the surface morphology directly reflects the change of the PCBM domains. As shown in Fig. 13, it is shown that the thermal treatment effectively leads to the growth of the PCBM domains and thus increases the root mean square roughness. However, comparing to the device without the cathode confinement, there is a smoother surface morphology for the device with the cathode confinement. As shown in the AFM phase images (Fig. 13 b and c), there is a smaller island size for the sample with the cathode confinement. The profile measurements (Fig. 13 e and f) also show that the average peak-to-peak height and the width of the surface morphology are reduced by 20% and 33% by using the cathode confinement. Since surface morphology change is mainly induced

by the aggregates of PCBM, the smoother surface morphology means that the cathode confinement can prevent the formation of too large underlying PCBM domains.

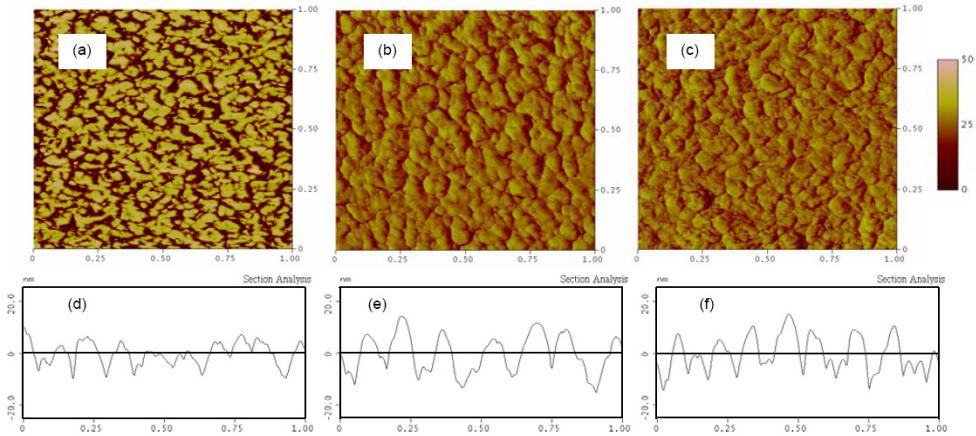

Fig. 13. Tapping-mode AFM phase images of Al covered P3HT:PCBM blend film: (a) sample without any thermal treatment and samples without (b) and with (c) the cathode confinement in the thermal treatment. Their corresponding cross sectional profiles are shown in (d) to (f) with root mean square roughness 5.5, 6.3 and 5.9 nm respectively.

It is well known that the main roles of annealing process are to induce the redistribution of PCBM and increase the crystallization of P3HT, so that the bicontinuous interpenetrating networks is achieved and meanwhile the optical absorption capability is enhanced. However, a too fast PCBM diffusion will lead to the formation of very large PCBM aggregates and thus destroy the optimal bicontinuous interpenetrating network. Besides, too large PCBM domains also reduce the interfacial contact area between P3HT and PCBM and lead to the inefficient exciton dissociation. In order to achieve a high performance, it is required to well control the PCBM domain size. It is shown here that the overgrowth of the PCBM domains in the thermal treatment is effectively inhibited by using the cathode confinement. Thus a better nanoscale morphology control is achieved. Similar metal confinement effect was also demonstrated on the organic surface by using silver cap [Peumans et al., 2003]. The improved morphology will decrease the exciton loss, facilitate the charger transport and thus increase J_{SC}.

J_{SC} is also directly related to the optical absorption of the active layer. In order to investigate the effects of cathode confinement on the optical absorption capability, the UV-Vis absorption spectra of the active layer capped with the Al electrode were measured. Because the annealed metal results in a slight variation of the light absorption, the optical spectra were obtained by subtracting the pure metal spectra. The results are shown in Fig. 14. All the samples show the typical absorption spectrum of P3HT:PCBM blend film with the absorption peak at the wavelength of 515 nm and shoulders at 550 nm and 604 nm. The thermal treatment obviously increases the optical absorption of the P3HT:PCBM film. However, there is a better optical absorption capability for the sample with the cathode confinement (e in Fig. 14) compared to the sample without the cathode confinement (d in Fig. 14). It is well known that the absorption capability of P3HT:PCBM system is directly related to the P3HT crystallites. The crystallization of P3HT was measured by XRD.

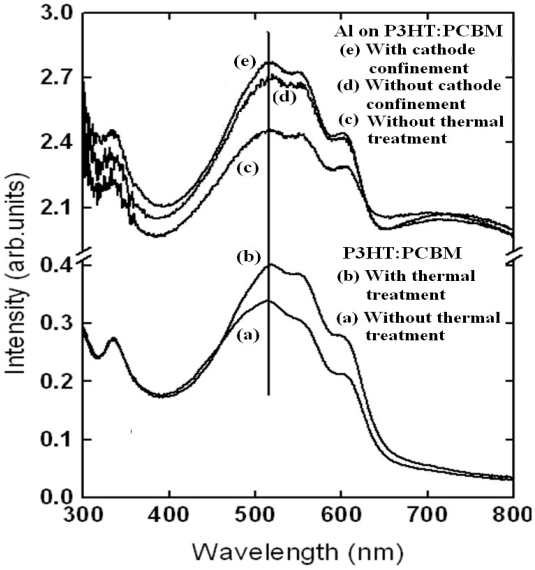

Fig. 14. Optical absorption spectra of various samples: (a) bare P3HT:PCBM blend film without thermal treatment (b) bare P3HT:PCBM blend film with thermal treatment (c) Al covered P3HT:PCBM blend film without the thermal treatment (d) Al covered P3HT:PCBM blend film with the thermal treatment done before cathode deposition (e) Al covered P3HT:PCBM blend film with the thermal treatment done after cathode deposition.

Fig. 15 shows the obtained XRD measurement results. A characteristic peak around $2\theta = 5.4°$ is observed for all the samples, which is associated with the lamella structure of thiophene rings in P3HT. Based on Bragg's law and Scherrer relation, the lattice constant (d) and the size of the polymer crystallites (L) can be determined:

$$n\lambda = 2d\sin\theta \tag{25}$$

$$L = \frac{0.9\lambda}{\Delta_{2\theta}\cos\theta} \tag{26}$$

where λ is the wavelength of the x-ray, θ the Bragg's angle, $\Delta_{2\theta}$ the smallest full width at half maximum of the peak. The extracted d and L are listed in Table 3. It is shown that all the samples show the lattice constant of 1.62 ± 0.01 nm that represents the P3HT crystallites in a-axis orientation. Thermal treatment increases the crystallization of P3HT. However, the increased magnitudes are different for the devices with and without the cathode confinement. The sample with the help of the cathode confinement in the thermal treatment shows the highest peak. As listed in Table 3, the size of the P3HT crystallites (L value of 17.7 nm) is increased by 36% by using the cathode confinement compared to without the cathode confinement (L value of 13 nm). The increased crystallite size may come from the effective inhibition of the strong PCBM diffusion by the cathode confinement. It has been shown [Swinnen et al., 2006] that a too strong diffusion of PCBM from the P3HT matrix would reduce the P3HT crystallization and optical absorption property. Because of the presence of

the cathode in the thermal treatment, the PCBM diffusion is slowed down. Thus it is easier for P3HT to be crystallized. The increased P3HT crystallites will enhance the active layer optical absorption capability and increase J_{SC}.

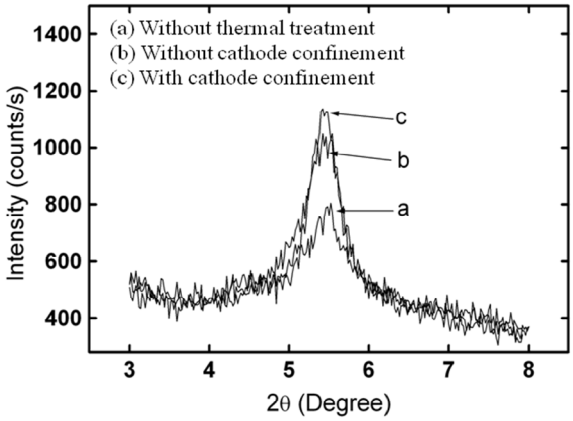

Fig. 15. X-ray diffraction spectra of various samples: (a) Al covered P3HT:PCBM blend film without the thermal treatment (b) Al covered P3HT:PCBM blend film with the thermal treatment done before cathode deposition (c) Al covered P3HT:PCBM blend film with the thermal treatment done after cathode deposition.

Samples	2θ [°]	$\Delta_{2\theta}$ [°]	h [counts/s]	L [nm]	d [nm]
Without thermal treatment	5.49	0.83	318	9.6	1.61
Without cathode confinement	5.44	0.61	596	13	1.625
With cathode confinement	5.44	0.45	617	17.7	1.625

Table 3. Summary of X-Ray Diffraction Peaks of P3HT:PCBM from Fig.15

3.3 Summary

P3HT:PCBM solar cells with the cathode confinement in the thermal treatment show better performance than the solar cells without the cathode confinement in the thermal treatment. The effects of the cathode confinement on the device performance have been investigated in this work. According to the XPS results, it is found that the Al-O-C bonds and P3HT-Al complexes are formed at the interface between the active layer and the cathode by using the cathode confinement. These chemical structures effectively reduce the contact resistance and improve the device performance. More importantly, the cathode confinement effectively improves the active layer morphology. According to the AFM, UV-Vis absorption spectra and XRD measurement results, it is found that the cathode confinement in the thermal treatment not only prevents the overgrowth of the PCBM domains, but also increases the crystallization of P3HT. With the help of cathode confinement in the thermal treatment, a better optical absorption and a more ideal bicontinuous interpenetrating networks can be obtained at the same time. This will effectively reduce the exciton loss and improve the charge transport capability. Thus an improved device performance is achieved.

4. Overall optimization of polymer solar cells

Because the active layer is very thin in compared with the incident light wavelength, the optical interference effect influences the absorption and J_{SC} as discussed in above. According to the simulated results based on the optical model, the thickness will be optimized around the first and second optical interference peaks in this part. In addition, the annealing process can efficiently improve the performance of P3HT:PCBM polymer solar cells. The performance is related to the annealing sequence, and post-annealing is more favored by the devices. Based on this conclusion, all the polymer solar cells were fabricated and post-annealed in this section. These devices were used to optimize the overall solar cell performance.

4.1 Experimental

The fabrication process is the same as above. The devices were fabricated on the ITO-coated glass substrates. After routine solvent cleaning (treated sequentially with detergent, de-ionized water, acetone, and isopropanol in an ultrasonic bath for about 15 minutes), the dried ITO glass substrates were treated with oxygen plasma for about three mins. Then the filtered PEDOT:PSS suspension was spin coated on the top of the ITO surface under ambient condition. The P3HT:PCBM solution dissolved in dichlorobenzene with a weight ratio of 1:0.8 was spin coated in the glove box. Finally, Al cathode was deposited by e-beam evaporation through a shadow mask. All the devices have same structure: ITO\PEDOT:PSS\P3HT:PCBM\Al, and only the thicknesses of the P3HT:PCBM active layers are different. The active layer thickness was controlled by changing the spin speed and solution concentration. Then different annealing temperatures are tested for the devices based on post-annealing to find the optimized conditions. The *J-V* characteristics were measured using a Keithley 2400 parameter analyzer in the dark and under a simulated light intensity of 100 mW/cm^2 (AM 1.5G) calibrated by an optical power meter.

4.2 Experimental results and discussion

4.2.1 Optical interference effects and active layer thickness optimization

The TMF method as discussed in section 2 is used to predict J_{SC} for the active layer thickness in a range from 50 nm to 250 nm for 1:0.8 P3HT:PCBM active layer. The results are plotted in Fig. 16. As predicted, obvious polymer solar oscillatory behavior is observed because of the very thin active layer compared with the light wavelength. When the P3HT:PCBM ratio is 1:0.8, the first and second optical interference peaks are found at the P3HT:PCBM layer thicknesses of around 85 nm and 230 nm. Both the two optical interference peaks should be used to optimize the active layer thickness.

According to the simulated results, the devices were fabricated around the first and the second optical interference peaks. The experimental results for the different active layer thicknesses are shown Fig. 17. As predicted, J_{SC} shows a periodic behavior with the variation of the active layer thickness. The J_{SC} increases from as low as 6.25 mA/cm^2 (for the device with active layer thickness, t=64 nm) to as high as 6.93 mA/cm^2 (for t=80 nm), and then decreases around the first interference peak. The same trend is observed around the second optical interference peak at a thickness of 208 nm. J_{SC} reaches a value as high as 10.37 mA/cm^2 at the second optical interference peak. The higher J_{SC} comes from the better absorption ability. It is obviously shown that the second peak can absorb more light than the first peak as shown in Fig. 18. Thus the second optical interference peak is more preferred to achieve a higher *PCE*. Then around this peak, the annealing conditions are investigated.

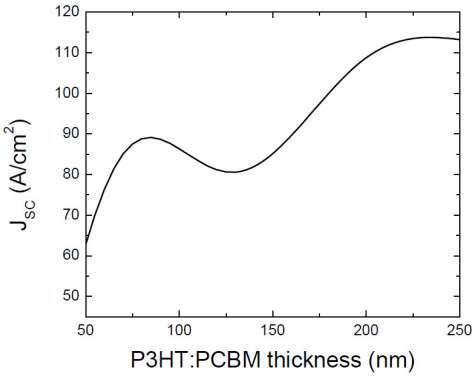

Fig. 16. J_{SC} versus P3HT:PCBM thickness, P3HT:PCBM with weight ratio of 1:0.8 and device structure of ITO/PEDOT:PSS/P3HT:PCBM/Al.

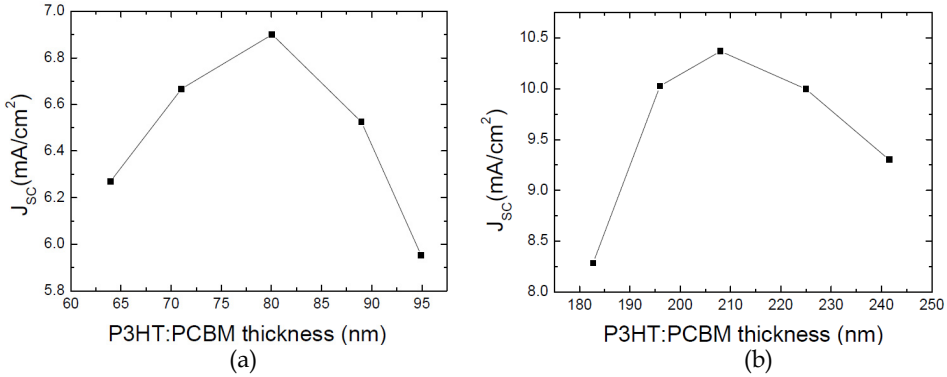

Fig. 17. Optimization of active layer thickness. (a) around the first optical interference peak, and (b) around the second optical interference peak. All devices were post-annealed at 160°C for 10 mins.

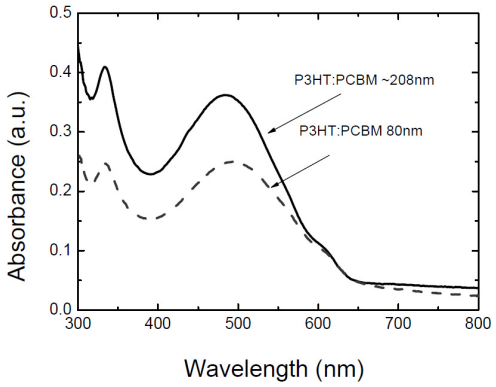

Fig. 18. UV-visible absorption spectra of P3HT:PCBM (about 80 nm thick and 208 nm thick).

4.2.2 Optimization of annealing conditions

The device performance depends greatly on annealing temperatures as clearly seen from Fig. 19. The reasons for the performance to be improved by the annealing process have been widely investigated and discussed in section 3. It is clear that for an efficient bulk HJ polymer solar cell, *D* and *A* domains must be small enough so that most of the excitons can diffuse into the *D/A* interfaces before they decay. At the same time, the interpenetrating transport network must be formed for the efficient charge transport. Thus, the morphology optimization is of great important. By varying the annealing condition, the morphology can be well controlled.

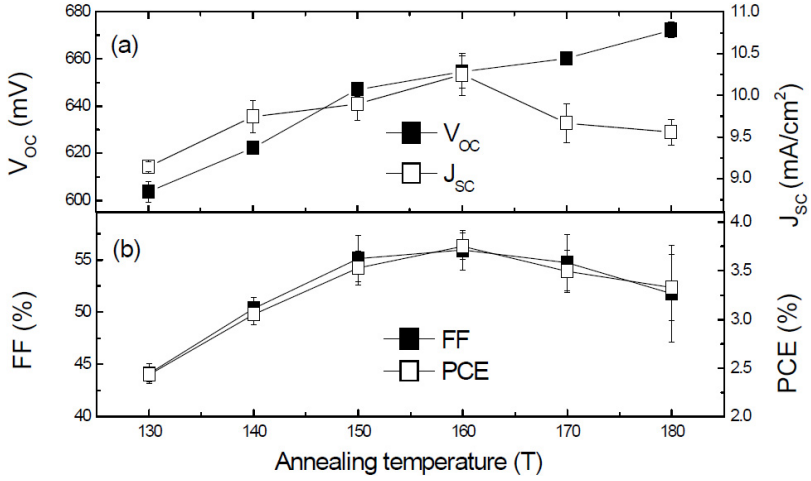

Fig. 19. (a) and (b): Relations of device performance and annealing conditions. The P3HT:PCBM layer thickness keeps constant of 208 nm.

These results were related to the better morphology as discussed in previous and also related to the increase of the charge carrier mobility. The same reason should also be responsible for our results. The highest *PCE* in our experiments is achieved when the annealing temperature is 160°C which is very close to the annealing temperatures reported by Ma (Ma et al., 2005). The analysis of changes in film morphology has shown that the changes in film crystallinity and aggregation within the film PCBM nanophase lead to the improved solar characteristics at this temperature. When the annealing temperature is increased, a steady enhancement of V_{OC} is observed because the e-beam evaporated Al can induce dipoles at the interface between active layer and cathode [Zhang et al., 2009]. As shown in Fig. 19, the device shows the optimized performance when it has been annealed at 160°C for 10 min.

5. Conclusion

In polymer solar cells, because of the optical interference effect, the total exciton generation rate does not increase monotonically with the increase of the active layer thickness, but behaves wave-like, which induces the corresponding variation of J_{SC}. The carrier lifetime also inffuence J_{SC} greatly. When the carrier lifetime is long enough, dissociation probability will play a very important role for a thicker active layer. J_{SC} will behave wave-like with the variation of active layer thickness. When the carrier lifetime is too short (drift length is

smaller than device thickness), accumulation of charges will appear near the electrode and J_{SC} will increase at the initial stage and then decrease rapidly with the increase of active layer thickness.

The experimental studies were carried out to investigate P3HT:PCBM based HJ polymer solar cells in this chapter. It was found that the strengthened contact due to the bonding reinforcements (Al-O-C bonds and P3HT-Al complex) at the active layer/metal interface for post-annealed device improves the charge collection at the cathode side. Carrier separation can be facilitated via the improved nanoscaled morphology of the post-annealed polymer blend. The Al capping layer promotes efficient formation of the P3HT crystallites and thus enhances the light harvesting property of the polymer blend. Evidence for the latter has been derived from the improved shape of the absorption spectrum. The results underline the importance of applying the most efficient annealing sequence in order to achieve the best solar device performance.

Based on above results, the overall performance of P3HT:PCBM bulk polymer solar cells were optimized. As predicted by the TMF method, an obvious polymer solar cell oscillatory behavior of J_{SC} was observed in the experiments. The devices were optimized around the first two optical interference peaks. It was found that the optimized thicknesses are 80 nm and 208 nm. Based on the post-annealing, different annealing temperatures have been tested. The optimized annealing condition was found to be 160^{o}C for 10 min in a nitrogen atmosphere.

6. References

Cheyns, D.; Poortmans, J.; Heremans, P.; Deibel, C.; Verlaak, S., Rand, B. P. & Genoe J. (2008). Analytical model for the open-circuit voltage and its associated resistance in organic planar heterojunction solar cells. *Physical Review B*, Vol. 77, No. 16, (April 2008), pp. 165332-1–165332-10, ISSN 1098-0121

Goodman, A. M. & Rose, A. (1971). Double Extraction of uniformly generated electron-hole pairs from insulators with nonjecting contacts. *Journal of Appllied Physics.* Vol. 42, No. 7, (June 1971). pp. 2823-2830. ISSN 0021-8979

Kim, H. J.; Park, J. H.; Lee, H. H.; Lee D. R.; & Kim, J. J. (2009). The effect of Al electrodes on the nanostructure of poly(3-hexylthiophene): Fullerene solar cell blends during thermal annealing, organic electronics, Vol. 10, No. 8, (December 2009). pp. 1505-1510. ISSN 1566-1199

Koster, L. J. A.; Smits, E. C. P.; Mihailetchi, V. D. & Blom, P. W. M. Device model for the operation of polymer/fullerene bulk heterojunction solar cells. *Physical Review B*, Vol. 72, No. 8, (August 2005) pp. 085205-1-085205-9. ISSN 1098-0121

Lacic, S. & Inganas, O. (2005). Modeling electrical transport in blend heterojunction organic solar cells. *Journal of Applied Physics*, Vol. 97, No. 12, (June 2005). pp. 124901-1-124901-7. ISSN 0021-8979

Ma, W.; Yang, C.; Gong, X.; Lee, K. & Heeger, A. J. (2005). Thermally stable, efficient polymer solar cells with nanoscale control of the interpenetrating network morphology, Advacned Functional Materials, Vol. 15, No.10, (October 2005).1617-1622. ISSN 1616-301X

Li, G.; Shrotriya, V. & Yao Y. (2005). Investigation of annealing effects and film thickness dependence of polymer solar cells based on poly(3-hexylthiophene). *Journal of Appllied Physics.*Vol. 98, No. 4 (August 2005), pp. 43704-1-43704-5. ISSN 0021-8979

Ling, Q. D.; Li, S.; Kang, E. T.; Neoh, K. G.; Liu, B. & Huang, W. (2002). Interface formation between the Al electrode and poly[2,7-(9,9-dihexylfluorene)-*co*-alt-2,5-(decylthiophene)] (PFT) investigated in situ by XPS , *Applied Surface Science*, Vol. 199, No. 1-4, (October 2002). pp. 74-82.

Monestier, F.; Simon, J. J.; Torchio, P.; Escoubas, L.; Flory, F.; Bailly, S.; Bettignies, R.; Guillerez, S. & Defranoux, C., Modeling the short-circuit current density of polymer solar cells based on P3HT:PCBM blend. *Solar Energy Materials & Solar Cells*, Vol. 91, No. 5, (March 2007). pp. 405-410. ISSN 0927-0248

Mihailetchi, V. D.; Xie, H.; Boer，B.; Koster L. J. A. & Blom, P. W. M. Charge Transport and Photocurrent Generation in Poly(3-hexylthiophene): Methanofullerene Bulk-Heterojunction Solar Cells. *Advacned Functional Materials*, Vol. 16, No. 5, (March 2006). pp. 699-708. ISSN 1616-301X

Pettersson, L. A. A.; Roman, L. S. & Inganas, O. (1999). Modeling photocurrent action spectra of photovoltaic devices based on organic thin films. *Journal of Applied Physics*, Vol. 86, No. 1, (1999). pp. 487-496. ISSN 0021-8979

Peumans, P.; Yakimov, A. & Forrest, S. R. (2003). Small molecular weight organic thin-film photodetectors and solar cells. *Journal of Applied Physics*, Vol. 93, No. 7, (April 2003). pp. 3693-3723. ISSN 0021-8979

Peumans, P.; Uchida, S. & Forrest, S. R. (2003). Efficient bulk heterojunction photovoltaic cells using small-molecular-weight organic thin films, *Nature*, Vol. 425, No. 6954, (September 2003). pp. 158-162.

Reeja-Jayan, B. & Manthiram, A. (2010). Influence of polymer–metal interface on the photovoltaic properties and long-term stabilityofnc-TiO2-P3HT hybrid solar cells,Solar Energy Materials & Solar Cells, Vol. 94, No. 5, (February 2010). pp. 907-914. ISSN 0927-0248

Swinnen, A.; Haeldermans, I.; Ven, M. V.; Haen, J. D.; Vanhoyland, G.; Aresu, S.; Olieslaeger, M. D. & Manca, J. (2006). Tuning the dimensions of C_{60}-based needlike srystals in blended thin films , *Advacned Functional Materials*, Vol. 16, pp. 760-765, 2006. ISSN 1616-301X

Zhang, C. F.; Tong, S. W.; Jiang, C. Y.; Kang, E. T.; Chan, D. S. H. & Zhu, C. X. (2008). Efficient multilayer organic solar cells using the optical interference peak, Applied Physics Letters, Vol. 93, No. 4, (August 2008). pp. 043307-1-043307-3.ISSN 0003-6951

Zhang, C. F.; Tong, S. W.; Jiang, C. Y.; Kang, E. T.; Chan, D. S. H. &Zhu, C. X. (2009). Enhancement in open circuit voltage induced by deep interface hole trapsin polymer-fullerene bulk heterojunction solar cells. Applied Physics Letters, Vol. 94, No. 10, (March 2009). pp. 103305-1-103305-3. ISSN 0003-6951

Zhang, C. F.; Hao, Y.; Tong, S. W.; Lin, Z. H.; Feng, Q; Kang, E. T. & Zhu, C. X. (2011). Effects of Cathode Confinement on the Performance of Polymer/Fullerene Photovoltaic Cells in the Thermal Treatment, *IEEE Transaction on Electron Devices*, Vol. 58, No. 3, (March 2011), pp. 835-842. ISSN 0018-9383

2

A New Guide to Thermally Optimized Doped Oxides Monolayer Spray-Grown Solar Cells: The Amlouk-Boubaker Optothermal Expansivity ψ_{AB}

M. Benhaliliba[1], C.E. Benouis[1],
K. Boubaker[2], M. Amlouk[2] and A. Amlouk[2]
[1]*Physics Department, Sciences Faculty, Oran University of Sciences and Technology Mohamed Boudiaf- USTOMB, POBOX 1505 Mnaouer- Oran,*
[2]*Unité de Physique des dispositifs à Semi-conducteurs UPDS, Faculté des Sciences de Tunis, Campus Universitaire 2092 Tunis,*
[1]*Algeria*
[2]*Tunisia*

1. Introduction

PVC Photovoltaic solar cells are unanimously recognized to be one of the alternative renewable energy sources to supplement power generation using fossils. It is also recognized that semiconductors layered films technology, in reducing production costs, should rapidly expand high-scale commercialization.
Despite the excellent achievements made with the earliest used materials, it is also predicted that other materials may, in the next few decades, have advantages over these front-runners. The factors that should be considered in developing new PVC materials include:

- Band gaps matching the solar spectrum
- Low-cost deposition/incorporation methods
- Abundance of the elements
- Non toxicity and environmental concerns,

Silicon-based cells as well as the recently experimented polymer and dye solar cells could hardly fit all these conditions. Transparent conducting oxides as ZnO, SnO_2 as well as doped oxides could be good alternative candidates.
In this context, the optothermal expansivity is proposed as a new parameter and a guide to optimize the recently implemented oxide monolayer spray-grown solar cells.

2. Solar cells technologies and design recent challenges

In spite of better performance of traditional junction-based solar cells, during the past few decades, reports have appeared in literature that describe the construction of cells based metal-oxides (Bauer et al., 2001; Sayamar et al., 1994; He et al., 1999; Tennakone et al., 1999;

Bandara & Tennakone, 2001) and composite nanocrystalline materials (Palomares et al., 2003; Kay & Gratzel, 2002). Since that time, several other semiconductors have been tested with less success.
Recent challenges concerning newly designed solar cells are namely Band-gap concerns, cost, abundance and environmental concerns.

2.1 Band gaps matching the solar spectrum

The recently adopted layered structure of PVC raised the problem of solar spectrum matching (Fig.1) as well as lattice mismatch at early stages. In fact, the heterogeneous structure: Contact/window layer/buffer layer/Contact causes at least three differently structured surfaces to adhere under permanent constraints. It is known that the electronic band gap is the common and initial choice-relevant parameter in solar cells sensitive parts design. It is commonly defined as the energy range where no electron states exist. It is also defined as the energy difference between the top of the valence band and the bottom of the conduction band in semiconductors. It is generally evaluated by the amount of energy required to free an outer shell electron the manner it becomes a mobile charge carrier. Since the band gap of a given material determines what portion of the solar spectrum it absorbs, it is important to choose the appropriate compound matching the incident energy range. The choice of appropriated materials on the single basis of the electronic band gap is becoming controversial due the narrow efficient solar spectrum width, along with new thermal and mechanical requirements. It is rare to have a complete concordance between adjacent crystalline structures particularly in band gap sense.

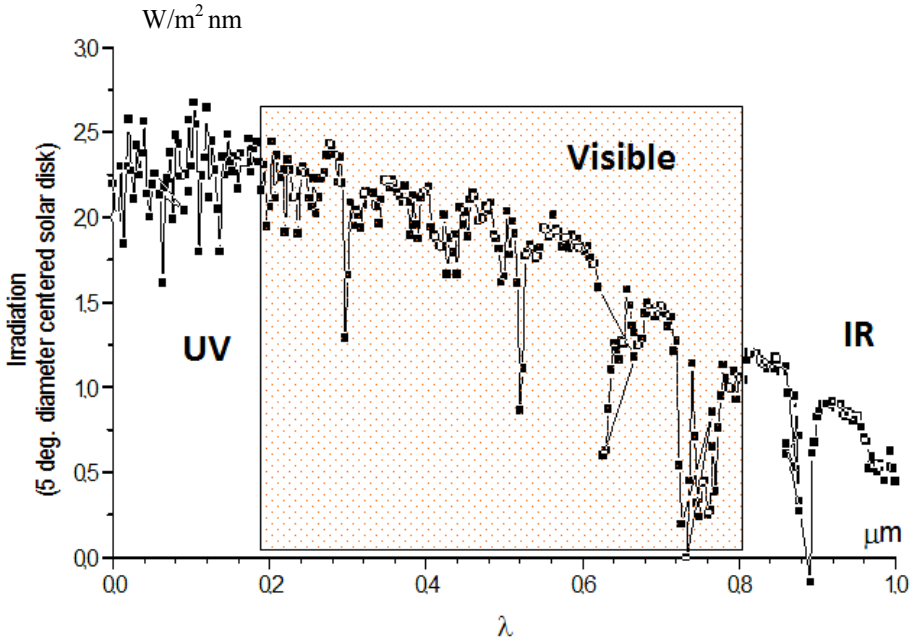

Fig. 1. Solar spectrum

For example, in silicon-based solar cells, recombination occurring at contact surfaces at which there are dangling silicon bonds (Wu, 2005) is generally caused by material/phase discontinuities. This phenomenon limits cell efficiency and decreases conversion quality.

2.2 Low-cost deposition/incorporation methods

Deposition techniques and incorporation methods have been developed drastically and several deposition improved methods have been investigated for fabrication of solar cells at high deposition rates (0.9 to 2.0 nm/s), such as hot wire CVD, high frequency and microwave PECVD, , and expanding thermal plasma CVD. Parallel to these improvements, vacuum conditions and chemical processes cost increased the manner that serial fabrication becomes sometimes limited. Nowadays, it is expected that low processing temperature allow using a wide range of low-cost substrates such as glass sheet, polymer foil or metal. These features has made the second-generation low- cost metal-oxides thin-film solar cells promising candidates for solar applications.

2.3 Abundance of the elements

The first challenge for PV cells designer is undoubtedly the abundance of materials for buffer and window layers. The ratio of abundance i. e. of Tungsten-to-Indium is around 104, that of of Zinc-to-Tin is around 40. Although efficiency of Indium and Gallium as active doping agents has been demonstrated and exploited (Abe & Ishiyama, 2006; Lim et al., 2005), their abundance had decreased drastically (510 and 80 tons, respectively as reported by U.S. Geological Survey 2008) with the last decades' exploitation.

2.4 Non toxicity and environmental concerns

Among materials being used, cadmium junctions (Cd) and selenium (Se) are presumed to cause serious health and environmental problems. Risks vary considerably with concentration and exposure duration. Other candidate materials haven't gone though enough tests to show reassuring safety levels (Amlouk, 2010).

3. Materials optimisation

3.1 Primal selection protocols

Cost and toxicity concerns led to less and less use of Se and Cd-like materials. Additionally, increasing interest in conjoint heat-light conversion took some bad heat-conducting materials out from consideration. Selection protocols are becoming more concentrated on thermal, mechanical and opto-electric performance.

Since thermal conductivity, specific heat and thermal diffusivity has always been considered as material intrinsic properties, while absorbance and reflexivity depend on both material and excitation, there was a need of establishing advanced physical parameters bringing these proprieties together.

3.2 Opto-thermal analysis

The Amlouk-Boubaker optothermal expansivity is defined by:

$$\psi_{AB} = \frac{D}{\hat{\alpha}} \tag{1}$$

Where D is the thermal diffusivity and $\hat{\alpha}$ is the effective absorptivity, defined in the next section.

3.2.1 The effective absorptivity

The effective absorptivity $\hat{\alpha}$ is defined as the mean normalized absorbance weighted by $I(\tilde{\lambda})_{\text{AM1.5}}$, the solar standard irradiance, with $\tilde{\lambda}$: the normalised solar spectrum wavelength:

$$\begin{cases} \tilde{\lambda} = \dfrac{\lambda - \lambda_{\min}}{\lambda_{\max} - \lambda_{\min}} \\ \lambda_{\min} = 200.0 \text{ nm} \ ; \lambda_{\max} = 1800.0 \text{ nm}. \end{cases} \tag{2}$$

and :

$$\hat{\alpha} = \frac{\int_0^1 I(\tilde{\lambda})_{\text{AM1.5}} \times \alpha(\tilde{\lambda}) d\tilde{\lambda}}{\int_0^1 I(\tilde{\lambda})_{\text{AM1.5}} d\tilde{\lambda}} \tag{3}$$

where: $I(\tilde{\lambda})_{\text{AM1.5}}$ is the Reference Solar Spectral Irradiance.

The normalized absorbance spectrum $\alpha(\tilde{\lambda})$ is deduced from the Boubaker polynomials Expansion Scheme *BPES* (Oyedum et al., 2009; Zhang et al., 2009, 2010a, 2010b; Ghrib et al., 2007; Slama et al., 2008; Zhao et al., 2008; Awojoyogbe and Boubaker, 2009; Ghanouchi et al.,2008; Fridjine et al., 2009 ; Tabatabaei et al., 2009; Belhadj et al., 2009; Lazzez et al., 2009; Guezmir et al., 2009; Yıldırım et al., 2010; Dubey et al., 2010; Kumar, 2010; Agida and Kumar, 2010). According to this protocol, a set of *m* experimental measured values of the transmittance-reflectance vector: $\left(T_i(\tilde{\lambda}_i); R_i(\tilde{\lambda}_i)\right)\Big|_{i=1..m}$

versus the normalized wavelength $\tilde{\lambda}_i\Big|_{i=1..m}$ is established. Then the system (4) is set:

$$\begin{cases} R(\tilde{\lambda}) = \left[\dfrac{1}{2N_0} \sum_{n=1}^{N_0} \xi_n \times B_{4n}(\tilde{\lambda} \times \beta_n) \right] \\ T(\tilde{\lambda}) = \left[\dfrac{1}{2N_0} \sum_{n=1}^{N_0} \xi_n^{'} \times B_{4n}(\tilde{\lambda} \times \beta_n) \right] \end{cases} \tag{4}$$

where β_n are the 4n-Boubaker polynomials B_{4n} minimal positive roots (N_0 is a given integer and ξ_n and $\xi_n^{'}$ are coefficients determined through Boubaker Polynomials Expansion Scheme BPES.

Finally, the normalized absorbance spectrum $\alpha(\tilde{\lambda})$ is calculated using the relation (5) :

$$\alpha(\tilde{\lambda}) = \frac{1}{d\sqrt{2}} \sqrt{\left(\ln \frac{1 - R(\tilde{\lambda})}{T(\tilde{\lambda})} \right)^2 + \left(\ln \frac{(1 - R(\tilde{\lambda}))^2}{T(\tilde{\lambda})} \right)^2} \tag{5}$$

where *d* is the layer thickness.

The effective absorptivity $\hat{\alpha}$ is calculated using (Eq. 3) and (Eq. 5).

3.2.2 The Optothermal expansivity ψ_{AB}

The Amlouk-Boubaker optothermal expansivity unit is m^3s^{-1}. This parameter, as calculated in Eq. (1) can be considered either as the total volume that contains a fixed amount of heat per unit time, or a 3D expansion velocity of the transmitted heat inside the material.

3.2.3 The optimizing-scale 3-D Abacus

According to precedent analyses, along with the definitions presented in § 3.2, it was obvious that any judicious material choice must take into account simultaneously and conjointly the three defined parameters: the band gap E_g, Vickers Microhardness H_υ and The Optothermal Expansivity ψ_{AB}. The new 3D abacus (Fig. 2) gathers all these parameters and results in a global scaling tool as a guide to material performance evaluation.

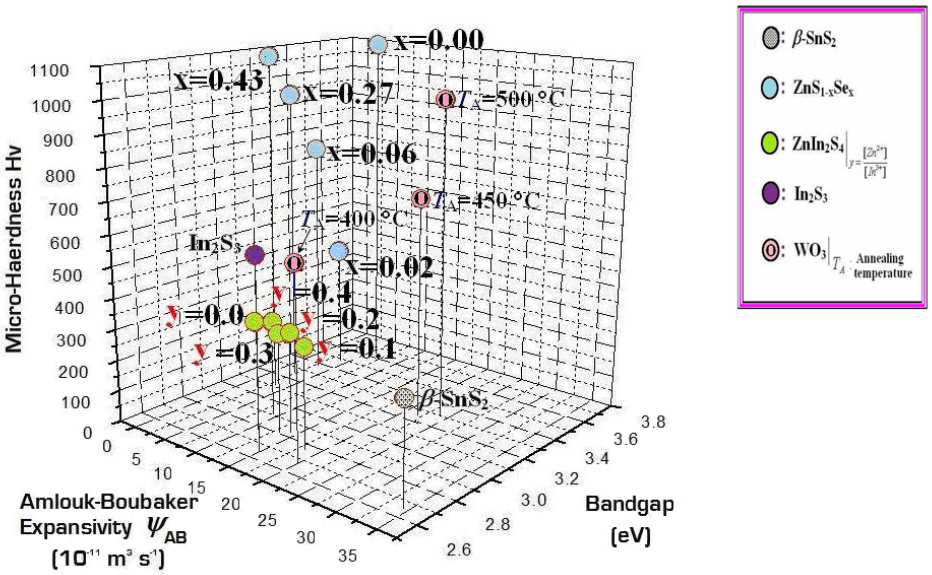

Fig. 2. The 3D abacus

For particular applications, on had to ignore one of the three physical parameters gathered in the abacus. The following 2D projections have been exploited:

The projection in H_υ - E_g plane, which is interesting in the case of a thermally neutral material.

It is the case, i.e. of the $ZnS_{1-x}Se_x$ compounds, it is obvious that the consideration of Band gap-Haredness features is mor important than thermal proprieties. The E_g - H_υ projection (Fig. 3) gives relevant information: the selenization process causes drastical loss of hardness in initially hard binary Zn-S material.

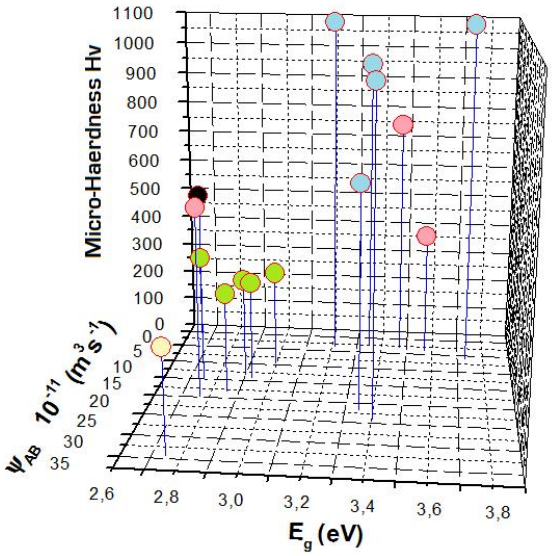

Fig. 3. The 3D abacus (E_g - Hυ projection)

This projection in ψ_{AB} - E_g plane is suitable for thick layers whose mechanical properties don't contribute significantly to the whole disposal hardness.

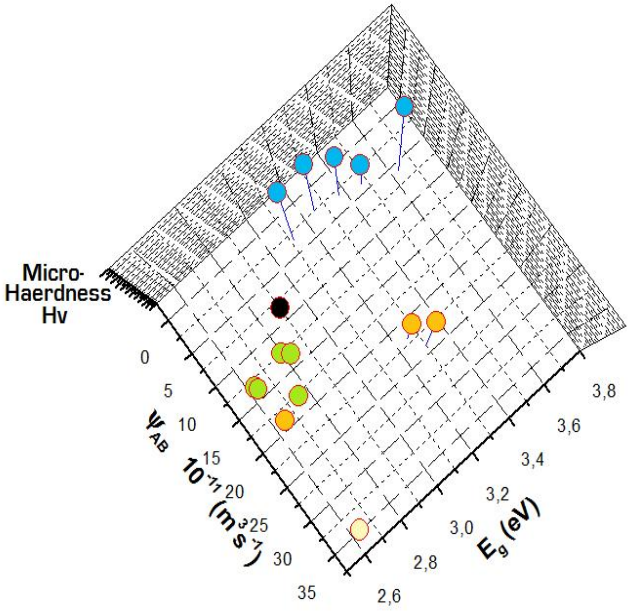

Fig. 4. The 3D abacus (ψ_{AB} - E_g projection)

The projection in ψ_{AB} - Hυ plane is useful for distinguishing resistant and good heat conductor materials, which is the case of the $ZnIn_2S_4$ materials.
In fact the effect of the Zinc-to-Indium ratio on the values of the Amlouk-Boubaker optothermal expansivity (Fig. 5) is easily observable in this projection (it is equivalent to an expansion of the values of the parameter ψ_{AB} into a wide range: [10-20] 10^{-11} m^3s^{-1}).

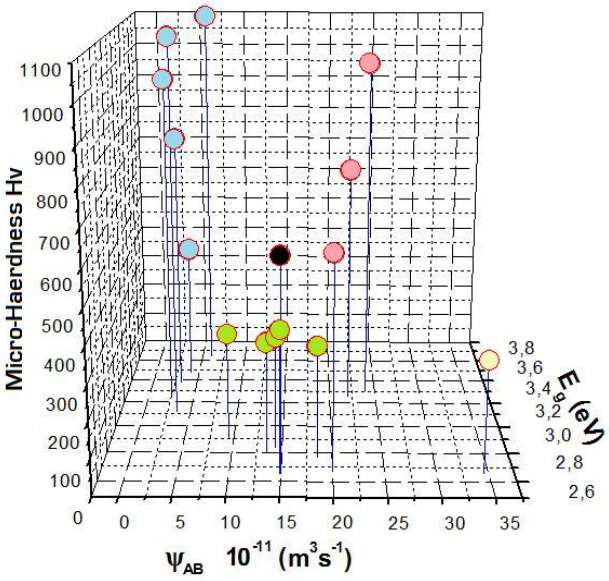

Fig. 5. The 3D abacus (ψ_{AB} - Hυ projection)

3.3 Investigation of the selected materials

According to the information given by the 3D abacus (Figures 3-5), some materials have been selected. ZnO and ZnO-doped layered materials, SnO_2 and SnO_2:F/SnO_2:F-SnS_2 compounds were among the most interesting ones.

3.3.1 ZnO and ZnO-doped layers

Zinc oxide (ZnO) is known as one of the most multifunctional semiconductor material used in different areas for the fabrication of optoelectronic devices operating in the blue and ultra-violet (UV) region, owing to its direct wide band gap (3.37 eV) at room temperature and large exciton binding energy (60 meV) (Coleman & Jagadish, 2006). On the other hand, it is one of the most potential materials for being used as a TCO because of its high electrical conductivity and high transmission in the visible region (Fortunato et al., 2009).
Zinc oxide can be doped with various metals such as aluminium (Benouis et al., 2007) indium (Benouis et al., 2010), and gallium (Fortunato et al., 2008). The conditions of deposition and the choice of the substrate are important for the growth of the films (Benhaliliba et al., 2010). The substrate choosen must present a difference in matching lattice less than 3% to have good growth of the crystal on the substrate (Teng et al., 2007; Romeo et

al., 1998). ZnO (both doped and undoped) is currently used in the copper indium gallium diselenide (CIGS, or Cu (In, Ga)Se2) thin-film solar cell (Wellings et al., 2008; Haung et al., 2002). ZnO is also promising for the application in the electronic and sensing devices, either as field effect transistors (FET), light sensor, gas and solution sensor, or biosensor.

In addition to its interesting material properties motivating research of ZnO as semiconductor, numerous applications of ZnO are well established. The world usage of ZnO in 2004 was beyond a million tons in the fields like pharmaceutical industry (antiseptic healing creams, etc.), agriculture (fertilizers, source of micronutrient zinc for plants and animals), lubricant, photocopying process and anticorrosive coating of metals.

In electronic engineering, Schottky diode are the most known ZnO-based unipolar devices. The properties of rectifying metal contacts on ZnO were studied for the first time in the late 60ties (Mead, 1965; Swank, 1966; Neville & Mead, 1970) while the first Schottky contacts on ZnO thin films were realized in the 80ties (Rabadanov et al., 1981; Fabricius et al., 1986).

The undoped and doped ZnO films grow with a hexagonal würtzite type structure and the calculated lattice parameters (a and c) are given in Table 1 (Benhaliliba et al. 2010).

Nature	Grain Size (Å)	Int. (%)	d (Å)	2θ (°)	Angle Shift (°)	TC	a (Å)	c (Å)	$(c-c_0)/c_0(x10^{-5})$
Undoped									
(100)	217	6.3	2.81	31.78	0.009	0.50	3.24	5.20	-61.4
(002)	358	25.7	2.60	34.44	-0.019	2.33			
(101)	254	19.4	2.47	36.24	-0.008	1.67			
IZO									
(100)	239	100	2.81	31.80	-0.050	2.24	3.24	5.20	-3.84
(002)	211	53.5	2.60	34.42	-0.019	1.19			
(101)	195	85.5	2.47	36.28	-0,028	1.95			
AZO									
(100)	206	70.7	2.81	31.80	-0.011	1.52	3.24	5.20	-115.23
(002)	225	70.5	2.60	34.46	-0.039	1.48			
(101)	195	100	2.47	36.28	-0.028	2.13			

Table 1.

Many significant differences were observed for the undoped, Al- and In-doped ZnO thin films. The films with low thickness (150 nm) have a random orientation with several peaks as reported by Wellings et al. (2008), Ramirez et al. (2007) and Abdullah et al. (2009). The same kind of growth was obtained by Tae et al. (1996) for 150 nm thick films. Whereas on FTO, the predominant ZnO film grew to a thickness of 200-300 nm as stated by Schewenzer et al. (2006). Figures (6-8) give some information about some information about ZnO and ZnO-doped layers.

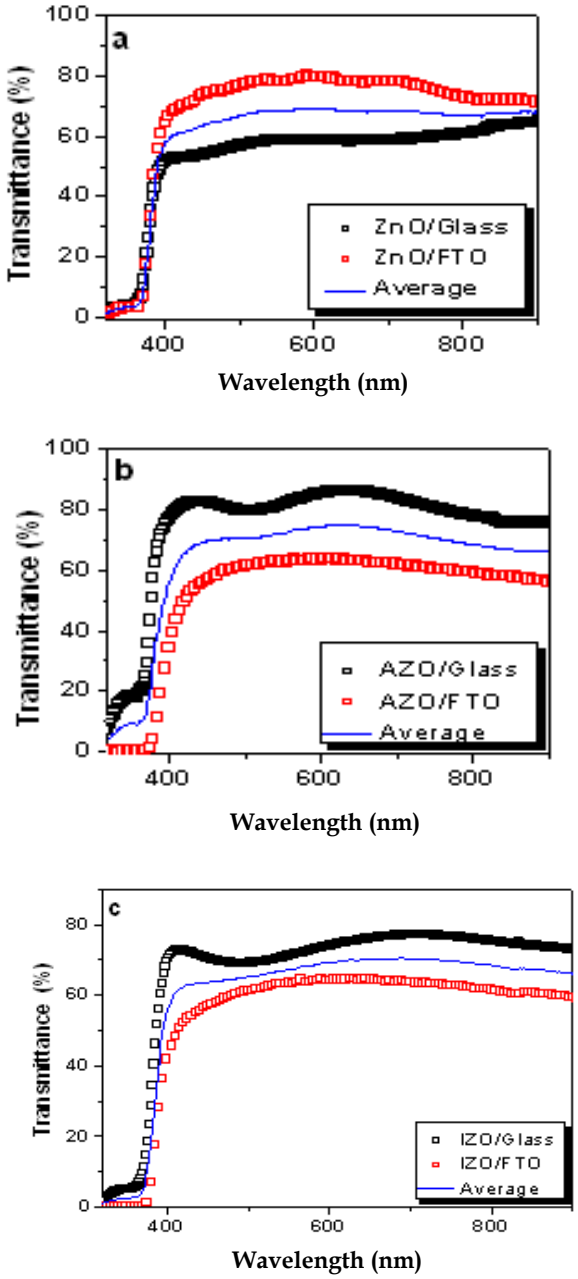

Fig. 6. Transmittance spectra, ZnO/Glass and ZnO/FTO (a), AZO/Glass and AZO/FTO (b), IZO/Glass and IZO/FTO (c).

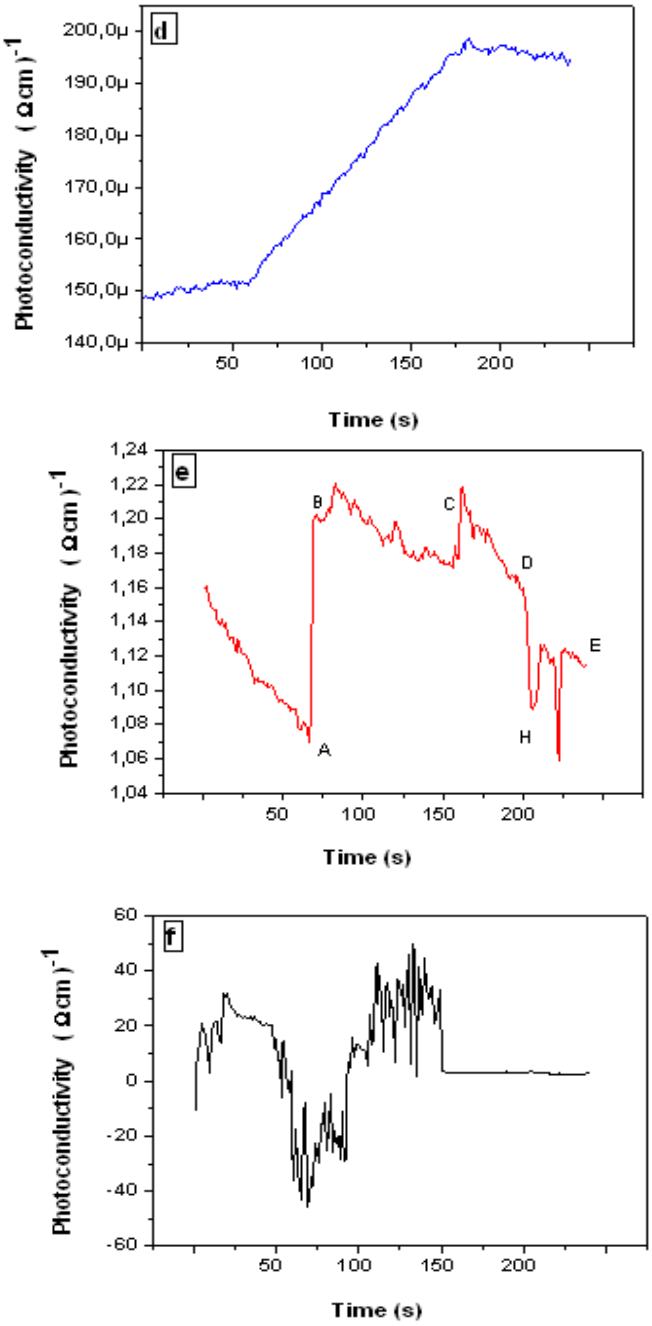

Fig. 7. Photoconductivity spectra versus time of ZnO/FTO (d), AZO/FTO (e), IZO/FTO (f).

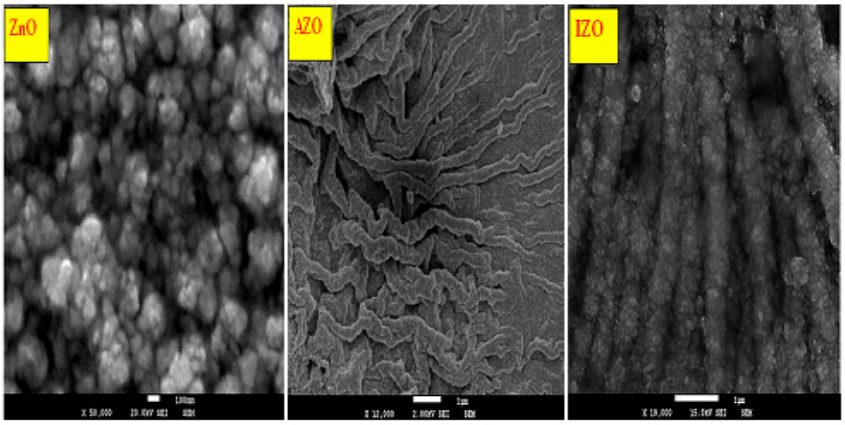

Fig. 8. SEM micrographs for (a) ZnO, (b) AZO and (c) IZO films, (bottom) white horizontal dashes indicate the scale (100 nm (ZnO), 1µm (AZO and IZO).

3.3.2 SnO_2:F-SnS_2 gradually grown layers

Tin oxide (SnO_2) is an *n*-type VI.II oxide semiconductor with a wide band gap (*E*g = 3.6 eV). Because of its good opto-electrical properties, and its ability to induce a high degree of charge compensation, it is widely used as a functional material for the optoelectronic devices, gas sensor, ion sensitive field effect transistors, and transparent coatings for organic light emitting diodes (Onyia & Okeke, 1989; Wang et al., 2006; Lee & Park, 2006; Yamada et al., Kane & Schweizer,1976).

In the last decades, pure and doped tin oxide compounds, prepared by several techniques (Manorama et al., 1999; Bruno et al., 1994; Brinzari et al., 2001; Wang et al., 2002) have been used for the preparation of high performance gas sensing and light emitting devices layers (Barsan, 1994; Goepel & Schierbaum, 1995; Ramgir et al. ,2005).

SnO_2 thin films are generally prepared using methanol CH_4O: 1.0 L, demineralised water and anhydrous tin tetrachloride $SnCl_4$. Formation of pure SnO_2 is resulting from the endothermic reaction:

$$SnCl_4 + 2H_2O \xrightarrow{methanol,440°C} SnO_2 + 4\overset{\frown}{HCl}$$

Approximately 0.9 µm-thick SnO_2 thin films are generally deposited on glass, under an approximated substrate temperature T_s=440°C.

XRD patterns of the as-grown SnO_2 films are shown in Fig. 9. Diagram analysis shows that the layers present a first set of (110)-(101)-(200) X-ray diffraction peaks followed by more important pair (211)-(301). According to JCDPS 88-0287 (2000) standards, these patterns refer to tetragonal crystalline structure.

It was reported by Yakuphanoglu (2009) and Khandelwal et al. (2009)that SnO_2 films structure depends wholly on elaboration technique, substrate material and thermal treatment conditions. This feature was also discussed by Purushothaman et al. (2009) and Kim et al. (2008) who presented temperature-dependent structure alteration of the SnO_2 layers.

Atomic force microscopy (AFM) 3D images of the SnO_2 are presented in Fig. 10.

The layers present a pyramidal-clusters rough structure, which is characteristic to many Sn-like metal oxides. This observation confirms the XRD results.

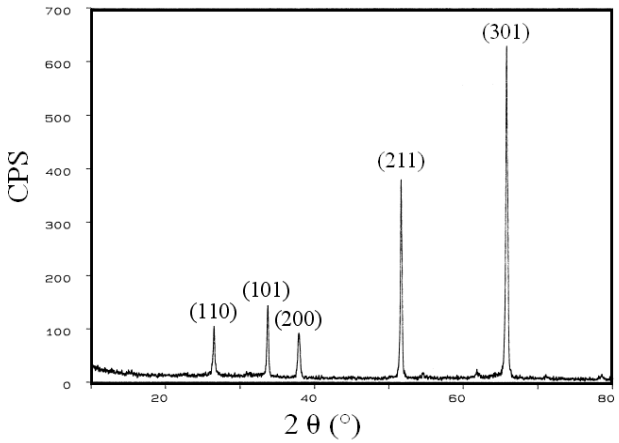

Fig. 9. XRD Diagram of SnO_2 thin layers prepared at T_s 440 °C.

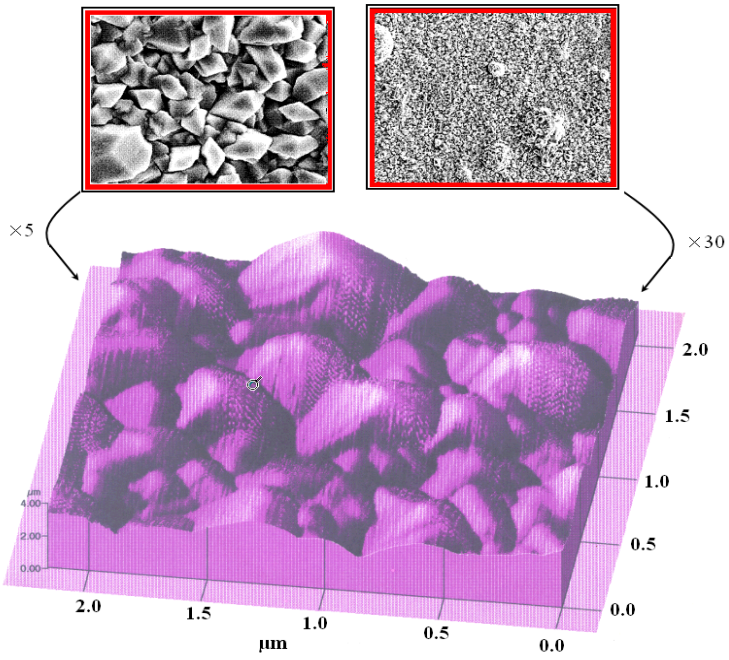

Fig. 10. SnO_2 layers 3D and 2D surface topography 2D (top) and 3D (bottom).

SnO_2:F-SnS_2 gradually grown layers have as intermediate precursors SnO2:F layers obtained by spray pyrolysis on glass substrates according to the coupled reactions :

$$(SnCl_4, 5H_2O)_n + 2nH_2O \xrightarrow[\text{Carrier gas}]{\text{Spray}} n\,SnCl_4\downarrow + \; 7n\,H_2O\uparrow$$

and

$$n\,SnCl_4 + n\,(NH_4^+, F^-) + 2n\,H_2O \xrightarrow[methanol]{440°C} n\,\underline{SnO_2{:}F} + 4n\,\overrightarrow{HCl} + n\,\overrightarrow{NH_3} + \frac{n}{2}\,\overrightarrow{H_2}$$

In the second reaction, ammonium florid acts on the deposited (and heated) tin tetrachloride by incorporation process due to ionic close electro-negativity and dimension (F^- and O^{2-} radii ratio is around 0.96). The obtained layers are n-type (Fig 11-a)
Hence, the first step of the protocol is indeed elaboration of the precursor SnO_2: F layer. In the second step, this layer is subjected to local annealing in a highly sulfured atmosphere (Fig 11-b). Under specific experimental conditions (Temperature, pressure, exposure time) SnS_2 compound appears selectively at the top of the precursor SnO_2: F layer. This obtained mini-layer is n-type (fig 11-b).

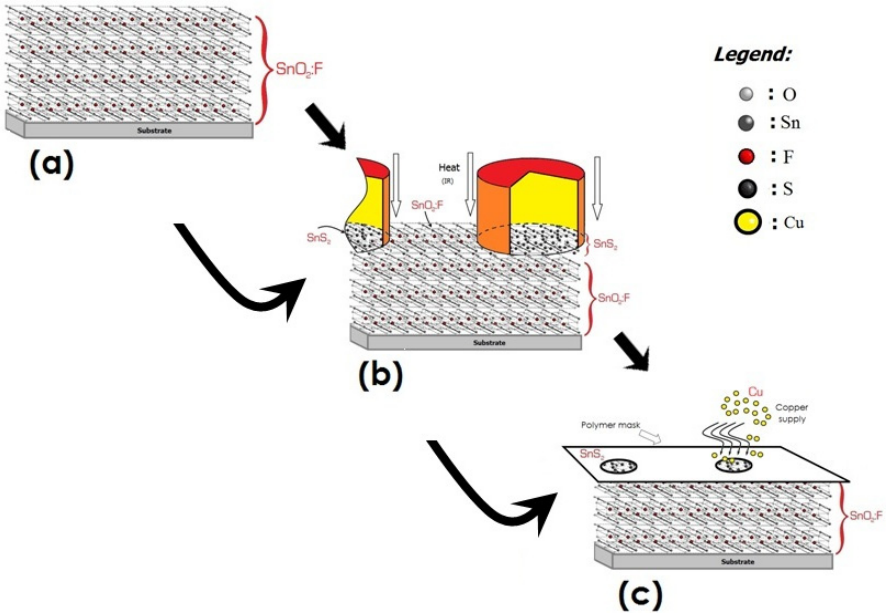

Fig. 11. TCO monolayer-grown: cell elaboration protocol

Finally, a neutral masking sheet is applied to the free surface in order to deposit copper (Cu) by evaporation, controlled dipping or even direct mechanical spotting. Due to the metallic diffusive properties, a multiphase CuSnS (Cu_2SnS_3,Cu_3SnS_4,Cu…) conducting compound appears at the free surfaces (Fig 11-c). This compound has been verified to have better mechanical performance than CuInS.

3.3.3 A sketch of the thermally optimized new monolayer grown cell

The first prototype of the proposed TCO monolayer-grown Solar cell is presented in Figure 12. The procedure can be applied to other oxides, namely Sb_xO_y, Sb_xS_y/MSbO (M=Cu, Ag,..) hetero-junction.

It has been experimented that n-type can be locally and partially transformed into p-WS_2, which results in a WO_3/WS_2 heterojunction, using the same sulfuration procedure detailed above.

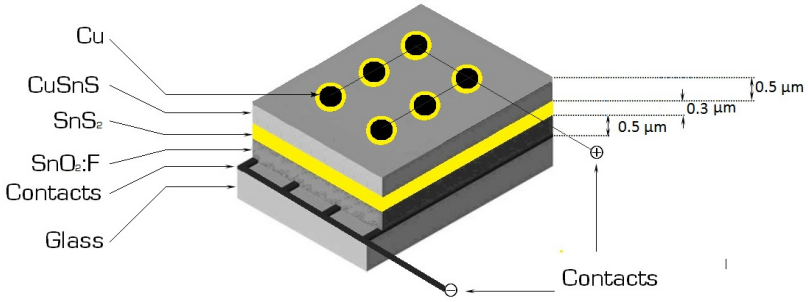

Fig. 12. TCO monolayer-grown Solar cell

The case of ZnO has been experimented but raised some problems, in fact it has been recorded that sulfuration process is never complete, and that an unexpected mixture $(ZnO)_x(ZnS)_y$ takes place.

4. Conclusion

In this chapter, a new physical parameter has been proposed as a guide for optimizing the recently implemented oxide monolayer spray-grown solar cells. This parameter led to the establishment of a 3D (bangap E_g -Vickers Microhardness $H\upsilon$ - Optothermal Expansivity ψ_{AB}) abacus. Thanks to optimizing features, some interesting materials have been selected for an original purpose: The TCO monolayer-grown Solar cell. The first prototype of the proposed TCO monolayer-grown Solar cell has been presented and commented. The perspective of using other oxides, namely Sb_xO_y, Sb_xS_y/MSbO (M=Cu, Ag,..) has been discussed.

5. References

Abdullah, H.N.P.Ariyanto, S.Shaari, B.Yuliarto and S.Junaidi, Am. J. Eng. and Appl. Sc. 2 (2009) 236-240.

Abe, Y. & Ishiyama N., (2006). Titanium-doped indium oxide films prepared by DC magnetron sputtering using ceramic target. J. Mater. Sci. 41, pp.7580-7584

Agida, M., Kumar, A. S., 2010. A Boubaker Polynomials Expansion Scheme Solution to Random Love's Equation in the Case of a Rational Kernel , J. of Theoretical Physics 7,319.

Amlouk, A.; Boubaker K.& Amlouk M., (2010). J. Alloys Compds, 490,pp. 602–604.

Awojoyogbe, O.B., Boubaker, K., 2008. A solution to Bloch NMR flow equations for the analysis of homodynamic functions of blood flow system using m- Boubaker polynomials. Curr. Appl. Phys. 9, 278–283.

Bandara, J. & Tennakone, K. J. (2001). Colloid Interface Sci. 236, pp. 375-382.

Barsan, N. Sens. Actuators, B, Chem. 17 (1994) 241.

Bauer, C.; Boschloo, G., Mukhtar, E. & Hagfeldt, A. (2001). J. Phys. Chem. B 105,pp. 5585-5591.

Belhadj, A., Onyango, O., Rozibaeva, N., 2009. Boubaker polynomials expansion scheme-related heat transfer investigation inside keyhole model. J. Thermo- phys. Heat Transfer 23, 639–640.

Benhaliliba, C. E. Benouis, M. S. Aida, F. Yakuphanoglu, A. Sanchez Juarez, J Sol-Gel Sci Technol (2010) 55:335–342 DOI 10.1007/s10971-010-2258-x.

Benhaliliba, C.E. Benouis, M.S. Aida, A. Sanchez Juarez, F. Yakuphanoglu, A. Tiburcio Silver, J. Alloys Compd. 506 (2010) 548-553.

Benouis, C.E. ; Benhaliliba, M. , Sanchez Juarez, A., Aida, M.S., F.Yakuphanoglu, F., (2010). Journal of Alloys and Compounds 490, pp. 62–67.

Benouis C.E., M. Benhaliliba, F. Yakuphanoglu, A. Tiburcio Silver, M.S. Aida, A. Sanchez Juarez, Synthetic Metals (2011). D.O.I. 10.1016/ J. Synthmet.2011.04.017.

Benouis, C.E. ; Sanchez-Juarez, A., Aida, M.S., (2007). Phys. Chem. News, 35, pp. 72-79.

Brinzari V., G. Korotcenkov, V. Golovanov, Thin Solid Films 391 (2001) 167.

Bruno, L.C. Pijolat, R. Lalauze, Sens. Actuators, B, Chem. 18–19 (1994) 195.

Coleman, V. A. & Jagadish C., (2006). Basic Properties and Applications of ZnO, and: chapter1 Zinc Oxide Bulk, Thin Films and Nanostructures C. Jagadish and S. Pearton Elsevier limited.

Dubey, B., Zhao, T.G., Jonsson, M., Rahmanov, H. 2010. A solution to the accelerated-predator-satiety Lotka–Volterra predator–prey problem using Boubaker polynomial expansion scheme. J. Theor. Biology 264, 154-160.

Fabricius H, Skettrup T, Bisgaard P. Appl Opt 1986;25:2764–7.

Fortunato, E.; Gonçalves, A., Pimentel, A., Barquinha, P., Gonçalves, G., Pereira, L., Ferreira, I. & Martins, R., (2009). Appl. Phys. A Mat. Sci. Proc. 96, pp.197-205.

Fortunato, E.; Raniero, L., Silva, L,. Gonçalves, A., Pimentel, A., Barquinha, P., Aguas, H., Pereira, L., Gonçalves, G., Ferreira, I., Elangovan, E., Martins, R., (2008). Sol. En. Mat. And Sol. Cells 92, pp.1605-1610.

Fridjine, S., Amlouk, M., 2009. A new parameter: an ABACUS for optimizing functional materials using the Boubaker polynomials expansion scheme. Mod. Phys. Lett. B 23, 2179–2182.

Ghanouchi, J., Labiadh, H., Boubaker, K., 2008. An Attempt to solve the heat transfer equation in a model of pyrolysis spray using 4q-order Boubaker polynomials. Int. J. Heat Technol. 26, 49–53.

Ghrib, T., Boubaker, K., Bouhafs, M., 2008. Investigation of thermal diffusivity–microhardness correlation extended to surface-nitrured steel using Boubaker Ginot, V. & Hervé, J. C. ,1994, Estimating the parameters of dissolved oxygen dynamics in shallow ponds, Ecol. Model. 73, 169-187.

Goepel, W. Schierbaum, K.D. Sens. Actuators, B, Chem. 26 (1995) 1.

Guezmir, N., Ben Nasrallah, T., Boubaker, K., Amlouk, M., Belgacem, S., 2009. Optical modeling of compound CuInS2 using relative dielectric function approach and Boubaker polynomials expansion scheme BPES. J. Alloys Compd. 481, 543–548.

Haung F.J, Rudmann, D., Bilger, G., Zogg, H., Tiwari, A.N., (2002) Thin Solid Films 403-404, pp. 293-296.

He, J.; Lindstrom, H., Hagfeldt, A. & Lindquist, S.E. (1999). J. Phys. Chem. B 103, pp. 8940-8951.

Kane, J. H.P. Schweizer, J. Electrochem. Soc. 123 (1976) 270.

Kay, A. & Gratzel, M. (2002). Chem. Mater 14, pp. 2930-2938.

Khandelwal, R. A. Pratap Singh, A. Kapoor, S. Grigorescu, P. Miglietta, N. Evgenieva Stankova, A. Perrone, Optics & Laser Tech. 41 (2009) 89

Kim, H. H. Park, H. J. Chang, H. Jeon, H. H. Park, Thin Solid Films, 517(2008) 1072

Kumar, A. S., 2010. An analytical solution to applied mathematics-related Love's equation using the Boubaker Polynomials Expansion Scheme, Journal of the Franklin Institute 347, 1755.

Lee, S.Y. B.O. Park, Thin Solid Films 510 (2006) 154.

Lim, J. H.; Yang E.-J., Hwang D.K., Yang J.H. (2005). Highly transparent and low resistance gallium-doped indium oxide contact to p-type GaN. Appl. Phys. Lett. 87,pp. 1-3

Manorama, S.V. C.V.G. Reddy, V.J. Rao, Nanostruct. Mater. 11 (1999) 643.
Mead CA. Phys Lett (1965). Pp.18-218.
Nasr, C.; Kamat, P.V.& Hotchandani, S. J. (1998). Phys. Chem. B 102, pp.10047-10052.
Neville RC, Mead CA. J Appl Phys 1970;41:3795.
Onyia, A.I. C.E. Okeke, J. Phys. D: Appl. Phys. 22 (1989) 1515.
Oyodum, O.D., Awojoyogbe, O.B., Dada, M., Magnuson, J., 2009. On the earliest definition of the Boubaker polynomials. Eur. Phys. J. Appl. Phys. 46, 21201–21203.
Palomares, E.; Cliford, J.N., Haque, S.A., Lutz, T.& Durrant, J.R. (2003). J. Am. Chem. Soc 125, pp. 475-481.
Purushothaman, K.K. M. Dhanashankar, G. Muralidharan, Current App. Physics 9 (2009) 67
Rabadanov RA, Guseikhanov MK, Aliev IS, Semiletov SA. Fizika (Zagreb)1981;6:72.
Ramgir, N.S. Mulla, I.S. Vijayamohanan, K.P. J. Phys. Chem., B 109 (2005) 12297.
Ramirez, D.D.Silva, H.Gomez, G.Riveros, R.E.Marotti, E.D.Dalchiele, Solar Energy Materiels and Solar Cells 31 (2007) 1458-1451.
Redmond, G.; Fitzmaurice, D. & Gratzel, M. (1994). Chem. Mater. 6, pp. 686-689.
Romeo, A.; Tiwari, A.N., & Zogg, H., 2nd World Conference and Exhibition on Photovoltaic Solar Energy Conversion 6-10 July 1998 Hofburg Kongresszentru, Vienna Austria.
Sayama, K.; Sugihara, H. & Arakawa H.(1998). Chem. Mater. 10, 3825-3830.
Schewenzer, B.J.R.Gommm and D.E.Morse, Langmuir 22 (2006) 9829-9831.
Slama, S., Bessrour, J., Bouhafs, M., BenMahmoud, K. B., 2009a .Numerical distribution of temperature as a guide to investigation of melting point maximal front spatial evolution during resistance spot welding using Boubaker polynomials. Numer. Heat Transfer Part A 55,401–408.
Slama, S., Boubaker, K., Bessrour, J., Bouhafs, M., 2009b. Study of temperature 3D profile during weld heating phase using Boubaker polynomials expansion. Thermochim. Acta 482, 8–11.
Slama, S., Bouhafs, M., Ben Mahmoud, K.B., Boubaker, A., 2008. Polynomials solution to heat equation for monitoring A3 point evolution during resistance spot welding. Int. J. Heat Technol. 26, 141–146.
Swank RK. Phys Rev 1966;153:844.
Tabatabaei, S., Zhao, T., Awojoyogbe, O., Moses, F., 2009. Cut-off cooling velocity profiling inside a keyhole model using the Boubaker polynomials expansion scheme. Heat Mass Transfer 45, 1247–1251.
TaeYoung Ma, Sang Hyun Kim, Hyun Yul Moon, Gi Cheol Park, Young Jin Kim, Ki Wan Kim, J.Appl.Phys. 35(1996) 6208-6211.
Teng, X.; Fan, H., Pan, S., Ye, C., Li, G., (2007). Materials letters 61, pp. 201-204.
Tennakone, K.; Kumara, G. R. R. A., Kottegoda, I. R. M. & Perera, V.P.S. (1999). J. Chem. Soc. Chem. Commun. 99, pp. 15-21.
Wang, H.C.Y. Li, M.J. Yang, Sens. Actuators B 119 (2006) 380.
Wang, Y. C. Ma, X. Sun, H. Li, Nanotechnology 13 (2002) 565.
Wellings, J.S.; Chaure, N.B., Heavens, S.N., Dharmadasa, I.M., (2008). Thin Solid Films, 516, pp. 3893-3898.
Wellings, J.S.N.B.Chaure, S.N.Heavens, I.M.Dharmadasa, Thin Solid Films, 516 (2008) 3893-3898.
Wu, L. Z.; Tian W.& Jiang X. T. (2005). Silicon-based solar cell system with a hybrid PV module. Solar Energy Materials and Solar Cells. 87, pp.637-645
Yakuphanoglu, F. Journal of Alloys and Compounds, 470 (2009) 55
Yamada Y., K. Yamashita, Y. Masuoka, Y. Seno, Sens. Actuators B 77 (2001) 12.
Zhao, T.G., Wang, Y.X., Ben Mahmoud, K.B., 2008. Limit and uniqueness of the Boubaker–Zhao polynomials imaginary root sequence. Int. J. Math. Comput. 1, 13–16.

3

Flexible Photovoltaic Textiles for Smart Applications

Mukesh Kumar Singh
Uttar Pradesh Textile Technology Institute,
Souterganj, Kanpur,
India

1. Introduction

In recent years alternative renewable energies including that obtained by solar cells have attracted much attention due to exhaustion of other conventional energy resources especially fossil-based fuels. Photovoltaic energy is one of the cleanest, most applicable and promising alternative energy using limitless sun light as raw material. Even though, inorganic solar cells dominate in the world photovoltaic market, organic solar cells as the new emerging photovoltaics has explored new possibilities for different smart applications with their advanced properties including flexibility, light-weight, and graded transparency. Low cost production and easy processing of organic solar cells comparing to conventional silicon-based solar cells make them interesting and worth employing for personal use and large scale applications . Today, the smart textiles as the part of technical textiles using smart materials including photoactive materials, conductive polymers, shape memory materials, etc. are developed to mimic the nature in order to form novel materials with a variety of functionalities. The solar cell-based textiles have found its application in various novel field and promising development obtaining new features. These photovoltaic textiles have found its application in military applications, where the soldiers need electricity for the portable devices in very remote areas. The photovoltaic textile materials can be used to manufacture power wearable, mobile and stationary electronic devices to communicate, lighten, cool and heat, etc. by converting sun light into electrical energy. The photovoltaic materials can be integrated onto the textile structures especially on clothes, however, the best promising results from an efficient photovoltaic fiber has to be come which can constitute a variety of smart textile structures and related products[1].

Fossil fuels lead to the emission of CO_2 and other pollutants and consequently human health is under pressure due to adverse environmental conditions. In consequence of that renewable energy options have been explored widely in last decades[2-3].

Unprecedented characteristics of photovoltaic (PV) cells attract maximum attention in comparision of other renewable energy options which has been proved by remarkable growth in global photovoltaic market[4].

Organic solar cells made of organic electronic materials based on liquid crystals, polymers, dyes, pigment etc. attracted maximum attention of scientific and industrial community due to low weight, graded transparency, low cost, low bending rigidity and environmental friendly processing potential[5-6]. Various photovoltaic materials and devices similar to solar

cells integrated with textile fabrics can harvest power by translating photon energy into electrical energy.

2. Driving forces to develop organic PV cells

Energy is the greatest technological problem of the 21st century. Energy conversion efficiency is a dominant factor to meet the increasing demand of energy worldwide. Solar energy looks easy alternative next to conventional sources, like electricity, coal and fuels. The use of solar energy can become more popular by developing photovoltaic (PV) cells of improved efficiency. The crystalline silicon PV cells are 12 % efficient with very high manufacturing cost. Thin-film cells based on CdTe, $CuInS_2$ and amorphous Si are promising, but In is expensive, Cd is toxic and amorphous Si isn't stable. A 10 % efficient cell can generate energy level equivalent to 100 W/m^2. Recently, the development of photovoltaic fibre, a great innovation in the field of photovoltaics made the technology more attractive and smart[7-12].

3. Classification of solar cells

Author has made an effort to classify the available solar cells.

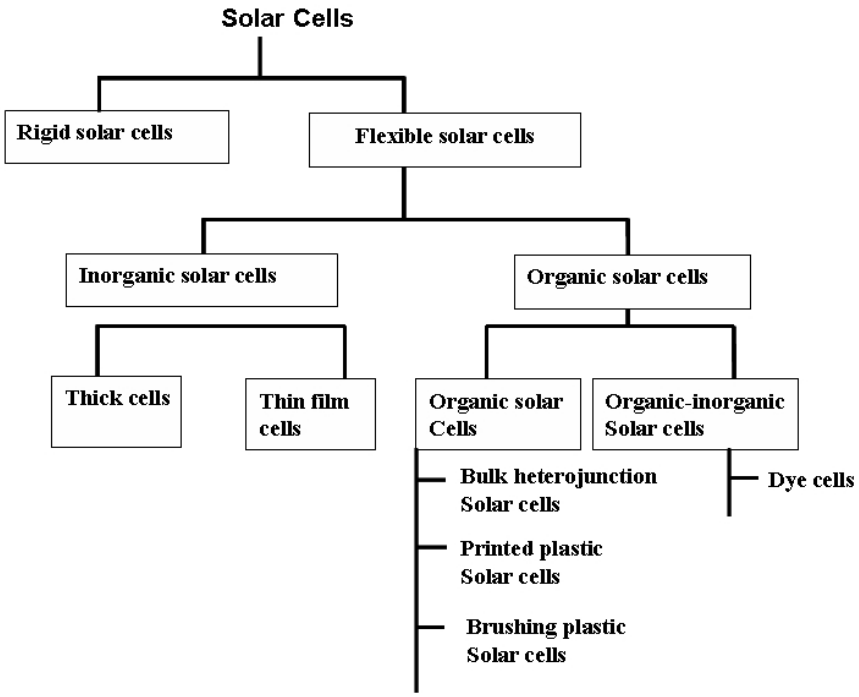

Fig. 1. Classification of Solar cells

Organic solar cells are discussed in detail in this chapter due to their higher compatibility to develop photovoltaic textiles.

4. Manufacturing of organic photovoltaic cells

Indium tin oxide (ITO) was used as a common transparent electrode in polymer-based solar cells due to its remarkable efficiency and ability of light transmission. However, it is quite expensive and generally too brittle to be used with flexible textile substrates. Therefore, highly conductive poly (3,4-ethylenedioxythiophene) doped with poly(styrene sulfonate) PEDOT:PSS, carbon nano-tube or metal layers are used to substitute ITO electrode. This can be a promising way to develop PV textiles for smart application due to its low cost and easy application features for future photovoltaic textile applications. A typical sequence of photovoltaic textiles manufacturing is exhibited in Fig. 2.

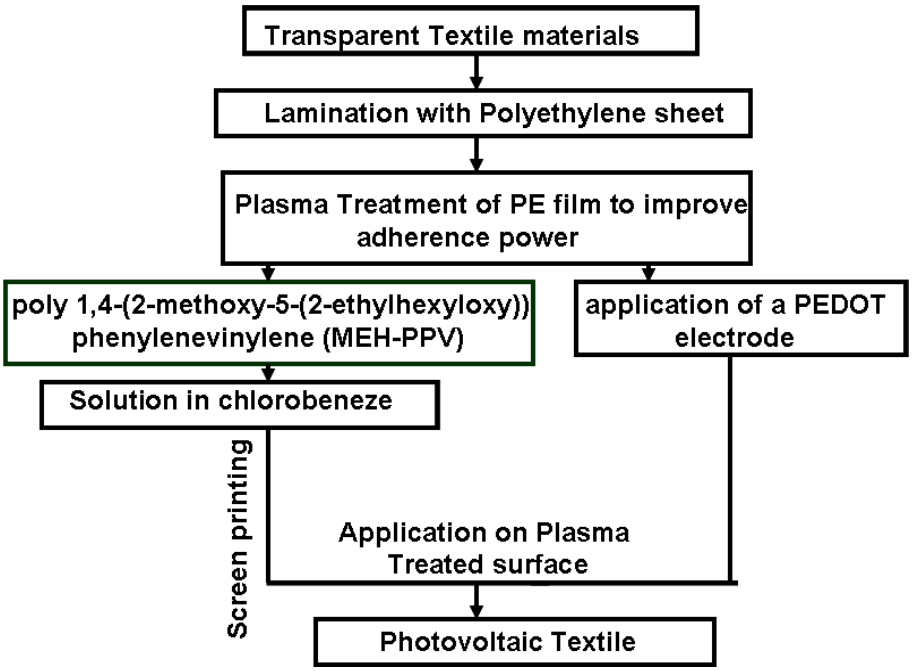

Fig. 2. A typical sequence of photovoltaic textiles manufacturing

A group of scientists has demonstrated the fabrication of an organic photovoltaic device with improved power conversion efficiency by reducing lateral contribution of series resistance between subcells through active area partitioning by introducing a patterned structure of insulating partitioning walls inside the device. Thus, the method of the present invention can be effectively used in the fabrication and development of a next-generation large area organic thin layer photovoltaic cell device[13].
The manufacturing of organic photovoltaic (PV) cells can be possible at reasonable cost by two techniques:

4.1 Roll-to-roll coating technique

A continuous roll-to-roll nanoimprint lithography (R2RNIL) technique can provide a solution for high-speed large-area nanoscale patterning with greatly improved throughput. In a typical

process, four inch wide area was printed by continuous imprinting of nanogratings by using a newly developed apparatus capable of roll-to- roll imprinting (R2RNIL) on flexible web base. The 300 nm line width grating patterns are continuously transferred on flexible plastic substrate with greatly enhanced throughput by roll-to- roll coating technique.
European Union has launched an European research project "HIFLEX" under the collaboration with Energy research Centre of the Netherland (ECN) to commercialize the roll to roll technique. Highly flexible Organic Photovoltaics (OPV) modules will allow the cost-effective production of large-area optical photovoltaic (OPV) modules with commercially viable Roll-to-Roll compatible printing and coating techniques.
Coatema, Germany with Renewable Technologies and Konarka Technologies has started a joint project to manufacture commercial coating machine. Coatema, Germany alongwith US Company Solar Integrated Technologies (SIT) has developed a process of hot-melt lamination of flexible photovoltaic films by continuous roll-to-roll technique[14]. Roll-to-roll (R2R) processing technology is still in neonatal stage. The novel innovative aspect of R2R technology is related to the roll to roll deposition of thin films on textile surfaces at very high speed to make photovoltaic process cost effective. This technique is able to produce direct pattern of the materials[15, 16].

4.2 Thin -film deposition techniques

Various companies of the world have claimed the manufacturing of various photovoltaic thin films of amorphous silicon (a-Si), copper indium selenide (CIGS), cadmium telluride (CdTe) and dye-sensitized solar cell (DSSC) successfully. Thin film photovoltaics became cost effective after the invention of highly efficient deposition techniques. These deposition techniques offer more engineering flexibilities to increase cell efficiencies, reflectance and dielectric strength, as well as act as a barrier to ensure a long life of the thin film photovoltaics and create high vapour barrier to save the chemistry of these types of photovoltaics[17-18].
A fibre shaped organic photovoltaic cell was produced by utilizing concentric thin layer of small molecular organic compounds as shown in Fig 3.

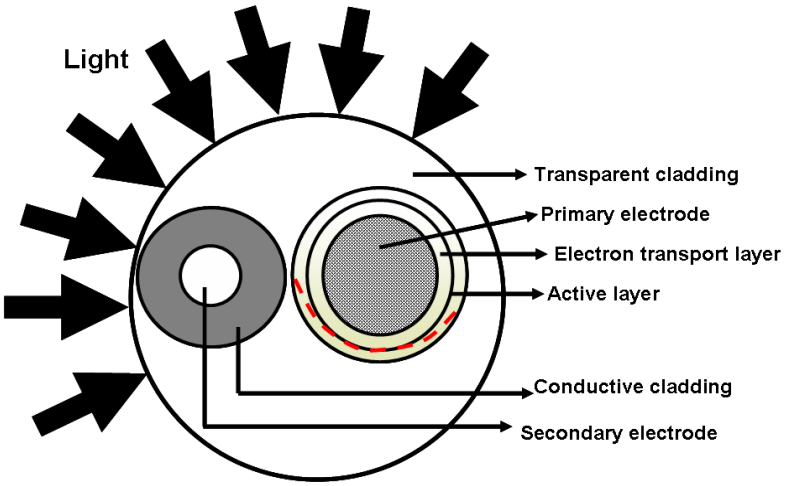

Fig. 3. Photovoltaic fibre

Thin metal electrode are exhibited 0.5% efficiency of solar power conversion to electricity which is lower than 0.76% that of the planner control device of fibre shape organic PV cells. Results are encouraged to the researchers to explore the possibility of weaving these fibres into fabric form.

4.2.1 Dye-sensitized photovoltaics

An exhaustive research on photovoltaic fibres based on dye-sensitized TiO_2-coated Ti fibers has opened up various gateways for novel PV applications of textiles. The cohesion and adhesion of the TiO_2 layer are identified as crucial factors in maintaining PV efficiency after weaving operation. By proper control of tension on warp and weft fibres, high PV efficiency of woven fabrics is feasible.

The deposition of thin porous films of ZnO on metalized textiles or textile-compatible metal wires by template assisted electro-deposition technique is possible. A sensitizer was adsorbed and the performance as photoelectrodes in dye-sensitized photovoltaic cells was investigated. The thermal instability of textiles restricts its use as photovoltaic material because process temperatures are needed to keep below 150°C. Therefore, the electro-deposition of semiconductor films from low-temperature aqueous solutions has become a most reliable technique to develop textile based photovoltaics. Among low-temperature solution based photovoltaic technologies; dye sensitized solar cell technology appears most feasible. If textile materials are behaved as active textiles, the maximum electrode distance in the range of 100 µm has to be considered. Loewenstein et al., (2008) and Lincot et al., (1998) have used Ag coated polyamide threads and fibers to deposit porous ZnO as semiconductor material . The crystalline ZnO films were prepared in a cathodic electrodeposition reaction induced by oxygen reduction in an aqueous electrolyte in presence of Zn^{2+} and eosinY as structure-directing agent[19-20].

Bedeloglu et al., (2009)[21] were used nontransparent non-conductive flexible polypropylene (PP) tapes as substrate without use of ITO layer. PP tapes were gently cleaned in methanol, isopropanol, and distilled water respectively and then dried in presence of nitrogen. 100nm thick Ag layer was deposited by thermal evaporation technique. In next step, a thin layer of poly(3,4-ethylenedioxythiophene) doped : poly(styrene sulfonate) PEDOT: PSS mixture solution was dip coated on PP tapes. Subsequently, poly [2-methoxy-5-(3, 7-dimethyloctyloxy)-1-4-phenylene vinylene] and 1-(3-methoxycarbonyl)-propyl-1-phenyl(6,6)C61, MDMO: PPV: PCBM or poly(3-hexylthiophene) and 1-(3-methoxycarbonyl)-propyl-1-phenyl(6,6)C61, P3HT: PCBM blend were dip coated onto PP tapes. Finally, a thin layer of LiF (7nm) and Al (10nm) were deposited by thermal evaporation technique.

The enhanced conductivity will always useful to improve the photovoltaic potential of poly(3,4-ethylene dioxythiophene):poly(styrene sulfonate) (PEDOT:PSS). Photovoltaic scientific community found that the conductivity of poly(3,4-ethylene dioxythiophene): poly(styrene sulfonate) (PEDOT:PSS), film is enhanced by over 100-folds if a liquid or solid organic compound, such as methyl sulfoxide (DMSO), N,Ndimethylformamide (DMF), glycerol, or sorbitol, is added to the PEDOT:PSS aqueous solution. The conductivity enhancement is strongly dependent on the chemical structure of the organic compounds. The aqueous PEDOT: PSS can be easily converted into film form on various substrates by conventional solution processing techniques and these films have excellent thermal stability and high transparency in the visible range[22-25].

Some organic solvents such as ethylene glycol (EG), 2-nitroethanol, methyl sulfoxide or 1-methyl-2-pyrrolidinone are tried to enhance the conductivity of PEDOT: PSS. The PEDOT:

PSS film which is soluble in water becomes insoluble after treatment with EG. Raman spectroscopy indicates that interchain interaction increases in EG treated PEDOT: PSS by conformational changes of the PEDOT chains, which change from a coil to linear or expanded-coil structure. The electron spin resonance (ESR) was also used to confirm the increased interchain interaction and conformation changes as a function of temperature. It was found that EG treatment of PEDOT: PSS lowers the energy barrier for charge among the PEDOT chains, lowers the polaron concentration in the PEDOT: PSS film by w 50%, and increases the electrochemical activity of the PEDOT: PSS film in NaCl aqueous solution by w100%. Atomic force microscopy (AFM) and contact angle measurements were used to confirm the change in surface morphology of the PEDOT: PSS film. The presence of organic compounds was helpful to increase the conductivity which was strongly dependent on the chemical structure of the organic compounds, and observed only with organic compound with two or more polar groups. Experimental data were enough to make a statement that the conductivity enhancement is due to the conformational change of the PEDOT chains and the driving force is the interaction between the dipoles of the organic compound and dipoles on the PEDOT chains[26].

Thin film PV structure offers following advantages [27-29]:

- Photovoltaic thin film structures are more efficient in comparison to their planar counterparts.
- Photovoltaic thin films offer increased surface area which is favourable for light trapping due to a reduction in specular reflectance but increased internal scattering, leading to increased optical path lengths for photon absorption.
- In Photovoltaic thin film structures, transport lengths for photoexcited carriers in the absorber are reduced and so electrons and holes do not need to travel over large distances before separation and collection.

4.2.2 Thin -film deposition technique

The thin film deposition of photovoltaic materials takes place by electron beam, resistance heating and sputtering techniques. These technologies differ from each other in terms of degree of sophistication and quality of film produced. A resistance-heated evaporation technology is relatively simple and inexpensive, but the material capacity is very small which restricts its use for commercial production line. Sputtering technique can be used to deposit on large areas and complex surfaces. Electron beam evaporation is the most versatile technique of vacuum evaporation and deposition of pure elements, including most metals, numerous alloys and compounds. The electron beam technology has an edge over its counterparts due to following merits of this technology:

- precise control at low or high deposition rates is possible
- possibilities of co-deposition and sequential deposition systems are available
- uniform low temperature deposition is possible
- excellent material utilization is possible
- higher evaporation rates are possible
- freedom from contamination is possible
- precise film composition and cooler substrate temperatures can be maintained

4.2.2.1 e-Vap® thin film deposition technology

Various frames of different electron beam sizes are offered by e-Vap® which are able to produce small research specimen to achieve commercial coating requirement with crucible

capacities from 2cc to 400cc. e-Vap® 100 miniature evaporation systems is a precise wire-fed electron beam source designed specifically for depositing monolayer thin films in ultrahigh vacuum environments capable to deposit metals at atomic level. e-Vap® 3000 and Caburn-MDC e-Vap® are other electron beam evaporation system of different capacity for a wide range of applications[30]. Various companies are working in the field of thin film photovoltaics as shown in Table 1.

Major companies	Technology	Status of manufacturing
Siemens Solar Industries (SSI), Global Solar	Copper Indium Diselenide	Initial Small Quantity Manufacture under 100 kW at SSI
First Solar, BP Solar, Matsushita	First Solar, BP Solar, Matsushita	First Solar Production under 1 MW, Others Lower
Solarex, United Solar, Canon, others	Amorphous Silicon	Commercial Production under 10 MW at Several Plants

Table 1. Photovoltaic thin film manufacturing

4.3 Printing of plastic solar cells

Organic semiconductor based solar cells can be integrated fast with textile substrates and molecular heterojunction cells can be printed using inkjet printing efficiently. This technology has opened new routes to produce organic solar cells. Credit of invention of printed solar cells goes to Konarka Technologies[31] for successful demonstration of manufacturing of solar cells by inkjet printing as shown in Fig.4 .

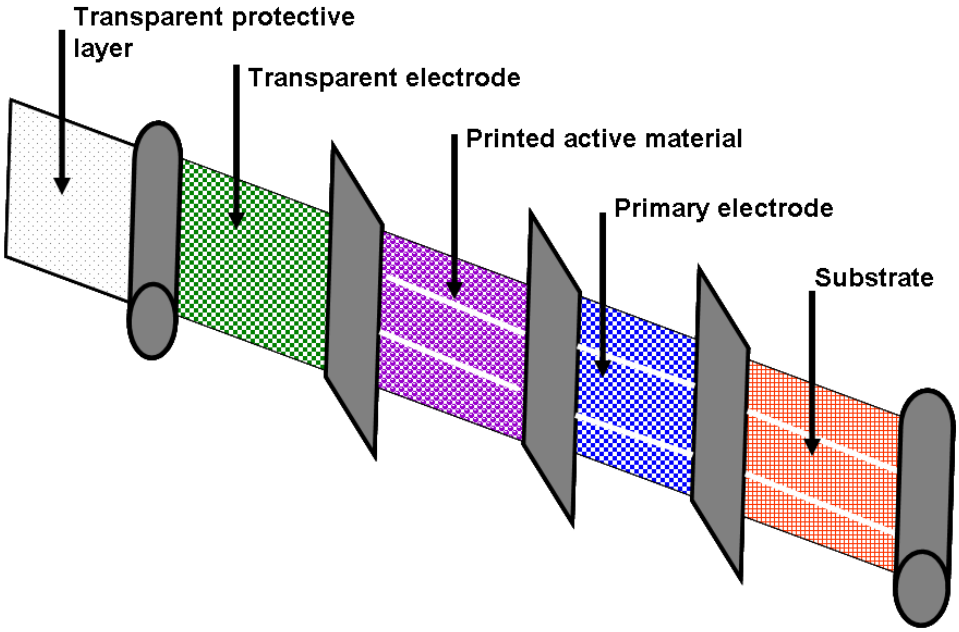

Fig. 4. Konarka's plastic photovoltaic cells by printing technology

The inkjet printing technology enables manufacturing of solar cells with multiple colors and patterns for lower power requirement products, like indoor or sensor applications. A mixture of high and low boiling solvents, (68% orthodichlorobenzene and 32% 1,3,5-trimethylbenzene), is found suitable for the production of inkjet printed organic solar cells with power conversion efficiency upto 3%. During the drying process and subsequent annealing, the suggested oDCB–mesitylene solvent mixture leads to an optimum phase separation network of the polymer donor and fullerene acceptor and therefore strongly enhances the performance. During drying and subsequent heat-setting process, the recommended ortho-dichlorobenzene (oDCB)-mesitylene solvent mixture leads to an optimum phase separation of polymer donor and fullerene acceptor as suggested by Pagliaro et al., (2008)[32]. Solvents formulation and temperature of printing table are two prime parameters to control the spreading and wetting of liquid on substrate surface. Fig.4 shows a schematic representation of organic film formation by inkjet printing.

In a typical case, the photoactive formulation is formed by blending poly(3-hexylthiophene) (P3HT) with fullerene [6,6]-phenyl C61 butyric acid methyl ester (PCBM) in a tetralene and oDCB–mesitylene solvent mixture. A uniform film and reliable printing with respect to the spreading and film formation was performed by keeping the inkjet platen temperature 40°C. The combination of higher/lower boiling solvent mixture, oDCB–mesitylene, offers following advantages:

a. oDCB with b.p.¼180°C can be used to prevent nozzle clogging and provide a reliable jetting of the printhead
b. the second component, mesitylene, with lower boiling point of 165°C of the solvent mixture, with a lower surface tension, is used to achieve optimum wetting and spreading of the solution on the substrate. It has a higher vapor pressure of 1.86mm Hg at 20°C and a lower boiling point of 165°C compared to oDCB and tetralene. It increases the drying rate of the solvent mixture, which is a critical parameter to decide the morphology of PV prints.

According to Hoth et al., (2007) for an efficient bulk heterojunction solar cell, precise control of the morphology is essential. The active layer deposition tool strategy decides the morphology. It was evident from AFM study of the inkjet printed active layers that the P3HT–PCBM blend films show significant difference in the grain size and surface roughness. The roughness of active layer surface affects the performance of the inkjet printed photovoltaic device. The credit of commercialization of power plastic cells (PPC) goes to Konarka alongwith a German firm Leonhard Kurz by opting simple, energy efficient, environmentally friendly, replicable and scalable process. The semiconducting conjugated polymers to make the photosensitive layers of the cell are created in batches of several liters each. Finally fluffy powder is formed and manufacturers combine it with standard industrial solvents to create an ink or coatable liquid. This coatable liquid is fed in reservoir of inkjet print head. Specific types of pumps are used to exert continuous pressure to maintain constant through put rate from orifice inkjet printhead throughout the printing process. Inkjet head has facility to move in different directions which helps to create various printing patterns of semiconducting polymer liquid on textile substrate layer by layer as shown in Fig.5. These layers are considerably thin. During deposition of semiconducting polymer cleanliness is very important and whole printing process is carried out in a clean room[31].

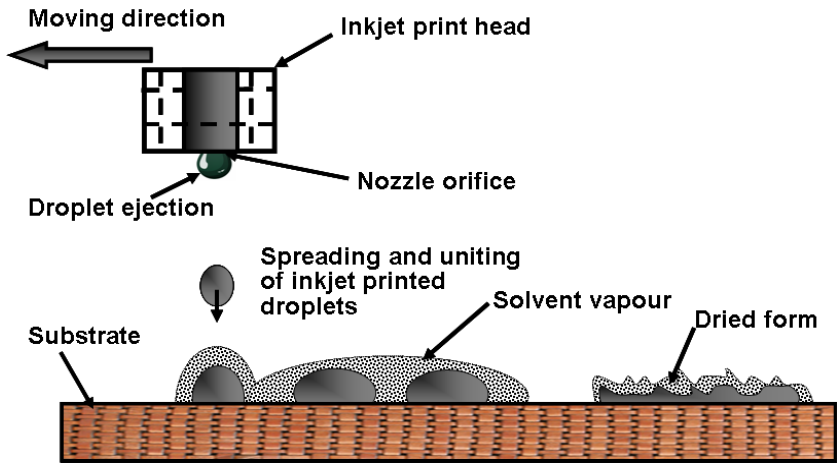

Fig. 5. Inkjet printing of photovoltaic cells

4.3.1 Advantages of inkjet printing

Inkjet printing of organic photovoltaic materials offers following advantages:

- Inkjet printing is a commonly used technique for controlled deposition of solutions of functional materials in specific locations on a substrate and can provide easy and fast deposition of polymer films over a large area.
- Organic solar cells can be processed with printing technologies with little or no loss compared to clean room, semiconductor technologies such as spin coating.
- Inkjet printing could become a smart tool to manufacturer solar cells with multiple colors and patterns for lower power requirement products, like indoor or sensor applications.
- Inkjet printing technique is considered very promising because the polymer devices can be fabricated very easily because of the compatibility with various substrates and it does not require additional patterning.

5. Significance of low bandgap polymers

The part of visible sunlight is lost by absorption in specific regions of the spectrum when passes through the atmosphere. The amount of loss depends on the air mass. Under ideal conditions, the available photons for the conversion to the electrons can be represented by the solar spectrum in photon flux as a function of wavelength. It is evident that photons must be harvest at longer wavelength but at longer wavelengths the energy of the charge carriers remains lower which restricts the voltage difference that the device can produce. Hence designing of optimum bandgap is essential. However, the practical efficiencies differ from theoretically predicted values. These above considerations are based on the fact that the low band gap polymers have the possibility to improve the efficiency of OPVs due to a better overlap with the solar spectrum. Hence to achieve maximum power generation in photovoltaic device low band gap materials are required. Majority of Photovoltaic devices are unable to convert light energy below 350–400 nm wavelengths efficiently into electrical energy because of poor absorption in the substrate and front electrodes. Although, this part

of light spectrum contains very little intensity and consequently do not have a major contribution and i.e only 1.4% to the total possible current. It is evident from above discussion that to increase the current realization λ_{max} have to increase from 650 to 1000nm, in turn decreasing the band gap. Poly (3-hexylthiophene) is a typical example of low badgap polymeric material has a band gap of 650nm (1.9 eV) which can harvest up to 22.4% of the available photons. Hence, it is necessary to fabricate the polymers having broad absorption to achieve increase in the efficiency of the solar cell[33-34].

6. Different techniques to manufacture photovoltaic textiles

Photovoltaics and textiles are two different areas where a successful collaboration brings very smart results. The integration of these two different sectors can be possible by adopting following techniques.
There are two basic techniques to manufacture PV textiles.

6.1 PV textiles by PV fibres

This technique is based on the development of photovoltaic fibres using Si-based /organic semiconducting coating or incorporation of dye-sensitized cells (DSC). Availability of PV fibre offer more freedom in the selection of structure for various type of applications[35-39].
The development of photovoltaic fibres offers advantages to manufacture large area active surfaces and higher flexibility to weave or knit etc[40].
Although, the problem of manufacturing textile structure by using dye-sensitized cells (DSC-PV) fibres into textile structure is still alive and require a optimization with respect to textile manufacturing operations. In a typical research work the working electrode of DSC-PV fibre is prepared by coating Ti wire with a porous layer of TiO_2. This working electrode is embedded in an electrolyte with titanium counter electrode. The composite structure is coated with a transparent cladding to ensure protection and structural integrity. The electrons from dye molecules are excited by photo energy and penetrated into the conduction band of TiO_2 and move to the counter electrode through external circuit and regenerate the electrolyte by happening of redox reaction. Ultimately the electrolyte regenerates the dye by means of reduction reaction.
The performance of DSC fibre is majorily depends on the grade of TiO_2 coating and its integration to Ti substrate. The integrity of Ti with TiO_2 will depend on the surface cleanliness and roughness of Ti, affinity between Ti and TiO_2 and other defects. The deposition of TiO_2 dye on Ti wire surface is performed by strategy as shown in Fig.6. The integrity of coating on Ti substrate is tested by using peel test, tensile test, four point bending test and scratch test. The amount of discontinuities is measured by optional microscopy and SEM[41-47].
The photovoltaic potential of dye-sensitized solar cells (DSSC) of Poly(vinyl alcohol) (PVA) was improved by spun it into nanofibers by electrospinning technique using PVA solution containing silver nitrate ($AgNO_3$). The silver nanoparticles were generated in electrospun PVA nanofibers after irradiation with UV light of 310~380 nm wavelength. Electrospun PVA/Ag nanofibers have exhibited I_{sc}, FF, V_{oc}, and η showed the values of 11.9~12.5 mA/cm^2, 0.55~10.59, 0.70~10.71 V, and 4.73~14.99%, respectively. When the silver was loaded upto 1% as dope additives in PVA solution, the resultant electrospun PVA/Ag nanofibres exhibited power conversion efficiency 4.99%, which is higher than that of dye sensitized solar cells (DSSC) using electrospun PVA nanofibers without Ag nanoparticles[48].

Ramier et al., (2008), concluded that the feasibility of producing textile structure from DSC-PV fibre is quite good. The deposition of TiO_2 on flexible fibre is expected to be quite fruiteful in order to maintain the structural integrity without comparing with PV performance[49].

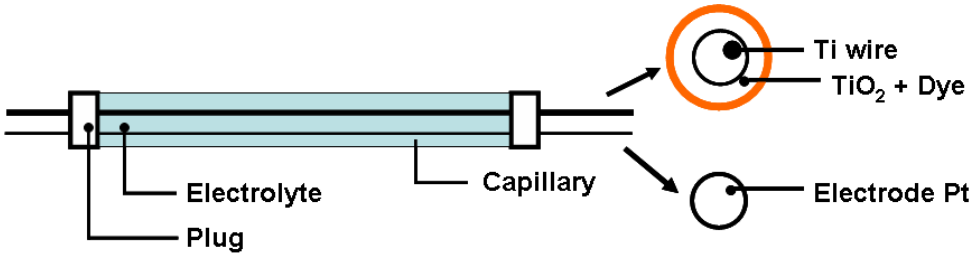

Fig. 6. A model DSC Photovoltaic fibre by surface deposition

Fibre based organic PV devices inroads their applications in electronics, lighting, sensing and thermoelectric harvesting. By successful patch up between commodity fibre and photovoltaic concept, a very useful and cost effective way of power harvesting is matured[50-52].

Coner et al.,[53] have developed a photovoltaic fibre by deposition of small Molecular weight organic compound in the form of concentric layer on long fibres. They manufactured the OPV fibre by vacuum thermal evaporation (VTE) of concentric thin films upto 0.48 mm thickness on polyamide coated silica fibre. Different control devices are based on OPV cells containing identical layer structures deposited on polyimide substrates. The OPV based fibre cells were defined by the shape of the substrate and 1 mm long cathodes. All fibre surfaces were cleaned well prior to deposition. Lastly, they concluded that performance of OPV fibre cells from ITO is inferior in terms of changes in illumination angle, enabling the optical photovoltaic (OPV) fibre containing devices to outperform its planar analog under favourable operating conditions. Light emitting devices are designed in such a way that becomes friendly to weave it. The light trapping on fibre surface can be improved by using external dielectric coating which is coupled with protective coating to enhance its service time. Successful PV fibre can be manufactured by opting appropriate material with more improved fabrication potential[54].

Dye sensitized solar cells (DSC) are low cost, applicable in wide range of application and simple to manufacture. These merits of dye-sensitized PV fibre makes it a potential alternative to the conventional silicon and thin film PV devices[55].

DSC works on the principle of optoelectronically active cladding on an optical fibre. This group was manufactured two type of PV fibre using polymethylmethacrylate (PMMA) baltronic quality diameter 1.3 to 2.0mm and photonium quality glass fibre with diameter 1.0 to 1.5 mm. Both virgin fibre were made electronically conductive by deposition of 130nm thick layer of ZnO:Al by atomic layer deposition technique with the help of P400 equipment. The high surface area photoelectric film for DSC was prepared in two steps. In first step TiO_2 in the form of solution or paste having TiO_2 nanoparticle is deposited on electronically conductive surface. In the second step dry layer of TiO_2 is sintered at 450-500°C for 30 minute to ensure proper adhesion to the fibre surface. PMMA fibre is suitable to survive upto 85°C. Hence mechanical compression is alternate technique to ensure the fixation.

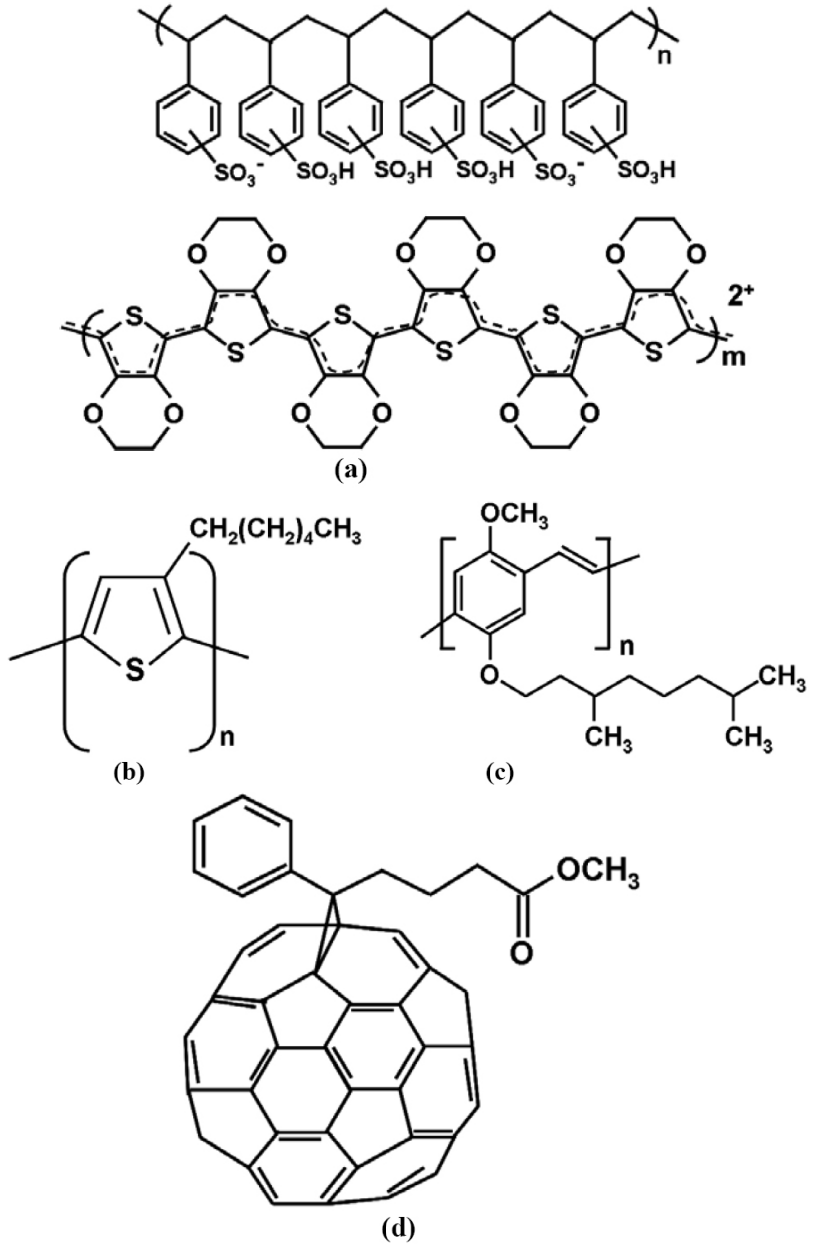

Fig. 7. Chemical configurations of (a) PEDOT:PSS (b) P3HT (c) MDMO-PPV (d) PCBM

Glass fibre is capable to withstand with sintering temperatures which inroads the possibilities of preparation of porous photoelectrodes on them. Commercially available TiO_2 paste was diluted to achieve appropriate viscosity with tarpin oil to make suitable for dip-coating. TiO_2

film was formed by dip coating and dried at room temperature upto 30 min before proper sintering between 475 to 500°C. Appropriately sintered fibres were then immersed in dye solution consisting of 0.32 ml of the cis-bis(isothiocyanate)bis(2,2-bipyridyl-4-4' dicarboxylato)-ruthenium(II) bis-tetrabutyl ammonium, Solaronix SA with trade name N719 dye in absolute ethanol for 48h. The dyeing of nonporous Polymethylmethacrylate (PMMA) fibre coated with nonporous TiO_2 layer was performed in the same dye bath. After complete senetization the excess dye was rinsed away with ethanol. A electrolyte solution was prepared with 0.5 M 4-tert butylpyridine and 0.5 M LiI, 0.05MI2 in 3 methoxypropionitrile (MePRN) with 5 wt% polyvinylidene fluoride-hexafluoro-propylene(PVDE-HFP) added as gelatinizing agent as used by Wang et al., (2004)[56].
Finally gelatinized iodine electrolyte was added next with dip coating from hot solution. Lastly the carbon based counter electrode was coated by means of a gel prepared by exhaustive grinding of 1.4g graphite powder and 0.49 grade carbon black simultaneously.

6.1.1 Manufacturing of photovoltaic fibres as per Bedeloglu et al.,[57-58] method

Bedeloglu et al., have used nontransparent PP as substrate. The PP tape was washed using methanol, isopropanol and water and then dried in N2 atmosphere. Thermal evaporation technique was used to deposit 100nm thick Ag contact layer on PP substrate. A filtered solution of PEDOT: PSS, chemical structure shown in Fig.7, in 5% dimethyl sulfoxide (DMSO) and stirred with 0.1% Triton X-100 to increase the thermal conductivity and cohesiveness properties. Stirred mixture of PEDOT: PSS were deposited on cleaned PP tapes at a thickness of 200 nm by dip coating technique. A blend of P3HT as conjugated polymer and PCBM was stirred upto 24h in chlorobenzene and then dip coated with thickness of 200 nm on top of PEDOT: PSS layer. Finishing of all PV structures was completed in vacuum chambers. An aluminium contact layer of approximately 3 nm thickness was deposited followed by 7nm thick Ag layer as anode. The purpose of Al layer was to avoid short circuiting between Ag and PEDOT: PSS films. The resultant photovoltaic fibre is shown in Fig.8.

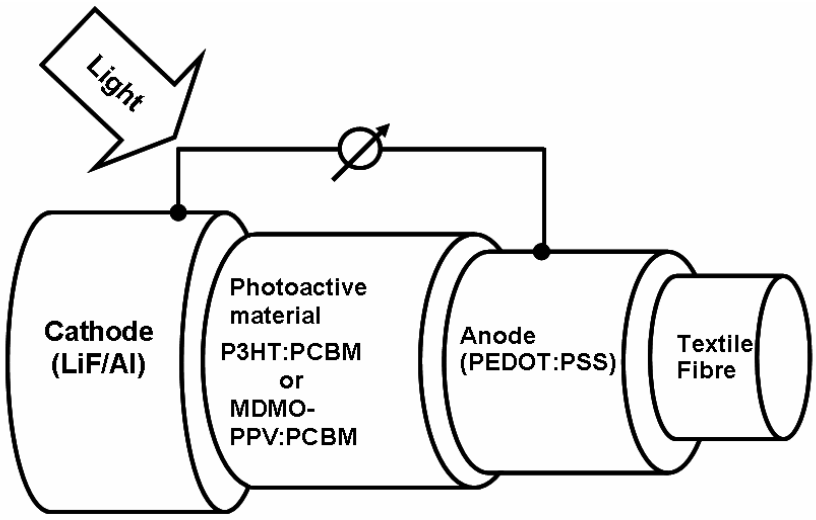

Fig. 8. Schematic representation of Photovoltaic fibre

A group of Turkish scientists has standardized a photovoltaic fibre manufacturing process. A monofilament supply cope is used to supply the basic filament for PV fibre manufacturing. This monofilament is cleaned in a bath by methanol solution and then further clean up by isopropanol solution in second bath. The cleaned fibre surface is washed with distill water followed by drying with dry nitrogen flow. The fibre is immersed in fourth bath containing mixture of PEDOT: PSS followed by oven drying at 50°C for 3 hr. The coated fibres are further immersed in another subsequent bath containing photoactive material solution and then dried out at 50°C for 15 min in oven. After drying, deposition of metal electrode takes place on fibre surface followed by deposition of anti-reflective materials by appropriate deposition technique. Finally a protective layer is laminated on fibre surface. In consequence of this process, a photovoltaic fibre is manufactured and become ready for power harvesting.

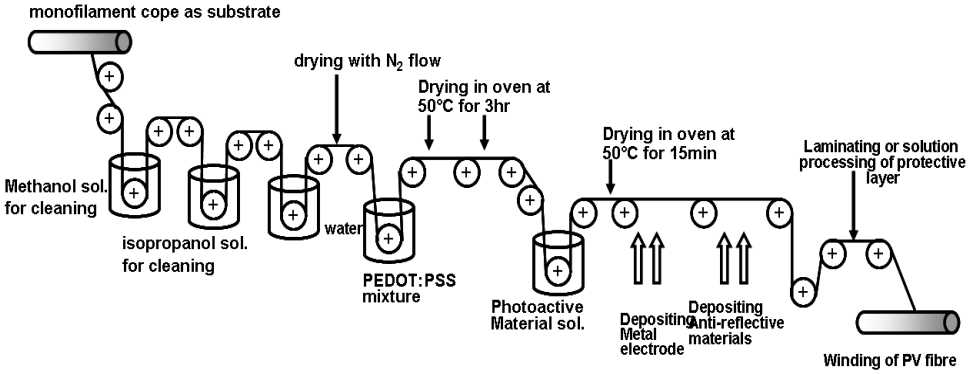

Fig. 9. Manufacturing process of Photovoltaic fibre as suggested by Bedeloglu et al.[21]

6.2 PV textiles by patching (attachment of PV cells to existing textile structures)

Under this technology a solar cell is manufactured separately and then patched onto textile structure by different ways. Thin film solar cells with adequate flexibility can be patched successfully on textile surfaces to impart PV effect. This technique is most appropriate to easily develop both small and large area structures with low cost, and light weight.

In a typical approach thin layers of polymer photovoltaics are laminated onto a textile substrate followed by plasma treatment and coating of PEDOT electrode. Subsequent screen printing of the active material and evaporation of the ultimate electrode finished the polymer photovoltaic that is fully integrated into the textile material[59].

Poly 1,4-(2-methoxy-5-(2-ethylhexyloxy))phenylenevinylene (MEH-PPV) was synthesized by polymerization of α,α′-dibromo-2-methoxy-5-(2-ethylhexyloxy) xylene as described by Neef and Ferraris. The purified MEH-PPV was characterized and found the Mw of 249,000 g mol^{-1} , polydispersity of 5.46 and a peak molecular weight Mp of 157,500 g mol^{-1}. A polyethylene terephthalate (PET) film of thickness 200 µm covered with 50 Ω^2 ITO layer was iched by 20% HCL and 5%HNO_3. A 250 µm thick polyethylene film was thermally laminated on polyethylene terephthalate (PET) surface. Both PET and PE surfaces was plasma treated using a 350-1 low power 3-phase AC plasma system as prescribed by Jensen and Glejbol (2003) in order to obtain optimum etching to get appropriate adherence with textile substrates[60-61].

Plasma treatment was followed by application of PEDOT electrode deformation by spray painting of an inhibited mixture of Iron (III) Tosylate and 3,4-Ethylene-dioxythiopene (EDT) through an aluminum mask. As the temperature reaches 50°C inhibitors are started to evaporate and polymerization of EDT initiated. After completing the polymerization, the PEDOT-coated textile was washed in cold water twice to washout excess tosylate, Iron (II) and inhibitor residuals and finally annealed in air at 50°C for 2 hour.
The materials that can generate electricity by photon conversion are loaded with fibres, yarns and textile structures inherently to offer PV effect.
Chlorobenzene was used to get the solution of MEH-PPV of $3.5gL^{-1}$. The solution was filtered through a filter of 2.7µm filter and coated on polyethylene terephthalate- Indium tin oxide (PET-ITO) substrate by doctor blade coating system. Consequently a homogeneous red colour film is coated on PET-ITO substrate. Cholorobenezene solution of $25gL^{-1}$ was used to get printed pattern of polymer by means of screen-printing. The masks were prepared by using threads of 27 micron diameter with 140, 180,200 and 220 fibres cm^{-1} mesh. Finally, the printed substrates were dried in absence of sunlight. Photovoltaic device was prepared by following manner. The PET-ITO-MEHPPV substrates were incorporated behind a mask and a layer of C60 and aluminium was deposited by thermal evaporation technique. After completing the evaporation the device was laminated on 100 micron PET substrate on electrode side. The screen printed photovoltaic textile was mounted on large evaporator and kept the distance between thermal source and substrate 65 cm. The PV textile holder was rotated at 30 rpm. The aluminium electrodes were prepared in the form of 300 nm thick layers. The evaporation chamber was filled with dry nitrogen after completing the 30 min cooling. Electrodes were integrated with textile substrate by using silver epoxy[62].

7. Characterization of photovoltaic textiles

Characterization of various photovoltaic textiles is essential to prove its performance before send to the market. Various characterization techniques collectively ensures the perfect achievement of the targets to manufacture the desired product.

7.1 Thickness and morphology of photovoltaic textiles

Scanning electron microscope is used to investigate the thickness and morphology of various donor, acceptor layers. Scanning electron microscopes from LEO Supra 35 and others can be used to measure the existence and thickness of various coated layers on various textile surfaces at nanometer level. Various layers on photovoltaic fibres become clearly visible with 50000X magnification. The thickness of the layers can be seen from SEM photographs by bright interface line between the polymer anode and the photoactive layer.

7.2 Current and voltage

In order to characterize the Photovoltaic fibres open circuit voltage, short circuit current density, current and voltage at the maximum power point under an illumination of 100 mW/cm^2 are carried out.
In order to calculate the Photovoltaic efficiency of Photovoltaic textiles, current verses voltage study is essential. To achieve this target a computer controlled sourcemeter equipped with a solar simulator under a range of illumination power is required with proper calibration. All photoelectrical characterizations are advised to conduct under nitrogen or argon atmosphere

inside a glove box to maintain the preciseness of observations. The overall efficiency of the PV devices can be representing by following equation.

$$\eta = \frac{V_{oc} \times I_{sc} \times FF}{P_{in}} = \frac{P_{out}}{P_{in}} \quad (1)$$

Where

V_{oc} is the open circuit voltage (for l=0) typically measured in volt (V)

I_{sc} is the short circuit current density (for V=0) in ampere /square meter (A/m^2)

P_{out} is the output electrical power of the device under illumination

P_{in} the incident solar radiation in (watt/meter^2) W/m^2

FF is the fill factor and can be explained by the following relationship:

$$FF = \frac{I_{mpp} \times V_{mpp}}{I_{sc} \times V_{oc}} \quad (2)$$

where,

V_{mpp} voltage at the maximum power point (MPP)

I_{mpp} is the current at the maximum power point (MPP)

Where the product of the voltage and current is maximized

To assure an objective measurement for precise comparison of various photovoltaic devices, characterization has to be performed under identical conditions.

An European research group has used Keithley 236 source measure unit in dark simulated AM 1.5 global solar conditions at an intensity of 100mW cm^{-2}. The solar simulator unit made by K.H. Steuernagel Lichttechnik GmbH was calibrated with the help of standard crystalline silicon diode. PV fibres were illuminated through the cathode side and I-V characteristics were measured. The semi-logarithmic I-V curves demonstrate the current density versus voltage behaviour of photovoltaic fibres under various conditions. It gives a comparative picture of voltage Vs current density as a function of various light intensities.

Durisch et al., (1996) has developed a computer based testing instrument to measure the performance of solar cells under actual outdoor conditions. This testing system consist a suntracked specimen holder, digital multimeters, devices to apply different electronic loads and a computer based laser printer. Pyranometers, pyrheliometers and a reference cell is used to measure and record the insulation. This instrument is able to test wide dimensions of photovoltaic articles ranging from 3mm X 3mm to 1 meter X 1.5meter. The major part of world's energy scientist community predicts that photovoltaic energy will play a decisive role in any sustainable energy future[63].

7.3 Electroluminescence

The institute for Solar Energy Research Hameln (ISFH) Emmerthal Germany introduced a new technique to characterize the solar cells based on electroluminescence. Electroluminescence can be defined as the emission of light resulting from a forward bias voltage application to the solar cells. The electrons recombine radioactively which are injected into the solar cells by transferring their extra energy to an emitted photon with available holes. The consequence of the electron and hole concentration is able to represent the intensity of the luminescence radiation. A powerful charge coupled device (CCD)

camera is used to capture the images of intensity distribution of the luminescence radiation. Generally, actual solar cells offer inhomogeneous electroluminescence images but for an ideal solar cell it must be homogeneous. A cooled 12 CCD camera is used to capture electroluminescence images. The flexibility to adjust the distance between the camera and the solar cells offers the potential to analyse wide variety of solar cells.

7.4 Fill factor

The quality of solar cells is measured in terms of fill factor. The fill factor for a ideal solar cell is one but as internal resistance of solar cell becomes large or bad contact becomes between layers, fill factor reduces. The fill factor of textile based photovoltaics remains low due to bad quality of electrodes and/or poor contact between different layers of materials[64].
It can be improved towards unit by selection of appropriate textile substrate and further optimization process parameters and processes.

7.5 Mechanical characterization

Textile substrates are subjected to different stresses under various situations. Hence usual tensile characterization is essential for photovoltaic textiles. For tensile testing of PV fibres, the constant rate of extension (CRE) based tensile testing machines are used at 1 mm per minute deformation rate using Linear Variable Differential Transformers (LVDT) displacement sensor. Fracture phenomenon is recorded by means of high resolution video camera integrated with tensile testers.
To study about the adhesion and crack formation in coating on textile structures, generally 30 mm gauge length is used in case of photovoltaic fibres. Fibre strength measuring tensile tester, integrated with an appropriate optical microscope to record the images of specimen at an acquisition rate of about one frame per second is used to record the dynamic fracture of PV fibres. Different softwares are available to analyse the image data like PAXit, Clemex, and Digimizer etc.

7.6 Absorption spectra of solid films

Various spectrophotometers like Varian Carry 3G UV-Visible were used to observe the ultraviolet visible absorption spectra of photovoltaic films. The thin films are prepared to study the absorption spectrum of solid films. In a typical study, a thin film was prepared by spin coating of solution containing 10 mg of P3HT and 8mg of PCBM and 4.5 mg of MDMO-PPV and 18 mg of PCBM (in case of 1:4)/ml with chlorobenzene as solvent. A typical absorption spectra of MDMO-PPV:PCBM and P3HT: PCBM is illustrated in Fig 10.

7.7 X-ray diffraction of photovoltaic structures

Crystallization process is very common phenomenon that takes place during photovoltaic structure development. The content of crystalline and amorphous regions in photovoltaic structures influences the photoactivity of photovoltaic structures. X-ray diffraction technique is capable to characterize the amount of total crystallinity, crystal size and crystalline orientation in photovoltaic structures.
Presently, thin film photovoltaics are highly efficient devices being developed in different crystallographic forms: epitaxial, microcrystalline, polycrystalline, or amorphous. Critical structural and microstructural parameters of these thin film photovoltaics are directly

related to the photovoltaic performance. Various X-ray techniques like x-ray diffraction for phase identification, texture analysis, high-resolution x-ray diffraction, diffuse scattering, x-ray reflectivity are used to study the fine structure of photovoltaic devices[65].

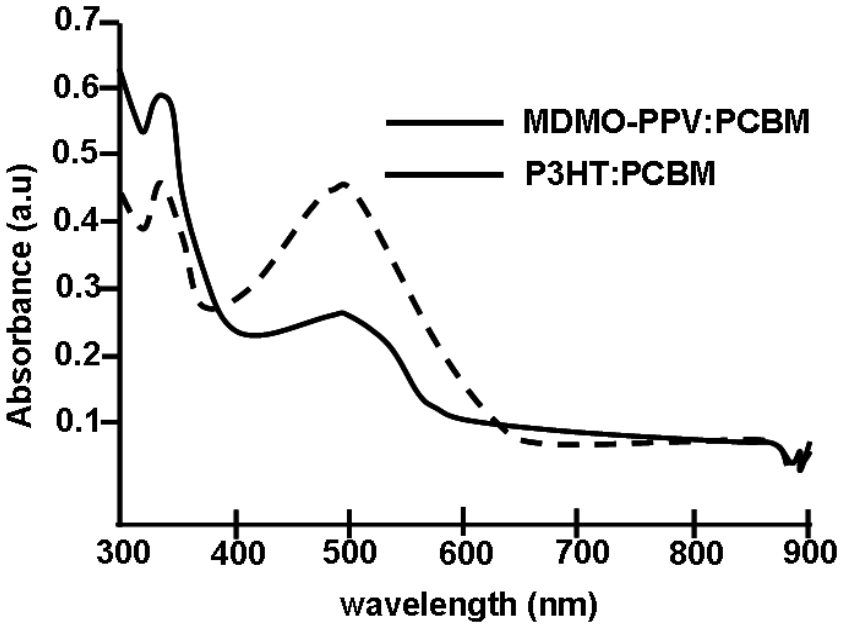

Fig. 10. Absorption spectra[57] for solutions of P3HTPCBM and MDMO-PPV-PCBM (with permission)

7.8 Raman spectroscopy

The Raman Effect takes place when light rays incidents upon a molecule and interact with the electron cloud and the bonds of that molecule. Spontaneous Raman effect is a form of scattering when a photon excites the molecule from the ground state to a virtual energy state. When the molecule relaxes it emits a photon and it returns to a different rotational or vibrational state.

Raman spectroscopy is majorly used to confirm the chemical bonds and symmetry of molecules. It provides a fingerprint to identify the molecules. The fingerprint region for organic molecules remains in the (wavenumber) range of 500–2000 cm^{-1}. Spontaneous Raman spectroscopy is used to characterize superconducting gap excitations and low frequency excitations of the solids. Raman scattering by anisotropic crystal offers information related to crystal orientation. The polarization of the Raman scattered light with respect to the crystal and the polarization of the laser light can be used to explore the degree of orientation of crystals[66].

The in situ morphological and optoelectronic changes in various photovoltaic materials can be observed by observing the changes in the Raman and photoluminescence (PL) feature with the help of a spectrometer. Various spectrums can be recorded at a definite integration time after avoiding any possibility of laser soaking of the sample[67].

8. Some facts about the photovoltaic textiles

- To achieve a highly efficient photovoltaic device, solar radiation needs to be efficiently absorbed. In case of solar cell the absorption of light causes electron hole pairs which are split into free carriers at the interface between the donor and the acceptor material.
- Active areas for photovoltaic fibres are generally found between 4 and 10mm^2.
- The power conversion efficiency of the MDMO-PPV:PCBM based photovoltaic fibre was higher than the P3HT:PCBM based photovoltaic fibres
- Due to circular cross-sectional shape of photovoltaic fibres, the light is absorbed at different angles
- Generally the photoactive layer thickness remain approximately between 280-350nm. A thick film can absorb more light compared to a thin film. By the increase of film thickness, the electrical field and the number of charge carriers decrease and consequently a decrease in the external quantum efficiency of the devices is observed. Although, the film thickness is restricted in presence of low-charge carrier. The optimum thickness is required to provide both maximum light absorption and maximum charge collection at the same fraction of moment. Optimization of thickness of various layers of photovoltaic fibres provides the possibility to increase the power conversion efficiency of polymer-based solar cells.
- The thickness of the layers for optimal photovoltaic fibre can be controlled by solution concentration and dipping time.
- Photovoltaic fibre based organic solar cells can be curled and crimped without losing any photovoltaic performance from their structure.
- Low power conversion efficiency of photovoltaic textiles is the real challenge in this field and can be improved by significant improvement in existing photovoltaic material and techniques. In case of organic solar cells, the optical band gap is very critical and it must be as narrow as possible because the polymers with narrow band gap are able to absorb more light at longer wavelengths, such as infrared and near-infrared. Hence low band gap polymers (<1.8 eV) can be used as better alternative for higher power harvesting efficiency in future if they are sufficiently flexible[68,69].
- The incorporation of C60 barrier layer can improve the performance of photovoltaic textiles.
- Generally the performance of freshly made photovoltaic textiles was found best because cell degradation happens fast when sun illumination takes place in absence of O_2 barriers.
- The self life of polymer based photovoltaics is short under ambient conditions[70].

9. Photovoltaic textile, developments at international level

The incorporation of polymer photovoltaics into textiles was demonstrated by Krebs et a., (2006) by two different strategies. Simple incorporation of a polyethyleneterphthalate (PET) substrate carrying the polymer photovoltaic device prepared by a doctor blade technique necessitated the use of the photovoltaic device as a structural element[71].
The total area of the device on PET was typically much smaller than the active area due to decorative design of aluminium electrode. Elaborate integration of the photovoltaic device into the textile material involved the lamination of a polyethylene (PE) film onto a suitably

transparent textile material that was used as substrate. Plasma treatment of PE-surface allowed the application of a PEDOT electrode that exhibited good adherence. Screen printing of a designed pattern of poly 1,4-(2-methoxy-5-(2-ethylhexyloxy) phenylenevinylene (MEH-PPV) from chlorobenzene solution and final evaporation of an aluminum electrode completed the manufacturing of power generating device. The total area of the textile device was 1000 cm^2 (25cm x 40cm) while the active area (190 cm^2) was considerably smaller due to the decorative choice of the active material.
Konarka Inc. Lowell, Mass., U.S.A demonstrated a successful photovoltaic fiber. Presently, a German company is engaged with Ecole Polytechnique Fédérale de Lausanne (EPFL) to optimize the fiber properties and weave it into the power-generating fabric. Solar textiles would able to generate renewable power generation capabilities. The photovoltaic fibres are able to woven in fabric form rather than attached or applied on other surfaces where integration remains always susceptible. The structures woven by photovoltaic fibres are able to covert into fabric, coverings, tents and garments.
Patterned photovoltaic polymer solar cells can be incorporated on PET clothing by sewing through the polymer solar cell foil using an ordinary sewing machine. Connections between cells were made with copper wire that could also be sewn into the garment. The solar cells were incorporated into a dress and a belt as shown in Fig.11 (Tine Hertz).

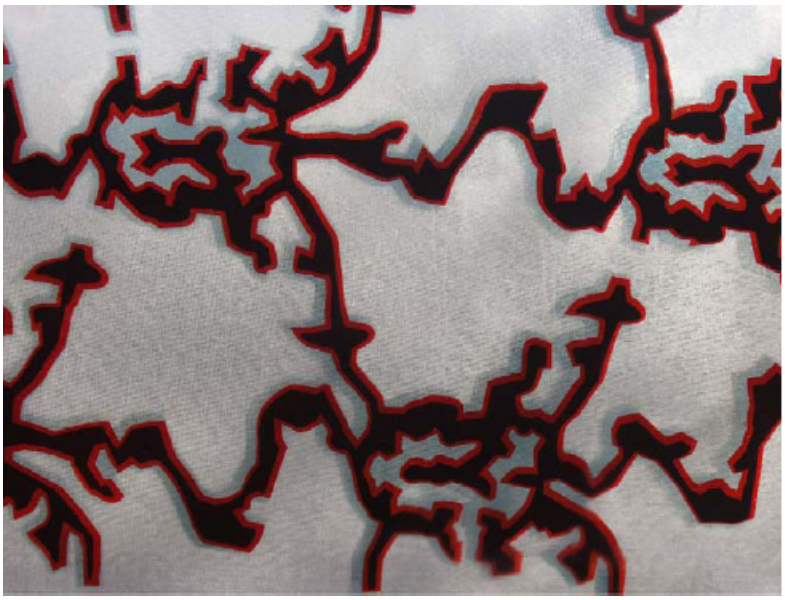

Fig. 11. Textile solar cell pattern designed by Tine Hertz and Maria Langberg of Danmarks Designkole

Shafarman et al., (2003) demonstrated thin film solar cells by using $CuInGaSe_2$ photovoltaic polymers and this film is more suitable for patching onto clothing into different patterns[72]. The polymer photovoltaics technology is in its infancy stage and many gaps need to be bridged before commercialization. Prototype printing machines are useful to apply PVs on textile surface into decorative pattern as shown in Fig. 11, 12,13.

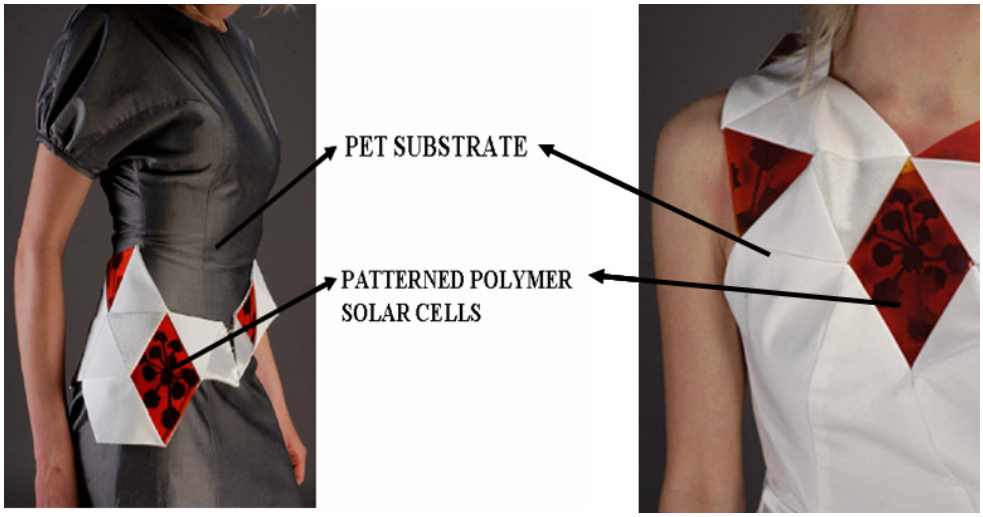

Fig. 12. Patterned polymer cell (with permission)

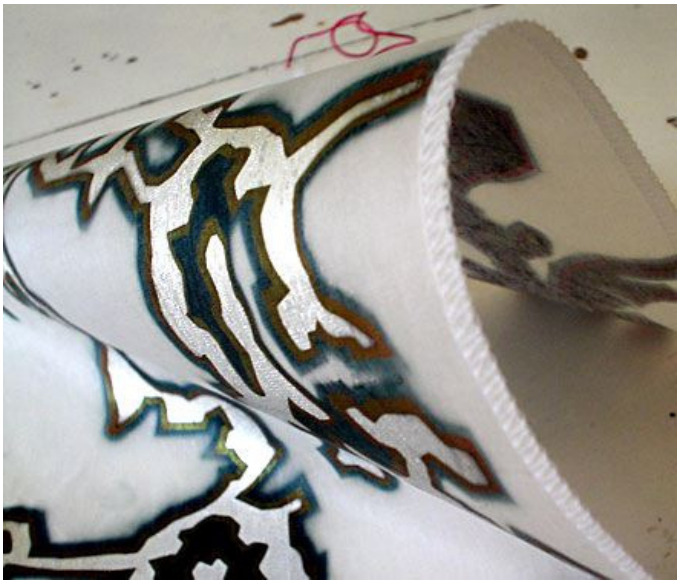

Fig. 13. Photovoltaic decorative patterns

Massachusetts Institute of Technology (MIT) Cambridge, Massachusetts revealed that the integration of solar cell technology in architecture creates designs for flexible photovoltaic materials that may change the way buildings receive and distribute energy. Sheila Kennedy of (MIT) used 3-D modeling software for her solar textiles designs, generating membrane-like surfaces that can become energy-efficient cladding for roofs or walls[73]. Solar textiles may also be used like tents as shown in Fig. 14.

Fig. 14. Photovoltaic textile as a tent (with permission)

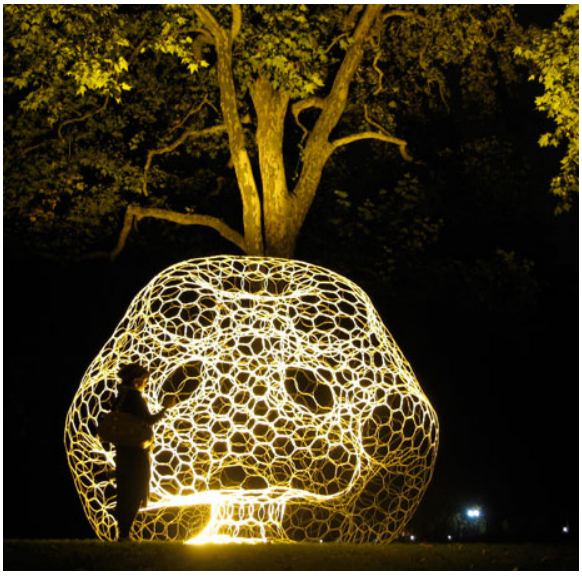

Fig. 15. A typical example of photovoltaic textile (with permission)

- Commission for Technology and Innovation (CTI) Switzerland also exhibited a keen interest in the development of photovoltaic textiles.
- Thuringian Institute of Textiles and Plastics Research (TITK) registered their remarkable presence in order to develop photovoltaic textiles[74].
- J Wilson and R Mather have created Power Textiles Ltd, a spin-off from Heriot-Watt University, Scotland to develop a process for the direct integration of solar cells on textiles.
- Konarka is developing solar photovoltaic fabric with joint effort of the university Ecole Polytechnique Fédérale de Lausanne (EPFL), Switzerland. Konarka has claimed that

they can produce a photovoltaic fiber. Presently, the Company is working with EPFL to optimize the fiber structure and weave it into the first power-generating fabric. Solar textiles would open up additional application areas for photovoltaics since renewable power generation capabilities can be tightly integrated

- In 2002, Konarka became the first company in the United States to license Dr. Michael Grätzel's dye-sensitized solar cell technology, which augmented its own intellectual property.
- Thuringian Institute of Textiles and Plastics Research (TITK), Breitscheidstraße Rudolstadt Germany, is a technically-oriented research institute, carrying out fundamental and applied research on PV textiles suitable to easily commercialize. The institute supports small and medium-sized enterprises in their innovation works with interdisciplinary scientific knowledge, innovative ideas, and knowledge of the industry and provision of modern technical infrastructure.
- Professor John Wilson and Dr Robert Mather of School of Textiles and Design, formerly the Scottish College of Textiles have created Power Textiles Ltd, a spin-off from Heriot-Watt University, to develop a process for the direct integration of solar cells on textiles.
- In a research work at American Institute of Physics, multiwall carbon nanotubes are introduced into poly(3-hexylthiophene) and [6,6] phenyl C_{61} butyric acid methyl fullerene, bulk heterojunction organic photovoltaic devices after appropriate chemical modification for compatibility with solution processable photovoltaics. To overcome the problem of heterogeneous dispersion of carbon nanotubes in organic solvents, multiwall CNT are functionalized by acid treatment. Pristine and acid treated multiwall carbon nanotubes have been incorporated into the active layer of photovoltaic polymers which results a fill factor of 0.62 and power harvesting efficiency of 2.3% under Air Mass 1.5 Global[75].
- Dephotex is going to develop photovoltaic textiles based on novel fibre under collaboration with European Union.
- Photovoltaic tents are developed by integration of flexible solar panels made by thin film technology by patching on tent fabric surface. The solar cells can run ventilation systems, lighting and other critical electrical functions, avoiding the need for both generators and the fuel to run them.

The integration of photovoltaic technology with UV absorption technology will open very smart passages to new product development. However, the above opinion is only a hypothesis of author. The textile materials which are stable against ultraviolet rays are more suitable to work as basic substrate. However, the production and integration of photovoltaic fibres into fabric form will solve many problems concerned about simple incorporation of a polymer photovoltaic on a textile substrate directly or by lamination of a thin layer of PVs onto textile material followed by plasma treatment and application of a PEDOT electrode onto the textile materials.

10. Conclusions

The incorporation of polymeric photovoltaics into garments and textiles have been explored new inroads for potential use in ''intelligent clothing'' in more smart ways. Incorporation of organic solar cells into textiles has been realized encouraging performances. Stability issues need to be solved before commercialization of various photovoltaic textile manufacturing techniques. The functionality of the photovoltaic textiles does not limited by mechanical stability of photovoltaics. Polymer-based solar cell materials and manufacturing techniques

are suitable and applicable for flexible and non-transparent textiles, especially tapes and fibers, with transparent outer electrodes.
The manufactured photovoltaic fibres may also be utilized to manufacture functional yarns by spinning and then fabric by weaving and knitting. Fibres and yarns subjected to various mechanical stresses during spinning, weaving and knitting may possibly damage the coating layers of photovoltaic fibres. These sensitive and delicate structures must be protected by applying special protective layers by noble coating techniques to produce photovoltaic textiles. Photovoltaic tents, curtains, tarpaulins and roofing are available to utilize the solar power to generate electricity in more green and clean fashion.

11. References

[1] Aernouts, T. 19th European Photovoltaics Conference, June 7–11, Paris, France, 2004.
[2] Lund P D Renewable energy 34, 2009, 53
[3] Yaksel I Renewable energy 4, 2008, 802
[4] European photovoltaic Ind. Asso. Global market outlook for photovoltaic until 2012. www.epia.org
[5] Gunes S, Beugebauer H and Saricftci N S Chem Rev. 107, 2007, 1324
[6] Coakley KM, ,cGehee M D, Chem Mater. 16,2004,4533
[7] Organic Photovoltaics: Mechanisms, Materials, and Devices, ed. S.-S. Sun and N. S. Sariciftci, Taylor & Francis, London, 2005.
[8] Organic Photovoltaics: Concepts and Realization, ed. C. J. Brabec, V. Dyakonov, J. Parisi and N. S. Sariciftci, Springer-Verlag, Heidelberg, 2003.
[9] Tang, C.W. Two-layer organic photovoltaic cell. Applied Physics Letters, 48, (1986) 183.
[10] Sariciftci, N.S., Smilowitz, L., Heeger, A.J. and Wudl, F. (1992) photoinduced electron transfer from a conducting polymer to buckminsterfullerene. Science, 258, 1992, 1474.
[11] Spanggaard, H. and Krebs, F.C. (2004) A brief history of the development of organic and polymeric photovoltaics. Solar Energy Materials and Solar Cells, 83, 125.
[12] Granstrom, M., Petritsch, K., Arias, A.C., Lux, A., Andersson, M.R. and Friend, R.H. (1998) Laminated fabrication of polymeric photovoltaic diodes. Nature, 395, 257.
[13] Yu J W, Chin B D, Kim J K and Kang N S Patent IPC8 Class: AH01L3100FI, USPC Class: 136259, 2007
[14] http://www.coatema.de/ger/downloads/veroeffentlichungen/news/0701_Textile%20Month_GB.pdf
[15] Krebs F C., Fyenbo J and Jørgensen Mikkel "Product integration of compact roll-to-roll processed polymer solar cell modules: methods and manufacture using flexographic printing, slot-die coating and rotary screen printing" *J. Mater. Chem.*, 20, 2010, 8994-9001
[16] Krebs F C., Polymer solar cell modules prepared using roll-to-roll methods: Knife-over-edge coating, slot-die coating and screen printing Solar Energy Materials and Solar Cells 93, (4), 2009, 465-475
[17] Luo P, Zhu Cand Jiang G Preparation of $CuInSe_2$ thin films by pulsed laser deposition the Cu–In alloy precursor and vacuum selenization, Solid State Communications, 146, (1-2), 2008, 57-60
[18] Solar energy: the state of art Ed: Gordon J Pub: James and James Willium Road London, 2001
[19] Loewenstein T., Hastall A., Mingebach M., Zimmermann Y., Neudeck A. and Schlettwein D., *Phys. Chem. Chem. Phys.*, 2008, 10,1844.
[20] Lincot D. and Peulon S., *J. Electrochem. Soc.*, 1998, 145, 864.
[21] Bedeloglua A,*, Demirb A, Bozkurta Y, Sariciftci N S, Synthetic Metals 159 (2009) 2043–2048
[22] Pettersson LAA, Ghosh S, Inganas O. Org Electron 2002;3:143.

[23] Kim JY, Jung JH, Lee DE, Joo J. Synth Met 2002;126:311.
[24] Kim WH, Ma¨kinen AJ, Nikolov N, Shashidhar R, Kim H, Kafafi ZH. Appl Phys Lett 80, (2002), 3844.
[25] Jonsson SKM, Birgerson J, Crispin X, Greczynski G, Osikowicz W, van der Gon AWD, SalaneckWR, Fahlman M. Synth. Met 1, 2003;139:
[26] Ouyang J, Xu Q, Chu C W, Yang Y,*, Lib G, Shinar Joseph S On the mechanism of conductivity enhancement in poly(3,4-ethylenedioxythiophene) : poly(styrene sulfonate) film through solvent treatment" Polymer 45, 2004, 8443–8450
[27] Grätzel M., *Nature*, 414, 338 (2001)
[28] Könenkamp R., Boedecker,K. Lux-Steiner M. C., Poschenrieder M., Zenia F., Levy-Clement C. and Wagner S., *Appl. Phys. Lett.*, 77, 2575 (2000)
[29] Boyle D. S., Govender K. and O'Brien P., *Chem Commun.*, 1, 80 (2002)
[30] http://www.caburn.com/resources/downloads/eVapcat.pdf
[31] Hoth, C.N., Choulis, S.A., Schilinsky, P. and Brabec, C.J. "High photovoltaic performance of inkjet printed polymer: fullerene blends" Advanced Materials, 19, 2007, 3973.
[32] M Pagliaro, G Palmisano, and R Ciriminna "Flexible Solar Cells" WILEY-VCH Verlag GmbH & Co. KGaA, Weinheim, 2008, 98-119
[33] Bundgaard E and Krebs F C Low band gap polymers for organic photovoltaics Solar Energy Materials and Solar Cells 91 (11), 2007, 954-985
[34] Kroon R, Lenes M, Jan C. Paul H, Blom W. M, Boer B de "Small Bandgap Polymers for Organic Solar Cells (Polymer Material Development in the Last 5 Years)" Polymer Reviews, 48, (3), 2008 , 531 - 582
[35] Rajahn M, Rakhlin M, Schubert M B "Amorphous and heterogeneous silicone based films" MRS Proc. 664, 2001
[36] Schubert MB, Werner J H, Mater. Today 9(42), 2006
[37] Drew C, Wang X Y, Senecal K, J of Macro. Mol. Sci Pure A 39, 2002, 1085
[38] Baps B, Eder K M, Konjuncu M, Key Eng. Mater. 206-213, 2002, 937
[39] Gratzel M, Prog. Photovolt: Res. Appl. 8, 2000, 171
[40] Bayinder M, Shapira O, Sayain Hazezewski D Viens J Abouraddy A F, Jounnopoulas A D and Fink Y Nature Mat. 4, 2005, 820
[41] Verdenelli M, Parole S, Chassagneux F, Lettof J M, Vincent H and Scharff J P, J of Eur. Ceram. Soc. 23, 2003, 1207
[42] Xie C, Tong W, Acta Mater, 53, 2005, 477
[43] Muller D, Fromm E Thin Mater. Solid Films 270, 1995, 411
[44] Hu M S and Evans A G, Acta Mater, 37, 1998, 917
[45] Yang Q D, Thouless M D, Ward S M, J of Mech Phys Solids, 47, 1999, 1337
[46] Agrawal D C, Raj R, Acta Mater, 37, 1989, 1265
[47] Rochal G, Leterrier Y, Fayet P, Manson J Ae, Thin Solid Films 437,2003, 204
[48] Park S H, Choi H J,Lee S B, Lee S M L, Cho S E, Kim K H, Kim Y K, Kim M R and Lee J K "Fabrications and photovoltaic properties of dye-sensitized solar cells with electrospun poly(vinyl alcohol) nanofibers containing Ag nanoparticles" Macromolecular Research 19(2), 2011, 142-146
[49] Ramiera J., Plummera C.J.G., Leterriera Y., Mansona J.-A.E.,_, Eckertb B., and Gaudianab R. "Mechanical integrity of dye-sensitized photovoltaic fibers" Renewable Energy 33 (2008), 314–319
[50] Hamedi M, Forchheimer R and Inganas O Nat Mat. 6, 2007, 357
[51] Bayindir M, Sorin F, Abouraddy A F, Viens J, Hart S D, Joannopoulus J D, Fink Y Nature 431, 2004, 826
[52] Yadav A, Schtein M, Pipe K P J of Power Sources 175, 2008, 909

[53] Coner O, Pipe K P Shtein M Fibre based organic PV devices Appl. Phys. Letters 92, 2008, 193306
[54] Ghas A P, Gerenser L J, Jarman C M, Pornailik J E, Appl. Phys. Lett. 86, 2005, 223503
[55] Regan R O, Gratzel M, Nature 353, 1991, 737
[56] Wang P, Zakeeruddin S M, Gratzel M and Fluorine J Chem. 125, 2004, 1241
[57] Bedeloglu A C, Demir A, Bozkurt Y and Sariciftci N S "A photovoltaic fibre design for smart textiles" Text. Res. J 80(11), 2010, 1065-1074
[58] Bedeloglu A C, Koeppe R, Demir A, Bozkurt Y and Sariciftci N S "Development of energy generating photovoltaic textile structures for smart application" Fibres and Polymers 11(3), 2010, 378-383
[59] Krebs F C, Biancardo M, Winther-Jensen B, Spanggard H and Alstrup J "Strategies for incorporation of polymer photovoltaics into garment and textiles" Sol. Ener. Mat. &Sol Cells 90, 2006, 1058-1067
[60] Neef C. J. and Ferraris J. P. MEH-PPV: Improved Synthetic Procedure and Molecular Weight Control" Macromolecules, 2000, 33 (7), pp 2311–2314
[61] Winther –Jensen B and Glejbol K "Method and apparatus for the excitation of a plasma" US Patent US6628084, Published on Sept., 9, 2003
[62] Bedeloglu A, Koeppe R, Demir A, Bozkurt Y and Sariciftci N S "Development of energy generating PV textile structure for smart applications" Fibres and Polym. 11(3), 2010, 378
[63] Durisch W, Urban J and Smestad G "Characterization of solar cells and modules under actual operating conditions" WERS 1996, 359-366
[64] Kim M S, Kim B G and Kim J "Effective Variables to Control the Fill Factor of Organic Photovoltaic Cells" ACS Appl. Mater. Interfaces, , 1 (6), 2009,1264–1269
[65] Wang W, Xia G , Zheng J , Feng L and Hao R "Study of polycrystalline ZnTe(ZnTe:Cu) thin films for photovoltaic cells" Journal of Materials Science: Materials in Electronics 18(4), 2007, 427-431
[66] Khanna, R.K. "Raman-spectroscopy of oligomeric SiO species isolated in solid methane". Journal of Chemical Physics 74 (4), (1981) 2108
[67] Miller S, Fanchini G, Lin Y Y, Li C, Chen C W, Sub W F and Chhowallaa M "Investigation of nanoscale morphological changes in organic photovoltaics during solvent vapor annealing" J. Mater. Chem., 2008, 18, 306–312
[68] Perzon E, Wang X, Admassie S, Inganas O, and Andersson M R "An alternative low band gap polyflourene for optoelectronic devices" Polymer 47, 2006, 4261-4268
[69] Campos L M, Tontcheva A, Gunes S, Sonmez G, Neugebauer H, Sariciftci N S and Wudl F "Extended photocurrent spectrum of a low band gap polymer in a bulk heterojunction solar cell" Chem. Mater. 17, 2005, 4031-4033
[70] Krebs F C, Carle J E, Cruys-Bagger N, Anderson M, Lilliedal M R, Hammond M A and Hvidt S, Sol. Eng Mater. Sol. Cells 86, 2005, 499
[71] Krebs F.C Spanggaard H.. Sol. Energy Mater. Sol. Cells 83 (2004) 125
[72] Shafarman, W.N., Stolt L., in: Luque A., and Hegedus S. (Eds.), Handbook of Photovoltaic Science and Engineering, Wiley, New York, 2003.
[73] http://www.silvaco.com.cn/tech_lib_TCAD/tech_info/devicesimulation/pdf/Solar_Cell.pdf
[74] www.titk.de/en/home/home.htm
[75] Applied Physics Letters / Volume 97 / Issue 3, 2010 / NANOSCALE SCIENCE AND DESIGN

4

Dilute Nitride GaAsN and InGaAsN Layers Grown by Low-Temperature Liquid-Phase Epitaxy

Malina Milanova[1] and Petko Vitanov[2]
[1]*Central Laboratory of Applied Physics, BAS*
[2]*Central Laboratory of New Energy & New Energy Sources, BAS*
Bulgaria

1. Introduction

A critical goal for photovoltaic energy conversion is the development of high-efficiency, low cost photovoltaic structures which can reach the thermodynamic limit of solar energy conversion. New concepts aim to make better use of the solar spectrum than conventional single-gap cells currently do. In multijunction solar cells based on III-V heterostructures, better spectrum utilization is obtained by stacking several solar cells. These cells have achieved the highest efficiency among all other solar cells and have the theoretical potential to achieve efficiencies equivalent to or exceeding all other approaches. Record conversion efficiencies of 40.7 % (King, 2008) and 41,1 (Guter at al., 2009) under concentrated light for triple- junction allows hoping for practical realization of gianed values of efficiency in more multiplejunction structures. The expectations will be met , if suitable novel materials for intermediate cascades are found, and these materials are grown of an appropriate quality. Models indicate that higher efficiency would be obtained for 4-junction cells where 1.0 eV band gap cell is added in series to proven InGaP/GaAs/Ge triple-junction structures. Dilute nitride alloys such as GaInAsN, GaAsSbN provide a powerful tool for engineering the band gap and lattice constant of III-V alloys, due to their unique properties. They are promising novel materials for 4- and 5-junction solar cells performance. They exhibit strong bowing parameters and hold great potential to extend the wavelength further to the infrared part of the spectrum.

The incorporation of small quantity of nitrogen into GaAs causes a dramatic reduction of the band gap (Weyeres et al., 1992), but it also deteriorates the crystalline and optoelectronic properties of the dilute nitride materials, including reduction of the photoluminescence intensity and lifetime, reduction of electron mobility and increase in the background carrier concentration. Technologically, the incorporation probability of nitrogen in GaAs is very small and strongly depends on the growth conditions. GaAsN- based alloys and heterostructures are primarily grown by metaloorganic vapor-phase epitaxy (MOVPE) (Kurtz et all, 2000; Johnston et all, 2005)) and molecular-beam epitaxy (MBE) (Kurtz et al. 2002; Krispin et al, 2002; Khan et al, 2007), but the material quality has been inferior to that of GaAs. A peak internal quantum efficiency of 70 % is obtained for the solar cells grown by MOCVD (Kurtz et al. 1999). Internal quantum values near to unit are reported for p-i-n

GaInAsN cell grown by MBE (Ptak et al 2005), but photovoltages in this material are still low. Recently chemical-beam epitaxy (Nishimura et al., 2007; Yamaguchi et al, 2008; Oshita et al, 2011) has been developed in order to improve the quality of the grown layer, but today it remains a challenge to grow dilute nitride materials with photovoltaic (PV) quality.
In this chapter we present some results on thick GaAsN and InGaAsN layers, grown by low-temperature Liquid-Phase Epitaxy (LPE). In the literature there are only a few works on dilute nitride GaAsN grown by LPE (Dhar et al., 2005; Milanova et al., 2009) and some data for InGaAsN (Vitanov et al., 2010).

2. Heteroepitaxy nucleation and growth modes

The mechanism of nucleation and initial growth stage of heteroepitaxy dependence on bonding between the layer and substrate across the interface. Since the heteroepitaxy requires the nucleation of a new alloy on a foreign substrate the surface chemistry and physics play important roles in determining the properties of heteroepitaxial growth. In the classical theory, the mechanism of heterogeneous nucleation is determined by the surface and interfacial free energies for the substrate and epitaxial crystal.
Three classical modes of initial growth introduced at first by Ernst Bauer in 1958 can be distinguished: Layer by layer or Frank–Van der Merwe FM two-dimension mode (Frank–Van der Merwe, 1949), Volmer–Weber VW 3D island mode (Volmer–Weber, 1926), and Stranski–Krastanov SK or layer-plus-island mode (Stranski–Krastanov, 1938) as the intermediate case. The layer by layer growth mode arises when dominates the interfacial energy between substrate and epilayer material. In the opposite case, for the weak interfacial energy when the deposit atoms are more strongly bound to each other than they are to the substrate, the island (3D), or VW mode results. In the SK case, 3D island are formed on several monolayers, grown in a layer-by-layer on a crystal substrate.
Schematically these growth modes are shown in the Figure 2.1.

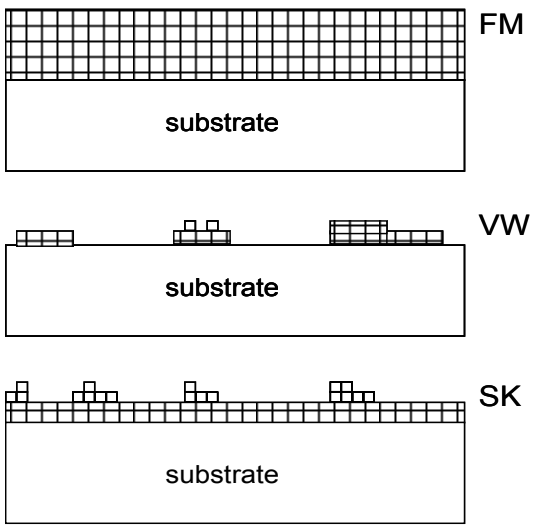

Fig. 2.1. Schematic presentation of FM, VW and SK growth modes

The growth modes in heteroepitaxy are defined based on thermodynamic models.
The sum of the film surface energy and the interface energy must be less than the surface energy of the substrate in order for wetting to occur and then layer by layer growth is expected. The VW growth mode is to be expected for a no wetting epitaxial layer. If γ and γ_0 are the surface free energies of the layer and substrate, respectively, and γ_i is the interfacial free energy the change in the free energy $\Delta\gamma$ associated with covering the substrate with epitaxial layer is:

$$\Delta\gamma = \gamma + \gamma_i - \gamma_0 \tag{2.1}$$

If minimum energy determinates the mode for nucleation and growth, the dominated mechanism will be two-dimensional for $\Delta\gamma < 0$ and three-dimensional for $\Delta\gamma > 0$. However, even in the case of a wetting epitaxial layer ($\Delta\gamma < 0$), the existence of mismatch strain can cause islanding after the growth of a few monolayers. This is because the strain energy , increases linearly with the number of strained layers. At some thickness, $\gamma+\gamma i$ exceeds γ_0 and the growth mode transforms from FM to SK resulting in 3D islands on the 2D wetting layer. Whereas it is clear that the VW growth mode is expected for a nonwetting epitaxial layer, the behavior of a wetting deposit is more complex and requires further consideration. Often the interfacial contribution in the limit of zero lattice mismatch and weak chemical interactions between the film and substrate at the interface can be neglected in comparison to the surface free energy ($\gamma i \approx 0$). In this case the growth mode is determined entirely by the surface free energies of the film and substrate material.
Instead of these three main growth modes additional growth modes and epitaxial growth mechanisms could be distinguished (Scheel, 2003): columnar growth, step flow mode, step bunching, and screw-island growth.
The structural quality of the layer and surface morphology strongly depend on the growth method and the main growth parameters: supersaturation, misorientation of the substrate and the difference of lattice constants between substrate and the epitaxial layer.
In the case of flat substrate, the supersaturation increases until surface nucleation of a new monolayer occurs and its growth cover the substrate, followed by the nucleation of the next monolayer. For compound of limited thermodynamic stability or with volatile constituents like GaAs, GaN, SiC the appearance of the growth mode is largely predetermined by the choice of the growth method due to the inherent high supersaturation in epitaxy from the vapor phase and adjustable low supersaturation in LPE.
The FM growth mode in LPE can only be obtained at quasi-zero misfit as it is established from thermodynamic theory (Van der Merwe, 1979) and demonstrated by atomistic simulations using the Lennard–Jones potential (Grabow and Gilmer, 1988) and also at low supersaturation. At high supersaturation a high thermodynamic driving force leads to a high density of steps moving with large step velocities over the surface and causes step bunching.
The VW mode is typical of VPE. Due to the high supersaturation a large number of surface nuclei arise, which then spread and form three-dimensional islands, that finally coalesce to a compact layer. Continued growth of a layer initiated by the VW mode often shows columnar growth which is a common feature in epitaxy of GaN and diamond. (Hiramatsu *et al*., 1991). The SK mode has been demonstrated by MBE growth of InAs onto GaAs substrate (Nabetani *et al*., 1994).

Observations, analyses and measurements of LPE GaAs on the formation of nuclei and surface terraces show that nuclei grow into well-defined prismatic hillocks bounded by only {100} and {111} planes and they are unique to each substrate orientation, and hillocks tend to coalesce into chains and then into parallel surface terraces (Mattes & Route, 1974). The hillock boundaries may cause local strain fields and variation of the incorporation rates of impurities and dopants, or the local strain may getter or rejects impurities during annealing processes. This inhomogeneity may be suppressed by providing one single step source or by using substrates of well-defined small misorientation. The FM growth mode and such homogeneous layers can only be achieved by LPE or by VPE at very high growth temperatures.

Only at low supersaturation, nearly zero misfit and small misorientation of the substrate the layer by-layer growth mode can be realized and used to produce low dislocation layers for ultimate device performance. Two-dimensional growth is desirable because of the need for multilayered structures with flat interfaces and smooth surfaces. A notable exception is the fabrication of quantum dot devices, which requires three-dimensional or SK growth of the dots. Even here it is desirable for the other layers of the device to grow in a two-dimensional mode. In all cases of heteroepitaxy, it is important to be able to control the nucleation and growth mode.

3. Pseudomorphic and metamorphic growth

One of the main requirements for high quality heterostructure growth is the lattice constant of the growth material to be nearly the same as those of the substrate. In semiconductor alloys the lattice constant and band gap can be modified in a wide range. The lattice parameter difference may vary from nearly 0 to several per cent as in the cases of GaAs-AlAs and InAs-GaAs system, respectively. The growth of dilute nitride alloys is difficult because of the wide immiscibility range, a large difference in the lattice constant value and very small atom radius of N atoms. The growth of thick epitaxial layers creates many problems which absent in the quantum-well structures.

At the initial stage of the growth when the epitaxial layer is of different lattice constant than the substrate in-plane lattice parameter of the growth material will coherently strain in order to match the atomic spacing of the substrate. The elastic energy of deformation due to the misfit in lattice constant destroys the epilayer lattice. The substrate is sufficiently thick and it remains unstrained by the growth of the epitaxial layer. If the film is thin enough to remain coherent to the substrate, then in the plane parallel to the growth surface, the thin film will adopt the in-plane lattice constant of the substrate, i.e. $a_{\parallel} = a_o$, where $a_{\parallel}$ is the in-plane lattice constant of the layer and a_o is the lattice constant of the substrate. This is the case of pseudomorphic growth, and the epitaxial layer is pseudomorphic. If the lattice constant of the layer is larger than that of the substrate as in the case of InGaAs on GaAs, under the pseudomorphic condition growth the lattice of the layer will be elastically compressed in the two in-plane directions. The lattice constant of the layer in the growth direction perpendicular to the interface (the so-called out-of plane direction) will be strained according the Poison effect and will be larger than the unstrained value and the layer lattice will tense in the growth direction. Schematically this situation is illustrated in Figure 3.1.

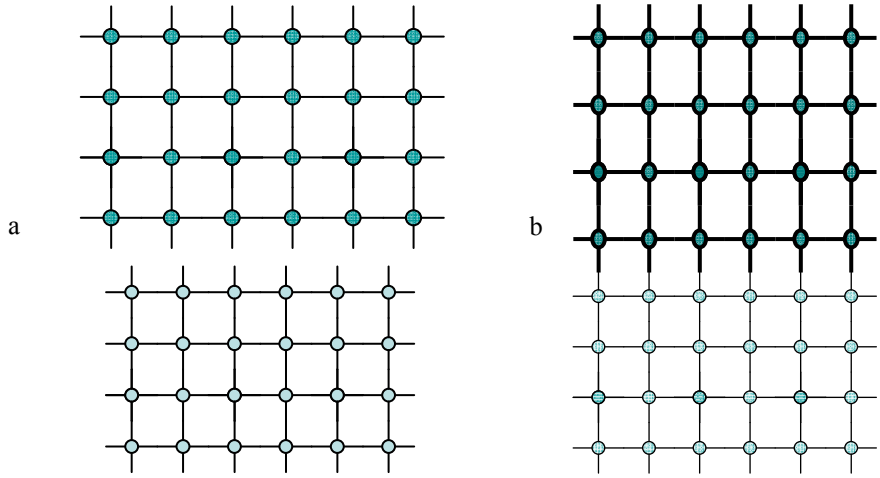

Fig. 3.1. Schematic presentation of atom arrangement for two materials with different cubic lattice constant: a) before growth; b) for pseudomorphic growth

In the case of the smaller lattice constant of the growth layer (GaAsN on GaAs for example), $a < a_o$ the layer will be elastically tensed in two in-plane directions and compressed in the growth directions (the out-of-plane lattice constant will be smaller than substrate lattice constant). Under pseudomorphic growth conditions the cubic lattice doesn't remain cubic: $a_{II} = a_o \neq a_\perp$. The out -of-plane lattice constant could be determined from the equation:

$$a_\perp = a[1 - D(a_{II}/a - 1)] \tag{3.1}$$

Where:
$a_\perp$ - out-of-plane lattice constant of the layer
a_{II} - in-plane lattice constant of the layer
a - lattice constant of the unstrained cubic epitaxial layer
$D = 2C_{12}/C_{11}$, where C_{11} and C_{12} are elastic constants of the grown layer
Beyond a given critical thickness η_c when a critical misfit strain ε is exceeded, a transition from the elastically distorted to the plastically relaxed configuration occurs. In this case both mismatch component differ from zero: $a_{II} \neq a_o \neq a_\perp$. The lattice constant misfit is:

$$f = (a - a_o)/a_o$$

$$f_\perp = (a_\perp - a_o)/a_o = (1+D-DR)f \tag{3.2}$$

$$f_{II} = (a_{II} - a_o)/a_o = Rf$$

R is a relaxation rate. For pseudomorphic growth R=0, and for full strain relaxation R =1
If the epilayer is thicker than the critical thickness, there will be sufficient strain energy in the layer to create dislocations to relieve the excess strain. The layer has now returned to its unstrained or equilibrium lattice parameters in both the in-plane and out-of-plane directions and the film to be 100% relaxed. Figure 3.2 shows schematically how a misfit dislocation can relieve strain in the heteroepitaxial structure.

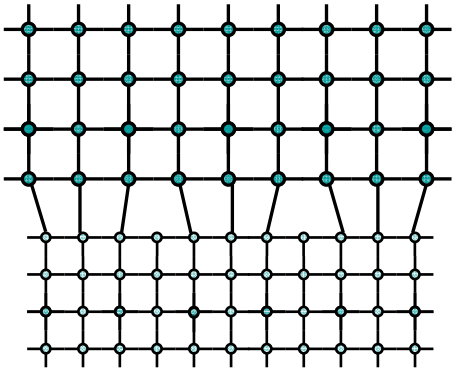

Fig. 3.2. Schematic presentation of the atom arrangement for metamorphic growth

In actual films, there is usually some amount of partial relaxation, although it can be very small in nearly coherent layers and nearly 100% in totally relaxed layers. For the partially relaxed layer, the in-plane lattice constant has not relaxed to its unstrained value. So some mismatch is accommodated by elastic strain, but a portion of the mismatch is accommodated by misfit dislocations (plastic strain).

There are two widely used models for calculations the critical thickness values: the Matthews-Blakeslee mechanical equilibrium model (Matthews.& Blakeslee, 1974) and the People-Bean energy equilibrium model (People & Bean, 1985). The People-Bean energy equilibrium model requires the total energy being at its minimum under critical thickness. According this model the elastic energy is equal to the dislocation energy at the critical thickness if the total elastic energy of the system with fully coherent interface is larger than the sum of the total system energy for the reduced misfit, due to the generation of dislocations, and the associated dislocation energy, and then begins the formation of interfacial dislocations.

Generally, the Matthews-Blakeslee model based on stemming from force balance, is the most often used to describe strain relaxation in thin films system. The equilibrium model of Matthews-Blakeslee assumes the presence of threading dislocations from the substrate. It gives mathematical relation for critical thickness by examining the forces originating from both the misfit strain F_ε and the tension of dislocation line F_L. The critical thickness h_c is defined as the thickness limit when the misfit strain force F_ε is equal to the dislocation tension force F_L(at h_c $F_\varepsilon = F_L$). For layers ticker than the critical thickness, the threading segment begins to glide and creates misfit dislocations at the interface to relieve the mismatch strain. The dislocations can easily move if dislocation lines and the Burgers vectors belong to the easy glide planes as {111} planes in face-centred cubic crystals.

In III-V semiconductors, the relaxation is known to occur by the formation of misfit dislocations and /or stacking faults. The usual misfit dislocations that are considered are located along the intersection of the glide plane and the interface plane. In zinc-blende crystal structures, on (100) oriented substrates the glide planes intersect the interface (110) which provides the corresponding line directions of misfit dislocations in such structures. The component of 60˚ dislocations perpendicular to the line directions contributes to strain relaxation. The 60˚ Burgers vector is b= ½ a_1 $\langle 110 \rangle$ and has a length along the interface perpendicular to the line $a / \sqrt{2}$.

Calculated values for critical thickness from People-Bean energy equilibrium and Matthews-Blakeslee force balance models are:

$$h_c = \frac{b(1-\nu)}{32\pi f^2(1+\nu)}\ln(h_c / b) \tag{3.3}$$

$$h_c = \frac{b}{4\pi f(1+\nu)}[\ln(h_c / b)+1] \tag{3.4}$$

Where:
$\nu = C_{12}/(C_{12}+C_{11})$ is Poison's ratio,
f is a lattice mismatch, $b = a/\sqrt{2}$ is a magnitude of Burgers vector
The calculated values of People-Bean models are larger than that of the Matthews-Blakeslee model. The measurements of dislocation densities in many cases showed no evidence of misfit dislocations for layer considerable ticker than Matthews-Blakeslee limit and nearly close to the energy-equilibrium thickness limit. Layers with thicknesses above the People-Bean limit can be considered to be completely relaxed, whereas layers below Matthews-Blakeslee limit values fully strained. Layers with thicknesses between these limits are metastable. They could be free of dislocations after growth, but are susceptible to relaxation during later high-temperature processing.
For the semiconductor devices based on the thick metamorphic structure the influence of the misfit dislocations which are located at the interface on active region could be reduced by growing the additional barrier layers before active region growth. Threading dislocations, which propagate up through the structure, are the most trouble for electronic devices since they can create defect states such as nonradiative centres and destroy the device properties.
There are a variety of techniques used to reduce the density of threading dislocations in a material. For planar structure a thick buffer layer with lattice parameter equal to that of the active layers is usually used for reduction of threading dislocations. However, these structures always have high threading dislocation densities. In most thick nearly relaxed heteroepitaxial layers, it is found that the threading dislocation density greatly exceeds that of the substrate. Some authors (Sheldon et al.1988, Ayers et al. 1992) are noted for a number of heteroepitaxial material systems that this dislocation density decreases approximately with the inverse of the thickness. The dislocation density could be reduced by postgrowth annealing.
A linearly graded buffers and graded superlattice also are effectively used for restricting dislocations to the plane parallel to the growth surface, and thus support the formation of misfit dislocation and suppress threading dislocation penetration in the active region.

3.1 X-ray diffraction characterization

The X-ray diffraction (XRD) method is an accurate nondestructive method for characterization of epitaxial structures. X-ray scans may be used for determination the lattice parameter, composition, mismatch and thicknesses of semiconductor alloys.
In XRD experiment a set of crystal lattice planes (hkl) is selected by the incident conditions and the lattice spacing d_{hkl} is determined through the well-known Brag's law:

$$2d\sin\theta_B = n\lambda \tag{3.1.1}$$

where n is the order of reflection and θ_B is the Brag angle
The crystal surface is the entrance and exit reference plane for the X-ray beams in Bragg scattering geometry and the incident and diffracted beams make the same angle with the lattice planes. Two types of rocking curve scan are used: symmetric when the Bragg diffraction is from planes parallel to crystal surface and asymmetric when the diffraction lattice planes are at angle φ to the crystal surface (Fig. 3.3).

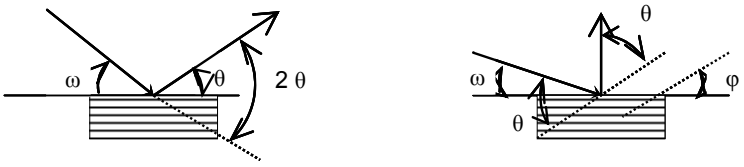

Fig. 3.3. Symmetric and asymmetric reflections from crystal surface

Let ω be the incidence angle with respect to the sample surface of a monochromatic X-ray beam. By rocking a crystal through a selected angular range, centered on the Bragg angle of a given set of lattice planes a diffraction intensity profile I(ω**)** is collected. For single layer heterostructure, the intensity profile will show two main peaks corresponding to the diffraction from the layer and substrate. The angular separation $\Delta\omega$ of the peaks account for the difference Δd_{hkl} between the layer and substrate lattice spacing. XRD do not directly provide the strain value on the crystal lattice. Te measurable quantities being the lattice mismatches $\Delta a_{\perp}/a_o$ and $\Delta a_{II}/a_o$, i. e $f_{\perp}$ and f_{II}. The relationship between lattice mismatch components and misfit f with respect to substrate is:

$$f = f_{\perp}\,(1\text{-}\nu)/(1+\nu) + 2\,\nu\, f_{II}/\,(1+\nu) \tag{3.1.2}$$

where ν is the Poisson ratio
This is the basic equation for the strain and composition characterization of heterostructures for cubic lattice materials. In the case of semiconductor alloys A_xB_{1-x} the composition x can be obtained if the relationship between composition and lattice constant is known. Poisson ratio is also composition depending and the use of Poisson ratio ν is only valid for isotropic materials. For a cubic lattice, it can only be applied for high symmetric directions as (001), (011), (111), but Poison ratio may be different along different directions ($\nu \approx 1/3$ for the most semiconductors alloys).
XRD can easily be employed to measure the lattice parameter with respect the substrate used as a reference. The strain and the composition of layer can be accurately determined if the dependence of the lattice parameter with the composition is known, the accuracy being mainly due to the precise knowledge of the lattice parameter –composition dependence.
In many cases a good approximation of a such dependence is given by Vegard law, which assumes that in the alloy A_xB_{1-x} the lattice of the alloy is proportional to the stoichiometric coefficient x:

$$a\,(x) = xa(\mathrm{A}) + (1\text{-}\,x)\,a(\mathrm{B}) \tag{3.1.3}$$

From this equation the stoichiometric coefficient x is obtained:

$$x = (a(x) - a(B))/\ (a(A) - a(B)) \tag{3.1.4}$$

If a(B) is the substrate lattice parameter, the composition x can be calculated from the measurement misfit f(x) value:

$$x = f(x)/f(AB) \tag{3.1.5}$$

Where:
$f(x)$ is the measured misfit value with respect to a(B) and
f(AB) is the misfit between compound A and compound B, used as reference.
In the case of $GaAs_{1-x}N_x$ and $In_xGa_{1-x}As_{1-y}N_y$ dilute nitride alloys relationship between lattice parameters and composition assuming Vegard's law are the foolowing:

$$a_{GaAs1-xNx} = x\ a_{GaN} + (1- x)\ a_{GaAs} \tag{3.1.6}$$

$$a_{\ InxGa1-xAs1-yNy} = x\ y a_{InN} + (1- x)y\ a_{GaN} + x(1- y)\ a_{InAs} + (1- x)\ (1- y)\ a_{GaAs} \tag{3.1.7}$$

The lattice parameter measurements method is one of the most accurate way to determine the composition, provided that the composition versus lattice parameter dependence is known. The comparison between composition values obtained from XRD and that, determined by other analytical techniques has allowed to measure the deviation from the linear Vegard's law in alloys.
Table 1. presents the values of elastic constants and lattice parameters for GaAs, InAs, GaN, InN binary compounds.

compound / Parameter	GaAs	InAs	GaN	InN
C_{11}, GPa	118.79	83.29	293	187
C_{12}, GPa	53.76	45.26	159	125
$a_{0,}$ nm	0.5653	0.60584	0.4508	0.4979

Table 1. Elastic constants and lattice parameters for some III-V compounds

4. Low-temperature LPE growth

Low-temperature LPE is the most simple, low cost and safe method for high-quality III-V based heterostructure growth. It remains the important growth technique for a wide part of the new generations of optoelectronic devices, since the competing methods, MBE and MOCVD, are complicated and expensive although they offer a considerable degree of flexibility and growth controllability. The lowering the growth temperature for Al-Ga-As system provides the minimal growth rate values of 1–10 Å/s, and they are comparable with MBE and MOCVD growth values (Alferov et al, 1986). At the early stages of the process two-dimensional layer growth occurs, which ensures structure planarity and makes it possible to obtain multilayer quantum well (QW) structures (Andreev et al, 1996).

The results of study the crystallization process in the temperature range 650-400 °C demonstrate precise layer composition and thickness controllability for the low-temperature LPE growth. A necessary requirements for successful devices fabrication is the optimal doping of the structure layers at low temperatures. The experiments (Milanova and Khvostikov, 2000) on doping using different type dopants covered large range of carrier concentrations: from 10^{16} to 10^{19} cm^{-3} for n $Al_xGa_{1-x}As$ layers ($0 \leq x < 0.3$); from 5×10^{17} cm^{-3} to well above 10^{19} cm^{-3} for p $Al_xGa_{1-x}As$ ($0 \leq x < 0.3$); and from 10^{16} to 10^{18} cm^{-3} for n- and p $Al_xGa_{1-x}As$ ($0.5 < x < 0.9$) layers. High quality multilayer heterostructures containing layers as thin as 2-20 nm, as well as several microns thick, with a smooth surface and flat interfaces have been grown by low-temperature LPE. The lowest absolute threshold current of 1.3mA (300 K) was obtained for buried laser diodes with a stripe width of ~ 1μm and cavity length of 125μm (Alferov et al, 1990).

High-efficiency solar cells for unconcentrated (Milanova et al, 1999) and concentrated solar cells (Andreev et al, 1999) have been fabricated by low-temperature LPE. The record conversion efficiency under ultra-high (>1000) concentration ratio solar radiation heve been achieved for GaAs single-junction solar cells based on multilayer AlGaAs/GaAs heterostructures (Algora et al, 2001).

The success of the LPE method is strongly depend on the graphite boat design used for epitaxy growth. The most widely used for LPE growth is a slide boat method. The conventional simple slide boat consists of a boat body in which are formed containers for liquid phase and a slider with one or more sits for the substrate (Fig. 4.1.). The slider moves the substrates under and out of the growth melt. This boat design has some disadvantages: the melt thicknesses is several millimeters and during growth from such semi-limited liquid-phase a portion of dissolved materials can not reach the substrate surface and forms stable seeds at a distance of 1 mm and more from the growth surface which deteriorate the planarity of the grown layer.

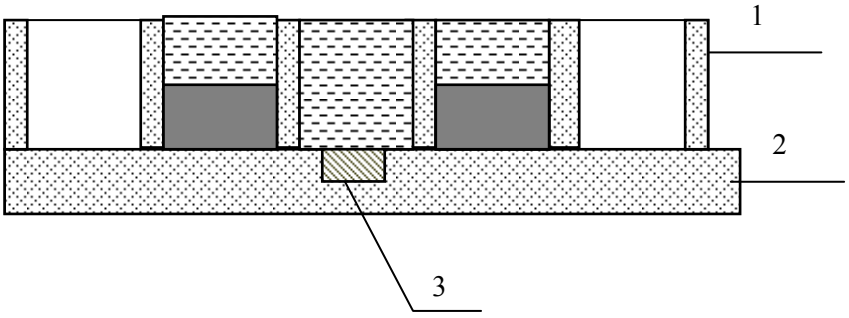

Fig. 4.1. Conventional slide boat for LPE growth: 1, body boat; 2, slider, 3, substrate.

Another drawback is the arising the defects on the layer surface due to the mechanical damage during its transfer from one melt to another. Also always on the surface of the melt present oxides films and it is difficult to completely removed these films even by long high-temperature baking. This is a critical problem for wetting of the substrate surface, especially for epitaxial process in Al-Ga-As system. A piston growth technique has been developed for LPE growth of AlGaAs heterostructures by Alferov at al (Alferov et al, 1975).

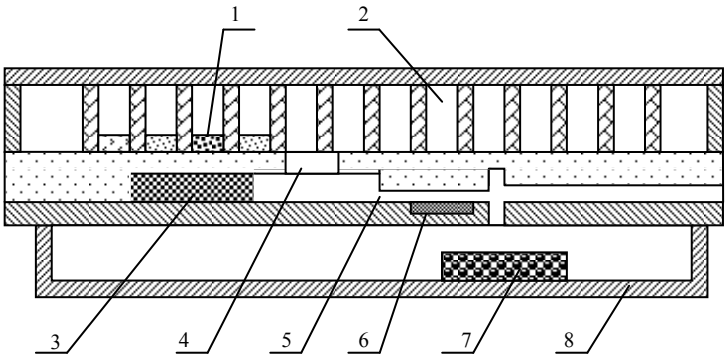

Fig. 4.2. Piston boat for growth of multilayer AlGaAs/GaAs heterostructures: 1, growth solution; 2, container for solution; 3, piston; 4, opening; 5, narrow slit; 6, substrate; 7, used solution; 8, container for used solutions.

The substrate surface in this boat after the first wetting is always covered by a melt and this solves difficulties of wetting during the growth of AlGaAs heterostructures in the range 600-400 °C. The piston boat design is shown in Figure 4.2. In this boat the melts of different compositions are placed in containers which can move along the boat body. The liquid phase falls down into the piston chamber and squeezes throw narrow slit into the substrate which allows mechanical cleaning of oxides films from liquid phase and insures a good wetting. The crystallization is carried out from the melt 0.5-1 mm thick. After the growth of the layer liquid phase is removed from the substrate by squeezing of the next melt. The last liquid phase is swept from the surface by shifting the substrate holder out side the growth chamber.

The liquid phase can not remove completely from the surface structure and cause a poor morphology of the last grown layer. The excess melt could be remove from the substrate by using additional wash melt, which may either has a poor adhesion to the substrate or may be relatively easy remove with post-growth cleaning and etching in selective etchants. Authors (Mishurnyi at al, 2002) suggest an original method to complete remove the liquid solution after epitaxy. The remained liquid phase is pulled up into the space between the substrate and vertical plates made of the same materials as the substrate assembled very closely to the substrate surface. This method is very useful for growth of multilayer heterostructures not containing Al in modified slide boat because prevent mixing of any liquids remaining. For the most multicomponent alloys such as InGaAsP, InGaAsSb, InPAsSb etc., lattice constant is very sensitive to composition variation and the piston boat is not suitable for their growth because of mixing of two deferent solutions. Slide boats with different design are used for fabrication of complicated multilayer heterostructure on the base of these multicomponent alloys. In order to improve the control of layer thicknesses and uniformity it is necessary the growth to be carried out using a finite melt. In this boat the liquid phase after saturations is transferred into the additional containers or growth chamber with finite space for the liquid phase. Figure 4.3 shows a schematic slide boat for epitaxy growth from finite melt.A critical requirement for the most multicomponent alloys, instead of AlGaAs, AlGaP, is precise determination of the growth temperature. The

temperature at the interface between the liquid phase and substrate can not be measured and common it is determined by measurements of the source component solubility (Mishurnyi et al, 1999) .

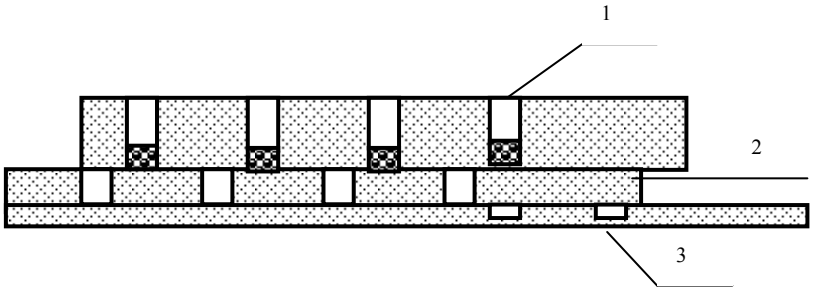

Fig. 4.3. Slide boat for growth from finite melt: 1, boat body with container for melts; 2, slider with container for finite melts; 3, slider for the substrates.

Slide boats with different design modification are used for growth of variety structures in different multicomponent system. A boat made of two different materials, sapphire (for body) and graphite (for slider), is suggested by Reynolds and Tamargo (Reynolds and Tamargo, 1984). This design reduces temperature variations around the perimeter of the substrate which contribute to unwanted 'edge' growth effects. Slide boats with narrowed melt contact for epitaxy of extremely thin epilayers have been used to grow active layer in single-quantum well lasers by (Alferov et al, 1985) and later by (Kuphal, 1991). Also a modified slide boat can be used for multilayer periodic structures growth (Arsent'ev et al, 1988). The use of two growth chambers with narrow slits makes it possible to produce such structures by means of repeated reciprocating movements of the slider with the substrate situated underneath these slits. Another variant of an LPE boat (Mishurnyi et la, 1997), which is a combination of the 'sliding' and 'piston' designs has been used successfully to grow InGaAsSb, AlGaAsSb and various multilayer structures on the basis of these materials.

5. Low-temperature LPE growth and characterization of dilute nitride GaAsN and InGaAsN thick layers

Dilute nitride III-V-N alloys with nitrogen content in the range of few percent, such as GaAsN and InGaAsN, are of considerable interest for application in multijunction solar cells.

The incorporation of nitrogen into group V sublattice causes profound effect on the band gap and properties of the dilute nitride material strongly differ from those of the conventional III-V alloys. While in conventional alloys a smaller lattice constant increases the band gap, the mixing of GaAs with few molar percent of GaN leads to giant reduction of its band gap due to the smaller covalent radius and large electronegativity of N atoms. The large changes in the electronic structure in dilute III–V nitrides could be explained by the band anticrossing model (BAC). The interaction between the localized levels introduced by a highly electronegative impurity, such as N in GaN_xAs_{1-x}, and the delocalized states of the host semiconductor causes a restructuring of the conduction band into E+ and E− subbands, which in this case effectively lowers the conduction band edge of the alloy.

Figure 5.1. shows the relationship between the lattice constant and band-gap energy in some III-V semiconductor alloys. In the case of InGaNAs adding In to GaAs increases the lattice constant, while adding N to GaAs decreases the lattice constant. In the same time the incorporation of In and N in GaAs leads to reduction of the band gap energy in the new alloy. Consequently, by adjusting the contents of In and N in quaternary InGaNAs alloys can be grown lattice-matched to GaAs layers because In and N have opposing strain effects on the lattice and make it possible to engineer a strain-free band gap layers suitable for different applications.

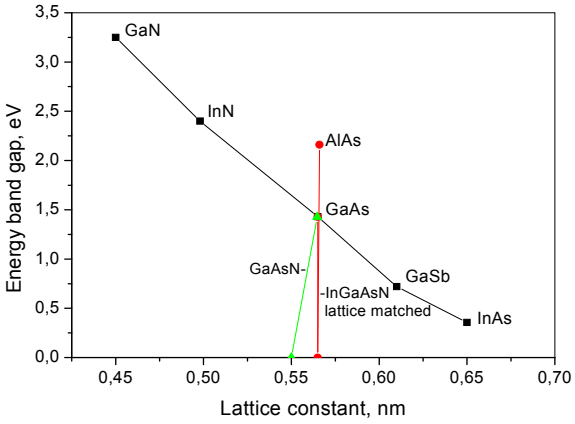

Fig. 5.1. Relationship between lattice constant and bad gap energy for some III-V semiconductor alloys

Recently a development of the spectral splitting concentrator photovoltaic system based on a Fresnel lens and diachronic filters has a great promise to reach super high conversion efficiencies (Khvostiokov et al. 2010). Module efficiency nearly 50% is expected for the system with three single-junction solar cells connected in series with band gap of 1.88-1.42-1.0 eV. The development of three optimized AlGaAs, GaAs and InGaAsN based cells is the best combination for application in such system if PV quality of the quaternary InGaAsN could be reached by LPE growth.

In this paper low-temperature LPE is proposed as a new growth method for dilute nitride materials. Because of its simplicity and low cost many experiments on GaInAsN and GaAsN growth under different condition and with different doping impurities could be made using LPE. The systematic study of their structural, optical and electrical properties by various methods make it possible to find optimized growth conditions for InGaAsN quaternary compounds lattice matched to GaAs substrate.

5.1 Growth and characterization of GaAsN layers

GaAsN compounds were grown by the horizontal graphite slide boat technique for LPE on (100) semi-insulating or n-type GaAs substrates. A flux of Pd-membrane purified hydrogen at atmospheric pressure was used for experiments. No special baking of the system was done before epitaxy. Starting materials for the solutions consisted of 99.9999 % pure Ga, polycrystalline GaAs and GaN. The charged boat was heated at 750°C for 1 h in a purified H_2 gas flow in order to dissolve the source materials and decrease the contaminants in the

melt. Epitaxial GaAsN layers 0.8-1.5 thick were grown from different initial temperatures varied in the range 560-650 °C at a cooling rate of 0.6 °C/min.

5.1.1 Structural characterization

XRD and SIMS techniques are used to determine N concentration in grown samples.
While SIMS measures the total nitrogen content in the layer, XRD determines the change in the lattice constant due to the substitution of nitrogen atoms on As-sublattice sites.
The N composition from XRD results could be estimated assuming Vegard's law. In many cases the Vegard's law is a good approximation for the lattice parameter dependence on the composition. The deviation from Vegard's law dependences on many parameters, for instance, the difference in the atom bond length, different atom electronegativity and elastic constants of the components in the alloy. For the ideal case N incorporates predominantly as substitutional N_{As} atoms in As- sublattice substituting As atoms. However, it is known that there are some other N configurations: N-As split interstitial; N-N split interstitial; and isolated N interstitial. Figure 5.2 presents the main configurations of N in GaAsN as substitutional atom N_{As} and as As-N and N-N split interstitials, respectively.
The influence of these N-related complexes on the lattice constant can be calculated on the base of the theoretical model of Chen (Chen et al. 1996) for analyzing the correlation between lattice parameters and point defects in semiconductors. According this model the lattice strain caused by the substitutional N_{As} is given by the following relation:

$$\frac{\Delta a}{a} = \mu \frac{x(r_N - r_{As})}{2(r_{Ga} + r_{As})} \tag{5.1.1}$$

where: r_N, r_{Ga},, r_{As} the covalent radii;
$\mu = (1+\nu)/(1-\nu)$, and v is the Poissn ratio
The lattice strained caused by split interstitial is:

$$\frac{\Delta a}{a} = \mu \frac{x(d_b - r_{Ga} - r_{As})}{2(r_{Ga} + r_{As})} \tag{5.1.2}$$

Where d_b is the distance of the N-As complex from its nearest neighbours:

$$d_b = \frac{\sqrt[3]{3}}{3} r_{si} + \sqrt{(r_{si} + r_{Ga})^2 + \frac{2}{3} r_{si}^2} \tag{5.1.3}$$

where $r_{si} = (r_N + r_{As})/2$ is an effective bond radius.

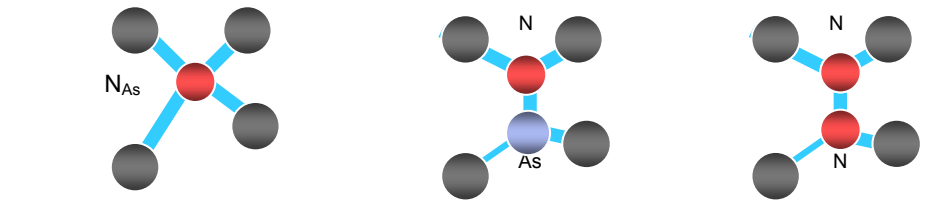

Fig. 5.2. The main configurations of nitrogen atoms in GaAsN
N-atom, As-atom Ga-atom

The effect of N-N interstitial is very small and can be neglected. Also the formation of an isolated N interstitial is unlikely due to a high formation energy (Li et al. 2001) and their concentrations in GaAsN is very small. While the substitutional N_{As} atoms compress the lattice constant , the N-As complexes expand the lattice constant of GaAsN in the growth direction, as shown in Figure 5.3. So, XRD results may underestimated the N composition due to the N-As and N-N split interstitials.

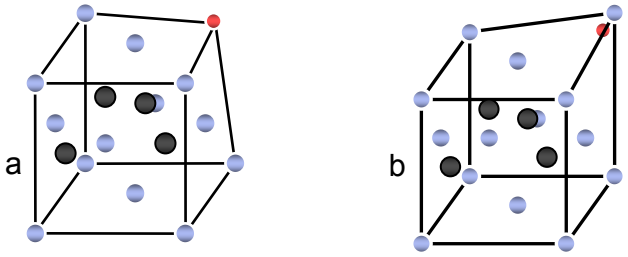

Fig. 5.3. Incorporation of N-atom in As-sublattice: a) as substitutional atom N_{As}; b) as As-N split interstitial

XRD rocking curves are recorded in the symmetrical (004) reflection. Fig. 5.4 shows the experimental XRD rocking curves of two GaAsN samples, 1.2 μm thick, with N composition of 0.3% and 0.62% and may consider that they are fuly relaxed. The N content determines the line shape of the main peak of the spectra: it manifests itself as a broad shoulder evolving into a weak separate peak shifted away to the right from the (004) GaAs substrate reflection. Our data show that N compositions measured by the two methods, SIMS and XRD, agree well and XRD measurements by using Vegard's law could be used to determine the lattice constant of GaAsN layers containing low N concentrations. These results are in a good agreement with the calculations from the theoretical model and the experimental results for small N concentration in the GaAsN reported in the literature. The deviation from Vegard's law has been observed for nitrogen concentration levels above 2.9 mol % GaN in the layer (Spruytte at all., 2001; Li et al. 2001).

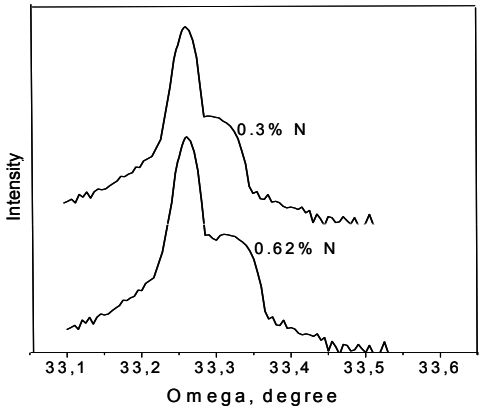

Fig. 5.4. XRD rocking curves for GaAsN samples with differenrt N content.

Unlike XRD used for assessing the incorporation of nitrogen in $GaAs_{1-x}N_x$ alloys grown by LPE the nitrogen bonding configurations and local atomic structures have been studied using x-ray photoelectron spectroscopy (XPS) and Fourier transform infrared (FTIR) spectroscopy. The XPS spectra have been measured over a range of binding energies from 1 to 550 eV. The X-ray photoelectron spectra of N 1s photoelectron and Ga LMM Auger lines recorded from the as grown $GaAs_{1-x}N_x$ samples prepared in different temperature ranges are shown in Fig 5.5. It is clearly seen the Ga Auger peak around 391 eV and the N 1*s* level photoemission peak of the samples. The variation of the intensity of the N 1*s* peak with respect to the Ga LMM peaks reflects is due to the different nitrogen content of the samples. Sample grown from higher initial epitaxy temperature of 650 ^oC contains 0.2% N and exhibits a N 1s peak with lower intensity and lower binding energy in comparison with the N 1s peak intensity of the sample grown in the lower temperature range (600-570 ^oC) with 0.5% N content. It has been established that lower epitaxy temperatures favours nitrogen incorporation in the layers. The N 1s spectra of the samples indicate that nitrogen atoms exist in a single-bonded configuration, the Ga-N bond, and interstitial nitrogen complexes is not observed, in contrast to data of high nitrogen content GaAsN samples where the additional nitrogen complex associated peak is recorded (Spruytte at all., 2001).

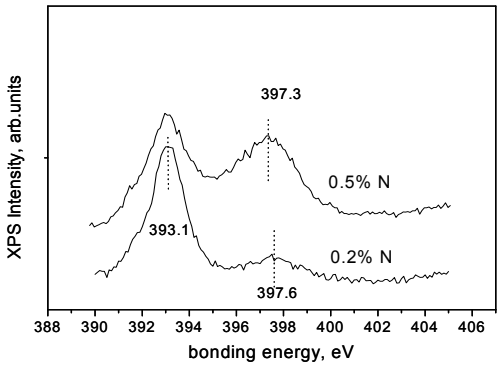

Fig. 5.5. XPS spectra of two GaAsN samples with different N content.

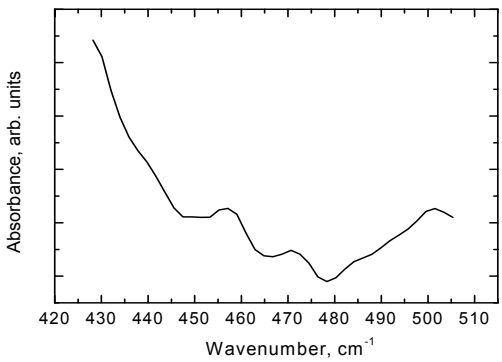

Fig. 5.6. FTIR spectrum of as grown GaAsN sample.

FTIR absorption spectra of an as grown $GaAs_{1-x}N_x$ layer on a n-GaAs substrate is plotted in Fig. 5.6. A peak at 472.6 cm^{-1}, attributed to a local vibrational mode of nitrogen at arsenic site in GaAs is clearly seen.

5.1.2 Electrical characterization

Electrical parameters of undoped GaAs and GaAsN layers with different nitrogen content grown on seminsulating (001) GaAs substrates are measured in the temperature range 80 – 300 K using van der Pauw geometry.

Figure 5.7. shows the temperature dependence of the Hall-concentration n_H on reciprocal temperature for two layers GaAsN with nitrogen concentration of 0.2% and 0.5%, respectively in comparison with undoped GaAs. It is seen that all samples are of n-type and for layers containing nitrogen electron concentration increases about one order of magnitude. This could be explained by the assumption that nitrogen behaves mainly as an isoelectronic donor, which arises from the local heterojunction scheme GaAs-GaN according to Belliache (Bellaiche et al., 1997). The results shown in figure indicate that the free carrier concentration increases strongly with the N concentration. The increase in n_H has also been observed in GaN_xAs_{1-x} doped with S (Yu et al., 2000a) and in Ga_{1-3x} $In_{3x}NxAs_{1-x}$ alloys doped with Se (Skierbiszewski at al., 2000). This large increase of the free electron concentration can be quantitatively explained by a combination of the band anticrossing model (Shan et al, 1999) and the amphoteric defect model (Walukiewicz, 1989). The later suggests that the maximum free carrier concentration in a semiconductor is determined by the Fermi energy with respect to the Fermi-level stabilization energy E_{FS} which is a constant for III-V semiconductors. Since the position of the valence band in GaAsN is independent of N concentration, the giant downward shift of the conduction band edge toward E_{FS} and the enhancement of the density of states effective mass in GaAsN lead to much larger concentration of uncompensated, electrically active donors for the same location of the Fermi energy relative to E_{FS}. In order to explain the large enhancement of the doping limits in dilute nitride alloys both the effects of band gap reduction and the increase in the effective mass have to be taken into account (Yu et al., 2000 b; Skierbiszewski at al., 2000).

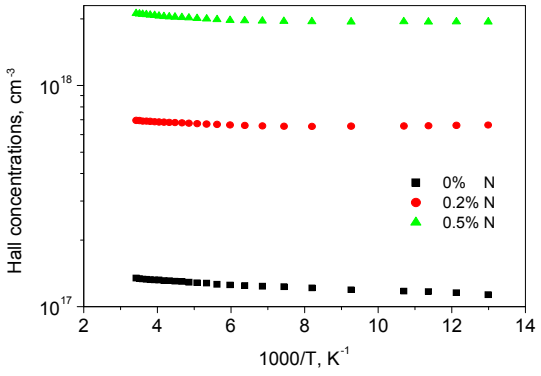

Fig. 5.7. Free carrier concentration as a function of inverse temperature for as grown GaAs, and two GaAsN layers with different N content

Figure 5.8. presents the temperature dependencies of the Hall-mobility for the same samples. The mobility of the dilute GaAsN samples is considerably lower due to space charge scattering contributions induced by N-related defects added to well-known scattering mechanisms such as phonon and ionized impurity scattering. The mobility maximums of both curves are almost at the same temperature with a relatively small difference of about 20K, which is an indication for scattering specificity. It is seen a well expressed low-temperature mobility decrease which could be explained by the temperature dependence of the GaAs conduction band edge energy, which is closer to the N defect levels at lower temperatures, increasing the scattering cross-section.

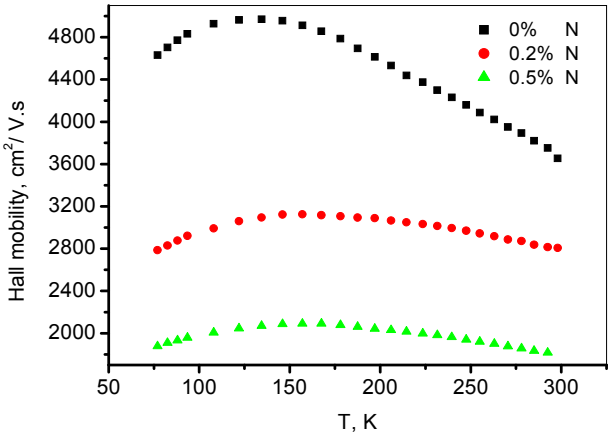

Fig. 5.8. Temperature dependence of Hall electron mobility for GaAs (full squares), and two GaAsN with: 0.2%N (full circles); 0.5%N (full triangles)

The mobility values of the dilute GaAsN samples is lower than those of the undoped GaAs layer but considerable higher than mobility values obtained in n-type GaAsN films with similar free electron concentration grown by MOCVD and MBE.

5.2 Growth and characterization of InGaAsN layers

Dilute InGaAsN layers have been prepared using the same technique as for GaAsN growth. A series of nearly-lattice matched InGaAsN epilayers 1.3-1.5 μm thick have been grown from In-rich solution containing 1.5 at.% polycrystalline GaN as a nitrogen source in the temperature range 615 – 580 °C at a cooling rate 0.6 °C/min.

5.2.1 Structural characterization

Typical XRD rocking curves for grown layers are plotted in the Fig. 5.9.
Two prominent peaks associated with the GaAs substrate and the quaternary InGaAsN layer are observed. The lattice mismatch $\Delta a/a_o$ determined from the XRD spectrum is ~ 0.1%. The *In*-concentration of the layers measured separately by X-ray microanalyses is 6.4%. Using Vegard's law the *N*- content in InGaAsN layers is determined to be 2.8%

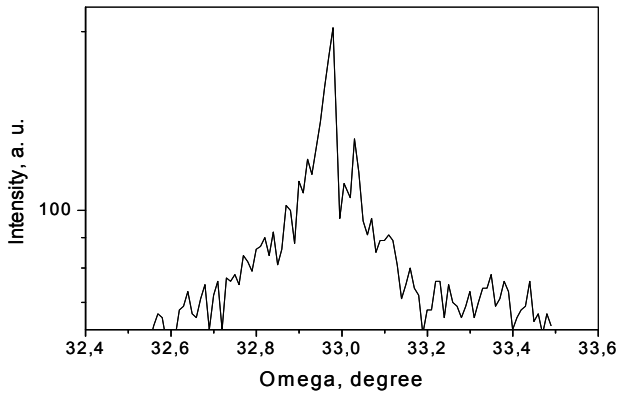

Fig. 5.9. XRD rocking curves of InGaAsN sample

The local structure of the InGaAsN is defined by Raman spectrum. In the Raman spectrum, presented in fig. 5.10. does not observed N-induced local mode LO2 , assigned to the vibration of isolated nitrogen atom bonded to four Ga neighbors ($N_{As}Ga_4$). Instead of this two LVM peaks at 454 and 490 cm^{-1} originated from In-N bonds in a local Ga_3In_1-N or Ga_2In_2-N configurations are appeared. Similar LVM peaks have been reported in the literature for as grown InGaAsN layers by MBE (Mintairov et al., 2001, Hashimoto et al., 2003) and for some MBE and MOCVD samples after annealing (Pavelescu et al.,2005; Kurtz et al. 2001). The experimentally observed local modes could be explained by theoretical analyses of the microscopic lattice structures related to the incorporation of N in InGaAsN alloys. The Monte Carlo simulation (Kim & Zunger, 2001) reveal that in InGaAsN quaternary alloys the "small atom–large atom" bond configuration i.e. "large cation-small anion" In-N + "small cation-large anion" Ga-As is preffered for better lattice-matched of the alloy to GaAs substrate, because introduces less strain. On the other hand, the cohesive energies of GaN is larger than that of InN, so the highly strained Ga-N + In-As configuration is preferred in terms of bond energy. In LPE growth under near to equilibrium conditions In-N bonds are more favorable since they reduce the sum of local strain plus chemical bond energies. The introduction of In changes N environment by formation short-range-ordered nitrogen centered N-In_nGa_{4-n} ($0 \le n \le 4$) clusters in InGaAsN alloy. In Ga-rich InGaAsN quaternary the most probably realized are the nearest –neighbor pair defects N_{As}-In_{Ga} in which one of the Ga atom in the neighborhood of N is replaced by a large size heavier In_{Ga} ($N_{As}In_{Ga}Ga_3$) and also a formation of a second nearest-neighbor complex $N_{As}In_{Ga}(2)Ga_2$ where two of four Ga atoms is replaced by two large-site and heavier In_{Ga} in the vicinity of N_{As}. The calculations using Green's function technique (Talwar, 2007) relieve the splitting of a triple degenerate N_{As} near to 471 cm^{-1} into a non-degenerate LVM ~ 462 cm^{-1} and a double degenerate LVM at 490cm^{-1} for the nearest –neighbor complex and three bands near to 481, 457, and 429 for second nearest-neighbor complex . The surface roughness of the samples has been examined by atomic force microscopy (AFM). A three-dimensional AFM image of an as grown 1.3 μm-thick InGaAsN layer is presented in Fig. 5.11. The measured root-mean-square (RMS) roughness on 1-micron area is 0.42 nm.

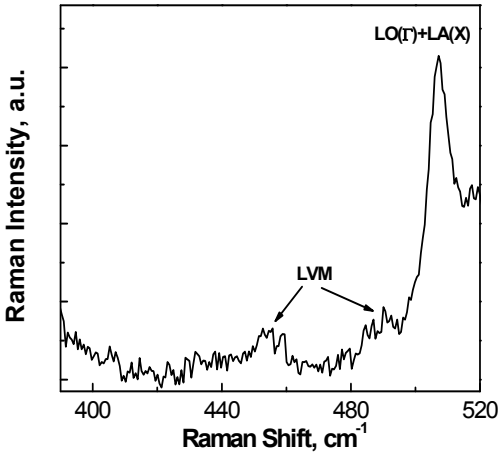

Fig. 5.10. Raman spectrum of as grown InGaAsN layer.

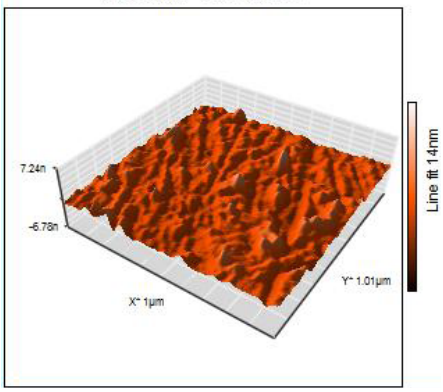

Fig. 5.11. AFM image of the surface of as grown InGaAsN.

5.2.2 Electrical characterization

In the Fig. 5.12 are plotted the temperature dependence of Hall concentrations n_H for lattice matched InGaAsN in comparison with a metamorphic InGaAs layer. For undoped InGaAs, n_H decreases linearity in the explored temperature range, 80 to 300K, typical for slightly degenerate III-V semiconductors. However, for N-containing films, two distinct temperature regimes with different temperature dependence of n_H are observed. The Hall electron concentration decreases as the temperature decreases down to about 200 K, indicating the presence of thermally activated deep donor levels within the dilute nitride bandgap. The saturation of n_H at low temperature (T < 200K) is attributed to fully ionized shallow donors. This behavior could be explained by the presence of two donor levels in the InGaAsN bandgap, one being a shallow N isoelectronic donor and the second a thermally activated deeper donor, presumably N-related deep-level defects typically associated with different N-N pair and N-cluster states (Zhang & Wei, 2001).

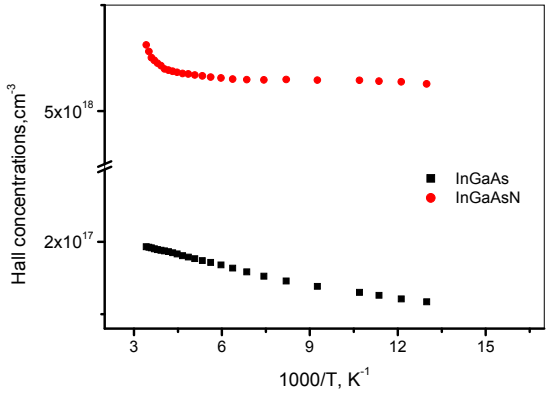

Fig. 5.12. Temperature dependence of free carrier concentrations for undoped InGaAs and lattice matched InGaAsN samples

The temperature dependence of Hall mobility for undoped InGaAs and InGaAsN layers grown from In-rich solution is similar to those for the GaAsN layers grown from Ga-rich solution as it is shown in Figures 5. 13 and 5. 14.

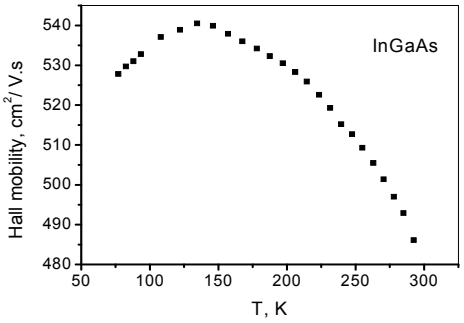

Fig. 5.13. Hall mobility as a function of temperature for undoped InGaAs sample

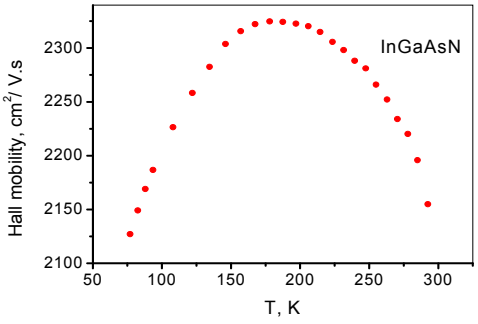

Fig. 5.14. Hall mobility as a function of temperature for lattice matched InGaAsN sample

The mobility of the metamorphic InGaAs structure is low, down to 500 $cm^2/V.s$, since it possibly contains threading dislocations of high density and the latter causes relatively poor material quality. High values over 2000 $cm^2/$ V.s for Hall mobility exhibits the lattice matched to GaAs substrate InGaAsN sample. These values are about the theoretical limit predicted by Fahy and O'Reilly (Fahy and O'Reilly, 2004) and among the highest reported for lattice matched thick InGaAsN layers.

6. Conclusion

Dilute nitride GaAsN and InGaAsN epitaxial layers have been prepared by low-temperature LPE using polycrystalline GaN as a source for nitrogen. The GaAsN layers, 0.8-1.5 μm thick, with 0.15-0.6 at. % N content in the solid have been grown from different initial epitaxy temperature varied in the range 650-550 °C. The lowering the epitaxy temperatures favors nitrogen incorporation in the layers. The Hall measurements reveal sharply increase of free carrier concentrations about one order of magnitude and decrease of Hall mobility for GaAsN samples in comparison with undoped GaAs.

Lattice-matched conditions for coherent growth of InGaAsN layers on GaAs have been found. The results suggest preferential In-N bond formation for high quality growth of these alloys. Temperature dependent electronic transport measurements show a thermally activated increase in the free carrier concentration at measurement temperatures higher than 200 K, suggesting the presence of carrier trapping levels below the GaAsN conduction band edge. Nearly lattice matched to GaAs substrate thick $In_xGa_{1-x}As_{1-y}N_y$ (x~ 6.4%, y~2.8%) layers exhibit high values over 2000 $cm^2/$ V.s for Hall electron mobility.

Further study is necessary in order to determine the potential of melt-grown quaternary InGaAsN alloys for solar cell application. This will be attained by: study the influence of growth conditions on the material quality in wide temperature range 450-600 °C and differentiation between intrinsic and extrinsic limitations for device performance; finding optimized growth conditions for InGaAsN lattice matched to GaAs with improved material quality ; extending the long-wavelength limit of GaAsN-based materials by the lowering the band gap energy of dilute nitride structure that can be lattice matched grown on GaAs.

The finale goal is a development of single-junction solar cells with high photovoltaic parameters.

7. References

Alferov Zh.I., Andreev V.M., Konnikov S.G., Larionov V.R. and Shelovanova G.N. (1975). Investigation of a new LPE method of obtaining Al-Ga-As heterostructures, *Kristall Technik*, Vol.10, No 2, pp 103-110.

Alferov Zh.I., Garbuzov D.Z., Arsent'ev I.N., Ber B.Ya., Vavilova L.S., Krasovskii V.V. and Chydinov A.V.(1985) Auger profiles of the composition and luminescence studies of liquid-phase grown InGaAsP

Alferov Zh.I., Andreev V.M., Vodnev A.A., Konnikov S.G., Larionov V.R., Pogrebitskii K.Yu. Rymiantsev V.D. and Khvostikov V.P.(1986). AlGaAs heterostructures with quantum-well layers, fabricated by low-temperature liquid-phase epitaxy, *Sov. Tech. Phys. Lett*., 12(9), 450–451.

Alferov Zh.I., Andreev V.M., A.Z. Mereutse, Syrbu A.V., Suruchanu G.I. and Yakovlev V.P.(1990). Super low-threshold (Ith = 1.3 mA, T= 300 K) quantum-well AlGaAs

lasers with uncoated mirrors prepared by liquid-phase epitaxy, *Sov. Tech. Phys. Lett.*, Vol.16, No 5, pp 339–340.

Algora C., Oritz E., Rey-Stolle I, Diaz V., Pena R., Andreev V. M., Khvostikov V. P., Rumyantsev V. D.(2001). A GaAs solar cell with an efficiency of 26.2% at 1000 suns and 25.0% at 2000 suns, *IEEE Trans. on Elec. Dev.*, Vol. 48, No 5, pp 840-844. ISSN: 0018-9383.

Andreev V. M., Kazantsev A. B., Khvostikov V. P., Paleeva E. V., Rumyantsev V. D. and Sorokina S. V. (1996). Quantum-well AlGaAs heterostructures grown by low-temperature liquid-phase epitaxy, *Materials Chemistry and Physics*, Vol. 45, No 2, p p.130-135.

Andreev V. M., Khvostikov V. P., Larionov V. R., Rumyantsev V. D., Paleeva E. V., Shvarts M. Z.(1999). High-efficiency AlGaAs/GaAs concentrator (2500 suns) solar cells *Fiz. Tekh. Poluprovodn*. Vol. 33, N0 9, pp 1070-1072.

Arsent'ev I.N., Bert N.A., Vasil'ev A.V., Garbuzov D.Z., Zhuravkevich E.V., Konnikov S.G., Kosogov A.O., Kochergin A.V., Faleev N.N. and Flaks L.I.(1988). Periodic multilayer In-Ga-As-P structures fabricated by liquid-phase epitaxy, *Sov. Tech. Phys. Lett.*, Vol 14, No 4, pp 264–266.

Ayers J.E., Schowalter L.J., and S.K. Ghandhi (1992). Post-growth thermal annealing of GaAs on Si(001) grown by organometallic vapor phase epitaxy, *J. Cryst. Growth*, Vol. 125, No1-2, pp. 329-335.

Bauer, E . (1958). Phaenomenologische Theorie der Kristallabscheidung an Oberflaechen, *Zeitschrift für Kristallographie*, Vol. 110, pp 372-394.

Bellaiche L., S. H. Wei, Zunger A., (1997) Band gaps of GaPN and GaAsN alloys, *Appl. Phys. Lett.*, Vol. 70, No 26, pp.3558-3560.

Chen N. F., Wang Y., He H, and Lin L. (1996). Effects of point defects on lattice parameters of semiconductors, *Physical Review B*, Vol. 54, No 12, (September 1996), pp 8516-8521.

Dhar S., Halder N., Mondal A., Bansal B., Arora B. M. (2005). Detailed studies on the origin of nitrogen-related electron traps in dilute GaAsN layers grown by liquid phase epitaxy, *Semiconductor Science and Technology*, Vol. 20, No. 12. pp. 1168-1172.

Fahy S., O'Reilly E. P. (2004), Theory of electron mobility in dilute nitride semiconductors, *Physica E*: *Low-dimensional systems and nanostructures*, Vol. 21, No 1-2, pp. 881-885.

Frank F.C. and Van der Merwe J.H. (1949). One-dimensional dislocations. II. Misfitting monolayers and oriented overgrowth, *Proc. R. Soc. London A*, Vol. 198, No 1053, (August 15, 1949), pp 216 -225.

Grabow M.H. and Gilmer,G.H. (1988). Thin film growth modes, wetting and cluster nucleation, *Surf. Science*, Vol. 194, No 3, pp 333-346

Guter W., Schöne J., Philipps S., Steiner M., Siefer G., Wekkeli A., Welser E, Oliva E, Bett A. and Dimroth F.(2009). Current-matched triple-junction solar cell reaching 41.1% conversion efficiency under concentrated sunlight, *Appl. Phys. Lett*. Vol. 94, No 2, 023504.

Johnston S. W., Kurtz S. R., Friedman D. J., Ptak A. J., Ahrenkiel R. K., and Crandall R. S. (2005). Observed trapping of minority-carrier electrons in *p*-type GaAsN during deep-level transient spectroscopy measurement, Appl. Phys. Lett. Vol 86, No 7, 072109.

Hashimoto A., Kitano T., Nguyen A.K., Masuda A., Yamamoto A., Tanaka S., Takahashi M., Moto A., Tanabe T., Takagishi S., Raman characterization of lattice-matched

GaInAsN layers grown on GaAs (001) substrates, *Solar Energy Materials & Solar Cells* 2003, Vol. 75, pp. 313–317.

Hiramatsu K., Itoh S., Amano H., Akasaki I., Kuwano N., Shiraishi T. and Oki K.(1991). Growth mechanism of GaN grown on sapphire with A1N buffer layer by MOVPE, *J. Cryst. Growth*, Vol.115, No 1-4 , (Desember,1991), pp 628-633.

Khan A, Kurtz S. R., Prasad S., Johnston S. W., and Gou J. (2007). Correlation of nitrogen related traps in InGaAsN with solar cell properties, *Appl. Phys. Lett.* Vol. 90, No 24, 243509.

Khvostikov V.P., Sorokina S.V., Potapovich N.S., Vasil'ev V.I., Vlasov A.S., Shvarts M.Z., Timoshina N.Kh., Andreev V.M., (2010). Single-junction solar cells for spectrum splitting PV system, *Proceedings of the 25th European PV Solar Energy Conference and Exhibition,* Valencia, Spain6-10 September 2010.

Kim K. and Zunger A., Spatial Correlations in GaInAsN Alloys and their effects on Band-Gap Enhancement and Electron Localization, *Phys. Rev. Lett.*, Vol. 86, No 12, pp. 2609-2612.

King R.(2008). Multijunction cells: record breakers, *NaturePhotonics*, Vol. 2, pp. 284– 285.

Krispin P., Spruytte S. G., Harris J. S., and Ploog K. H. (2002) Electron traps in Ga(As,N) layers grown by molecular-beam epitaxy, *Appl. Phys. Lett.* Vol. 80, No 12, pp 2120-2122.

Kuphal E. (1991). Liquid Phase Epitaxy, *Appl. Phys. A* 52, pp 380–409.

Kurtz S. R, Allerman A. A., Jones E. D., Gee J. M., Banas J. J., and Hammons B. E. (1999) InGaAsN solar cells with 1.0 ev band gap, lattice matched to GaAs, *Applied Physics Letters*, Vol. 74, No 5, pp. 729–731.

Kurtz S. R., Allerman A. A., Seager C. H., Sieg R. M., and Jones E. D. (2000), Minority carrier diffusion, defects, and localization in InGaAsN, with 2% nitrogen, *Applied Physis Letters*, Vol. 77, No 3, pp. 400–402.

Kurtz S., Webb J., Gedvilas L., Friedman D., Geisz J., Olson J., King R., Joslin D., & Karam N., *Appl. Phys. Lett.*, 2001, Vol. 78, No 6, pp. 748 -750.

Kurtz S. R., Klem J. F., Allerman A. A., Sieg R. M., Seager C. H., & Jones E. D. (2002) Minority carrier diffusion and defects in InGaAsN grown by molecular beam epitaxy, *Appl. Phys. Lett.*, Vol. 80, No 8, pp. 1379-1381.

Li W., Pessa M., & Likonen J. (2001) Lattice parameter in GaNAs epilayers on GaAs: Deviation from Vegard's law, *Appl. Phys. Lett.*, Vol. 78, No 19, pp. 2864-2866.

Mattes B.L. and Route R.K.(1974). LPE growth of GaAs: Formation of nuclei and surface terraces , *J. Cryst. Growth*, Vol. 27, (December 1974), pp 133-141.

Matthews J. W.& Blakeslee A. E. (1974). Defects in epitaxial multilayers: I. Misfit dislocations, *J. Cryst. Growth*, Vol. 27, (December 1974) pp. 118-125.

Milanova M., Mintairov A., Rumyantsev V., Smekalin K.(1999). Spectral characteristics of GaAs solar cells grown by LPE, *J. of Electronic Mat.*, Vol 28, No 1, pp 35-37.

Milanova M. and Khvostikov V.(2000). Growth and doping of GaAs and AlGaAs layers by lowtemperature liquid-phase epitaxy, *J. Crystal Growth,* Vol. 219, No 10, pp 193–198.

Milanova M., Kakanakov R., Koleva G., Arnaudov B., Evtimova S., Vitanov P., Goranova E.,. Bakardjieva Vl, Alexieva Z.(2009) Incorporation of nitrogen in melt grown GaAs , *J. Optoelectronics and Advanced Materials*, Vol. 11, No. 10, pp. 1471-1474.

Mintairov A. M., Blagnov P. A.,. Merzj J. L, Ustinov V. M. & Vlasov A. S. (2001). Vibrational study of nitrogen incorporation in InGaAsN alloys, *9th Int. Symp. "Nanostructures: Physics and Technology"* NC.13p, St Petersburg, Russia, June 18-22, 2001.

Mishurnyi V.A., de AndaF., Gorbatchev A.Yu., Vasil'ev V.I., Faleev N.N.(1997). InGaAsSb growth from Sb-rich solutions, *J. Crystal Growth,* Vol. 180, pp 34–39.

Mishurnyi V.A., de Anda F., Hernandes del Castillo I.C. and Gorbatchev A.Yu.(1999). Temperature determination by solubility measurements and a study of evaporation of volatile components in LPE, *Thin Solid Films,*Vol. 340, pp 24–27.

Mishurnyi V.A., de Anda F. and Gorbatchev A.Yu.(2002). Some problems on the phase diagrams research in LPE, *Current Top. Crystal Growth Res.*, Vol. 6, pp 115–125.

Nabetani Y., Ishikawa T., Noda S. and Sasaki A.(1994). Initial growth stage and optical properties of a three-dimensional InAs structure on GaAs, *Journal of Applied Physics*, (July, 1994) Vol. 76, No 1, pp 347-351.

Nishimura K., Lee H.-S. , Suzuki H., Ohshita Y., & Yamaguchi M. (2007) Chemical Beam Epitaxy of GaAsN Thin Films with Monomethylhydrazine as N Source, *Jpn. J. Appl. Phys.,* Vol. 46, pp. 2844-2847.

Ohshita Y, N. Kojima T. Tanaka T. HondaM. Inagaki and M. Yamaguchi Novel material for super high efficiency multi-junction solar cells *J. Cryst. Growth*, Vol 38, No 1, (March 2011) pp 328-331.

Pavelescu E.-M., Wagner J., Komsa H.-P., Rantala T. T., Dumitrescu M.& Pessa M., Nitrogen incorporation into GaInNAs lattice-matched to GaAs: The effects of growth temperature and thermal annealing, *J. Appl. Phys.*, 2005, Vol.78, No 8, pp. 083524-1-4.

People R.& Bean J. C. (1985) Calculation of critical layer thickness versus lattice mismatch for Ge_xSi_{1-x}/Si strained-layer heterostructures, *Appl. Phys. Lett.*, Vol. 47, No 3, pp. 322-324.

Ptak A. J., Friedman D. J., Kurtz S., & Keihl J.(2005). Enhanced depletion width GaInNs solar cells grown by molecular beam epitaxy, *Proceedings of 31IEEE PVSC*, pp. 603–606, Orlando, Florida, USA, January 3-7, 2005.

Reynolds C.L. and Tamargo M.C. (1984) LPE appartus with improved thermal geometry, US Patent 4 470 368.

Scheel H.J.(2003) Control of Epitaxial Growth Modes for High-performance Devices, In: *Crystal Growth Technology*, Scheel H.J.& Fukuda T., pp. 623-642, John Wiley & Sons, Ltd.

Shan W, Walukiewicz W, Ager JW, Haller EE, Geisz JF, Friedman DJ, Olson JM, Kurtz SR. (1999) Band Anticrossing in GaInNAs Alloys. *Phys. Rev. Lett.*, Vol. 82, No 6, pp 1221–1224.

Sheldon P., Jones K.M., Al-Jassim M.M., & Yacobi B.G.(1988) Dislocation density reduction through annihilation in lattice-mismatched semiconductors grown by molecular beam epitaxy, *J. Appl. Phys.*, Vol. 63, No 11, pp. 5609-5611.

Skierbiszewski C., Perlin P., Wisniewski P., Knap W., Suski T., Walukiewicz W., Shan W., Yu K. M., Ager J. W., Haller E. E., Geisz J. F., and Olson J. M. (2000) Large, nitrogen-induced increase of the electron effective mass in $In_yGa_{1-y}N_xAs_{1-x,}$ *Appl. Phys. Lett.* Vol 76, No 17, pp 2409-2411.

Spruytte S. G., Coldren C. W., Harris J. S., Wampler W., Krispin P., Ploog K., & Larson M. C. (2001) Incorporation of nitrogen in nitride-arsenides: Origin of improved luminescence efficiency after anneal, *J. Appl. Phys.*, Vol. 89, No 8 , pp. 4401-4406.

Stranski I. N. and Krastanov L. V. (1939). *Abhandlungen der Mathematisch-Naturwissenschaft lichen Klasse.,* Akademie der Wissenschaften und der Literatur in Mainz, Vol. 146, p. 797.

Talwar D. N. (2007) Chemical bonding of nitrogen in dilute InAsN and high In-content GaInAsN, Phys. Stat. Sol. (c) Vol. 4, No. 2, pp. 674– 677.

Van der Merwe J.H (1979), Critical Reviews in Solid State and Materials Science, in *Chemistry and Physics of Solid Surfaces*, editor R. Vanselow, CRC Press, Boca Raton, 1979, 209 p.

Vitanov P., Milanova M., Arnaudov B., Evtimova S., Goranova E., Koleva G., Bakardjieva Vl. & Popov G. (2010) Study of melt-grown GaAsN and InGaAsN epitaxial layers (2010). *Journal ofPhysics:ConferenceSeries*, Vol. 253, pp. 012045-1-6.

Volmer M. & Weber A.,(1926). Keimbildung in übersättigten Gebilden, *Z. Physik Chem.*, Vol.119, pp 277-301.

Walukiewicz W., (1996) Amphoteric native defects in semiconductors, *Appl. Phys. Lett.*, Vol. 54, No 21, pp. 2094-2096.

Weyeres M., Sato M., & Ando H.(1992) Red shift of photoluminescence and absorption in dilute gaasn alloy layers, *Japanese Journal of Applied Physics*, Vol. 31, pp. L853.

Yamaguchi M., Nishimura K., Sasaki T., Suzuki H., Arafune K., Kojima N., Ohsita Y., Okada Y., Yamamoto A., Takamoto T. & Araki K. (2008). Novel materials for high-efficiency III-V multi-junction solar cells, *Solar Energy*, Vol. 82, No 2, pp. 173-180.

Yu K. M., Walukiewicz W., Shan W., J. Wu, Ager J. W., HallerE. E., Geisz J. F., & Ridgway M. C. (2000a). Nitrogen-induced enhancement of the free electron concentration in sulfur implanted GaN_xAs_{1-x} , *Appl. Phys. Lett.* Vol. 77, No 18, pp 2858-2860.

Yu K. M., Walukiewicz, W., Shan W., Ager J. W., Wu J., Haller E. E., Geisz J. F., Friedman D. J. and Olson J. M. (2000b) Nitrogen-induced increase of the maximum electron concentration in group III-N-V alloys. *Phys. Rev. B*, Vol. 61, No 20, pp.R13337-R13340.

Zhang S. B.& Wei S. H. (2001). Nitrogen Solubility and Induced Defect Complexes in Epitaxial GaAs:N, *Phys. Rev. Lett.*, Vol. 86, No 9, pp. 1789–1792.

5

Organic-Inorganic Hybrid Solar Cells: State of the Art, Challenges and Perspectives

Yunfei Zhou,
Michael Eck and Michael Krüger
University of Freiburg/Freiburg Materials Research Centre
Germany

1. Introduction

Novel photovoltaic (PV) technologies are currently investigated and evaluated as approaches to contribute to a more environmental friendly energy supply in many countries. One of the driving forces are the aims to reduce the emission of green house gases and the dependency on importing fossil energy resources from political unstable countries. Additionally the wish to replace nuclear power by greener and less threatening technologies will enhance the development of regenerative energy supply in many countries especially after the recent nuclear catastrophe at Fukushima nuclear power plant in Japan in March 2011. This will include the more rapid implementation of existing mature PV technologies but also the development and improvement of novel PV approaches such as organic PV (OPV) and dye-sensitized solar cells (DSSCs) together with new efficient strategies for energy storage and distribution to make electric power, deriving from PVs, available whenever and wherever it is needed.

The so-called 1st generation of solar cells based on e.g. bulk crystalline and polycrystalline silicon is still dominating the PV market. However, so-called 2nd generation solar cells mainly consisting out of thin film solar cells based on CdTe, Copper Indium Gallium Selenide (CIGS), and amorphous silicon gained distribution of ca. 25% in market share today worldwide. It is expected that this number will increase significantly within the next years. While for the 1st and 2nd generation solar cells commercial solar panels are available with decent power conversion efficiencies (PCEs) and lifetimes, the emerging 3rd generation solar cells such as OPV and DSSCs technologies are still in the development phase. Some commercially available products have recently entered the market such as e.g. solar bags representing niche products, which are so far not suitable for competing with traditional large scale applications of solar panels of the 1st and 2nd generations. In traditional solar panels the differences between best solar cell and average solar cell efficiencies are much smaller than for the emerging solar cell technologies with the consequence that modules of 3rd generation solar cells still suffer from too low performance. In Table 1 the best cell and module efficiencies of different PV technologies are compared. It has to be mentioned that especially for the emerging new PV technologies the average efficiencies are significantly lower than the results of the best cells.

PV Technology	Best cell PCEs	Average cell PCEs	Best module PCEs	Average module PCEs
Si (bulk)	25.0% (monocryst.) (Zhao et al., 1998) 20.4% (polycryst.) (Schultz et al., 2004) 10.1% (amorphous) (Benagli et al., 2009)	---	22.9% (monocryst.) (Zhao et al., 1997) 17.55% (polycryst.) (Schott, 2010)	14-17.5% (monocryst.) 13-15% (polycryst.) 5-7% (amorphous)
CIGS (thin film)	20.3% Jackson et al., (2011)	---	15.7% (MiaSolé, 2010)	10-14%
CdTe (thin film)	16.7% (Wu X. et al., 2001)	---	10.9% (Cunningham et al., 2000)	~10%
DSSC	11.2% (Han et al., 2006)	5-9%	5,38% (Goldstein et al., 2009)	---
OPV (thin film)	8.3% (Konarka, 2010) 8.3% (Heliatek, 2010) 8.5% (Mitsubishi, 2011)	3-5%	3.86% (Solarmer, 2009)	1-3%

Table 1. Comparison of best and average PCE values of single solar cells and modules of different PV technologies.

2. Device structures and working principle

Organic-inorganic hybrid solar cells are typically thin film devices consisting out of photoactive layer(s) between two electrodes of different work functions. High work function, conductive and transparent indium tin oxide (ITO) on a flexible plastic or glass substrate is often used as anode. The photoactive light absorbing thin film consists out of a conjugated polymer as organic part and an inorganic part out of e.g. semiconducting nanocrystals (NCs). A top metal electrode (e.g. Al, LiF/Al, Ca/Al) is vacuum deposited onto the photoactive layer finally. A schematic illustration of a typical device structure is shown in Fig. 1a. Generally there are two different structure types for photoactive layers - the bilayer structure (Fig. 1b) and the bulk heterojunction structure (Fig. 1c). The latter one is usually realized by just blending the donor and acceptor materials and depositing the blend on a substrate. In contrast to bulk inorganic semiconductors, photon absorption in organic semiconductor materials does not generate directly free charge carriers, but strongly bound electron-hole pairs so-called excitons (Gledhill et al., 2005). Since the exciton diffusion lengths in conjugated polymers are typically around 10-20 nm (Halls et al., 1996) the optimum distance of the exciton to the donor/acceptor (D/A) interface, where charge transfer can take place and excitons dissociate into free charge carriers, should be in the same length range. Therefore the bulk-heterojunction structure was introduced where the electron donor and acceptor materials are blended intimately together (Halls et al., 1995). The interfacial area is dramatically increased and the distance that excitons have to travel to reach the interface is reduced. After exciton dissociation into free charge carriers, holes and electrons are transported via polymer and NC percolation pathways towards the respective electrodes. Ideally, an interdigital donor acceptor configuration would be a perfect structure for efficient exciton dissociation and charge transport (Fig. 1d). In such a structure, the distance from exciton generation sites, either in the donor or the acceptor phase, to the D/A

interface would be in the range of the exciton diffusion length. After exciton dissociation, both holes and electrons will be transported within their pre-structured donor or acceptor phases along a direct percolation pathway to the respective electrodes. This interdigital structure can be realized by various nanostructuring approaches, which will be discussed in detail later in the section 6.2.2.

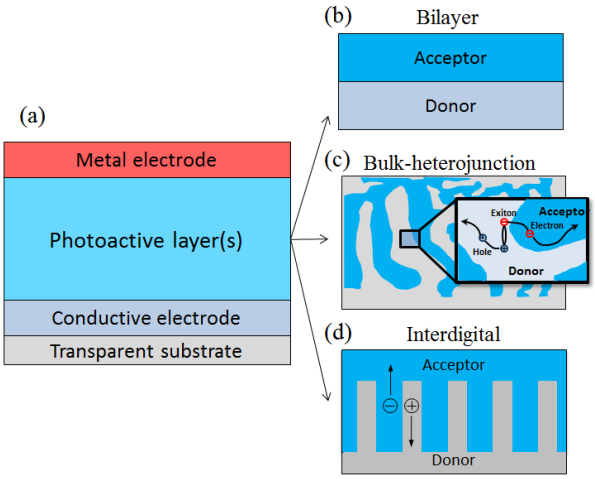

Fig. 1. Schematic illustration of typical device structures for hybrid solar cells.

In hybrid solar cells, photocurrent generation is a multistep process. Briefly, when a photon is absorbed by the absorbing material, electrons are exited from the valance band (VB) to the conduction band (CB) to form excitons. The excitons diffuse to the donor/acceptor interface where charge transfer can occur leading to the dissociation of the excitons into free electrons and holes. Driven by the internal electric field, these carriers are transported through the respective donor or acceptor material domains and are finally collected at the respective electrodes. To sum up, there are four main steps: photon absorption, exciton diffusion, charge separation as well as charge carrier transport and collection. The physics of organic/hybrid solar cells is reviewed in detail elsewhere (Greenham, 2008; Saunders & Turner, 2008).

3. Donor-acceptor materials

Due to the decreased size of NCs down to the nanometer scale, quantum effects occur, thus a number of physical (e.g. mechanical, electrical, optical, etc.) properties change when compared to those of bulk materials. For example, the quantum confinement effect (Brus, 1984) can be observed once the diameter of the material is in the same magnitude as the wavelength of the electron wave function. Along with the decreasing size of NCs, the energy levels of NCs turn from continuous states to discrete ones, resulting in a widening of the band gap apparent as a blue shift in the absorption and photoluminescence (PL) spectra. In general, there are two distinct routes to produce NCs: by physical approaches where they can be fabricated by lithographic methods, ion implantation, and molecular beam deposition; or by chemical approaches where they are synthesized by colloidal chemistry in

solution. Colloidal synthetic methods are widely used and are promising for large batch production and commercial applications. The unique optical and electrical properties of colloidal semiconductor NCs have attracted numerous interests and have been explored in various applications like light-emitting diodes (LEDs) (Kietzke, 2007), fluorescent biological labeling (Bruchez et al., 1998), lasers (Kazes et al., 2002), and solar cells (Huynh et al., 2002).
Colloidal NCs synthesized in organic media are usually soluble in common organic solvents thus they can be mixed together with conjugated polymers which are soluble in the same solvents. With suitable band gap and energy levels, NCs can be incorporated into conjugated polymer blends to form so-called bulk-heterojunction hybrid solar cells (Borchert, 2010; Reiss et al., 2011; Xu & Qiao, 2011; Zhou, Eck et al., 2010). CdS, CdSe, CdTe, ZnO, SnO_2, TiO_2, Si, PbS, and PbSe NCs have been used so far as electron acceptors. In Table 2 different donor-acceptor combinations in 3rd generation solar cells are shown together with the respective highest achieved PCEs from laboratory devices.
Bulk-heterojunction hybrid solar cells are still lagging behind the fullerene derivative-based OPVs in respect of device performance. Nevertheless, they have the potential to achieve better performance while still maintaining the benefits such as potentially low-cost, thin and flexible, and easy to produce. By tuning the diameter of the NCs, their band gap as well as their energy levels can be varied due to the quantum size effect. Furthermore, quantum confinement leads to an enhancement of the absorption coefficient compared to that of the bulk materials (Alivisatos, 1996). As a result, in the NCs/polymer system, both components have the ability to absorb incident light, unlike the typical polymer/fullerene system where the fullerene contributes very little to the photocurrent generation (Diener & Alford, 1998; Kazaoui & Minami, 1997). In addition, NCs can provide stable elongated structures on the length scale of 2-100 nm with desirable exciton dissociation and charge transport properties (Huynh et al., 2002).

Donor	Acceptor	PCE(%)	Reference
Polymer	C_{60} derivative	8.3	(Konarka, 2010)
Polymer	CdSe Tetrapods	3.19	(Dayal et al., 2010)
Polymer	Polymer	2.0	(Frechet et al., 2009)
Small molecule	Small molecule	8.3	(Heliatek, 2010)
Dye	TiO_2	11.2	(Han et al., 2006)

Table 2. Donor-acceptor combinations and best PCEs of 3rd generation solar cells.

Fig. 2 illustrates commonly used donor and acceptor materials in bulk-heterojunction hybrid solar cells. The conjugated polymers usually act as electron donors and semiconductor NCs with different shapes such as spherical quantum dots (QDs), nanorods (NRs) and tetrapods (TPs) as well as the C_{60} derivative PCBM as electron acceptor materials.
In Fig. 3 the energy levels (in eV) of commonly used conjugated polymers as donors and NCs as acceptors for bulk-heterojunction hybrid solar cells are summarized and compared. The Fermi levels of the electrodes and the energy levels of PCBM are shown as well. The variation of the values for the energy levels are deriving from different references and are due to different applied measurement methods for extracting the respective values of the lowest unoccupied molecular orbitals and highest occupied molecular orbitals (HOMO-LUMO) levels such as cyclic voltammetry (CV), X-ray photoelectron spectroscopy (XPS), ultra-violet photoelectron spectroscopy (UPS). The data for the respective HOMO-LUMO levels have been extracted from various references which are given in a recent review article (Zhou, Eck et al., 2010).

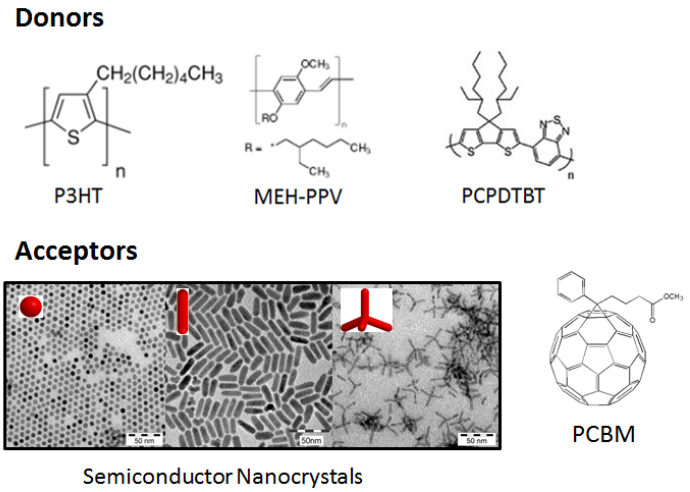

Fig. 2. Up: Chemical structures of commonly used conjugated polymers as electron donors for bulk-heterojunction hybrid solar cells. Shown are Poly(3-hexylthiophene-2,5-diyl) (P3HT), Poly[2-methoxy-5-(2-ethylhexyloxy)-1,4-phenylenevinylene](MEH-PPV), and Poly[2,6-(4,4-bis-(2-ethylhexy)-4H-cyclopenta[2,1-b;3,4-b]-dithiophene)-alt-4,7-(2,1,3-benzothiadiazole)](PCPDTBT). Down: Differently shaped semiconductor NCs as well as the chemical structure of [6,6]-Phenyl C_{61} butyric acid methyl ester (PCBM) as electron acceptors.

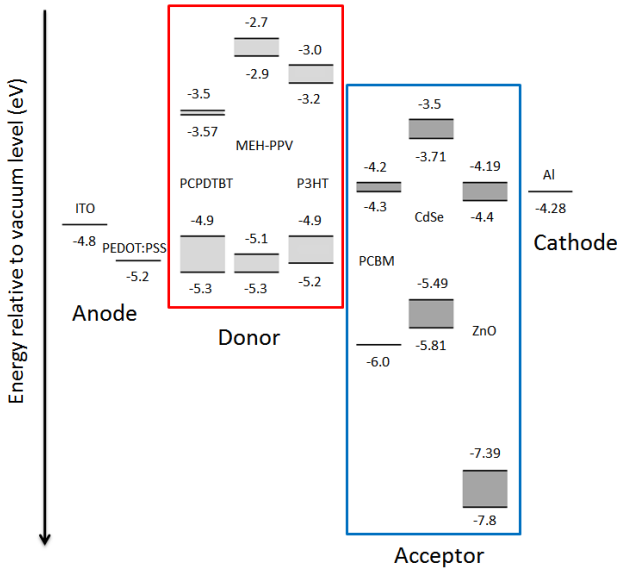

Fig. 3. Energy levels (in eV) of commonly used conjugated polymers as electron donors and NCs as electron acceptors in bulk-heterojunction hybrid solar cells.

Energy levels of donor and acceptor materials should match for efficient charge separation at the D/A interface. PL spectroscopy is a simple and useful method to investigate if a material combination can be an appropriate D/A system (Greenham et al., 1996). Because pure polymers such as P3HT and MEH-PPV exhibit a strong PL behaviour, its PL intensity is quenched by the addition of NCs with matching energy levels. This is an indication that charge transfer occurs from polymer to NCs. However, the observation of PL quenching is not necessarily a proof of charge separation within the D/A system because Förster resonance energy transfer (FRET) could also happen from larger band gap materials to smaller band gap materials, leading to strong PL quenching as well (Greenham et al., 1996). Therefore, additional methods such as photoinduced absorption (PIA) spectroscopy and light-induced electron spin resonance (L-ESR) spectroscopy are used in order to exclude PL quenching due to FRET. A detailed review on these two methods has been recently published (Borchert, 2010).

4. CdSe NCs based hybrid solar cells

CdSe NCs were the first NCs being incorporated into solar cells which still exhibit the highest PCEs compared to devices with NCs from other materials, and are still under extensive studies for utilization in hybrid solar cells. CdSe NCs have some advantages: they absorb at a useful spectral range for harvesting solar emission from 300 nm to 650 nm, they are good electron acceptors in combination with conjugated polymers, and the synthetic methods for their synthesis are well-established. The incorporation of CdSe spherical quantum dots into polymer for hybrid solar cells was firstly reported in 1996 (Greenham et al., 1996). At a high concentration of NCs of around 90% by weight (wt%), external quantum efficiencies (EQE) up to 10% were achieved, indicating an efficient exciton dissociation at the polymer/NCs interface. Although the phase separation, between the polymer and the NCs was observed to be in the range of 10-200 nm, the PCEs of devices were very low of about 0.1%. This was attributed to an inefficient electron transport between the individual NCs. After different shapes of NCs were synthetically available (Peng X. G. et al., 2000), different elongated CdSe structures were utilized in hybrid solar cells as electron acceptor materials.
Meanwhile numerous approaches were published regarding the synthesis of various morphologies and structures of CdSe NCs such as QDs, NRs and TPs and their application in hybrid solar cells. A significant advance was reported in 2002 (Huynh et al., 2002), when efficient hybrid solar cells based on elongated CdSe NRs and P3HT were obtained. Elongated NRs were used for providing elongated pathways for effective electron transport. Additionally, P3HT was used as donor material instead of MEH-PPV since it has a comparatively high hole mobility and absorbs at a longer wavelength range compared to PPV derivatives (Schilinsky et al., 2002). By increasing the NRs length, improved electron transport properties were demonstrated resulting in an improvement of the EQE. The optimized devices consisting out of 90wt% pyridine treated nanorods (7 nm in diameter and 60 nm in length) and P3HT exhibited an EQE over 54% and a PCE of 1.7%. Later on, 1,2,4-trichlorobenzene (TCB), which has a high boiling point, was used as solvent for P3HT instead of chlorobenzene. It was found that P3HT forms fibrilar morphology when TCB was used as solvent providing extended pathways for hole transport, which resulted in improved device efficiencies up to 2.6% (Sun & Greenham, 2006). Further improvement was achieved by using CdSe TPs, since TPs always have an extension perpendicular to the electrode for more efficient electron transport in comparison to NRs which are preferentially

oriented more parallel to the electrode (Hindson et al., 2011). Devices based on pyridine treated CdSe TPs exhibited efficiencies up to 2.8% (Sun et al., 2005). Recently, by using the lower band gap polymer PCPDTBT, which can absorb a higher fraction of the solar emission, an efficiency of 3.19% was reported (Dayal et al., 2010). This value is up to date the highest efficiency for colloidal NCs based bulk-heterojunction hybrid solar cells.

Elongated or branched NCs in principal can provide more extended and directed electrical conductive pathways, thus reducing the number of inter-particle hopping events for extracting electrons towards the electrode. However, device performance does not only benefit from the shape of the NCs, but also from their solubility and surface modification which influence significantly the charge transfer and carrier transport behavior. Despite the relatively high intrinsic conductivity within the individual NCs, the electron mobility through the NC network in hybrid solar cells is quite low, which could be mainly attributed to the electrical insulating organic ligands on the NC surface. Ginger *et al.* have investigated charge injection and charge transfer in thin films of spherical CdSe NCs covered with TOPO ligand sandwiched between two metal electrodes (Ginger & Greenham, 2000). Very low electron mobilities in the order of 10^{-5} $cm^2V^{-1}s^{-1}$ were measured, whereas the electron mobility of bulk CdSe is in the order of 10^2 $cm^2V^{-1}s^{-1}$ (Rode, 1970). In most cases, the ligands used for preventing aggregation during the growth of the NCs contain long alkyl chains, such as oleic acid (OA), trioctylphosphine oxide (TOPO) or hexadecylamine (HDA), form electrically insulating layers preventing an efficient charge transfer between NCs and polymer, as well as electron transport between the individual NCs (Greenham et al., 1996; Huynh et al., 2003). In order to overcome this problem, post-synthetic treatment on the NCs has been investigated extensively. Fig. 4 shows two general strategies of post-synthetic treatment on NCs for improving the performance of hybrid solar cells – ligand exchange from original long alkyl ligands to shorter molecules e.g. pyridine, and chemical surface treatment and washing for reducing the ligand shell. A combination of ligand shell reduction and ligand exchange afterwards might further improve the solar cell performance by enhancing the electron transport in the interconnected NC network.

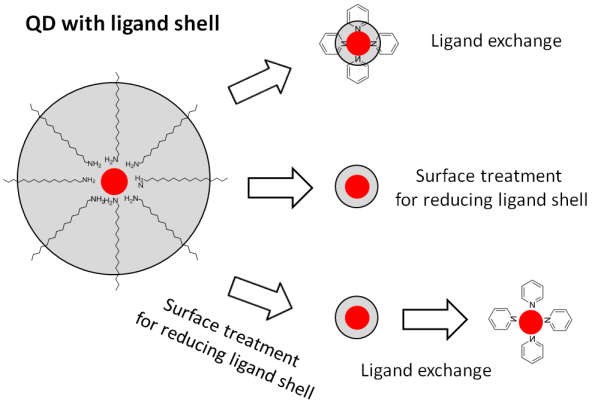

Fig. 4. Schematic illustration of two post-synthetic QD treatment strategies to enhance the PCEs in hybrid solar cells: ligand exchange (up) and reduction of the ligand surface of QDs by applying a washing procedure (middle). A combination of the two approaches might be beneficial for further enhancing the performance of hybrid solar cells (down).

Pyridine ligand exchange is the most commonly used and effective postsynthetic procedure so far, leading to the state-of-the-art efficiencies for hybrid solar cells (Huynh et al., 2002). Generally, as-synthesized NCs are washed by methanol several times and consequently refluxed in pure pyridine at the boiling point of pyridine under inert atmosphere overnight. This pyridine treatment is believed to replace the synthetic insulating ligand with shorter and more conductive pyridine molecules.

Treatments with other materials such as chloride (Owen et al., 2008), amine (Olson et al., 2009), and thiols (Aldakov et al., 2006; Sih & Wolf, 2007) were also investigated. Aldakov et al. systematically investigated CdSe NCs modified by various small ligand molecules with nuclear magnetic resonance (NMR), optical spectroscopy and electrochemistry, although their hybrid devices exhibited low efficiencies (Aldakov et al., 2006). Olson *et al.* reported on CdSe/P3HT blended devices exhibiting PCEs up to 1.77% when butylamine was used as a shorter capping ligand for the NCs (Olson et al., 2009). In an alternative approach, shortening of the insulating ligands by thermal decomposition was demonstrated and led to a relative improvement of the PCEs of the CdSe/P3HT-based solar cells (Seo et al., 2009).

However, NCs after ligand exchange with small molecules tend to aggregate and precipitate out of the organic solvent because long alky chain ligands are replaced (Huynh et al., 2002; Huynh et al., 2003), resulting in difficulties to obtain stable mixtures of NCs and polymer. Recently, a new strategy for post-synthetic treatment on spherical CdSe QDs was demonstrated (Zhou, Riehle et al., 2010), where the NCs were treated by a simple and fast hexanoic acid-assisted washing procedure. One advantage of avoiding the exchange of the synthesis capping ligands is that the QDs retain a good solubility after acid treatment, resulting in reproducible performance as well as allowing a high loading of the CdSe QDs in the blend, which is preferable for an efficient percolation network formation during the annealing step of the photoactive composite film. Devices with optimized ratios of QDs to P3HT exhibited reproducible PCEs up to 2.1% after spectral mismatch correction (Zhou, Eck et al., 2010) (Fig. 5a). This is the highest reported value for a CdSe QD / P3HT based hybrid solar cell so far. It is notable that the FF is relatively high up to 0.54, implying a good charge carrier transport capability in the devices. A simple reduced ligand sphere model was proposed to explain the possible reason for improved photovoltaic device efficiencies after acid treatment as shown in Fig. 5b (Zhou, Riehle et al., 2010). By the assistance of hexanoic acid this "immobilized" insulating spheres formed by HDA ligands are effectively reduced in size due to the salt formation of HDA. This organic salt is also much more easily dissolved in the supernatant solution than unprotonated HDA and can be separated easily from the QDs by subsequent centrifugation.

In addition, extended investigations on TOP/OA capped CdSe QDs suggested that the hexanoic acid treatment is also for this ligand system applicable for improving the device performance. Although these two kinds of QDs have different sizes (5.5 nm for HDA-capped QDs and 4.7 nm for TOP/OA capped QDs) which could result in different energy levels of QDs as well, after acid treatment both devices exhibit PCEs of 2.1% (Zhou et al., 2011) as shown in Fig. 6. Furthermore, using low band gap polymer PCPDTBT, optimized devices based on acid treated TOP/OA CdSe QDs were achieved and exhibited the highest efficiency of 2.7% for CdSe QD based devices so far (Zhou et al., 2011).

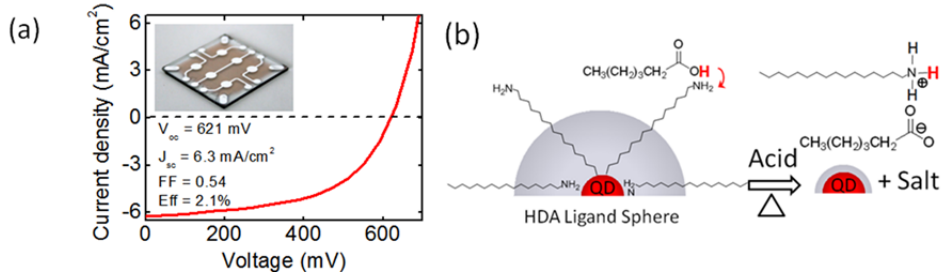

Fig. 5. (a) J-V characteristic of a hybrid solar cell device containing 87 wt% CdSe QDs and P3HT as photoactive layer under AM1.5G illumination, exhibiting a PCE of 2.1% after spectral mismatch correction (Inset: Photograph of the hybrid solar cell device structure) [Zhou, Eck et al., 2010] – Reproduced by permission of The Royal Society of Chemistry. (b) Schematic illustration of the proposed QD sphere model: an outer insulating HDA ligand sphere is supposed to be responsible for the insulating organic layer in untreated QDs directly taken out of the synthesis matrix and is effectively reduced in size by methanol washing and additional acid treatment. Reprinted with permission from [Zhou, Riehle et al., 2010]. Copyright [2010], American Institute of Physics..

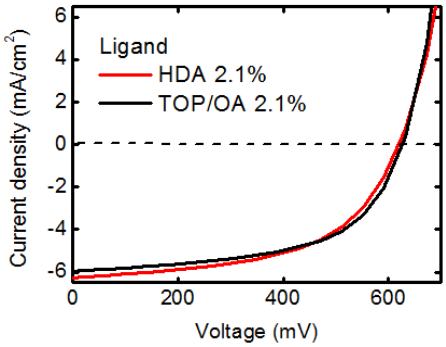

Fig. 6. Comparison of J-V characteristics of the best devices fabricated based on HDA or TOP/OA ligand capped CdSe QDs and P3HT, exhibiting similar PCEs of 2.1%.

5. Hybrid solar cells based on other NCs

Other semiconductor NCs than CdSe were also used for hybrid solar cells. ZnO NCs have attracted a lot of attention because they are less toxic than other II-VI semiconductors and are relatively easy to synthesize in large quantities. Devices based on blends of MDMO-PPV and ZnO NCs at an optimized NC content (67 wt%) presented a PCE of 1.4% (Beek et al., 2004). By using P3HT as donor polymer which has a higher hole mobility together with an in-situ synthesis approach of ZnO directly in the polymer matrix, the efficiency was optimized up to 2% using a composite film containing 50 wt% ZnO NCs (Oosterhout et al., 2009). However, because of the relatively large band gap, the contribution to the absorption of light from ZnO NCs is very low. Another disadvantage is the low solubility of ZnO NCs in solvents which are commonly used for dissolving conjugated polymers (Beek et al., 2006).

This problem of processing ZnO NCs together with polymers to obtain well-defined morphologies limits up to now the further improvement of the solar cell performance of ZnO based hybrid solar cells.

Low band gap NCs such as CdTe, PbS, PbSe, $CuInS_2$ and $CuInSe_2$ NCs are promising acceptor materials due to their ability of absorbing light at longer wavelengths which may allow an additional fraction of the incident solar spectrum to be absorbed. For instance, CdTe NCs have a smaller band gap compared to CdSe NCs, while their synthesis routes are similar to CdSe NCs (Peng & Peng, 2001). However, suitable CdTe/polymer systems have not yet been found, and reported PCEs based on CdTe/MEH-PPV are quite below 0.1% (Kumar & Nann, 2004). A systematic investigation on hybrid solar cells based on MEH-PPV blended with $CdSe_xTe_{1-x}$ tetropods demonstrated a steady PCE decrease from 1.1% starting from CdSe to 0.003% with CdTe (Zhou et al., 2006). The reason of the dramatically decrease in efficiency could be attributed to the possibility that energy transfer rather than charge transfer could occur from the polymer to CdTe NCs in CdTe/Polymer blends, resulting in an insufficient generation of free charge carriers (van Beek et al., 2006; Zhou et al., 2006). However there is one work reporting over 1% efficiency using vertically aligned CdTe nanorods combined with poly(3-octylthiophene) (P3OT), indicating that CdTe NCs may be useful for hybrid solar cells when the energy levels are matching to the polymers (Kang et al., 2005). Further lowering of the NC band gap could be achieved by using semiconductors such as PbS or PbSe. Watt et al. have developed a novel surfactant-free synthetic route where PbS NCs were synthesized in situ within a MEH-PPV film (Watt et al., 2004; Watt et al., 2005). $CuInS_2$ and $CuInSe_2$ which have been successfully used in inorganic thin film solar cells are promising for hybrid solar cells as well. Although an early study performed by Arici et al. (Arici et al., 2003) showed very low efficiencies <0.1%, recent progress on colloidal synthesis methods for high quality $CuInS_2$ (Panthani et al., 2008; Yue et al., 2010) might stimulate the development to more efficient photovoltaic devices. In general, using low band gap NCs as electron acceptors in polymer/NCs systems has been not successful yet, because energy transfer from polymer to low band gap NCs is the most likely outcome, resulting in inefficient exciton dissociation.

Recently it has been demonstrated that Si NCs are a promising acceptor material for hybrid solar cells due to the abundance of Si compounds, non-toxicity, and strong UV absorption. Hybrid solar cells based on blends of Si NCs and P3HT with a PCE above 1% have been reported (Liu et al., 2009). Si NCs were synthesized by radio frequency plasma via dissociation of silane, and the size can be tuned between 2 nm and 20 nm by changing chamber pressure, precursor flow rate, and radio frequency power. Devices made out of 50 wt% Si NCs, 3-5 nm in size, exhibited a PCE of 1.47% under AM1.5 G illumination which is a promising result (Liu et al., 2010).

The distribution of ligand-free NCs into the conjugated polymer matrix should be of great advantage for the resulting hybrid solar cells. This can be realized by an "in situ" synthesis approach of NCs directly in the polymer matrix. First attempts have been performed with a one pot synthesis of PbS in MEH-PPV by Watt et al. (Watt et al. 2005). Although the size distribution and concentration of synthesized NCs was not optimized, a PCE of 1.1 % was reached using this method. Liao et al. demonstrated successfully a direct synthesis of CdS nanorods in P3HT, leading to hybrid solar cells with PCEs up to 2.9% (Liao et al., 2009).

Table 3 summarized the selected performance parameters of hybrid solar cells based on colloidal NCs and conjugated polymers.

NC	Shape	Polymer	PCE(%)	Reference
CdSe	TP	PCPDTBT	3.19	(Dayal et al., 2010)
CdSe	TP	OC_1C_{10}-PPV	2.8	(Sun et al., 2005)
CdSe	QD	PCPDTBT	2.7	(Zhou et al., 2011)
CdSe	NR	P3HT	2.65	(Wu & Zhang, 2010)
CdSe	NR	P3HT	2.6	(Sun & Greenham, 2006)
CdSe	TP	APFO-3	2.4	(Wang et al., 2006)
CdSe	Hyperbranched	P3HT	2.2	(Gur et al., 2007)
CdSe	QD	P3HT	2.0	(Zhou, Riehle et al., 2010)
CdSe	QD	P3HT	1.8	(Olson et al., 2009)
CdSe	NR	P3HT	1.7	(Huynh et al., 2002)
ZnO	-	P3HT	2.0	(Oosterhout et al., 2009)
ZnO	-	P3HT	1.4	(Beek et al., 2004)
CdS	NR	P3HT	2.9	(Liao et al., 2009)
CdTe	NR	MEH-PPV	0.05	(Kumar & Nann, 2004)
CdTe	NR	P3OT	1.06	(Kang et al., 2005)
PbS	QD	MEH-PPV	0.7	(Gunes et al., 2007)
PbSe	QD	P3HT	0.14	(Cui et al., 2006)
Si	QD	P3HT	1.47	(Liu et al., 2010)

Table 3. Selected performance parameters of hybrid solar cells reported in literature based on colloidal NCs and conjugated polymers.

6. Challenges and perspectives

6.1 Extension of the photon absorption and band gap engineering

Absorption of a large fraction of the incident photons is required for harvesting the maximum possible amount of the solar energy. Generally, incident photons are mainly absorbed by the donor polymer materials and partially also from the inorganic NCs. For example in blends containing 90 wt% CdSe nanoparticles in P3HT, about 60% of the total absorbed light energy can be attributed to P3HT due to its strong absorption coefficient (Dayal et al., 2010). Using P3HT as donor polymer, hybrid solar cells with spherical QDs, NRs, and hyperbranched CdSe NCs exhibited the best efficiencies of 2.0%(Zhou, Riehle et al., 2010), 2.6%(Sun & Greenham, 2006; Wu & Zhang, 2010), and 2.2%(Gur et al., 2007), respectively. However, due to the insufficient overlap between the P3HT absorption spectrum and the solar emission spectrum (Scharber et al., 2006), further improving of the PCE values seems to be difficult to obtain with this polymer system.

Assuming that all photons up to the band gap edge are absorbed and converted into electrons without any losses (i.e. external quantum efficiency (EQE) is constant 1), crystalline silicon with a band gap of 1.1 eV can absorb up to 64% of the photons under AM1.5 G illumination, with a theoretical achievable current density J_{sc} of about 45 mA/cm^2. While in the case of P3HT having a band gap of 1.85 eV, only 27% photons can be absorbed, resulting in a maximal J_{sc} of 19 mA/cm^2. By using a low band gap polymer with a band gap of e.g. about 1.4 eV, 48% photons can be absorbed leading to a maximum J_{sc} up to 32 mA/cm^2 (Zhou, Eck et al., 2010). Nevertheless, lowering the band gap of photo-absorbing materials below a certain limit will lead to a decrease in device efficiency, because the energy of absorbed photons with a larger energy than the band gap will be wasted as the electrons and holes relax to the band edges.

Most low band gap polymers are from the material classes of thiophene, fluorene, carbazole, and cylopentadithiophene based polymers, which are reviewed in detail in several articles (Kamat, 2008; Riede et al., 2008; Scharber et al., 2006). Among those low band gap polymers, PCPDTBT (chemical structure shown in Fig.2) with a band gap of ~1.4 eV and a relatively high hole mobility up to 1.5×10^{-2} $cm^2V^{-1}s^{-1}$ (Morana et al., 2008) appears to be an excellent candidate as a photon-absorbing and electron donating material (Soci et al., 2007). OPVs based on PCPDTBT:$PC_{70}BM$ system achieved already efficiencies up to 5.5% (Peet et al., 2007) and 6.1%(Park et al., 2009). Recently, a bulk-heterojunction hybrid solar cell based on CdSe tetrapods and PCPDTBT was reported by Dayal et al.(Dayal et al., 2010) with an efficiency of 3.13%. Devices based on PCPDTBT and CdSe TPs, exhibited an EQE of >30% in a broad range from 350 nm to 800 nm, which is the absorption band of the polymer. It is notable that the devices reached very high J_{sc} values above 10 mA/cm^2, indicating that the broad absorption ability of the photoactive hybrid film consequently contributes to the photocurrent. Zhou et al. reported on a direct comparison study of using PCPDTBT and P3HT as donor polymer for CdSe QDs based hybrid solar cells (Zhou et al., 2011). Fig. 7a shows the comparison of the best cells fabricated from blends of P3HT:CdSe and PCPDTBT:CdSe. The PCPDTBT based device showed a considerable enhancement of PCE to 2.7% compared to the P3HT based device mainly due to the increase of J_{sc}. Fig. 7b shows the EQE spectrum of photovoltaic devices comparing the two different polymers. The PCPDTBT based device showed a broader EQE spectrum from 300 nm to 850 nm, and considerable photocurrent contribution from the QDs was observed at 400 nm region where the QD absorption is strong. This implies that both components of the PCPDTBT:CdSe system contribute to the absorption of incident photons and to the photocurrent generation. The energy levels of donor and acceptor materials also play an important role determining the V_{oc} and consequently device efficiency. The optimum LUMO offset between donor and acceptor has been investigated by many research groups. An offset energy of 0.3 eV was found to be sufficient for charge transfer (Brabec et al., 2002; Bredas et al., 2004). Therefore, fitting of the donor and acceptor energy levels as well as band gap engineering are desirable for eliminating energy losses during the charge transfer process. Scharber et al. demonstrated a relationship between PCEs of solar cells, band gaps, and the offsets between donor and acceptor LUMO levels of the donor materials.

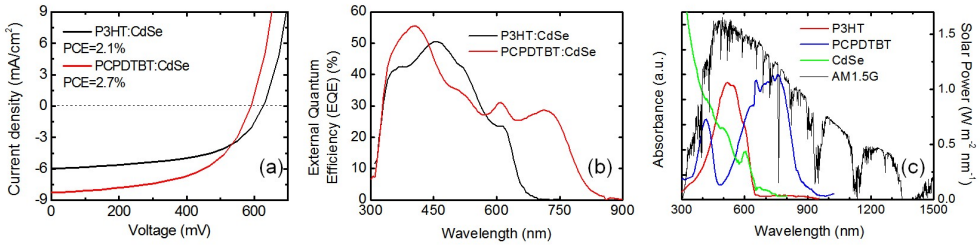

Fig. 7. (a) J-V characteristics of the best solar cells fabricated from blends of P3HT:CdSe and PCPDTBT:CdSe with a PCEs of 2.1% and 2.7% respectively. (b) EQE spectra of the P3HT:CdSe and PCPDTBT:CdSe devices (c) Absorption spectra of CdSe QDs, P3HT, PCPDTBT in thin films, in comparison with the AM1.5G solar emission spectrum.

As a result, for PCEs of devices exceeding 10%, a donor band gap <1.74 eV and a LUMO level <-3.92 eV are required (Scharber et al., 2006). In addition, Dennler et al. demonstrated

that for a minimum energy offset of 0.3 eV between the donor and acceptor LUMO levels, PCEs of >10% are practical available for a donor polymer with an ideal optical band gap of ~1.4 eV (Riede et al., 2008). Recently, Xu et al. predicted the highest achievable cell efficiencies in polymer/NCs hybrid solar cells by considering the polymer band gaps and polymer LUMO energy levels (Xu & Qiao, 2011). Fig. 9 illustrates the 3D contour plots of polymer LUMO levels, polymer band gaps, and calculated device efficiencies for three representative inorganic NCs with CBs at ~4.2 eV (TiO_2), ~4.4 eV (ZnO) and ~3.7 eV (CdSe). Assuming all of the photons are absorbed by the polymers and the V_{oc} equals to the energy offset between the polymer HOMO and the NC LUMO, device efficiencies beyond 10% can be achieved by using polymers with optimal band gaps and LUMO levels.

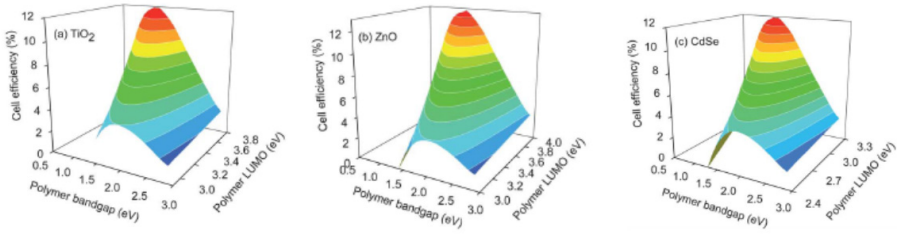

Fig. 8. 3D contour plots of polymer LUMO energy levels, polymer band gaps and cell efficiencies in a single junction solar cell structure with three representative inorganic semiconductor acceptors of (a) TiO2; (b) ZnO; and (c) CdSe. The conversion efficiencies of solar cells were calculated by assuming IPCE =65%, FF=60% under AM 1.5 with an incident light intensity of 100 mW cm^2. [Xu & Qiao, 2011] – Reproduced by permission of The Royal Society of Chemistry.

Another approach to increase the photon absorption in the active layer is to use light trapping structures as substrates or as electrodes. Light trapping can be used to overcome the problem of insufficient absorption in thin film solar cells in general (Rim et al., 2007). Nano- and microstructures of the photoactive film material can be utilized to enlarge the total pathway of incident light through the active layer. An early attempt for realizing a light trapping structure in organic solar cells was made by Roman et al. (Roman et al., 2000), who used a sub micrometer patterned grating created by lithography to mold the active layer in a way that it exhibits a cross sectional saw tooth characteristic on its surface. The subsequently deposited aluminum top electrode is then acting as a reflactive layer. Furthermore Niggemann et al. created buried nanoelectrodes (Niggemann et al., 2004) requiring an inverted cell design by using a structured aluminium coated electrode, and microprisms (Niggemann et al., 2008) as light trapping substrate for organic solar cells. So far light trapping was only applied on pure organic solar cells, but because of the similar device structure these attempts can also be applied to hybrid solar cells.

6.2 Enhancing of the charge carrier transport in hybrid solar cells

The film morphology plays a decisive role in the performance of a hybrid solar cell. Both the nano-phase separation and the charge extraction must be optimized for a highly efficient solar cell. For an optimal nano-phase separation the acceptor material must be homogeneously distributed in the blend. For optimizing the charge extraction towards the electrodes, continuous percolation pathways should exist for the charges to move towards

the respective electrodes. For optimized hybrid films with suitable nano-phase separation the solvents used for the donor-acceptor blends must suit well for both the NCs and the polymer. In order to improve the dispersibility of the NCs inside the NC/polymer mixture, pyridine is added in a certain optimal concentration to the P3HT solvent chloroform. The experiment resulted in a reduction of the surface roughness of the hybrid film which was measured by AFM and in a higher EQE for hybrid devices (Huynh et al., 2003).
The crystallinity of the conjugated polymer is another important factor to consider for improving the hole extraction towards the anode of the solar cell. Therefore P3HT is a suitable material (Sharma et al., 2010). Greenham's group reported that using TCB as a solvent with a slow evaporation rate, in contrast to chloroform, is enhancing the self organization of the polymer and thereby the efficiency of a P3HT/CdSe (NR) solar cell (Sun & Greenham, 2006). Additionally during the the thermal treatment interfacial and access ligands (e.g. pyridine) are removed (Huynh et al., 2003). By treating the blend at temperatures of ca. 110°C it is reported that oxygen is removed from the P3HT (Olson et al., 2009). Erb et. al reported that the crystallinity of P3HT is improving significantly after thermal annealing which can be observed by the extension of the absorption spectra to longer wavelengths after thermal treatment of the polymer (Erb et al., 2005).

6.2.1 Visualization of the nanomorphology of thin hybrid films

An AFM analysis of the active layer of the hybrid blend reveals information about the surface topography. Here the roughness is mostly regarded as indicator for the quality of the nanophase separation of NC and polymer phases. An AFM image of the surface of a CdSe/P3HT hybrid film is shown in Fig. 9a. In addition TEM can be used for the investigation of thin hybrid films. The two dimensional image delivers information about the distribution of donor and acceptor materials in the film (Fig. 9b). Hereby the quality of the mixing and the tendency of NC aggregation as well as nanophase separation can be observed. A relatively new approach for the analysis of the nanomorphology in hybrid solar cells is the use of 3D TEM tomography, where a series of TEM images are taken of the sample subsequently at different tilt angles.

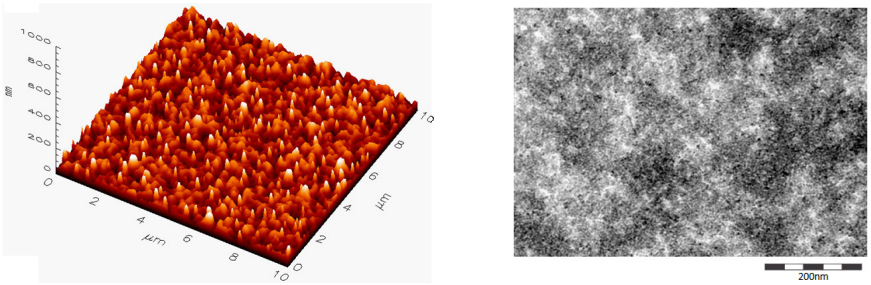

(a) (b)

Fig. 9. (a) AFM image of the surface of a spin coated CdSe/P3HT blend film, (b) TEM of a CdSe/P3HT thin film. The white areas represent the polymer phase and the dark areas the NC phase.

With the help of a computer software a three dimensional tomographic view of the donor-acceptor blend can be achieved (Fig. 10). This method is especially well suited for hybrid solar cells because they exhibit a high contrast between the inorganic NCs and the organic

polymer. The obtained visualization of the internal material distribution gives an important feedback for solar cell development.
In Fig. 10a a 3D visualization of a P3HT/ZnO thin hybrid film is shown (Oosterhout et al., 2009). The volume fraction of NCs present in the active area could be successfully extracted. Furthermore the fraction of NCs connected to the top electrode could be calculated, which was decreasing from 93% for a 57 nm thin film to 80% for a 167 nm thin film. This decrease could be correlated with the decrease of the IQE. Surprisingly despite of the better IQE, thinner films are showing a considerably coarser nanophase separation with only 60% of the fraction of the P3HT lying at a distance of 10 nm or less to the next acceptor, while this value was nearly 100% for the 167 nm thick film.
Fig.10b shows analyzed blends of OC_1C_{10}-PPV/CdSe by 3D TEM tomography (Hindson et al., 2011). It was demonstrated that the better performance of CdSe NR based devices is due to the higher connectivity between the NCs leading to a total fraction of ca. 90% NRs being connected to the top electrode while for QD based cells the fraction of connected NCs for the same weight ratio was found to be only 78%. It was additionally found that the alignment of the NRs is mostly horizontal, since 82% are aligned within 10° of the x-y-plane.

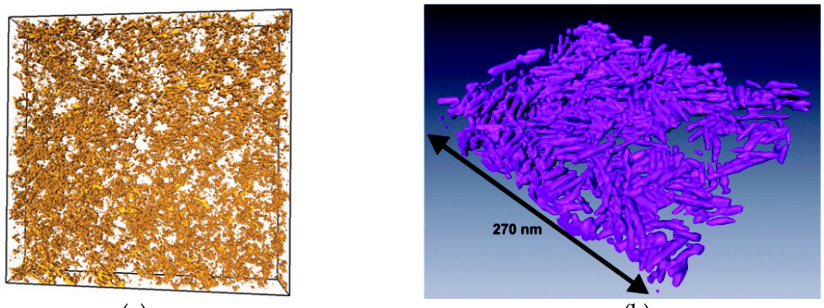

(a) (b)

Fig. 10. (a) 3D visualizations of the a hybrid P3HT/ZnO hybrid film. Reprinted by permission from Macmillan Publishers Ltd: [Nature Materials] (Oosterhout et al., 2009), copyright (2009).; (b) Distribution of NRs within a OC_1C_{10}-PPV/CdSe-NR hybrid film based on TEM tomography. Reprinted with permission from (Hindson et al., 2011). Copyright 2011 American Chemical Society.

6.2.2 Morphology control by nanostructuring approaches

Morphology control on the nanoscale is a key issue to reduce the recombination of excitons. The optical absorption length within the donor material of the film is of about 100 nm (Peumans et al., 2003), while the generated excitons have a diffusion length of only 10 nm to 20 nm (Halls et al., 1996). Even if an exciton reaches the donor-acceptor interface before it recombines, the generated free charges must be extracted over continuous percolation pathways directly to the respective electrodes without being trapped or getting lost by charge recombination.
An interpenetrated donor acceptor structure on the nanoscale, as illustrated in Fig. 1d, would considerably improve the exciton diffusion, charge collection and charge transfer efficiency resulting in higher EQE value and so leading to a higher solar cell efficiency (Sagawa et al., 2010). Figure 1d is showing a conceptual design of an ideal structure of donor

and acceptor phases within the heterojunction solar cell. Different nanostructuring approaches for hybrid heterojunction solar cells have been developed to implement such a device structure. A common method is the use of a porous template and the subsequent filling of the pores by a semiconducting material in order to fabricate vertically aligned nanopillars. One possibility to obtain porous templates is the anodic oxidation of Al to alumina, so-called Anodic Aluminum Oxidation (AAO) (Jessensky et al., 1998; Liu, P. A. et al., 2010). Here, vertical channels with diameters between 20 nm to 120 nm are formed by a first electrochemical oxidation and etching step, followed by a 2nd subsequent etching step for pore widening. The pores can be filled by different methods including simple pore filling, electrochemical deposition and vapor-liquid solid (VLS) growth processes. In principle the lengths, diameters and distances of the formed aligned nanopillars and nanowires can be controlled by the respective dimensions of the template and etching conditions. The height can be controlled by the thickness of the aluminium layer. In Fig. 11 a SEM image of an AAO template fabricated in our laboratory is shown. In a similar way the anodization of titanium films can lead to porous TiO_2 films and structures. The fabrication of vertically aligned tubes with pore diameters between 10 nm (Chen et al., 2007) and 100 nm (Macák et al., 2005) are reported. The main technical relevant differences to the AAO template is that TiO_2 itself is a semiconductor, while Al_2O_3 is an insulator, and that the pores in the TiO_2 template are closed at the bottom towards the ITO and so the filled in semiconducting material is not in contact with the electrode.

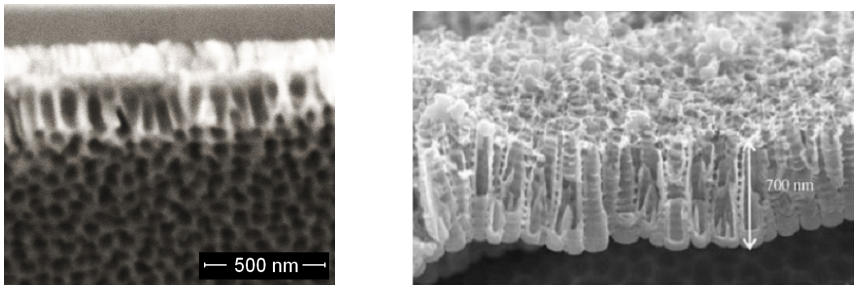

Fig. 11. Left: Side view SEM image of a porous AAO membrane manufactured by anodic oxidation of aluminium at 40 V in the presence of 0.3 M oxalic acid; right: Side view SEM image of porous TiO_2 nanotubes fabricated by anodization of titanium. (Macák et al., 2005). Copyright Wiley-VCH Verlag GmbH & Co. KGaA. Reproduced with permission.

One notable example for the integration of a nanostructuring method into solar cell device fabrication is the use of AAO templates for the deposition of CdS by a VLS process leading to aligned nanopillars. Subsequent chemical vapor deposition (CVD) of CdTe resulted into a nanostructured all inorganic solar cell with an impressive PCE of ca. 6% (Fan et al., 2009). A few attempts to use vertically aligned nanopillars to obtain nanostructured hybrid solar cells also exist (Kuo et al., 2008; Ravirajan et al., 2006). These approaches resulted so far in devices with significant lower efficiencies compared to state of the art hybrid solar cells without additional nanostructuring steps. One example for the utilization of an AAO template for a nanostructured hybrid solar cell was published by Kuo et al. (Kuo et al., 2008) and is schematically illustrated in Fig. 12a together with its energy level diagram (Fig. 12b). A direct comparison between a nanostructured bulk-heterojunction hybrid solar cell and a bilayer based hybrid solar cell was performed. First, free standing nanopillars of TiO_2 were

formed by spin coating of a TiO_2 dispersion onto the AAO template. After sintering at 450°C for 1 h and the subsequent removal of the 300 nm thick AAO template by NaOH, the TiO_2 nanopilllars were obtained. By covering the TiO_2 structure with P3HT via spin coating and subsequent evaporation of Au contacts, hybrid solar cells were manufactured with a PCE of 0.512% in comparison to 0.12% for the bilayer structure of the same donor-acceptor material composition. By this method an inverted solar cell was created, using gold as top electrode. A drawback in this design is that donor and acceptor materials are in direct contact with the ITO substrate, where both, holes and electrons, could be extracted leading to additional recombination events at the ITO electrode which lowers the overall solar cell efficiency.

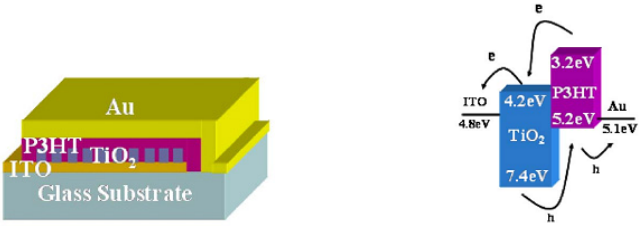

(a) (b)

Fig. 12. (a) Schematic illustration of an inverted TiO_2/P3HT hybrid solar cell manufactured by Kuo et al. using an AAO template for formation of parallel aligned TiO_2 nanopillars subsequently filled by P3HT; (b) Schematic illustration of the energy level diagram of the fabricated hybrid solar cell. Reprinted with permission from [Kuo et al., 2008]. Copyright [2008], American Institute of Physics.

It was demonstrated that by filling of the AAO template with a conjugated polymer, aligned polymer nanopillars were obtained exhibiting an increased hole mobility due to an improved vertical alignment of the polymeric chains within the AAO template (Coakley et al., 2005). The hole mobility rose by a factor of 20 from $3x10^{-4}$ $cm^2V^{-1}s^{-1}$ for a flat polymer layer in diode configuration to $6x10^{-3}$ $cm^2V^{-1}s^{-1}$ for the aligned polymer inside the AAO pores. After the AAO template was removed the spacings between the obtained polymer pillars can in principle be filled with an acceptor material like e.g. NCs from a deposited dispersion. This leads to a nanostructured hybrid solar cell with an interdigital device structure as illustrated in Fig. 1d.

Since TiO_2 is a semiconductor and could already be used as electron acceptor together with a conjugated donor polymer, the pores of a porous TiO_2 film could be directly filled with a donor polymer to obtain a nanostructured bulk-heterojunction hybrid film. Recently Lim et al. demonstrated the successful infiltration of P3HT into TiO_2 nanotubes of diameters of 60 nm to 80 nm. However, the diameters of the filled pores were above the desired diameters for an efficient charge extraction, so the reproducible and complete filling of the TiO_2 nanotubes is still one of the main challenges to be solved before this nanostructuring method can be implemented into hybrid solar cells.

Another method which was successfully applied for the formation of a nanostructured bulk-heterojunction organic solar cell is nanoimprint lithography (NIL). An AAO template was used as a mask for etching a Si substrate using a two-step inductively coupled plasma (ICP) etching process (Aryal et al., 2008). Thereby a silicon mold as shown in Fig. 13a is formed.

This mold is then used for creating NRs in a film of a conjugated polymer (e.g. regioregular P3HT). The created polymeric rods (Fig. 13c) show an increased crystallinity and preferential alignment of the polymer molecules in the vertical direction (Aryal et al., 2009) as well. The spacing between the polymer rods can then be filled with an acceptor material. After the evaporation of a top electrode the hybrid solar cell would be complete.
Kim et al. used NIL to create a nanostructured solar cell combining the molded polydithiophene derivative TDPDT with PCBM leading to a PCE of 0.8% compared to 0.25% of a bilayer structure (Kim et al., 2007).

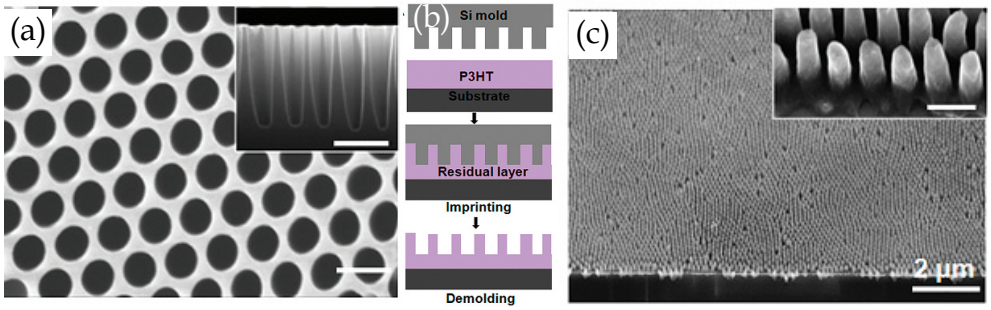

Fig. 13. (a) Silicon mold created by ICP etching using a AAO template as mask (inset image: side view of the mold); (b) illustration of the molding process applied to P3HT; (c) molded parallel aligned P3HT nanopillars. Reprinted with permission from (Aryal et al., 2009). Copyright 2009 American Chemical Society.

7. Outlook

Hybrid solar cells are still lagging behind the PCBM based OPV technology in respect of device performance and maturity for commercialization. They are currently under development and evaluation in basic research and have the potential for further significant improvement. The additional absorption of photons by semiconductor NCs, their potential to utilize multiple excitons generation and their higher electron conductivity compared to organic acceptor materials are some of the reasons behind. Novel device structures, the implementation of nanostructuring methods and the development of lower band gap material able to convert the NIR and IR parts of the solar spectrum into electrical energy will probably lead soon to PCE values of 10% and beyond for OPV technologies (Dennler et al., 2009). It is expected that the hybrid solar cell technologies also benefit from this development since device structure, nanostructuring methods and the development of novel low band gap polymers are overlapping aspects with pure OPV approaches. Progress in the development of organic-inorganic hybrid material design will not only be beneficial for the development of hybrid solar cells but also for various applications such as light emitting diodes, photodetectors etc. and have therefore a broader application potential beyond photovoltaics. In addition the energy levels in inorganic-organic hybrid materials can be tuned more easily compared to pure organic composites based on to the size quantization effects occurring in semiconductor nanostructures which might be beneficial for dedicated applications and allows a broad design flexibility for the variation of material composites.
Nevertheless one can clearly deduce from Table 1 that in all 1st and 2nd generation of PV technologies, differences between module PCEs and values of the best research cells are

much smaller than in the case of DSSCs, OPV and hybrid solar cell technologies. Therefore the enhancement of the average module efficiencies of 3rd generation solar cells is one key issue to be addressed in order to extend this technology to wide range applications substituting traditional solar panels. In addition long-term stabilities of 3rd generation solar cells have to be improved tremendously to compete with existing PV technologies otherwise their utilization will be limited to small applications in devices with a limited lifetime such as e.g. disposable sensors and actuators. In case of hybrid solar cells the exploration of additional donor-acceptor materials is necessary, in order to replace toxic compounds by more environmental friendly materials.

8. Acknowledgment

Financial support from the German Federal Ministry of Education and Research (BMBF) within the project "NanoPolySol" under the contract No. 03X3517E as well as from the German Research Foundation (DFG) graduate school GRK 1322 "Micro Energy Harvesting" is gratefully acknowledged.

9. References

Aldakov, D.; Chandezon, F.; De Bettignies, R.; Firon, M.; Reiss, P. & Pron, A. (2006). Hybrid organic-inorganic nanomaterials: ligand effects. *European Physical Journal-Applied Physics*, Vol. 36, Nr. 3, pp. 261-265, ISSN 1286-0042

Alivisatos, A. P. (1996). Semiconductor clusters, nanocrystals, and quantum dots. *Science Science*, Vol. 271, Nr. 5251, pp. 933-937, ISSN 0036-8075

Arici, E.; Sariciftci, N. S. & Meissner, D. (2003). Hybrid solar cells based on nanoparticles of CuInS2 in organic matrices. *Adv Funct Mater*, Vol. 13, Nr. 2, pp. 165-171, ISSN 1616-301X

Aryal, M.; Buyukserin, F.; Mielczarek, K.; Zhao, X. M.; Gao, J. M.; Zakhidov, A. & Hu, W. C. (2008). Imprinted large-scale high density polymer nanopillars for organic solar cells. *Journal of Vacuum Science & Technology B*, Vol. 26, Nr. 6, pp. 2562-2566, ISSN 1071-1023

Aryal, M.; Trivedi, K. & Hu, W. C. (2009). Nano-Confinement Induced Chain Alignment in Ordered P3HT Nanostructures Defined by Nanoimprint Lithography. *Acs Nano*, Vol. 3, Nr. 10, pp. 3085-3090, ISSN 1936-0851

Babel, A. & Jenekhe, S. A. (2002). Electron transport in thin-film transistors from an n-type conjugated polymer. *Adv Mater Adv Mater*, Vol. 14, Nr. 5, pp. 371-374, ISSN 0935-9648

Beek, W. J. E.; Wienk, M. M. & Janssen, R. A. J. (2004). Efficient hybrid solar cells from zinc oxide nanoparticles and a conjugated polymer. *Adv Mater Adv Mater*, Vol. 16, Nr. 12, pp. 1009-1013, ISSN 0935-9648

Beek, W. J. E.; Wienk, M. M. & Janssen, R. A. J. (2006). Hybrid solar cells from regioregular polythiophene and ZnO nanoparticles. *Adv Funct Mater Adv Funct Mater*, Vol. 16, Nr. 8, pp. 1112-1116, ISSN 1616-301X

Benagli S.; Borrello D.; Vallat-Sauvain E.; Meier J.; Kroll U.; Hötzel J.; Spitznagel J.; Steinhauser J.; Castens L., & Djeridane Y. (2009). High-efficiency amorphous silicon devices on LPCVD-ZnO TCO prepared in industrial KAI-M R&D reactor. *24th European Photovoltaic Solar Energy Conference*, Hamburg, pp. 2293 - 2298

Borchert, H. (2010). Elementary processes and limiting factors in hybrid polymer/nanoparticle solar cells. *Energ Environ Sci* , Vol. 3, Nr. 11, pp. 1682-1694, ISSN 1754-5692

Brabec, C. J.; Winder, C.; Sariciftci, N. S.; Hummelen, J. C.; Dhanabalan, A.; van Hal, P. A. & Janssen, R. A. J. (2002). A low-bandgap semiconducting polymer for photovoltaic devices and infrared emitting diodes. *Adv Funct Mater Adv Funct Mater*, Vol. 12, Nr. 10, pp. 709-712, ISSN 1616-301X

Bredas, J. L.; Beljonne, D.; Coropceanu, V. & Cornil, J. (2004). Charge-transfer and energy-transfer processes in pi-conjugated oligomers and polymers: A molecular picture. *Chem Rev Chem Rev*, Vol. 104, Nr. 11, pp. 4971-5003, ISSN 0009-2665

Bruchez, M.; Moronne, M.; Gin, P.; Weiss, S. & Alivisatos, A. P. (1998). Semiconductor nanocrystals as fluorescent biological labels. *Science*, Vol. 281, Nr. 5385, pp. 2013-2016, ISSN 0036-8075

Brus, L. E. (1984). Electron Electron and Electron-Hole Interactions in Small Semiconductor Crystallites - the Size Dependence of the Lowest Excited Electronic State. *J Chem Phys*, Vol. 80, Nr. 9, pp. 4403-4409, ISSN 0021-9606

Chen, X.; Schriver, M.; Suen, T. & Mao, S. S. (2007). Fabrication of 10 nm diameter TiO2 nanotube arrays by titanium anodization. *Thin Solid Films*, Vol. 515, Nr. 24, pp. 8511-8514, ISSN 0040-6090

Coakley, K. M.; Srinivasan, B. S.; Ziebarth, J. M.; Goh, C.; Liu, Y. X. & McGehee, M. D. (2005). Enhanced hole mobility in regioregular polythiophene infiltrated in straight nanopores. *Advanced Functional Materials*, Vol. 15, Nr. 12, pp. 1927-1932, ISSN 1616-301X

Cui, D. H.; Xu, J.; Zhu, T.; Paradee, G.; Ashok, S. & Gerhold, M. (2006). Harvest of near infrared light in PbSe nanocrystal-polymer hybrid photovoltaic cells. *Appl Phys Lett Appl Phys Lett*, Vol. 88, Nr. 18, pp. 183111, ISSN 0003-6951

Cunningham, D.; Davies, K.; Grammond, L.; Mopas, E.; O Connor, N.; Rubchich, M.; Sadeghi, M.; Skinner, N., & Trumbly, T. (2000). *28th IEEE Photovoltaic Specialists Conference*, Alaska, USA, pp. 13-18

Dayal, S.; Kopidakis, N.; Olson, D. C.; Ginley, D. S. & Rumbles, G. (2010). Photovoltaic Devices with a Low Band Gap Polymer and CdSe Nanostructures Exceeding 3% Efficiency. *Nano Lett Nano Lett*, Vol. 10, Nr. 1, pp. 239-242, ISSN 1530-6984

Dayal, S.; Reese, M. O.; Ferguson, A. J.; Ginley, D. S.; Rumbles, G. & Kopidakis, N. (2010). The Effect of Nanoparticle Shape on the Photocarrier Dynamics and Photovoltaic Device Performance of Poly(3-hexylthiophene):CdSe Nanoparticle Bulk Heterojunction Solar Cells., pp. 3629-2635

Dennler, G.; Scharber, M. C. & Brabec, C. J. (2009). Polymer-Fullerene Bulk-Heterojunction Solar Cells. *Adv Mater Adv Mater*, Vol. 21, Nr. 13, pp. 1323-1338, ISSN 0935-9648

Diener, M. D. & Alford, J. M. (1998). Isolation and properties of small-bandgap fullerenes. *Nature Nature*, Vol. 393, Nr. 6686, pp. 668-671, ISSN 0028-0836

Erb, T.; Zhokhavets, U.; Gobsch, G.; Raleva, S.; Stuhn, B.; Schilinsky, P.; Waldauf, C. & Brabec, C. J. (2005). Correlation between structural and optical properties of composite polymer/fullerene films for organic solar cells. *Advanced Functional Materials*, Vol. 15, Nr. 7, pp. 1193-1196, ISSN 1616-301X

Fan, Z. Y.; Razavi, H.; Do, J. W.; Moriwaki, A.; Ergen, O.; Chueh, Y. L.; Leu, P. W.; Ho, J. C.; Takahashi, T.; Reichertz, L. A.; Neale, S.; Yu, K.; Wu, M.; Ager, J. W. & Javey, A.

(2009). Three-dimensional nanopillar-array photovoltaics on low-cost and flexible substrates. *Nature Materials*, Vol. 8, Nr. 8, pp. 648-653, ISSN 1476-1122

Frechet, J. M. J.; Holcombe, T. W.; Woo, C. H.; Kavulak, D. F. J. & Thompson, B. C. (2009). All-Polymer Photovoltaic Devices of Poly(3-(4-n-octyl)-phenylthiophene) from Grignard Metathesis (GRIM) Polymerization. *J Am Chem Soc J Am Chem Soc*, Vol. 131, Nr. 40, pp. 14160-14161, ISSN 0002-7863

Ginger, D. S. & Greenham, N. C. (2000). Charge injection and transport in films of CdSe nanocrystals. *J Appl Phys J Appl Phys*, Vol. 87, Nr. 3, pp. 1361-1368, ISSN 0021-8979

Gledhill, S. E.; Scott, B. & Gregg, B. A. (2005). Organic and nano-structured composite photovoltaics: An overview. *J Mater Res J Mater Res*, Vol. 20, Nr. 12, pp. 3167-3179, ISSN 0884-2914

Goldstein, J.; Yakupov, I. & Breen, B. (2010). Development of large area photovoltaic dye cells at 3GSolar. *Solar Energy Materials and Solar Cells*, Vol. 94, Nr. 4, pp. 638-641, ISSN 0927-0248

Greenham, N. C. (2008) Hybrid Polymer/Nanocrystal Photovoltaic Devices, in Organic Photovoltaics (eds C. Brabec, V. Dyakonov and U. Scherf), Wiley-VCH Verlag GmbH & Co. KGaA, Weinheim, Germany.

Greenham, N. C.; Peng, X. G. & Alivisatos, A. P. (1996). Charge separation and transport in conjugated-polymer/semiconductor-nanocrystal composites studied by photoluminescence quenching and photoconductivity. *Phys Rev B Phys Rev B*, Vol. 54, Nr. 24, pp. 17628-17637, ISSN 1098-0121

Gunes, S.; Fritz, K. P.; Neugebauer, H.; Sariciftci, N. S.; Kumar, S. & Scholes, G. D. (2007). Hybrid solar cells using PbS nanoparticles. *Sol Energ Mat Sol C Sol Energ Mat Sol C*, Vol. 91, Nr. 5, pp. 420-423, ISSN 0927-0248

Gur, I.; Fromer, N. A.; Chen, C. P.; Kanaras, A. G. & Alivisatos, A. P. (2007). Hybrid solar cells with prescribed nanoscale morphologies based on hyperbranched semiconductor nanocrystals. *Nano Lett Nano Lett*, Vol. 7, Nr. 2, pp. 409-414, ISSN 1530-6984

Halls, J. J. M.; Pichler, K.; Friend, R. H.; Moratti, S. C. & Holmes, A. B. (1996). Exciton diffusion and dissociation in a poly(p-phenylenevinylene)/C-60 heterojunction photovoltaic cell. *Appl Phys Lett Appl Phys Lett*, Vol. 68, Nr. 22, pp. 3120-3122, ISSN 0003-6951

Halls, J. J. M.; Walsh, C. A.; Greenham, N. C.; Marseglia, E. A.; Friend, R. H.; Moratti, S. C. & Holmes, A. B. (1995). Efficient Photodiodes from Interpenetrating Polymer Networks. *Nature Nature*, Vol. 376, Nr. 6540, pp. 498-500, ISSN 0028-0836

Han, L.; Fukui, A.; Fuke, N.; Koide, N., & Yamanaka, R. (2006). *4th World Conference on Photovoltaic Energy Conversion (WCEP-4)*, Hawai, USA

Heliatek, Heliatek and IAPP achieve production-relevant efficiency record for organic photovoltaic cells, (11-10-2010), available at: http://www.heliatek.com/news-19

Hindson, J. C.; Saghi, Z.; Hernandez-Garrido, J. C.; Midgley, P. A. & Greenham, N. C. (2011). Morphological Study of Nanoparticle-Polymer Solar Cells Using High-Angle Annular Dark-Field Electron Tomography. *Nano Letters*, Vol. 11, Nr. 2, pp. 904-909, ISSN 1530-6984

Huynh, W. U.; Dittmer, J. J. & Alivisatos, A. P. (2002). Hybrid nanorod-polymer solar cells. *Science Science*, Vol. 295, Nr. 5564, pp. 2425-2427, ISSN 0036-8075

Huynh, W. U.; Dittmer, J. J.; Libby, W. C.; Whiting, G. L. & Alivisatos, A. P. (2003). Controlling the morphology of nanocrystal-polymer composites for solar cells. *Advanced Functional Materials*, Vol. 13, Nr. 1, pp. 73-79, ISSN 1616-301X

Huynh, W. U.; Dittmer, J. J.; Teclemariam, N.; Milliron, D. J.; Alivisatos, A. P. & Barnham, K. W. J. (2003). Charge transport in hybrid nanorod-polymer composite photovoltaic cells. *Phys Rev B Phys Rev B* , Vol. 67, Nr. 11, pp. 115326, ISSN 1098-0121

Jackson P.; Hariskos D.; Lotter E.; Paetel S.; Wuerz R.; Menner R.; Wischmann W. & Powalla M., (2011). New world record efficiency for Cu(In,Ga)Se2 thin-film solar cells beyond 20%. *Progress in Photovoltaics: Research and Applications*. Published online. DOI: 10.1002/pip.1078

Jessensky, O.; Muller, F. & Gosele, U. (1998). Self-organized formation of hexagonal pore arrays in anodic alumina. *Applied Physics Letters*, Vol. 72, Nr. 10, pp. 1173-1175, ISSN 0003-6951

Kamat, P. V. (2008). Quantum Dot Solar Cells. Semiconductor Nanocrystals as Light Harvesters. *J Phys Chem C J Phys Chem C*, Vol. 112, Nr. 48, pp. 18737-18753, ISSN 1932-7447

Kang, Y. M.; Park, N. G. & Kim, D. (2005). Hybrid solar cells with vertically aligned CdTe nanorods and a conjugated polymer. *Appl Phys Lett Appl Phys Lett*, Vol. 86, Nr. 11, ISSN 0003-6951

Kazes, M.; Lewis, D. Y.; Ebenstein, Y.; Mokari, T. & Banin, U. (2002). Lasing from semiconductor quantum rods in a cylindrical microcavity. *Adv Mater Adv Mater*, Vol. 14, Nr. 4, pp. 317, ISSN 0935-9648

Kietzke, T. (2007). Recent Advances in Organic Solar Cells., Vol. 2007, pp. 40285

Kim, M. S.; Kim, J. S.; Cho, J. C.; Shtein, M.; Guo, L. J. & Kim, J. (2007). Flexible conjugated polymer photovoltaic cells with controlled heterojunctions fabricated using nanoimprint lithography. *Applied Physics Letters*, Vol. 90, Nr. 12, ISSN 0003-6951

Konarka Technologies, Konarka's Power Plastic Achieves World Record 8.3% Efficiency Certification from National Energy Renewable Laboratory (NREL), (29-11-2010), available at: http://www.konarka.com/index.php/site/pressreleasedetail/konarkas_power_plastic_achieves_world_record_83_efficiency_certification_fr

Kumar, S. & Nann, T. (2004). First solar cells based on CdTe nanoparticle/MEH-PPV composites. *J Mater Res J Mater Res*, Vol. 19, Nr. 7, pp. 1990-1994, ISSN 0884-2914

Kuo, C. Y.; Tang, W. C.; Gau, C.; Guo, T. F. & Jeng, D. Z. (2008). Ordered bulk heterojunction solar cells with vertically aligned TiO2 nanorods embedded in a conjugated polymer. *Applied Physics Letters*, Vol. 93, Nr. 3, ISSN 0003-6951

Liao, H. C.; Chen, S. Y. & Liu, D. M. (2009). In-Situ Growing CdS Single-Crystal Nanorods via P3HT Polymer as a Soft Template, for Enhancing Photovoltaic Performance. *Macromolecules*, Vol. 42, Nr. 17, pp. 6558-6563, ISSN 0024-9297

Lim, S. L.; Liu, Y. L.; Liu, G.; Xu, S. Y.; Pan, H. Y.; Kang, E. T. & Ong, C. K. (2011). Infiltrating P3HT polymer into ordered TiO2 nanotube arrays. *Physica Status Solidi A-Applications and Materials Science*, Vol. 208, Nr. 3, pp. 658-663, ISSN 1862-6300

Liu, C. Y.; Holman, Z. C. & Kortshagen, U. R. (2009). Hybrid Solar Cells from P3HT and Silicon Nanocrystals. *Nano Lett Nano Lett*, Vol. 9, Nr. 1, pp. 449-452, ISSN 1530-6984

Liu, C. Y.; Holman, Z. C. & Kortshagen, U. R. (2010). Optimization of Si NC/P3HT Hybrid Solar Cells., Vol. 20, Nr. 13, pp. 2157-2164

Liu, P. A.; Singh, V. P. & Rajaputra, S. (2010). Barrier layer non-uniformity effects in anodized aluminum oxide nanopores on ITO substrates. *Nanotechnology*, Vol. 21, Nr. 11, ISSN 0957-4484

Macak, J. M.; Tsuchiya, H. & Schmuki, P. (2005). High-aspect-ratio TiO2 nanotubes by anodization of titanium. *Angewandte Chemie-International Edition*, Vol. 44, Nr. 14, pp. 2100-2102, ISSN 1433-7851

MiaSolé, MiaSolé Achieves 15.7% Efficiency with Commercial-Scale CIGS Thin Film Solar Modules, (2-12-2010), available at: http://www.miasole.com/sites/default/files/MiaSole_release_Dec_02_2010. pdf

Mitsubishi Chemical, 8.5% efficient small molecule organic solar cell, (8-3-2011), available at: http://www.physorg.com/pdf218812262.pdf

Morana, M.; Wegscheider, M.; Bonanni, A.; Kopidakis, N.; Shaheen, S.; Scharber, M.; Zhu, Z.; Waller, D.; Gaudiana, R. & Brabec, C. (2008). Bipolar charge transport in PCPDTBT-PCBM bulk-heterojunctions for photovoltaic applications. *Adv Funct Mater Adv Funct Mater*, Vol. 18, Nr. 12, pp. 1757-1766, ISSN 1616-301X

Musselman, K. P.; Mulholland, G. J.; Robinson, A. P.; Schmidt-Mende, L. & MacManus-Driscoll, J. L. (2008). Low-Temperature Synthesis of Large-Area, Free-Standing Nanorod Arrays on ITO/Glass and other Conducting Substrates. *Advanced Materials*, Vol. 20, Nr. 23, pp. 4470-4475, ISSN 0935-9648

Musselman, K. P.; Wisnet, A.; Iza, D. C.; Hesse, H. C.; Scheu, C.; MacManus-Driscoll, J. L. & Schmidt-Mende, L. (2010). Strong Efficiency Improvements in Ultra-low-Cost Inorganic Nanowire Solar Cells. *Advanced Materials*, Vol. 22, Nr. 35, pp. E254-E258, ISSN 0935-9648

Niggemann, M.; Glatthaar, M.; Gombert, A.; Hinsch, A. & Wittwer, V. (2004). Diffraction gratings and buried nano-electrodes - architectures for organic solar cells. *Thin Solid Films*, Vol. 451-52, pp. 619-623, ISSN 0040-6090

Niggemann, M.; Riede, M.; Gombert, A. & Leo, K. (2008). Light trapping in organic solar cells. *Physica Status Solidi A-Applications and Materials Science*, Vol. 205, Nr. 12, pp. 2862-2874, ISSN 1862-6300

Olson, J. D.; Gray, G. P. & Carter, S. A. (2009). Optimizing hybrid photovoltaics through annealing and ligand choice. *Sol Energ Mat Sol C Sol Energ Mat Sol C*, Vol. 93, Nr. 4, pp. 519-523, ISSN 0927-0248

Oosterhout, S. D.; Wienk, M. M.; van Bavel, S. S.; Thiedmann, R.; Koster, L. J. A.; Gilot, J.; Loos, J.; Schmidt, V. & Janssen, R. A. J. (2009). The effect of three-dimensional morphology on the efficiency of hybrid polymer solar cells. *Nat Mater Nat Mater*, Vol. 8, Nr. 10, pp. 818-824, ISSN 1476-1122

Owen, J. S.; Park, J.; Trudeau, P. E. & Alivisatos, A. P. (2008). Reaction chemistry and ligand exchange at cadmium-selenide nanocrystal surfaces. *J Am Chem Soc J Am Chem Soc*, Vol. 130, Nr. 37, pp. 12279-12281, ISSN 0002-7863

Panthani, M. G.; Akhavan, V.; Goodfellow, B.; Schmidtke, J. P.; Dunn, L.; Dodabalapur, A.; Barbara, P. F. & Korgel, B. A. (2008). Synthesis of CuInS2, CuInSe2, and Cu(InxGa1-x)Se-2 (CIGS) Nanocrystal "Inks" for Printable Photovoltaics. *Journal of the American Chemical Society*, Vol. 130, Nr. 49, pp. 16770-16777, ISSN 0002-7863

Park, S. H.; Roy, A.; Beaupre, S.; Cho, S.; Coates, N.; Moon, J. S.; Moses, D.; Leclerc, M.; Lee, K. & Heeger, A. J. (2009). Bulk heterojunction solar cells with internal quantum

efficiency approaching 100%. *Nat Photonics Nat Photonics*, Vol. 3, Nr. 5, pp. 297-302, ISSN 1749-4885

Peet, J.; Kim, J. Y.; Coates, N. E.; Ma, W. L.; Moses, D.; Heeger, A. J. & Bazan, G. C. (2007). Efficiency enhancement in low-bandgap polymer solar cells by processing with alkane dithiols. *Nature Materials*, Vol. 6, Nr. 7, pp. 497-500, ISSN 1476-1122

Peng, X. G.; Manna, L.; Yang, W. D.; Wickham, J.; Scher, E.; Kadavanich, A. & Alivisatos, A. P. (2000). Shape control of CdSe nanocrystals. *Nature Nature*, Vol. 404, Nr. 6773, pp. 59-61, ISSN 0028-0836

Peng, Z. A. & Peng, X. G. (2001). Formation of high-quality CdTe, CdSe, and CdS nanocrystals using CdO as precursor. *J Am Chem Soc J Am Chem Soc*, Vol. 123, Nr. 1, pp. 183-184, ISSN 0002-7863

Peumans, P.; Yakimov, A. & Forrest, S. R. (2003). Small molecular weight organic thin-film photodetectors and solar cells. *J Appl Phys J Appl Phys*, Vol. 93, Nr. 7, pp. 3693-3723, ISSN 0021-8979

Ravirajan, P.; Peiro, A. M.; Nazeeruddin, M. K.; Graetzel, M.; Bradley, D. D. C.; Durrant, J. R. & Nelson, J. (2006). Hybrid polymer/zinc oxide photovoltaic devices with vertically oriented ZnO nanorods and an amphiphilic molecular interface layer. *Journal of Physical Chemistry B*, Vol. 110, Nr. 15, pp. 7635-7639, ISSN 1520-6106

Riede, M.; Mueller, T.; Tress, W.; Schueppel, R. & Leo, K. (2008). Small-molecule solar cells - status and perspectives. *Nanotechnology Nanotechnology*, Vol. 19, Nr. 42, pp. 424001, ISSN 0957-4484

Rim, S. B.; Zhao, S.; Scully, S. R.; McGehee, M. D. & Peumans, P. (2007). An effective light trapping configuration for thin-film solar cells. *Applied Physics Letters*, Vol. 91, Nr. 24, ISSN 0003-6951

Rode, D. L. (1970). Electron mobility in II-VI semiconductors. *Phys Rev B-Solid St Phys Rev B-Solid St*, Vol. 2, Nr. 10, pp. 4036-4044

Roman, L. S.; Inganas, O.; Granlund, T.; Nyberg, T.; Svensson, M.; Andersson, M. R. & Hummelen, J. C. (2000). Trapping light in polymer photodiodes with soft embossed gratings. *Advanced Materials*, Vol. 12, Nr. 3, pp. 189-+, ISSN 0935-9648

Sagawa, T.; Yoshikawa, S. & Imahori, H. (2010). One-Dimensional Nanostructured Semiconducting Materials for Organic Photovoltaics. *Journal of Physical Chemistry Letters*, Vol. 1, Nr. 7, pp. 1020-1025, ISSN 1948-7185

Saunders, B. R. & Turner, M. L. (2008). Nanoparticle-polymer photovoltaic cells. *Advances in Colloid and Interface Science*, Vol. 138, Nr. 1, pp. 1-23, ISSN 0001-8686

Scharber, M. C.; Wuhlbacher, D.; Koppe, M.; Denk, P.; Waldauf, C.; Heeger, A. J. & Brabec, C. L. (2006). Design rules for donors in bulk-heterojunction solar cells - Towards 10 % energy-conversion efficiency. *Adv Mater Adv Mater*, Vol. 18, Nr. 6, pp. 789-794, ISSN 0935-9648

Schilinsky, P.; Waldauf, C. & Brabec, C. J. (2002). Recombination and loss analysis in polythiophene based bulk heterojunction photodetectors. *Appl Phys Lett Appl Phys Lett*, Vol. 81, Nr. 20, pp. 3885-3887, ISSN 0003-6951

Schott Solar, SCHOTT Solar Presents Champion Multicrystalline Module, (7-9-2010), available at: http://www.schott.com/english/news/press.html?NID=2948

Schultz, O.; Glunz, S. W. & Willeke, G. P. (2004). Multicrystalline silicon solar cells exceeding 20% efficiency. *Progress in Photovoltaics*, Vol. 12, Nr. 7, pp. 553-558, ISSN 1062-7995

Seo, J.; Kim, W. J.; Kim, S. J.; Lee, K. S.; Cartwright, A. N. & Prasad, P. N. (2009). Polymer nanocomposite photovoltaics utilizing CdSe nanocrystals capped with a thermally cleavable solubilizing ligand. *Appl Phys Lett Appl Phys Lett*, Vol. 94, Nr. 13, pp. 133302, ISSN 0003-6951

Sih, B. C. & Wolf, M. (2007). CdSe nanorods functionalized with thiol-anchored oligothiophenes. *J Phys Chem C J Phys Chem C*, Vol. 111, Nr. 46, pp. 17184-17192, ISSN 1932-7447

Soci, C.; Hwang, I. W.; Moses, D.; Zhu, Z.; Waller, D.; Gaudiana, R.; Brabec, C. J. & Heeger, A. J. (2007). Photoconductivity of a low-bandgap conjugated polymer. *Adv Funct Mater Adv Funct Mater*, Vol. 17, Nr. 4, pp. 632-636, ISSN 1616-301X

Solarmer Energy, Press release, (18-6-2009), available at: http://www.printedelectronicsnow.com/news/2009/06/23/solamer_energy_picks_up_speed_in_flexible_solar_panel_development_

Su, Z. X. & Zhou, W. Z. (2008). Formation Mechanism of Porous Anodic Aluminium and Titanium Oxides. *Advanced Materials*, Vol. 20, Nr. 19, pp. 3663-3667, ISSN 0935-9648

Sun, B. Q. & Greenham, N. C. (2006). Improved effciency of photovoltaics based on CdSe nanorods and poly(3-hexylthiophene) nanofibers. *Physical Chemistry Chemical Physics*, Vol. 8, Nr. 30, pp. 3557-3560, ISSN 1463-9076

Sun, B. Q.; Snaith, H. J.; Dhoot, A. S.; Westenhoff, S. & Greenham, N. C. (2005). Vertically segregated hybrid blends for photovoltaic devices with improved efficiency. *J Appl Phys J Appl Phys*, Vol. 97, Nr. 1, pp. 014914, ISSN 0021-8979

van Beek, R.; Zoombelt, A. P.; Jenneskens, L. W.; van Walree, C. A.; Donega, C. D.; Veldman, D. & Janssen, R. A. J. (2006). Side chain mediated electronic contact between a tetrahydro-4H-thiopyran-4-ylidene-appended polythiophene and CdTe quantum dots. *Chem-Eur J Chem-Eur J*, Vol. 12, Nr. 31, pp. 8075-8083, ISSN 0947-6539

Wang, P.; Abrusci, A.; Wong, H. M. P.; Svensson, M.; Andersson, M. R. & Greenham, N. C. (2006). Photoinduced charge transfer and efficient solar energy conversion in a blend of a red polyfluorene copolymer with CdSe nanoparticles. *Nano Lett Nano Lett*, Vol. 6, Nr. 8, pp. 1789-1793, ISSN 1530-6984

Watt, A. A. R.; Blake, D.; Warner, J. H.; Thomsen, E. A.; Tavenner, E. L.; Rubinsztein-Dunlop, H. & Meredith, P. (2005). Lead sulfide nanocrystal: conducting polymer solar cells. *Journal of Physics D-Applied Physics*, Vol. 38, Nr. 12, pp. 2006-2012, ISSN 0022-3727

Watt, A.; Thomsen, E.; Meredith, P. & Rubinsztein-Dunlop, H. (2004). A new approach to the synthesis of conjugated polymer-nanocrystal composites for heterojunction optoelectronics. *Chemical Communications*, Nr. 20, pp. 2334-2335, ISSN 1359-7345

Wu X.; Keane J.C.; Dhere R.G.; DeHart C.; Duda A.; Asher S.; Levi D.H., & Sheldon P. (2001). 16.5%-efficient CdS/CdTe polycrystalline thin-film solar cell. *17th European Photovoltaic Solar Energy Conference*, München, pp. 995-1000

Wu, Y. & Zhang, G. (2010). Performance Enhancement of Hybrid Solar Cells Through Chemical Vapor Annealing., Vol. 10, pp. 1628-1631

Xu, T. & Qiao, Q. (2011). Conjugated polymer-inorganic semiconductor hybrid solar cells. *Energy & Environmental Science*, DOI: 10.1039/c0ee00632g

Yue, W. J.; Han, S. K.; Peng, R. X.; Shen, W.; Geng, H. W.; Wu, F.; Tao, S. W. & Wang, M. T. (2010). CuInS2 quantum dots synthesized by a solvothermal route and their

application as effective electron acceptors for hybrid solar cells. *Journal of Materials Chemistry*, Vol. 20, Nr. 35, pp. 7570-7578, ISSN 0959-9428

Zhao, J. H.; Wang, A. H.; Green, M. A. & Ferrazza, F. (1998). 19.8% efficient "honeycomb" textured multicrystalline and 24.4% monocrystalline silicon solar cells. *Applied Physics Letters*, Vol. 73, Nr. 14, pp. 1991-1993, ISSN 0003-6951

Zhao, J.; Wang, A.; Yun, F.; Zhang, G.; Roche, D. M.; Wenham, S. R. & Green, M. A. (1997). 20,000 PERL silicon cells for the '1996 world solar challenge' solar car race. *Progress in Photovoltaics*, Vol. 5, Nr. 4, pp. 269-276, ISSN 1062-7995

Zhou, Y. F.; Eck, M. & Krüger, M. (2010). Bulk-heterojunction hybrid solar cells based on colloidal nanocrystals and conjugated polymers. *Energy & Environmental Science*, Vol. 3, Nr. 12, pp. 1851-1864, ISSN 1754-5692

Zhou, Y. F.; Riehle, F. S.; Yuan, Y.; Schleiermacher, H. F.; Niggemann, M.; Urban, G. A. & Krueger, M. (2010). Improved efficiency of hybrid solar cells based on non-ligand-exchanged CdSe quantum dots and poly(3-hexylthiophene). *Appl Phys Lett Appl Phys Lett*, Vol. 96, Nr. 1, pp. 013304, ISSN 0003-6951

Zhou, Y.; Eck, M.; Veit, C.; Zimmermann, B.; Rauscher, F.; Niyamakom, P.; Yilmaz, S.; Dumsch, I.; Allard, S.; Scherf, U. & Krueger, M. (2011). Efficiency enhancement for bulk-heterojunction hybrid solar cells based on acid treated CdSe quantum dots and low bandgap polymer PCPDTBT. *Solar Energy Materials and Solar Cells*, Vol. 95, Nr. 4, pp. 1232-1237, ISSN 0927-0248

Zhou, Y.; Li, Y. C.; Zhong, H. Z.; Hou, J. H.; Ding, Y. Q.; Yang, C. H. & Li, Y. F. (2006). Hybrid nanocrystal/polymer solar cells based on tetrapod-shaped CdSexTe1-x nanocrystals. *Nanotechnology Nanotechnology*, Vol. 17, Nr. 16, pp. 4041-4047, ISSN 0957-4484

6

Relation Between Nanomorphology and Performance of Polymer-Based Solar Cells

Almantas Pivrikas[1,2]
[1]*Physical Chemistry, Linz Institute for Organic Solar Cells, Johannes Kepler University Linz*
[2]*School of Chemistry and Molecular Biosciences, Centre for Organic Photonics and Electronics, The University of Queensland, Brisbane*
Austria

1. Introduction

Global warming and climate change has sparked the interest in alternative energy sources.(Cox et al., 2000) Although solar power reaching the surface of the Earth is able to meet the demands of humanity at the present,(Turner, 1999) an important question remains: how to convert the solar power into electrical power efficiently and at low costs.(Glaser, 1968) Polymer-based organic solar cells offer a possible solution for low cost photovoltaic energy conversion.(Wohrle & Meissner, 1991) In general, organic electronics has created an immense academic interest due to unlimited and flexible molecular engineering possibilities, allowing new organic materials with tailored physical properties to be synthesized.(Forrest, 2005b)
The most promising aspect of organic solar cells is their potential economic advantage due to large-scale production posibilities using continuous and large scale roll-to-rool printing and coating techniques allowing to deposit the active film, electrodes, sealing layers, antireflecting coatings and other components on flexible substrates all-at-once.(Krebs, 2009) Various aesthetic form factors, usually considered to be important for the solar panel integration into buildings can be achieved with this type of solar cell. Desired device form, color and a wide range of applications including solar power stations, roof-tops, portable devices, textile integrated power supplies and other consumer products can be envisioned.
The relation between fabrication costs of photovoltaic modules and power conversion efficiency defines the market success, therefore both factors have to be considered from academic and industrial perspective.(Brabec, 2004) Due to low dielectric constants and weak van der Waals forces binding the organic molecules into a solid, excitons (electron and hole pair strongly bounded by Coulomb attraction) are the primary photoexcitations in organic solids.(Schwoerer & Wolf, 2007) In order to achieve high power conversion efficiency of organic solar cells excitons have to be separated into mobile charge carriers for photocurrent generation.(Forrest, 2005a) The bulk-heterojunction concept is employed to overcome the short exciton diffusion distance. The photoactive film of heterojunction is formed from the donor and acceptor materials which are phase-separated on the nanometer length scale, to facilitate the photo-induced charge transfer as well as create a percolating pathways for charge transport to the electrodes.(Brabec et al., 2001; Halls et al., 1995) Therefore, the

nanomorphology of polymeric solar cells plays a crucial role for the performance of the devices.
Historically, thermal annealing of the film has been used to induce the phase separation between donor and acceptor in bulk-heterojunction blends.(Padinger et al., 2003) However, thermal treatment creates an additional fabrication step in the whole device fabrication process. Later, various methods have been tested and employed to control the nanomorphology of the blends, namely use of solvents with different boiling points (choice of solvent), reduction of drying speed (rate of drying and vapor annealing), changing the solubility of materials, melting of bilayers and the use of processing additives.(Pivrikas et al., 2010b) The later method has received great academic interest as it removes the need for post-production treatment while at the same time allowing fine control of the nanomorphology in various donor-acceptor blends.(Lee et al., 2008)
In this work the factors limiting the power conversion efficiency of excitonic polymer-based bulk-heterojunction solar cells are discussed. Various methods allowing the film nanomorphology to be controlled are reviewed. The use of processing additives to control the phase separation for the formation of an interpenetrating network and how this impacts the power conversion efficiency is described.

2. Excitonic polymer-based solar cells

Polymer-based bulk-heterojunction solar cells (BHSC) have already shown certified efficiencies above 8 % demonstrating ability to compete with inorganic solar cell systems (eg. amorphous silicon cells fabricated on flexible substrates). Efficiencies exceeding 10% for solution processed solar cells are expected to be achieved soon.(Nayak et al., 2011) The power conversion efficiency of BHSCs is determined by the photophysical processes under operational conditions. A fundamental understanding of the relation between light absorption charge separation, charge transport, recombination, and film nanostructure as well as between the various thin film fabrication and processing parameters (such as solvent composition, solution concentration, deposition atmosphere and process temperature) is needed for further improvements. These important parameters can be controlled to some extent by adjusting the required film composition or device structure.(Gunes et al., 2007)

2.1 Solar cell device structure

The typical device structure of most organic optoelectronic devices, including organic light-emitting diodes and solar cells, is shown in Fig. 1. The front electrode is based on a transparent conducting oxide, such as indium tin oxide (ITO), that serves as the high-work-function, positive electrode.(Brabec et al., 2001) To further improve the quality of the ITO electrode and aid hole (positive charge carrier) extraction from the active film, poly(3,4-ethylenedioxythiophene)-poly(styrene sulfonate) (PEDOT-PSS) layer (tens of nanometers thick) is coated on top, forming a smooth surface which is essential in thin film devices. The photoactive film, the donor and acceptor bulk-heterojunction blend is deposited on top of the PEDOT-PSS layer. The whole device is finished by thermally evaporating the back contact (negative electrode) under high vacuum. To achieve the built-in electric field needed for most devices to operate, the back electrode must be made from a low-work-function metal that serves as the negative electrode. In the operation of a typical polymer-fullerene bulk-heterojunction solar cell, electrons generated in the active layer are collected by the back electrode (anode), and holes are collected at the opposite electrode (cathode).

2.2 Solar cell fabrication techniques

While academic research is highly concentrated on improving the power conversion efficiency, there are other important aspects needed for commercial success, such as cell stability, degradation, low manufacturing costs with rapid large scale production. This has been summarized by the Venn diagram as the unification of challenges when trying to combine power conversion efficiency, processability and stability into final devices.(Jorgensen et al., 2008)

Solution processing is attractive for fabricating organic optoelectronic devices mainly due to its simplicity and applicability for large scale and low-cost production. Thin films can be formed in various ways: a) printing techniques including screen printing, pad printing, gravure printing, flexographic printing and offset printing; b) coating techniques including pin coating, doctor blading, casting, painting, spray coating, slot-die coating, curtain coating, slide coating and knife-over-edge coating. The only technique that in both categories is inkjet printing.

Spin coating has been the most common technique for polymeric solar cell fabrication with numerous reviews and fundamental studies available.(Norrman et al., 2005) This technique, widely used in the microelectronics industry to deposit photoresist on silicon wafers, allows for the reproducible formation of highly homogeneous films over large areas. A typical spin coating process involves application of a solution (with the organic semiconductors dissolved in a solvent) to a substrate which is then either accelerated to the required angular velocity or is already spinning at it, Fig. 2.(Krebs, 2009) A large portion of the solution is wasted leaving a thin film on the substrate. Film thickness, morphology and surface topography strongly depend on the rotational speed, viscosity, volatility, diffusivity, molecular weight and concentration of the solutes and solvents used.(Cohen & Gutoff, 1992)

2.3 Current-Voltage dependence of solar cells

The most important figure of merit describing the performance of a solar cell is the power conversion efficiency, which is determined from the current voltage characteristics of the solar cells under operational conditions. Typical current-voltage characteristics of solar cells under illumination is shown in Fig. 3.(Deibel & Dyakonov, 2010)

The accurate measurement of the PCE according to international standards has been described in the literature,(Shrotriya et al., 2006) and is eesential for reproducibility and comparison of results between different laboratories. The Shockley diode equation describes the

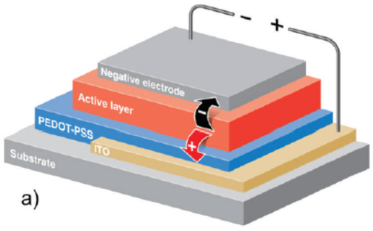

Fig. 1. Schematic sandwich-type structure of organic solar cells showing an organic semiconductor active film between two metal electrodes with different work functions (typically ITO/PEDOT-PSS as positive and Ca/Al as negative contacts). Reprinted with permission from (Shaheen, 2007). Copyright 2007 Society of Photo-Optical Instrumentation Engineers.

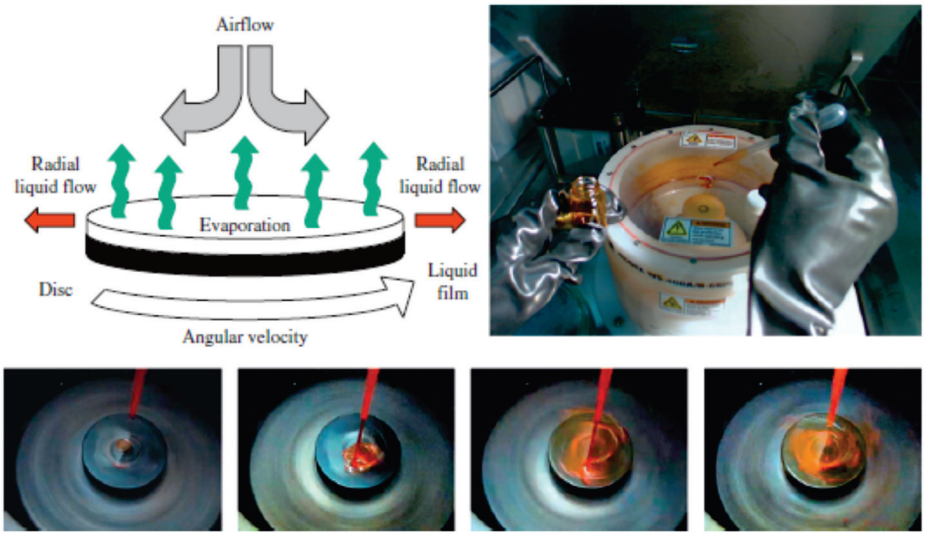

Fig. 2. Spin coating of organic solar cells from solution. Reprinted with permission from (Krebs, 2009). Copyright 2009, with permission from Elsevier.

current-voltage dependence of an ideal diode.(Shockley & Queisser, 1961) In the dark under forward bias the injection current increases exponentially with applied bias, whereas under reverse bias, current saturates at low applied voltages due to blocking contacts. This leads to a rectifying behaviour as can be clearly seen in the log-lin plot in Fig. 3. A description of the non-ideal device (typical organic solar cells) requires addition of series (Rs) and paralell (Rp) resistances. Rs is connected in series with the ideal diode and it describes the contact resistances such as injection barriers and sheet resistances. Rp arises due to the influence of local shunts between the two electrodes, i.e. additional current paths circumventing the diode. Typically in organic solar cells, a strong photocurrent dependence of applied electric field is observed manifesting as a non-saturated current at -1V reverse bias (Fig. 3). The field-dependent photocurrent arises due to:

a) field dependent mobile charge carrier generation, since an exciton has to dissociate into mobile carriers;(Oesterbacka et al., 2010)

b) charge carrier collection due to Hecht's law, if the extracted charge saturates at electric fields wheere the film thickness is larger than the carrier drift distance.(Hecht, 1932)

c) electric field dependent carrier mobility.(Pivrikas, Ullah, Sitter & Sariciftci, 2011)

In addition to electric field dependent mobility, the charge transport in disordered organic solar cells is also carrier concentration dependent. This effect arises due to the hopping nature of charge transport, where at higher carrier concentrations the carrier hopping probability between localized states increases (loosely speaking due to a higher density of localized states resulting in better electron wavefunction overlap) and therefore the carrier mobility increases.(PIVRIKAS, ULLAH, SINGH, SIMBRUNNER, MATT, SITTER & SARICIFTCI, 2011)

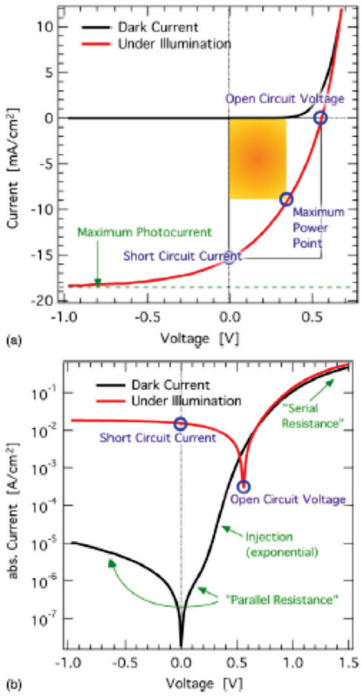

Fig. 3. Typical schematic current-voltage (I-V) dependence of the organic solar cell in the dark and under illumination. Reprinted with permission from (Deibel & Dyakonov, 2010). Copyright 2010, with permission from Institute of Physics.

2.4 Power conversion efficiency

PCE is defined as the ratio of the electrical power produced by a solar cell to the optical power of incident light (P_{light}):(Luque & Hegedus, 2003)

$$PCE = \frac{j_{SC} V_{OC} FF}{P_{light}} \tag{1}$$

where j_{SC} is the short circuit current density, V_{OC} is the open circuit voltage, $FF = V_{MP} j_{mp} / V_{OC} j_{SC}$ is the fill factor representing the maximum area in the fourth quadrant of the I-V characteristics of solar cells, V_{MP} and jmp are the voltage and current, respectively, at the point of maximum power, and P_{light} is the power of incoming light under Standard Test Conditions (1000 W/m2, AM 1.5 (Air Mass) solar reference spectrum, temperature during measurements 25 C).[15] To maximize the PCE values, all these parameters have to be maximized. The open circuit voltage of BHSC is determined by the energy of the quasi-Fermi levels of both semiconductors (donor and acceptor) as well as the Fermi levels of the electrodes.(Scharber et al., 2006) The short circuit current j_{SC} depends on electrical carrier drift (induced by electric field) and diffusion (induced by concentration gradient). Apart from the absorption on the film, charge carrier concentration and mobility are the main factors influencing the photocurrent regardless of the transport mechanism (drift or diffusion).(Nelson, 2003)

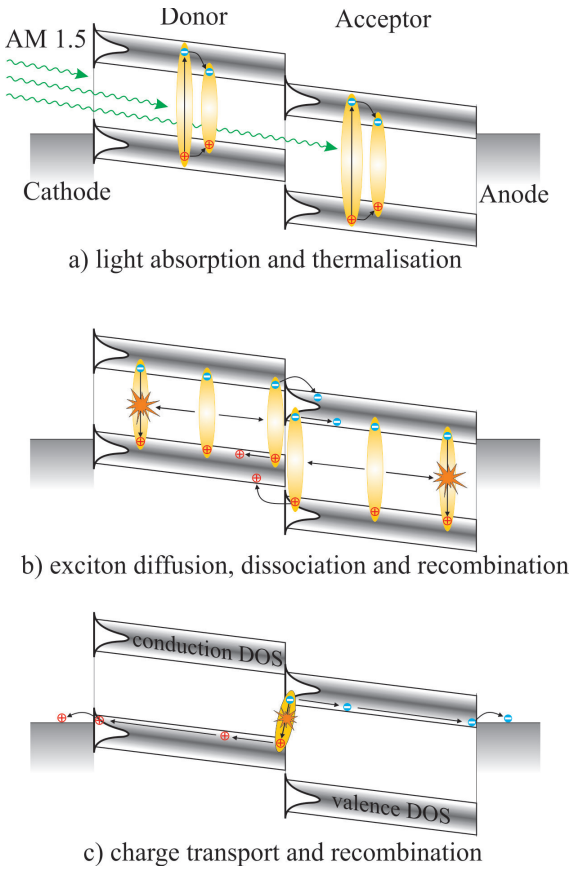

Fig. 4. Factors limiting power conversion efficiency of excitonic solar cells. Reprinted with permission from (Pivrikas, 2010). Copyright 2010 IEEE.

The PCE of organic solar cells is influenced by many different photophysical processes and parameters. Simplified energy-level diagrams of organic solar cells utilizing donor and acceptor materials is shown in Fig. 2.(Pivrikas et al., 2010a)

2.5 Power conversion efficiency limiting mechanisms in excitonic solar cells

The first factor limiting the PCE is the absorption of light in the film. Ideally, as much as possible of the incident solar irradiance should be absorbed.(Pivrikas et al., 2010a) The Beer-Lambert law determines the light absorption profile in homogeneously distributed and scatter-free medium. Optical interference effects can also influence the light absorption profile in thin multilayer films.(Dennler et al., 2009) As can be seen in Fig. 4 some part of absorbed light energy is lost due to a thermalization process - charge relaxtion within the Density of States (DOS) to the lower energy levels to form an occupational-DOS within localized DOS.(Bassler, 1993; Juska et al., 2003; Osterbacka et al., 2003)

The second efficiency limiting process is exciton dissociation into mobile charge carriers. Due to low dielectric constants and consequently weak Coulombic field screening in the organic

materials (relative static permittivity is around 3) the primary photoexcitation is an exciton, which does not create the photocurrent.(Luque & Hegedus, 2003) The exciton diffusion length describes how far an exciton can diffuse within its lifetime. The concept of heterojunction between two organic semiconductors (donor and acceptor) is used to split an exciton into mobile charge carriers. Efficient exciton dissociation (charge transfer) takes place at the interface between donor and acceptor if a suitable offset in energy level exists, as shown in Fig. 4 b).(Pivrikas et al., 2010a) The excited state Charge Transfer (CT) complex (sometimes called exciplex) might be formed after the dissociation of an exciton meaning that positive and negative charge carriers might remain bounded by the Coulomb attraction at the donor acceptor interface, which would not contribute to photocurrent.
The charge carrier transport (collection) to the electrodes is the third important limiting processes. As shown in Fig. 4 c), mobile electrons and holes must be transported to the opposite electrodes. The driving force can be either diffusion, related to the carrier concentration gradients, and/or drift due to a built-in electric field. An important aspects of charge transport are the charge extraction at the semiconductor-metal interface. The energy level alignment between the metal and semiconductor, free charge carrier concentration in the film (doping level) as well as the trapping level concetration, carrier capture and release times from capture centers determine the interfacial properties of the device. Non-blocking contact without energetical barrier for charge carrier extraction is required to be present at the interface.(Baranovski, 2006) The disordered nature of solution processed films of organic semiconductors results in low charge carrier mobilities (tzpically 10^{-3} - 10^{-7} $cm^2V^{-1}s^{-1}$ in π-conjugated polymers). The mobility of the slower charge carrier limits the photocurrent, and therefore the efficiency of the solar cell due to accumulation of charge carriers. Since the photocurrent under operation conditions typically approach space charge limited current, second order recombination processes become dominant due to high charge carrier concentration, and the carrier lifetime becomes shorter than the transit time.(Pivrikas et al., 2010a)

2.6 Bulk-heterojunction solar cells

The light absorption coefficient, α, in a disordered organic film is usually high, on the order of 10^5 cm^{-1}. This allows thin films, on the order of hundreds of nanometers, to be used in solar cells. However, the exciton diffusion length in most organic materials is of the order of 10 nm. If the exciton is to diffuse to the interface between the two materials (donor-acceptor) in order to separate into mobile charge carriers, these two materials must be blended on this length scale. Furthermore, the donor-acceptor phases must for bi-continuous network with percolating pathways for electron and hole transport to the elctrodes. This is the operating principle of the BHSC shown in Fig. 5.(Sariciftci, 2006) The film nano-morphology is crucially important for the efficiency of solar cells.(Ma et al., 2005) The nanoscale phase-separation phase separation between donor and acceptor in BHSC plays an important role relating the device properties and performance to the solar cell fabrication methods. Typical donor is poly(3-hexylthiophene-2,5-diyl) (P3HT) and acceptor is [6,6]-phenyl-C61-butyric acid methyl ester (PCBM)

3. Methods to control the morphology of BHSC

The formation and the size of nanoscale domains of donor and acceptor phases are strongly dependent on the film fabrication techniques and conditions. Beyond the selection of suitable materials there are several parameters that must be carefully controlled when fabricating

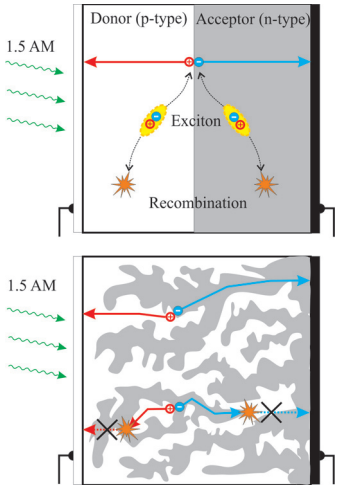

Fig. 5. Bilayer and bulk-heterojunction solar cells. Reprinted with permission from (Pivrikas et al., 2010a). Copyright 2009, with permission from Elsevier.

BHSC, such as the solution concentration, deposition temperature, donor-acceptor blend ratio, spin speeds using solvents with different boiling points, solvent evaporation kinetics, vapour pressure, solubility, and polarity.(Pivrikas et al., 2010b)
Various methods allowing the control of the film nano-morphology have been introduced in the past.(Chen, Hong, Li & Yang, 2009; Peet et al., 2009) Initially it was observed that the PCE of BHSC significantly increases upon a postproduction treatment, e.g. thermal annealing of solar cells with applied external voltage.(Hoppea & Sariciftci, 2004; Padinger et al., 2003) Other methods used in the past to control the morphology of BHSC involve the use of appropriate solvents with specific boiling point that allow either the increase or decrease of the solvent evaporation rate.(Kim, Choulis, Nelson, Bradley, Cook & Durrant, 2005; Shaheen et al., 2001; Yu et al., 1995) Other methods, such as reducing the drying speed of spin-coated films,(Li et al., 2005; Mihailetchi et al., 2006; Vanlaeke et al., 2006) solubility matching(Troshin et al., 2009) and the melting of bilayers have also been used.(Kim, Liu & Carroll, 2006) It was observed that chemical additives can substitute the post production treatment of BHSC.(Lee et al., 2008) Processing additives are an attractive concept due to the simplicity and suitability for large scale production.

3.1 Thermal annealing of devices

Thermal annealing, by controlling the temperature and annealing time, is typically applied to either the final device or BHJ films in order to improve the nanoscale phase separation between donor and acceptor.(Ma et al., 2005; Sun et al., 2007; Xin et al., 2008; Zhang, Choi, Haliburton, Cleveland, Li, Sun, Ledbetter & Bonner, 2006) Significant improvement in photovoltaic performance after annealing is typically observed in P3HT/PCBM blends.(Padinger et al., 2003) Thermal annealing has the advantage in that it can be applied independently of the film deposition technique. Thermal annealing has also been shown to enhance the crystallinity of the polymer, such as for P3HT, increasing the PCE and the photocurrent due to increased carrier mobility.(Erb et al., 2005) Furthermore, the interconnections between the polymer/fullerene phazes in the interpenetrating network are

enhanced as a result of phase separation between the donor and acceptor on meso (> 100 nm) and nanoscales (< 20 nm).(Kim, Cook, Tuladhar, Choulis, Nelson, Durrant, Bradley, Giles, McCulloch, Ha et al., 2006; Ma et al., 2005)
The effect of thermal annealing on film morhology was clearly demonstrated by bright-field (BF) transmission electron microscopy (TEM) images, recorded in slight defocussing conditions in a P3HT/PCBM blends, as shown in Fig. 6.(Yang et al., 2005)

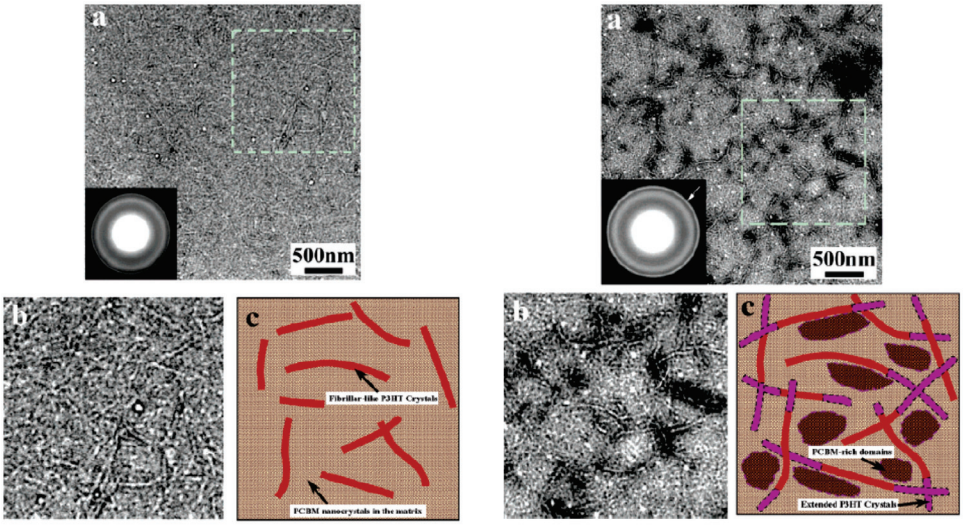

Fig. 6. Transmission Electron Microscopy (TEM) images show the overview (a) and zoomed in (b), and the corresponding schematic representation (c) of the photoactive layer solar cells. Left (a)-(c) images: pristine unannealed P3HT and PCBM blend. Right (a)-(c) images: thermal annealed P3HT and PCBM blend. Insets in (a) figures is the corresponding SAED pattern. The dash line bordered regions represent the extension of existing P3HT crystals in the pristine film or newly developed PCBM-rich domains during the annealing step. The arrow is to indicate the increased intensity of (020) Debye-Scherrer ring from P3HT crystals compared to the SAED pattern shown in the inset of Figure 2a. Reprinted with permission from (Yang et al., 2005). Copyright 2005 American Chemical Society.

As can be seen, fibrillar-like P3HT domains (brighter in contrast compared to background) overlap with each other over the whole film. The inset of Fig. 6 shows the selected area electron diffraction (SAED) pattern of the film. The outer ring corresponds to a distance of 0.39 nm, which is typical pi-pi stacking distance of P3HT chains.(Ihn et al., 1993) The crystallinity of P3HT crystals is not very pronounced as seen from the low intensity of the reflection ring. The inner ring in the SAED pattern, corresponding to a d-spacing of 0.46 nm, is seen to be even more diffuse and has been attributed by the nanometer sized PCBM nanocrystals that are homogeneously dispersed throughout the film. Fig. 6 a) shows the BF TEM images of the composite film after annealing (120 C for 60 min). The most pronounced feature in the BF TEM image of the annealed sample is the increased contrast and the appearance of bright fibrillar P3HT crystals throughout the entire film. The width of these crystals remains almost constant compared to the pristine composite film, but on average their length was found to increase over 50 %. The increased crystallinity of P3HT after thermal treatment

is visible from the increased intensity of the reflection ring in the SAED pattern (inset of Fig. 6 a)). Larger and darker PCBM rich areas can be observed suggesting an increased phase demixing between P3HT and PCBM. It was concluded that the crystallinity of P3HT is improved upon annealing and the demixing between the two components is increased, but large-scale phase separation does not occur. The resulting interpenetrating networks composed of P3HT crystals with a high aspect ratio and aggregated nanocrystalline PCBM domains provide continuous pathways in the entire photoactive layer for efficient hole and electron transport.

In order to further understand the extent of thermal annealing, 2-D X-ray scattering in a grazing incidence geometry (GIWAXS) was used to study the development of the crystalline structure of P3HT and PCBM during the interdiffusion process at various temperatures. 2D GIWAXS patterns of as-prepared P3HT/PCBM bilayers and annealed samples are shown in Fig. 7.(Treat et al., 2011) The diffraction patterns for P3HT shows that the *a*-axis of the P3HT crystals is predominantly oriented perpendicular to the substrate and the *b*-axis (pi-stacking)

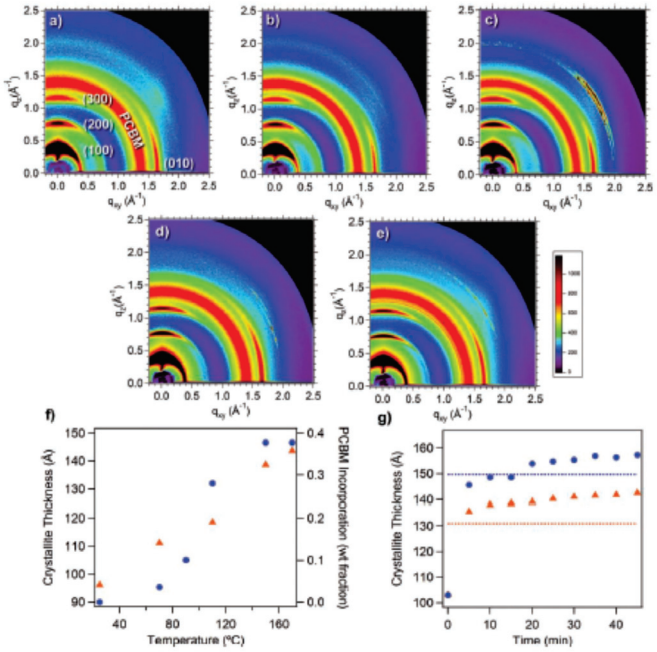

Fig. 7. Two-dimensional GIWAXS of a P3HT/PCBM bilayer on Si a) as-cast and annealed at b) 70 C, c) 110 C, d) 150 C, and e) 170 C for 5 min. f) The Scherrer equation was used to extract the P3HT crystallite thickness along the a- axis from the full-width-at-half-maximum of the (100) reflection. PCBM incorporation from the DSIMS measurements was plotted for comparison at various annealing temperatures. g) Growth in the crystal thickness with time using in-situ heating 2D GIWAXS of a P3HT/PCBM bilayer on Si at 110 C (orange) and 170 C (blue). The Scherrer equation was used to determine crystal thickness from the (100) reflection corresponding to P3HT. The dotted line corresponds to a neat P3HT/Si sample heated for 5 min at 110 C (orange) and 170 C (blue). Copyright 2011 Wiley. Used with permission from (Treat et al., 2011).

is oriented parallel - which is the typically observed P3HT orientation. Upon annealing the as-prepared films at various temperatures, the d-spacing along the *a*-axis of the P3HT crystal was found to remain constant, indicating that during the interdiffusion process, the PCBM does not interpenetrate between the side chains of the P3HT crystal structure.(Mayer et al., 2009) The peak width of the diffraction ring, corresponding to the aggregates of PCBM does not change during the interdiffusion process, showing that PCBM remains in an amorphous state with aggregates large enough to scatter incident X-rays. Only a small change in the distribution of P3HT crystal orientations was found to be present at various levels of interdiffusion, while the intensity of the (200) peak of P3HT increased by nearly a factor of two on annealing at 170 C. It was shown that the interdiffusion process has little effect on the crystalline regions of the P3HT film, where the diffusion of PCBM into P3HT occurs within the disordered regions of P3HT.

To determine how interdiffusion within this system affects the growth of the P3HT crystallites, the P3HT crystallite size along the *a*-axis for the bilayer films was compared to pure P3HT films heated under similar conditions (Fig. 7 (f)-(g)). The P3HT crystallite size was estimated using the Scherrer equation and plotted against the fraction of PCBM within the P3HT layer (Fig. 7 (f)). The crystallite size was found to increase with increasing annealing temperature regardless of the level of interdiffusion. The P3HT crystallite size in the bilayer system was found to increase most rapidly during the first 5 min of annealing, where the crystallite thickness was approching that for a neat P3HT film heated under similar conditions (Fig. 7 (g)).

3.2 Solvent effects

Postproduction treatment requires a rather well controlled environment, it adds an additional fabrication costs to the solar cell manufacturing process, which might not be attractive for large-scale industrial production. Furthermore, some material systems, like the low band gap organic semiconductor poly[2,6-(4,4-bis-(2-ethylhexyl)-4H-cyclopenta[2,1-b;3,4-b0]-dithiophene)-alt-4,7-(2,1,3-benzothiadiazole)] (PCPDTBT) blended with [6,6]-phenyl C71-butyric acid methyl ester (C71-PCBM), do not shown any improvement upon thermal annealing.

Phase separation and molecular self-organization can be influenced by solvent evaporation since the solvent establishes the film evolution environment. Slow drying or solvent annealing techniques have also been used to control the morphology of the blends by changing the rate of solvent removal.(Li et al., 2005; Li, Yao, Yang, Shrotriya, Yang & Yang, 2007; Sivula et al., 2006) The use of different solvents and their effect on the film nano-structure of BHSC has been studied in detail in the past.(Li, Shrotriya, Yao, Huang & Yang, 2007) High boiling point solvents were used with the device placed in an enclosed container, in which the atmosphere rapidly saturates with the solvent.

Grazing-incidence x-ray diffraction (GIXRD) studies provided evidence that the solvent evaporation rate directly influences the polymer chain arrangement in the film.(Chu et al., 2008) It was shown that the use of higher boiling point solvent strongly improves the PCE of MDMO-PPV and PCBM blends.(Shaheen et al., 2001) Higher PCE values due to improved film morphology and crystallinity have been reached by substituting chloroform with chlorobenzene for P3HT/PCBM BHSC.(Ma et al., 2005) The difference between chlorobenzene and 1,2-dichloro benzene for use as a solvent was shown in the novel low bandgap polymer PFco-DTB and C71-PCBM blend systems, where chlorobenzene resulted in films with higher

roughness.(Yao et al., 2006) Non-aromatic solvents have shown to be able to affect the photovoltaic performance of MEH-PPV and PCBM blends.(Yang et al., 2003)
An interesting method to study the morphology of BHSC optically by recording exciton lifetime images within the photoactive layer of P3HT and PCBM has been demonstrated by Huan et al.(Huang et al., 2010) Using a confocal optical microscopy combined with a fluorescence module they were able to image the spacial distrubution of exciton lifetime for both slow and fast dried films, as shown in Fig. 8.

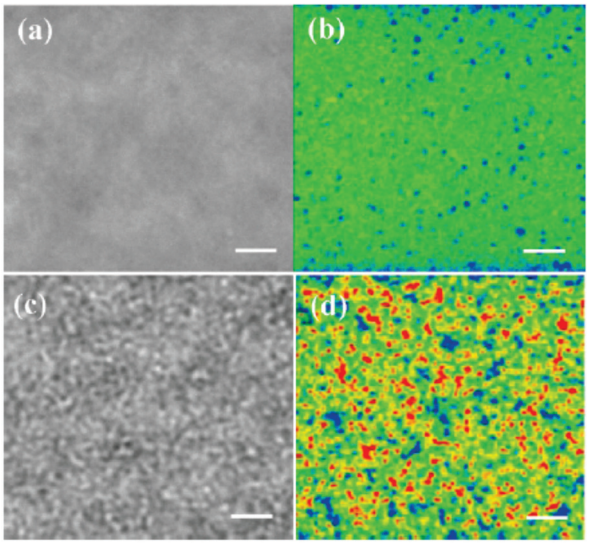

Fig. 8. (a, c) Transmitted images and (b, d) exciton lifetime images of the BHJ film prepared from rapidly and slowly grown methods, respectively, measured after excitation at 470 nm using a picosecond laser microscope (512 $\times$ 512 pixels). Scale bars: 2 μm. Reprinted with permission from (Huang et al., 2010). Copyright 2010 American Chemical Society.

The transmitted image of the rapidly grown film (Fig. 8 (a)) shows a uniform and featureless characteristics throughout the structure, indicating that P3HT and PCBM were mixed well within the films. This monotonous transmitted image corresponds to a uniform exciton lifetime distribution. Fig. 8 (c)-(d) shows transmitted and exciton lifetime images for the slowly dried films. The bright spots are emissions from many polymer chains that have stacked or aggregated into a bulk cluster leading to a reduced PL quenching. The red regions (P3HT-rich domains Fig. 8 (d)) correspond to the bright spot of the transmitted image (Fig. 8 (c)). In agreement with previous studies, the images showed that the active layers during slow solvent evaporation provide a 3D pathways for charge transport reflecting better cell performance.

3.3 Processing additives

This method is based on the usage of a third non-reacting chemical compound, a processing additive, to the donor and acceptor solution. Improvement of the performance of polymer/fullerene photovoltaic cells doped with triplephenylamine has been reported.(Peet et al., 2009) The ionic solid electrolyte (LiCF3SO3) used as a dopant also resulted in enhanced PCE of MEH-PPV/PCBM blends due to an optimized polymer morphology, improved

electrical conductivity and in situ photodoping.(Chen et al., 2004) A copolymer including thieno-thiophene units (DHPT3) has been used as a nucleating agent for crystallization in the active layer of P3HT and PCBM BHSC.(Bechara et al., 2008) It was demonstrated that the addition of DHPT3 in P3HT/PCBM thin films induces a structural ordering of the polythiophene phase, leading to improved charge carrier transport properties and stronger active layer absorption. High-performance P3HT/PCBM blends were fabricated using quick drying process and 1-dodecanethiol as an additive.(Ouyang & Xia, 2009) Ternary blends of P3HT, PCBM and poly(9,9-dioctylfluorene-co-benzothiadiazode) (F8BT) showed enhanced optical absorption and partly improved charge collection.(Kim, Cook, Choulis, Nelson, Durrant & Bradley, 2005) A few volume percent of 1,8-diiodooctane in o-xylene was used to dissolve poly(9,9-di-n-octylfluorene) PFO allowing the control of film morphology.(Peet et al., 2008) Block-copolymers and diblock copolymers with functionalized blocks have also shown to be able to influence the film morphology.(Sivula et al., 2006; Sun et al., 2007; Zhang, Choi, Haliburton, Cleveland, Li, Sun, Ledbetter & Bonner, 2006)

3.3.0.1 "Bad" solvent effect

The incorporation of other solvents into the host solvent is capable of controlling the film morphology of BHSC.(Chen et al., 2008; Wienk et al., 2008; Xin et al., 2008; Zhang, Jespersen, Björström, Svensson, Andersson, Sundstr"om, Magnusson, Moons, Yartsev & Ingan"as, 2006) In some cases, changes in the solvent composition lead to interchain order that cannot be obtained by any other method.(Campbell et al., 2008; Moulee et al., 2008; Peet et al., 2007) The use of nitrobenzene as an additive has been shown to improve the phase-separation between the donor and acceptor (P3HT/PCBM blend), where P3HT was shown to be present in both amorphous and crystalline phase.(Moule & Meerholz, 2008; van Duren et al., 2004)

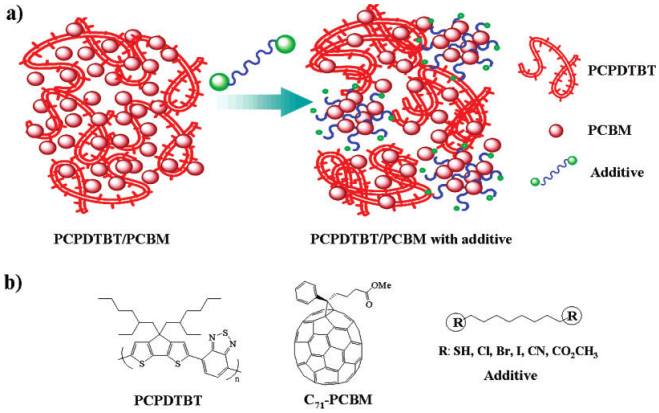

Fig. 9. Schematic depiction of the role of the processing additive in the self-assembly of bulk heterojunction blend materials (a) and structures of PCPDTBT, C71-PCBM, and additives (b). Reprinted with permission from (Lee et al., 2008). Copyright 2008 American Chemical Society.

The concept of mixing a host solvent with a "bad" solvent has been explored resulting in solvent-selection rules for desired film morphology.(Alargova et al., 2001) Solvents, distinctly dissolving one component of the blend, induce the aggregation of nanofibers and nanoparticles in the solvent prior to film deposition.(Yao et al., 2008) It was shown

that (independent of the concentration of the additive) fullerene molecules crystallized into distributed aggregates in the presence of a "bad" solvent in the host solvent. Well aligned P3HT aggregates resulting in high degree of crystallinity due to the interchain $\pi - \pi$ stacking were observed upon addition of hexane.(Li et al., 2008; Rughooputh et al., 1987) The addition of 1-chloronaphthalene (a high boiling point solvent) into dichlorobenzene has also resulted in similar self-organization of polymer chains.(Chen et al., 2008) It was shown that in the blends of poly(2,7-(9,9-dioctyl-fluorene)-alt-5,5-(40,70-di-2-thienyl-20,10,3-benzothiadiazole)) and PCBM dissolved in chloroform with a small addition of chlorobenzene, a uniform domain distribution was attained, whereas the addition of xylene or toluene into the chloroform host solvent resulted in larger domains, stronger carrier recombination and a smaller photocurrent. Alkane-thiol based compounds were extensively used as processing additives in the past.(Lee et al., 2008) The photoconductivity response was shown to increase strongly in polymer/fullerene composites by adding a small amount of alkane-thiol based compound to the solution prior to the film deposition.(Coates et al., 2008; Peet et al., 2006) By incorporating a few volume percent of alkanethiols into the PCPDTBT/C71-PCBM BHSC (Fig. 9) it was shown that the PCE improves almost by a factor of two.(Alargova et al., 2001; Peet et al., 2007)

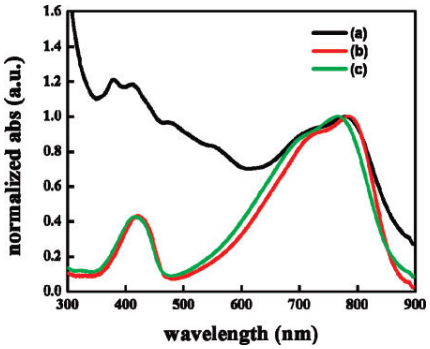

Fig. 10. UV-visible absorption spectra of PCPDTBT/C71-PCBM films processed with 1,8-octanedithiol: before removal of C71-PCBM with alkanedithiol (black); after removal of C71-PCBM with alkanedithiol (red) compared to the absorption spectrum of pristine PCPDTBT film (green). Reprinted with permission from (Lee et al., 2008). Copyright 2008 American Chemical Society.

The alkanedithiol effect was explained by the ability of alkanedithiols to selectively dissolve the fullerene component, where the polymer is less soluble, Fig. 9 The effect has been proven by removing the fullerene domains by dipping the BHJ film into an alkanedithiol solution and measuring light absorption before and after dipping.(Lee et al., 2008) The normalized absorption spectra (shown in Fig. 10) demonstrate that after dipping the film the absorption matches that of the pristine polymer.

As a consequence, "bad" solvent addition provides a means to select solvent-additives in order to control the phase-separation in BHSC. It was shown that during film processing the fullerene stays longer in its dissolved form, due to the rather high boiling point of alkanedithiol (> 160 C), allowing for self-aligning and phase-separation between the polymer and fullerene as suggested in Fig. 7 b). Two effects control the morphology of the blends:

a) selective solubility of one of the components;

b) a high boiling of the additive compared to the host solvent.

The concentration of the processing additive allows the amount of phase-separation between the donor and the acceptor to be controlled.

3.3.0.2 Different processing additives

1,8-di(R)octanes with various functional groups (R) allow control of the film morphology.(Peet et al., 2007) The best results were obtained with 1,8-diiodooctane. Progressively longer alkyl chains, namely 1,4-butanedithiol, 1,6-hexanedithiol, 1,8-octanedithiol or 1,9-nonanedithiol were used to manipulate the morphology of solution processed films. It was concluded that approximately six methylene units are required for the alkanedithiol to have an appreciable effect on the morphology.

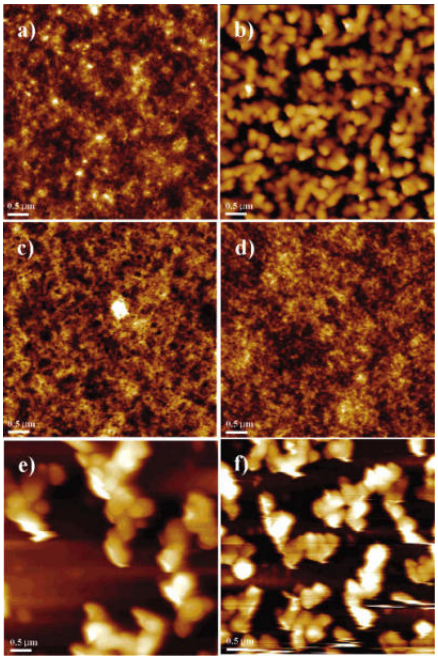

Fig. 11. AFM topography of films cast from PCPCTBT/C71-PCBM with additives: (a) 1,8-octanedithiol, (b) 1,8-cicholorooctane, (c) 1,8-dibromooctane, (d) 1,8-diiodooctane, (e) 1,8-dicyanooctane, and (f) 1,8-octanediacetate. Reprinted with permission from (Chen, Yang, Yang, Sista, Zadoyan, Li & Yang, 2009). Copyright 2009 American Chemical Society.

Fig. 11 shows a Atomic Force Microscopy (AFM) surface topography of films cast from PCPCTBT/C71-PCBM with the various processing additives.(Lee et al., 2008) The 1,8-octanedithiol (a), 1,8-dibromooctane (c), and 1,8-diiodooctane (d) resulted in phase-segregated morphologies with finer domain sizes than those obtained with 1,8-dichlorooctane (b), 1,8-dicyanooctane (e), and 1,8-octanediacetate (f). The morphology of films processed with 1,8-diiodooctane showed more elongated domains than those processed with 1,8-octanedithiol and 1,8-dibromooctane. The 1,8-di(R)octanes with SH, Br, and I, gave finer domain sizes and exhibited more efficient device performances than those with $R = Cl$, CN, and CO_2CH_3. The AFM images of the BHJ films processed using 1,8-di(R)octanes with

$R = Cl$, CN, and CO_2CH_3 showed large scale phase separation with round-shape domains and no indication of a bicontinuous network.

3.3.0.3 Concentration of processing additives

Once the most effective thiol functional group has been indentified, it is interesting to find how the concentration of the processing additive in solution affects the film morphology. The effect of additive concentration in the solution was clearly observed in surface topography images in AFM.(Chen, Yang, Yang, Sista, Zadoyan, Li & Yang, 2009)

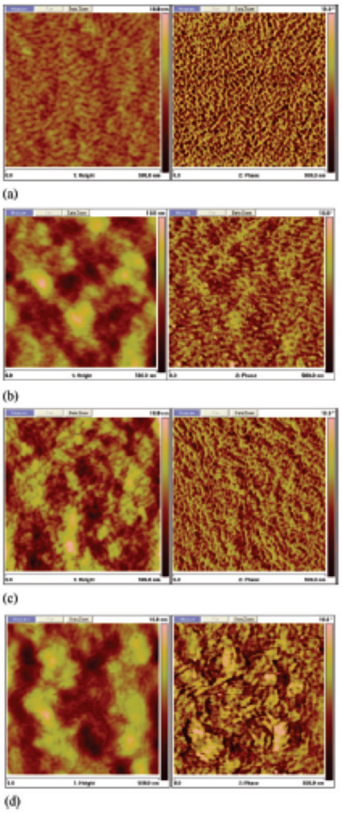

Fig. 12. Tapping mode AFM images of films with different amounts of 1,8-octanedithiol in 500 nm $\times$ 500 nm. Left: topography. Right: phase images. (a) 0 μL, (b) 7.5 μL, (c) 20 μL, and (d) 40 μL of 1,8-octanedithiol. The scale bars are 10.0 nm in the height images and 10.0 $^\circ$ in the phase images. Reprinted with permission from from (Chen, Yang, Yang, Sista, Zadoyan, Li & Yang, 2009). Copyright 2009 American Chemical Society.

AFM images (a), (b), (c), and (d) of Fig. 12 show the height (left) and phase (right) images of polymer films with 0, 7.5, 20, and 40 μL of 1,8-octanedithiol, respectively, showing an increasing trend in roughness with increasing amount of 1,8-octanedithiol. The domain sizes were found to be consistent with the higher crystallization observed with increasing amount of 1,8-octanedithiol. Finely dispersed structures were observed when there was no

1,8-octanedithiol added. The AFM results were consistent with PL spectra showing higher PL intensity with increased 1,8-octanedithiol concentration.
AFM provides information about the film surface only, the bulk of the film has been studied using synchrotron-based grazing incidence X-ray diffraction (GIXD) in P3HT:PCBM blends.(Chen, Yang, Yang, Sista, Zadoyan, Li & Yang, 2009) Fig. 13 (a) represents 2-D GIXD

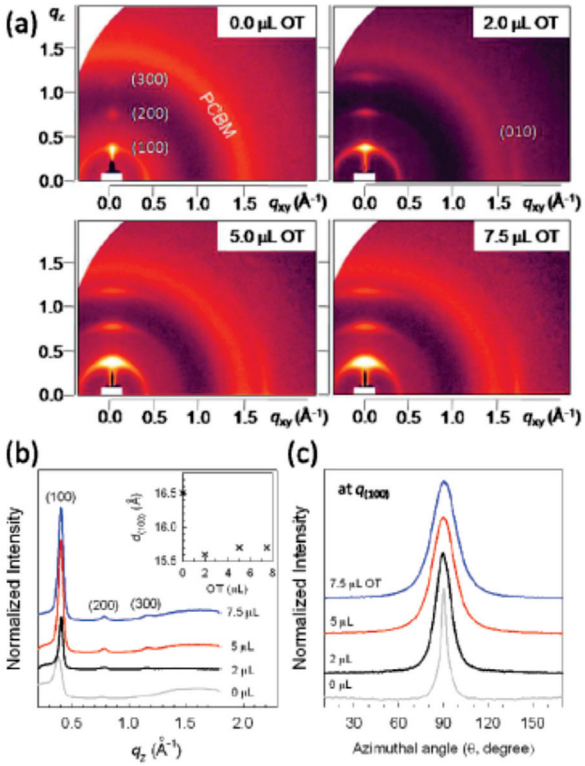

Fig. 13. (a) 2D GIXD patterns of films with different amounts of 1,8-octanedithiol. (b) 1D out-of-plane X-ray and (c) azimuthal scan (at $q^{(100)}$) profiles extracted from (a). Inset of b: calculated interlayer spacing in the (100) direction with various amounts of 1,8-octanedithiol. Reprinted with permission from (Chen, Yang, Yang, Sista, Zadoyan, Li & Yang, 2009). Copyright 2009 American Chemical Society.

patterns of the as-spun P3HT:PCBM films with different concentrations of 1,8-octanedithiol. It was found that the hexyl side chains and backbone of P3HT are oriented perpendicular and parallel to the surface, respectively regardless of 1,8-octanedithiol concentration. However, the crystallinity of P3HT in the films significantly increases in the presence of 1,8-octanedithiol and tends to keep steady above 5 μL 1,8-octanedithiol, as seen from in 1-D out of-plane X-ray profiles normalized by film thicknesses (see Fig. 13 (b). The average interlayer spacing was observed to change significantly in the presence of 1,8-octanedithiol. It was concluded that the interaction between P3HT is stronger in the presence of 1,8-octanedithiol with the P3HT crystallinity improved due to stacking. The size distribution of P3HT crystals was found to be broader with increasing amount of 1,8-octanedithiol, as shown in Fig. 13 (c).

Improved crystallization of P3HT and broader crystal size distribution at higher 1,8-octanedithiol concentrations was explained by solvent volume ratios. During the film fabrication, the main solvent evaporates faster than the additive solvent resulting in a sudden increase of the volume ratio of the additive solvent to the main solvent. Polymer molecules lower their internal energy by aggregating when the additive solvent volume ratio reaches a critical point. At higher additive concentrations, the time required to reach this point is reduced and aggregation is stronger. As a result, polymer molecules aggregate with larger average domain sizes due to the stronger driving force and broader size distributions arises due to the shorter aggregation time.

4. Schematic structures of bulk-heterojunction film morphology

The morphological studies discussed above highlight the importance of phase separation between donor and acceptor, and reveal a schematic film structures for polymer-based bulk-heterojunction solar cells, as shown in Fig. 14..(Hoppe et al., 2006; Huang et al., 2010; Peumans et al., 2003)
In the top Fig. 14 (a), the percolated pathways for electrons and holes is created allowing them to reach the respective electrodes. In Fig. 14 b the situation for an enclosed PCBM cluster is shown: here electrons and holes will recombine, since percolation is insufficient.
The center Fig. 14 show that the lower surface energy of P3HT, relative to PCBM, provides the driving force for the interconcentration gradient observed in both the rapidly (a) and slowly (b) grown films. The film prepared through a rapidly grown process leads to an extremely homogeneous blends. A greater number of percolating pathways are formed in slow grown films.
Furthermore, the effect of annealing on the interface morphology of a mixed-layer device was modeled using a cellular model, as shown in Fig. 14 (bottom) for different temperatures. Annealing temperatures has been shown to crucially influence the morphology of the mixed-layer device, while the modeled morphology resemble experimentally measured devices.

5. Processing additive effect on solar cell performance

The photophysical effects of 1,8-octanedithiol (ODT) additives on PCPDTBT and C71-PCBM composites and device performance were studied using photo-induced absorption spectroscopy.(Hwang et al., 2008) Reduced carrier loss due to recombination was found in BHJ films processed using the additive. From photobleaching recovery measurements reduced carrier losses were demonstrated. However, it was concluded that the amount of the reduction is not sufficient to explain the observed increase in the power conversion efficiency (by a factor of 2). Carrier mobility measurements in Field Effect Transistor (FET) configuration demonstrated that the electron mobility increased in the PCPDTBT:C71-PCBM when ODT is used as an additive, resulting in enhanced connectivity of C71-PCBM networks.(Cho et al., 2008) This work also showed that if the ODT was not completely removed from the BHJ films by placing them in high vacuum ($> 10^{-6}$ torr) the hole mobility actually decreased, implying that residual ODT may act as a hole trap. It was concluded that the improved electron mobility was the primary cause of the improved power conversion efficiency, while the hole mobility was found to be relatively insensitive to the additive.

5.1 Power conversion efficiency and current-voltage dependence

In order to clarify the effect of chemical additives on the photophysical properties and photovoltaic performance, regioregular P3HT and PCBM bulk-heterojunction solar cells were fabricated in four different ways:
(1) as produced films (untreated, no alkyl thiol);
(2) thermally annealed films (refereed to as treated in text, no alkyl thiol);
(3) as produced films with alkyl thiol (refereed to as treated in text, with alkyl thiol);
(4) thermally annealed films with alkyl thiol (refereed to as treated in text, with alkyl thiol).
The fabrication procedures were kept the same for all four types of cells. The details on device preparation can be found elsewhere.(Pivrikas et al., 2008)
Current-voltage (I-V) characteristics under illumination of devices are shown in Fig. 15. Untreated solar cells gave the worst performance with the least short circuit current and low fill factor. However, these cells demonstrate a relatively higher open circuit voltage, but, due to a low short circuit current and a low fill factor, their power conversion efficiency was low, around 1 %. The difference in photocurrents between annealed cells and these with alkyl thiol

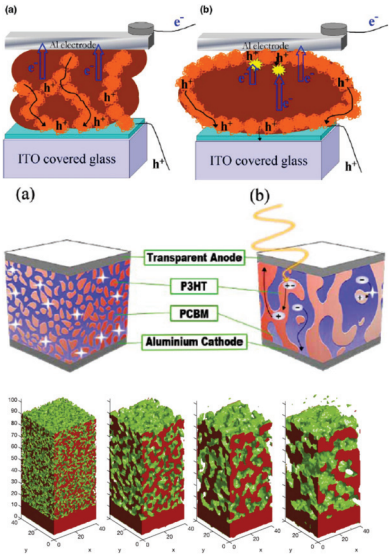

Fig. 14. Schematic structures of the film nanomorphology of bulk-heterojunction blends - all emphasizing the importance of the interpenetrating network in polymer-based solar cells. Top figures: (a) chlorobenzene and (b) toluene cast MDMO-PPV and PCBM blend layers. Center figures: vertical phase morphology of (a) rapidly and (b) slowly grown P3HT and PCBM blends. Bottom figures: the simulated effects of annealing on the interface morphology of a mixed-layer photovoltaic cell. The interface between donor and acceptor is shown as a green surface. Donor is shown in red and acceptor is transparent. Top figures reprinted with permission from (Hoppe et al., 2006), copyright 2006, with permission from Elsevier. Middle figures reprinted with permission from (Huang et al., 2010), copyright 2010 American Chemical Society. Bottom figures adapted by permission from Macmillan Publishers Ltd: (Peumans et al., 2003), copyright 2003.

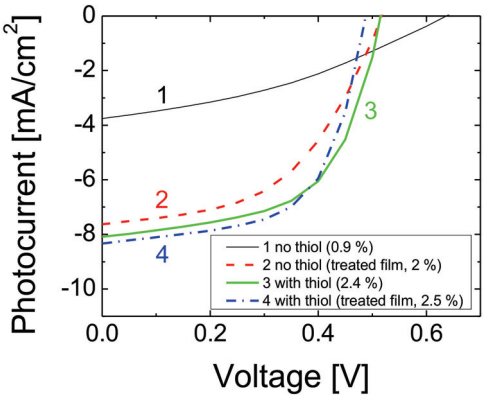

Fig. 15. Current-voltage characteristics demonstrating significant performance improvement under illumination (1000 W/m^2, 1.5 AM) for P3HT/PCBM bulk-heterojunction solar cells prepared in different ways: as produced (thin line), annealed (thick dashed line), thiol added (thick line), thiol added and annealed (thick dash dot line). Reprinted with permission from (Pivrikas et al., 2008). Copyright 2008, with permission from Elsevier.

is small, except that treated cells have lower fill factors and therefore slightly lower efficiency as compared to those with alkyl thiol additive, Fig. 16.

5.2 Light absorption and external quantum efficiency

In order to clarify the factors determining OPV device efficiency, the incident photon to current efficiency (IPCE), alternatively called External Quantum Efficiency (EQE) is measured, since it provides information on light absorption spectra, charge transport and recombination losses. The effect of thermal treatment versus processing addictive, as well as the effect of additive concentration, was studied and shown in Fig. 16. In Fig. 16 (a) and (d) the light absorption and Beer-Lambert absorption coefficient are shown as a function of wavelength. In agreement with previous observations, an increase in optical absorption is seen for treated cells. The red-shift of the absorption and characteristic vibronic shoulders are clearly pronounced in treated cells (at around 517 nm, 556 nm and 603 nm) both arising from strong interchain interactions within high degree of crystallinity in P3HT. In solution, no peak shift was observed, suggesting that the influence of the additive on P3HT happens during the solvent drying (or spin coating) process and not in the solution state. The increase in optical absorption at higher additive concentrations demonstrates that more energy can be harvested in solar cells, therefore, these cells have better photovoltaic performance due to a larger amount of photons being absorbed in the film.

While PCBM is known to quench the PL of P3HT effectively in the well mixed blends.(Chen, Yang, Yang, Sista, Zadoyan, Li & Yang, 2009) The photoluminescence was shown to increase with increasing amount of 1,8-octanedithiol (Fig. 16 (b)), suggesting that the phase separation between the P3HT and PCBM is increasing since the exciton diffusion distance is on the same order of magnitude.(Xu & Holdcroft, 1993; Zhokhavets et al., 2006)

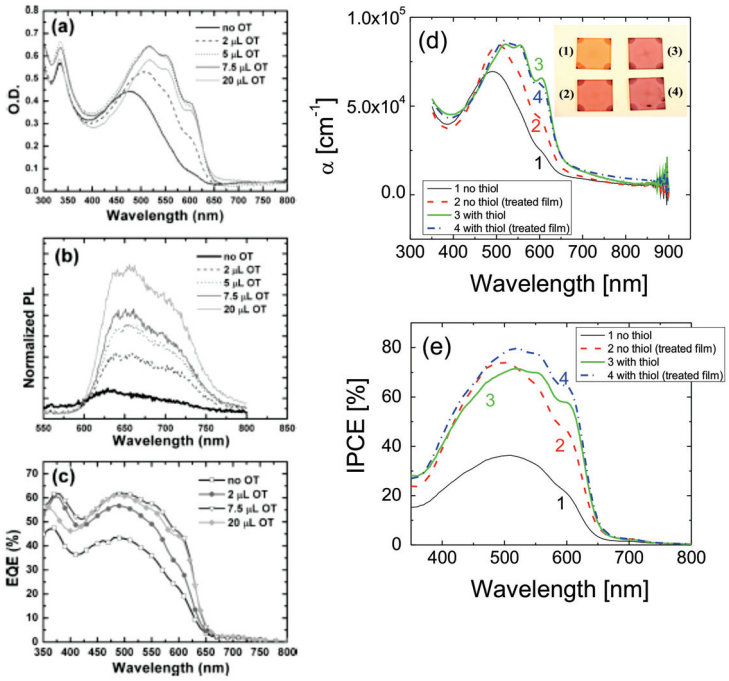

Fig. 16. Changes in light absorption (a) and photoluminescence (PL) (b) and External Quantum Efficiency (EQE) (c) shown at various amounts of processing additive (OT is 1,8-octanedithiol) used during film preparation. Changes in light absorption (d) and incident photon to current efficiency (IPCE) in (e) measured in pristine and treated (annealed films and films fabricated with processing additive) films. Strong red-shift in absorption, appearance of absorption peaks, higher IPCE values in treated films or films with processing additive well agrees with improved OPV performance. Thermal annealing of films fabricated with processing additive results in no change in OPV performance. Figures on the left reprinted with permission from (Chen, Yang, Yang, Sista, Zadoyan, Li & Yang, 2009). Copyright 2009 American Chemical Society. Figures on the right reprinted with permission from (Pivrikas et al., 2008). Copyright 2008, with permission from Elsevier.

A strong improvement in IPCE was observed in treated solar cells. The IPCE dependence approximately follows the light absorption curve, as the same characteristic absorption peaks are reproduced in the optical absorption spectra (Fig. 16). From the IPCE studies it was concluded that the improvement in the performance of solar cells is not only due to the increased optical absorption, but also due to improved transport (higher carrier mobility) and/or reduced recombination losses (eg. due to longer charge carrier lifetime), which again confirms the benefits of improved interpenetrating network between donor and acceptor.

5.3 Charge transport

Since it was found from ICPE studies that the film morphology not only improves the light absorption, but also results in better charge transport, it is important to quantify this improvement. In order to understand the difference in charge transport properties in treated

and untreated cells, dark IV curves were recorded for all 4 types of treated cells shown in Fig. 17.(Pivrikas et al., 2008)

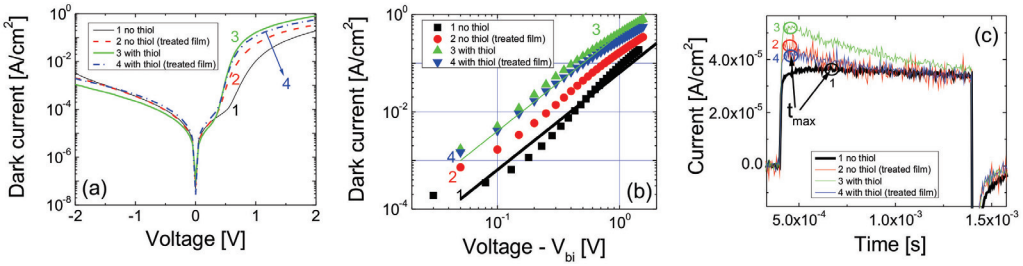

Fig. 17. The improvement in charge carrier mobility in treated (annealed films and films fabricated with processing additive) compared to pristine films demonstrated by two methods: dark current-voltage injection and CELIV. (a) log-lin plot showing the rectification ratio in forward and reverse bias and insignificant differences in leakage current in reverse bias. (b) log-log plot in forward bias showing much higher injection current levels in treated blends. (c) faster carrier extraction in treated films compared to pristine directly measured by CELIV current transients. Improvement in the carrier mobility can be seen from the shift in the position of extraction maximum, while experimental conditions (film thicknesses and applied voltages) were kept similar. Thermal annealing of films fabricated with processing additive results in no change in performance. Reprinted with permission from (Pivrikas et al., 2008). Copyright 2008, with permission from Elsevier.

The dark current in the region of negative applied voltage (the reverse bias, positive voltage on Al, negative on ITO), is similar in all cells, showing that current injection is contact limited. A significant rectification ratio is observed for all types of studied cells. The dark leakage current in reverse bias is rather high, but similar for all cells.

Due to the different nanomorphologies of the interpenetrating network, the dark conductivity is expected to increase in the cells with higher conversion efficiency, because of improved conductivity of the films (assuming the injection is not limited by the contact). The dark injection current in forward bias is observed to be significantly higher in treated cells. In Fig. 17 (b) the dark injection current in forward bias is plotted in log-log scale for all devices. Faster charge carrier mobilities in all cells were estimated from these dependences using the Mott-Gurney Law. As can be directly seen from the magnitude of injection current, the highest mobility was observed in the films with chemical additives, confirming the beneficial effect of chemical additives for charge transport in bulk-heterojunction solar cells. From CELIV measurements, shown in Fig. 17 (c) it was demonstrated that charge carrier mobility is mainly reponsible for improvements in OPV performance.

However, the charge carrier recombination processes in operating devices has yet to be clarified. It was shown that the typically expected Langevin bimolecular charge carrier recombination can be avoided in highly efficiency P3HT and PCBM blends.(Pivrikas et al., 2005) Non-Langevin carrier recombination was shown to be crucially important in low mobility organic photovoltaic devices, since the requirement for the slower carrier mobility can be reduced without recombination losses. This implies that close to unity Internal quantum efficiency can be reached in low bandgap organic materials with very low carrier mobility if reduced bimolecular recombination (non-Langevin) is present in the device.

6. Conclusions

The film nanomorphology of bulk heterojunction solar cells determines the power conversion efficiency through photophysical properties such as light absorption, exciton dissociation, charge transport and recombination. The nano-morphology can be controlled by a variety of different methods. Thermal annealing of fabricated solar cells can be successfully substituted with slow drying of the solvent or chemical additives. These methods induce the phase separation between the donor and acceptor in the bulk-heterojunction, which results in red-shifted light absorption, improved exciton dissociation, faster charge carrier transport, and reduced recombination. Segregated donor-enriched and/or acceptor-enriched phases can be formed resulting in an interpenetrating bicontinuous network with the domain sizes comparable to the exciton diffusion length. Interconnected pathways for electromn and hole transport to the electrodes are required. This structure is essential for the photovoltaic performance of polymer-based solar cells. Therefore, reproducible, low cost nano-structure control is crucially important for fabrication of high efficiency OPV suitable for commercialization. In order to be able to control and predict the film nano-morphology of novel materials, an understanding of the material parameters governing the phase separation is required.

7. Acknowledgements

The author would like to Dr. Paul Schwenn for helpful discussions during manuscript preparation.

8. References

Alargova, R., Deguchi, S. & Tsujii, K. (2001). Stable colloidal dispersions of fullerenes in polar organic solvents, *Journal of the American Chemical Society* 123(43): 10460–10467.

Baranovski, S. (2006). *Charge transport in disordered solids with applications in electronics*, John Wiley & Sons Inc.

Bassler, H. (1993). Charge transport in disordered organic photoconductors a monte carlo simulation study, *physica status solidi (b)* 175(1): 15–56.

Bechara, R., Leclerc, N., Lévêque, P., Richard, F., Heiser, T. & Hadziioannou, G. (2008). Efficiency enhancement of polymer photovoltaic devices using thieno-thiophene based copolymers as nucleating agents for polythiophene crystallization, *Applied Physics Letters* 93: 013306.

Brabec, C. (2004). Organic photovoltaics: technology and market, *Solar energy materials and solar cells* 83(2-3): 273–292.

Brabec, C., Sariciftci, N., Hummelen, J. et al. (2001). Plastic solar cells, *Advanced Functional Materials* 11(1): 15–26.

Campbell, A., Hodgkiss, J., Westenhoff, S., Howard, I., Marsh, R., McNeill, C., Friend, R. & Greenham, N. (2008). Low-temperature control of nanoscale morphology for high performance polymer photovoltaics, *Nano letters* 8(11): 3942–3947.

Chen, F., Tseng, H. & Ko, C. (2008). Solvent mixtures for improving device efficiency of polymer photovoltaic devices, *Applied Physics Letters* 92: 103316.

Chen, F., Xu, Q. & Yang, Y. (2004). Enhanced efficiency of plastic photovoltaic devices by blending with ionic solid electrolytes, *Applied physics letters* 84: 3181.

Chen, H., Yang, H., Yang, G., Sista, S., Zadoyan, R., Li, G. & Yang, Y. (2009). Fast-grown interpenetrating network in poly (3-hexylthiophene): Methanofullerenes solar cells processed with additive, *The Journal of Physical Chemistry C* 113(18): 7946–7953.

Chen, L., Hong, Z., Li, G. & Yang, Y. (2009). Recent progress in polymer solar cells: manipulation of polymer: fullerene morphology and the formation of efficient inverted polymer solar cells, *Advanced Materials* 21(14-15): 1434–1449.

Cho, S., Lee, J., Moon, J., Yuen, J., Lee, K. & Heeger, A. (2008). Bulk heterojunction bipolar field-effect transistors processed with alkane dithiol, *Organic Electronics* 9(6): 1107–1111.

Chu, C., Yang, H., Hou, W., Huang, J., Li, G. & Yang, Y. (2008). Control of the nanoscale crystallinity and phase separation in polymer solar cells, *Applied Physics Letters* 92: 103306.

Coates, N., Hwang, I., Peet, J., Bazan, G., Moses, D. & Heeger, A. (2008). 1, 8-octanedithiol as a processing additive for bulk heterojunction materials: Enhanced photoconductive response, *Applied Physics Letters* 93: 072105.

Cohen, E. & Gutoff, E. (1992). *Modern coating and drying technology*, VCH.

Cox, P., Betts, R., Jones, C., Spall, S. & Totterdell, I. (2000). Acceleration of global warming due to carbon-cycle feedbacks in a coupled climate model, *Nature* 408(6809): 184–187.

Deibel, C. & Dyakonov, V. (2010). Polymer–fullerene bulk heterojunction solar cells, *Reports on Progress in Physics* 73: 096401.

Dennler, G., Scharber, M. & Brabec, C. (2009). Polymer-fullerene bulk-heterojunction solar cells, *Advanced Materials* 21(13): 1323–1338.

Erb, T., Zhokhavets, U., Gobsch, G., Raleva, S., ST "uHN, B., Schilinsky, P., Waldauf, C. & Brabec, C. (2005). Correlation between structural and optical properties of composite polymer/fullerene films for organic solar cells, *Advanced Functional Materials* 15(7): 1193–1196.

Forrest, S. (2005a). The limits to organic photovoltaic cell efficiency, *MRS bulletin* 30(01): 28–32.

Forrest, S. (2005b). The path to ubiquitous and low-cost organic electronic appliances on plastic, *Gravitational, electric, and magnetic forces: an anthology of current thought* p. 120.

Glaser, P. (1968). Power from the sun: Its future, *Science* 162(3856): 857.

Gunes, S., Neugebauer, H. & Sariciftci, N. (2007). Conjugated polymer-based organic solar cells, *Chemical reviews* 107(4): 1324–1338.

Halls, J., Walsh, C., Greenham, N., Marseglia, E., Friend, R., Moratti, S. & Holmes, A. (1995). Efficient photodiodes from interpenetrating polymer networks.

Hecht, K. (1932). Zum mechanismus des lichtelektrischen primärstromes in isoliereden kristallen, *Z. Phys* 77: 235.

Hoppe, H., Glatzel, T., Niggemann, M., Schwinger, W., Schaeffler, F., Hinsch, A., Lux-Steiner, M. & Sariciftci, N. (2006). Efficiency limiting morphological factors of mdmo-ppv: Pcbm plastic solar cells, *Thin solid films* 511: 587–592.

Hoppea, H. & Sariciftci, N. (2004). Organic solar cells: An overview, *J. Mater. Res* 19(7): 1925.

Huang, J., Chien, F., Chen, P., Ho, K. & Chu, C. (2010). Monitoring the 3d nanostructures of bulk heterojunction polymer solar cells using confocal lifetime imaging, *Analytical chemistry* 82(5): 1669–1673.

Hwang, I., Cho, S., Kim, J., Lee, K., Coates, N., Moses, D. & Heeger, A. (2008). Carrier generation and transport in bulk heterojunction films processed with 1, 8-octanedithiol as a processing additive, *Journal of Applied Physics* 104(3): 033706–033706.

Ihn, K., Moulton, J. & Smith, P. (1993). Whiskers of poly (3-alkylthiophene) s, *Journal of Polymer Science Part B: Polymer Physics* 31(6): 735–742.

Jorgensen, M., Norrman, K. & Krebs, F. (2008). Stability/degradation of polymer solar cells, *Solar Energy Materials and Solar Cells* 92(7): 686–714.

Juska, G., Genevičius, K.,
"Osterbacka, R., Arlauskas, K., Kreouzis, T., Bradley, D. & Stubb, H. (2003). Initial transport of photogenerated charge carriers in π-conjugated polymers, *Physical Review B* 67(8): 081201.

Kim, K., Liu, J. & Carroll, D. (2006). Thermal diffusion processes in bulk heterojunction formation for poly-3-hexylthiophene/c60 single heterojunction photovoltaics, *Applied physics letters* 88(18): 181911–181911.

Kim, Y., Choulis, S., Nelson, J., Bradley, D., Cook, S. & Durrant, J. (2005). Device annealing effect in organic solar cells with blends of regioregular poly (3-hexylthiophene) and soluble fullerene, *Applied Physics Letters* 86(6): 063502–063502.

Kim, Y., Cook, S., Choulis, S., Nelson, J., Durrant, J. & Bradley, D. (2005). Effect of electron-transport polymer addition to polymer/fullerene blend solar cells, *Synthetic metals* 152(1-3): 105–108.

Kim, Y., Cook, S., Tuladhar, S., Choulis, S., Nelson, J., Durrant, J., Bradley, D., Giles, M., McCulloch, I., Ha, C. et al. (2006). A strong regioregularity effect in self-organizing conjugated polymer films and high-efficiency polythiophene: fullerene solar cells, *nature materials* 5(3): 197–203.

Krebs, F. (2009). Fabrication and processing of polymer solar cells: a review of printing and coating techniques, *Solar Energy Materials and Solar Cells* 93(4): 394–412.

Lee, J., Ma, W., Brabec, C., Yuen, J., Moon, J., Kim, J., Lee, K., Bazan, G. & Heeger, A. (2008). Processing additives for improved efficiency from bulk heterojunction solar cells, *Journal of the American Chemical Society* 130(11): 3619–3623.

Li, G., Shrotriya, V., Huang, J., Yao, Y., Moriarty, T., Emery, K. & Yang, Y. (2005). High-efficiency solution processable polymer photovoltaic cells by self-organization of polymer blends, *Nature Materials* 4(11): 864–868.

Li, G., Shrotriya, V., Yao, Y., Huang, J. & Yang, Y. (2007). Manipulating regioregular poly (3-hexylthiophene):[6, 6]-phenyl-c61-butyric acid methyl ester blends-route towards high efficiency polymer solar cells, *Journal of Materials Chemistry* 17(30): 3126–3140.

Li, G., Yao, Y., Yang, H., Shrotriya, V., Yang, G. & Yang, Y. (2007). Şsolvent annealingŤ effect in polymer solar cells based on poly (3-hexylthiophene) and methanofullerenes, *Advanced Functional Materials* 17(10): 1636–1644.

Li, L., Lu, G. & Yang, X. (2008). Improving performance of polymer photovoltaic devices using an annealing-free approach via construction of ordered aggregates in solution, *J. Mater. Chem.* 18(17): 1984–1990.

Luque, A. & Hegedus, S. (2003). *Handbook of photovoltaic science and engineering*, John Wiley & Sons Inc.

Ma, W., Yang, C., Gong, X., Lee, K. & Heeger, A. (2005). Thermally stable, efficient polymer solar cells with nanoscale control of the interpenetrating network morphology, *Advanced Functional Materials* 15(10): 1617–1622.

Mayer, A., Toney, M., Scully, S., Rivnay, J., Brabec, C., Scharber, M., Koppe, M., Heeney, M., McCulloch, I. & McGehee, M. (2009). Bimolecular crystals of fullerenes in conjugated polymers and the implications of molecular mixing for solar cells, *Adv. Funct. Mater* 19(8): 1173–1179.

Mihailetchi, V., Xie, H., de Boer, B., Popescu, L., Hummelen, J., Blom, P. & Koster, L. (2006). Origin of the enhanced performance in poly (3-hexylthiophene):[6, 6]-phenyl c-butyric acid methyl ester solar cells upon slow drying of the active layer, *Applied physics letters* 89: 012107.

Moule, A. & Meerholz, K. (2008). Controlling morphology in polymer–fullerene mixtures, *Advanced Materials* 20(2): 240–245.

Moulee, A., Tsami, A., B
"unnagel, T., Forster, M., Kronenberg, N., Scharber, M., Koppe, M., Morana, M., Brabec, C., Meerholz, K. et al. (2008). Two novel cyclopentadithiophene-based alternating copolymers as potential donor components for high-efficiency bulk-heterojunction-type solar cells, *Chemistry of Materials* 20(12): 4045–4050.

Nayak, P., Bisquert, J. & Cahen, D. (2011). Assessing possibilities and limits for solar cells, *Advanced Materials* .

Nelson, J. (2003). *The physics of solar cells*, Imperial College Press London.

Norrman, K., Ghanbari-Siahkali, A. & Larsen, N. (2005). 6 studies of spin-coated polymer films, *Annu. Rep. Prog. Chem., Sect. C: Phys. Chem.* 101: 174–201.

Oesterbacka, R., Pivrikas, A., Juska, G., Poskus, A., Aarnio, H., Sliauzys, G., Genevicius, K., Arlauskas, K. & Sariciftci, N. (2010). Effect of 2-d delocalization on charge transport and recombination in bulk-heterojunction solar cells, *IEEE Journal of Selected Topics in Quantum Electronics* 16(6): 1738–1745.

Osterbacka, R., Geneviius, K., Pivrikas, A., Juka, G., Arlauskas, K., Kreouzis, T., Bradley, D. & Stubb, H. (2003). Quantum efficiency and initial transport of photogenerated charge carriers in [pi]-conjugated polymers, *Synthetic metals* 139(3): 811–813.

Ouyang, J. & Xia, Y. (2009). High-performance polymer photovoltaic cells with thick p3ht: Pcbm films prepared by a quick drying process, *Solar Energy Materials and Solar Cells* 93(9): 1592–1597.

Padinger, F., Rittberger, R. & Sariciftci, N. (2003). Effects of postproduction treatment on plastic solar cells, *Advanced Functional Materials* 13(1): 85–88.

Peet, J., Brocker, E., Xu, Y. & Bazan, G. (2008). Controlled β-phase formation in poly (9, 9-di-n-octylfluorene) by processing with alkyl additives, *Advanced Materials* 20(10): 1882–1885.

Peet, J., Kim, J., Coates, N., Ma, W., Moses, D., Heeger, A. & Bazan, G. (2007). Efficiency enhancement in low-bandgap polymer solar cells by processing with alkane dithiols, *Nature Materials* 6(7): 497–500.

Peet, J., Senatore, M., Heeger, A. & Bazan, G. (2009). The role of processing in the fabrication and optimization of plastic solar cells, *Advanced Materials* 21(14-15): 1521–1527.

Peet, J., Soci, C., Coffin, R., Nguyen, T., Mikhailovsky, A., Moses, D. & Bazan, G. (2006). Method for increasing the photoconductive response in conjugated polymer/fullerene composites, *Applied physics letters* 89(25): 252105–252105.

Peumans, P., Uchida, S. & Forrest, S. (2003). Efficient bulk heterojunction photovoltaic cells using small-molecular-weight organic thin films, *Nature* 425(6954): 158–162.

Pivrikas, A., Juška, G., Mozer, A., Scharber, M., Arlauskas, K., Sariciftci, N., Stubb, H. &
"Osterbacka, R. (2005). Bimolecular recombination coefficient as a sensitive testing parameter for low-mobility solar-cell materials, *Physical review letters* 94(17): 176806.

Pivrikas, A., Neugebauer, H. & Sariciftci, N. (2010a). Charge carrier lifetime and recombination in bulk heterojunction solar cells, *Selected Topics in Quantum Electronics, IEEE Journal of* 16(6): 1746–1758.

Pivrikas, A., Neugebauer, H. & Sariciftci, N. (2010b). Influence of processing additives to nano-morphology and efficiency of bulk-heterojunction solar cells: A comparative review, *Solar Energy* .

Pivrikas, A., Stadler, P., Neugebauer, H. & Sariciftci, N. (2008). Substituting the postproduction treatment for bulk-heterojunction solar cells using chemical additives, *Organic Electronics* 9(5): 775–782.

PIVRIKAS, A., ULLAH, M., SINGH, T., SIMBRUNNER, C., MATT, G., SITTER, H. & SARICIFTCI, N. (2011). Meyer-neldel rule for charge carrier transport in fullerene devices: A comparative study, *Organic electronics* 12(1): 161–168.

Pivrikas, A., Ullah, M., Sitter, H. & Sariciftci, N. (2011). Electric field dependent activation energy of electron transport in fullerene diodes and field effect transistors: GillŠs law, *Applied Physics Letters* 98: 092114.

Rughooputh, S., Hotta, S., Heeger, A. & Wudl, F. (1987). Chromism of soluble polythienylenes, *Journal of Polymer Science Part B: Polymer Physics* 25(5): 1071–1078.

Sariciftci, N. (2006). Morphology of polymer/fullerene bulk heterojunction solar cells, *Journal of Materials Chemistry* 16(1): 45–61.

Scharber, M., M
"uhlbacher, D., Koppe, M., Denk, P., Waldauf, C., Heeger, A. & Brabec, C. (2006). Design rules for donors in bulk-heterojunction solar cellsŮtowards 10% energy-conversion efficiency, *Advanced Materials* 18(6): 789–794.

Schwoerer, M. & Wolf, H. (2007). *Organic molecular solids*, Wiley Online Library.

Shaheen, S., Brabec, C., Sariciftci, N., Padinger, F., Fromherz, T. & Hummelen, J. (2001). 2.5% efficient organic plastic solar cells, *Applied Physics Letters* 78: 841.

Shockley, W. & Queisser, H. (1961). Detailed balance limit of efficiency of p-n junction solar cells, *Journal of Applied Physics* 32(3): 510–519.

Shrotriya, V., Li, G., Yao, Y., Moriarty, T., Emery, K. & Yang, Y. (2006). Accurate measurement and characterization of organic solar cells, *Advanced Functional Materials* 16(15): 2016–2023.

Sivula, K., Ball, Z., Watanabe, N. & Fréchet, J. (2006). Amphiphilic diblock copolymer compatibilizers and their effect on the morphology and performance of polythiophene: fullerene solar cells, *Advanced Materials* 18(2): 206–210.

Sun, S., Zhang, C., Ledbetter, A., Choi, S., Seo, K., Bonner, C., Drees, M. & Sariciftci, N. (2007). Photovoltaic enhancement of organic solar cells by a bridged donor-acceptor block copolymer approach, *Applied physics letters* 90(4): 043117–043117.

Treat, N., Brady, M., Smith, G., Toney, M., Kramer, E., Hawker, C. & Chabinyc, M. (2011). Interdiffusion of pcbm and p3ht reveals miscibility in a photovoltaically active blend, *Laser Physics Review* 1: 82–89.

Troshin, P., Hoppe, H., Renz, J., Egginger, M., Mayorova, J., Goryachev, A., Peregudov, A., Lyubovskaya, R., Gobsch, G., Sariciftci, N. et al. (2009). Material solubility-photovoltaic performance relationship in the design of novel fullerene derivatives for bulk heterojunction solar cells, *Adv. Funct. Mater* 19: 779–788.

Turner, J. (1999). A realizable renewable energy future, *Science* 285(5428): 687.

van Duren, J., Yang, X., Loos, J., Bulle-Lieuwma, C., Sieval, A., Hummelen, J. & Janssen, R. (2004). Relating the morphology of poly (p-phenylene vinylene)/methanofullerene blends to solar-cell performance, *Advanced Functional Materials* 14(5): 425–434.

Vanlaeke, P., Vanhoyland, G., Aernouts, T., Cheyns, D., Deibel, C., Manca, J., Heremans, P. & Poortmans, J. (2006). Polythiophene based bulk heterojunction solar cells: Morphology and its implications, *Thin Solid Films* 511: 358–361.

Wienk, M., Turbiez, M., Gilot, J. & Janssen, R. (2008). Narrow-bandgap diketo-pyrrolo-pyrrole polymer solar cells: The effect of processing on the performance, *Advanced Materials* 20(13): 2556–2560.

Wohrle, D. & Meissner, D. (1991). Organic solar cells, *Advanced Materials* 3(3): 129–138.

Xin, H., Kim, F. & Jenekhe, S. (2008). Highly efficient solar cells based on poly (3-butylthiophene) nanowires, *Journal of the American Chemical Society* 130(16): 5424–5425.

Xu, B. & Holdcroft, S. (1993). Molecular control of luminescence from poly (3-hexylthiophenes), *Macromolecules* 26(17): 4457–4460.

Yang, C., Qiao, J., Sun, Q., Jiang, K., Li, Y. & Li, Y. (2003). Improvement of the performance of polymer/c60 photovoltaic cells by small-molecule doping, *Synthetic metals* 137(1-3): 1521–1522.

Yang, X., Loos, J., Veenstra, S., Verhees, W., Wienk, M., Kroon, J., Michels, M. & Janssen, R. (2005). Nanoscale morphology of high-performance polymer solar cells, *Nano Letters* 5(4): 579–583.

Yao, Y., Hou, J., Xu, Z., Li, G. & Yang, Y. (2008). Effects of solvent mixtures on the nanoscale phase separation in polymer solar cells, *Advanced Functional Materials* 18(12): 1783–1789.

Yao, Y., Shi, C., Li, G., Shrotriya, V., Pei, Q. & Yang, Y. (2006). Effects of c70 derivative in low band gap polymer photovoltaic devices: Spectral complementation and morphology optimization, *Applied physics letters* 89(15): 153507–153507.

Yu, G., Gao, J., Hummelen, J., Wudl, F. & Heeger, A. (1995). Polymer photovoltaic cells: enhanced efficiencies via a network of internal donor-acceptor heterojunctions, *Science* 270(5243): 1789.

Zhang, C., Choi, S., Haliburton, J., Cleveland, T., Li, R., Sun, S., Ledbetter, A. & Bonner, C. (2006). Design, synthesis, and characterization of a-donor-bridge-acceptor-bridge-type block copolymer via alkoxy-and sulfone-derivatized poly (phenylenevinylenes), *Macromolecules* 39(13): 4317–4326.

Zhang, F., Jespersen, K., Björström, C., Svensson, M., Andersson, M., Sundstr"om, V., Magnusson, K., Moons, E., Yartsev, A. & Ingan"as, O. (2006). Influence of solvent mixing on the morphology and performance of solar cells based on polyfluorene copolymer/fullerene blends, *Advanced Functional Materials* 16(5): 667–674.

Zhokhavets, U., Erb, T., Hoppe, H., Gobsch, G. & Serdar Sariciftci, N. (2006). Effect of annealing of poly (3-hexylthiophene)/fullerene bulk heterojunction composites on structural and optical properties, *Thin Solid Films* 496(2): 679–682.

7

One-Step Physical Synthesis of Composite Thin Film

Seishi Abe
Research Institute for Electromagnetic Materials
Japan

1. Introduction

Quantum-dot solar cells have attracted much attention because of their potential to increase conversion efficiency of solar photo conversion up to almost 66% by utilizing hot photogenerated carriers to produce higher photovoltages or higer photocurrents (Nozik, 2002). Specifically, the optical-absorption edge of a semiconductor nanocrystal is often shifted due to the quantum-size effect. The optical band gap can then be tuned to the effective energy region for absorbing maximum intensity of the solar radiation spectrum (Landsberg et al., 1993; Kolodinski et al., 1993). Furthermore, quantum dots produce multiple electron-hole pairs per -photon through impact ionization, whereas bulk semiconductor produces one electron-hole pair per -photon.

Wide gap semiconductor sensitized by semiconductor nanocrystal is candidate material for such use. The wide gap materials such as TiO_2 can only absorb the ultraviolet part of the solar radiation spectrum. Hence, the semiconductor nanocrystal supports absorbing visible (vis)- and near-infrared (NIR) -light. Up to now, various nanocrystalline materials [InP (Zaban et al., 1998), CdSe (Liu & Kamat, 1994), CdS (Weller, 1991; Zhu et al., 2010), PbS (Hoyer & Könenkamp, 1995), and Ge (Chatterjee et al., 2006)] have been investigated, for instance, as the sensitizer for TiO_2. Alternatively, a wide-gap semiconductor ZnO is also investigated, since the band gap and the energetic position of the valence band maximum and conduction band minimum of ZnO are very close to that of TiO_2 (Yang et al., 2009). Most of these composite materials were synthesized through chemical techniques, however, physical deposition, such as sputtering, is also useful. In addition, package synthesis of the composite thin film is favorable for low cost product of solar cell.

In this chapter, Ge/TiO_2 and PbSe/ZnSe composite thin film are presented, and they were prepared through rf sputtering and hot wall deposition (HWD), with multiple resources for simultaneous deposition. The package synthesis needs the specific material design for each of the preparation techniques. In the rf sputtering, the substances for nanocrystal and matrix are appropriately selected according to the difference in heat of formation (Ohnuma et al., 1996). Specifically, Ge nanocrystals are thermodynamically stable in a TiO_2 matrix, since Ti is oxidized more prominently than Ge along the fact that the heat of formation of GeO_2 is greater than those of TiO_2 (Kubachevski & Alcock, 1979). Larger difference in the heat of formation [e.g., Ge/Al-O (Abe et al., 2008a)] can provide thermodynamically more stable nanocrystal. Hence, the crystalline Ge was homogeneously embedded in amorphous Al oxide matrix, and evaluated unevenness of the granule size was ranged from 2 to 3nm, according to high resolution electron microscopy (HREM). In the HWD, on the other hand,

the substances for nanocrystal and matrix are also selected following thermodynamic insolubility. The HWD technique, which is a kind of thermal evaporation, causes unintentional increase of the substrate-temperature due to the thermal irradiation. Hence, simultaneous HWD evaporation from multiple resources often produces solid solution [e.g., $Pb_{1-x}Ca_xS$ (Abe & Masumoto, 1999)]. Hence, package synthesis of the composite thin film needs insolubility material system. The bulk PbSe-ZnSe system, for instance, is found to phase-separate at thermal equilibrium state (Oleinik et al., 1982). It is therefore expected that PbSe nanocrystals phase-separate from the ZnSe matrix in spite of the simultaneous evaporation from PbSe- and ZnSe-resource.
Accordingly, the two thermodynamic material-designs, heat of formation for rf sputtering and insolubility system for HWD, are employed here for package synthesis of composite thin film. This chapter focuses on one-step physical synthesis of Ge/TiO_2 composite thin films by rf sputtering and PbSe/ZnSe composite thin films by HWD, as candidate materials for quantum dot solar cell.

2. Ge/TiO_2 composite thin films

TiO_2 mainly has crystal structures of rutile, anatase and brookite. It is believed that the anatase structure is favorable for the matrix, since carrier mobility and photoconductivity in the anatase structure exceed those in the rutile structure (Tang et al., 1994). It is difficult to forecast how the crystal structure of the TiO_2 matrix will be formed in such composite films. In fact, Ge/TiO_2 films prepared by rf sputtering employing a mixture target of TiO_2 and Ge powder hitherto contained anatase- and rutile -structure almost equally (Chatterjee, 2008). Hence, it is investigated here that the composition of Ge/TiO_2 films is thoroughly varied for preparing the anatase structure of the TiO_2 matrix while retaining vis-NIR absorption of Ge quantum dots.

2.1 Anatase-dominant matrix in Ge/TiO_2 thin films prepared by rf sputtering

The present study employed a new method of preparing Ge/TiO_2 films using a composite target of a Ge chip set on a TiO_2 disk, and their composition has been thoroughly changed. Figure 2-1(a) depicts the X-ray diffraction (XRD) pattern of Ge/TiO_2 thin films as a function of Ge concentration. In this case, the additional oxygen ratio in argon is kept constant at 0%. Labels A through E indicate Ge concentrations of 0, 1.9, 6.8, 8.1, and 21at.% by adopting 0, 1, 2, 3, and 21 Ge chips. XRD patterns first exhibited an amorphous state in as-deposited films, and several diffraction peaks began to appear at 723 K when the post-annealing temperature was raised from 673 to 873K in 50K steps. These peaks were assigned to TiO_2, and the films were therefore crystallized at around 723K (not shown here). A single-phase rutile structure is observed at a Ge concentration of 0at.% in the figure, corresponding to simple preparation of pure TiO_2 thin film. In our preliminary experiment for preparing the TiO_2 thin films, a single-phase anatase structure was obtained for oxygen ratios exceeding 0.5% and the successive post-annealing treatment. An insufficient oxygen ratio thus seems to cause formation of the rutile structure. Next, with a slight addition of Ge in the pattern of B, distinct diffraction peaks of anatase structure begin to appear, and the (101) Bragg reflection is dominant. Further addition of Ge, as seen in patterns C and D, produces different behavior in orientation, increasing the peak intensity at (004) reflection of the anatase structure. Finally, dominant, broad peaks of Ge can be observed with excess Ge addition in pattern E. The average size of the Ge nanogranules is estimated to be about 6.6nm based on the full-width at half maximum of the XRD peak employing Scherrer's equation (Scherrer, 1918). According to the variation of Ge concentration, the anatase structure is favorably promoted in patterns B, C, and D.

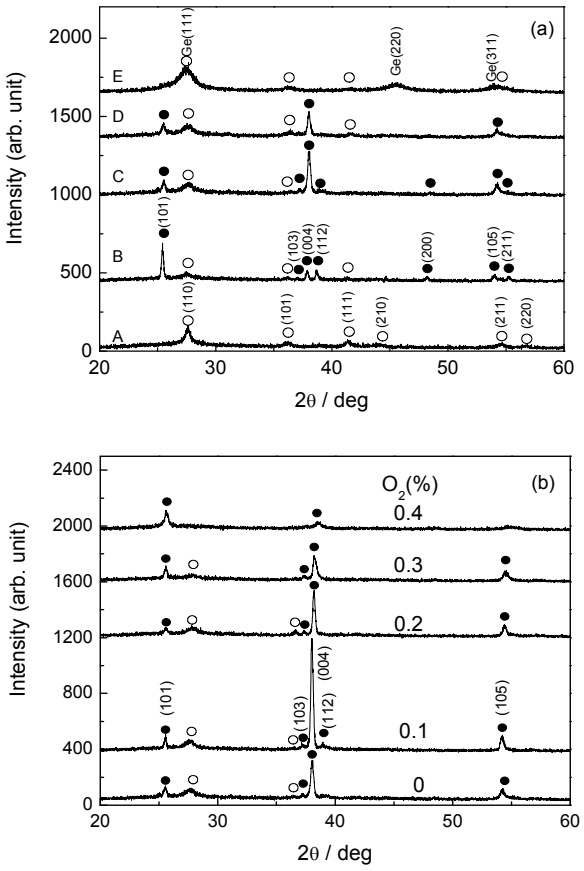

Fig. 2.1. (a) XRD patterns of Ge/TiO_2 composite films versus Ge concentrations. (•) indicates anatase structure, and (○), rutile structure. (b) Same patterns versus additional oxygen ratio in argon. (•) indicates anatase structure, and (○), rutile structure (b) (after Abe et al., 2008b).

Figure 2-1(b) depicts the XRD pattern of Ge/TiO_2 thin films as a function of the additional oxygen ratio in argon. In this case, the oxygen ratio is varied from 0 to 0.4%, and the number of Ge chips is kept constant at 2. When the ratio is increased to 0.1%, the (004) Bragg reflection becomes more prominent as seen in the figure. A further increase of the oxygen ratio then indicates weakness. An anatase-dominant structure with strong intensity at (004) reflection is thus observed at an oxygen ratio of 0.1%. We cannot observe an XRD peak of Ge in the pattern within the precision of our experiment technique, possibly due to the relatively low Ge concentration of 5.8at.%. This c-axis growth behavior in an anatase-dominant structure seems to be unique even though the composite film is deposited on a glass substrate. Thus, the crystal structure of TiO_2 matrix is found to be changed with respect to the Ge number and the oxygen ratio as illustrated in Figs. 2-1(a) and 2-1(b).

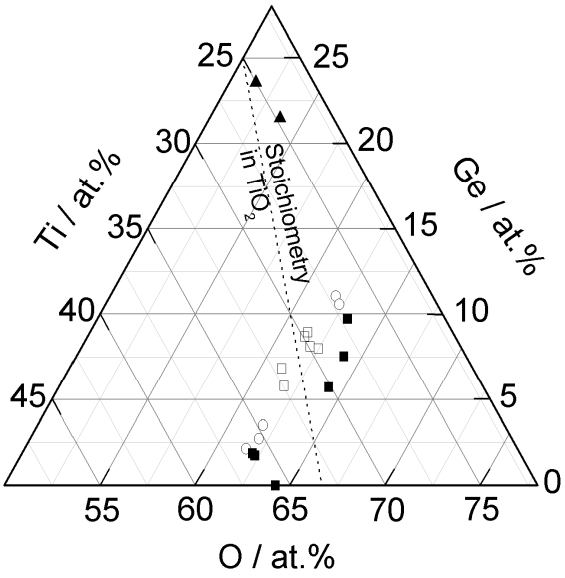

Fig. 2.2. Compositional plane of crystal structure of TiO_2 matrix in Ge/TiO_2 composite films. (○) indicates anatase structure, and (▲), rutile structure. (■) indicates coexistence of anatase and rutile structure. In particular, (□) indicates anatase-dominant structure with strong intensity at (004) reflection (after Abe et al., 2008b).

The relation between the analyzed composition of the films and the structure of TiO_2 matrix is summarized in Fig. 2-2 based on these results. The stoichiometric composition of TiO_2 is also plotted as a dotted line. The single phase of anatase structure (○) can be seen in the figure, but its visible absorption is quite weak. These films therefore do not achieve the present objective. A mixed phase containing anatase- and rutile -structure (■) appears in a wide range of Ge concentrations. In particular, an anatase-dominant structure with strong (004) reflection (□) is found at a Ge concentration of 6 to 9at.% near the stoichiometric composition of TiO_2. The optical absorption will be discussed using the following figure. The rutile structure (▲) is observed at a relatively high Ge concentration range. In these films, diffraction peaks of Ge nanogranules were observed at the same time [Fig. 2-1(a)]. Accordingly, the anatase-dominant structure with strong (004) reflection (□) is regarded to be the most optimized structure in the present study. As a further optimization, total gas pressure was varied from 2mTorr to 10mTorr in the optimized composition range. The (004) Bragg reflection was maximized at a gas pressure of 6mTorr; however, a slight amount of rutile structure still remained.

In the above sections, the structural optimization of the TiO_2 matrix in the Ge/TiO_2 composite films was focused. Next, we shall investigate the optical properties. Figure 2-3 depicts the typical optical absorption spectra of Ge/TiO_2 thin films thus optimized. For comparison, the spectrum of TiO_2 thin film is also presented in the figure. Ge has an indirect band-gap structure (Macfarlane et al., 1957), and the square root of absorbance is employed. As seen in the figure, the onset absorption can be confirmed at around 1.0eV in contrast to UV absorption of TiO_2 thin films due to its energy band gap of 3.2eV in the anatase

structure. They can favorably cover the desirable energy region for high conversion efficiency (Loferski, 1956). Therefore, it should be pointed out that valuable characteristics of vis-NIR absorption and anatase-dominant structure of TiO_2 matrix are simultaneously retained in the Ge/TiO_2 composite thin films as a result of compositional optimization. Ge addition is first motivated to demonstrate the quantum size effect, then, it is worthy of note that its addition also effectively controls the crystal structure of the TiO_2 matrix. Consequently, a single phase of anatase structure cannot be obtained. However, extensive progress can be made in structural formation of the TiO_2 matrix as a result of exhaustive compositional investigation. Based on these results, Ge/TiO_2 thin films having an anatase-dominant structure of TiO_2 matrix and vis-NIR absorption should also be regarded as candidate materials for quantum dot solar cell.

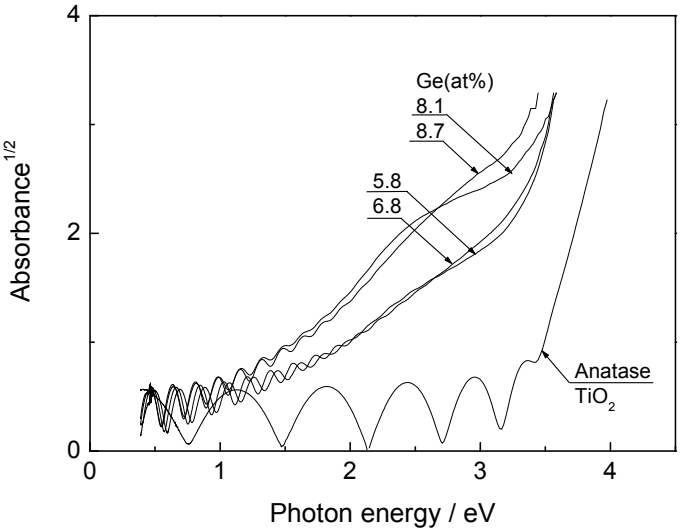

Fig. 2.3. Typical optical absorption spectra of Ge/TiO_2 composite films with anatase-dominant structure of TiO_2 matrix (after Abe et al., 2008b).

2.2 Solubility range and energy band gap of powder-synthesized $Ti_{1-x}Ge_xO_2$ solid solution

As a reason for the vis-NIR absorption, the quantum size effect probably appeared owing to the presence of Ge nanogranules. However, a ternary solid solution of $Ti_{1-x}Ge_xO_2$ is possibly formed as a matrix during the postannealing, and the solubility range of Ge and its energy band gap are hitherto unclear. Therefore, the reason for the vis-NIR absorption requires further investigation. To demonstrate whether the matrix exhibits the vis-NIR absorption, powder synthesis of a ternary $Ti_{1-x}Ge_xO_2$ solid solution is carried out. Specifically, the Ge/TiO_2 composite thin film contains multiple phases, and it is then difficult to focus on the matrix characteristics. In this section, $Ti_{1-x}Ge_xO_2$ solid solution is powder-synthesized, and the fundamental properties of solubility range of Ge and the energy band gap are investigated to clarify whether the ternary solid solution exhibits the vis-NIR absorption.

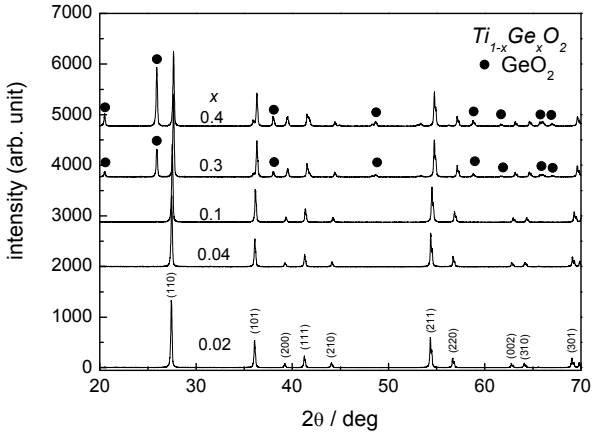

Fig. 2.4. Typical powder XRD patterns of $Ti_{1-x}Ge_xO_2$ solid solution with respect to x. Filled circle indicates GeO_2 (after Abe , 2009).

In a previous section, Ge nanogranules and TiO_2 matrix were thermally crystallized at an annealing temperature of 873K (Abe et al., 2008). Accordingly, a similar temperature of 923K was preliminary adopted to synthesize the $Ti_{1-x}Ge_xO_2$ solid solution. In this case, four samples (x = 0.05, 0.1, 0.2, and 0.3) were mixed and heat-treated for 20 days to achieve thermal equilibrium. However, a single phase of the $Ti_{1-x}Ge_xO_2$ solid solution could not be obtained, forming two phases of GeO_2 and anatase-structured TiO_2 according to the XRD pattern. For reference, there was a slight decrease in the lattice constant at x=0.05 estimated from the (004) reflection of anatase structure in comparison with those of the TiO_2 standard powder, and gradually increased with increasing x in the range exceeding 0.05. Thus, the solubility limit of Ge was found to be quite narrow (less than 0.05) at 923K. In addition, no energy shift of the optical absorption edge can be seen with respect to x. Therefore, an adequately high temperature of 1273K is alternatively adopted here in anticipation of a wide solubility range of Ge.

Figure 2-4 depicts typical powder XRD pattern of the $Ti_{1-x}Ge_xO_2$ solid solution. In the range below 0.1, all the XRD peaks can be assigned to rutile structure and shift toward greater angle as x increases owing to the difference in ionic radii between Ti and Ge (Shannon, 1976; Takahashi et al., 2006). In addition, an XRD peak of GeO_2 cannot be observed within the precision of the experimental technique. Such peak shift was also observed on the TiO_2-GeO_2 solid solution synthesized through sol-gel method within a Ge concentration range below 10 mol% (Kitiyanan et al., 2006) or 1.5 mol% (S. Chatterjee & A. Chatterjee, 2006). It is suggested that the present sample possibly forms a solid solution of $Ti_{1-x}Ge_xO_2$. The solubility range of Ge is therefore found to be enlarged as a result of elevating the temperature from 923 to 1273K. The standard powder of TiO_2 employed here has anatase structure, since the matrix of the Ge/TiO_2 composite thin films had anatase-dominant structure (Abe et al., 2008b). However, the product thus powder-synthesized resulted in rutile structure because of phase transition from anatase to rutile at 973K (The Mark Index, 1968). In contrast, the GeO_2 peaks, which are indicated by a filled circle, begin to appear in the range exceeding 0.3. Their peak positions seem to remain the same with respect to x, suggesting no solubility range of Ti in GeO_2 at 1273 K. The two phases of the $Ti_{1-x}Ge_xO_2$ and GeO_2 are therefore formed in such concentration range.

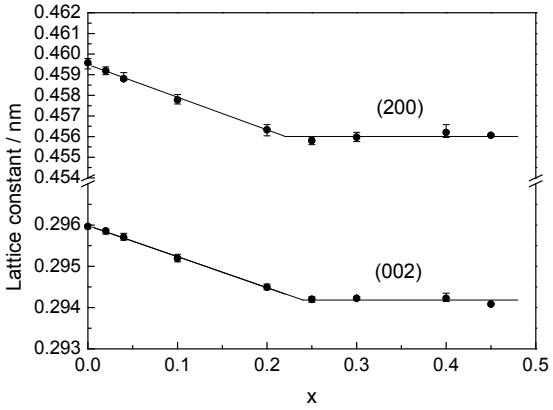

Fig. 2.5. Lattice constant of $Ti_{1-x}Ge_xO_2$ solid solution vs Ge concentration (after Abe , 2009).

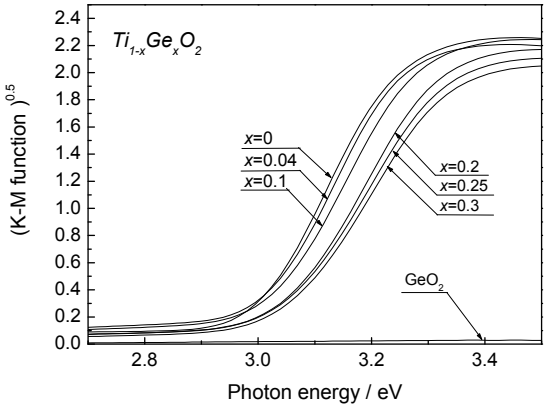

Fig. 2.6. Typical optical absorption spectra of $Ti_{1-x}Ge_xO_2$ solid solution vs Ge concentration (after Abe , 2009).

Next, the solubility limit of Ge in the $Ti_{1-x}Ge_xO_2$ is determined through the variation of the lattice constant. Figure 2-5 depicts the lattice constant of the $Ti_{1-x}Ge_xO_2$ solid solution as a function of x. Here, the lattice constant of the tetragonal system is estimated from the (200) and (002) reflections. Their peak intensities were found to be relatively weak (Fig. 2-4), but the peak position can be distinctly determined from Lorentzian fitting of the spectra, containing a measurement error of about 0.06 deg in 2θ as a result of four repetitive measurements. Accordingly, the lattice constant results in containing a maximum calculation error of about 0.0006 nm. In the preliminary experiment, a mass reduction during the heat treatment was found to be less than 0.1% in standard powders of TiO_2 and GeO_2, suggesting a small amount of sublimation. The nominal content of Ge is therefore employed here as a composition of the product. It is clearly seen in the figure that the lattice constant in both reflections is first decreased linearly in proportion to x, and becomes constant irrespective of x in the range exceeding 0.25. According to Vegard's law (Vegard, 1921), an on-setting composition x to deviate from the linearity is regarded as a solubility

limit of Ge. It is therefore determined to be 0.23 ± 0.01 at 1273 K, having 0.22 at (200) and 0.24 at (002) reflection. Thus, the two-phase region consistently involves the fixed composition of $Ti_{0.77}Ge_{0.23}O_2$ and GeO_2. It can be clearly explained in terms of Gibb's phase rule. Specifically, the number of degrees of freedom is simply estimated to be 1, since the present ternary system has a component of 2. Thus, the state of the system is completely fixed at a given temperature of 1273K. Based on these results, the relation between the lattice constant L (nm) and x in the solubility range is expressed as follows: L=0.4595-0.0162x at (200) reflection and L=0.2960-0.0075x at (002) reflection.

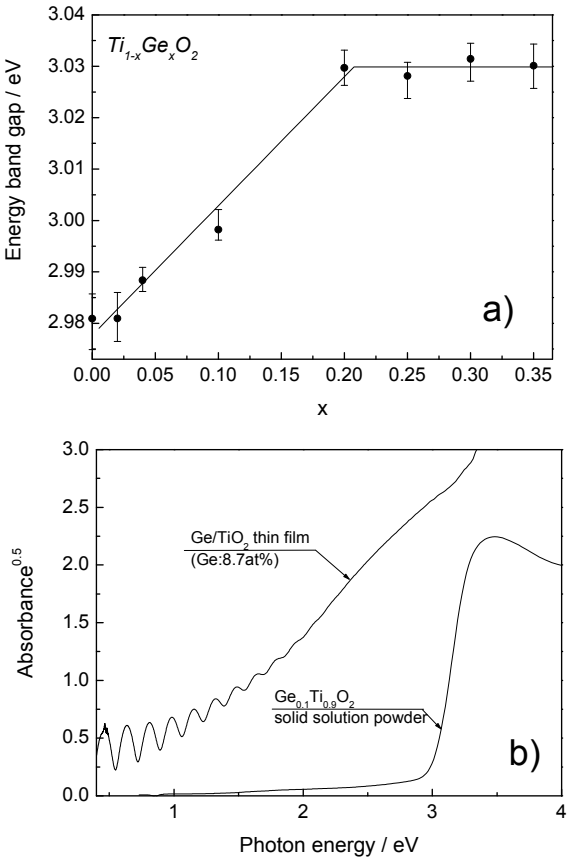

Fig. 2.7. (a) Energy band gap of $Ti_{1-x}Ge_xO_2$ solid solution at room temperature vs Ge concentration. (b) Absorption spectra of the Ge/TiO_2 thin film and a solid solution of the $Ti_{1-x}Ge_xO_2$ powder (after Abe , 2009).

In comparison, the lattice constant of the matrix in the Ge/TiO_2 composite thin films also decreased with increasing Ge concentration, ranging from 0.9495 to 0.9400nm estimated from the (004) reflection of anatase structure. In this case, the postannealing was performed at 873K for 60min. Such decreasing tendency of the lattice constant is the same as those of the $Ti_{1-x}Ge_xO_2$ powder despite the fact that the crystal structure is different in both samples,

having a rutile structure for the powder and an anatase structure for the composite films. Therefore, the matrix of the composite film possibly formed a solid solution of $Ti_{1-x}Ge_xO_2$. Subsequently, optical absorption should be investigated regardless of whether the solid solution exhibits the vis-NIR absorption.

Figure 2-6 plots the optical absorption spectra of the powder-synthesized $Ti_{1-x}Ge_xO_2$ solid solution. These spectra are derived from the square root of Kubelka-Munk function (Kubelka & Munk, 1931) because of the indirect band gap structure of TiO_2 (Macfarlane et al., 1957). For comparison, the spectrum of GeO_2 is also shown. It is clearly seen that the GeO_2 is appreciably transparent in the measured range from 2.7 to 3.5 eV, whereas the optical absorption edge of the $Ti_{1-x}Ge_xO_2$ can be clearly observed at approximately 3 eV, and shift to the greater energy region as x increases. Therefore, the solid solution of $Ti_{1-x}Ge_xO_2$ is found to unexhibit the vis-NIR absorption.

Just for reference, the band gap can be estimated from a linear extrapolation to zero of the optical absorption edge, and is then summarized in Fig. 2-7(a). Error bars indicative of the possible variation in energy gap are used to plot the data. The energy band gap increases monotonically from 2.98 to 3.03 eV with respect to x, and becomes constant in the range exceeding 0.25. The energy shift is therefore achieved to be 0.05 eV at a solubility limit of 0.23. In fact, the Ge/TiO_2 composite thin films were compositionally optimized at a relatively low Ge concentration of 6 to 9at.% (Abe et al., 2008b), which indicates the total amount of Ge contained in both the matrix and the nanogranules. Hence, the energy shift in the matrix of the composite thin film is considered to be negligibly small (less than 0.01 eV). From these results, the matrix of the Ge/TiO_2 composite thin films possibly formed a solid solution of $Ti_{1-x}Ge_xO_2$ during the post annealing, but did not exhibit the vis-NIR absorption.

Figure 2-7(b) depicts the optical absorption spectra of the Ge/TiO_2 thin film and a solid solution of the $Ti_{1-x}Ge_xO_2$ powder. Here, Ge concentration in the film was analyzed to be 8.7 at.%, and a similar concentration of x=0.1 in the powder was also presented for comparison. The absorption spectrum of the $Ti_{1-x}Ge_xO_2$ powder was obtained by means of the Kubelka-Munk function (Kubelka & Munk, 1931) through a diffused reflectance spectrum. The vis-NIR absorption was clearly observed in the Ge/TiO_2 film, while an optical absorption edge of the synthesized powder was observed at UV region. It was therefore concluded that the $Ti_{1-x}Ge_xO_2$ solid solution unexhibited such vis-NIR absorption.

2.3 Quantum size effect of Ge in TiO_2 matrix

In the previous sections, valuable characteristics of the vis-NIR absorption and the anatase-dominant structure of TiO_2 matrix were simultaneously retained in the Ge/TiO_2 composite thin films. However, it was unclear whether the vis-NIR absorption (Fig. 2-3) was due to the presence of Ge nanogranules, since an X-ray diffraction peak of Ge was not observed in the optimized composition range. In this section, we have investigated the presence of Ge nanogranules embedded in the anatase-dominant structure of TiO_2 thin films, and clarified the reason for the vis-NIR absorption.

Figure 2-8 depicts the size distribution of nanogranules in the Ge/TiO_2 composite thin films. These profiles were estimated from small angle X-ray spectroscopy (SAXS) analysis of Guinier fitting for an experimental result (the inset in Fig.2-8). In this case, Ge chips of 3 and the oxygen ratio of 0.3% was adopted during the deposition, and Ge concentration was analyzed to be 8.7at.%, and the film exhibited the vis-NIR absorption [Fig. 2-7(b)]. In the pinhole-collimated apparatus of SAXS measurement, X-ray was injected perpendicularly to the film surface, providing in-plane structural characteristic. As can be seen in the figure, the

size profile distributed broadly, and mean radius of nanogranules was estimated to be 1.9 nm (3.8nm in diameter), ranging the radius from ~0.5 to 8nm. The SAXS analysis therefore strongly suggested that nanoscale material was embedded in the film, possibly attributing to Ge nanogranules or another phase of the $Ti_{1-x}Ge_xO_2$ matrix. Successively, the size of $Ti_{1-x}Ge_xO_2$ matrix was estimated by HREM.

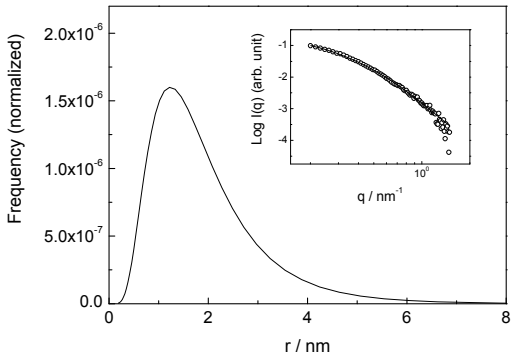

Fig. 2.8. Size distribution of nanogranules derived from the SAXS analysis. The inset depicts SAXS spectrum (after Abe et al., 2008c).

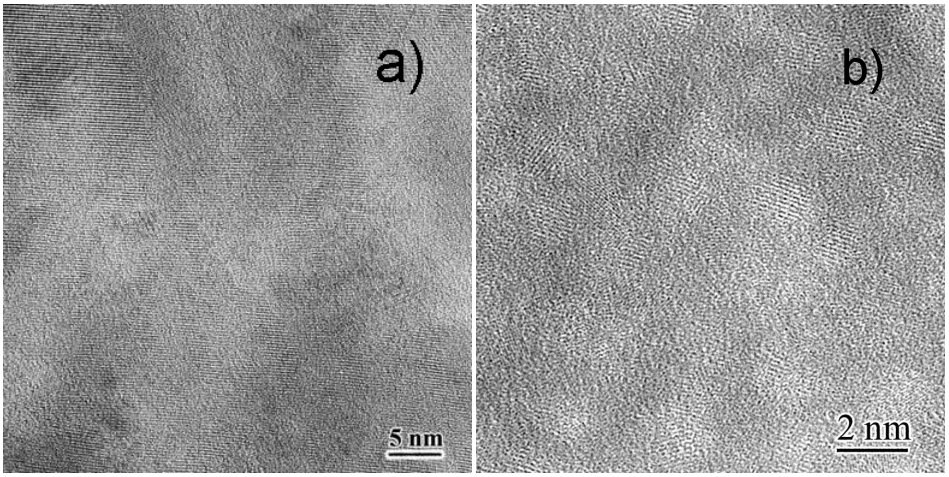

Fig. 2.9. (a) HREM image of anatase structure of the matrix in Ge/TiO_2 thin films (Abe et al., 2008c). (b) HREM image of Ge nanogranules embedded in the matrix (after Abe et al., 2008b).

Figure 2-9(a) presents the HREM image of the anatase-structured matrix at an oxygen ratio of 0.3%. Lattice image of the anatase structure was clearly observed, and size of their grains was estimated to be ~30nm. The size exceeded that of the nanogranules estimated by SAXS. Figure 2-9(b) presents an HREM image of Ge nanogranules embedded in Ge/TiO_2 composite film at a Ge concentration of 8.7at.%. In the figure, the slightly bright contrast

region with spherical geometry corresponds to Ge nanogranule, and their lattice image can be clearly seen. The average size is estimated to be about 2nm. Furthermore, their average size is also estimated to be about 5nm by SAXS analysis. These estimated sizes are found to be close each other, and the Ge nanogranules are sufficiently small to create the quantum size effect because of the exciton Bohr radius of 24.3nm in Ge (Maeda et al., 1991). Therefore, the shift of optical absorption (Fig. 2-3) is reasonably due to the Ge nanogranules embedded in $Ti_{1-x}Ge_xO_2$ matrix.

3. PbSe/ZnSe composite thin films

Co-sputtering thus employed in the above section is useful for forming a composite thin film consisting of semiconductor nanocrystals embedded in a matrix because of its simple preparation process and consequent low cost. In the material design, based on the heat of formation, nanocrystal and matrix are clearly phase-separated in spite of the co-deposition from multiple sources (Abe et al., 2008b; Ohnuma et al., 1996). However, it is generally found that sputtering techniques often damage a film due to contamination of the fed gas and high-energy bombardment of the film surface. Thermal evaporation in a high-vacuum atmosphere seems to be better as a preparation technique from the point of view of film quality. In addition, the present study focuses on the insolubility of the material system, since simultaneous evaporation from multiple sources often provides a solid solution (Nill, et al., 1973; Holloway & Jesion, 1982; Abe & Masumoto, 1999).

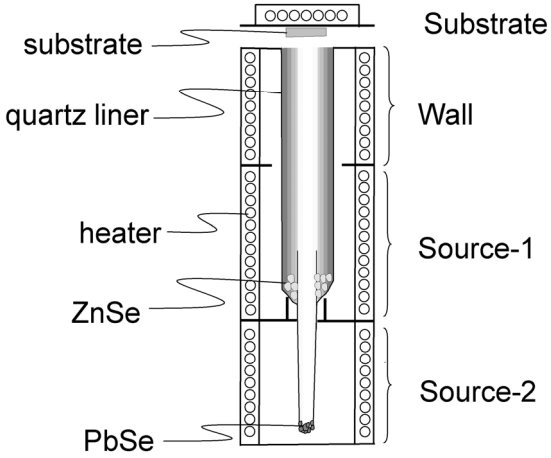

Fig. 3.1. HWD apparatus used in the study. It consists of four electric furnaces for substrate, wall, source-1, and source-2 (after Abe, 2011).

The PbSe-ZnSe system is a candidate for the composite. In the bulk thermal equilibrium state, the mutual solubility range is quite narrow, less than 1mol%, at temperatures below 1283K (Oleinik et al., 1982). In addition, a composite thin film of PbSe nanocrystal embedded in ZnSe matrix is capable of exhibiting the quantum size effect because of the relatively large exciton Bohr radius of 46nm in PbSe (Wise, 2000) and the relatively wide band gap of 2.67eV in ZnSe (Adachi & Taguchi, 1991). Hence, the optical gap of PbSe nanocrystals will probably be tuned to the maximum solar radiation spectrum. The

dendritic PbSe nanostructure (Xue, 2009) and ZnSe nanobelt array (Liu, 2009), for instance, are hitherto investigated, but there is no report for one-step synthesis of PbSe/ZnSe composite thin film. Furthermore, an evaporation technique should be carefully selected, since the techniques involving a thermal non-equilibrium state, such as molecular beam epitaxy, increase the solubility limit (Koguchi et al., 1987). The use of HWD, which can provide an atmosphere near thermal equilibrium, is therefore indicated here (Lopez-Otero, 1978). Based on these considerations, one-step synthesis of a PbSe/ZnSe composite thin film was investigated by simultaneous HWD from multiple sources.

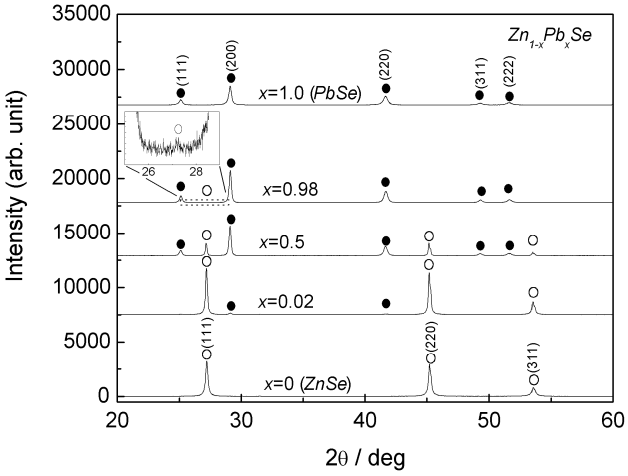

Fig. 3.2. XRD pattern of powder-synthesized $Zn_{1-x}Pb_xSe$ with respect to x. Dots indicate PbSe and circles indicate ZnSe (after Abe, 2011).

A PbSe/ZnSe composite thin film was prepared by the HWD method. Figure 3-1 is a schematic diagram of the HWD apparatus used. There were four electric furnaces in the apparatus, designated as substrate, wall, source-1, and source-2. Each temperature could be controlled independently. In the HWD method, deposition and re-evaporation are continuously repeated upon a film surface, resulting in achieving a state near thermal equilibrium (Lopez-Otero, 1973). PbSe and ZnSe were used as evaporation sources and were synthesized from elements of Pb, Zn, and Se with 6N purity. The PbSe and ZnSe sources were located at furnaces of source-2 and source-1 for simultaneous evaporation to a glass substrate (Corning #7059). Here, the temperatures were kept constant at 573K for the substrate, 773K for the wall, and 973K for source-1 (ZnSe). The source-2 (PbSe) temperature was varied from 763 to 833K to provide different PbSe concentrations.

The bulk PbSe-ZnSe phase diagram is now revealed at ZnSe concentrations below 45at.% (Pb-rich side) (Oleinik et al., 1982), although the phase diagram of the Zn-rich side still remains unclear. Powder synthesis of a PbSe-ZnSe system was investigated prior to investigating the film preparation. Figure 3-2 depicts the powder XRD pattern of the $Zn_{1-x}Pb_xSe$ system. In the powder synthesis, the bulk PbSe and ZnSe thus synthesized was used as starting materials. The desired composition of the system was prepared in an agate mortar and vacuum-sealed in a quartz tube for heat treatment at 1273K for 48h. Finally, the samples were successively water-quenched to maintain the solubility range at

a synthesis temperature then crushed into powder for the following experiment setup. At x=0, all of the XRD peaks are assigned to the zinc-blend structure of ZnSe, with a lattice constant of 0.5669nm, estimated from the XRD peaks in a high-2θ range from 100° to 155°, using the Nelson-Riley function (Nelson & Riley, 1945). The XRD peak of PbSe with an NaCl structure appears at Pb concentrations exceeding 0.02. The lattice constant of the ZnSe at x=0.02 is the same as at x=0, within the precision of the experiment technique. This result indicates that the solubility range of Pb in ZnSe is negligible. In contrast, the lattice constant of PbSe is estimated to be 0.6121nm at x=1.0 and 0.6117nm at x=0.98. A slight decrease in the lattice constant is seen in PbSe, due to the difference in ionic radii of Pb and Zn. Weak XRD peaks of ZnSe are also observed at x=0.98 as seen in the inset for easier viewing. This result indicates that the solubility range of Zn in PbSe is less than 0.02 at 1273K. The result is in good agreement with the previous result (Oleinik et al., 1982). The phase separation of the PbSe-ZnSe system is thus also seen on the Zn-rich side in the thermal-equilibrium state. The film preparation for PbSe/ZnSe composite is next investigated based on these results.

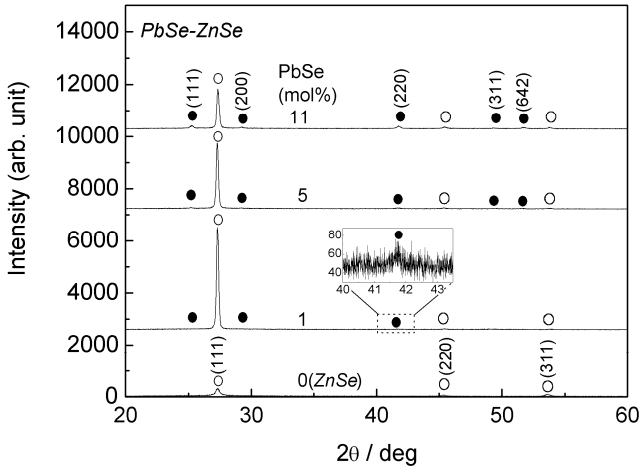

Fig. 3.3. XRD pattern of the PbSe/ZnSe composite thin films. Dots indicate PbSe and circles indicate ZnSe (after Abe, 2011).

The two sources were simultaneously evaporated to prepare a PbSe/ZnSe composite thin film. In the apparatus used, thermal radiation from the wall- and the source-furnace induced an unintentional increase of the substrate temperature up to 515K without use of the substrate-furnace. The deposition rate of the film was almost the same irrespective of the substrate temperature in the range from 515K to 593K. A homogeneous color is observed visually in these films. Above a substrate temperature of 593K, the deposition rate abruptly decreased with increasing temperature, since re-evaporation of PbSe from the film surface became dominant. The films visually exhibit an inhomogeneous yellowish and metallic color, probably caused by a significant reduction in the PbSe while the ZnSe remained, due to the relatively high vapor pressure of PbSe (Mills, 1974). The wall temperature also induced similar behavior. A substrate temperature of 573K and a wall temperature of 773K are therefore adopted throughout the present study.

Figure 3-3 depicts the XRD pattern for the PbSe/ZnSe composite thin films. The weak XRD peak of PbSe at 1mol% is enlarged in the inset for easier viewing. At a PbSe concentration of 0mol% (i.e., pure ZnSe), polycrystalline ZnSe with a zinc-blend structure is observed, with PbSe phase appearing at concentrations exceeding 1mol%. The solubility range of Pb in ZnSe is therefore found to be quite narrow, less than 1mol%, corresponding well to the bulk result (Fig. 3-2). The composite films thus deposited on a glass substrate exhibit a reasonably polycrystalline structure, but dominant (111) growth is seen in the ZnSe phase irrespective of x. At 1mol%, the lattice constant at the PbSe (220) peak is estimated to be 0.6118nm, close to that of the bulk result (Fig. 3-2). This result suggests that there is also a narrow solubility range on the Pb-rich side. The phase-separating PbSe-ZnSe system is therefore maintained not only in the bulk product, but also in the film thus obtained, despite the simultaneous evaporation from multiple sources. This result demonstrates that an atmosphere near thermal equilibrium was achieved in the HWD apparatus used.

Figure 3-4(a) presents a bright-field TEM image of the PbSe/ZnSe composite thin film containing 5mol%PbSe. Dark isolated grains with sizes of 25nm to 50nm are seen dispersed along the grain boundary of the bright area. Figures 3-4(b-e) present an scanning transmission electron microscopy (STEM) - energy dispersive spectroscopy (EDX) elemental mapping of the sample through X-ray detection of Zn K (red), Se K (blue), and Pb L (green). Similar morphology is also seen in the bright-field STEM image [Fig. 3-4(b)]. The dark grains indicate the absence of elemental Zn [Fig. 3-4(c)] and the presence of Se and Pb [Figs. 3-4 (d and e)]. It is thus determined that the dark grains are nanocrystalline PbSe. The other region is widely covered with the elements Zn and Se [Figs. 3-4 (c and d)], reasonably assumed to compose ZnSe. It is therefore determined that isolated PbSe nanocrystals are dispersed in the ZnSe matrix. The nanocrystals are estimated to be sufficiently small to exhibit the quantum-size effect because of the exciton Bohr radius of 46nm in PbSe (Wise, 2000).

Figure 3-5 depicts optical absorption spectra for the PbSe/ZnSe composite thin films. For comparison, the spectrum of a pure ZnSe thin film is also presented in the figure. PbSe and ZnSe have direct band structures (Theis, 1977; Zemel et al., 1965) and the absorbance squared is employed here. At a 0mol%PbSe, the optical absorption edge of ZnSe is clearly observed at 2.7eV. Weak absorption then broadly appears at a PbSe concentration of 1mol% in the visible region, together with the optical absorption edge of ZnSe. Such multiple absorptions are also seen in the spectra at concentrations up to 7mol%, indicating the obvious phase separation of the PbSe-ZnSe system. The broad absorption edge shifts toward the lower-energy region as the PbSe content increases. In particular, onset absorption can be confirmed at approximately 1.0eV at 16mol%PbSe, favorably covering the desirable energy region for high conversion efficiency (Loferski, 1956). Therefore, it should be noted that the PbSe/ZnSe composite thin film exhibits the valuable characteristic of vis-NIR absorption.

However, it is unclear whether the shift of the optical absorption edge is due to the PbSe nanocrystals, since the mean grain size of the PbSe remains almost the same at 27nm irrespective of the PbSe content, according to the XRD result (Fig. 3-3) using Scherrer's equation (Scherrer, 1918). A PbSe-ZnSe solid-solution system cannot provide continuous change of the energy band gap because of the quite narrow solubility range (Fig. 3-3). In contrast, the PbSe nanocrystals are sufficiently smaller than the exciton Bohr radius of PbSe (Fig. 3-4). Therefore, this obvious shift is assumed to be responsible for the quantum-size effect of the PbSe nanocrystals embedded in the ZnSe matrix. The minimal appearance of infrared absorption at 16mol%PbSe strongly suggests that relatively large-scale PbSe grains are partially involved in the composite film, since the energy band gap of bulk PbSe is

0.27eV (Zemel et al., 1965). Another TEM image also indicates the presence of relatively large PbSe crystals of approximately 100nm, even with a small amount of 5mol%PbSe (not shown here). Hence, the mean grain size of the PbSe is bimodally distributed in the composite. These large-scale PbSe grains probably dominate the full width at half maximum value of the XRD peak, resulting in no obvious relation between the optical absorption shift and the PbSe grain size. The size control of the nanocrystalline PbSe is therefore insufficient in the present study. The substrate temperature thus adopted seems to assist in the aggregation of PbSe nanocrystals. However, a one-step synthesis of the composite package has the potential to lead to low-cost production of next-generation solar cells.

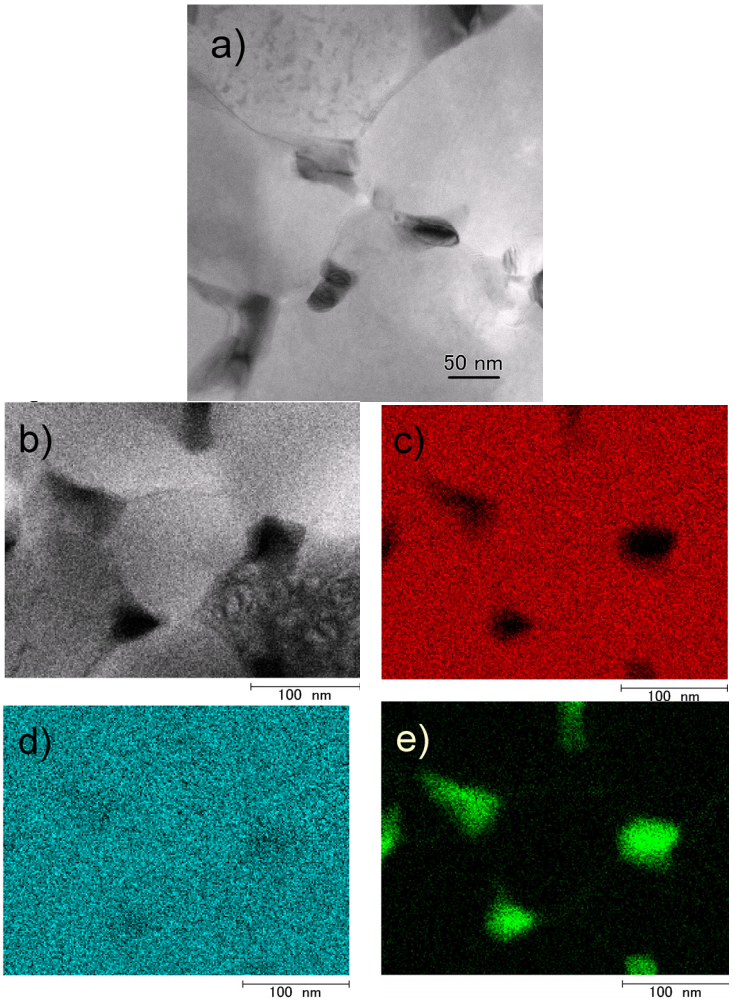

Fig. 3.4. Direct observation of PbSe/ZnSe composite thin film containing 5mol%PbSe. (a) Bright-field TEM image. (b) Bright-field image of STEM mode. (c) Elemental mapping of Zn (red), (d) Se (blue), and (e) Pb (green) (after Abe, 2011).

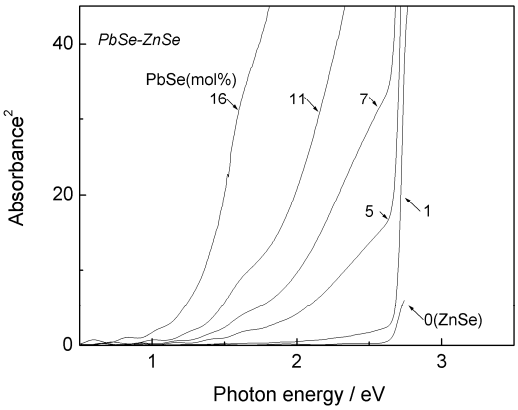

Fig. 3.5. Optical absorption spectra for PbSe/ZnSe composite thin films (after Abe, 2011).

4. Conclusion

This chapter has been focused on one-step physical synthesis of Ge/TiO_2 and PbSe/ZnSe composite thin film as candidate materials for quantum dot solar cell. It should be pointed out in the Ge/TiO_2 that the anatase-dominant structure appears in the restricted composition range as a result of optimization of Ge chip numbers and additional oxygen ratio in argon. Furthermore, their optical absorption edge is obviously shifted to vis-NIR region. The solubility range of Ge in the $Ti_{1-x}Ge_xO_2$ powder is estimated to be 0.23 ± 0.01 at 1273 K. In addition, their optical absorption edge is obviously shifted to the UV region as x increases. Thus, the $Ti_{1-x}Ge_xO_2$ solid solution does not exhibit the vis-NIR absorption. In contrast, SAXS and HREM results clearly indicated that the Ge nanogranules were embedded in the matrix. The size was sufficiently small to appear the quantum size effect. Thus, the both valuable characteristics are simultaneously retained in the Ge/TiO_2 composite films. In the PbSe/ZnSe, the solubility limit of Pb in ZnSe is quite narrow, less than 1mol% in the film form, indicating that an atmosphere near thermal equilibrium is achieved in the apparatus used. Elemental mapping indicates that isolated PbSe nanocrystals are dispersed in the ZnSe matrix. The optical absorption edge shifts toward the lower-photon-energy region as the PbSe content increases. In particular, onset absorption can be confirmed at approximately 1.0eV with 16mol%PbSe, favorably covering the desirable energy region for high conversion efficiency. The insolubility material system and the HWD technique enable a one-step synthesis of PbSe/ZnSe composite thin film.

5. Acknowledgment

The present work was supported in part by a Grant-in-Aid for Scientific Research from the Japan Society for the Promotion of Science (No.21360346). The author is grateful to Dr. M. Ohnuma [National Institute for Materials Science (NIMS), Tsukuba, Japan], Dr. D. H. Ping (NIMS), and Dr. S. Ohnuma [Research Institute for Electromagnetic Materials (RIEM), Sendai, Japan] for collaborating in this work. The author gratefully acknowledges the valuable comments and continuous encouragement of President T. Masumoto (RIEM). The author is also grateful to Mr. N. Hoshi and Mr. Y. Sato (RIEM) for assisting in the experiments.

6. References

Abe, S. & Masumoto, K. (1999). Compositional plane and properties of solid solution semiconductor $Pb_{1-x}Ca_xS_{1-y}Se_y$ for mid-infrared lasers, *Journal of Crystal Growth*, Vol.204, pp. 115-121.

Abe, S, Ohnuma, M, Ping, D. H., Ohnuma, S. (2008a). Single dominant distribution of Ge nanogranule embedded in Al-oxide thin film, *Journal of Aplied Physics*, Vol. 104, pp. 104305 1-3.

Abe, S, Ohnuma, M, Ping, D. H., Ohnuma, S (2008b). Anatase-Dominant Matrix in Ge/TiO_2 Thin Films Prepared by RF Sputtering Method , *Applied Physics Express*, Vol. 1, pp. 095001 1-3.

Abe, S, Ohnuma, M, Ping, D. H., Ohnuma, S (2008c). Preparation of Ge nanogranules embedded in Anatase-dominant TiO_2 thin films by RF sputtering, *Proceedings of 14th International Conference on Thin Films (ICTF 14)*, pp.101-104.

Abe, S (2009). Solubility Range and Energy Band Gap of Powder-Synthesized $Ti_{1-x}Ge_xO_2$ Solid Solution , *Japanese Journal of Applied Physics*, Vol. 48, pp. 081605 1-3

Abe, S (2011). One-step synthesis of PbSe/ZnSe composite thin film, *Nanoscale Research Letters* Vol. 6, pp.324 1-6.

Adachi, S. & Taguchi, T. (1991). Optical properties of ZnSe,: *Physical Review B*, Vol. 43, pp. 9569-9577.

Chatterjee, S. Goyal, A. & Shah, I. (2006). Inorganic nanocomposites for next generation photovoltaics, *Materials Letters.* Vol.60, pp. 3541-3543.

Chatterjee, S. & Chatterjee, A. (2008). Optoelectronic properties of Ge-doped TiO_2 nanoparticles. *Japanese Journal of Applied Physics*, Vol. 47, pp. 1136-1139.

Chatterjee, S. (2008). Titania-germanium nanocomposite as a photovoltaic material, *Solar Energy*, Vol.82, pp. 95-99.

Holloway, H. & Jesion, G. (1982). Lead strontium sulfide and lead calcium sulfide, two new alloy semiconductors, *Physical Review B*, Vol. 26, pp. 5617-5622.

Hoyer, P. & Könenkamp, R. (1995). Photoconduction in porus TiO_2 sensitized by PbS quantum dots, *Appied Physics Letters*, Vol. 66, pp. 349-351.

Kitiyanan, A. Kato, T. Suzuki, Y. & Yoshikawa, S. (2006). The use of binary TiO_2-GeO_2 oxide electrodes to enhanced efficiency of dye-sensitized solar cells, *Journal of Photochemistry and Photobiology A*, Vol. 179, pp. 130-134.

Koguchi, N. Kiyosawa, T.& Takahashi, S. (1987). Double hetero structure of $Pb_{1-x}Cd_xS_{1-y}Se_y$ lasers grown by molecular beam epitaxy, *Journal of Crystal Growth*, Vol. 81, pp. 400-404.

Kolodinski, S. Werner, J. H. Wittchen, T. & Queisser, H.J. (1993). Quantum efficiencies exceeding unity due to impact ionization in silicon solar cells, *Applied Physics Letters*, Vol. 63, pp. 2405-2407.

Kubachevski, O & Alcock, C. B. (1979). *Metallurgical Thermochemistry*, Pergamon.

Kubelka, P. & Munk, F. (1931). Ein Beitrag zur Optik der Far-banstriche, *Zeitschrift Technische Physik* Vol. 12, pp. 593-601.

Landsberg, P. T. Nussbaumer, H. & Willeke, G. (1993). Band−band impact ionization and solar cell efficiency , *Journal of Applied Physics*, Vol. 74, pp. 1451-1452.

Liu, D. & Kamat, P. V. (1993). Photoelectrochemical behavior of thin CdSe and coupled TiO_2/CdSe semiconductor films, *Journal of Physical Chemistory*, Vol. 97, pp. 10769-10773.

Liu, J. & Xue, D. (2009). Solution-based route to semiconductor film: Well-aligned ZnSe nanobelt arrays, *Thin Solid Films*, Vol. 517, pp. 4814-4817.

Loferski, J. J. (1956). Theoretical considerations covering the choice of the optinum semiconductor for photovoltaic solar energy conversion, *Journal of Applied Physics*, Vol. 27, pp.777-784.

Lopez-Otero, A. (1978). Hot wall epitaxy, *Thin Solid Films*, Vol. 49, pp. 3-57.

Macfarlane, G. G. McLean, T. P. Quarrington, J. E. & Roberts, V. (1957). Fine structure in the absorption-edge spectrum of Ge, *Physical Review* , Vol. 108, pp. 1377-1383.

Maeda, Y. Tsukamoto, N. Yazawa, Y. Kanemitsu, Y. & Masumoto, Y. (1991). Visible photoluminescence of Ge microcrystals embeddded inSiO_2, *Applied Physics Letters*, Vol. 59, pp. 3168-3170.

Mills, K. C. (1974). *Thermodynamic data for inorganic sulphide, selenides and Tellurides*. Butterworth.

Nelson, J. B. & Riley, D. P. (1945). An experimental investigation of extrapolation methods in the derivation of accurate unit-cell dimensions of crystals, *Proceedings of Physical Society* Vol. 57, pp. 160.

Nill, K. W. Sreauss, A. J. & Blum, F. A. (1973). Tunable cw Pb0.98Cd0.02S diode lasers emitting at 3.5 μm: Applications to ultrahigh-resolution spectroscopy, *Applied Physics Letters* Vol. 22, pp. 677-679.

Nozik, A. J. (2002). Quantum dot solar cells, *Physics E*, Vol. 14, pp.115-120.

Ohnuma, S. Fujimori, H. Mitani, S. & Masumoto, T. (1996). High-frequency magnetic properties in metal-nonmetal granular films, *Journal of Applied Physics,* Vol. 79, pp. 5130-5135.

Oleinik, G.S. Mizetskii, P.A. & Nizkova, A.I. (1982). Nature of the interaction between lead and zic chalcogenides, *Inorganic Materials*, Vol. 18, pp. 734-735.

Scherrer, P. (1918). Bestimmung der Größe und der inneren Struktur von Kolloidteilchen mittels Röntgenstrahlen, *Göttinger Nachrichten*, Vol. 2, pp. 98-100.

Shannon, R. D. (1976). Revised effective ionic radii and systematic studies of interatomic distances in halides and chalcogenides, *Acta Crystallography, Sect. A*, Vol. 32, pp. 751-767.

The Merck Index (Merck & Co, New Jersey, 1968) 8th ed., p. 1054.

Takahasi, Y. Kitamura, K. Iyi, N. & Inoue, S. (2006). Phase-stability and photoluminescence of $BaTi(Si, Ge)_3O_9$, *Journal of Ceramic Society of Japan*, Vol. 114, pp. 313-317.

Tang, H. Prasad, K. Sanjinès, R.P. Schmid, E. & Lévy F. (1994). Electrical and optical properties of TiO_2 anatase thin films, *Journal of Appied Physics*, Vol. 75, pp. 2042-2047.

Theis, D. (1977). Wavelength modulated reflectivity spectra of ZnSe and ZnS from 2.5 to 8 eV, *Physica Status Solidi* (B), Vol. 79, pp.125-130.

Vegard, L. (1921). Die Konstitution der Mischkristalle und die Raumerfüllung der Atome, *Z. Phys*. Vol. 5, pp. 17-26.

Weller, H.. (1991). Quantum sized semiconcuctor particles in solution in modified layers, *Berichte der Bunsengeselleschaft Physical Chemistry,* Vol. 95, pp. 1361-1365.

Wise, F. W. (2000). Lead salts quantum dots: the limit of strong confinement, *Accounts of Chemical Research*, Vol. 33, pp. 773-780.

Xue, D. (2009). A template-free solution method based on solid-liquid interface reaction towards dendritic PbSe nanostructures, *Modern Physics Letters B*, Vol. 23, pp. 3817-3823.

Yang, W. Wan, F. Chen, S. Jiang, C. (2009). Hydrothermal growth and application of ZnO nanowire films with ZnO and TiO_2 buffer layers in dye-sensitized solar cells, *Nanoscale Research Letters*, Vol. 4, pp. 1486-1492.

Zaban, A. Micic, O. I. Gregg, B. A. & Nozik, A. J., (1998). Photosensitization of nanoporus TiO_2 electrodes with InP quantum dots, *Langmuir*, Vol. 14, pp. 3153-3156.

Zemel, J. N. Jensen, J. D. & Schoolar, R. B. (1965). Electrical and optical properties of epitaxial films of PbS, PbSe, PbTe, and SnTe, *Physical Review*, Vol. 140, pp. A330-A342.

Zhu, G. Su, F. Lv, T. Pan, L. Sun, Z. (2010). Au nanoparticles as interfacial layer for CdS quantum dot-sensitized solar cells, *Nanoscale Research Letters*, Vol. 5, pp. 1749-1754.

8

Cuprous Oxide as an Active Material for Solar Cells

Sanja Bugarinović[1], Mirjana Rajčić-Vujasinović[2], Zoran Stević[2] and Vesna Grekulović[2]
[1]*IHIS, Science and Technology Park "Zemun", Belgrade,*
[2]*University of Belgrade, Technical faculty in Bor, Bor*
Serbia

1. Introduction

Growing demand for energy sources that are cleaner and more economical led to intensive research on alternative energy sources such as rechargeable lithium batteries and solar cells, especially those in which the sun's energy is transformed into electrical or chemical. From the ecology point of view, using solar energy does not disturb the thermal balance of our planet, either being directly converted into heat in solar collectors or being transformed into electrical or chemical energy in solar cells and batteries. On the other hand, every kilowatt hour of energy thus obtained replaces a certain amount of fossil or nuclear fuel and mitigates any associated adverse effects known. Solar energy is considered to be one of the most sustainable energy resources for future energy supplies.

To make the energy of solar radiation converted into electricity, materials that behave as semiconductors are used. Semiconductive properties of copper sulfides and copper oxides, as well as compounds of chalcopyrite type have been extensively investigated (Rajčić-Vujasinović et al., 1994, 1999). One of the important design criteria in the development of an effective solar cell is to maximize its efficiency in converting sunlight to electricity. A photovoltaic cell consists of a light absorbing material which is connected to an external circuit in an asymmetric manner. Charge carriers are generated in the material by the absorption of photons of light, and are driven towards one or other of the contacts by the built-in spatial asymmetry. This light driven charge separation establishes a photo voltage at open circuit, and generates a photocurrent at short circuit. When a load is connected to the external circuit, the cell produces both current and voltage and can do electrical work.

Solar technology, thanks to its advantages regarding the preservation of the planetary energy balance, is getting into an increasing number of application areas. So, for example, Rizzo et al. (2010) as well as Stević & Rajčić-Vujasinović (in Press) describe hybrid solar vehicles, while Vieira & Mota (2010) show a rechargeable battery with photovoltaic panels.

The high cost of silicon solar cells forces the development of new photovoltaic devices utilizing cheap and non-toxic materials prepared by energy-efficient processes. The Cu–O system has two stable oxides: cupric oxide (CuO) and cuprous oxide (Cu_2O). These two oxides are semiconductors with band gaps in the visible or near infrared regions. Copper and copper oxide (metal-semiconductor) are one of the first photovoltaic cells invented (Pollack and Trivich, 1975). Cuprous oxide (Cu_2O) is an attractive semiconductor material that could be

used as anode material in thin film lithium batteries (Lee et al, 2004) as well as in solar cells (Akimoto et al., 2006; Musa et al., 1998; Nozik et al., 1978; Tang et al., 2005). Its semiconductor properties and the emergence of photovoltaic effect were discovered by Edmond Becquerel 1839th[1] experimenting in the laboratory of his father, Antoine-César Becquerel.

Cu_2O is a p-type semiconductor with a direct band gap of 2.0–2.2 eV (Grozdanov, 1994) which is suitable for photovoltaic conversion. Tang et al. (2005) found that the band gap of nanocrystalline Cu_2O thin films is 2.06 eV, while Siripala et al. (1996) found that the deposited cuprous oxide exhibits a direct band gap of 2.0 eV, and shows an n-type behavior when used in a liquid/solid junction. Han & Tao (2009) found that n-type Cu_2O deposited in a solution containing 0.01 M copper acetate and 0.1 M sodium acetate exhibits higher resistivity than p-type Cu_2O deposited at pH 13 by two orders of magnitude. Other authors, like Singh et al. (2008) estimated the band gap of prepared Cu_2O nanothreads and nanowires to be 2.61 and 2.69 eV, which is larger than the direct band gap (2.17 eV) of bulk Cu_2O (Wong & Searson, 1999). The higher band gap can be attributed to size effect of the present nanostructures. Thus the increase of band gap as compared to the bulk can be understood on the basis of quantum size effect which arises due to very small size of nanothreads and nanowires in one-dimension.

Cuprous oxide attracts the most interest because of its high optical absorption coefficient in the visible range and its reasonably good electrical properties (Musa et al., 1998). Its advantages are, in fact, relatively low cost and low toxicity. Except for a thin film that can be electrochemically formed on different substrates (steel, TiO_2), cuprous oxide can be obtained in the form of nano particles with all the benefits offered by nano-technology (Daltin et al., 2005; Zhou & Switzer, 1998). Nanomaterials exhibit novel physical properties and play an important role in fundamental research.

The unit cell of Cu_2O with a lattice constant of 0.427 nm is composed of a body centered cubic lattice of oxygen ions, in which each oxygen ion occupies the center of a tetrahedron formed by copper ions (Xue & Dieckmann, 1990). The Cu atoms arrange in a fcc sublattice, the O atoms in a bcc sublattice. The unit cell contains 4 Cu atoms and 2 O atoms. One sublattice is shifted by a quarter of the body diagonal. The space group is Pn3m, which includes the point group with full octahedral symmetry. This means particularly that parity is a good quantum number. Figure 1 shows the crystal lattice of Cu_2O. Molar mass of Cu_2O is 143.09 g/mol, density is 6.0 g/cm^3 and its melting and boiling points are 1235°C and 1800°C, respectively. Also, it is soluble in acid and insoluble in water.

Cuprous oxide (copper (I) oxide Cu_2O) is found in nature as cuprite and formed on copper by heat. It is a red color crystal used as a pigment and fungicide. Rectifier diodes based on this material have been used industrially as early as 1924, long before silicon became the standard. Cupric oxide (copper(II) oxide CuO) is a black crystal. It is used in making fibers and ceramics, gas analyses and for Welding fluxes. The biological property of copper compounds takes important role as fungicides in agriculture and biocides in antifouling paints for ships and wood preservations as an alternative of Tributyltin compounds.

In solar cells, Cu_2O has not been commonly used because of its low energy conversion efficiency which results from the fact that the light generated charge carriers in micron-sized Cu_2O grains are not efficiently transferred to the surface and lost due to recombination. For randomly generated charge carriers, the average diffusion time from the bulk to the surface is given by:

[1] http://pvcdrom.pveducation.org/MANUFACT/FIRST.HTM

$$\tau = r^2 / \pi^2 D \quad (1)$$

where r is the grain radius and D is the diffusion coefficient of the carrier (Rothenberger et al., 1985, as cited in Tang et al., 2005). If the grains radius is reduced from micrometer dimensions to nanometer dimensions, the opportunities for recombination can be dramatically reduced. The preparation of nano crystalline Cu_2O thin films is a key to improving the performance of solar application devices. Nanotechnologies in this area, therefore, given their full meaning. In the last decade the scientific literature, abounds with works again showing progress in research related to obtaining the cuprous oxide.

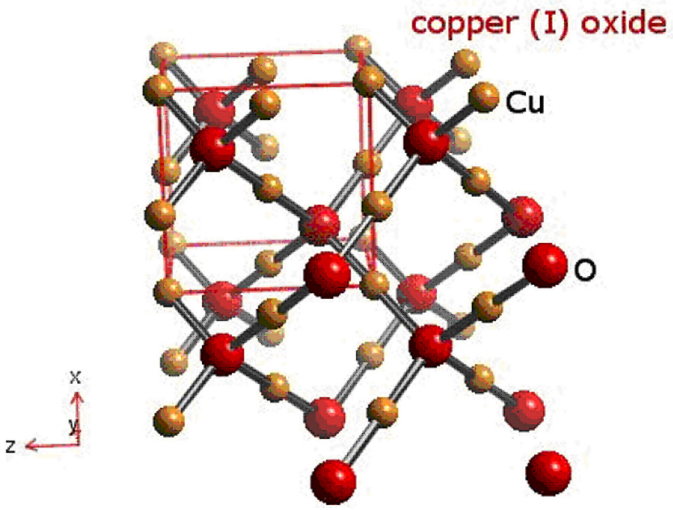

(http://www.webelements.com/compounds/copper/dicopper_oxide.html)

Fig. 1. Crystal structure of Cu_2O

This chapter presents an overview of recent literature concerning cuprous oxide synthesis and application as an active material in solar cells, as well as our own results of synthesis and investigations of Cu_2O thin films using electrochemical techniques.

2. Methodologies used for the synthesis of cuprous oxide

The optical and electrical properties of absorber materials in solar cells are key parameters which determine the performance of solar cells. Hence, it is necessary to tune these properties properly for high efficient device. Electrical properties of Cu_2O, such as carrier mobility, carrier concentration, and resistivity are very dependent on preparation methods.
Cuprous oxide thin films have been prepared by various techniques like thermal oxidation (Jayatissa et al., 2009; Musa et al., 1998; Sears & Fortin, 1984), chemical vapor deposition (Kobayashi et al. 2007; Maruyama, 1998; Medina-Valtierra et al., 2002; Ottosson et al., 1995; Ottosson & Carlsson, 1996), anodic oxidation (Fortin & Masson, 1982; Sears and Fortin, 1984; Singh et al., 2008), reactive sputtering (Ghosh et al., 2000), electrodeposition (Briskman, 1992; Daltin et al., 2005; Georgieva & Ristov, 2002; Golden et al., 1996; Liu et al., 2005; Mizuno et al., 2005; Rakhshani et al., 1987, Rakhshani & Varghese, 1987; Santra et al., 1999; Siripala et

al., 1996; Tang et al., 2005; Wang et al., 2007; Wijesundera et al., 2006), plasma evaporation (Santra et al., 1992), sol–gel-like dip technique (Armelao et al., 2003; Ray, 2001) etc. Each of these methods has its own advantages and disadvantages. In most of these studies, a mixture of phases of Cu, CuO and Cu_2O is generally obtained and this is one of the nagging problems for non-utilizing Cu_2O as a semiconductor (Papadimitropoulos et al., 2005). Pure Cu_2O films can be obtained by oxidation of copper layers within a range of temperatures followed by annealing for a small period of time.
Results obtained using different methods, especially thermal oxidation and chemical vapor evaporation for synthesis of cuprous oxide thin films, are presented in next sections, with special emphasis on the electrochemical synthesis of cuprous oxide.

2.1 Thermal oxidation

Polycrystalline cuprous oxide can be formed by thermal oxidation of copper under suitable conditions (Rai, 1988). The procedure involves the oxidation of high purity copper at an elevated temperature (1000–1500^{0}C) for times ranging from few hours to few minutes depending on the thickness of the starting material (for total oxidation) and the desired thickness of Cu_2O (for partial oxidation). Process is followed by high-temperature annealing for hours or even days.
Sears & Fortin (1984) synthesized cuprous oxide films on copper substrates to a thickness of a few micrometers, using both thermal and anodic oxidation techniques. The measurements carried out on the anodic oxide layers indicate an unwanted but inevitable incorporation of other compounds into the Cu_2O. They found that the photovoltaic properties of the resulting Cu_2O/Cu backwall cells depend critically on the copper surface preparation, as well as on the specific conditions of oxidation. Backwall cells of the thermal variety with thicknesses down to 3 μm do not quite yet approach the performance of the best Cu_2O front cells, but are much simpler to grow. Serious difficulties with shorting paths in the case of thermally grown oxide and with the purity of the Cu_2O in the anodic case will have to be solved before a solar cell with an oxide layer thickness in the 1.5 to 2 μm range can be produced.
Musa et al. (1998) produced the cuprous oxide by thermal oxidation and studied its physical and electrical properties. The oxidation was carried out at atmospheric pressure in a high-temperature tube furnace. During this process the copper foils were heated in the range of 200 to 1050°C. Cu_2O has been identified to be stable at limited ranges of temperature and oxygen pressure. It has also been indicated that during oxidation, Cu_2O is formed first, and after a sufficiently long oxidation time CuO is formed (Roos & Karlson, 1983, as cited Musa et al., 1998). It has been suggested that the probable reactions that could account for the presence of CuO in layers oxidised below 1000 °C are:

$$2Cu_2O + O_2 \rightarrow 4CuO \quad (2)$$

$$Cu_2O \rightarrow CuO + Cu \quad (3)$$

The unwanted CuO can be removed using an etching solution consisting of FeCl, HCl, and 8 M HNO_3 containing NaCl. The results of the oxidation process as deduced from both XRD and SEM studies indicate that the oxide layers resulting from oxidation at 1050^{0}C consist entirely of Cu_2O. Those grown below 1040^{0}C gave mixed oxides of Cu_2O and CuO. It was observed that in general the lower the temperature of oxidation, the lower the amount of Cu_2O was present in the oxide. Thermodynamic considerations indicate that the limiting temperature for the

elimination of CuO from the oxide layer was found to be 1040^0C. For thermal oxidation carried out below 1040^0C, Cu_2O is formed first and it is then gradually oxidised to CuO depending on the temperature and time of reaction. Pure unannealed Cu_2O layers grown thermally in air are observed to exhibit higher resistivity and low hole mobility. A significant reduction in resistivity and an increase in mobility values were obtained by oxidizing the samples in the presence of HCl vapour, followed by annealing at 500^0C. Cu_2O layers grown in air without the annealing process gave resistivities in the range $2x10^3$ – $3x10^3$ Ωcm. A substantial reduction in the resistivity of the samples was achieved by doping with chlorine during growth and annealing. An average mobility of 75 $cm^2\ V^{-1}\ s^{-1}$ at room temperature was obtained for eight unannealed Cu_2O samples. This average value increased to 130 $cm^2\ V^{-1}\ s^{-1}$ after doping the samples with chlorine and annealing. The SEM studies indicate that the annealing process results in dense polycrystalline Cu_2O layers of increased grain sizes which are appropriate for solar-cell fabrication. Figure 2 presents the micrograph of the surface morphology of a copper foil partially oxidised at 970^0C for 2 min. The sample was neither annealed nor etched. The surface shows the black CuO coat formed on the violet-red Cu_2O after the oxidation process. The surface morphology is porous and amorphous in nature. The structure formed by this oxidation process is of the form $CuO/Cu_2O/Cu/Cu_2O/CuO$.

Jayatissa et al. (2009) prepared cuprous oxide (Cu_2O) and cupric oxide (CuO) thin films by thermal oxidation of copper films coated on indium tin oxide (ITO) glass and non-alkaline glass substrates. The formation of Cu_2O and CuO was controlled by varying oxidation conditions such as oxygen partial pressure, heat treatment temperature and oxidation time. Authors used X-ray diffraction, atomic force microscopy and optical spectroscopy to determinate the microstructure, crystal direction, and optical properties of copper oxide films. The experimental results suggest that the thermal oxidation method can be employed to fabricate device quality Cu_2O and CuO films that are up to 200–300 nm thick.

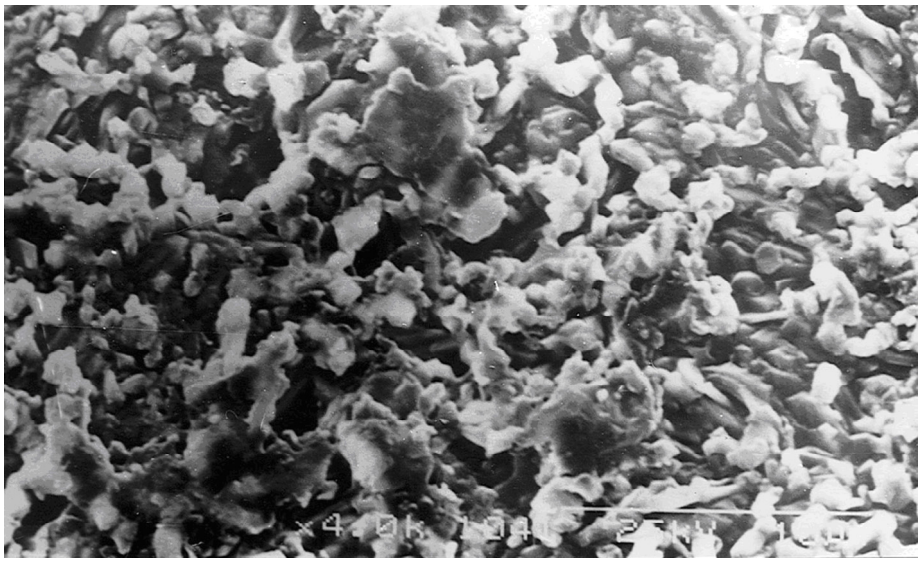

Fig. 2. SEM micrograph of unetched and unannealed sample oxidised at 970^0C for 2 min showing CuO coating (Musa et al., 1998)

2.2 Chemical vapor deposition

Chemical vapor deposition is a chemical process used to produce high-purity, high-performance solid materials. The films may be epitaxial, polycrystalline or amorphous depending on the materials and reactor conditions. Chemical vapor deposition has become the major method of film deposition for the semiconductor industry due to its high throughput, high purity, and low cost of operation. Several important factors affect the quality of the film deposited by chemical vapor deposition such as the deposition temperature, the properties of the precursor, the process pressure, the substrate, the carrier gas flow rate and the chamber geometry.

Maruyama (1998) prepared polycrystalline copper oxide thin films at a reaction temperature above 280^0C by an atmospheric-pressure chemical vapor deposition method. Copper oxide films were grown by thermal decomposition of the source material with simultaneous reaction with oxygen. At a reaction temperature above 280^0C, polycrystalline copper oxide films were formed on the borosilicate glass substrates. Two kinds of films, i.e., Cu_2O and CuO, were obtained by adjusting the oxygen partial pressure. Also, there are large differences in color and surface morphology between the CuO and Cu_2O films obtained. Author found that the surface morphology and the color of CuO film change with reaction temperature. The CuO film prepared at 300^0C is real black, and the film prepared at 500^0C is grayish black.

Medina-Valtierra et al. (2002) coated fiber glass with copper oxides, particularly in the form of $6CuO•Cu_2O$ by chemical vapor deposition method. The authors' work is based on design of an experimental procedure for obtaining different copper phases on commercial fiberglass. Films composed of copper oxides were deposited over fiberglass by sublimation and transportation of $(acac)_2Cu(II)$ with a O_2 flow (oxidizing agent), resulting in the decomposition of the copper precursor, deposition of Cu^0 and Cu^0 oxidation on the fiberglass over a short range of deposition temperatures. The copper oxide films on the fiberglass were examined using several techniques such as X-ray diffraction (XRD), visible spectrophotometry, scanning electronic microscopy (SEM) and atomic force microscopy (AFM). The films formed on fiberglass showed three different colors: light brown, dark brown and gray when Cu_2O, $6CuO•Cu_2O$ or CuO, respectively, were present. At a temperature of 320°C only cuprous oxide is formed but at a higher temperature of about 340°C cupric oxide is formed. At a temperature of 325°C $6CuO\text{-}Cu_2O$ is formed. The decomposition of precursor results in the formation of a zero valent copper which upon oxidation at different temperature gives different oxides.

Ottosson et al. (1995) deposited thin films of Cu_2O onto MgO (100) substrates by chemical vapour deposition from copper iodide (CuI) and dinitrogen oxide (N_2O) at two deposition temperatures, 650°C and 700°C. They found that the pre-treatment of the substrate as well as the deposition temperature had a strong influence on the orientation of the nuclei and the film. For films deposited at 650°C several epitaxial orientations were observed: (100), (110) and (111). The Cu_2O(100) was found to grow on a defect MgO(100) surface. When the substrates were annealed at 800°C in N_2O for 1 h, the defects in the surface disappeared and only the (110) orientation was developed during the deposition. The films deposited at 700°C (without annealing of the substrates) displayed only the (110) orientation.

Markworth et al. (2001) prepared cuprous oxide (Cu_2O) films on single-crystal MgO(110) substrates by a chemical vapor deposition process in the temperature range 690–790°C. Cu_2O (a=0.4270 nm) and MgO (a=0.4213 nm) have cubic crystal structures, and the lattice mismatch between them is 1.4%. Due to good lattice match, chemical stability, and low cost,

MgO single crystals are particularly effective substrates for the growth of Cu_2O thin films. Authors found that the Cu_2O films grow by an island-formation mechanism on MgO substrate. Films grown at 690°C uniformly coat the substrate except for micropores between grains. However, at a growth temperature of 790°C, an isolated, three-dimensional island morphology develops.
Kobayashi et al. (2007) investigated the high-quality Cu_2O thin films grown epitaxially on MgO (110) substrate by halide chemical vapor deposition under atmospheric pressure. CuI in a source boat was evaporated at a temperature of 883 K, and supplied to the growth zone of the reactor by N_2 carrier gas, and O_2 was also supplied there by the same carrier gas. Partial pressure of CuI and O_2 were adjusted independently to 1.24×10^{-2} and 1.25×10^{3} Pa. They found that the optical band gap energy of Cu_2O film calculated from absorption spectra is 2.38 eV. The reaction of CuI and O_2 under atmospheric pressure yields high-quality Cu_2O films.

2.3 Other methods

Several novel methods for the synthesis of cuprous oxide (i.e. reactive sputtering, sol-gel technique, plasma evaporation,) and some results obtained using these techniques are presented in this part. For example, Santra et al. (1992) deposited thin films of cuprous oxide on the substrates by evaporating metallic copper through a plasma discharge in the presence of a constant oxygen pressure. Authors found two oxide phases before and after annealing treatment of films. Before annealing treatment, cuprous oxide was identified and after annealing in a nitrogen atmosphere, cuprous oxide changes to cupric oxide. The results of optical absorption measurement show that the band gap energies for Cu_2O and CuO are 2.1 eV and 1.85 eV, respectively. Thin films prepared in the absence of a reactive gas and plasma were also deposited on glass substrates and in these films the presence of metallic copper was identified.
Ghosh et al. (2000) deposited cuprous oxide and cupric oxide by RF reactive sputtering at different substrate temperatures, namely, at 30, 150 and 300^{0}C. They used atomic force microscopy for examination of the properties of the prepared oxides films related to surface morphology. It was found for the film deposited at 30^{0}C, that, 8-10 small grains of size ~40 nm diameter agglomerate together and make a big grain of size ~120 nm. At the temperature of 150^{0}C the grain size becomes 160 nm. The grain size decreases to 90 nm at 300^{0}C. From thickness and deposition time, the deposition rates of the films are found to be 8, 11.5 and 14.0 nm/min for substrate temperature corresponding to 30, 150 and 300^{0}C, respectively. Optical band gap of the films deposited at 30, 150 and 300^{0}C are 1.75, 2.04 and 1.47 eV, respectively. Different phases of copper oxides are found at different temperatures of deposition. CuO phase is obtained in the films prepared at a substrate temperature of 300^{0}C.
Sol gel-like dip technique is a very simple and low-cost method, which requires no sophisticated specialized setup. For example, Armelao et al. (2003) used a sol-gel method to synthesize nanophasic copper oxide thin films on silica slides. They used copper acetate monohydrate as a precursor in ethanol as a solvent. Authors observed formation of CuO crystallites in the samples annealed under inert atmosphere (N_2) up to 3 h. A prolonged treatment (5 h) in the same environment resulted in the complete disappearance of tenorite and in the formation of a pure cuprite crystalline phase. Also, under reducing conditions, the formation of CuO, Cu_2O and Cu was progressively observed, leading to a mixture of Cu(II) and Cu(I) oxides and metallic copper after treatment at 900^{0}C for 5 h.

All the obtained films have nanostructure with an average crystallite size lower than 20 nm.
Nair et al. (1999) deposited cuprous oxide thin films on glass substrate using chemical technique. The glass slides were dipped first in a 1 M aqueous solution of NaOH at the temperature range 50-90°C for 20 s and then in a 1 M aqueous solution of copper complex. X-ray diffraction patterns showed that the films, as prepared, are of cuprite structure with composition Cu_2O. Annealing the films in air at 350^0C converts these films to CuO. This conversion is accompanied by a shift in the optical band gap from 2.1 eV (direct) to 1.75 eV (direct). The films show p-type conductivity, ~ 5 x 10^{-4} Ω^{-1} cm^{-1} for a film of thickness 0.15 μm.

3. Electrochemical synthesis

3.1 Electrodeposition

Synthesis of Cu_2O nanostructures by the methods described in the previous part demands complex process control, high reaction temperatures, long reaction times, expensive chemicals and specific method for specific nanostructures. A request for obtaining nanometer particles, cause complete change of technology in which Cu_2O is formed on the cathode by reduction of Cu^{2+} ions from the organic electrolyte. The possible reactions during the cathodic reduction of copper (II) lactate solution are:

$$2Cu^{2+} + H_2O + 2e^{-} = Cu_2O + 2H^{+} \quad (4)$$

$$Cu^{2+} + 2e^{-} = Cu \quad (5)$$

$$Cu_2O + 2H^{+} + 2e^{-} = 2Cu + H_2O \quad (6)$$

The electrodeposition techniques are particularly well suited for the deposition of single elements but it is also possible to carry out simultaneous depositions of several elements and syntheses of well-defined alternating layers of metals and oxides with thicknesses down to a few nm. So, electrodeposition is a suitable method for the synthesis of semiconductor thin films such as oxides. This method provides a simple way to deposit thin Cu(I) oxide films onto large-area conducting substrates (Lincot, 2005). Thus, the study of the growth kinetics of these films is of considerable importance. In this section we present some results of electrochemical deposition of cuprous oxide obtained by various authors.
Rakhshani et al. (1987) cathodically electrodeposited Cu(I) oxide film onto conductive substrates from a solution of cupric sulphate, sodium hydroxide and lactic acid. Films of Cu_2O were deposited in three different modes, namely the potentiostatic mode, the mode with constant WE potential with respect to the CE and the galvanostatic mode. The composition of the films deposited under all conditions was Cu_2O with no traces of CuO. The optical band gap for electrodeposited Cu_2O films was 1.95 eV. Deposition temperature played an important role in the size of deposited grains. Films were photoconductive with high dark resistivities. Also, Rakhshani & Varghese (1987) electrodeposited cuprous oxide thin films galvanostatically on 0.05 mm thick stainless steel substrates at a temperature of 60^0C. The deposition solution with pH 9 consisted of lactic acid (2.7 M), anhydrous cupric sulphate (0.4 M), and sodium hydroxide (4 M). Authors found that all the films deposited at 60 °C consisted only of Cu_2O grains a few

μm in size and preferentially oriented along (100) planes parallel to the substrate surface. A band gap was found and it was 1.90-1.95 eV.

Mukhopadhyay et al. (1992) deposited Cu_2O films by galvanostatic method on copper substrates. An alkaline cupric sulphate (about 0.3 M) bath containing NaOH (about 3.2 M) and lactic acid (about 2.3 M) was used as the electrolyte at pH 9. The bath temperatures were 40, 50 and 60°C. XRD analysis indicated a preferred (200) orientation of the Cu_2O deposited film. The deposition kinetics was found to be independent of deposition temperature and linear in the thickness range studied (up to about 20 μm). The electrical conductivity of Cu_2O films was found to vary exponentially with temperature in the 145-300^{0}C range with associated activation energy of 0.79 eV.

Golden et al. (1996) found that the reflectance and transmittance of the electrodeposited films of cuprous oxide give a direct band gap of 2.1 eV. Namely, authors used electrodeposition method for obtaining the films of cuprous oxide by reduction of copper (II) lactate in alkaline solution (0.4 M cupric sulfate and 3 M lactic acid). Films were deposited onto either stainless steel or indium tin oxide (ITO) substrates. Deposition temperatures ranged from 25 to 65 °C. They found that the cathodic deposition current was limited by a Schottky-like barrier that forms between the Cu_2O and the deposition solution. A barrier height of 0.6 eV was determined from the exponential dependence of the deposition current on the solution temperature. At a solution pH 9 the orientation of the film is [100], while at a solution pH 12 the orientation changes to [111]. The degree of [111] texture for the films grown at pH 12 increased with applied current density.

Siripala et al. (1996) deposited cuprous oxide films on indium tin oxide (ITO) coated glass substrates in a solution of 0.1 M sodium acetate and 1.6 x 10^{-2} M cupric acetate and the effect of annealing in air has been studied too. Electrodeposition was carried out for 1.5 h in order to obtain films of thicknesses in the order of 1 μm. Authors concluded that the electrodeposited Cu_2O films are polycrystalline with grain sizes in the order of 1-2 μm and the bulk crystal structure is simple cubic. They concluded that there is no apparent change in the crystal structure when heat treated in air at or below 300°C. Annealing in air changes the morphology of the surface creating a porous nature with ring shaped structures on the surface. Annealing above 300°C causes decomposition of the yellow-orange colour Cu_2O film into a darker film containing black CuO and its complexes with water.

Zhou & Switzer (1998) deposited Cu_2O films on stainless steel disks by the cathodic reduction of copper (II) lactate solution (0.4 M cupric sulfate and 3 M lactic acid). The pH of the bath was between 7 and 12 and the bath temperature was 60°C. Authors concluded that the preferred orientation and crystal shape of Cu_2O films change with the bath pH and the applied potential. They obtained pure Cu_2O films at bath pH 9 with applied potential between -0.35 and -0.55 (SCE) or at bath pH 12.

Mahalingam et al. (2000) deposited cuprous oxide thin films on copper and tin-oxide-coated glass substrates by cathodic reduction of alkaline cupric lactate solution (0.45 M $CuSO_4$, 3.25 M lactic acid and 0.1 M NaOH). The deposition was carried out in the temperature range of 60-80^{0}C at pH 9. Galvanostatic deposition on tin-oxide-coated glass and copper substrates yields reddish-grey Cu_2O films. All the films deposited are found to be polycrystalline having grains in the range of 0.01 - 0.04 μm. The deposition kinetics is found to be linear and independent of the deposition temperature. From the optical absorption measurements, authors found that the deposit of cuprous oxide films has a refractive index of 2.73, direct band gap of 1.99 eV, and extinction coefficient of 0.195. After deposition on temperature of 70^{0}C, cuprous oxide films were annealed in air for 30 min at different temperatures (150, 250

and 350^{0}C) to obtain their room temperature resistivity. It showed a decrease in resistivity of Cu_2O film of the order of 10^7 Ωcm to 10^4 Ωcm. The explanation of such behavior may be due to increase in hole conduction.

Georgieva & Ristov (2002) deposited the cuprous oxide (Cu_2O) films using a galvanostatic method from an alkaline $CuSO_4$ bath containing lactic acid and sodium hydroxide (64 g/l anhydrous cupric sulphate ($CuSO_4$), 200 ml/l lactic acid ($C_3H_6O_3$) and about 125 g/l sodium hydroxide (NaOH)). The electrodeposition temperature was 60^{0}C. Authors obtained polycrystalline films of 4–6 μm in thickness with optical band gap of 2.38 eV.

Daltin et al. (2005) applied potentiostatic deposition method to obtain cuprous oxide nanowires in polycarbonate membrane by cathodic reduction of alkaline cupric lactate solution (0.45 M Cu(II) and 3.25 M lactate). Authors found that the optimum electrochemical parameters for the deposition of nanowires are: pH 9.1, temperature 70^{0}C, and applied potential -0.9 V (SSE). The morphology of the nanowires was analyzed by SEM. The obtained nanowires had uniform diameters of about 100 nm and lengths up to 16 μm. Scanning electron micrograph of electrodeposited Cu_2O nanowires are presented in Figure 3.

Liu et al. (2005) investigated the electrochemical deposition of Cu_2O films onto three different substrates (indium tin oxide film coated glass, n-Si wafer with (001) orientation and Au film evaporated onto Si substrate). For the film grown on ITO, electrical current increases gradually during deposition, while for the films growth on both Si and Au substrates, the monitored current decreases monotonically. Authors considered that the continuous decrease in current reflects different deposition mechanisms. In the case of Si substrate, the decrease of the current may be the result of the formation of an amorphous SiO_2 layer on the Si surface, which limits the current. For the Au surface, the decrease in measured current is due to the resistivity increase as a result of Cu_2O film formation. Cu_2O crystals with microsized pyramidal shape were grown on ITO substrate. Nanosized and pyramidal shaped Cu_2O particles were formed on Si substrate and the film grown on Au substrate shows a (100) orientation with much better crystallinity.

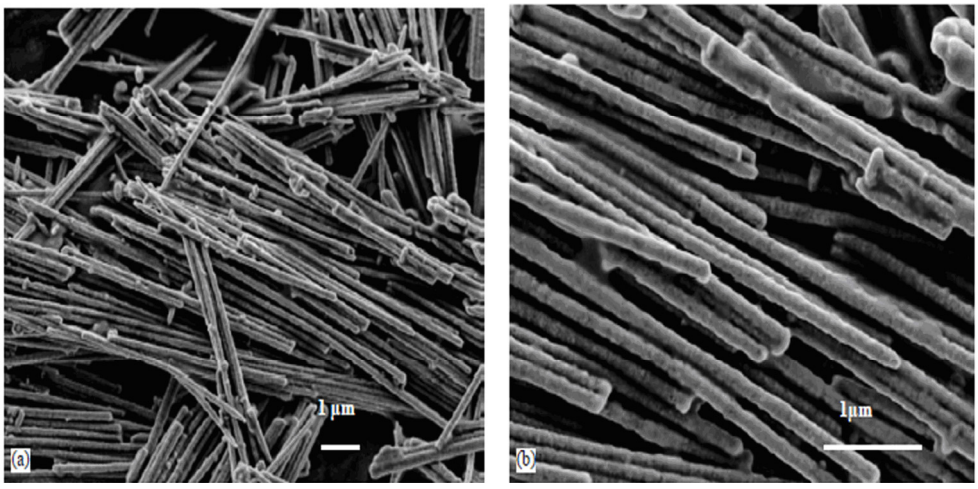

Fig. 3. (a) Scanning electron micrograph of electrodeposited Cu_2O nanowires. Bath temperature 70^{0}C, pH 9.1, E -1.69 V/$_{SSE}$. (b) Enlarged (a) (Daltin et al., 2005)

Tang et al. (2005) investigated the electrochemical deposition of nanocrystalline Cu_2O thin films on TiO_2 films coated on transparent conducting optically (TCO) glass substrates by cathodic reduction of cupric acetate (0.1 M sodium acetate and 0.02 M cupric acetate). Authors concluded that the pH and bath temperature strongly affect the composition and microstructure of the Cu_2O thin films. The effect of bath pH on electrodeposition of Cu_2O thin film was investigated by selecting a bath temperature of 30^0C and an applied potential of -245 mV (SCE). Authors found that the films deposited at pH 4 are mostly metallic Cu and only little Cu_2O. In the region of pH 4 to pH 5.5, the deposited films are a composite of Cu and Cu_2O, while the films deposited at pH between 5.5 and 6 are pure Cu_2O. Pure Cu_2O deposited at bath temperature between 0 and 30^0C produced spherically shaped grains with 40~50 nm in diameter. The bath temperature must be controlled in the range of 0-30^0C to obtain nanocrystalline Cu_2O thin film. At a temperature of 45°C, a highly branched dendrite formed, and the grain size increased to 200–500 nm. At the temperature above 60°C, a ring-shaped structure with a porous surface was observed. Optical absorption measurements indicate that annealing at 200^0C can improve the transmittance of the nanocrystalline Cu_2O thin films. Figure 4 shows SEM photographs of Cu_2O films deposited at various bath temperatures.

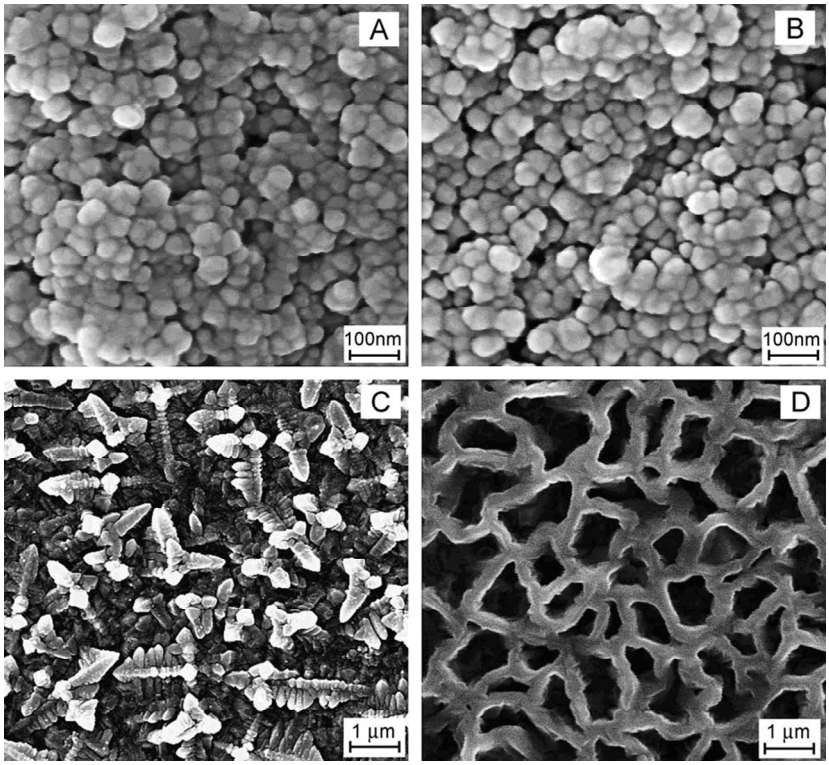

Fig. 4. SEM photographs of Cu_2O films deposited at various bath temperatures: (A) 0^0C, (B) 30^0C, (C) 45^0C, and (D) 60^0C (Tang et al., 2005)

Wijesundera et al. (2006) investigated the potentiostatic electrodeposition of cuprous oxide and copper thin films. Electrodeposition was carried out in an aqueous solution containing

sodium acetate and cupric acetate. The results of their investigation show that the single phase polycrystalline Cu_2O can be deposited from 0 to -300 mV (SCE). Also, co-deposition of Cu and Cu_2O starts at - 400 mV (SCE). At the deposition potential from -700 mV (SCE) a single phase Cu thin films are produced. Single phase polycrystalline Cu_2O thin films with cubic grains of 1–2 μm can be possible at the deposition potential around -200 mV (SCE).
Wang et al. (2007) cathodically electrodeposited cuprous oxide films from 0.4 M copper sulfate bath containing 3 M lactic acid. The bath pH was carefully adjusted between 7.5 and 12.0 by controlled addition of 4 M NaOH. The electrodeposition was done on Sn-doped indium oxide substrates. The influence of electrodeposition bath pH on grain orientation and crystallite shape was examinated. Authors found that three orientations, namely, (100), (110), and (111) dominate as the bath pH is increased from ~ 7.5 to ~ 12.
Recently, Hu et al. (2009) electrodeposited Cu_2O thin films onto an indium tin oxide (ITO) coated glass by a two-electrode system with acid and alkaline electrolytes under different values of direct current densities. Copper foils were used as the anodes, and the current density between the anode and cathode varied between 1 mA cm^{-2} and 5 mA cm^{-2}. It was obtained that the microstructure of Cu_2O thin films produced in the acid electrolyte changes from a ring shape to a cubic shape with the increase of direct current densities. The microstructure of Cu_2O thin films produced in the alkaline electrolyte has a typical pyramid shape. The electrocrystallization mechanisms are considered to be related to the nucleation rate, cluster growth, and crystal growth. To investigate the initial stage of nucleation and cluster growth, different current densities with the same deposition time were applied. Figure 5 shows that a relatively large cluster size and a relatively small number of nucleation sites were obtained under a current density of 1 $mAcm^{-2}$. At a high current density of 5 $mAcm^{-2}$, more nucleation sites and a small cluster size were obtained.

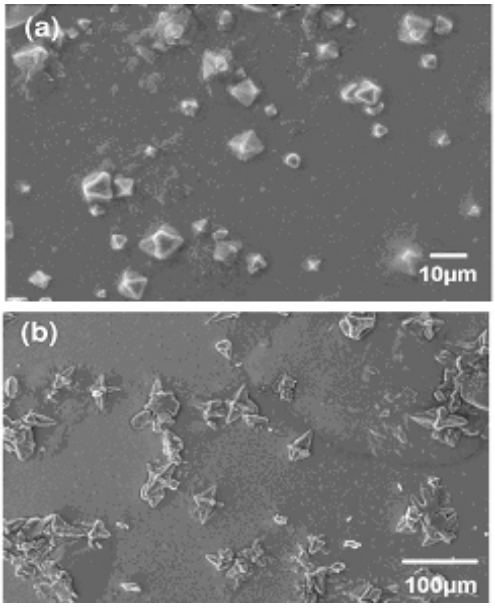

Fig. 5. The Cu_2O films synthesized under different current densities with the same deposition time (Hu et al., 2009)

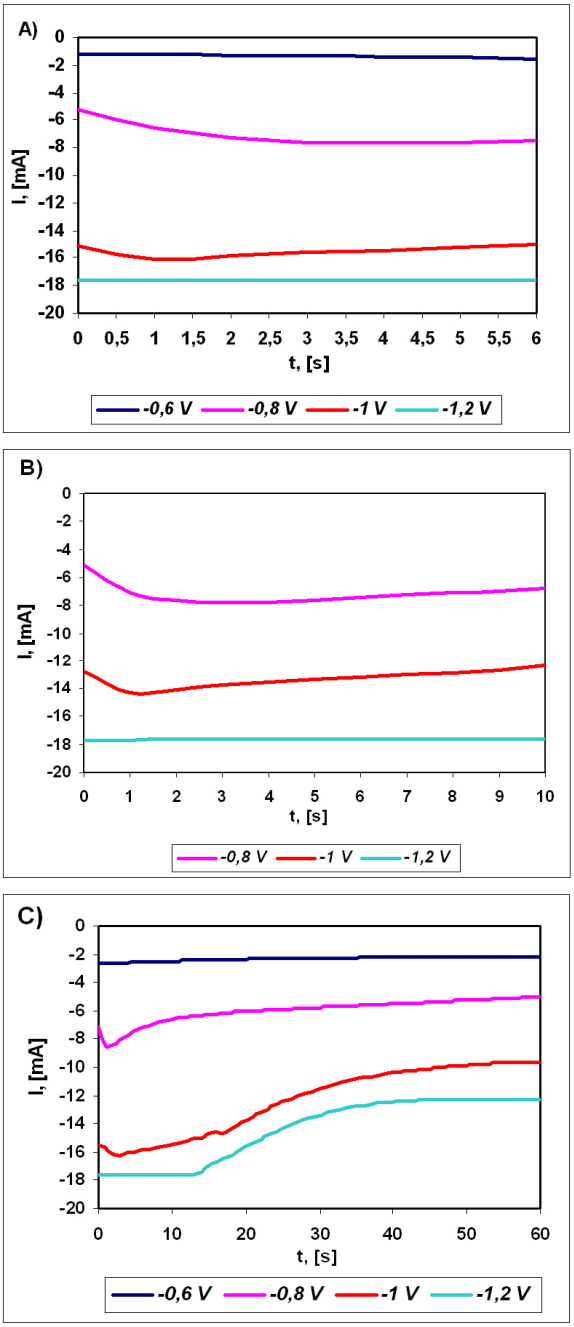

Fig. 6. Current density vs. time curves for electrodeposition of Cu_2O thin film on titanium electrode (electrodeposition time: (A) 6 s, (B) 10 s and (C) 60 s; t = 25 ^oC, pH 9.22)

Bugarinović et al. (2009) investigated the electrochemical deposition of thin films of cuprous oxide on three different substrates (stainless steel, platinum and copper). All experiments of Cu_2O thin films deposition were performed at room temperature. Using experimental technique described elsewhere (Stević & Rajčić-Vujasinović, 2006; Stević & et al., 2009), electrodeposition was carried out in in a copper lactate solution as an organic electrolyte (0.4 M copper sulfate and 3 M lactic acid, pH 7-10 is set using NaOH). The conditions are adjusted so that the potentials which arise Cu_2O and CuO are as different as possible. Characterization of obtained coatings was performed by cyclic voltammetry. The results indicate that the composition of the substrate strongly affects electrochemical reactions. Reaction with the highest rate took place on a copper surface, while the lowest rate was obtained on the platinum electrode. The results show that the co-deposit of Cu_2O and Cu was obtained at - 800 mV (SCE) on stainless steel electrode. The same authors investigated the electrodeposition of cuprous oxide thin film on titanium electrode. The obtained results are presented in Figure 6.

Cuprous oxide thin films were deposited at potentials -0.6 V, -0.8 V, -1.0 V and 1.2 V with respect to SCE. All experiments were carried out for a duration of 6 s, 10 s and 1 minute. When the electrodeposition lasted 6 s (Fig. 6A), obtained currents depended on applied potentials. Lowest current of 1mA was obtained at the potential of -0.6 V vs. SCE, while the highest value of 17.9 mA was reached at -1.2 V (SCE). When the electrodeposition time was 10 s (Fig. 6B), curves current vs. time had similar shape as the previous, but when the process duration prolongates to 60 s (Fig. 6C), currents obtained at higher potentials (-1.0 V and -1.2 V vs. SCE) decrease after about 15 s and stabilise again after about 40 s at some lower value (nearly 80% of the previous ones). Maximum theoretical thicknesses of Cu_2O film for every applied potential and all process durations were calculated. The lowest thickness of 7 nm was obtained for 6 s with potential of -0.6 V (SCE). More negative potentials and the increase of time lead to the increase of the film thickness. Theoretical value of the Cu_2O film thickness for the longest time (60 s) and most negative potential (-1.2 V vs. SCE) is about 900 nm.

3.2 Anodic oxidation

In spite of the simple equipment and easy process control, cathodic synthesis demands expensive chemicals as a big dissadventage. On the other hand, anodic oxidation of copper in alkaline solution is one of the standard methodologies for producing cuprous oxide powders used for marine paints and for plants preservation. Those powders are composed of particles of micrometer scale. However, solar sells, for their part, require particles or films of much smaller dimensions in order to achieve higher efficiency. Passive protecting layers formed on copper during anodic oxidation in alkaline solutions are widely investigated and described in electrochemical literature. The structure of those films formed on copper in neutral and alkaline solutions consists mainly of Cu_2O and CuO or $Cu(OH)_2$. Applying in situ electrochemical scanning tunneling microscopy (STM), Kunze et al. (2003) found that in NaOH solutions, a Cu_2O layer is formed at $E > 0.58\text{-}0.059$ pH (V vs. SHE). A $Cu_2O/Cu(OH)_2$ duplex film is found for $E > 0.78\text{-}0.059$ pH (V vs. SHE). In borate buffer solutions, oxidation to Cu_2O leads to non-crystalline grain like structure, while a crystalline and epitaxial Cu_2O layer has been observed in 0.1 M NaOH indicating a strong anion and/or pH effect on the crystallinity of the anodic oxide film.

Stanković et al. (1998; 1999) investigated the effect of different parameters such as temperature, pH and anodic current density on CuO powder preparation. The lowest value

of average crystallite size was obtained at pH 7.5, whereas the highest value was obtained at pH 9.62. They found a strong dependence of grain size and cupric oxide purity on current density. The average srystallite size increased from 45 nm (at a current density of 500 Am^{-2}) to 400 nm (at a current density of 4000 Am^{-2}), other conditions being as follows: pH 7.5, temperature of 353 K and 1.5 M Na_2SO_4.

There have been a number of papers on anodic formation of thin Cu_2O layers (< 1 μm) using alkaline solutions, but some work has been done with slightly acidic solutions. For example, backwall Cu_2O/Cu photovoltaic cells have been prepared by Sears and Fortin (Sears & Fortin, 1983) with the Cu_2O layer being about 1 μm thick. They used and compared two methods of oxidation – thermal and anodic. The condition of the underlying copper surface is expected to influence the resulting parameters of thin solar cells, so they examined the influence of the surface preparation of the starting copper (i.e., polishing technique, thermal annealing). All this experience can help in researching the optimal way of production of nanostructured Cu_2O powders or films.

Recently, Singh et al. (2008) reported synthesis of nanostructured Cu_2O by anodic oxidation of copper through a simple electrolysis process employing plain water as electrolyte. They found two different types of Cu_2O nanostructures. One of them belonged to particles collected from the bottom of the electrolytic cell, while the other type was located on the copper anode itself. The Cu_2O structures collected from the bottom consist of nanowires (length, ~ 600–1000 nm and diameter, ~ 10–25 nm). It may be mentioned that the total length of Cu_2O nanothread and nanowire is comprised of several segments. These were presumably formed due to interaction between nanothreads/nanowires forming the network in which the Cu_2O nanothread/nanowire configuration finally appears. When the electrolysis conditions were maintained at 10 V for 1 h, the representative TEM microstructure revealed the presence of dense Cu_2O nanowire network (length, ~ 1000 nm, diameter, ~ 10–25 nm). The X-ray diffraction pattern obtained from these nanomaterials, could be indexed to a cubic system with lattice parameter, a = 0.4269 ± 0.005 nm. These tally quite well with the lattice parameter of Cu_2O showing that the material formed under electrolysis conditions consists of cubic Cu_2O lattice structure.

In addition to the delaminated nanostructures, investigations of the copper anode, which were subjected to electrolysis runs, revealed the presence of another type of nanostructure of Cu_2O. Authors propose that the higher applied voltage (e.g. 8 V or 10 V) for electrolysis represents the optimum conditions for the formation of nanocubes. These nanocubes reflect the basic cubic unit cell of Cu_2O.

4. Conclusion

Copper oxides, especially cuprous oxide, are of interest because of their applications in solar cell technology. The semiconductor cuprous oxide Cu_2O film has been of considerable interest as a component of solar cells due to its band gap energy and high optical absorption coefficient. Since the properties of cuprous oxide not only depend upon the nature of the material but also upon the way they are synthesized, different methods and results obtained on the synthesis of cuprous oxide by various researchers are discussed in this chapter. The properties of the prepared cuprous oxide films related to surface morphology are presented too. In this chapter, the point is made on electrodeposition of cuprous oxide because electrodeposition techniques are particularly well suited for the deposition of metal oxides with thicknesses down to a few nm. The

results obtained show that the cuprous oxide can be used as a potential active material for solar cells application.

5. Acknowledgment

This work was supported by Ministry of Science and Technological Development of Republic of Serbia, Project No. OI 172 060.

6. References

Akimoto, K.; Ishizuka, S.; Yanagita, M.; Nawa, Y.; Paul, G. K. & Sakurai, T. (2006). Thin Film Deposition of Cu_2O and Application for Solar Cells. *Solar Energy*, Vol. 80, No.6, (June 2006), pp. 715–722, ISSN 0038-092X

Armelao, L.; Barreca, D.; Bertapelle, M.; Bottaro, G.; Sada, C. & Tondello, E. (2003). A Sol–gel Approach to Nanophasic Copper Oxide Thin Films. *Thin Solid Films,* Vol.442, No.1-2, (October 2003), pp. 48–52, ISSN 0040-6090

Briskman, R.N. (1992). A Study of Electrodeposited Cuprous Oxide Photovoltaic Cells. *Solar Energy Materials and Solar Cells*, Vol.27, No.4, (September 1992), pp. 361–368, ISSN 0927-0248

Bugarinović, S.J.; Grekulović, V.J.; Rajčić-Vujasinović, M.M.; Stević, Z.M. & Stanković, Z.D. (2009). Electrochemical Synthesis and Characterization of Copper(I) Oxide (in Serbian). *Hemijska Industrija,* Vol.63, No.3, (May-June 2009), pp. 201-207, ISSN 0367-598X

Daltin, A-L.; Addad, A. & Chopart, J-P. (2005). Potentiostatic Deposition and Characterization of Cuprous Oxide Films and Nanowires. *Journal of Crystal Growth*, Vol.282, No.3-4, (September 2005), pp. 414-420, ISSN 0022-0248

Fortin, E. & Masson, D. (1982). Photovoltaic Effects in Cu_2O-Cu Solar Cells Grown by Anodic Oxidation. *Solid-State Electronics*, Vol.25, No.4, (April 1982), pp. 281-283, ISSN 0038-1101

Georgieva, V. & Ristov, M. (2002). Electrodeposited Cuprous Oxide on Indium Tin Oxide for Solar Applications. *Solar Energy Materials and Solar Cells*, Vol.73, No.1, (May 2002), pp. 67–73, ISSN 0927-0248

Ghosh, S.; Avasthi, D.K.; Shah, P.; Ganesan, V.; Gupta, A.; Sarangi, D.; Bhattacharya, R. & Assmann, W. (2000). Deposition of Thin Films of Different Oxides of Copper by RF Reactive Sputtering and Their Characterization. Vacuum, Vol.57, No.4, (June 2000), pp. 377-385, ISSN 0042-207X

Golden, T.D.; Shumsky, M.G.; Zhou, Y.; Vander Werf, R.A.; Van Leeuwen, R.A. & Switzer, J.A. (1996). Electrochemical Deposition of Copper (I) Oxide Films. *Chemistry of Materials*, Vol. 8, No.10, (October 1996), pp. 2499–2504, ISSN 0897-4756

Grozdanov, I. (1994). Electroless Chemical Deposition Technique for Cu_2O Thin Films. *Materials Letters*, Vol.19, No.5-6, (May 1994), pp. 281–285, ISSN 0167-577X

Han, K. & Tao, M. (2009). Electrochemically Deposited p–n Homojunction Cuprous Oxide Solar Cells. *Solar Energy Materials and Solar Cells,* Vol. 93, No.1, (January 2009), pp.153-157, ISSN 0927-0248

Hu, F.; Chan, K.C. & Yue, T.M. (2009). Morphology and Growth of Electrodeposited Cuprous Oxide under Different Values of Direct Current Density. *Thin Solid Films*, Vol. 518, No.1, (November 2009), pp. 120–125, ISSN 0040-6090

Jayatissa, A.H.; Guo, K. & Jayasuriya, A.C. (2009). Fabrication of Cuprous and Cupric Oxide Thin Films by Heat Treatment. *Applied Surface Science*, Vol.255, No.23, (September 2009), pp. 9474-9479, ISSN 0169-4332

Kobayashi, H.; Nakamura , T. & Takahash, N. (2007). Preparation of Cu_2O Films on MgO (110) Substrate by Means of Halide Chemical Vapor Deposition under Atmospheric Pressure. *Materials Chemistry and Physics*, Vol.106, No.2-3, (December 2007), pp. 292-295, ISSN 0254-0584

Kunze, J.; Maurice, V.; Klein, L.H.; Strehblow, H.H. & Marcus, P. (2003). In Situ STM Study of the Effect of Chlorides on the Initial Stages of Anodic Oxidation of Cu(111) in Alkaline Solutions. *Electrochimica Acta*, Vol.48, No.9, (April 2003), pp.1157-1167, ISSN 0013-4686

Lee, Y.H.; Leu, I.C.; Chang, S.T.; Liao, C.L. & Fung, K.Z. (2004). The Electrochemical Capacities and Cycle Retention of Electrochemically Deposited Cu_2O Thin Film Toward Lithium. *Electrochimica Acta*, Vol.50, No.2-3, (November 2004), pp. 553–559, ISSN 0013-4686

Lincot, D. (2005). Electrodeposition of semiconductors. *Thin Solid Films*, Vol. 487, No.1-2, (September 2005), pp. 40–48, ISSN 0040-6090

Liu, Y.L.; Liu, Y.C.; Mu, R.; Yang, H.; Shao, C.L.; Zhang, J.Y.; Lu, Y.M.; Shen, D.Z. & Fan, X.W. (2005). The Structural and Optical Properties of Cu_2O Films Electrodeposited on Different Substrates. *Semiconductor Science and Technology*, Vol.20, No.1, pp. 44-49, (January 2005), ISSN 0268-1242

Mahalingam, T.; Chitra, J.S.P.; Rajendran, S.; Jayachandran, M. & Chockalingam, M.J. (2000). Galvanostatic deposition and characterization of cuprous oxide thin films. *Journal of Crystal Growth*, Vol. 216, No.1-4, (June 2000), pp. 304–310, ISSN 0022-0248

Markworth, P.R.; Liu, X.; Dai, J.Y.; Fan, W.; Marks, T.J. & Chang, R.P.H. (2001). Coherent Island Formation of Cu_2O Films Grown by Chemical Vapor Deposition on MgO (110). *Journal of Materials Research,* Vol.16, No.8, (August 2001), pp. 2408-2414, ISSN 0884-2914

Maruyama, T. (1998). Copper Oxide Thin Films Prepared from Copper Dipivaloylmethanate and Oxygen by Chemical Vapor Deposition. *Japanese Journal of Applied Physics*, Vol. 37, No.7A, pp. 4099-4102, ISSN 0021-4922

Medina-Valtierra, J.; Ramırez-Ortiz, J.; Arroyo-Rojas, V.M.; Bosch, P. & De los Reyes, J.A. (2002). Chemical Vapor Deposition of $6CuO \bullet Cu_2O$ Films on Fiberglass. *Thin Solid Films*, Vol. 405, No.1-2, (February 2002), pp. 23–28, ISSN 0040-6090

Mizuno, K.; Izaki, M.; Murase, K.; Shinagawa, T.; Chigane, M.; Inaba, M.; Tasaka, A. & Awakura, Y. (2005). Structural and Electrical Characterizations of Electrodeposited p-type Semiconductor Cu_2O Films. *Journal of The Electrochemical Society*, Vol.152, No.4, pp. C179–C182, ISSN 0013-4651

Mukhopadhyay, A.K.; Chakraborty, A.K.; Chatterjee, A.P. & Lahiri, S.K. (1992). Galvanostatic Deposition and Electrical Characterization of Cuprous Oxide Thin Films. *Thin Solid Films*, Vol.209, No.1, (March 1992), pp. 92-96, ISSN 0040-6090

Musa, A.O.; Akomolafe, T. & Carter, M.J. (1998). Production of Cuprous Oxide, a Solar Cell Material, by Thermal Oxidation and a Study of Its Physical and Electrical Properties. *Solar Energy Materials and Solar Cells*, Vol.51, No.3-4, (February 1998), pp. 305-316, ISSN 0927-0248

Nair, M.T.S.; Guerrero, L.; Arenas, O.L. & Nair, P.K. (1999). Chemically Deposited Copper Oxide Thin Films: Structural, Optical and Electrical Characteristics. *Applied Surface Science*, Vol.150, No.1-4, (August 1999), pp. 143-151, ISSN 0169-4332

Nozik, A.J. (1978). Photoelectrochemistry: Applications to Solar Energy Conversion. *Annual Review of Physical Chemistry*, Vol.29, No.1, (October 1978), pp. 189-222, ISSN 0066-426X

Ottosson, M.; Lu, J. & Carlsson, J-O. (1995). Chemical Vapour Deposition of Cu_2O on MgO(100) from CuI and N_20: Aspects of Epitaxy. *Journal of Crystal Growth*, Vol.151, No.3-4, (June 1995) pp. 305-311, ISSN 0022-0248

Ottosson, M. & Carlsson, J-O. (1996). Chemical Vapour Deposition of Cu_2O and CuO from CuI and O_2 or N_2O. *Surface and Coatings Technology*, Vol. 78, No.1-3, (January 1996), pp. 263-273, ISSN 0257-8972

Papadimitropoulos, G.; Vourdas, N.; Vamvakas, V.Em. & Davazoglou, D. (2005). Deposition and Characterization of Copper Oxide Thin Films. *Journal of Physics: Conference Series, Vol.* 10, No.1, pp. 182–185, ISSN 1742-6588

Pollack, G.P. & Trivich, D. (1975). Photoelectric Properties of Cuprous Oxide. *Journal of Applied Physics*, Vol.46, No.1, (January 1975), pp. 163–172, ISSN 0021-8979

Rai, B.P. (1988). Cu_2O Solar Cells: A Review. S*olar Ceils,* Vol.25, No.3, (December 1988), pp. 265–272, ISSN 0379-6787

Rajčić-Vujasinović, M.; Stević, Z. & Djordjević, S. (1994). Application of Pulse Potential for Oxidation of Natural Mineral Covellite (in Russian). *Zhurnal prikladnoi khimii (Russian Journal of Applied Chemistry)*, Vol.67, No.4, pp. 594-597, ISSN 1070-4272

Rajčić-Vujasinović, M.M.; Stanković, Z.D. & Stević, Z.M. (1999). The Consideration of the Analogue Electrical Circuit of the Metal or Semiconductor/Electrolyte Interfaces Based on the Time Transient Analysis. *Elektrokhimiya (Russian Journal of Electrochemistry*), Vol.35, No.3, pp. 347-354, ISSN 1023-1935

Rakhshani, A.E.; Al-Jassar, A.A. & Varghese, J. (1987). Electrodeposition and Characterization of Cuprous Oxide. *Thin Solid Films,* Vol.148, No.2, (April 1987), pp. 191-201, ISSN 0040-6090

Rakhshani, A.E. & Varghese, J. (1987). Galvanostatic Deposition of Thin Films of Cuprous Oxide. *Solar Energy Materials*, Vol.15, No.4, (May-June 1987), pp. 237-248, ISSN 0165-1633

Ray, S.C. (2001). Preparation of Copper Oxide Thin Film by The Sol–Gel-Like Dip Technique and Study of Their Structural and Optical Properties. *Solar Energy Materials and Solar Cells*, Vol.68, No.3-4, (June 2001), pp. 307-312, ISSN 0927-0248

Rizzo, G.; Arsie, I. & Sorrentino, M. (October 2010). Hybrid Solar Vehicles, In: *Solar Collectors and Panels, Theory and Applications*, Manyala, R. (Ed.), pp. 79-96, Sciyo, ISBN 978-953-307-142-8, Available from: http://www.intechopen.com/articles/show/title/hybrid-solar-vehicles

Santra, K., Sarkar, C.K.; Mukherjee, M.K & Ghosh, B. (1992). Copper Oxide Thin Films Grown by Plasma Evaporation Method. *Thin Solid Films,* Vol. 213, No.2, (June 1992), pp.226-229, ISSN 0040-6090

Santra, K.; Chatterjee, P. & Sen Gupta, S.P. (1999). Powder Profile Studies in Electrodeposited Cuprous Oxide Films. *Solar Energy Material and Solar Cells*, Vol. 57, No.4, (April 1999), pp. 345–358, ISSN 0927-0248

Sears, W.M. & Fortin, E. (1984). Preparation and properties of Cu_2O/Cu photovoltaic cells. *Solar Energy Materials*, Vol.10, No.1, (April-May 1984), pp. 93-103, ISSN 0165-1633

Singh, D.P.; Singh, J.; Mishra, P.R.; Tiwari, R.S. & Srivastava, O.N. (2008). Synthesis, characterization and application of semiconducting oxide (Cu_2O and ZnO) nanostructures. *Bulletin of Materials Science*, Vol.31, No.3, (June 2008), pp. 319–325, ISSN 0250-4707

Siripala, W., Perera, L.D.R.D., De Silva, K.T.L.; Jayanetti, J.K.D.S. & Dharmadasa, I.M. (1996). Study of Annealing Effects of Cuprous Oxide Grown by Electrodeposition Technique. *Solar Energy Materials and Solar Cells*, Vol.44, No.3, (November 1996), pp. 251–260, ISSN 0927-0248

Stanković, Z.; Rajčić-Vujasinović, M.; Vuković, M.; Krčobić, S. & Wragg, A.A. (1998). Electrochemical Synthesis of Cupric Oxide Powder. Part I: Influence of pH. *Journal of Applied Electrochemistry*, Vol.28, No.12, (December 1998), pp. 1405-1411, ISSN 0021-891X

Stanković, Z.; Rajčić-Vujasinović, M.; Vuković, M.; Krčobić, S. & Wragg, A.A. (1999). Electrochemical Synthesis of Cupric Oxide Powder. Part II: Process Conditions. *Journal of Applied Electrochemistry*, Vol.29, No.1, (January 1999), pp. 81-85, ISSN 0021-891X

Stević, Z. & Rajčić-Vujasinović, M. (2006). Chalcocite as a Potential Material for Supercapacitors. *Journal of Power Sources*, Vol.160, No.2, (October 2006), pp. 1511-1517, ISSN 0378-7753

Stević, Z.; Rajčić-Vujasinović, M. & Dekanski, A. (2009). Estimation of Parameters Obtained by Electrochemical Impedance Spectroscopy on Systems Containing High Capacities. *Sensors*, Vol.9, No.9, (September 2009), pp. 7365-7373, ISSN 1424-8220

Stević, Z. & Rajčić-Vujasinović, M. (In press). Supercapacitors as a Power Source in Electrical Vehicles, in: Electric Vehicles / *Book 1.* Soylu, S. (Ed). ISBN 978-953-307-287-6

Tang, Y.; Chen, Z.; Jia, Z.; Zhang, L. & Li, J. (2005). Electrodeposition and Characterization of Nanocrystalline Films Cuprous Oxide Thin Films on TiO_2. *Materials Letters*, Vol.59, No.4, (February 2005), pp. 434–438, ISSN 0167-577X

Vieira, J.A.B. & Mota, A.M. (2010). Maximum Power Point Tracker Applied in Batteries Charging with Photovoltaic Panels, In: *Solar Collectors and Panels, Theory and Applications*, Ochieng, R.M. (Ed.), pp. 211-224, Sciyo, ISBN 978-953-307-142-8, Available from: http://www.intechopen.com/articles/show/title/maximum-power-point-tracker-applied-to-charging-batteries-with-pv-panels

Wang, L.C.; de Tacconi, N.R.; Chenthamarakshan, C.R.; Rajeshwar, K. & Tao, M. (2007). Electrodeposited Copper Oxide Films: Effect of Bath pH on Grain Orientation and Orientation-dependent Interfacial Behavior. *Thin Solid Films*, Vol. 515, No.5, (January 2007), pp. 3090–3095, ISSN 0040-6090

Wijesundera, R.P., Hidaka, M., Koga, K., Sakai, M. & Siripala, W. (2006). Growth and Characterization of Potentiostatically Electrodeposited Cu_2O and CuO Thin Films. *Thin Solid Films*, Vol.500, No.1-2, (April 2006), pp. 241–246, ISSN 0040-6090

Wong, E.M. & Searson, P.C. (1999). ZnO Quantum Particle Thin Films Fabricated by Electrophoretic Deposition. *Applied Physics Letters*, Vol.74, No.20, (May 1999), pp. 2939-2941, ISSN 0003-6951

Xue, J. & Dieckmann, R. (1990). The Non-Stoichiometry and the Point Defect Structure of Cuprous Oxide ($Cu_{2-\delta}O$). *Journal of Physics and Chemistry of Solids*, Vol. 51, No.11, pp. 1263-1275, ISSN 0022-3697

Zhou, Y. & Switzer, J.A. (1998). Electrochemical Deposition and Microstructure of Copper (I) Oxide Films. *Scripta Materialia*, Vol.38, No.11, (May 1998), pp. 1731-1738, ISSN 1359-6462

9

Bioelectrochemical Fixation of Carbon Dioxide with Electric Energy Generated by Solar Cell

Doo Hyun Park[1], Bo Young Jeon[1] and Il Lae Jung[2]
[1]*Department of Biological Engineering, Seokyeong University, Seoul*
[2]*Department of Radiation Biology, Environmental Radiation Research Group, Korea Atomic Energy Research Institute, Daejeon, Korea*

1. Introduction

Atmospheric carbon dioxide has been increased and was reached approximately to 390 mg/L at December 2010 (Tans, 2011). Rising trend of carbon dioxide in past and present time may be an indicator capable of estimating the concentration of atmospheric carbon dioxide in the future. Cause for increase of atmospheric carbon dioxide was already investigated and became general knowledge for the civilized peoples who are watching TV, listening to radio, and reading newspapers. Anybody of the civilized peoples can anticipate that the atmospheric carbon dioxide is increased continuously until unknowable time in the future but not in the near future. Carbon dioxide is believed to be a major factor affecting global climate variation because increase of atmospheric carbon dioxide is proportional to variation trend of global average temperature (Cox et al., 2000). Atmospheric carbon dioxide is generated naturally from the eruption of volcano (Gerlach et al., 2002; Williams et al., 1992), decay of organic matters, respiration of animals, and cellular respiration of microorganisms (Raich and Schlesinger, 2002; Van Veen et al., 1991); meanwhile, artificially from combustion of fossil fuels, combustion of organic matters, and cement making-process (Worrell et al., 2001). Theoretically, the natural atmospheric carbon dioxide generated biologically from the decay of organic matter and the respirations of organisms has to be fixed biologically by land plants, aquatic plants, and photosynthetic microorganisms, by which cycle of atmospheric carbon dioxide may be nearly balanced (Grulke et al., 1990). All of the human-emitted carbon dioxide except the naturally balanced one may be incorporated newly into the pool of atmospheric greenhouse gases that are methane, water vapor, fluorocarbons, nitrous oxide, and carbon dioxide (Lashof and Ahuja, 1990). The airborne fraction of carbon dioxide that is the ratio of the increase in atmospheric carbon dioxide to the emitted carbon dioxide variation was typically about 45% over 5 years period (Keeling et al., 1995). Canadell at al (2007) reported that about 57% of human-emitted carbon dioxide was removed by the biosphere and oceans. These reports indicate that the airborne fraction of carbon dioxide is at least 43-45%, which may be the balance emitted by human activity.

The land plants are the largest natural carbon dioxide sinker, which have been decreased globally by deforestation (Cramer et al., 2004). Especially, tropical and rainforests are being

cut down for different purpose and by different reason and some of the forest are being burned for slash and burn farming. The atmospheric carbon dioxide and other greenhouse gases are increased in proportion to the deforestation (McKane et al. 1995). Deforestation causes part of the released carbon dioxide to be accumulated in the atmosphere and the global carbon cycle to be changed (Robertson and Tiejei, 1988). The releasing carbon dioxide and changing carbon cycle increase the greenhouse effect and may raise global temperature. The greenhouse effect is generated naturally by the infrared radiation, which is generated from incoming solar radiation, absorbed into atmospheric greenhouse gases and re-radiated in all direction (Held and Soden). The gases contributing to the greenhouse effect on Earth are water vapor (36-70%), carbon dioxide (9-26%), methane (4-9%), and ozone (3-7%) (Kiehl et al., 1977). Especially, water vapor can amplify the warming effect of other greenhouse gases, such that the warming brought about by increased carbon dioxide allows more water vapor to enter the atmosphere (Hansen, 2008). The greenhouse effect can be strengthened by human activity and enhanced by the synergetic effect of water vapor and carbon dioxide because the elevated carbon dioxide levels contribute to additional absorption and emission of thermal infrared in the atmosphere (Shine et al., 1999). The major non-gas contributor to the Earth's greenhouse effect, cloud (water vapor), also absorb and emit infrared radiation and thus have an effect on net warming of the atmosphere (Kiehl et al., 1997). Elevation of carbon dioxide is a cause for greenhouse effect, by which abnormal climate, desertification, and extinction of animals and plants may be induced (Stork, 1997). However, carbon dioxide is difficult to be controlled in the industry-based society that depends completely upon fossil fuel. If the elevation of carbon dioxide was unstoppable or necessary evil, the technique to convert biologically the atmospheric carbon dioxide to stable polymer in the condition without using fossil fuel must be developed. All of the land and aquatic plants convert mainly carbon dioxide to biomolecule in coupling with oxygen generation; however, a total of 16.5% of the forest (230,000 square miles) was affected by deforestation due to the increase of fragmented forests, cleared forests, and boundary areas between the fragmented forests (Skole et al., 1998). Decline of plants may be a cause to activate generation of the radiant heat because the visible radiation of solar energy absorbed for photosynthesis can be converted to additional radiant heat.

Solar cell is the useful equipment capable of physically absorbing solar radiation and converting the solar energy to electric energy (O'Regan and Grätzel, 1991). The radiant heat generated from the solar energy may be decreased in proportion to the electric energy produced by the solar cells. Electrochemical redox reaction can be generated from electric energy by using a specially designed bioreactor equipped with the anode and cathode separated with membrane, which is an electrochemical bioreactor. The electric energy generated from the solar energy can be converted to biochemical reducing power through the electrochemical redox mediator. The biochemical reducing power (NADH or NADPH) is the driving force to generate biochemical energy, ATP. The biochemical reducing power and ATP are essential elements that activate all biochemical reactions for biosynthesis of cell structure and production of metabolites.

2. Electrochemical redox mediator

The electrochemical reduction reaction generated in cathode can't catalyze reduction of NAD^+ or $NADP^+$ both *in vitro* and *in vivo* without electron mediator. Various ion radicals that are methyl viologen, benzyl viologen, hydroquinone, tetracyanoquinodimethane, and

neutral red (NR) have been used as electron mediator to induce electrochemical redox reaction between electrode and electron carriers that are NAD^+, FAD, and cytochrome C (Pollack et al., 1996; Park et al., 1997; Wang and Du, 2002; Kang et al., 2007). In order to *in vivo* drive and maintain bacterial metabolism with electrochemical reducing power as a sole energy source, only NAD^+ or $NADP^+$ is required to be reduced by coupling redox reaction between electron mediator and biochemical electron carrier (Park and Zeikus, 1999; 2000). NR can catalyze the electrochemical reduction reaction of NAD^+ both *in vivo* and *in vitro* but no electron mediator except the NR can. NR is a water-soluble structure composed of phenazine ring with amine, dimethyl amine, methyl, and hydrogen group as shown in Fig 1. The dimethyl amine group is redox center for electron-accepting and donating in coupling with phenazine ring; meanwhile, the amine, methyl, and hydrogen are structural group. Redox potential of NR is -0.325 volt (vs. NHE), which is 0.05 volt lower than NAD^+. The electrochemical redox reaction of NR can be coupled to biochemical redox reaction as follows:

$$[\ NR_{ox} + 2e^- + 1H^+ \rightarrow NR_{red};\ NR_{red} + NAD^+ \rightarrow NR_{ox} + NADH\ ]$$

NAD^+ can be reduced in coupling with biochemical redox reaction as follows:

$$[\ NAD^+ + 2e^- + 2H^+ \rightarrow NADH + H^+]$$

Commonly, NR_{ox} and NAD^+ are reduced to NR_{red} and NADH, respectively by accepting two electrons and one proton.

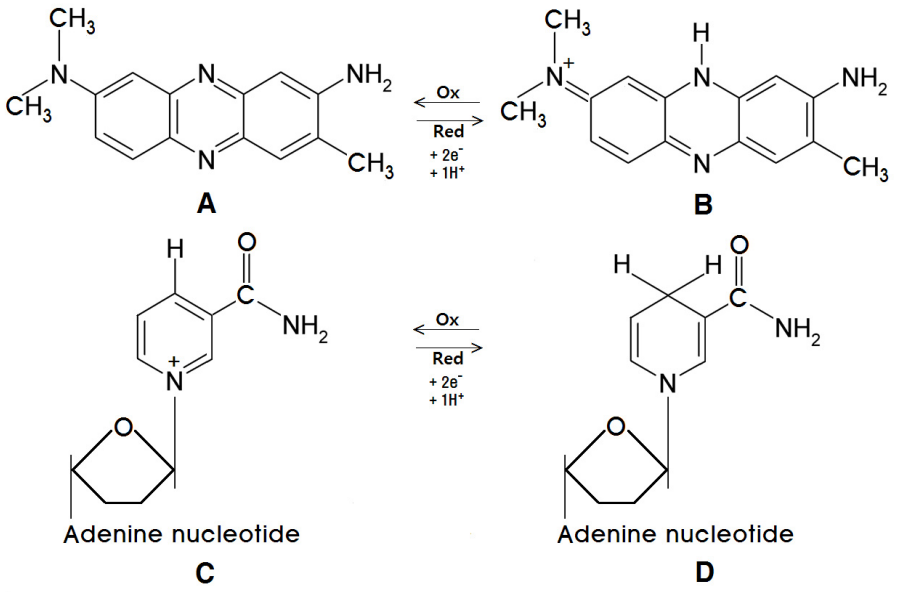

Fig. 1. Molecular structure of neutral red, which can be electrochemically oxidized (A) or reduced (B). The reduced neutral red can catalyze reduction reaction of NAD^+ (C) to NADH (D) without enzyme catalysis. Ox and Red indicate oxidation and reduction, respectively.

Theoretically, the water-soluble NR may be reduced at the moment when contacted with electrode and catalyze biochemical reduction of NAD^+ at the moment when contacted with bacterial cell or enzyme. A part of NR may be contacted with electrode or bacterial cell in water-based reactant but most of that is dissolved or dispersed in the reactant. In order to induce the effective electrochemical and biochemical reaction in the bacterial culture, NR and bacterial cells have to contact continuously and simultaneously with electrode. This can be accomplished by immobilization of NR in graphite felt electrode based on the data that most of bacterial cells tend to build biofilm spontaneously on surface of solid material and the graphite felt is matrix composed of $0.47 m^2/g$ of fiber (Park et al., 1999). The amino group of NR can bind covalently to alcohol group of polyvinyl alcohol by dehydration reaction, in which polyvinyl-3-imino-7-dimethylamino-2-methylphenazine (polyvinyl-NR) is produced as shown in Fig 2. The polyvinyl-NR is a water-insoluble solid electron mediator to catalyze electrochemically reduction reaction of NAD^+ like the water-soluble NR (Park and Zeikus, 2003). The polyvinyl-NR immobilized in graphite felt (NR-graphite) functions as a cathode for electron-driving circuit, an electron mediator for conversion of electric energy to electrochemical reducing power, and a catalyst for reduction of NAD^+ to NADH. The electrochemical bioreactor equipped with the NR-graphite cathode is very useful to cultivate autotrophic bacteria that grow with carbon dioxide as a sole carbon source and electrochemical reducing power as a sole energy source (Lee and Park, 2009).

3. Separation of electrochemical redox reaction

The biochemical reducing power can be regenerated electrochemically by NR-graphite cathode (working electrode) that functions as a catalyst, for which H_2O has to be electrolyzed on the surface of anode (counter electrode) that functions as an electron donor. The working electrode is required to be separated electrochemically from the counter electrode by specific septa that are the ion-selective Nafion membrane (Park and Zeikus, 2003; Kang et al., 2007; Tran et al., 2009), the ceramic membrane (Park and Zeikus, 2003; Kang et al., 2007; Tran et al., 2009), the modified ceramic membrane with cellulose acetate film (Jeon et al, 2009B), and the micro-pored glass filter, by which the electrochemical reducing power in the cathode compartment can be maintained effectively. Jeon and Park (2010) developed a combined anode that was composed of cellulose acetate film, porous ceramic membrane and porous carbon plate as shown in Fig 3. The combined anode functions as a septum for electrochemical redox separation between anode and cathode, an anode for electron-driving circuit, and a catalyst for electrolysis of H_2O. The major function of anode is to supply electrons required for generation of electrochemical reducing power in the working electrode (NR-graphite cathode), in which H_2O functions as an electron donor.
The strict anaerobic bacteria that are methanogens, sulfidogens, and anaerobic fermenters grow in the condition with lower oxidation-reduction potential than -300 mV (vs. NHE) (Ferry, 1993; Gottschalk, 1985), which can be induced electrochemically inside of the carbon fibre matrices of NR-cathode under only non-oxygen atmosphere. The NR-cathode can catalyze biochemical regeneration of NADH and generation of hydrogen but can't catalyze scavenging of oxygen and oxygen radicals at around 25^oC and 1 atm. The combined anode can protect effectively contamination of catholyte with the atmospheric oxygen by unidirectional evaporation of water from catholyte to atmosphere through the combined anode as shown in Fig 4. The driving force for the unidirectional evaporation of water may be generated naturally by the difference of water pressure between catholyte and outside atmosphere (Jeon et al., 2009A).

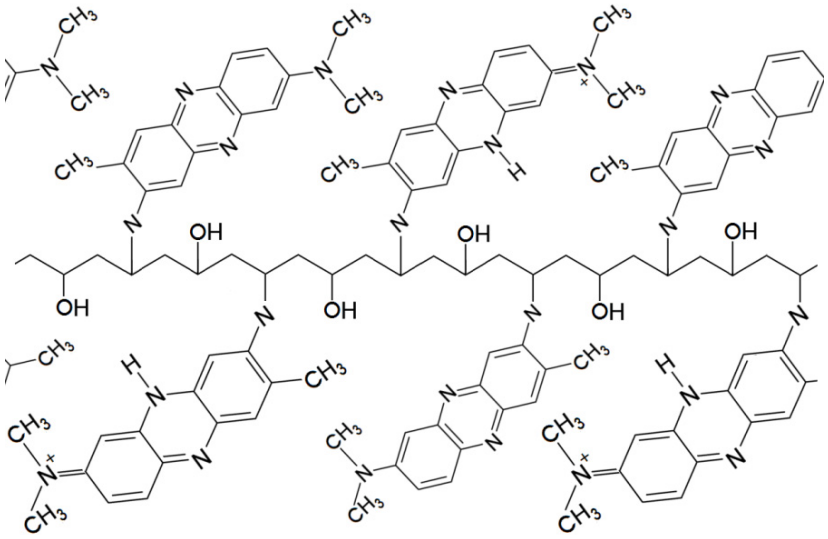

Fig. 2. Schematic structure of polyvinyl-NR that is produced by covalent bond between amine of NR and alcohol of polyvinyl alcohol. The polyvinyl-NR can bind physically to graphite cathode surface.

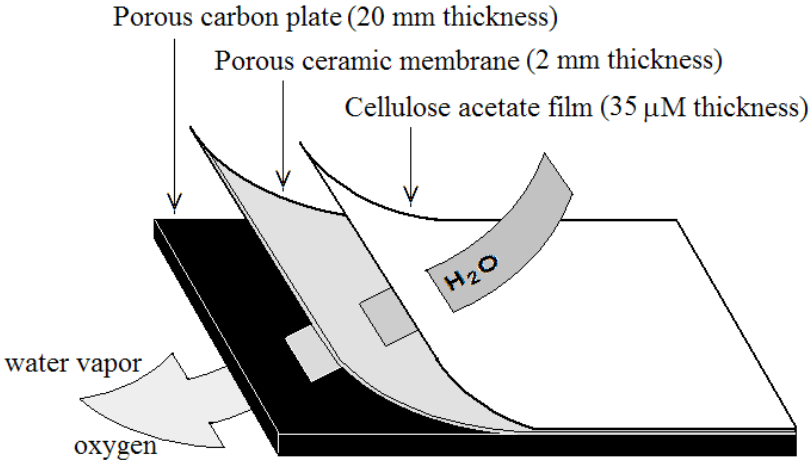

Fig. 3. Schematic structure of a combined anode composed of cellulose acetate film, porous ceramic membrane and porous carbon plate. Water or gas can penetrate across the cellulose acetate film but solutes can't.

Practically, the hydrogenotrophic methanogens are useful microorganisms for carbon dioxide fixation using the electrochemical bioreactor. However, most of the reducing power that is electrochemically generated in the NR-graphite cathode may be consumed to

maintain the proper oxidation-reduction potential for growth of the hydrogenotrophic methanogens in the condition without chemical reducing agent. This may be a cause to decrease the regeneration effect of the biochemical reducing power and free energy in the electrochemical bioreactors. In natural ecosystem, hydrogen sulfide produced metabolically by sulfidogens in coupling with oxidation of organic acids functions as the chemical reducing agent to maintain the proper environmental condition for growth of the methanogens (Thauer et al., 1977; Oremland et al., 1989; Zinder et al., 1984).

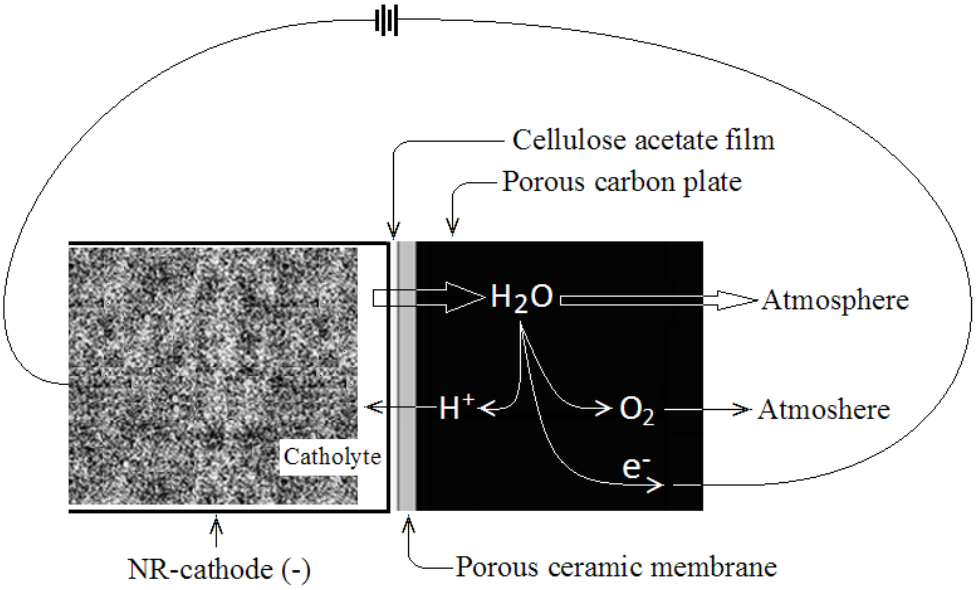

Fig. 4. Schematic structure of the combined anode composed of cellulose acetate film, porous ceramic membrane, and porous carbon plate, in which protons, electrons, and oxygen generated from water by the electrolysis may be transferred separately to the catholyte, the NR-cathode, and the atmosphere. Water is transferred from catholyte to atmosphere through the combined anode by difference of water pressure between catholyte and atmosphere.

Meanwhile, the growth condition for facultative anaerobic mixotrophs is not required to be controlled electrochemically because the metabolic function of the facultative anaerobic mixotrophs is not influenced critically by the oxidation-reduction potential. Accordingly, the combined anode may be replaced by the glass filter (pore, 1-1.6 μm) that permits transfer of water and diffusion of ions and soluble compounds. Water transferred from catholyte to anolyte through the glass filter by difference of pressure and volume is electrolysed into oxygen, protons, and electrons in the anode compartment. The protons, electrons, and oxygen are transferred separately to the catholyte, the NR-cathode, and the atmosphere as shown in Fig 5. The water in the anode compartment equipped at the center of catholyte is consumed continuously by electrolysis and refilled spontaneously from catholyte by difference of volume and pressure between the catholyte and anolyte.

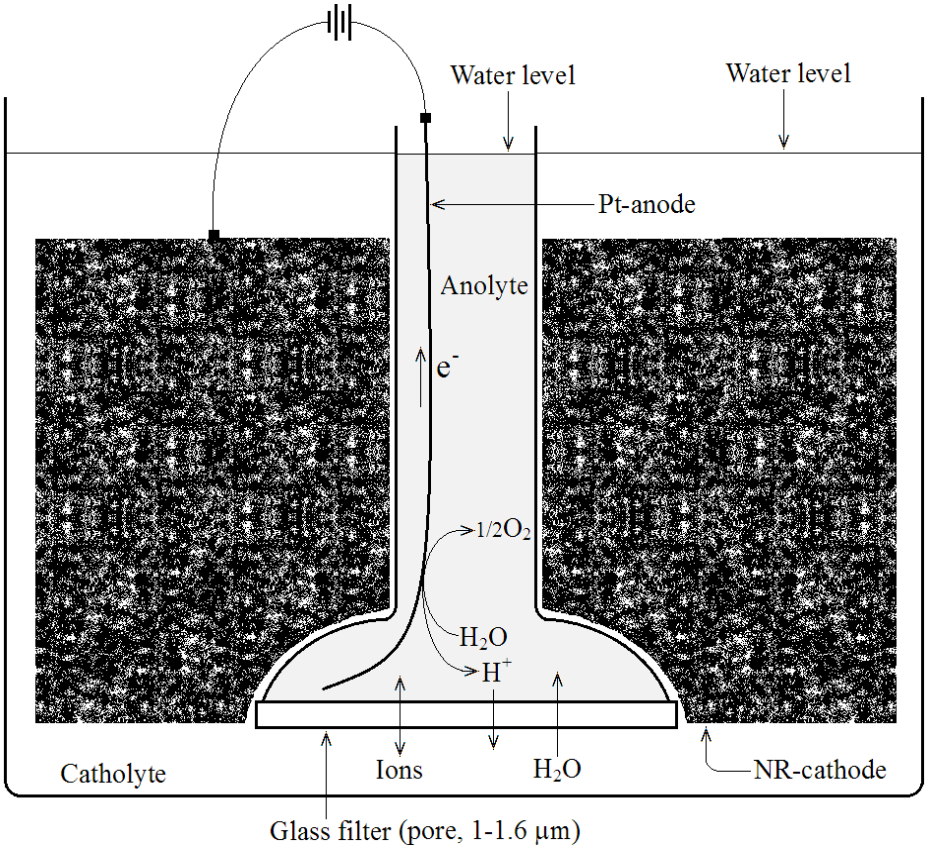

Fig. 5. Schematic structure of the anode and cathode compartment separated by glass filter. Protons, electrons, and oxygen generated from water by the electrolysis may be transferred separately to the catholyte, the NR-cathode, and the atmosphere.

4. Enrichment of hydrogenotrophic methanogens

A specially designed electrochemical bioreactor is composed of the combined anode (Fig 4) and NR-graphite cathode for enrichment of the hydrogenotrophic methanogens as shown in Fig 6. Oxygen-free and carbonate-saturated wastewater was supplied continuously from a wastewater reservoir as shown in Fig 7. The electrochemical bioreactor was operated with the electricity generated from the solar panel. The wastewater obtained from sewage treatment plant was used without sterilization, to which 50 mM of sodium bicarbonate was added. The contaminated oxygen was consumed by bacteria growing intrinsically in the wastewater reservoir. Hydrogenotrophic methanogens grow with the free energy and reducing power generated by the coupling redox reaction of carbon dioxide and hydrogen (Ferguson and Mah, 1983; Na et al., 2007; Zeikus and Wolfe, 1972). Hydrogen generated from the electrolysis of water can't function to maintain the proper oxidation reduction

potential for methanogenic bacteria in the electrochemical bioreactor owing to the micro-solubility. The micro-pore formed by the fiber matrices of NR-graphite cathode may be proper micro-environment for the growth of hydrogenotrophic methanogens because hydrogen generated from NR-graphite cathode may be captured in the micro-pores and the lower oxidation-reduction potential than -300 mV (vs. NHE) may be maintained by the electrochemical reducing power.

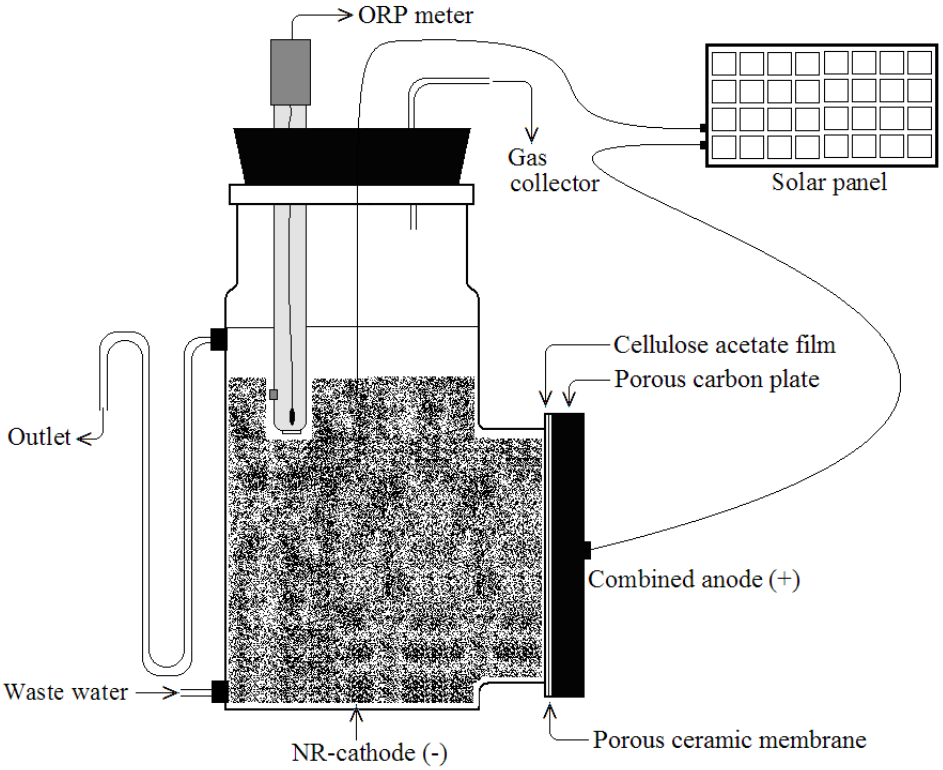

Fig. 6. Schematic structure of an electrochemical bioreactor, in which the anode compartment was replaced with the combined anode composed of cellulose acetate film, porous ceramic membrane and porous carbon plate. Water is electrolyzed in the porous carbon plate and separated into proton, electron, and oxygen.

Methyl compounds, hydrogen, low molecular weight fatty acids, hydrogen, and carbon dioxide are produced by various fermentation bacteria in the anaerobic digestive sludge. The methanogens grow syntrophically in the bioreactor cultivating anaerobic digestive sludge, which is composed of various organic compounds and anaerobic bacterial community (Stams et al., 2009; Katsuyam et al., 2009). When the anaerobic digestive sludge was applied to the electrochemical bioreactor (Fig 6 and 7), the hydrogenotrophic methanogens that are *Methanobacterium* sp., *Methanolinea* sp., and *Methnoculleus* sp. were enriched predominantly (Jeon et al., 2009B). The predominated hydrogenotrophic methanogens consumed and

produce actively carbon dioxide and methane, respectively, using the electrochemical reducing power generated from the solar panel (Cheng et al., 2011). Practically, the methane production and carbon dioxide consumption were significantly increased in the electrochemical bioreactor as shown in Fig 8.

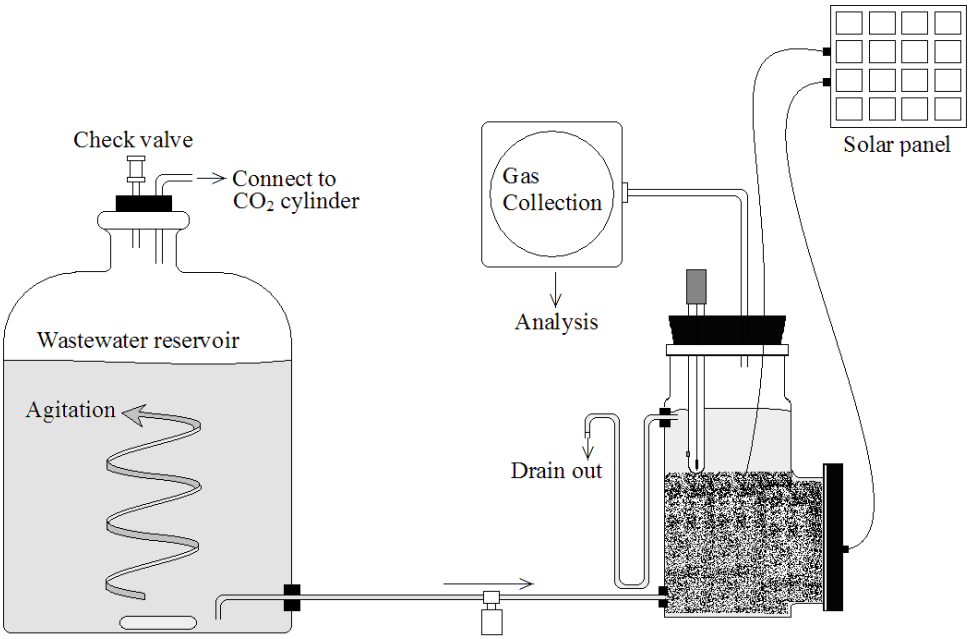

Fig. 7. Schematic structure of an electrochemical bioreactor for continuous culture of hydrogenotrophic methanogens. The wastewater saturated with carbon dioxide is supplied continuously to the electrochemical bioreactor and headspace of wastewater reservoir was refilled continuously with pure carbon dioxide without oxygen contamination.

Bacteriological conversion of carbon dioxide to methane using the electrochemical reducing power may be a technique for fixation of carbon dioxide without combustion of fossil fuel; however, may not be a way for long term storage of carbon. Cell structures of bacteria are composed of peptidoglycan, phospholipid, proteins, nucleic acids, and carbohydrates that are biochemically stable polymers (Caldwell, 1995). Bacterial cells themselves can be the carbon storage by freezing or drying without the specific engineering process. Hydrogenotrophic methanogens may not be proper carbon storage because they consume the reducing power and free energy ineffectively to maintain the lower oxidation-reduction potential than -300 mV, grow more slowly than other autotrophic bacteria, and produce the unstable metabolite (methane).

Facultative anaerobic mixotrophs, on the other hand, not only grow heterotrophically in the condition with organic carbons but also grow autotrophically in the condition with electron donors and carbon dioxide (Johson, 1998; Morikawa and Imanaka, 1993). The metabolism and physiological function of the facultative anaerobic mixotrophs are not influenced by oxygen. These are useful character of the facultative anaerobic mixotrophs to cultivate with

wastewater containing other reduced organic and inorganic compounds and exhaust containing carbon dioxide, and the electrochemical reducing power as the electron donor (Skirnisdottir et al., 2001).

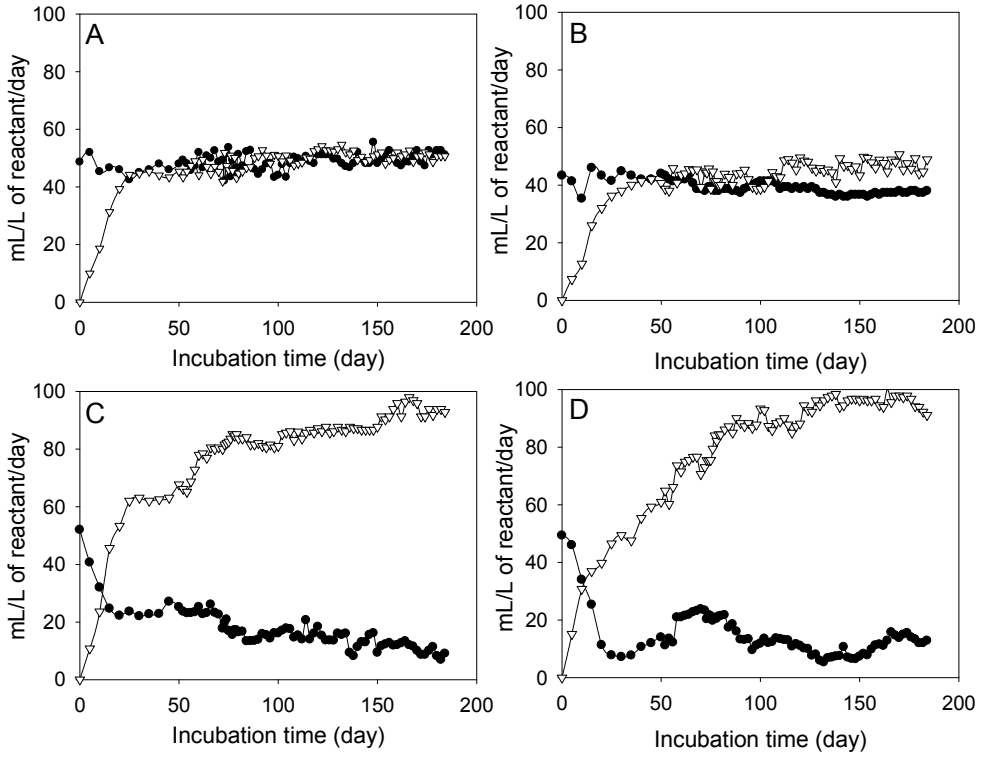

Fig. 8. Carbon dioxide consumption (●) and methane production (▽) by anaerobic digestive sludge cultivated in conventional bioreactor (reactors A and B) and electrochemical bioreactor (reactors C and D). Duplicate reactors were operated to enhance the comparability between the conventional bioreactor and the electrochemical bioreactor.

5. Enrichment and cultivation of carbon dioxide-fixing bacteria

A cylinder-type electrochemical bioreactor composed of the built-in anode compartment and NR-graphite cathode was employed to enrich the facultative anaerobic mixotrophs capable of fixing carbon dioxide with electrochemical reducing power as shown in Fig 9. The NR-cathode was separated electrochemically from anode compartment by the glass filter (Fig 5). Mixture of the bacterial community obtained from aerobic wastewater treatment reactor, forest soil, and anaerobic wastewater was cultivated in the cylinder-type electrochemical bioreactor to enrich selectively carbon dioxide-fixing bacteria with the electrochemical reducing power generated from NR-graphite cathode. DC -3 volt of electricity that was generated by a solar panel was charged to NR-graphite cathode to induce generation of electrochemical reducing power. Electricity is the easiest energy to

transfer and supply to any electronic device. The electrochemical bioreactor is also the simplest electronic device to convert electric energy to biochemical reducing power. The wastewater and exhausted gas can be used directly without purification or separation as the nutrient source for bacterial metabolism. Experimentally, the electricity generated from the 25 cm^2 of the solar panel is very enough for operation of the 10 L of electrochemical bioreactor.

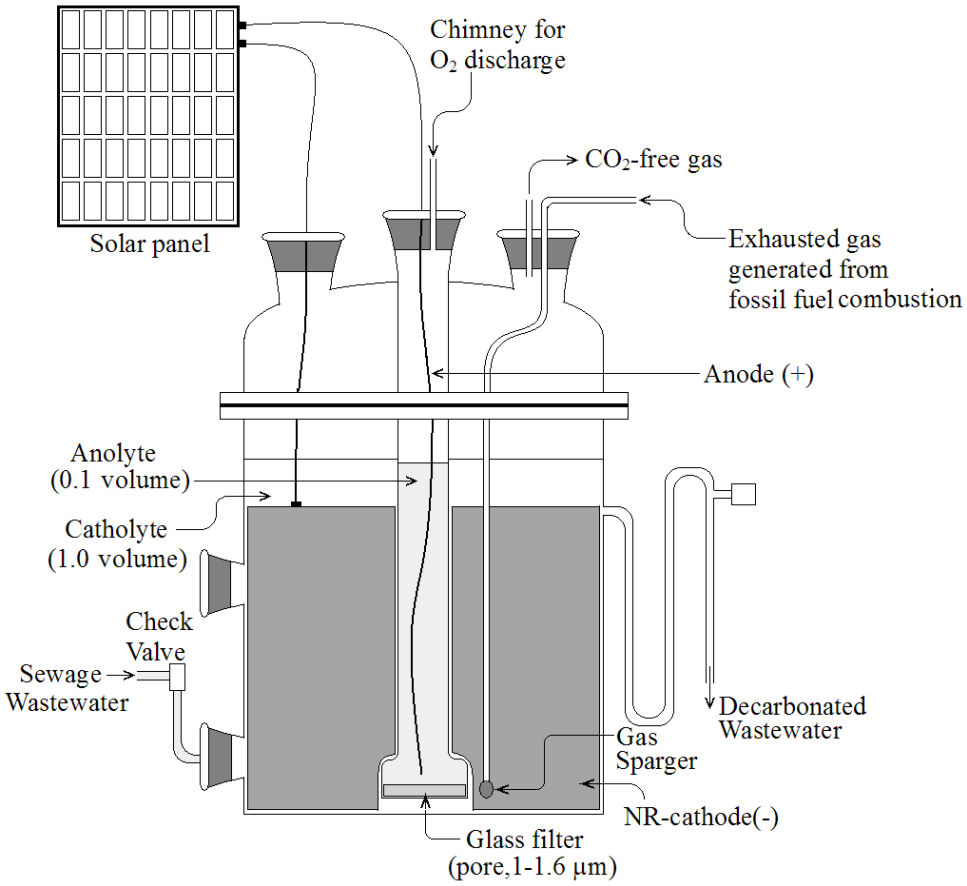

Fig. 9. Schematic diagram of the cylinder-type electrochemical bioreactor equipped with a built-in anode compartment for the cultivation of CO_2-fixing bacteria. The glass filter septum equipped at the bottom end of the anode compartment functions as redox separator between anode and cathode compartment and micropore for transfer of catholyte to anode compartment.

During enrichment of the carbon dioxide-fixing bacteria using the cylinder-type electrochemical bioreactor, bacterial community was changed significantly as show in Fig 10. Some of bacteria community was increased or enriched as shown in the box A and C but decreased or died out as shown in the box B and D. These phenomena are a clue that the

bacterial species that can fix carbon dioxide with electrochemical reducing power are adapted selectively to the reactor condition but other bacteria that can't generate biochemical reducing power from the electrochemical reducing power are not. The DNA bands were extracted from TGGE gel and sequenced. Identity of the bacteria was determined based on the 16S-rDNA sequence homology.

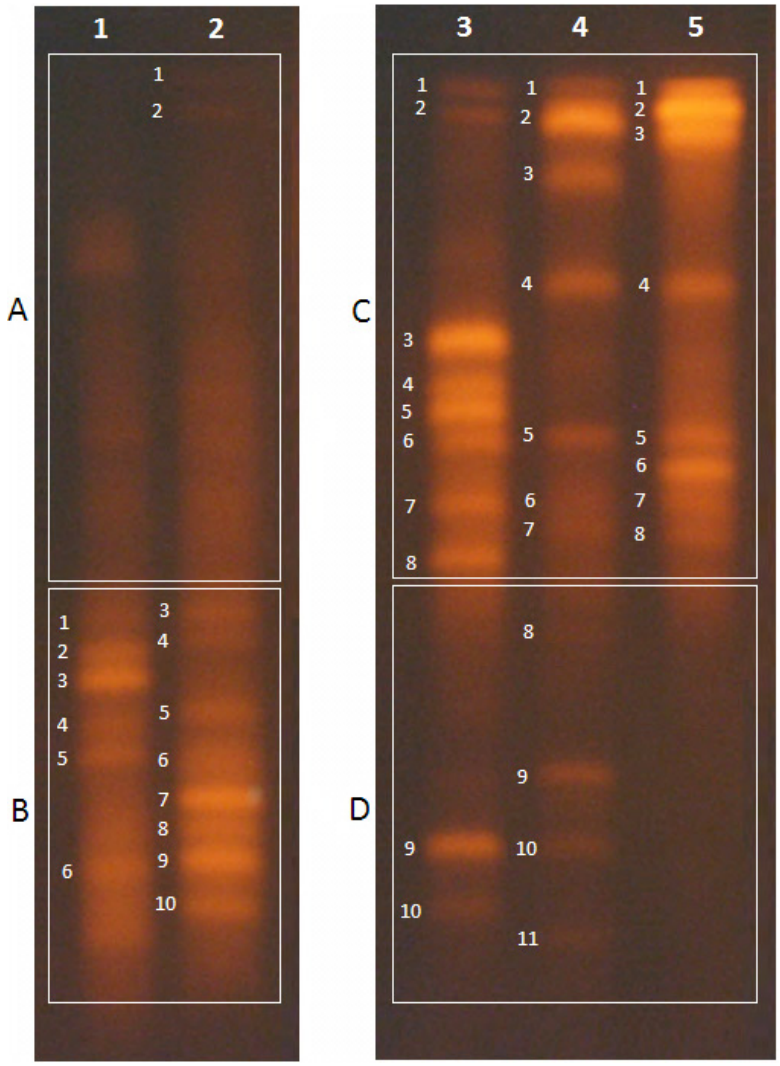

Fig. 10. TGGE patterns of 16S-rDNA variable regions amplified with chromosomal DNA extracted from bacterial communities enriched in the cylinder-type electrochemical bioreactors. 50 ml of bacterial culture was isolated from the electrochemical bioreactor at the initial time immediately after inoculation (lane1), 2nd week (lane 2), 8th week (lane 3), 16th week (lane 4), and 24th week of incubation time (lane 5).

Lane	Band	Genus or Species	Homology (%)	Accession No.
1 (initial)	1	Uncultured *Burkholderia* sp.	98	FJ393136
	2	Groundwater biofilm bacterium	98	FJ204452
	3	*Hydrogenophaga* sp.	98	FM998722
	4	Uncultured bacterium sp.	97	HM481230
	5	*Aquamicrobium* sp.	98	GQ254286
	6	Uncultured *Actinobacterium* sp.	99	FM253013
2 (2nd week)	1	Uncultured bacterium sp.	97	AF234127
	2	Uncultured bacterium sp.	97	EU532796
	3	Uncultured *Clostridum* sp.	99	FJ930072
	4	Uncultured *Polaromonas* sp.	99	HM486175
	5	Uncultured *Rhizobium* sp.	100	FM877981
	6	*Raoultella planticola*	98	EF551363
	7	Unidentified bacterium	98	AV669107
	8	Uncultured bacterium	99	HM920740
	9	Uncultured bacterium	97	GQ158957
	10	Uncultured *Klebsiella* sp.	98	GQ416299
3 (8th week)	1	Uncultured bacterium sp.	97	AF234127
	2	Uncultured bacterium sp.	97	EU532796
	3	*Enterococcus* sp.	98	DQ305313
	4	Uncultured bacterium	98	HM820223
	5	*Aerosphaera taera*	99	EF111256
	6	*Alcaligenes* sp.	98	GQ383898
	7	Uncultured bacterium	98	HM231340
	8	Uncultured bacterium sp.	97	FJ675330
	9	*Stenotrophomonas* sp.	98	EU635492
	10	Uncultured *Klebsiella* sp.	98	GQ416299
4 (16th week)	1	Uncultured bacterium sp.	97	AF234127
	2	Uncultured bacterium sp.	97	EU532796
	3	Uncultured bacterium sp.	98	HM575088
	4	*Alcaligenes* sp.	98	GQ200556
	5	*Alcaligenes* sp.	98	GQ383898
	6	Uncultured bacterium	98	HM231340
	7	*Achromobacter* sp.	96	GQ214399
	8	Uncultured *Lactobacillales* bacterium sp.	96	HM231341
	9	Uncultured *Ochrombacterum* sp.	97	EU882419
	10	*Stenotrophomonas* sp.	98	EU635492
	11	*Tissierella* sp.	96	GQ461822
5 (24th week)	1	Uncultured bacterium sp.	97	AF234127
	2	Uncultured bacterium sp.	97	EU532796
	3	Uncultured bacterium sp.	98	HM820116
	4	*Alcaligenes* sp.	98	GQ200556
	5	*Alcaligenes* sp.	97	GQ383898
	6	*Enterococcus sp.*	99	FJ513901
	7	Uncultured bacterium	98	HM231340
	8	*Achromobacter* sp.	96	GQ214399

Table 1. The homologous bacterial species with the sequences of DNA extracted from TGGE bands (Fig 10), which were identified based on the GenBank database.

Some anaerobic bacteria (*Hydrogenophaga* sp. and *Clostridium* sp.) that may be originated from the anaerobic wastewater treatment reactor are detected at the initial cultivation time but disappeared after 8th week of incubation time (Kang and Kim, 1999; Willems et al., 1989; Lamed et al., 1988). On the other hand, the bacteria that are capable of fixing carbon dioxide by autotrophic or mixotrophic metabolism were enriched as shown in Table 1. All of the enriched bacteria may not be the carbon dioxide-fixing bacteria but *Achromobacter* sp. and *Alcaligenes* sp. are known to fix carbon dioxide autotrophically or mixotrophically (Freter and Bowien, 1994: Friedrich, 1982; Hamilton et al., 1965; Leadbeater and Bowien, 1984; Ohmura et al.). During the enrichment of the carbon dioxide-fixing bacteria, carbon dioxide consumption was increased and reached to stationary phase after 15th week of incubation time as shown in Fig 11. Various organic compounds contained in the bacterial cultures that were originated from anaerobic wastewater treatment reactor, aerobic wastewater treatment reactor, and forest soil might be consumed completely and then carbon dioxide-fixing bacteria might grow selectively. The carbon dioxide consumption was increased initially and then reached to stationary phase after 15th week of incubation time, which is proportional to the enrichment time of the *Achromobacter* sp. and *Alcaligenes* sp.

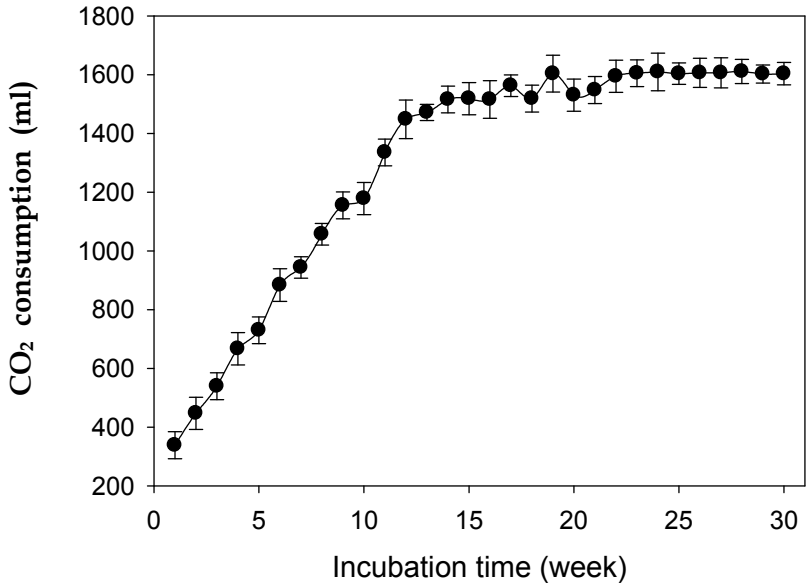

Fig. 11. Weekly consumption of CO_2 in the electrochemical bioreactor from the initial incubation time to 30 weeks. CO_2 consumption was analyzed weekly and the gas reservoir was refilled with 50±1% of CO_2 to N_2 at 4-week intervals.

Before and after enrichment, the bacterial community grown in the cylinder-type electrochemical bioreactor was analyzed using the pyrosequencing technique (Van der Bogert et al., 2011). The classifiable sequences obtained by the pyrosequencing were identified based on the Ribosomal Database Project (RDP), and defined at the 100 % sequence homologous level. The most abundant sequences (17.96%) obtained from the bacterial culture before enrichment was identified as *Brevundimonas* sp., and the abundance

of sequences identified with *Alcaligenes* sp. and *Achromobcter* sp. was 0.98 and 0.12%, respectively. Meanwhile, the most abundant sequences (43.83%) obtained from the bacterial culture after enrichment was identified as *Achromobacter* sp., and the most classifiable sequences were also identified as *Achromobacter* sp. and *Alcaligenes* sp. as shown in Table 2.

Before enrichment				After enrichment			
Classifiable sequences	Abundance (%)	Bacterial genus	Homology (%)	Classifiable sequences	Abundance (%)	Bacterial genus	Homology (%)
876	17.96	*Brevundimonas*	100	2248	43.83	*Achromobacter*	100
153	3.14	*Pseudomonas*	100	748	14.58	*Achromobacter*	100
111	2.28	*Hydrogenophaga*	100	595	5.87	*Stenotrophomonas*	100
99	2.03	*Delftia*	100	301	2.28	*Achromobacter*	100
86	1.76	*Stenotrophomonas*	100	263	1.77	*Achromobacter*	100
70	1.44	*Pseudomonas*	100	219	1.23	*Achromobacter*	100
53	1.09	*Parvibaculum*	100	117	0.90	*Achromobacter*	100
52	1.07	*Brevundimonas*	100	91	0.66	*Achromobacter*	100
48	0.98	*Alcaligenes*	100	63	0.57	*Alcaligenes*	100
32	0.66	*Comamonas*	100	46	0.53	*Achromobacter*	100
31	0.64	*Bacillus*	100	34	0.49	*Achromobacter*	100
26	0.53	*Bosea*	100	29	0.49	*Castellaniella*	100
21	0.43	*Devosia*	100	27	0.45	*Achromobacter*	100
17	0.35	*Acidovorax*	100	25	0.45	*Achromobacter*	100
12	0.25	*Brevundimonas*	100	25	0.39	*Stenotrophomonas*	100
12	0.25	*Sphaerobacter*	100	23	0.16	*Achromobacter*	100
11	0.23	*Brevundimonas*	100	23	0.14	*Alcaligenes*	100
9	0.18	*Acinetobacter*	100	20	0.12	*Achromobacter*	100
9	0.18	*Sphaerobacter*	100	14	0.10	*Alcaligenes*	100
8	0.16	*Brevundimonas*	100	14	0.10	*Pseudomonas*	100
7	0.14	*Hyphomicrobium*	100	11	0.08	*Achromobacter*	100
7	0.14	*Thermomonas*	100	10	0.08	*Achromobacter*	100
6	0.12	*Achromobacter*	100	8	0.06	*Achromobacter*	100
6	0.12	*Brevundimonas*	100	7	0.06	*Achromobacter*	100
4	0.10	*Devosia*	100	7	0.06	*Achromobacter*	100
3	0.08	*Pseudoxanthomonas*	100	6	0.04	*Alcaligenes*	100
3	0.06	*Castellaniella*	100	6	0.04	*Achromobacter*	100
3	0.06	*Gordonia*	100	6	0.04	*Achromobacter*	100

Table 2. Relative abundances of dominant bacterial taxa in the bacterial culture before and after enrichment. The relative abundances were estimated from the proportion of classifiable sequences, excluding those sequences that could not be classified below the genus level and 100% homology with the specific bacterial genus.

The *Achromobacter* sp. described in previous research was a facultative chemoautotroph (Hamilton *et al*., 1965; Romanov *et al*., 1977); however, it grew autotrophically with electrochemical reducing power under a CO_2 atmosphere and consumed CO_2 in this study. This result demonstrates that *Achromobacter* sp. grown in the electrochemical bioreactor may be a chemoautotroph capable of fixing CO_2 with the electrochemical reducing power. Meanwhile, various articles have reported that *Alcaligenes* sp. grew autotrophically (Frete and Bowien, 1994; Doyle and Arp. 1987; Leadbeater and Bowien, 1984) or heterotrophically (Reutz *et al*., 1982). According to these articles, *Alcaligenes* spp. are capable of growing autotrophically with a gas mixture of H_2, CO_2, and O_2, as well as heterotrophically under air on a broad variety of organic substrates. *Alcaligenes* spp. metabolically oxidize H_2 to regenerate the reducing power during autotrophic growth under H_2-CO_2 atmosphere (Hogrefe *et al*., 1984). The essential requirement for the autotrophic growth of both *Achromobacter* spp. and *Alcaligenes* spp. under CO_2 atmosphere is to regenerate reducing power in conjunction with metabolic H_2 oxidation, which may be replaced by the electrochemical reducing power on the basis of the results obtained in this research. The electrochemical reducing power required for the cultivation of carbon-dioxide fixing bacteria can be produced completely by the solar panel, by which atmospheric carbon dioxide may be fixed by same system to the photosynthesis.

6. Strategy of atmospheric carbon dioxide fixation using the solar energy

In global ecosystem, land plants, aquatic plants, and photoautotrophic microorganisms produce biomass that is original source of organic compounds (O'Leary, 1988). Autotrophs that are growing naturally or cultivating artificially have fixed the atmospheric carbon dioxide generated by heterotrophs, by which the atmospheric carbon dioxide may be balanced ecologically. However, the carbon dioxide generated from the combustion of organic compounds (petroleum and coal) that are not originated from biomass may be accumulated additionally in the atmosphere, inland water, and sea water. The solar radiation that reaches to the earth may not be limited for photosynthesis of phototrophs or electric generation of solar cells; however, the general habitats for growth of the phototrophs have been decreased by various human activities and the places for installation of the solar cells are limited to the habitats for human. If the solar cells were installed in the natural habitats, phototrophic fixation of carbon dioxide may be decreased in proportion to the electricity generation by the solar cells. The constructions of new cities, farmlands, golf courses, ski resorts, and sport grounds cause to convert the forests to grass field whose ability for carbon dioxide fixation is greatly lower than the forest. Consequently, the plantation of trees and grasses in the habitable lands or cultivation of algae and cyanobacteria in the habitable waters can't be the way to decrease additionally the atmospheric carbon dioxide.

Carbon dioxide has been fixed biologically by photoautotrophic, chemoautotrophic and mixotrophic organisms. The photoautotrophic bacteria assimilate carbon dioxide into organic compounds for cell structures with reducing power regenerated by the solar radiation under atmospheric condition (Kresge et al., 2005). The chemoautotrophs assimilate carbon dioxide into cell structure in coupling with production of methane or acetic acid with reducing power regenerated by hydrogenase under strict anaerobic hydrogen atmosphere (Perreault et al., 2007). The mixotrophs assimilate carbon dioxide into biomolecules with reducing power regenerated in coupling with metabolic oxidation of organic or inorganic compounds (Eiler, 2006). The photoautotrophs, chemoautotrophs, and mixotrophs can reduce metabolically carbon dioxide to organic carbon with the common reducing power (NADH or NADPH), which, however, are regenerated by

different metabolisms. The photoautotrophs, especially cyanobacteria that fix carbon dioxide by completely same metabolism (Calvin cycle) with plants, appear as if they are ideal organism to fix biologically carbon dioxide without chemical energy; however, they are unfavorable to be cultivated in the tank-type bioreactor owing to the limitation of reachable distance of solar radiation in aquatic condition. The chemoautotrophs may be useful to produce methane and acetic acid from carbon dioxide; however, they can grow only in the limit condition of the lower redox potential than -300 mV (vs. NHE) and with hydrogen. The mixotrophs can grow in the condition with electron donors, which are regardless of organic or inorganic compounds, for regeneration of reducing power under aerobic and anaerobic condition. This is the reason why the facultative anaerobic mixotrophs may be more effective than others to fix the atmospheric carbon dioxide directly by simple process. Especially, the cylinder-type electrochemical bioreactor equipped with the built-in anode compartment (Fig 9) is an optimal system for the cultivation or enrichment of facultative anaerobic mixotrophs. Basements of buildings or villages are used generally for maintenances or facilities for wastewater collection, electricity distribution, tap water distribution, and garage. The basements can't be the habitats for cultivation of plants with the natural sun light but can be utilized for cultivation of the carbon dioxide-fixing bacteria with electric energy generated from the solar cells that can be installed on the rooftop as shown in Fig 12.

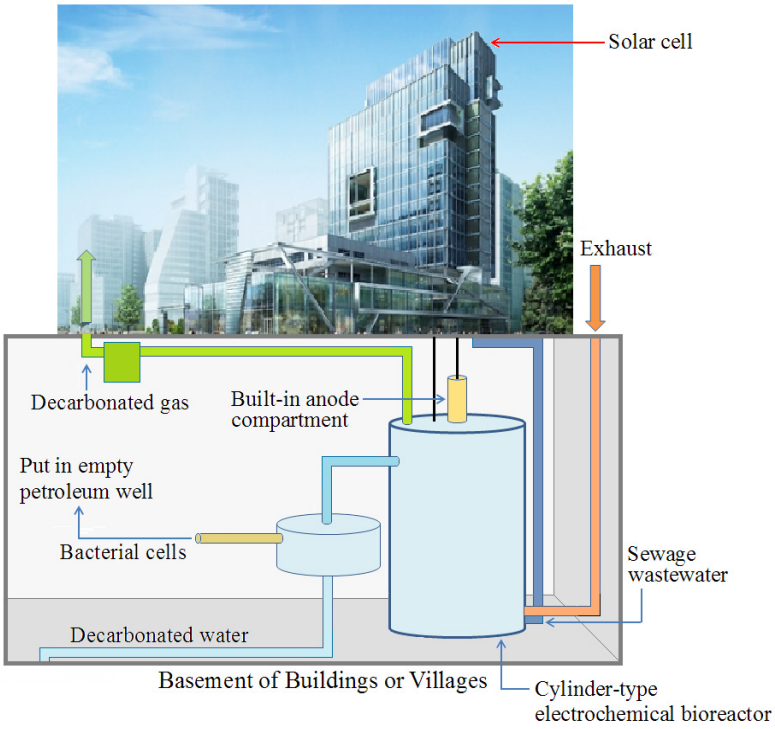

Fig. 12. Schematic structure of the electrochemical bioreactors installed in the building basement. The carbon dioxide-fixing bacteria can be cultivated using the electric energy generated by the solar cells.

The facultative anaerobic mixotrophs assimilate heterotrophically organic compounds contained in the wastewater into the structural compounds of bacterial cells under oxidation condition but autotrophically carbon dioxide into the biomass under condition with high balance of biochemical reducing power ($NADH/NAD^+$). DC electricity generated from the solar cells can be transferred very conveniently to the cylinder-type electrochemical bioreactor without conversion, which is the energy source for increase of biochemical reducing power balance. A part of the atmospheric carbon dioxide has been generated from the combustion system of fossil fuel, which may be required to be return to the empty petroleum well. To store the bacterial cells in the empty petroleum well is to return the carbon dioxide generated from petroleum combustion to the original place. The peptidoglycans, phospholipids, proteins, and nucleic acids that are major ingredients of bacterial cell structures are stable chemically to be stored in the empty petroleum well owing to the non-oxygenic condition. Conclusively, what the atmospheric carbon dioxide originated from the petroleum and coal is returned to the original place again may be best way to decrease the greenhouse effect.

7. Conclusion

The atmospheric carbon dioxide originated from petroleum and coal is required to be completely isolated from the ecological material cycles. The carbons in the ecological system are accumulated as the organic compounds in the organisms and as the carbon dioxide in the atmosphere, which is cycled via the photosynthesis and respiration, especially, plants are the biggest pool for carbon storage. However, the forest and plant-habitable area has been decreased continuously by human activities.

The cultivation of cyanobacteria and single cell algae with solar energy may be the best way to isolated effectively carbon dioxide from atmosphere but is possible in the water pool-type reactor located in the plant-habitable area. In other words, the forests or grass lands may be replaced by the water pools, by which the effect of carbon dioxide fixation has to be decreased. The cyanobacteria and algae can be cultivated in the bioreactor using lamp light operated with electric energy that is generated from solar cells, for which the solar energy has to be converted to electric energy and then converted again to the light energy. These phototrophic microorganisms have been studied actively and applied to produce nutrient sources and pharmacy. The goal for cultivation of the phototrophic microorganisms is to produce the utilizable materials but not to fix carbon dioxide like the agricultural purpose.

The carbon compounds of the organic nutritional compounds contained in the sewage wastewater are the potential carbon dioxide, which may be the useful medium for cultivation of the mixotrophic bacteria capable of fixing carbon dioxide. The maximal balance of anabolism to catabolism is theoretically 0.4 to 0.6 in the mixotrophic bacteria growing with organic carbons as the energy source, in which the carbon dioxide can't be the source for both anabolism and catabolism; however, the balance can be changed by the external energy like the electrochemical reducing power. In the condition with both the organic carbons and the electrochemical reducing power as the energy source, the balance of anabolism to catabolism may be increased to be higher than 0.4 due to the carbon dioxide assimilation that is generated in coupling with the redox reaction of

biochemical reducing power electrochemically regenerated. The electrochemical reducing power can induce regeneration of NADH and ATP, by which both the assimilation of organic carbon and carbon dioxide into bacterial structure compounds can be activated. The goal of cultivation of bacterial cells using the cylinder-type electrochemical is to assimilate the atmospheric carbon dioxide to the organic compounds for bacterial structure without the combustion of fossil fuel and without production of metabolites. Some metabolites that are methane and acetic acid can be generated by the strict anaerobic bacteria under anaerobic hydrogen-carbon dioxide atmosphere but not useful for industrial utility owing to the cost for production. Meanwhile, the methane and acetic acid produced from the organic compounds in the process for treatment of wastewater or waste materials may be useful as the by-product for the industrial utility. The cell size and structural character of bacteria permits to put directly the bacterial cells in the empty petroleum well without any process, by which the atmospheric carbon dioxides are returned to the original place.

8. Acknowledgement

Writing of this chapter was supported by the New & Renewable Energy of the Korea Institute of Energy Technology Evaluation and Planning (KETEP) grant funded by the Korea government Ministry of Knowledge Economy (2010T1001100334)

9. References

Caldwell, D.R. 1995. Microbial physiology and metabolism. Pp. 5-23. Wm. C. Brown Publishers. Oxford. England.

Canadell, J.G., C.R. Quéré, M.R. Raupach, C.B. Field, E.T. Buitenhuis, P. Cialis, T.J. Conway, N.P. Gillett, R.A. Houghton, and G. Marland. 2007. Contributions to accelerating atmospheric CO_2 growth from economic activity, carbon intensity, and efficiency of natural sinks. PNAS 104: 18866-18870.

Cheng, K.Y., G. Ho, and R. Cord-Ruwisch. 2011. Novel methanogenic rotatable bioelectrochemical system operated with polarity inversion. Environ. Sci. Technol. 45: 796-802.

Cox, P.M., R.A. Betts, C.D. Jones, S.A. Spall, and I.J. Totterdell. 2000. Acceleration of global warming due to carbon-cycle feedbacks in a coupled climate model. Nature 4008: 184-187.

Cramer, W., A. Bondeau, S. Schaphoff, W. Lucht, B. Smith, and S. Sitch. 2004. Tropical forests and the global carbon cycle: impacts of atmospheric carbon dioxide, climate change and rate of deforestation. Phil. Trans. R. Soc. Lond. B 359: 331-343.

Dhillon, A., M. Lever, K.G. Lloyd, D.B. Albert, M.L. Sogin, and A. Teske. 2005. Methanogen diversity evidenced by molecular characterization of methyl coenzyme M reductase A (mcrA) genes in hydrothermal sediments of the Suaymas Basin. Appl. Environ. Microbiol. 71: 4592-4601.

Eiler, A. 2006. Evidence for the ubiquity of mixotrophic bacteria in the upper ocean: implications and consequences. Appl. Environ. Microbiol. 72: 7431-7437.

Ferguson, T.J., and R.A. Mah. 1983. Isolation and characterization of an H_2-oxidizing thermophilic methanogen. Appl. Environ. Microbiol. 45: 265-274.

Ferry, J.G. 1993. Methanogenesis: Ecology, Physiology, Biochemistry and Genetics. Chapman & Hall, New York.

Freter, A., and B. Bowien. 1994. Identification of a novel gene, aut. involved in autotrophic growth of *Alcaligenes eutrophus*. J. Bacteriol. 176: 5401-5408.

Friedrich, C., 1982. Derepression of hydrogenase during limitation of electron donor and derepression of ribulosebiophosphate carboxylase during carbon limitation of *Alcaligenes eutrophus*. J. Bacteriol. 149:203-210.

Gerlach, T.M., K.A. McGee, T. Elias, A.J. Sutton, and M.P. Doukas. 2002. Carbon dioxide emission rate of Kilauea volcano: Implications for primary magma and the summit reservoir. J. Geophys. Res. 107:2189-2203.

Gottschalk, G. 1985. Bacterial metabolism, Second Edition, Pp. 252-260. Springer-Verlag, New York.

Grulke, N.E., G.H. Riechers, W.C. Oechel, U. Hjelm, and C. Jaeger. 1990. Carbon balance in tussock tundra under ambient and elevated atmosphere. Oecologia 83: 485-494.

Hamilton, R.R., R.H. Burris, P.W. Wilson, and C.H. Wang. 1965. Pyruvate metabolism, carbon dioxide assimilation, and nitrogen fixation by an *Achromobacter* species. J. Bacteriol. 89:647-653.

Hansen, K. 2008. Water vapor confirmed as major in climate change. News topics from NASA. http://www.nasa.gov/topics/earth/features/vapor_warming.html

Held, I.M., and B.J. Soden. 2000. Water vapor feedback and global warming. Annu. Rev. Energ. Environ. 25: 441-475.

Hogrefe, C., D. Römermann, and B. Friedrich. 1984. *Alcaligenes eutrophus* hydrogenase gene (Hox). J. Bacteriol. 158, 43-48.

Jeon, B.Y., and D.H. Park. 2010. Improvement of ethanol production by electrochemical redox combination of *Zymomonas mobilis* and *Saccharomyces cerevisiae*. J. Microbiol. Biotechnol. 20: 94-100.

Jeon, B.Y., S.Y. Kim, Y.K. Park, and D.H. Park. 2009A. Enrichment of hydrogenotrophic methanogens in coupling with methane production using electrochemical bioreactor. J. Microbiol. Biotechnol. 19: 1665-1671.

Jeon, B.Y., T.S. Hwang, and D.H. Park. 2009B. Electrochemical and biochemical analysis of ethanol fermentation of *Zymomonas mobilis* KCCM11336. J. Microbiol. Biotechnol. 19: 666-674.

Johnson, D.B. 1998. Biodiversity and ecology of acidophilic microorganisms. FEMS Microbiology Ecology 27: 307-317.

Kang, B., and Y.M. Kim. 1999. Cloning and molecular characterization of the genes for carbon monoxide dehydrogenase and localization of molybdopterin, flavin

adenine dinucleotide, and iron-sulfur centers in the enzyme of *Hydrogenophaga pseudoflava*. J. Bacteriol. 181: 5581-5590.

Kang, H.S., B.K. Na, and D.H. Park. 2007. Oxidation of butane to butanol coupled to electrochemical redox reaction of NAD^+/NADH. Biotech. Lett. 29: 1277-1280.

Katsuyama, C., S. Nakaoka, Y. Takeuchi, K. Tago, M. Hayatsu, and K. Kato. 2009. Complementary cooperation between two syntrophic bacteria in pesticide degradation. J. Theoretical Biol. 256: 644-654.

Keeling, C.D., T.P. Whorf, M. Wahlen, and J. Vanderplicht. 1995. Interannual extremes in the rate of rise of atmospheric carbon-dioxide since 1980, Nature. 375: 666-670.

Kiehl, J., T. Kevin, and E. Trenberth. 1997. Earth's annual global mean energy budget. Bulletin of the American Meteological Society 78: 197-208.

Lamed, R.J., J.H. Lobos, and T.M. Su. 1988. Effects of stirring and hydrogen on fermentation products of *Clostridium thermocellum*. Appl. Environ. Microbiol. 54: 1216-1221.

Lashof, D.A., and D.R. Ahuja. 1990. Relative contributions of greenhouse gas emission to global warming. Nature 344: 529-531.

Leadbeater, L., and B. Bowien. 1984. Control autotrophic carbon assimilation *Alcaligenes eutrophus* by inactivation and reaction of phosphoribulokinase. J. Bacteriol. 57: 95-99.

Lee, W.J., and D.H. Park. 2009. Electrochemical activation of nitrate reduction to nitrogen by *Ochrobactrum* sp. G3-1 using a noncompartmetned electrochemical bioreactor. J. Microbiol. Biotechnol. 19: 836-844.

McKane, R.B., E.B. Rastetter, J.M. Melillo, G.R. Shaver, C.S. Hopkinson, D.N. Femandes, D.L. Skole, and W.H. Chomentowski. 1995. Effects of global change on carbon storage in tropical forests of south America. Global Biochemical Cycle 9: 329-350.

Morikawa, M., and T. Imakawa. 1993. Isolation of a new mixotrophic bacterium which can fix aliphatic and aromatic hydrocarbons anaerobically. J. Ferment. Bioengin. 4: 280-283.

Na, B.K., T.K. Hwang, S.H. Lee, D.H. Ju, B.I. Sang, and D.H. Park. 2007. Development of bioreactor for enrichment of chemolithotrophic methanogen and methane production. Kor. J. Microbiol. Biotechnol.. 35: 52-57.

O'Leary, M.H. 1988. Carbon isotopes in photosynthesis. BioScienece 38: 328-336.

Kresge, N., R.D. Simoni, and R.L. Hill. 2005. The discovery of heterotrophic carbon dioxide fixation by Harland G Wood. J. Biol. Chem. 139:365-376.

Ohmura, N., K. Sasaki, N. Matsumoto, and H. Saiki. 2002. Anaerobic respiration using Fe^{3+}, S^o, and H_2 in the chemoautotrophic bacterium *Acidithiobacillus ferroxidans*. J. Bacteriol. 184: 2081-2087.

O'Regan, B., and M. Grätzel. 1991. A low-cost, high-efficiency solar cell based on dye-sensitized colloidal TiO_2 films. Nature 353: 737-740.

Oremland, R.S., R.P. Kiene, I. Mathrani, M.J. Whitica, and D.R. Boone. 1989. Description of an estuarine methylotrophic methanogen which grows on dimethyl sulfide. Appl. Environ. Microbiol. 55: 994-1002.

Park, D.H., and Z.G. Zeikus. 1999. Utilization of electrically reduced neutral red by *Actinobacillus succinogenes*: physiological function of neutral red in membrane-driven fumarate reduction and energy conservation. J. Bacteriol. 181: 2403-2401.

Park, D.H., and J.G. Zeikus. 2000. Electricity generation in microbial fuel cells using neutral red as an electronophore. Appl. Environ. Microbiol. 66:1292-1297.

Park, D.H., and J.G. Zeikus. 2003. Improved fuel cell and electrode designs for producing electricity from microbial degradation. Biotechnol. Bioengin. 81: 348-355.

Park, D.H., B.H. Kim, B. Moore, H.A.O. Hill, M.K. Song, and H.W. Rhee. 1997. Electrode reaction of *Desulforvibrio desulfuricans* modified with organic conductive compounds. Biotech. Technique. 11: 145-148.

Park, D.H., M. Laiveniek, M.V. Guettler, M.K. Jain, and J.G. Zeikus. 1999. Microbial utilization of electrically reduced neutral red as the sole electron donor for growth of metabolite production. Appl. Environ. Microbiol. 2912-2917.

Perreault, N.N., C.W. Greer, D.T. Andersen, S. Tille, G. Lacrampe-Couloume, B. Sherwood, and L.G. Whyte. 2008. Heterotrophic and autotrophic microbial populations in cold perennial springs of the high arctic. Appl. Environ. Microbiol. 74: 6898-6907.

Petty, G.W. 2004. A first course in atmospheric radiation, pp. 29-251, Sundog Publishing.

Pollack, J.D., J. Banzon, K. Donelson, J.G. Tully, J.W. Davis, K.J. Hackett, C. Agbayyim, and R.J. Miles. 1996. Reduction of benzyl viologen distinguishes genera of the class *Mollicute*s. Int. J. System. Bacteriol. 46: 881-884.

Reutz, I., P. Schobert, and B. Bowien. 1982. Effect of phosphoglycerate mutase deficiency on heterotrophic and autotrophic carbon metabolism of *Alcaligenes eutrophus*. J. Bacteriol. 151: 8-14.

Raich, J.W., and W.H. Schlesinger. 2002. The global carbon dioxide flux in soil respiration and its relationship to vegetation and climate. Tellus 44:81-99.

Robertson, G.P., and J.M. Tiejei. 1988. Deforestation alters denitrification in a lowland tropical rain forest. Nature 136: 756-759.

Romanova, A.K., A.V. Nozhevnikova, J.G. Leonthev, and S.A. Alekseeva. 1977. Pathways of assimilation of carbon oxides in *Seliberia carboxydohydrogena* and *Achromobacter carboxydus*. Microbiology 46, 719-722.

Schmidt, G.A., R. Ruedy, R.L. Miller, and A.A. Lacis. 2010. Attribution of the present-day total greenhouse effect. J. Geophys. Res. 115, D20106, doi:10.1029/ 2010JD014287.

Shine, K.P., M. Piers, and de F. Forster. 1999. The effect of human activity on radiative forcing of climate change: a review of recent developments. Global and Planetary Change 20:205-225.

Skirnisdottir, S., G.O. Hreggvidsson, O. Holst, and J.K. Kristjansson. 2001. Isolation and characterization of a mixotrophic sulfur-oxidizing *Thermus scotoductus*. Extremophiles. 5: 45-51.

Skole, D.L., W.A. Salas, and C. Silapathong. 1998. Interannual variation in the terrestrial carbon cycle: significance of Asian tropic forest conversion to imbalanced in the global carbon budget. Pp. 162-186 in J.N Galoway and J.M. Melillo, eds. Asian change in the context of global change. Cambridge: Cambridge University Press.

Stams, A.J.M., and C.M. Plugge. 2009. Electron transfer in syntrophic communities of anaerobic bacteria and archaea. Nature Rev. Microbiol. 7: 568-577.

Stork, N.E. 1977. Measuring global biodiversity and its decline. Pp. 46-68 in M.L. Reaka-Kudia at al., eds. Biodiversity LL: Understanding and protecting our natural resources. Washington, DC: Joseph Henry Press.

Tans, P. 2011. "Trends in atmospheric carbon dioxide". National Oceanic & Atmospheric Administration, Earth system Research Laboratory of Global Monitoring Division. Retrieved 2011-01-19.

Thauer, R.K., K. Jungermann, and K. Decker. 1977. Energy conservation in chemotrophic anaerobic bacteria. Bacteriol. Rev. 41: 100-180.

Tran, H.T., D.H. Kim, S.J. Oh, K. Rasool, D.H. Park, R.H. Zhang, and D.H. Ahn. 2009. Nitrifying biocathode enable effective electricity generation and sustainable wastewater treatment with microbial fuel cell. Water Sci. Technol. 59: 1803-1808.

Van der Bogert, B., W.M. de Vos, E.G. Zoetendal, and M. Kleerevezem. 2011. Microarray analysis and barcoded pyrosequencing provide consistent microbial profiles. Appl. Environ. Microbiol. 77: 2071-2080.

Van Veen, J.A., E. Liljeroth, and J.J.A. Lekkerkerk. 1991. Carbon fluxes in plant-soil systems at elevated atmospheric CO2 levels. Ecol. Appl. 1: 175-181.

Wang, S., and D. Du. 2002. Studies on the electrochemical behavior of hydroquinone at L-cysteine self-assembled monolayers modified gold electrode. Sensors 2: 41-49.

Willems, A., J. Busse, M. Goor, B. Pot, E. Falsen, E. Jantzen, B. Hoste, M. Gillis, K. Kersters, G. Auling, and J. Delay. 1989. *Hydrogenophaga*, a new genus of hydrogen-oxidizing bacteria that includes *Hydrogenophaga flava* comb. nov. (formerly *Pseudomonas flava*). *Hydrogenophaga palleronii* (formerly *Pseudomonas palleroni*), *Hydrogenophaga pseudoflava* (formerly *Pseudomonas pseudoflava* and "*Pseudomonas carboxydoflava*"), and *Hydrogenophaga taeniospiralis* (formerly *Pseudomonas taeniospiralis*). Int. J. Syst. Bacteriol. 39: 319-333.

Williams, S.N., S.J. Schaefer, V.M. Lucia, and D. Lopez. 1992. Global carbon dioxide emission to the atmosphere by volcanoes. Geochim. Cosmochim. Acta. 56: 1765-1770.

Worrell, E., L. Price, N. Martin, C. Hendriks, and L.O. Meida. 2001. Carbon dioxide emissions from the global cement industry. Ann. Rev. Energy Environ. 26: 303-329.

Zeikus, J.G., and R.S. Wolfe. 1972. *Methanobacterium thermoautotrophicum* sp. nov.: An anaerobic autotrophic, extreme thermophile. J. Bacteriol. 109: 707-713.

Zinder, S.H., S.C. Cardwell, T. Anguish, M. Lee, and M. Koch. 1984. Methanogenesis in a thermophilic (58°C) anaerobic digester: *Methanothrix* sp. as an important aceticlastic methanogen. Appl. Environ. Microbiol. 47: 796-807.

10

Semiconductor Superlattice-Based Intermediate-Band Solar Cells

Michal Mruczkiewicz, Jarosław W. Kłos and Maciej Krawczyk
Faculty of Physics, Adam Mickiewicz University, Poznań
Poland

1. Introduction

The efficiency of conversion of the energy of photons into electric power is an important parameter of solar cells. Together with production costs, it will determine the demand for the photovoltaic device and its potential use (Messenger & Ventre, 2004). The design of artificial nanostructures with suitably adjusted properties allows to increase the performance of solar cells. The proposed concepts include, among others, third-generation devices such as tandem cells, hot carrier cells, impurity photovoltaic and intermediate-band cells (Green, 2003). In this chapter we discuss the theoretical model of intermediate-band solar cell (IBSC), the numerical methods of determining the band structure of heterostructures, and the latest reported experimental activities. We calculate the efficiency of IBSCs based on semiconductor superlattices. The detailed balance efficiency is studied versus structural and material parameters. By adjusting these parameters we tailor the band structure to optimize the efficiency.

The background of the concept of IBSC lies in the impurity solar cell concept proposed by (Wolf, 1960) and presented in Fig. 1. The idea was to increase the efficiency by the introduction of intermediate states within a forbidden gap of the semiconductor. This allows the absorption of low-energy photons and causes them to contribute to the generated photocurrent via two-photon absorption. However, as shown experimentally by (Guettler & Queisser, 1970), the introduction of intermediate levels via impurities will create non-radiative recombination centers and cause a degradation of the solar cell efficiency. This effect was studied theoretically by (Würfel, 1993) and (Keevers & Green, 1994), with the conclusion that the introduced impurity levels can increase the efficiency in some cases, but only marginally. However the research in this field is still active and recently the optical transition between CB and IB band in the GaN_xAs_{1-x} alloys was proved experimentally (López et al., 2011; Luque, 2011).

Another, more sophisticated approach to the concept of impurity solar cell was proposed by (Barnham & Duggan, 1990). A further discussion in (Araujo & Martí, 1995), (Luque & Martí, 2001), (Martí et al., 2006) led to the conclusion that the problems related to the impurity states in the solar cell concept might be overcome if the impurities interacted strongly enough to form an impurity band (IB). In such conditions the electron wave functions in the IB are delocalized, causing the radiative recombinations to predominate over the non-radiative ones. The efficiency of the system was described by (Luque & Martí, 1997) on the basis of the extended Shockly-Queisser model (Shockley & Queisser, 1961), the most commonly used

and described in detail in the next section. Many extended versions of the model have been developed, such as that proposed by (Navruz & Saritas, 2008) in a study of the effect of the absorption coefficient, or the model of (Lin et al., 2009), considering the carrier mobility and recombinations.

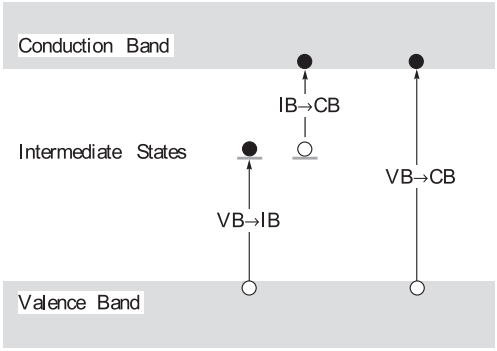

Fig. 1. Model of single-gap solar cell with impurity states introduced. Two possible ways of electron-hole creation are shown: via one-photon absorption in a transition from the valence band to the conduction band (VB→CB), and via two-photon absorption, in which the electron is excited from the valence band to the impurity state (VB→IB) by one photon, and from the impurity state to the conduction band (IB→CB) by another photon.

2. Theoretical model

2.1 Single gap solar cell

Unlike the thermodynamic limits (Landsberg & Tonge, 1980), the limit efficiency considered in the Shockley-Queisser detailed balance model of single-gap solar cell (SGSC) (Shockley & Queisser, 1961) incorporates information on the band structure of the semiconductor and the basic physics. The model includes a number of fundamental assumptions, which allow to evaluate, question and discuss its correctness. All incident photons of energy greater than the energy gap (E_G) of the semiconductor are assumed to participate in the generation of electron-hole pairs. Other assumptions include that no reflection occurs on the surface of the solar cell, the probability of absorption of a photon with energy exceeding the energy gap and creation of electron-hole pair equals one, and so does the probability of collection of the created electron-hole pairs. In the detailed balance model only radiative recombinations between electrons and holes are allowed, by Planck's law proportional to the temperature of the cell. According to this model, all the carriers relax immediately to the band edges in thermal relaxation processes.

The current-voltage equation of the cell under illumination can be written in the following form:

$$J(V) = J_{SC} - J_{Dark}(V), \tag{1}$$

where J_{SC} is the short circuit current, extracted from the cell when its terminals are closed and the load resistance is zero; the short circuit current is independent of the voltage, but depends on the illumination; the dark current J_{Dark} is the current that flows through the p-n

junction under applied voltage, in the case of a solar cell, produced at the terminals of the device under the load resistance R. The detailed balance efficiency is defined as the ratio of the output power P_{out} extracted from the cell to the input power P_{in} of the incident radiation:

$$\eta = \frac{P_{out}}{P_{in}} = \frac{J_m V_m}{P_{in}}, \tag{2}$$

where V_m and J_m is the voltage and current, respectively, that corresponds to the optimal value of the output power.
Both P_{in} and $J(V)$ can be defined in terms of fluxes of absorbed and emitted photons. Let β_s be the incident photon flux, or the number of incident photons per second per square meter received from the sun and the ambient. By Planck's law, describing the blackbody radiation:

$$\beta_s(E) = \frac{2F_s}{h^3c^2} \frac{E^2}{e^{E/k_b T_a} - 1}, \tag{3}$$

where h is the Planck constant, c is the velocity of light, k_b is a Boltzman constant and T_a is a temperature of the ambient. F_s is a geometrical factor determined by the half of the angle subtended by the sunlight:

$$F_s = \pi \sin^2 \frac{\Theta_{sun}}{2}. \tag{4}$$

In all the examples discussed in this chapter the maximum concentration of sunlight, corresponding to $\Theta_{sun} = 180\,^\circ$, is assumed. For that reason there is no need to describe the incident photon flux cming from the ambient and the photon flux described by the equation (3) is the total incident photon flux. The radiation of the sun is coming from all directions. If a flat solar panel receives radiation over a hemisphere, the geometrical factor becomes π, which is equivalent to the cell illuminated with $\Theta_{sun} = 180\,^\circ$.
The input power will be the total energy of all the incident photons:

$$P_{in} = \int_0^\infty E\beta_s(E)\, dE. \tag{5}$$

The short circuit current can be expressed as the elementary charge multiplied by the number of absorbed photons, with the absorption coefficient $a(E)$:

$$J_{SC} = q \int a(E)\beta_s(E)\, dE = q \int_{E_G}^\infty \beta_s(E)\, dE, \tag{6}$$

where the absorption coefficient $a(E)$ (zero for energies lower than the bandgap, one otherwise) determines the lower boundary of the integral.
The dark current is related to the number of photons emitted by the p-n junction:

$$J_{Dark}(V) = q \int e(E)\beta_e(E,V))\, dE, \tag{7}$$

where $e(E)$ is an emission coefficient which describe the probability of the photon emission. The generalized form of Planck's law of blackbody radiation (Landau & Lifshitz, 1980) describes the dependence of the flux β_e of photons emitted by the device on the chemical

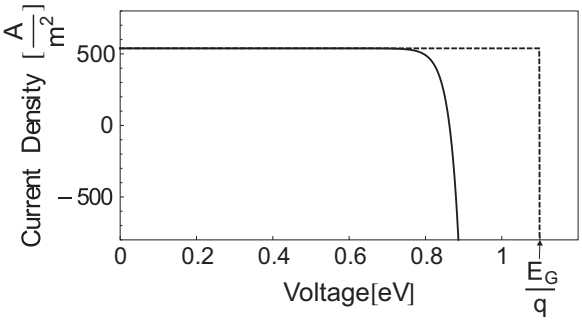

Fig. 2. The current-voltage characteristic of an SGSC with $E_G = 1.1$ eV. The solid and dashed lines represent the $J(V)$ function for a flat cell without concentrators, placed on Earth at a temperature of 300 K and at absolute zero (the temperature corresponding to the ultimate efficiency), respectively.

potential difference, which can be defined by the potential at the terminals:

$$\beta_e(E, \Delta\mu) = \frac{2F_e}{h^3c^2} \frac{E^2}{e^{(E-\Delta\mu)/k_bT_c} - 1}, \tag{8}$$

where T_c is the temperature of the cell, and $\Delta\mu$ is the chemical potential difference defined as the difference of the quasi-Fermi levels (defined in the next Section):

$$\Delta\mu = E_{FC} - E_{FV} = qV. \tag{9}$$

The lower boundary of the integral (7) depends on the emissivity, $e(E)$ (one for energies above E_G, zero otherwise) of the p-n junction, and thus determines the maximum voltage of the junction (the maximum load resistance that can be applied). Above this voltage the device will emit light.
The current-voltage function (1) becomes:

$$J(V) = q \int_{E_G}^{\infty} (\beta_s(E) - \beta_e(E, V))\, dE. \tag{10}$$

Figure 2 presents the current-voltage characteristics of a cell with bandgap E_G at different temperatures. As established above, the maximum voltage (at $T = 0$ K) is determined by E_G. In the limit of $T = 0$ K temperature the value of efficiency achieves its maximum value for the specific solar cell, i.e., the ultimate efficiency.

2.2 Intermediate band solar cells

In this section we will show how to extend the expression (10) to the case of the cell with intermediate band. The model IBSC device, shown in Fig. 3, includes emitters n and p, for separation and extraction of the carriers, and an intermediate band (IB) absorber material placed between them. It is desirable that the IB be thermally separated from the valence band (VB) and the conduction band (CB), so that the number of electrons in the IB can only be changed via photon absorption or emission. This assumption allows to introduce three

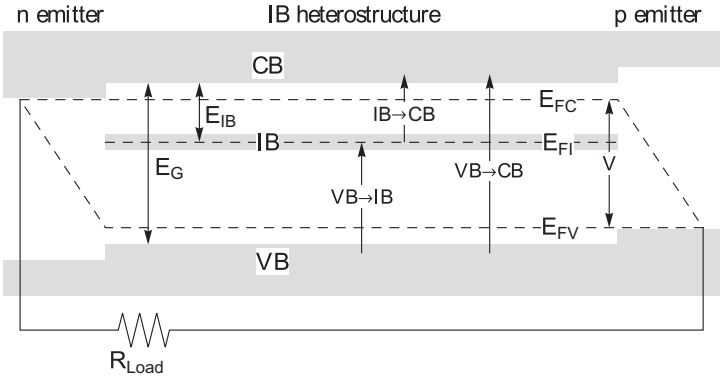

Fig. 3. Model of the band structure of a solar cell with intermediate band. The terminals of the solar cell are connected to the n and p emitters. The possible excitation processes, via one-photon or two-photon absorption, are indicated by arrows. Up down arrows indicate energy differences between band edges.

quasi-Fermi levels, one for each band, to describe the population of electrons within the bands. An infinite mobility of electrons is assumed, to ensure constant quasi-Fermi levels across the junction and minimize the occurrence of non-radiative light traps. The introduction of the IB can improve the efficiency by allowing the absorption of low-energy photons, and thus overcome the problems of the impurity level concept. In Fig. 3 the lowest energy difference between the bands is seen to depend on the value of E_{IB}, the energy difference between the IB and the CB; E_{IB} determines also the threshold energy of the absorbed photons.

In the basic version of the model, the absorption and emission coefficients between each band are assumed to be as presented in Fig. 4. It would probably be more realistic, but still advantageous, to assume that the absorption coefficients corresponding to different transitions are constant, but differ in value. Since the photons that contribute to the transitions between VB and CB predominate in the incident light, the transitions between IB are CB are much weaker that those between VB and IB. According to Martí et al. (2006), the problem has not yet been studied systematically. However, this assumption seems to reflect the behavior of real systems. Thus, the absorption coefficient for different transitions will fulfill the relation:

$$\alpha_{VC} > \alpha_{VI} > \alpha_{IC}. \tag{11}$$

This allows to assume specific values of the absorption coefficients in Fig. 4, but implies that the absorption between IB and CB will be marginal, and so will be the current generated by two-photon absorption.

The assumed form of the absorption and emission functions allows to specify the boundaries of the integrals in the expression for the photon flux absorbed or emitted by the band, analogously to the SGSC model. Three fluxes are distinguished, one for each of the three transitions: VB-CB, VB-IB and IB-CB. Each of the three fluxes contains information on the number of absorbed and emitted photons per unit of time per unit of area:

$$\int_{E_G}^{\infty} \left(\beta_s(E) - \beta_e(E,\mu)\right)\, dE, \tag{12}$$

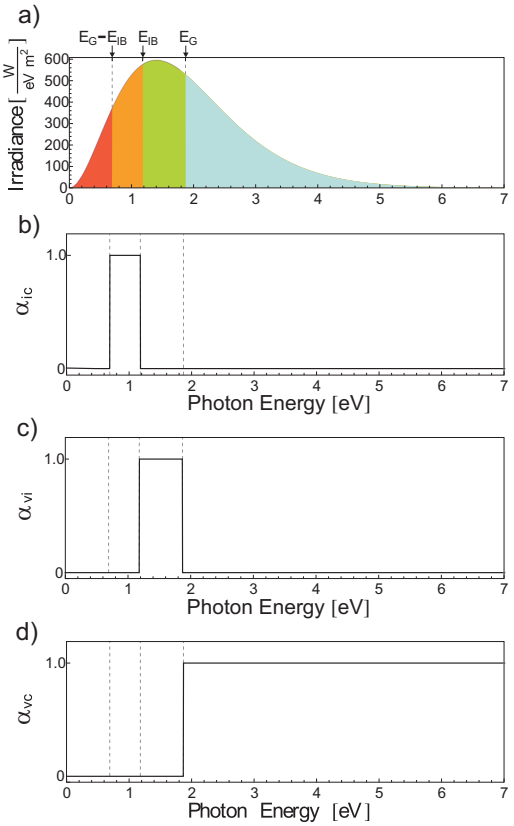

Fig. 4. (a) Radiant emittance of a blackbody at a temperature of 5760 K. Below, plots of the absorption coefficients for (b) IB→CB, (c) VB→IB and (d) VB→CB transitions. The shape of these functions depends on the energy gap and the assumptions made. The depicted forms allow to determine the integral boundaries in equations (12), (13) and (14).

$$\int_{E_G - E_{IB}}^{E_G} \left(\beta_s(E) - \beta_e(E, \mu_1)\right)\, dE, \tag{13}$$

$$\int_{E_{IB}}^{E_G - E_{IB}} \left(\beta_s(E) - \beta_e(E, \mu_2)\right)\, dE, \tag{14}$$

where:

$$\mu_1 = E_{FC} - E_{FI}, \tag{15}$$

$$\mu_2 = E_{FI} - E_{FV}. \tag{16}$$

In the equilibrium state the number of electrons in the IB must be constant, which implies that the increase/decrease due to the VB-IB transition must be equal to the decrease/increase due

to the IB-CB transition:

$$\int_{E_G-E_{IB}}^{E_G} (\beta_s(E) - \beta_e(E,\mu_1))\, dE = \int_{E_{IB}}^{E_G-E_{IB}} (\beta_s(E) - \beta_e(E,\mu_2))\, dE. \tag{17}$$

The separation of the quasi-Fermi levels is determined by the applied load resistance and the voltage produced at the terminals of the solar cell:

$$qV = E_{FC} - E_{FV} = (E_{FC} - E_{FI}) + (E_{FI} - E_{FV}) = \mu_1 + \mu_2. \tag{18}$$

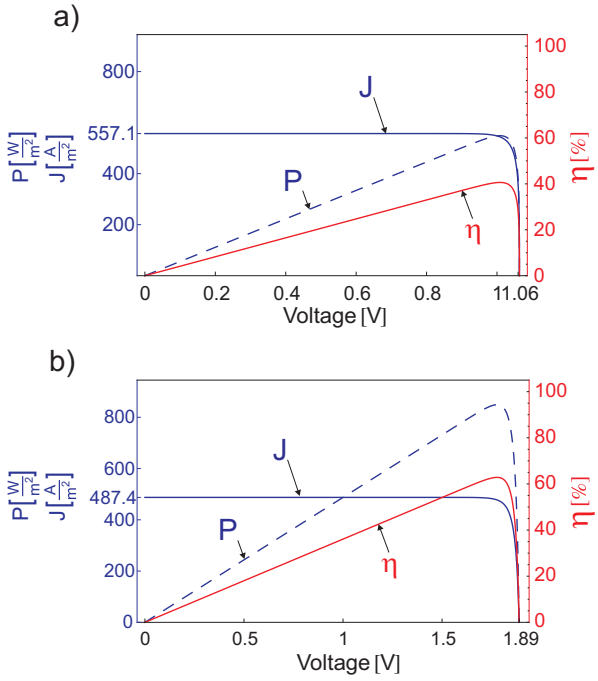

Fig. 5. Voltage dependence of the current density, J, output power P and efficiency η for (a) a single-gap solar cell with $E_G = 1.08$ eV; (b) an intermediate-band solar cell with $E_G = 1.9$ eV, $E_{IB} = 0.69$ eV. The cell has a temperature of 300 K; the incident light is characterized by the blackbody radiation at 5760 K and has a maximum concentration. The band alignment corresponds to the maximum efficiency.

With the last two equations we can calculate the quasi-Fermi level separation for a given voltage (Ekins-Daukees et al., 2005), and thus obtain the current-voltage characteristic. Figure 5 shows the J-V characteristics of (a) an SGSC and (b) an IBSC. The assumed energy gap and intermediate band energy level correspond to the highest possible efficiency of the cell illuminated by sunlight characterized by the 5760 K blackbody radiation, with a maximum concentration. Presented in the same graph, the output power plot shows an increase in efficiency. The short circuit current value is lower in the case of IBSC, but the significant

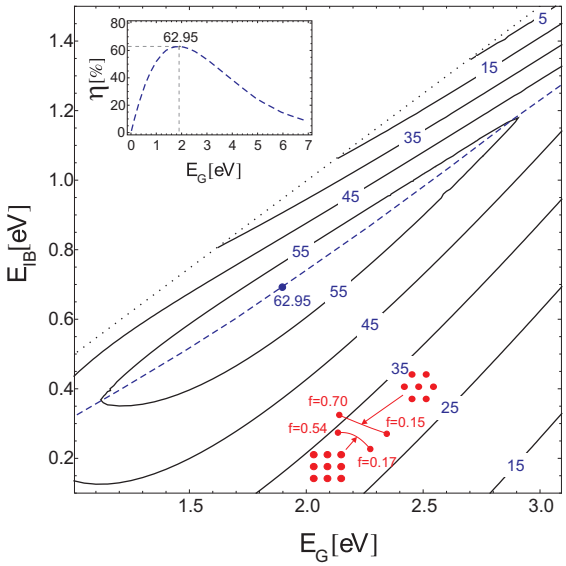

Fig. 6. Contour plot depicting the detailed balance efficiency η versus the energy gap E_G and the distance E_{IB} between the intermediate band bottom and the CB bottom. The values of E_{IB} range from 0 to $\frac{E_G}{2}$. However, according to the model assumed the efficiency is symmetric with respect to E_{IB} in the range from 0 to E_G. the inset in the top-left corner shows the η in dependence on E_G along the dashed line marked in the main figure. The inset shows the changes of E_G, E_I (and η) for AlGaAs supperlattices in dependence on filling fraction (cf. Fig. 11, 12).

increase in the operating voltage leads to a net increase in the efficiency. An explanation of the decrease in the short circuit current in the IBSC (when low-energy photon are absorbed) is provided by Fig. 4, showing the absorption coefficient dependence in the optimal IBSC. The high power absorbed by the cell is seen to contribute to the two-photon processes.
The contour plot in Fig. 6 shows the efficiency versus the bandgap and the distance between IB and CB. These results are important for the understanding of the potential of the IB concept. Later in this chapter they will be compared with simulation data, analyzed in terms of the material parameters used.
If the bandwidth of the solar cell is wider than the distance from the intermediate band to the nearest band, the spectral selectivity might be disturbed. However, these processes are not considered in this chapter. The bandwidth is assumed to only affect the absorption and emission spectra in one of the narrow gaps, changing the boundaries of the integrals in equation (17):

$$\int_{E_G-E_{IB}}^{E_G} (\beta_s(E) - \beta_e(E,\mu_1))\, dE = \int_{E_{IB}-\Delta IB}^{E_G-E_{IB}} (\beta_s(E) - (\beta_e(E,\mu_2))\, dE, \tag{19}$$

where ΔIB is the intermediate band width.

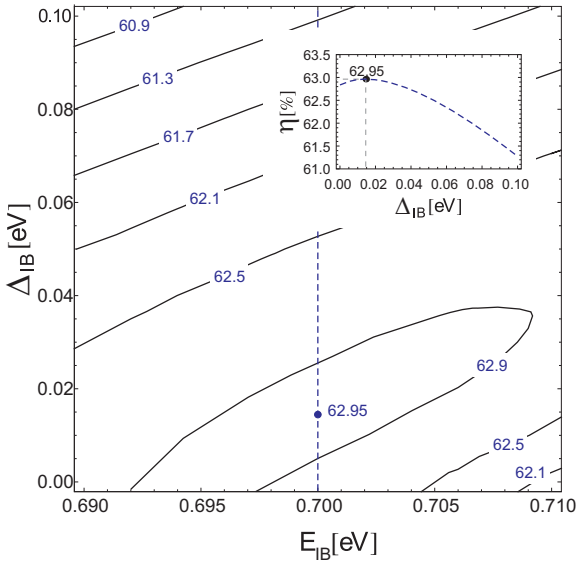

Fig. 7. Detailed balance efficiency of an IBSC with a fixed energy gap $E_G = 1.90$ eV versus the width Δ_{IB} and position E_{IB} of the intermediate band. In the inset, the profile of the efficiency function across the dashed line in the contour plot is shown.

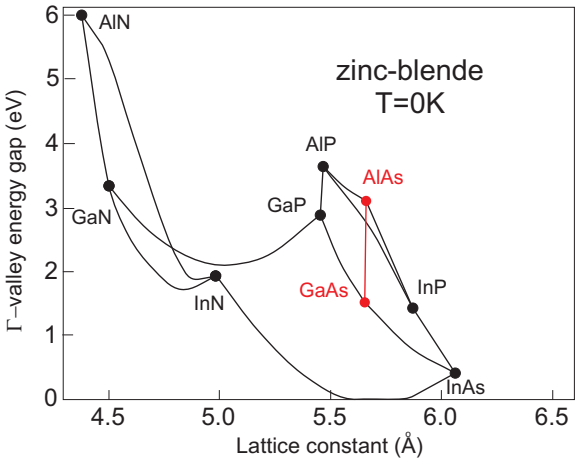

Fig. 8. Energy gap width versus lattice constant for selected III-V group semiconductor compounds. Red line corresponds to the ternary alloy AlGaAs. Note the lattice constant does not change significantly with changing Al concentration in the alloy. (The data have been taken from (Vurgaftman et al., 2001))

In this case an increase in the width of the intermediate band will result in increased absorption, since the gap will shrink. On the other hand, the maximum applicable voltage will decrease with increasing bandwidth, as the emission function will be affected. As shown in Fig. 7, for a fixed energy gap the maximum efficiency may increase. The inset presents the efficiency plotted versus the IB width for energy gap $E_G = 1.90$ eV and intermediate band level $E_{IB} = 0.7$ eV, measured to the top edge of the IB. A maximum is found to occur for $\Delta IB = 0.015$ [eV]; the maximum value is $\eta = 62.96\%$. An improvement by 0.04% is reported in (Green, 2003). An increase by 0.03% is achieved in the cell illuminated by the 6000 K blackbody radiation for $\Delta IB = 0.02$ eV.

3. Calculation of the band structure

We consider a 2D semiconductor superlattice which consists of a periodic array of semiconductor inclusions embedded in a semiconductor matrix. Such a system has an artificially introduced periodicity with a lattice constant much larger than the interatomic distances. As a result of introducing this additional periodicity the conduction and valence bands split into a set of minibands. In this regime of length and energy we can regard the system as continuous on the atomic scale and, in the case of direct gap semiconductors, use the effective parameters describing the position and curvature of the conduction band bottom and the valence band top. Then, the miniband structure of the conduction and valence bands can be calculated with the aid of effective Hamiltonians with spatially dependent effective parameters (Bastart, 1988; Burt, 1999; Califano & Harison, 2000). In the case of semiconductors with a relatively wide gap, such as AlGaAs, the electronic system can be decoupled from the system of light and heavy holes. Also, the stress at the inclusion/matrix interfaces can be neglected in materials of this kind, because of the small atomic lattice constant changes related to the different concentration of Al in the alloy (see Fig. 8). Thus, the simple BenDaniel-Duke Hamiltonian (BenDaniel & Duke, 1966) can be used for electrons in the vicinity of point Γ of the solid semiconductor structure:

$$\left[-\alpha\left(\frac{\partial}{\partial x}\frac{1}{m^*(\boldsymbol{r})}\frac{\partial}{\partial x}+\frac{\partial}{\partial y}\frac{1}{m^*(\boldsymbol{r})}\frac{\partial}{\partial y}+\frac{\partial}{\partial z}\frac{1}{m^*(\boldsymbol{r})}\frac{\partial}{\partial z}\right)+E_C(\boldsymbol{r})\right]\Psi_e(\boldsymbol{r})=E\Psi_e(\boldsymbol{r}), \qquad (20)$$

where $\boldsymbol{r}$ is the position vector in 3D space. The dimensionless constant $\alpha = 10^{-20}\hbar^2/(2m_e e) \approx 3.80998$ (m_e and e are the free electron mass and charge, respectively) allows to express the energy and the spatial coordinates in eV and Å, respectively; m^* is the effective mass of the electron; E_C denotes the conduction band bottom. Both parameters are periodic with the superlattice period:

$$\begin{aligned} m^*(\mathbf{r}+\mathbf{R}) &= m^*(\mathbf{r}),\\ E_C(\mathbf{r}+\mathbf{R}) &= E_C(\mathbf{r}), \end{aligned} \qquad (21)$$

where $\boldsymbol{R}$ is a lattice vector of the superlattice. We have used the following empirical formulae for a linear extrapolation of the material parameter values in GaAs and AlAs to estimate their values in the $Al_xGa_{1-x}As$ matrix: $E_C = 0.944x$ and $m^* = 0.067 + 0.083x$, x is a concentration of the Al in GaAs (Shanabrook et al., 1989; Vurgaftman et al., 2001).
In the case of a zinc blende structure (e.g., AlGaAs) both the light- and heavy-hole bands must be taken into account. The Schrödniger equation for each component of the envelope function

for light-holes, Ψ_{lh} and heavy-holes Ψ_{hh} reads (Datta, 2005):

$$-\begin{pmatrix} \hat{P}+\hat{Q} & 0 & -\hat{S} & \hat{R} \\ 0 & \hat{P}+\hat{Q} & \hat{R}^* & \hat{S}^* \\ -\hat{S}^* & \hat{R} & \hat{P}-\hat{Q} & 0 \\ \hat{R}^* & \hat{S} & 0 & \hat{P}-\hat{Q} \end{pmatrix} \mathbf{\Psi}_h(\boldsymbol{r}) = E\mathbf{\Psi}_h(\boldsymbol{r}), \tag{22}$$

where

$$\mathbf{\Psi}_h(\boldsymbol{r}) = \left(\Psi_{lh\uparrow}(\boldsymbol{r}), \Psi_{lh\downarrow}(\boldsymbol{r}), \Psi_{hh\downarrow}(\boldsymbol{r}), \Psi_{hh\uparrow}(\boldsymbol{r}) \right)^T. \tag{23}$$

The subscripts *lh* and *hh* label the components of the envelope function for the light and heavy holes, respectively. The symbols $\uparrow$ and $\downarrow$ refer to bands related to opposite z components of the light- and heavy-hole spins. The operators $\hat{P}$, $\hat{Q}$, $\hat{R}$ and $\hat{S}$ have the form:

$$\begin{aligned}
\hat{P} &= E_V(\boldsymbol{r}) + \alpha \left(\frac{\partial}{\partial x}\gamma_1(\boldsymbol{r})\frac{\partial}{\partial x} + \frac{\partial}{\partial y}\gamma_1(\boldsymbol{r})\frac{\partial}{\partial y} + \frac{\partial}{\partial z}\gamma_1(\boldsymbol{r})\frac{\partial}{\partial z} \right), \\
\hat{Q} &= \alpha \left(\frac{\partial}{\partial x}\gamma_2(\boldsymbol{r})\frac{\partial}{\partial x} + \frac{\partial}{\partial y}\gamma_2(\boldsymbol{r})\frac{\partial}{\partial y} - 2\frac{\partial}{\partial z}\gamma_2(\boldsymbol{r})\frac{\partial}{\partial z} \right), \\
\hat{R} &= \alpha\sqrt{3}\left[-\left(\frac{\partial}{\partial x}\gamma_2(\boldsymbol{r})\frac{\partial}{\partial x} - \frac{\partial}{\partial y}\gamma_2(\boldsymbol{r})\frac{\partial}{\partial y} \right) + i\left(\frac{\partial}{\partial x}\gamma_3(\boldsymbol{r})\frac{\partial}{\partial y} + \frac{\partial}{\partial y}\gamma_3(\boldsymbol{r})\frac{\partial}{\partial x} \right) \right], \\
\hat{S} &= \alpha\sqrt{3}\left[\left(\frac{\partial}{\partial x}\gamma_3(\boldsymbol{r})\frac{\partial}{\partial z} + \frac{\partial}{\partial z}\gamma_3(\boldsymbol{r})\frac{\partial}{\partial x} \right) - i\left(\frac{\partial}{\partial y}\gamma_3(\boldsymbol{r})\frac{\partial}{\partial z} + \frac{\partial}{\partial z}\gamma_3(\boldsymbol{r})\frac{\partial}{\partial y} \right) \right].
\end{aligned} \tag{24}$$

The Luttinger parameters γ_1, γ_2, γ_3, describe, the effective masses $1/(\gamma_1+\gamma_2)$ and $1/(\gamma_1-\gamma_2)$ of light and heavy holes near point Γ of the atomic lattice are, like the position of the valence band top E_V, periodic in the superlattice structure:

$$\begin{aligned}
\gamma_\beta(\mathbf{r}+\mathbf{R}) &= \gamma_\beta(\mathbf{r}), \\
E_V(\mathbf{r}+\mathbf{R}) &= E_V(\mathbf{r}),
\end{aligned} \tag{25}$$

where the subscript β is $1, 2$ or 3. For periodic heterostructures consisting of a triangular or square lattice-based system of GaAs rods embedded in $Al_xGa_{1-x}As$, the following material parameter values, dependent on the concentration of Al in aluminium gallium arsenide, can be assumed (Shanabrook et al., 1989; Vurgaftman et al., 2001):

$$\begin{aligned}
E_V &= 1.519 + 0.75x, \\
\gamma_1 &= 6.85 - 3.40x, \\
\gamma_2 &= 2.10 - 1.42x, \\
\gamma_3 &= 2.90 - 1.61x.
\end{aligned} \tag{26}$$

We are interested in the calculation of the spectra of a finite-thickness periodic layer of inclusions (see Fig. 9). In such superlattices, when the superlattice period and the layer thickness are of the order of a few nanometers the lowest miniband within the CB is detached from the other CB minibands. Moreover, the higher CB minibands overlap to form a continuous energy range without minigaps.

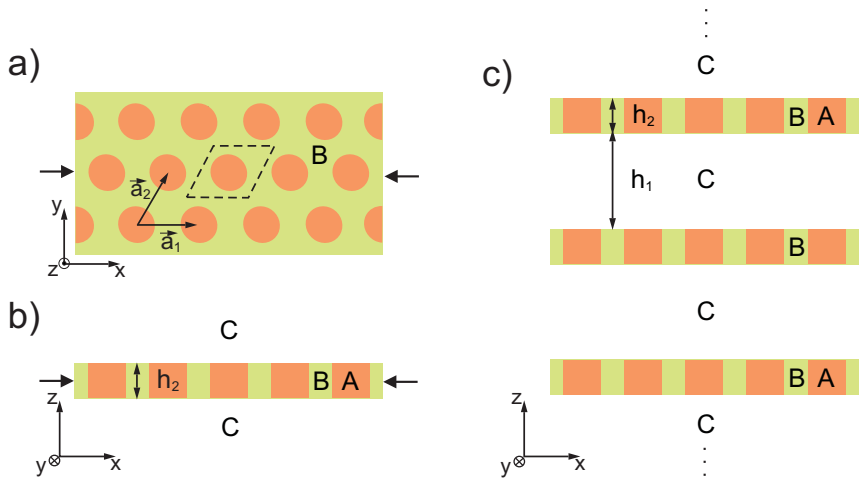

Fig. 9. Structure of a periodic slab with inclusions in triangular lattice, (a) top and (b) side view. Letters A, B and C denote the inclusion, matrix and spacer materials, respectively. The arrows indicate the cross-section plane. Dashed parallelogram in (a) delimits the unit cell, which reproduces the whole plane when translated by superlattice vectors $\boldsymbol{a}_1$ and $\boldsymbol{a}_1$. (c) The supercell structure used in the plane wave method: an infinite stack of replicas of the periodic slab.

In the VB all the minibands overlap or are separated by extremely narrow minigaps. Let us assume for simplicity that the total spectrum can by approximated by the model with a single gap (delimited by the top of the highest VB miniband and the bottom of the block of higher CB minibands) and a single intermediate band formed by the first (lowest) CB miniband. This simplification allows us to calculate the detailed balance efficiency of solar energy conversion for a superlattice-based solar cell using the model with a single intermediate band within the gap.

3.1 Plane wave method

We have calculated the band structure of electrons and holes by the plane wave method (PWM), a technique successfully applied to studying the electronic states in semiconductor heterostructures with quantum dots and wires of different shape and size, as well as interdiffusion and strain effects on electronic bands (Cusack et al., 1996; Gershoni et al., 1988; Li & Zhu, 1998; Li et al., 2005; Ngo et al., 2006; Tkach et al., 2000). By Fourier-expanding the spatially dependent structural parameters: m^*, γ_β, E_C, E_V, and the electron and hole envelope functions the differential equations (20) and (22) can be transformed to a set of algebraic equations for the Fourier coefficients of the envelope functions. This set of equations has the form of an eigenvalue problem with eigenvalues being the energies of successive minibands for the selected wave vector.

The PWM can only be applied to periodic systems. The structure under consideration is finite in one direction, though. To adopt the method to the case considered we calculate the spectrum of an infinite stack of weakly coupled periodic layers, as presented in Fig. 9(c). If

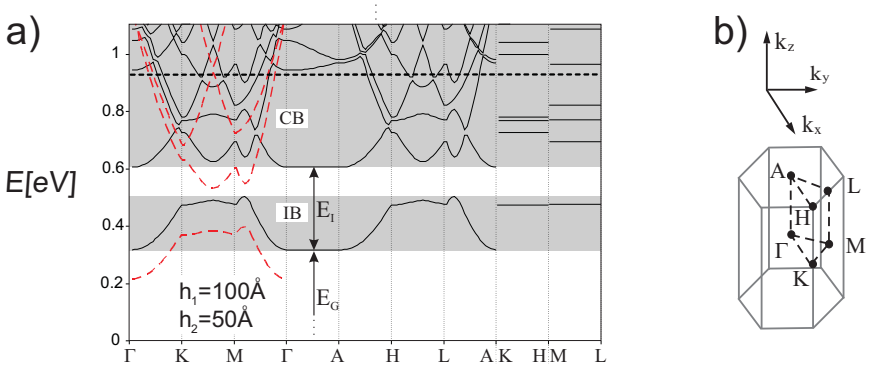

Fig. 10. (a) Electronic minibands in the structure presented in Fig. 9, with GaAs cylinders (material A) embedded in $Al_{0.35}Ga_{0.65}As$ slabs (B) separated by an AlAs spacer (C). Red dashed line represents bands in a 2D superlattice formed by an array of infinitely long rods (i.e., for $k_z = 0$). For a sufficiently thick spacer layer the minigaps are dispersionless in the z direction (lines K-H and M-L in the Brillouin zone shown in (b)). This proves a good separation of the periodic slabs. The calculations were performed for a superlattice with lattice constant a = 50 Å and filling fraction $f = 0.3$. The reference energy level $E = 0$ eV corresponds to the CB bottom in solid GaAs. The slab thickness h_2 is 50 Å and the AlAs spacer thickness h_1 is 100 Å.

the distance between adjacent layers is large and the potential in the spacer material C forms a high barrier both for electrons and holes, the spectrum of the system is very close to that of a single isolated layer (Rodríguez-Bolívar et al., 2011).
Figure 10(a) shows the electronic spectrum of the structure presented in Fig. 9, with circular GaAs rods embedded in AlGaAs slabs. Adjacent GaAs/AlGaAs slabs are separated by an AlAs spacer, relatively thick and with a high potential to ensure a good separation of the periodic slabs. This is reflected in the flat dispersion in the z direction (high-symmetry lines K-H, M-L, Γ-A) and the repeated shape of the dispersion branches $\Gamma - K - M - \Gamma$ and $A - H - L - A$. Thus, the case considered proves equivalent to that of a single periodic slab. In the considered range of structural parameter values the electronic spectrum includes one clearly detached miniband and a continuous block of minibands above it. The VB minibands (not shown in Fig. 10) overlap. Thus, the model with a single intermediate band (formed by the first CB miniband) within the energy gap (between the VB and the block of CB minibands) can be used for the calculation of the detailed balance efficiency.

4. Detailed balance efficiency of periodic semiconductor slab

We calculate the electronic and hole spectra of periodic semiconductor layers with different filling fraction values. The filling fraction is defined as the ratio of the in-plane cross-section S_{inc} of the inclusion to the area S of the unit cell area:

$$f = \frac{S_{inc}}{S}. \tag{27}$$

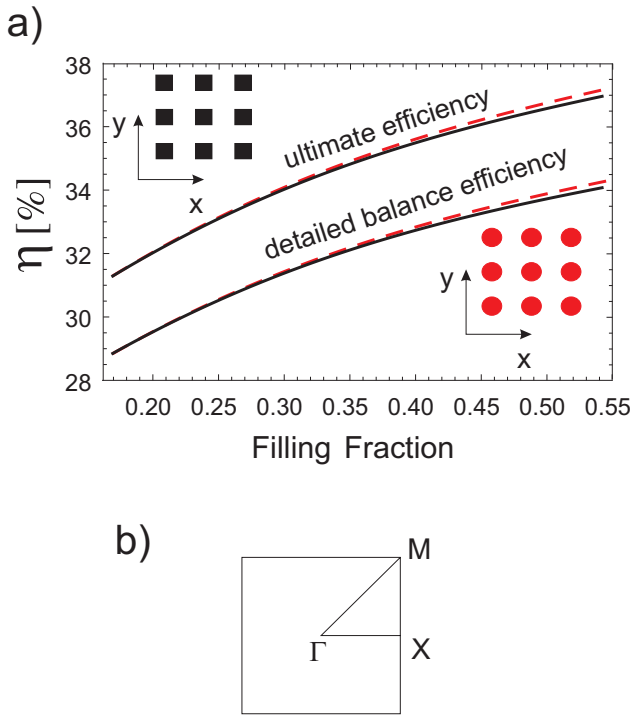

Fig. 11. (a) Detailed balance efficiency and ultimate efficiency of solar energy conversion versus filling fraction for a slab (of thickness h_2=50Å) with cylinders (dashed red line) and square prisms (solid black line) arranged in a square lattice (the lattice constant of the superlattice is $a = 50$ Å). The inclusion, slab and spacer materials are GaAs, $Al_{0.35}Ga_{0.65}As$ and AlAs, respectively. (b) The high-symmetry line in the first Brillouin zone used in the search of absolute minigaps.

We consider two shapes of the inclusions: cylinders and square prisms, and two lattices: the square and triangular lattice. Thus, four combinations of the system geometry are possible. For each combination we calculate the position and width of the valence and conduction bands versus the filling fraction. The following parameters of the band structure are extracted from the calculations:

- the width of the energy gap E_G between the top of the VB and the bottom of the block of CB minibands,
- the shift E_I between the bottom of the first CB miniband and the bottom of the block of higher CB minibands,
- the width ΔE_I of the intermediate band (the first CB miniband).

All three parameters are used in the calculation of the detailed balance efficiency of solar energy conversion for four geometries mentioned above.

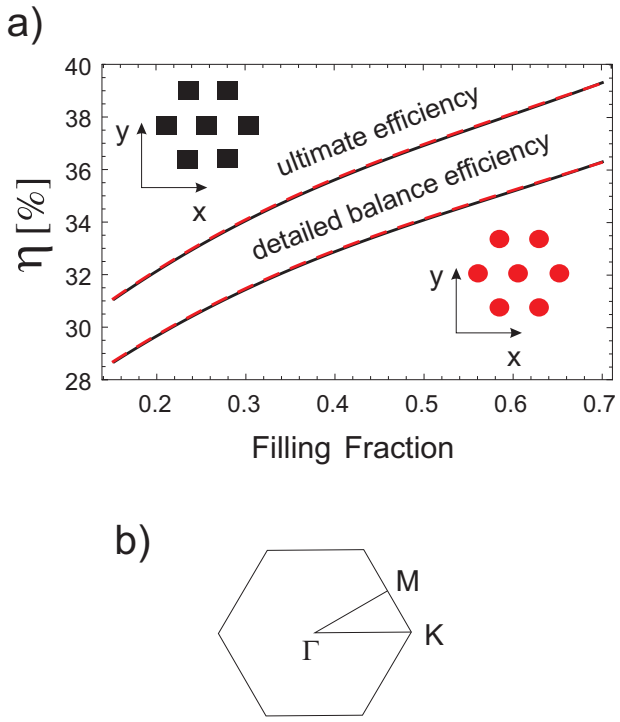

Fig. 12. (a) Detailed balance efficiency and ultimate efficiency of solar energy conversion versus filling fraction for a slab (of thickness h_2=50Å) with cylinders (dashed red line) and square prisms (solid black line) arranged in a triangular lattice (the lattice constant of the superlattice is $a = 50$ Å). The inclusion, slab and spacer materials are GaAs, $Al_{0.35}Ga_{0.65}As$ and AlAs, respectively. (b) The high-symmetry line in the first Brillouin zone used in the search of absolute minigaps.

The lattice constant of the superlattice is fixed at $a = 50$ Å. The assumed thickness of the periodic slab is $h_2 = 50$ Å. A maximum efficiency can be observed in this size range, with the thickness of the periodic slab comparable to the lattice constant of the superlattice. The inclusion and matrix materials are GaAs and $Al_{0.35}Ga_{0.65}As$, respectively. A thick AlAs spacer (of thickness $h_1 = 100$Å) ensures a good separation of adjacent periodic slabs in the PWM supercell calculations. We used $15x15x15$ and $13x13x13$ plane waves in the calculations of the electronic and hole spectra, respectively.

Figures 11(a) and 12(a) present the calculated ultimate efficiency and detailed balance efficiency versus filling fraction. To investigate the width of the absolute minibands/minigaps we calculated the electronic and hole spectra along the high-symmetry lines shown in Figs.11(b) and 12(b) for square and triangular lattices. The assumed upper bound of ≈ 0.7 of the filling fraction range in Fig. 12 (triangular lattice) corresponds to the maximum filling fraction values, or touching adjacent inclusions, in the considered structures: 0.68 for

cylindrical inclusions and 0.86 for inclusions in the shape of square prism. The upper limit of filling fraction for square lattice $\approx$ 0.55 in Fig. 11 results form minibands crossing (and disappearing of the minigap between the lowest conduction miniband and the rest of the minibands in CB) for higher values of f. The lower limit of the filling fraction, $f = 0.15$, is assumed for accuracy of the results obtained by the PWM. A good convergence of results is achieved for intermediate filling fraction values (far from 0 and 1).
The shape of the inclusions is seen to play no important role as long as the filling fraction value is kept. This is evidenced by the overlapping of the solid black and dashed red lines, referring to structures with square prisms and cylinders, respectively, in Figs. 11 and 12. Only in the square lattice case, a minor difference in the efficiency is seen to occur due to the inclusion shape in the range of larger filling fraction values.
Crucial for the efficiency are the lattice symmetry and the filling fraction. In the considered structures the efficiency tends to be higher in the case of the triangular lattice. The maximum values of ultimate (detailed balance) efficiency, 39.5% (35.5%) for the triangular lattice, are reached for large filling fraction values, corresponding to inclusions getting in touch. For this lattice type the efficiency grows monotonically with increasing filling fraction. In the case of the square lattice the filling fraction dependence of the ultimate (detailed balance) efficiency has a maximum of 37% (34%) for filling fraction value $f \approx 0.55$ for which the band crossing appears. For both lattice types the efficiency changes more rapidly in the range of low filling fraction values.
The change of filling fraction affects on the band structure and the values of E_G and E_I parameters which determine the efficiency of solar energy conversion in the supperlatice based solar cell. In the inset in Fig. 6 the detailed balance efficiency as a function of E_G and E_I was plotted (see the curves marked in red) for considered structures. We showed the results for systems with circular inclusions only because the week dependence of η on the inclusion shape. One can notice that the structure (or material) more suitable for solar cell application than the considers supperlattices has to poses slightly smaller energy gap E_G and much bigger separation between IB and CB, E_I. It is evident (see Fig. 8) that materials with better values of the energy gap can be chosen, e.g., InAs/GaAs (Jolley et al., 2010; Zhou et al., 2010) where the lattice mismatch between compounds induces stress which modify the band structure (39% detailed balance efficiency is predicted (Tomić, 2010), other compounds form III-V group ($InAs/Al_xGa_{1-x}As$, $InAs_{1-x}N_y/AlAs_xSb_{1-x}$, and $InAs_{1-z}N_z/Al_x[Ga_yIn_{1-y}]_{1-x}P$) where 60% detailed balance efficiency at maximum gap concentration where recently calculated (Linares et al., 2011).

5. Experiments

One of the first important experiments related directly to the concept of IBSC was the study by Luque et al. (2005), in which two main operating principles required from the IBSC (the production of photocurrent from photons of energy below the bandgap and the occurrence of three separate quasi-Fermi levels) were confirmed by measurements of quantum efficiency and electroluminescence. In the paper Martí et al. (2006) claim they demonstrate for the first time the production of photocurrent with a simultaneous absorption of two sub-bandgap energy photons, and prove the possibility of obtaining the photocurrent by two-photon absorption processes in InAs/(Al,Ga)As quantum dot (QD) structures.

Although the first experiments prove the possibility of photocurrent production by two-photon absorption, many obstacles still prevent the achievement of satisfactory performance. In another study, Martí et al. (2007) demonstrate that strain-induced dislocations can propagate from the QD region to the p emitter, resulting in a decrease in the minority carrier lifetime and, consequently, reducing the efficiency. Most of the conclusions drawn from the recent experiments point out the common problem of decrease in open-circuit voltage. These effects are investigated in Jolley et al. (2010).

6. Conclusions

We have examined thoroughly the effect of the (super)lattice symmetry and the cross-sectional shape of the rods on the efficiency of the solar cells based on thin slabs of quantum wire arrays by comparing structures consisting of GaAs cylinders or square prisms, embedded in $Al_xGa_{1-x}As$ and disposed in sites of square or triangular lattice. We show the gain in efficiency of semiconductor slabs with 2D periodicity in comparison with the efficiency of monolithic semiconductors (with a single bandgap). The key role in the gain of efficiency is played by the lowest conduction miniband, which, detached from the overlapping conduction minibands, acts as an intermediate band that opens an extra channel for carrier transitions between the valence band and the conduction band. Another parameter of vital importance for the efficiency of solar-energy conversion is the distance between the top of the highest valence miniband and the bottom of the overlapping conduction minibands. This distance, determines the energy of utilized carriers. Even though the obtained values of the width of the minigap are not optimal to obtain maximal efficiency (Bremner et al., 2009; Luque & Martí, 1997; Shao et al., 2007), the increase in efficiency is significant as compared to the bulk solar cells (Kłos & Krawczyk, 2009). The impact of the discretisation of the valence band on the efficiency of the photovoltaic effect is be much lesser than that of the discretisation of the conduction band, and, in the first approximation, can be regarded as limited to a shift in valence band top in the evaluation of solar cell efficiency (Kłos & Krawczyk, 2009).

7. References

Araujo, G. L. & Martí, A., (1995). Electroluminescence coupling in multiple quantum well diodes and solar cells, *Appl. Phys. Lett.* Vol. 66: 894Ű895.

Ashcroft, N. W. & Mermin, D. N., (1976) *Solid State Physics*, Saunders Collage Publishing.

Barnham, K. W. J. & Duggan, G., (1990). A new approach to high-efficiency multi-band-gap solar cells, *J. Appl. Phys.* Vol. 67: 3490-3493.

Bastard, G. (1988). *Wave Mechanics Applied to Semiconductor Heterostructures*, Les editions de Physique, Paris.

BenDaniel, D. J. & Duke, C. B. (1966). Space-charge effects on electron tunneling, *Phys. Rev.* Vol. 152: 683-692.

Bremner, S. P., Levy, M. Y. & Honsberg, C.B. (2009). Limiting efficiency of an intermediate band solar cell under a terrestrial spectrum, *Appl. Phys. Lett.* Vol. 92: 171110-1-3.

Burt, M.G. (1999). Fundamentals of envelope function theory for electronic states and photonic modes in nanostructures, *J. Phys.: Condens. Matter* Vol. 11, R53-R83.

Califano, M. & Harison, P. (2000). Presentation and experimental validation of a single-band, constant-potential model for self-assembled InAs/GaAs quantum dots, *Phys. Rev. B* Vol. 61: 10959-10965.

Cusack, M. A., Briddon, P. R. & Jaros, M. (1996). Electronic structure of InAs/GaAs self-assembled quantum dots, *Phys. Rev. B* Vol. 54: R2300-R2303.

Datta, S. (2005). *Quantum Transport: Atom to Transistor*, Cambridge University Press, Cambridge.

Ekins-Daukes, N. J., Honsberg, C. B. & Yamaguchi M., (2005). Signature of intermediate band materials from luminescence measurements, *Presented at the 31st IEEE Photovoltaic Specialists Conference*.

Gershoni, D., Temkin, H., Dolan, G. J., Dunsmuir, J., Chu, S. N. G. & Panish, M. B. (1988). Effects of two-dimensional confinement on the optical properties of InGaAs/InP quantum wire structures, *Appl. Phys. Lett.* Vol. 53: 995-997.

Green, M. A. (2003). *Third Generation Photovoltaics: Advanced Solar Energy Conversion*, Springer-Verlag, Berlin.

Guettler, G. & Queisser, H. J. (1970). Impurity photovoltaic effect in silicon, *Energy. Conversion* Vol. 10(2): 51-5.

Jolley, G., Lu, H. F., Fu, L., Tan, H. H. & Jagadish, C. (2010). Electron-hole recombination properties of $In_{0.5}Ga_{0.5}As$/GaAs quantum dot solar cells and the influence on the open circuit voltage, *Appl. Phys. Lett.* Vol. 97: 123505-1-3.

Keevers, M.J. & Green, M.A., (1994). Efficiency improvements of silicon solar cells by the impurity photovoltaic effect, *J. Appl. Phys.* Vol. 75: 4022-4031.

Kłos, J. W. & Krawczyk, M., (2009). Two-dimensional GaAs/AlGaAs superlattice structures for solar cell applications: Ultimate efficiency estimation, *J. Appl. Phys.* Vol. 106: 093703-1-9.

Kłos, J. W. & Krawczyk, M., (2010). Electronic and hole spectra of layered systems of cylindrical rod arrays: aolar cell application, *J. Appl. Phys.* Vol. 107: 043706-1-5.

Krawczyk, M. & Kłos, J. W., (2010). Electronic and hole minibands in quantum wire arrays of different crystallographic structure, *Physics Letters A* Vol. 374: 647-654.

Landau, L.D. & Lifshitz, E.M., (1980). *Statistical Physics*, Part 1. Vol. 5 (3rd ed.). Butterworth-Heinemann.

Landsberg, P. T. & Tonge, G. (1980). Thermodynamic energy conversion efficiencies, *J. Appl. Phys.* 51: R1-R20.

Li, S.-S. & Zhu, B.-F. (1998). Electronic structures of GaAs/AlAs lateral superlattices, *J. Phys.: Condend. Matter* Vol. 10: 6311-6319.

Li, S.-S., Chang, K. & Xia, J.-B. (2005). Effective-mass theory for hierarchical self-assembly of GaAs/$Al_xGa_{1-x}As$ quantum dots, *Phys. Rev. B* Vol. 71: 155301-1-7.

Lin, A. S., Wang, W. & Phillips, J. D., (2009). Model for intermediate band solar cells incorporating carrier transporta and recombination, *J. Appl. Phys.* Vol. 105: 064512-1-8.

Linares, P. G., Martí, A., Antolín, E. & Luque , A. (2011). III-V compound semiconductor screening for implementing quantum dot intermediate band solar cells, *J. Appl. Phys.* Vol. 109: 014313-1-8.

López, N., Reichertz, L. A., Yu, K. M., Campman, K. & Walukiewicz, W. (2011). Engineering the electronic band structure for multiband solar cells, *Phys. Rev. Lett.* Vol. 106: 028701-1-4.

Luque, A. & Martí, A. (1997). Increasing the efficiency of ideal solar cells by photon induced transitions at intermediate levels, *Phys. Rev. Lett* Vol. 78: 5014-5018.

Luque, A. & Martí, A., (2001). A metallic intermediate band high efficiency solar cell, *Prog. Photovolt. Res. Appl.* Vol. 9(2): 73-86.

Luque, A., Martí, A., López, N., Antolín, E., Cánovas, E., Stanley, C., Farmer, C., Caballero, L. J., Cuadra, L. & Balenzategui, J. L., (2005). Experimental analysis of the quasi-Fermi level split in quantum dot intermediate-band solar cells, *Appl. Phys. Lett.* Vol. 87: 083505-1-3.

Luque, A. & Martí, A., (2011). Towards the intermediate band, *Nature Photonics* Vol. 5: 137-138.

Martí, A., López, N., Antolín, E., Cánovas, E., Stanley, C., Farmer, C., Cuadra, L. & Luque, A., (2006). Novel semiconductor solar cell structures: The quantum dot intermediate band solar cell, *Thin Solid Films* Vol. 511-512: 638-644.

Martí, A., Antolín, E., Stanley, C., Farmer, C., López, N., Díaz, P., Cánovas, E., Linares, P. G. & Luque, A., (2006). Production of photocurrent due to intermediate-to-conduction-band transitions: a demonstration of a key operating principle of the intermediate-band solar cell, *Phys. Rev. Lett.* Vol. 97: 247701-1-4.

Martí, A., López, N., Antolín, E., Cánovas, E., Luque, A., Stanley, C., Farmer, C. & Díaz, P., (2007). Emitter degradation in quantum dot intermediate band solar cells, *Appl. Phys. Lett.* Vol. 90: 233510-1-3.

Messenger, R. A. & Ventre, J. (2004). *Photovoltaic Systems Engineering*, CRC Press, Florida.

Navruz, T. S. & Saritas, M., (2008). Efficiency variation of the intermediate band solar cell due to the overlap between absorption coefficients, *Solar Energy Materials & Solar Cells* Vol. 92: 273-282

Nelson, J. (2003). *The Physics of Solar Cells*, Imperial College, UK.

Ngo, C. Y., Yoon, S. F., Fan, W. J. & Chua, S. J. (2006). Effects of size and shape on electronic states of quantum dots, *Phys. Rev. B* Vol. 74: 245331-1-10.

Rodríguez-Bolívar, S., Gómez-Campos, F. M., Luque-Rodríguez, A., López-Villanueva, J. A., Jiménez-Tejada, J. A. & Carceller, J. E. (2011). Miniband structure and photon absorption in regimented quantum dot systems, *J. Appl. Phys.* Vol. 109: 074303-1-7.

Shanabrook, B. V., Glembocki, O. J., Broido, D. A. & Wang, W. I. (1989). Luttinger parameters for GaAs determined from the intersubband transitions in GaAs/$Al_xGa_{1-x}As$ multiple quantum wells, *Phys. Rev. B* Vol. 39: 3411-3414.

Shao, Q., Balandin, A. A., Fedoseyev, A. I. & Turowski, M. (2007). Intermediate-band solar cells based on quantum dot supracrystals, *Appl. Phys. Lett.* Vol. 91: 163503-1-3.

Shockley, W. & Queisser, H. J. (1961). Detailed balance limit of efficiency of p-n junction solar cells, *J. Appl. Phys.* Vol. 32, 510-519.

Tkach, N. V., Makhanets, A. M. & Zegrya, G. G. (2000). Energy spectrum of electron in quasiplane superlattice of cylindrical quantum dots, *Semicond. Sci. Technol.* Vol. 15: 395-398.

Tomić, S. (2010). Intermediate-band solar cells: Influence of band formation on dynamical processes in InAs/GaAs quantum dot arrays, *Phys. Rev. B* Vol. 82: 195321-1-15.

Vurgaftman, I., Meyer, J. R. & Ram-Mohan, L. R. (2001). Band parameters for III-V compound semiconductors and their alloys, *J. Appl. Phys.* Vol. 89: 5815-5875.

Wolf, M. (1960). Limitations and possibilities for improvements of photovoltaic solar energy converters, *Proc. IRE* Vol. 48: 1246-1263.

Würfel, P. (1993). Limiting efficiency for solar cells with defects from a three-level model, *Sol. Energy Mater. Sol. Cells* Vol. 29: 403-413.

Zhou, D., Sharma, G., Thomassen, S. F., Reenaas, T. W. & Fimland, B. O. (2010). Optimization towards high density quantum dots for intermediate band solar cells grown by molecular beam epitaxy, *Appl. Phys. Lett.* Vol. 96: 061913-1-3.

11

Solar to Chemical Conversion Using Metal Nanoparticle Modified Low-Cost Silicon Photoelectrode

Shinji Yae
University of Hyogo
Japan

1. Introduction

The storage of solar energy is one of the key technologies in making solar energy a major energy resource for humans (Turner et al., 2004). Solar hydrogen, which is produced by splitting water using solar energy, can be considered the perfect renewable energy. Hydrogen is an energy medium that can be easily stored and transported. It can generate not only thermal energy but also electricity using fuel cells and mechanical energy using hydrogen engines. Hydrogen returns to water via such energy generation. Therefore, solar hydrogen can form the basis of a clean, renewable energy cycle.

1.1 Solar hydrogen production with photoelectrochemical solar cells

Solar hydrogen production, that is, water splitting by photoelectrochemical solar cells equipped with a titanium dioxide (TiO_2) photoelectrode has been attracting much attention since Fujishima and Honda's report in 1972 (Fujishima & Honda, 1972). Photoelectrochemical solar cells have important and unique features (Licht, 2002, Nakato, 2000). They are fabricated simply by immersing a semiconductor electrode and a counterelectrode into an electrolyte solution (Fig. 1). They can convert solar energy not only to electricity (Fig. 1a) but also directly to storable chemical energy (Figs. 1b and 2) such as water splitting into hydrogen and oxygen (Arakawa et al., 2007, Fujishima & Honda, 1972, Grätzel, 1999, Khaselev & Turner, 1998, Lin et al., 1998, Miller et al., 2005, Park & Bard, 2005, Sakai et al., 1988), the decomposition of hydrogen iodide into hydrogen and iodine (Nakato et al., 1998, Nakato, 2000, Takabayashi et al., 2004, 2006), and the reduction of carbon dioxide to hydrocarbons or carbon monoxide (Hinogami et al., 1997, 1998). For the photovoltaic photoelectrochemical solar cell (Fig. 1a), two electrodes are immersed in a redox electrolyte solution. Opposite reactions such as the oxidation of the reductant to an oxidant on an n-type semiconductor electrode and the reduction of the oxidant to the reductant on the counterelectrode occur through solar illumination. Thus, the composition of redox electrolyte solution does not change, and only electricity is obtained as usual solid-state solar cells. For the photo to chemical conversion type of photoelectrochemical solar cells (Fig. 1b), different reactions occur on the electrodes, for example, the oxidation of iodide ions to iodine (triiodide ions) and

hydrogen evolution. This decomposition of hydrogen iodide is an 'up-hill' reaction. Thus, solar energy is directly converted to chemical energy using this type of photoelectrochemical solar cells. The junction of an electrolyte solution and a semiconductor can generate a high-energy barrier, thus reaching a high photovoltage level even with a low-cost, low-quality semiconductor. However, water splitting using titanium dioxide encounters serious difficulty in achieving hydrogen evolution. There are three solutions to this difficulty: using another semiconductor with an energy band gap that is wider than titanium dioxide; using a multi-photon system equipped with multi-photoelectrodes in series or a tandem-type photoelectrode; and using a hydrogen-producing semiconductor, such as silicon (Si), and an oxidation reaction other than oxygen evolution, such as oxidation of iodide ions into iodine.

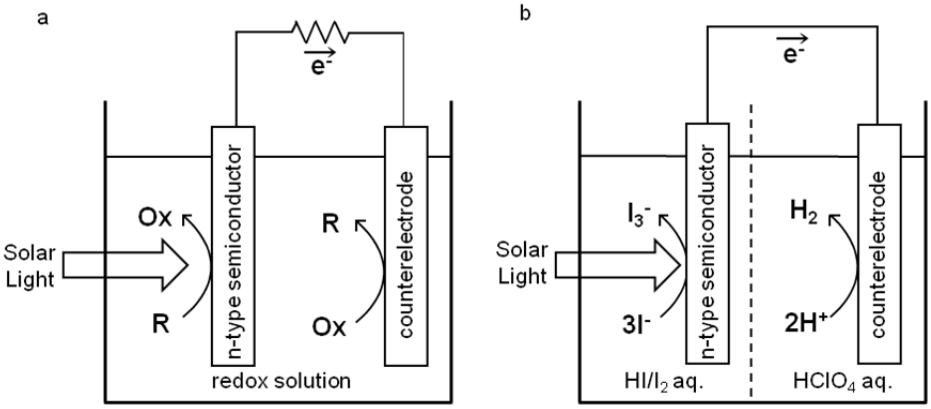

Fig. 1. Schematic illustrations of PEC solar cells. a) photovoltaic type; b) solar-to-chemical conversion type.

The Gibbs energy change for decomposition of hydrogen iodide (HI) into hydrogen (H_2) and iodine (I_2) (triiodide ion (I_3^-)) in an aqueous solution (see equations 1, 2 and 3) is smaller than that for water splitting. Thus, silicon photoelectrodes, which have a narrower energy band gap than titanium dioxide, can decompose hydrogen iodide with no external bias (Figs. 1b, 2 and equations (1)-(3)). The efficiency of a solar-to-chemical conversion via the photoelectrochemical decomposition of hydrogen iodide using single-crystalline silicon electrodes reached 7.4% (Nakato, 2000, Nakato et al., 1998, Takabayashi et al., 2004, 2006). Fuel cells using hydrogen gas and iodine solution can generate electricity via the reverse reaction of hydrogen iodide decomposition (equation (3)). Therefore, this system can form a solar energy cycle in a similar manner as the cycle consisting of water splitting and hydrogen-oxygen fuel cells.

Anode	$3I^- + 2h^+ \rightarrow I_3^-$	(1)
Cathode	$2H^+ + 2e^- \rightarrow H_2$	(2)
Total reaction	$2HI \rightarrow H_2 + I_2\ (I_3^-)$	(3)

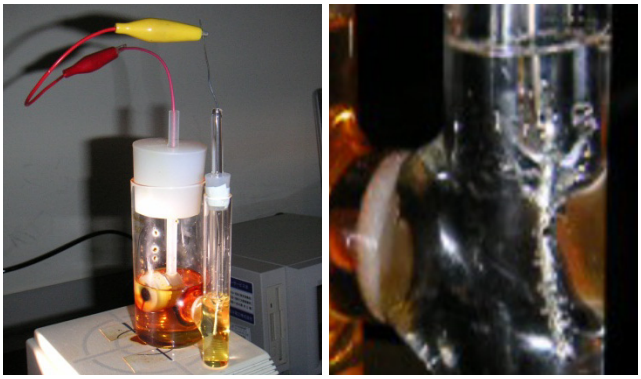

Fig. 2. Photoelectrochemical solar cell produces hydrogen gas via photodecomposition of hydrogen iodide with no external bias.

1.2 Metal nanoparticle modification of semiconductor electrode

Unfortunately, bare semiconductors can easily corrode or be passivated in aqueous solutions, and do not have enough catalytic activity for electrochemical reactions. Modifying the semiconductor surface with metal nanoparticles eliminates these problems without lowering the high energy barrier feature (Allongue et al., 1992, Hinogami et al., 1997, 1998, Jia et al., 1996, Nakato, 2000, Nakato et al., 1988, 1998, Nakato & Tsubomura 1992, Takabayashi et al., 2004, 2006, Yae et al., 1994a). The operation principle of this type of solar cells is explained as follows (Nakato et al., 1988, Nakato & Tsubomura 1992). Figure 3 shows a schematic illustration of cross section of a platinum (Pt)-nanoparticle modified n-type silicon (n-Si) photoelectrode. Photogenerated holes in n-Si transfer to the redox solution through the Pt particles, thus leading to a steady photocurrent. With no Pt particle, the photocurrent decays rapidly. The surface band energies of n-Si are modulated by the deposition of Pt particles. However, the effective barrier height is nearly the same as that for bare n-Si in case where the size of the Pt particles (or more correctly, the size of the areas of direct Pt-Si contacts) is small enough, much smaller than the width of the space charge layer. Thus, a very high barrier height, nearly equal to the energy band-gap, can be obtained if one chooses a electrochemical reaction with an enough high potential. Also, a major part of the n-Si surface is covered with a thin Si-oxide layer and passivated, and hence the electron-hole recombination rate at the n-Si surface is maintained quite low. For these reasons, very high photovoltage can be generated.

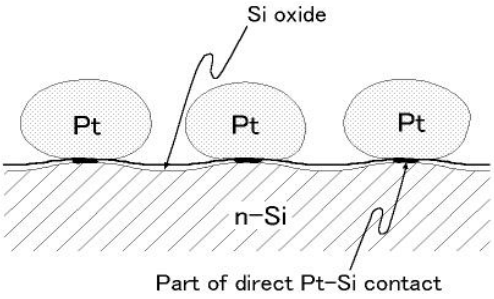

Fig. 3. Schematic illustration of cross section of a Pt-nanoparticle-modified n-Si photoelectrode.

In this study, Pt-nanoparticle modified multicrystalline Si wafers and microcrystalline Si (μc-Si:H) thin films (Yae et al., 2007a, b) are used as photoelectrodes in the photodecomposition of hydrogen iodide for low-cost and efficient production of solar hydrogen. We also attempt solar water splitting using a multi-photon system equipped with the microcrystalline Si thin film and metal-oxide photoelectrodes in series (Yae et al., 2007b).

2. Platinum nanoparticle modified porous multicrystalline silicon

Multicrystalline silicon is the most common material of the present conventional solar cells. We applied multicrystalline Si to solar hydrogen production by the photodecomposition of hydrogen iodide. To improve the conversion efficiency and stability of photoelectrochemical solar cells, multicrystalline n-type Si wafers were catalyzed with platinum nanoparticles and antireflected with a porous Si layer. The Pt nanoparticles were deposited on the multicrystalline Si substrates by electroless displacement deposition immersing substrates in a metal salt solution including hydrofluoric acid (Yae et al., 2006a, 2007c, 2008). The porous Si layers were formed by metal-particle-assisted hydrofluoric acid etching immersing metal-particle modified Si wafers in a hydrofluoric acid solution (Yae et al., 2003, 2006a, 2009).

2.1 Platinum nanoparticle formation by electroless displacement deposition

The metal nanoparticles play a tremendously important role in photoelectrochemical solar cells for photovoltaic and photochemical conversion of solar energy (Nakato et al., 1988, Nakato & Tsubomura 1992). The kind, particle density and size of nanoparticles influence the stability and conversion efficiency of solar cells. Thus, controlling the size and distribution density (particle density) of metal nanoparticles on semiconductor, multicrystalline Si in this case, is important for obtaining efficient photoelectrochemical solar cells. As well-controlled and low-cost methods of depositing metal nanoparticles on Si, we have been utilizing several methods such as simply dropping a solution of colloidal metal particles (Yae et. al., 1994a), preparing a Langmuir-Blodgett layer of nanoparticles (Jia et al., 1996, Yae et. al., 1994b, 1996), electrodeposition (Yae et. al., 2001, 2008), and electroless displacement deposition (Yae et al., 2007c, 2008). We choose the electroless displacement deposition to prepare Pt nanoparticles on multicrystalline Si wafers (Yae et al., 2006a). The electroless deposition of metals is a simple process involving only the immersion of substrates into metal-salt solutions. The electroless deposition is classified into autocatalytic and displacement depositions (Paunovic & Schlesinger, 2006). The electroless displacement deposition of metals onto Si uses a simple solution containing metal-salt and hydrofluoric acid. The deposition reaction is local galvanic reaction expressed by equations (4) and (5) consisting of the cathodic deposition of metal on Si accompanying positive hole injection into the valence band of Si and the anodic dissolution of Si. Various kinds of metals can be deposited on Si using this method (Chemla et al., 2003, Gorostiza et al., 1996, 2003, Nagaraha et al., 1993, Yae et al., 2007c, 2008).
Deposition of metal on Si:

$$M^{n+} \rightarrow M + nh^{+} \tag{4}$$

Anodic oxidation and dissolution of Si in an hydrofluoric acid solution:

$$Si + 4HF_2^{-} + 2h^{+} \rightarrow SiF_6^{2-} + 2HF + H_2 \tag{5}$$

or

$$Si + 2H_2O + 4h^+ \rightarrow SiO_2 + 4H^+ \quad (5)$$

$$SiO_2 + 6HF \rightarrow SiF_6^{2-} + 2H^+ + 2H_2O \quad (5)$$

Non-polished multicrystalline n-type Si wafers (cast, ca. 2 Ω cm, 0.3 mm thick) were washed with acetone, and etched with 1 mol dm^{-3} sodium hydroxide or potassium hydroxide solution at 353 K for saw damage layer removal. Before deposition of Pt particles, the wafers were treated by one of two pretreatment methods (hereafter, we call these pretreatments method A and method B). Method A: the wafers were washed with acetone, immersed in a CP-4A (a mixture of hydrofluoric acid, nitric acid, acetic acid, and water) solution for three min, and then immersed in a 7.3 mol dm^{-3} hydrofluoric acid solution for two min. Method B: the wafers were immersed in 14 mol dm^{-3} nitric acid at 353 K for 30 min after method A treatment. The multicrystalline Si wafer was immersed in a $1.0x10^{-3}$ mol dm^{-3} hexachloroplatinic (IV) acid solution containing 0.15 mol dm^{-3} hydrofluoric acid at 313 K for 30-120 s.

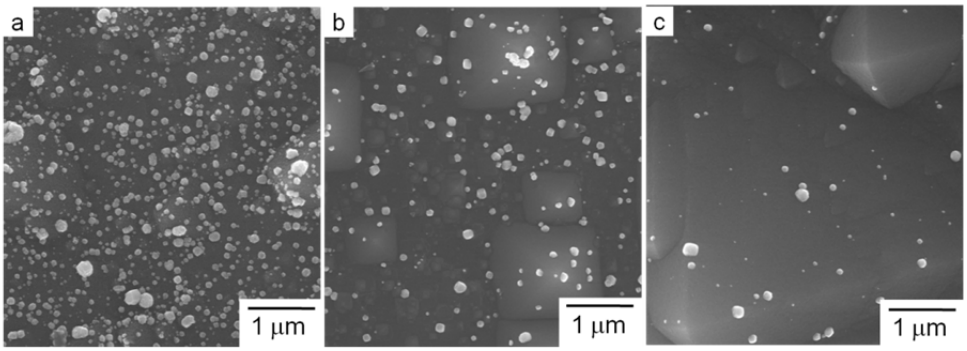

Fig. 4. Typical scanning electron microscopic (SEM) images of multicrystalline n-Si wafers pretreated by method A (image a) or B (b and c) and immersed in the Pt displacement deposition solution for 120 (a and b) or 30 s (c).

Figure 4 shows typical scanning electron microscopic (SEM) images of Pt deposited multicrystalline Si wafers. Spherical Pt-nanoparticles were sparsely scattered on the multicrystalline Si surfaces. Thin Si oxide layer formed by immersing the multicrystalline Si wafers in nitric acid solution (method B) decreased the particle density from $4x10^9$ to $0.9x10^9$ cm^{-2} (Figs. 4a and b). Shortening the immersion time from 120 to 30 s decreased the average particle size from 87 to 67 nm (Figs. 4b and c). The size and particle density of electrolessly deposited Pt nanoparticles on multicrystalline Si can be controlled by changing the deposition conditions. This is consistent with our previously reported results on single-crystalline silicon aside from high particle density (Yae et al., 2007c).

2.2 Porous silicon formation by metal-particle-assisted hydrofluoric acid etching

The antireflection of the semiconductor surface is an effective method for improving the energy conversion efficiency of solar cells (Sze, 1981, Nelson, 2003). The surface texturization by anisotropic etching is a common antireflection method for single crystalline Si solar cells. However, multicrystalline Si cannot be uniformly texturized by the anisotropic etching caused by its variety of orientations of crystallites. The metal-particle-assisted hydrofluoric acid etching can form both macroporous and microporous layers on

multicrystalline Si wafers, which are modified with fine metal particles, by simply immersing the wafers in an hydrofluoric acid solution without a bias and a particular oxidizing agent (Yae et al. 2006a, 2009). In previous papers, we reported that porous layer formation by this etching for 24 h decreased the reflectance of Si and increased the solar cell characteristics, which are not only photocurrent density but also photovoltage (Yae et al. 2003, 2005, 2006a, 2009).

2.2.1 Etching mechanism

The metal-particle-assisted hydrofluoric acid etching of Si proceeds by a local galvanic cell mechanism requiring photoillumination onto Si or dissolved oxygen in the solution (Yae et al. 2005, 2007d, 2009, 2010). Figure 5 shows a schematic diagram of n-Si and electrochemical reaction (equations (5), (6) and (7)) potential in a hydrofluoric acid solution. The local cell reaction consists of anodic dissolution of Si (equation (5)) and cathodic reduction of oxygen (equation (6)) and/or protons (equation (7)) on catalytic Pt particles. Under the photoillumination, photogenerated holes in the Si valence band anodically dissolve Si on the whole photoirradiated surface of Si. Under the dark condition, the etching proceeds by holes injected into the Si valence band with only cathodic reduction of oxygen on Pt particles, and thus the etching is localized around the Pt particles. The localized anodic dissolution produces macropores, which have Pt particles on the bottom, on the Si surface as shown in Fig. 6. We previously revealed two points about metal-particle-assisted hydrofluoric acid etching of Si: 1) the etching rate increased with photoillumination intensity on Si wafers and dissolved oxygen concentration in hydrofluoric acid solution; and 2) the time dependence of photoillumination intensity on the Si sample in the laboratory, which is ca. 0.2 mW cm^{-2} illumination for 6 h, dark condition for 12 h and then ca. 0.2 mW cm^{-2} illumination for 6 h, is suitable to produce the macro- and microporous combined structure effective for improving

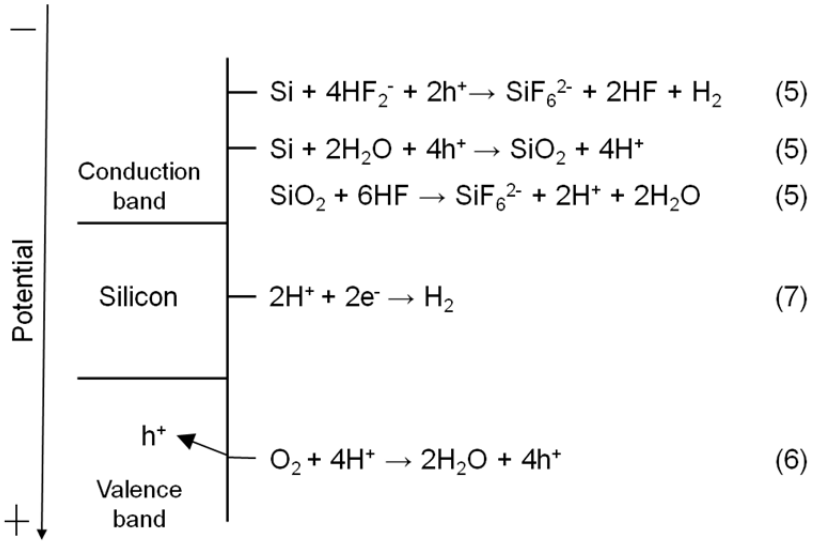

Fig. 5. Schematic diagram of silicon and electrochemical reaction potential in a hydrofluoric acid solution.

the solar cell characteristics (Yae et al. 2005, 2006b, 2009). In this section, we applied this method to the Pt-nanoparticle-modified multicrystalline n-Si to improve the solar cell characteristics, and attempted to shorten the etching time by controlling etching conditions such as the photoillumination intensity and the dissolved oxygen concentration.

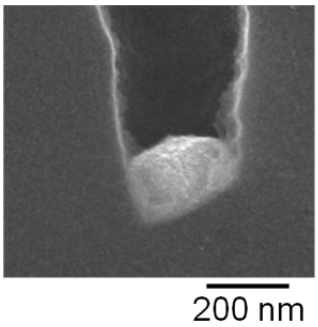

Fig. 6. Typical cross-sectional scanning electron micrograph of silicon macropore having a Pt particle on the bottom.

2.2.2 Porous structure control

The Pt-nanoparticle modified multicrytalline n-Si wafers were immersed in a 7.3 mol dm^{-3} hydrofluoric acid aqueous solution at 298 K. In some cases, oxygen gas bubbling was applied to the solution, and/or the n-Si wafers were irradiated with a tungsten-halogen lamp during immersion in the solution in a dark room. The reflectance of Si wafers was measured using a spectrophotometer in the diffuse reflection mode with an integrating sphere attachment.

Preparation conditions	Pretreatment	Pt deposition time (s)	Prorous layer formation (matal-particle-assisted hydrofluoric acid ethcing) conditions	Total etching time (h)
a	A	120	without light control for 24 h	24
b	B	120	without light control for 24 h	24
c	B	120	under 40 mW cm^{-2} with no bubbling for 3 h	3
d	B	120	40 mW cm^{-2} with no bubbling for 2 h and then in the dark with oxygen bubbling for 4 h	6
e	B	120	adding under 40 mW cm^{-2} with oxygen bubbling for 0.5 h to condition d	6.5
f	B	60	40 mW cm^{-2} with no bubbling for 2 h and then in the dark with oxygen bubbling for 4 h	6
g	B	60	adding under 40 mW cm^{-2} with oxygen bubbling for 0.5 h to condition f	6.5

Table 1. Preparation conditions of Pt nanoparticle modified porous multicrystalline n-Si

The deposition conditions of Pt-nanoparticles and metal-particle-assisted hydrofluoric acid etching conditions are listed in Table 1. Figure 7 shows typical scanning electron microscopic images of multicrystalline n-Si wafers that were pretreated by method A (image a) or B (image b) and metal-particle-assisted hydrofluoric acid etching without light control for 24 h (conditions a and b in Table 1). Macropores, whose diameter is 0.3–1 μm, were formed on whole surfaces of multicrystalline n-Si wafers. The density of pores, i.e. porosity, of n-Si wafer pretreated by method B is lower than that for method A. This is consistent with the Pt particle density on multicrystalline Si surface before etching (Fig. 4a and b). Both samples showed an orange photoluminescence under UV irradiation, thus microporous layers were formed on both samples.

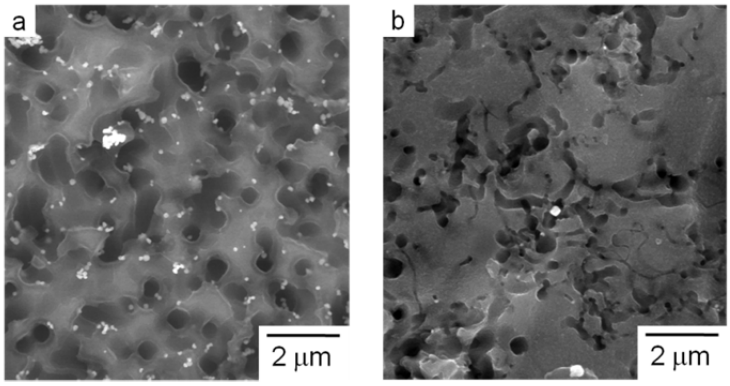

Fig. 7. Typical scanning electron microscopic images of Pt nanoparticle modified porous multicrystalline n-Si. Preparation conditions: images a and b are for conditions a and b in Table 1, respectively.

Figure 8 shows typical scanning electron microscopic images of multicrystalline n-Si that were pretreated by method B and metal-particle-assisted hydrofluoric acid etching under control of the photoillumination and the dissolved oxygen concentration (conditions c to g in Table 1). A microporous layer giving photoluminescence and no macropores was formed by etching under photoillumination without any gas bubbling estimated dissolved oxygen concentration of solution is ca. 5 ppm (Fig. 8a, condition c). The etching under the dark condition with oxygen gas bubbling (the solution was saturated with oxygen) after the etching under photoillumination produced macro- and microporous combined structure on the multicrystalline n-Si wafer (Fig. 8b, condition d). The morphology of the Si surface is similar to that formed by the etching without light control and gas bubbling for 24 h (Fig. 7b, condition b). Addition of the photoillumination with oxygen bubbling to the preceding conditions enlarged the macropore size and microporous layer thickness (Fig. 8c, condition e). Shortening the immersion time of multicrystalline n-Si wafers in the Pt displacement deposition solution, i.e. reduction of particle size and particle density of Pt on the wafers, reduced the number of macropores on the etched n-Si wafers (Figs. 8d and e, conditions f and g, respectively). The structure change in the porous layer of multicrystalline n-Si by changing the photoillumination intensity and dissolved oxygen concentration is consistent with our previously reported results on single crystalline n-Si (Yae et al., 2005, 2006b, 2009).

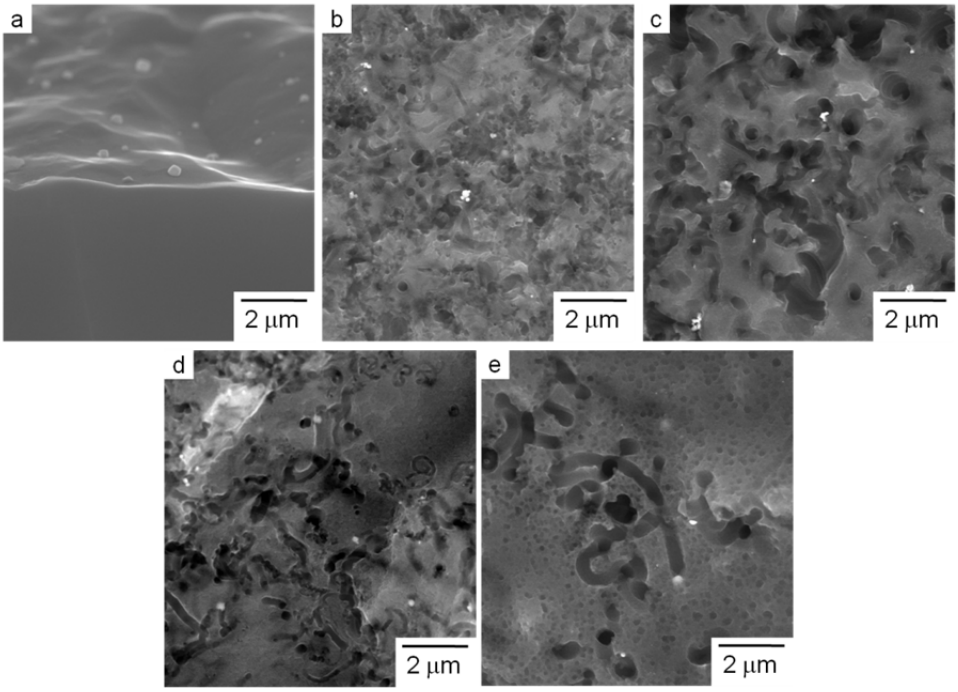

Fig. 8. Typical scanning electron microscopic images of Pt nanoparticle modified porous multicrystalline n-Si. Preparation conditions: images a, b, c, d, and e are for conditions c, d, e, f, and g in Table 1, respectively.

2.2.3 Antireflection effect

The macroporous layer formation changed the surface color of multicrystalline n-Si wafers to dark gray. Figure 9 shows the reflectance spectra of multicrystalline n-Si wafers. The porous layer prepared by the etching without light control and gas bubbling for 24 h reduced the reflectance from over 30% to under 6.2% (curves a and b) (Yae et al., 2006a, 2009). The porous layers prepared by the etching under the conditions d and g of Table 1 gave reflectance between 8 and 17% (curves c and d). This value is higher than that of the wafer prepared under the non-controlled conditions, but much lower than the non-etched wafer.

2.3 Photovoltaic photoelectrochemical solar cells

To evaluate electrical characteristics of photoelectrodes, we prepared photovoltaic photoelectrochemical solar cells (Fig. 1a) equipped with the Pt-nanoparticle modified porous multicrystalline n-Si photoelectrode. The multicrystalline n-Si electrode and Pt-plate counterelectrode were immersed in a redox electrolyte solution. Just before measuring the solar cell characteristics, the multicrystalline n-Si electrode was immersed in a 7.3 mol dm^{-3} hydrofluoric acid solution for two min under the elimination of dissolved oxygen by bubbling pure argon gas into the solution. This treatment is important to obtain high photovoltage caused by halogen atom termination of Si surface as mentioned below. A mixed solution of 7.6 mol dm^{-3} hydroiodic acid (HI) and 0.05 mol dm^{-3} iodine (I_2) was used

as a redox electrolyte solution of the photovoltaic photoelectrochemical solar cell. Photocurrent density versus potential (*j-U*) curves were obtained with a cyclic voltammetry tool. The potential of the n-Si wafer was measured with respect to the Pt counterelectrode. The multicrystalline n-Si was irradiated with a solar simulator (AM1.5G, 100 mW cm^{-2}) through the quartz window and a redox electrolyte solution ca. 3 mm thick.

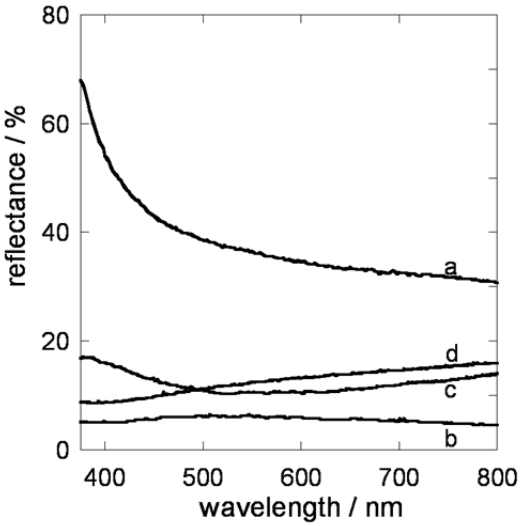

Fig. 9. Reflectance spectra of multicrystalline n-Si wafers: curve a after immersion in sodium hydroxide solution for saw damage layer removal; b, c, and d prepared under the conditions a, d, and g in Table 1, respectively.

2.3.1 Effect of particle density and size of platinum nanoparticles

Figure 10 show typical photocurrent density versus potential (*j-U*) curves of Pt-nanoparticle modified multicrystalline n-Si photoelectrodes having no porous layer pretreated under the same conditions as the specimens of Fig. 4. The decrease in particle density and size of Pt-nanoparticles increased the open-circuit photovoltage (V_{OC}) and short-circuit photocurrent density (j_{SC}) of photovoltaic photoelectrochemical solar cells from curve a to curve c of Fig. 10. Thus, the conversion efficiency (η^S) of the solar cells increased from 3.8% to 5.0%.

The reason for the increase in photocurrent density of the photoelectrochemical solar cells is the decrease of surface coverage of Pt-nanoparticles on Si. The surface coverage is 20% and 5% for Fig. 4a and b, respectively. This decrease is expected to increase the intensity of solar light reaching the Si surface by 19%. This is almost consistent with the increase in the short-circuit photocurrent density by 17%. The average open-circuit photovoltage of 12 samples is 0.42 V. This is lower than that for Pt-nanoparticle-electrolessly-deposited single crystalline n-Si electrodes (0.50 V in the average of 76 samples). This is explained by the following two reasons. 1) Lower quality of multicrystalline Si than single crystalline: The characteristics of multicrystalline Si solar cells are commonly lower than those of single crystalline. Thus, not only photovoltage but also the short-circuit photocurrent density and fill factor (*F.F.*) of photoelectrochemical solar cells are 12.1 mA cm^{-2} and 0.57 lower than those of single

crystalline (18.3 mA cm^{-2} and 0.60 on average, respectively). 2) Insufficient density of termination of Si surface bonds with iodine atoms: The termination of Si surface bonds with iodine atoms shifts the flat band potential of Si toward negative, and thus increases the photovoltage of photoelectrochemical solar cells using hydroiodic acid and iodine redox electrolyte (Fujitani et al., 1997, Ishida et al., 1999, Yae et al., 2006a, Zhou et al., 2001). An electrolyte solution of 8.6 mol dm^{-3} hydrobromic acid (HBr) and 0.05 mol dm^{-3} bromine (Br_2) has sufficient negative redox potential to generate high open-circuit photovoltage without the termination. Using the hydrobromic acid and bromine electrolyte solution increases the photovoltage by 0.06 V for multicrystalline and 0.03 V for single-crystalline n-Si electrodes from those using hydroiodic acid and iodine electrolyte solution. This result indicates that the density of the termination of multicrystalline n-Si surface bonds with iodine atoms is insufficient for generating high photovoltage.

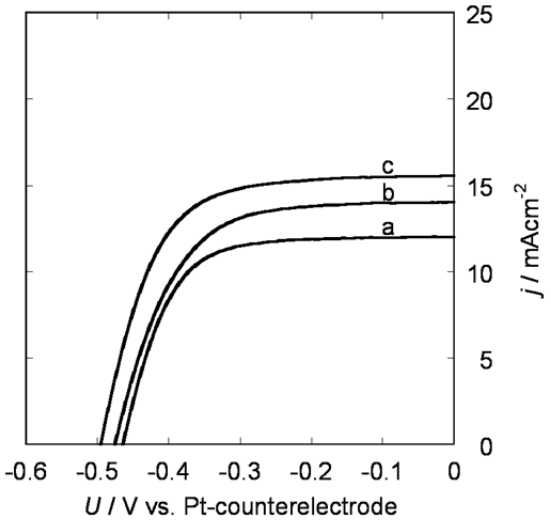

Fig. 10. Photocurrent density versus potential (*j-U*) curves of photovoltaic photoelectrochemical solar cells equipped with Pt-nanoparticle modified multicrystalline n-Si photoelectrode having no porous layer pretreated under the same conditions as the specimens of Fig. 4. Pretreatment: method A (image a), B (b and c); Pt deposition time: 120 (a and b), 30 s (c).

2.3.2 Effect of porous layer

Table 2 and Figure 11 indicate the average characteristics and typical photocurrent density versus potential (*j-U*) curves of photovoltaic photoelectrochemical solar cells equipped with a Pt-nanoparticle modified porous multicrystalline n-Si electrode prepared under the conditions listed in Table 1. The characteristics of photoelectrodes prepared under the conditions a and b as those for the wafers indicated in Fig. 7 show that the combination of the controlling particle density and size of Pt particles, and the formation of porous layer using metal-particle-assisted etching obtained a large increase in the conversion efficiency (η^S) from 3.8% for curve a in Fig. 10 and 2.9% in average of 12 samples to 5.1% in the average (Table 2). The formation of

continuous microporous layer (Figs. 8a and 11a, and condition c in Table 1) increased photovoltage (V_{OC}), and decreased fill factor (*F.F.*) of the solar cells. The formation of macro- and microporous combined structure (Figs. 8b and c, and conditions d and e in Table 1, respectively) increased photocurrent density (j_{SC}) and fill factor (*F.F.*), and thus increased the conversion efficiency (η^S) of solar cells (Fig. 11b, and conditions d and e in Table 2). The decrease of particle density and size of Pt particles (Figs. 8d and e, and conditions f and g in Table 1, respectively) increased photocurrent density (j_{SC}) and conversion efficiency (η^S) (Fig. 11c, and conditions f and g in Table 2). The conversion efficiency of solar cells reached 7.3% of curve c in Fig. 11 and 6.1% in the average of 4 samples (Table 2), and the etching time was shortened to 6.5 h from 24 h by controlling the photoillumination intensity and the dissolved oxygen concentration during etching (condition g in Table 1 and 2).

Preparation conditions see Table 1	No. of tested samples	Open-circuit photovoltage V_{OC} (V)	Short-circuit photocurrent density j_{SC} (mA cm^{-2})	Fill factor *F.F.*	Efficiency η^S (%)
a	21	0.47	13.8	0.60	3.9
b	7	0.50	16.6	0.62	5.1
d	17	0.46	17.6	0.60	4.9
e	3	0.50	17.4	0.63	5.5
f	3	0.49	18.0	0.66	5.8
g	4	0.50	19.5	0.63	6.1

Table 2. Characteristics of photovoltaic photoelectrochemical solar cells equipped with Pt-nanoparticle modified porous multicrystalline n-Si electrode prepared under the conditions in Table 1. Average values are indicated.

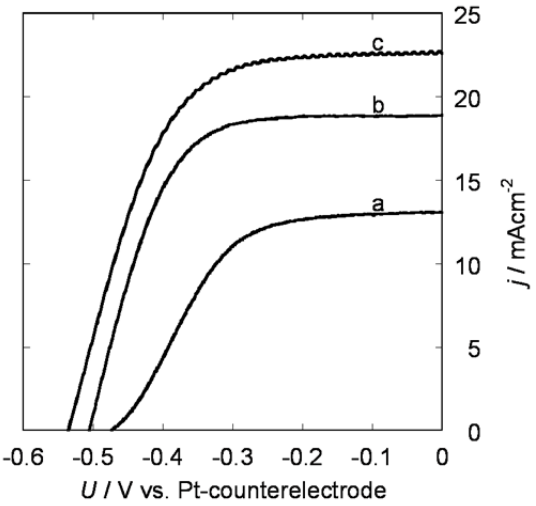

Fig. 11. Photocurrent density versus potential (*j-U*) curves of photovoltaic photoelectrochemical solar cells equipped with a Pt-nanoparticle modified porous multicrystalline n-Si electrode. Preparation conditions: curves a, b, and c, are for conditions c, d, and g listed in Table 1, respectively.

The increase in photocurrent density of photoelectrochemical solar cells equipped with Pt-nanoparticle modified multicrystalline n-Si electrode by the Pt-particle-assisted hydrofluoric acid etching is ca. 15% lower than the 30-40% estimated with reduction of the reflectance from 33% to 5-14% at the light wavelength of 700 nm. This difference can be explained by the difference in the refractive index between air (1.000), water (1.332 at 633 nm) and Si (3.796 at 1.8 eV (689 nm)) (Lide, 2004). The reflectance of Si is calculated at 34% in the air and 23% in the water. Using 23% as the initial value of reflectance estimates the increase in photocurrent density by the etching at 12-23%. This value is consistent with the experimental result of ca. 15%.
The photovoltage of photoelectrochemical solar cells equipped with Pt-nanoparticle modified multicrystalline n-Si electrode was improved by formation of the porous layer by Pt-particle-assisted hydrofluoric acid etching (Table 2). The photovoltage increase by the etching in dark conditions for 24 h was 0.01 V (V_{OC}: 0.43 V) in the average of eight samples, much lower than the 0.05 V (V_{OC}: 0.47 V) by the etching in a laboratory without light control (condition a in Table 1 and 2). These results show that the microporous layer effectively increases the photovoltage of such photoelectrochemical solar cells. This increase is explained by the following two possible mechanisms. 1) Screening Pt-nanoparticles' modulation of Si surface band energies by the microporous layer: The photovoltage of an n-Si electrode modified with metal particles depends on the distribution density of metal particles and the size of the direct metal-Si contacts. While metal particles are necessary as electrical conducting channels and catalysts of electrochemical reactions, the particles modulate the Si surface band energies. Thus, larger direct metal-Si contacts than a suitable size and/or a higher distribution density of metal particles than a suitable value reduce the effective energy barrier height, and then reduce the photovoltage of solar cells. The presence of a moderately thick microporous layer between the metal particles and bulk n-Si screens the modulation and thus raises the energy barrier height of the n-Si electrode, as discussed in the previous paper (Kawakami et al., 1997). 2) Increase in density of termination of Si surface bonds with iodine atoms: As we discussed in the previous section, the low open-circuit photovoltage (0.42 V) of the flat (nonporous) multicrystalline n-Si electrodes can be caused by the insufficient density of the termination of Si surface bonds with iodine atoms. Using the hydrobromic acid and bromine electrolyte solution increased the average open-circuit photovoltage of porous n-Si electrodes prepared under the condition a in Table 1 by 0.03 V for multicrystalline and 0.02 V for single-crystalline n-Si from those of using hydroiodic acid and iodide electrolyte solution. This result indicates that the density of the termination of the multicrystalline n-Si surface bonds with iodine atoms is increased to sufficient value for generating high V_{OC} by forming the microporous layer.

2.4 Solar to chemical conversion (solar hydrogen production)

In the preceding section, we prepared the efficient photovoltaic photoelectrochemical solar cells using the Pt-nanoparticle modified porous multicrystalline n-Si electrode. In this section, these electrodes were used for solar to chemical conversion via the photoelectrochemical decomposition of hydrogen iodide (HI) to iodine (I_2 or I_3^-) and hydrogen gas (H_2), that is, solar hydrogen. A two-compartment cell was used (Fig. 1b). The multicrystalline n-Si electrode was used as a photoanode in the mixed solution of hydroiodic acid and iodine of the anode compartment. A platinum plate was used as a counterelectrode in the perchloric acid ($HClO_4$) solution of the cathode compartment. Both compartments were separated with a porous glass plate. Figure 12 shows the typical photocurrent density versus potential (j-U) curve for the

multicrystalline n-Si electrode prepared under the condition g in Table 1 and 2. The potential (*U*) of the electrode was measured versus the Pt-plate counterelectrode in the perchloric acid solution of the cathode compartment (Fig. 1b). The short-circuit photocurrent density of 21.7 mA cm^{-2} was obtained. The solution color at the Si surface darkened, and gas evolution occurred at the Pt cathode surface. These results clearly show that the photoelectrochemical solar cell equipped with the Pt-nanoparticle modified porous multicrystalline n-Si electrode can decompose hydrogen iodide into hydrogen and iodine with no external bias, as shown in the equations (1), (2) and (3) in the section 1.1.

The dashed curve in Fig. 12 shows the current density versus the potential (*j-U*) curve of Pt electrode, which was in the anode compartment, instead of the Si electrode of the above cell for hydrogen iodide decomposition (Fig. 1b). The onset potential of the anodic current was 0.25 V versus the Pt-counterelectrode in the cathode compartment. This value indicates that the Gibbs energy change for the hydrogen iodide decomposition in the present solutions is 0.25 eV. The energy gain of solar to chemical conversion using the photoelectrochemical solar cell is calculated at 5.4 mW cm^{-2} by the product of the Gibbs energy change per the elementary charge and the short-circuit photocurrent density of 21.7 mA cm^{-2} under simulated solar illumination (AM1.5G, 100 mW cm^{-2}). Thus, we calculate the efficiency of solar to chemical conversion (solar hydrogen production) via the photoelectrochemical decomposition of hydrogen iodide at 5.4%. The average in solar-to-chemical-conversion efficiency of five samples was 4.7%.

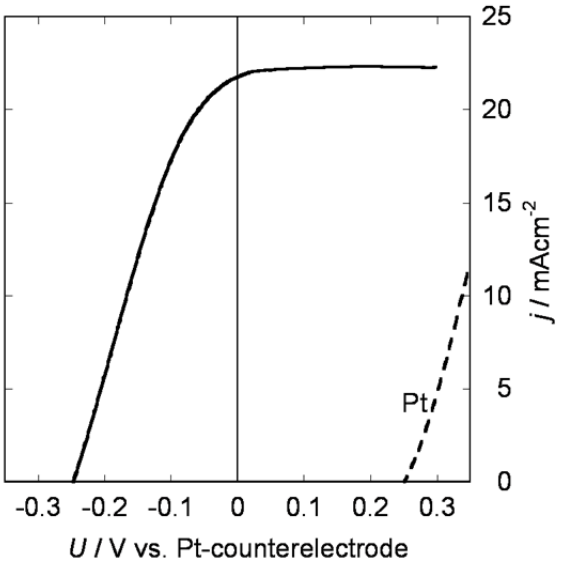

Fig. 12. Photocurrent density versus potential (*j-U*) curve (solid line) for solar-to-chemical conversion type of photoelectrochemical solar cell equipped with Pt-nanoparticle modified porous multicrystalline n-Si electrode prepared under condition g in Table 1. The two-compartment cell for photodecomposition of hydrogen iodide (Fig. 1b) was used. Dashed line: Pt electrode measured in the anode compartment of the two-compartment cell instead of the Si photoelectrode.

In Section 2, it was described that platinum-nanoparticle modified porous multicrystalline silicon electrodes prepared by electroless displacement deposition and metal-particle-assisted hydrofluoric acid etching can generate hydrogen (solar hydrogen) and iodine through the photoelectrochemical decomposition of hydrogen iodide in aqueous solution with no external bias at the solar-to-chemical conversion efficiency of 5.4%. The control of particle density and size of Pt particles by changing the initial surface condition of Si and deposition condition of Pt, and the control of porous layer structure by changing the etching conditions improve the conversion efficiency.

3. Platinum nanoparticle modified microcrystalline silicon thin films

Hydrogenated microcrystalline silicon (μc-Si:H) thin films are promising new materials for low-cost solar cells. The microcrystalline Si thin film approach has several advantages, including minimal use of semiconductor resources, large-area fabrication using low-cost chemical vapor deposition (CVD) methods, and no photodegradation of the solar cell's characteristics (Matsumura, 2001, Meier et al., 1994, Yamamoto et al., 1994). We applied microcrystalline Si thin films to solar hydrogen production by the photodecomposition of hydrogen iodide (Yae et al., 2007a, 2007b) and solar water splitting(Yae et al., 2007b). Figure 13 schematically shows a cross-section of the microcrystalline silicon thin-film photoelectrode. Photoelectrochemical solar cells require neither a p-type semiconductor layer nor a transparent conducting layer, which is necessary to fabricate solid-state solar cells.

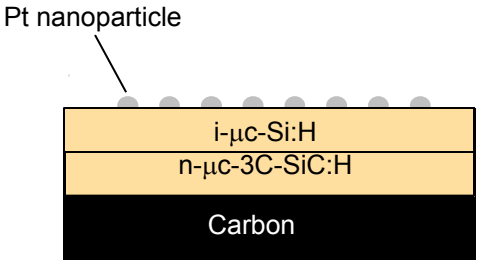

Fig. 13. Schematic cross-section of Pt-nanoparticle modified microcrystalline Si thin-film photoelectrode.

3.1 Preparation of photoelectrodes and photovoltaic photoelectrochemical solar cells

Hydrogenated microcrystalline silicon thin films were deposited onto polished glassy carbon (Tokai Carbon) substrates by the hot-wire catalytic chemical vapor deposition (cat-CVD) method (Matsumura et al. 2003). A 40-nm-thick n-type hydrogenated microcrystalline cubic silicon carbide (n-μc-3C-SiC:H) layer was deposited on the substrates using hydrogen-diluted monomethylsilane and phosphine gas at temperatures of 1700°C for the rhenium filament. An intrinsic hydrogenated microcrystalline silicon (i-μc-Si:H) layer, with thickness of 2-3 μm, was deposited on the n-type layer using monosilane gas at 1700°C for the tantalum filament. The microcrystalline silicon thin film electrodes were prepared by connecting a copper wire to the backside of the substrate with silver paste and covering it with insulating epoxy resin.

We deposited the Pt nanoparticles on the microcrystalline silicon surface using electroless displacement deposition as for the multicrystalline Si photoelectrodes (section 2.1). Figure 14 shows an scanning electron microscopic (SEM) image of the microcrystalline silicon film's surface after immersion in the Pt deposition solution for 120 s. Platinum nanoparticles of 3-200 nm in size and 1.5 x 10^{10} cm^{-2} in particle density were scattered on the film. The size and distribution density of Pt particles varied with the deposition conditions, such as oxide layer formation on the films before deposition and the immersion time of films in the deposition solution. The distribution density is much higher than that for a single-crystalline n-Si wafer, but the changing behaviors of the size and distribution density are similar to those of the single crystalline (Yae et al., 2007c, 2008).

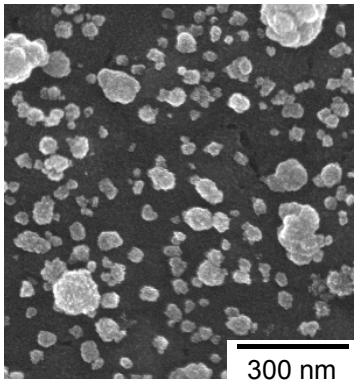

Fig. 14. Scanning electron microscopic image of Pt-nanoparticle modified microcrystalline Si thin film surface.

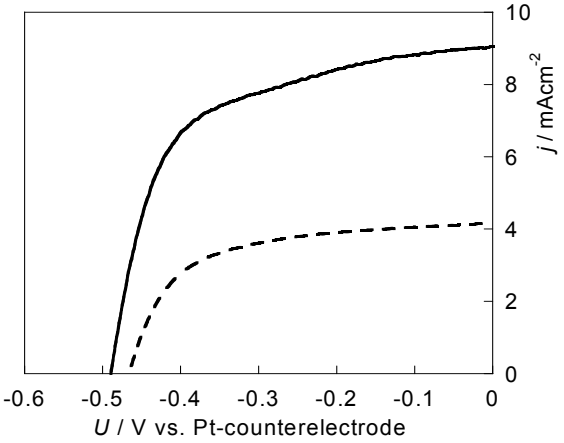

Fig. 15. Photocurrent density versus potential (*j-U*) curves for photovoltaic photoelectrochemical solar cell equipped with the Pt-nanoparticle modified microcrystalline Si photoelectrode measured in the 7.6 mol dm^{-3} (M) hydroiodic acid (HI)/0.05 M iodine (I_2) (dashed line) and 3.0 M HI/0.002 M I_2 (solid line) redox solutions.

For the photovoltaic photoelectrochemical solar cell (Fig. 1a), the Pt-nanoparticle-modified microcrystalline silicon thin film electrode and Pt-plate counterelectrode were immersed in a hydroiodic acid and iodine redox electrolyte solution as for the multicrystalline Si photoelectrodes (section 2.3). Figure 15 shows the photocurrent density versus potential (*j-U*) curves for the photovoltaic solar cell. The microcrystalline silicon film was stably adherent to the glassy carbon substrate after completing the photoelectrochemical measurements in these highly acidic solutions. The open-circuit photovoltage was 0.47-0.49 V. This is higher than the 0.3 V value obtained for the microcrystalline silicon thin film electrode covered with a continuous 1.5-nm-thick Pt layer, which was deposited using the electron-beam evaporation method. These results clearly indicate that the Pt-nanoparticle-modified microcrystalline silicon thin film electrodes work by using the same mechanism as the Pt-nanoparticle-modified single-crystalline n-Si electrodes, which work as ideal semiconductor photoelectrodes for generating high photovoltage and stable photocurrent described in previous sections 1.2 and 2.3.1. The reduction of redox electrolyte concentration increased the short-circuit photocurrent density to 9.1 from 4.2 mA cm^{-2} (Fig. 15, solid line). This increase is caused by a decrease in the visible light absorption of the triiodide (I_3^-) ion in the redox solution. The increased photocurrent raised open-circuit photovoltage to 0.49 V, and thus the photovoltaic conversion efficiency reached 2.7%.

3.2 Solar to chemical conversion (solar hydrogen production) via hydrogen iodide decomposition

The Pt-nanoparticle modified microcrystalline Si thin film electrode were used for solar to chemical conversion via the photoelectrochemical decomposition of hydrogen iodide to iodine and hydrogen gas as the multicrystalline Si photoelectrodes (section 2.4). For the photoelectrochemical decomposition of hydrogen iodide, a two-compartment cell was used (Fig. 1b and 2).

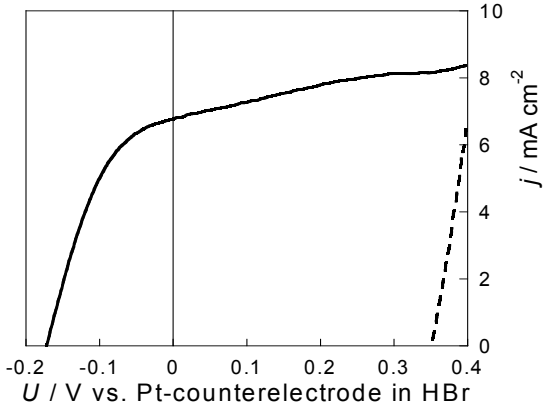

Fig. 16. Photocurrent density versus potential (*j-U*) curve (Solid line) for the Pt-nanoparticle modified microcrystalline Si thin film electrode measured in the hydroiodic acid and iodine mixture solution of the anode compartment of the two-compartment cell for solar to chemical conversion (solar hydrogen production, Fig. 1b). Dashed line: Pt electrode measured in the anode compartment of the two-compartment cell instead of the Si photoelectrode. Electrolyte solutions: anode compartment: 3.0 M HI/0.002 M I_2; cathode compartment: 3.0 M HBr.

The solid line in Fig. 16 shows the photocurrent density versus potential (*j-U*) curve for the Pt-nanoparticle-modified microcrystalline Si thin film electrode measured in the hydroiodic acid and iodine mixture solution of the anode compartment of the two-compartment cell. The potential of the electrode was measured versus the Pt counterelectrode in the hydrobromic acid solution of the cathode compartment. In the short-circuit condition under the simulated solar illumination, we obtained a shirt-circuit photocurent density of 6.8 mA cm^{-2}, the solution color on the photoelectrode surface darkened, and gas evolution occurred at the Pt cathode surface. These results clearly show that the photoelectrochemical solar cell equipped with the Pt-nanoparticle-modified microcrystalline Si thin film electrode can decompose hydrogen iodide into hydrogen gas and iodine with no external bias with 2.3% of solar-to-chemical conversion efficiency.

3.3 Hydrogen production via solar water splitting using multi-photon system

A multi-photon system equipped with the microcrystalline Si thin film and titanium dioxide (TiO_2) photoelectrodes in series (Fig. 17) was prepared based on a work in literature using a dye-sensitization-photovoltaic cell and a tungsten trioxide (WO_3) photoanode (Grätzel, 1999). A titanium dioxide photoanode and a Pt cathode (counterelectrode) were immersed in a perchloric acid ($HClO_4$) aqueous solution in a quartz cell. A photovoltaic photoelectrochemical solar cell equipped with the Pt-nanoparticle-modified microcrystalline Si electrode (section 3.1) was connected to the titanium dioxide photoanode and Pt cathode in series. Simulated solar light irradiated to the titanium dioxide photoelectrode. The titanium dioxide, which has a 3-eV energy band gap, absorbs the short-wavelength part (UV) of the solar light. The long-wavelength part of the solar light transmitted by the titanium dioxide and quartz cell reaches the Pt-nanoparticle-modified microcrystalline Si thin-film of the photovoltaic photoelectrochemical solar cell. The photovoltaic cell applies bias between the titanium dioxide photoanode and the Pt cathode in a perchloric acid aqueous solution for splitting water to hydrogen and oxygen.

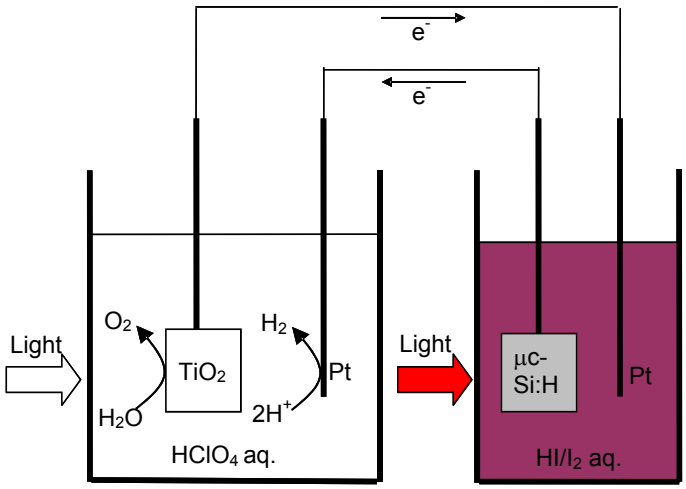

Fig. 17. Schematic illustration of multi-photon system equipped with titanium dioxide and microcrystalline Si photoelectrodes for solar water splitting.

The titanium dioxide photoanode was prepared as follows. Transparent conductive tin oxide (SnO_2)-coated glass plates were used as substrates. Titanium dioxide powder (P-25, average crystallite size: 21 nm) was ground with nitric acid, acetyl acetone, surfactant (Triton X-100), and water in a mortar. The obtained paste was coated on the substrate and dried. The titanium dioxide-nanoparticle film was heated in air at 500°C for three hours. The titanium dioxide electrode was prepared by connecting a copper wire to the bare part of the conductive tin oxide film with silver paste and covering it with insulating epoxy resin.

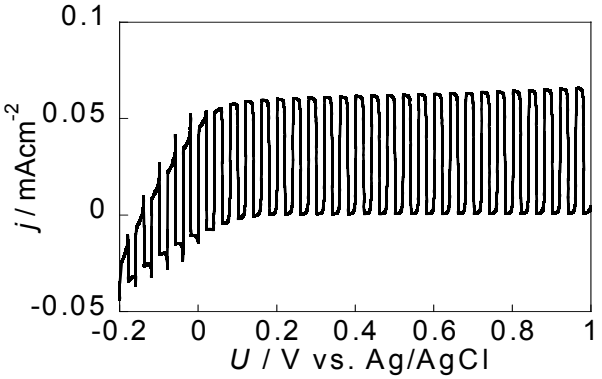

Fig. 18. Photocurrent density versus potential (*j-U*) curve for the titanium dioxide photoelectrode in a perchloric acid aqueous solution under chopped simulated solar illumination.

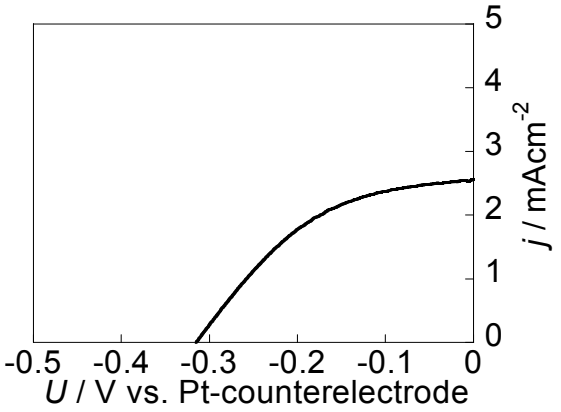

Fig. 19. Photocurrent density versus potential (*j-U*) curve for the photovoltaic photoelectrochemical solar cell equipped with a Pt-nanoparticle-modified microcrystalline Si electrode in the redox solution under simulated solar light illumination through the titanium dioxide photoelectrochemical cell.

Figure 18 shows the photocurrent density versus potential (*j-U*) curve for the titanium dioxide photoelectrode in a perchloric acid aqueous solution under simulated solar illumination. The dissolved oxygen in the solution was eliminated by using argon gas flow into the solution before the measurement. The anodic photocurrent starts to generate at -0.14 V vs. Ag/AgCl. This onset potential is more positive than -0.24 V vs. Ag/AgCl for hydrogen evolution, and thus this electrode cannot split water into hydrogen and oxygen without external bias. Figure 19 shows the photocurrent density versus potential (*j-U*) curve for the photovoltaic photoelectrochemical solar cell equipped with a Pt-nanoparticle-modified microcrystalline Si electrode in the redox solution under simulated solar light illumination through the titanium dioxide photoelectrochemical cell. The shirt-circuit photocurrent density was decreased from 5.3 mA cm^{-2} for the cell under direct solar light illumination to 2.6 mA cm^{-2} by light attenuation with the titanium dioxide cell. The multi-photon system (Fig. 17) using the same titanium dioxide and Pt-nanoparticle-modified microcrystalline Si electrodes as those in Figs. 18 and 19 indicated the photocurrent density versus potential (*j-U*) curve of Fig. 20. This system generated anodic photocurrent at a potential that was more negative than -0.24 V vs. Ag/AgCl for hydrogen evolution. Figure 21 shows that steady photocurrent was obtained for the multi-photon system in the short-circuit condition (Fig. 17). Tiny gas bubble formed on the Pt cathode during measurement under the short-circuit condition. These results show that this multi-photon system can split water into hydrogen and oxygen with no external bias with solar light. Since two photoelectrodes of titanium dioxide and Pt-nanoparticle-modified microcrystalline Si were connected in series, photovoltage was the sum of the two electrodes' values and photocurrent was the lower of the two electrodes' values. Therefore, the photocurrent density for water splitting was determined by that of the titanium dioxide electrode and very low. The photocurrent density, and thus hydrogen production by solar water splitting, is expected to increase by using a semiconductor with a narrower band gap, such as tungsten trioxide, instead of titanium dioxide. The theoretical simulation obtained 8 mA cm^{-2} of shirt-circuit photocurrent density, that is, 10% of solar-to-chemical conversion efficiency for solar water splitting for the tungsten trioxide and Si multi-photon system.

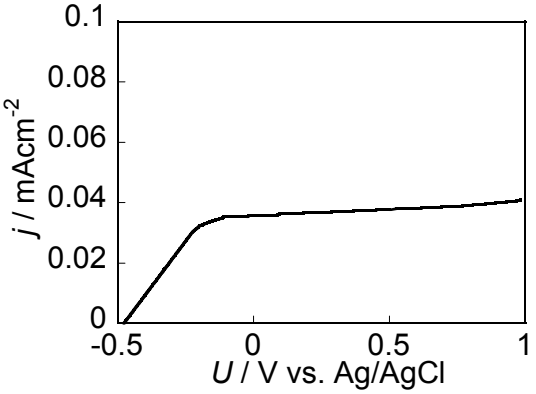

Fig. 20. Photocurrent density versus potential (*j-U*) curve for the multi-photon system (Fig. 17) using the same titanium dioxide thin film and Pt-nanoparticle modified microcrystalline Si photoelectrodes and electrolyte solutions as those in Figs. 18 and 19 under simulated solar light illumination.

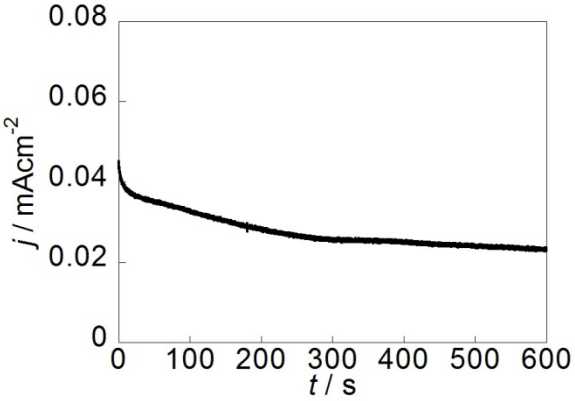

Fig. 21. Short-circuit photocurrent density (j) as a function of time (t) for the multi-photon system of Fig. 20 under simulated solar illumination.

4. Conclusion

Multicrystalline silicon wafers and microcrystalline silicon thin films, which are common and prospective low-cost semiconductor materials for solar cells, respectively, were successfully applied to produce solar hydrogen via photodecomposition of hydrogen iodide and solar water splitting. These photoelectrochemical solar cells have the following advantages: 1) simple fabrication of a cell by immersing the electrode in an electrolyte solution; 2) there is no need for a p-type semiconductor or a transparent conducting layer; and 3) direct solar-to-chemical conversion (fuel production). Modification of silicon surface with platinum nanopartilces by electroless displacement deposition and porous layer formation by metal-particle-assisted hydrofluoric acid etching improve solar cell characteristics. The solar-to-chemical conversion efficiency reached 5% for the photodecomposition of hydrogen iodide, and hydrogen gas evolution was obtained by the solar water splitting with no input of external electricity.

5. Acknowledgment

The author is grateful to Prof. H. Matsuda, Dr. N. Fukumuro (University of Hyogo), Dr. S. Ogawa, Prof. N. Yoshida, Prof. S. Nonomura (Gifu University), Mr. S. Sakamoto (Nippon Oikos Co., Ltd.), and Prof. Y. Nakato (Osaka University) for co-work and valuable discussions. The author would like to thank the students who collaborated: H. Miyasako, T. Kobayashi, K. Suzuki, and A. Onaka. The author is grateful to Prof. Y. Uraoka of Nara Institure of Science and Technology for the simulation of the solar water splitting using the multi-photon system. The present work was partly supported by the following programs: Grants-in-Aid for Scientific Research (C) from the JSPS (17560638, 20560676, and 23560875), Grants-in-Aid for education and research from Hyogo Prefecture through the University of Hyogo, Core Research for Evolutional Science and Technology (CREST) from the Japan Science and Technology Agency (JST), and Research for Promoting Technological Seeds from JST. The author wishes to thank Nippon Sheet Glass Co., Ltd. for donating transparent conductive tin oxide coated glass plates. Figures 15 and 16 were reprinted from ref. Yae et al., 2007a, copyright Elsevier (2007).

6. References

Allongue, P., Blonkowski, S., & Souteyrand, E. (1992). *Elecrochim. Acta,* Vol. 37, 781.

Arakawa, H., Shiraishi, C., Tatemoto, M., Kishida, H., Usui, D., Suma, A., Takamisawa, A., & Yamaguchi, T. (2007). *Proc. SPIE*, Vol. 6650, *Solar Hydrogen and Nanotechnology II*, Guo, J. (Ed.), San Diego, 665003.

Chemla, M., Homma, T., Bertagna, V., Erre, R., Kubo, N., & Osaka, T. (2003). *J. Electroanal. Chem.*, Vol. 559, 111.

Fujishima, A. & Honda, K. (1972). *Nature,* Vol. 238, 37.

Fujitani, M., Hinogami, R., Jia, J. G., Ishida, M., Morisawa, K., Yae, S., & Nakato, Y. (1997). *Chem. Lett.*, 1041.

Grätzel, M. (1999). *Cattech*, Vol. 3, 4.

Gorostiza, P., Servat, J., Morante, J. R., & Sanz, F. (1996). *Thin Solid Films*, Vol. 275, 12.

Gorostiza, P., Allongue, P., Díaz, R.; Morante, J. R., & Sanz, F. (2003). *J. Phys. Chem. B*, Vol. 107, 6454.

Hinogami, R., Nakamura, Y., Yae, S., & Nakato, Y. (1997). *Appl. Surf. Sci.*, Vol. 121/122, 301.

Hinogami, R., Nakamura, Y., Yae, S., & Nakato, Y. (1998). *J. Phys. Chem. B*, Vol. 102, 974.

Ishida, M., Morisawa, K., Hinogami, R., Jia, J. G., Yae, S., & Nakato, Y. (1999). *Z. Phys. Chem.*, Vol. 212, 99.

Jia, J.-G., Fujitani, M., Yae, S., & Nakato, Y. (1996). *Electrochim. Acta*, Vol. 42, 431.

Kawakami, K., Fujii, T., Yae S., & Nakato, Y. (1997). *J. Phys. Chem. B*, Vol. 101, 4508.

Khaselev, O. & Turner, J. A. (1998). *Science*, Vol. 280, 542.

Licht, S. (Vol. Ed.). (2002). *Semiconductor Electrodes and Photoelectrochemistry*, Bard. A. J. & Stratmann, M. (Series Eds.), *Encyclopedia of Electrochemistry*, Vol. 6, Wiley-VCH, Weinheim.

Lide, D. R. (Ed.). (2004). *CRC Handbook of Chemistry and Physics*, CRC Press, Boca Raton, 85th Ed., pp. 10-232, 10-234 and 12-150.

Lin, G. H., Kapur, M., Kainthla, R. C., & Bockris, J. O'M. (1989). *Appl. Phys. Lett.*, Vol. 55, 386.

Matsumura, H. (2001). *Thin Solid Films,* Vol. 395, 1.

Matsumura, H., Umemoto, H., Izumi, A., & Masuda, A. (2003). *Thin Solid Films,* Vol. 430, 7.

Meier. J., Flückiger, R., Keppner, H., & Shah, A. (1994). *Appl. Phys. Lett.,* Vol. 65, 860.

Miller, E. L., Marsen, B., Paluselli, D., & Rocheleau, R. (2005). *Electrochem. Solid-State Lett.*, Vol. 8, A247.

Nagahara, L. A., Ohmori, T., Hashimoto, K., & Fujishima, A. (1993). *J. Vac. Sci. Technol. A*, Vol. 11, 763.

Nakato, Y., Ueda, K., Yano, H., & Tsubomura, H. (1988). *J. Phys. Chem.*, Vol. 92, 2316.

Nakato, Y. & Tsubomura, H. (1992). *Elecrochim. Acta*, Vol. 37, 897.

Nakato, Y., Jia, J. G., Ishida, M., Morisawa, K., Fujitani, M., Hinogami, R., & Yae, S. (1998). *Electrochem. Solid-State Lett.*, Vol. 1, 71.

Nakato, Y. (2000). Photoelectrochemical Cells, In: *Wiley Encyclopedia of Electrical and Electronics Engineering Online*, Webster, J. (Ed.), John Wiley & Sons, Available from: http://www.interscience.wiley.com

Nelson, J. (2003). *The Physics of Solar Cells*, Imperial College Press, London, pp. 276-279.

Paunovic, M., Schlesinger, M. (2006). *Fundamentals of Electrochemical Deposition 2nd. Ed.*, John Wiley & Sons, New York.

Park, J. H. & Bard, A. J. (2005). *Electrochem. Solid-State Lett.*, Vol. 8, G371.

Sakai, Y., Sugahara, S., Matsumura, M., Nakato, Y., & Tsubomura, H. (1988). *Can. J. Chem.*, Vol. 66, 1853.

Sze, S. M. (1981). *Physics of Semiconductor Devices*, John Wiley & Sons, New York, 2nd Ed., pp. 811-816.

Takabayashi, S., Nakamura, R., & Nakato, Y. (2004). *J. Photochem. Photobiol. A*, Vol. 166, 107.

Takabayashi, S., Imanishi, A., & Nakato, Y. (2006). *Comptes Rendus Chimie*, Vol. 9, 275.

Turner, J. A., Williams, M. C., & Rajeshwar, K. (2004). *Interface*, Vol. 13, No. 3, 24.

Yae, S., Tsuda, R., Kai, T., Kikuchi, K., Uetsuji, M., Fujii, T., Fujitani, M., & Nakato, Y. (1994). *J. Electrochem. Soc.*, Vol. 141, 3090.

Yae, S., Nakanishi, I., Nakato, Y., Toshima, N., & Mori, H. (1994). *J. Electrochem. Soc.*, Vol. 141, 3077.

Yae, S., Fujitani, M., Nakanishi, I., Uetsuji, M., Tsuda, R., & Nakato, Y. (1996). *Sol. Energy Mater. Sol. Cells*, Vol. 43, 311.

Yae, S., Kitagaki, M., Hagihara, T., Miyoshi, Y., Matsuda, H., Parkinson, B. A., & Nakato, Y. (2001). *Electrochim. Acta*, Vol. 47, 345.

Yae, S., Kawamoto, Y., Tanaka, H., Fukumuro, N., & Matsuda, H. (2003). *Electrochem. Comm.*, Vol. 5, 632.

Yae, S., Tanaka, H., Kobayashi, T., Fukumuro, N., & Matsuda, H. (2005). *Phys. Stat. Sol. (c)*, Vol. 2, 3476.

Yae, S., Kobayashi, T., Kawagishi, T., Fukumuro, N., & Matsuda, H. (2006). *Solar Energy*, Vol. 80, 701.

Yae, S., Kobayashi, T., Kawagishi, T., Fukumuro, N., & Matsuda, H. (2006). *The Electrochemical Society Proceedings Series*, Vol. PV2004-19, *Pits and Pores III: Formation, Properties and Significance for Advanced Materials*, Schmuki, P., Lockwood, D. J., Ogata, Y. H., Seo, M., & Isaacs, H. S. (Eds.). 141.

Yae, S., Kobayashi, T., Abe, M., Nasu, N., Fukumuro, N., Ogawa, S., Yoshida, N., Nonomura, S., Nakato, Y., & Matsuda, H. (2007). *Sol. Energy Mater. Sol. Cells*, Vol. 91, 224.

Yae, S., Onaka, A., Abe, M., Fukumuro, N., Ogawa, S., Yoshida, N., Nonomura, S., Nakato, Y., & Matsuda, H. (2007). *Proc. SPIE*, Vol. 6650, *Solar Hydrogen and Nanotechnology II*, Guo, J. (Ed.), San Diego, 66500E.

Yae, S., Nasu, N., Matsumoto, K., Hagihara, T., Fukumuro, N., & Matsuda, H. (2007). *Electrochim. Acta*, Vol. 53, 35.

Yae, S., Abe, M., Kawagishi, T., Suzuki, K., Fukumuro, N., & Matsuda, H. (2007). *Trans. Mater. Res. Soc. Jpn.*, Vol. 32, 445.

Yae, S., Fukumuro, N., & Matsuda, H. (2008). Electrochemical Deposition of Metal Nanoparticles on Silicon, In: *Progress in Nanoparticles Research*, Frisiras, C. T. (Ed.), pp. 117-135, Nova Science Publishers, Inc., New York.

Yae, S., Fukumuro, N., & Matsuda, H. (2009). Porous Silicon Formation by Metal Particle Enhanced HF etching, In: *Electroanalytical Chemistry Research Trends*, Hayashi, K. (Ed.), pp. 107-126, Nova Science Publishers, New York.

Yae, S., Tashiro, M., Abe, M., Fukumuro, N., & Matsuda, H. (2010). *J. Electrochem. Soc.*, Vol. 157, D90.

Yamamoto, K., Nakashima, A., Suzuki, T., Yoshimi, M., Nishio, H., & Izumina, M. (1994). *Jpn. J. Appl. Phys.* Vol. 33, L1751.
Zhou, X., Ishida, M., Imanishi, A., & Nakato, Y. (2001). *J. Phys. Chem. B*, Vol. 105, 156.

12

Progress in Organic Photovoltaic Fibers Research

Ayse Bedeloglu
Dokuz Eylül University,
Turkey

1. Introduction

Energy management including production, distribution and usage of energy is an important issue, which determines internal and external policy and economical situation of countries. For generating electrical energy, use of traditional energy sources in particular fossil based fuels through long ages, caused environmental problems, in recent years. Renewable energy technologies using power of wind, sun, water, etc. can be remedies to hinder negative effects of pollution, emissions of carbon dioxide and irreversible climate change problem, which it caused. Photovoltaic technology, which converts photons of the sun into electrical energy by using semiconductors, is one of the most environmental friendly sources of renewable energy (Dennler et al., 2006a). Solar cells are used in many different fields such as in solar lambs and calculators, on roofs and windows of buildings, satellites and space craft, textile structures (fibers, fabrics and garments) and accessories (bags and suitcases).

In addition, there is an increasing interest in organic electronics from a wide range of science disciplines in which researchers search for novel, efficient and functional materials and structures. Organic materials based optoelectronic devices such as organic photovoltaics (organic solar cells), organic light emitting diodes and organic photo detectors (Curran et al., 2009) are desirable in many applications due to interesting features of organic materials such as cost advantage and flexibility. Production of electrical energy, which is necessary in both industrial and human daily life by converting sunlight using organic solar cells (organic photovoltaic technology) via easy and inexpensive techniques is also very interesting (Günes et al., 2007).

A photovoltaic textile, which is formed by combining a textile structure with a solar cell, and on which carries physical properties of textile and working principle of solar cell together, can generate electricity for powering different electrical devices. Photovoltaic fiber providing more compatibility to textiles in terms of flexibility and lightness owing to its thin and polymer-based structure may be used in a wide variety of applications such as tents, jackets, soldier uniforms and marine fabrics. This review is organized as follows: In the first section, an overview of photovoltaic technology, smart textiles and photovoltaic textiles will be presented. In the second section, a general introduction to organic solar cells and organic semi conductors, features, the working principle, manufacturing techniques, and characterization of organic solar cells as well as polymer based organic solar cells and studies about nanofibers and flexible solar cells will be given. In the third part, recent studies about photovoltaic fiber researches, production methods, and materials used and

application areas will be recounted. Finally, suggestions on future studies and the conclusions will be given.

1.1 Photovoltaic technology

"Photovoltaic" is a marriage of two words: "photo", which means light, and "voltaic", which means electricity. Electrical energy produced by solar cells is one of the most promising sustainable alternative energy and can provide energy demand of the world, in the future (Green, 2005). Today, silicon based solar cells having the highest power conversion efficiency are dominated in the market; however they have still high production costs. Electricity generation by solar cells is still more expensive than that of fossil fuels due to materials and manufacturing processes used in solar cells and installation costs. However, photovoltaic technology, compared to traditional energy production technologies, have interesting features such as using endless and abundant source of sun's energy, direct, environmental friendly and noiseless energy generation without the need of additional generators, customization according to requirements, having low maintenance costs and portable modules producing power ranging between milliwatt to megawatts even in remote areas, which make it unique (Dennler et al., 2006a). A photovoltaic system can convert sun light into electricity on both sunny and cloudy days (European PhotoVoltaic Industry Association (EPIA), 2009). The worldwide cumulative photovoltaic power installed reached about 23GW, in the beginning of 2010 and produces about 25TWh of electricity on a yearly basis (European PhotoVoltaic Industry Association (EPIA), 2010).

The electricity produced by solar cells can be utilized in many applications such as cooling, heating, lighting, charging of batteries and providing power for different electrical devices (Curran et al., 2009). Solar cells using silicon wafers are classified as first generation technology having high areal production costs and moderate efficiency. Thin-film solar cells using Amorphous silicon (a-Si), Cadmium telluride (CdTe) and Copper indium gallium (di)selenide (CIGS) as second generation technology have advantages such as increased size of the unit of manufacturing and reduction in material costs. However, this technology has modest efficiency beside these advantages compared to first generation technology. Therefore, third generation technology concept has been developed to eliminate disadvantages of earlier photovoltaic technologies (Green, 2005). There are two approaches in third generation photovoltaic technology. The first one aims to achieve very high efficiencies and second one tries to achieve cost per watt balance via moderate efficiency at low cost. Therefore, this uses inexpensive semiconductor materials and solutions at low temperature manufacturing processes. The third generation photovoltaics use various technologies and grouped under organic solar cells (Dennler et al., 2006a).

1.2 Smart textiles

Humankind has always been inspired to mimic intelligence of nature to create novel materials and structures with fascinating functions. Over the last decades, in industrial and daily life, paralleling to growth in world population and advancements in science and technology, human requirements have changed and begun to diverge from each other. Therefore, different functional products have emerged according to expectations and requirements of human kind. One of these, intelligent materials, can coordinate their characteristic behavior according to changes of external or internal stimulus (chemical, mechanical, thermal, magnetic, electrical and so on) as in biological systems and have different functions owing to their unique molecular structure (Mattila, 2006; Tani et al.,

1998). Intelligent materials and structures can sense and react and more, adapt it and perform a function of changes (Takagi, 1990; Tao, 2001).Intelligent material systems consist of three parts: a sensor, a processor and an actuator. Intelligent materials can provide advancements in many fields of science for energy generation, medical treatments, and engineering applications and so on.

There are also many application areas for interactive textiles, which use intelligent materials such as shape memory alloys or polymers, phase change materials, conductive materials and etc. Intelligent textiles are defined as structures that are capable of sensing external and internal stimuli and respond or adapt to them in a pre-specified way. Knowledge from different scientific fields (biotechnology, microelectronics, nanotechnology and so on) is required for intelligent textile research (Mattila, 2006). Intelligent textiles find uses in many applications ranging from space to healthcare and entertainment.

Power supply by using discrete batteries is an important obstacle towards functionality of intelligent textiles. Besides, flexibility, comfort and durability are other parameters concerned to manufacture consistent products (Coyle & Diamond, 2010). Flexible solar cells (Schubert & Werner, 2006), micro fuel cells (Gunter et al., 2007; enfucell, 2011), power generation by body motion and body heat (Beeby, 2010; Starner, 1996) can be some alternatives to the traditional batteries. Photovoltaic fibers and textiles can overcome this power supply problem since they use the working principle of solar cells.

1.3 Photovoltaic textiles

Small electronic devices such as personal digital assistants, mobile phones, mp3 players, and notebook computers, usually use traditional batteries of which energy is used up in a short time. Integration of flexible solar cells into apparels and fabrics, which cells are positioned in/on the textile, can provide required electrical energy for these portable electronic devices (Schubert & Werner, 2006). Photovoltaic textiles can be formed by integrating solar cells into textile structure or making textile structure itself from photovoltaic materials. Photovoltaic textile research needs cooperation of different sciences consisting of textile, electronics, physics and chemistry. Incorporation of solar cells with fibers and textiles that are flexible can extend the applications of photovoltaics from military and space applications to lighting and providing power for consumer electronics of humankind in daily usage.

Textile based solar cells are also named as photovoltaic textiles, solar textiles, energy harvesting textiles, solar powered textiles in the literature. Photovoltaic textiles, which are high value added intelligent products, and, which have a large application area, can benefit textile industry by increasing its competitiveness with long term development.

Power conversion efficiency and price properties beside the flexibility, weight, comfort, durability and washability properties of the products are also important from a customer point of view. Position of the flexible solar cells on fabric is also important to take efficient irradiation from the light source. Places of needed wires, controllers and batteries, which have to be lightweight under the cloth, are needed to be concerned to develop viable photovoltaic textiles (Schubert & Werner, 2006).

In recent years, there has been an increase in studies about developing photovoltaic fibers which can take charge in different textile and clothing applications. An active photovoltaic fiber, which is produced by using advanced design and suitable materials, and, which consist of adequate smooth layers, efficiency and stability, is capable of forming a flexible fabric by suitable knitting or weaving techniques, or integrating as a yarn into a cloth to generate power for electronic devices by converting sunlight (DeCristofano, 2009)

Fiber based photovoltaics take the advantage of being flexible and lightweight. Integration of photovoltaic fibers into fabrics and clothes is easy to manufacture wearable technology products. Small surface of a fiber also provide large area photoactive surfaces in the case of fabric, so higher power conversion efficiency can be obtained.
Traditional solar cells using silicon based semiconductors are generally rigid and are not suitable to be used with textiles. The thin film solar cells based on inorganic semiconductors can be made flexible and however they are more suitable for patching onto fabrics (Schubert & Werner, 2006).
Inexpensive electricity production can be achieved, when both low-cost and high efficient manufacturing of photovoltaic cells are achieved. A potential alternative approach to conventional rigid solar cells is organic solar cells, which can be coated on both rigid and flexible substrates using easy processing techniques. In addition, the polymer based organic solar cells can be used to produce fully flexible photovoltaic textiles easily, in any scale, from fibers to fabrics and using low-cost methods.

2. Organic photovoltaic technology

2.1 Organic semiconductors

Organic semiconductors, which are generally considered as intrinsic wide band gap semiconductors (band gap>1.4 eV), have many advantages to be used in solar cells. For example, organic semiconductors of which electronic band gap can be engineered by chemical synthesis with low-cost (Günes et al., 2007) have generally high absorption coefficients.
Organic semiconductors consist of different chemical structures (Nunzi, 2002) including polymers, oligomers, dendrimers, dyes, pigments, liquid crystals (Yilmaz Canli et al., 2010) etc. In carbon-based semiconductors, conductivity is obtained by conjugation, which single and double bonds between the carbon atoms alternate (Pope & Swenberg, 1999).
Conjugated organics are challenging materials for solar cells owing to their semiconducting and light absorbing features. As a compound of organic solar cells, organic semiconductors can be processed by thermal evaporation techniques or solution based coating or printing techniques at low temperatures (Deibel & Dyakonov, 2010).

2.2 Organic solar cells

As a promising renewable energy source, organic photovoltaics have attracted attention during the last decades resulting in significant progress in cell efficiency exceeded 5% (AM1.5, 1000 W/m^2) (Green et al., 2010) in the conventional bulk heterojunction solar cell architecture consisting of a polymer donor and fullerene acceptor blend. Organic solar cells achieving photovoltaic energy conversion by organic semiconductor or conductor are compatible with flexible substrates like textiles for use in novel application areas.
Photovoltaic effect, production of electricity by converting photons of the sunlight, occurs in an organic solar cell by the following steps (Nunzi, 2002): Absorption of photons of the light in the solar cell and exciton (electron-hole pair) creation; separation of charges and carriers generation from exciton dissociation; transport and then collection of charges by respective electrodes (Günes et al., 2007; Nunzi, 2002)
There are some approaches such as using conjugated polymers (Antonradis et al., 1994) and their blends (Granström et al., 1998; Halls et al., 1995; Yu & Heeger, 1995), small molecules (Tang, 1986; Wöhrle & Meissner, 1991) polymer-small molecule bilayers (Jenekhe & Yi, 2000;

Breeze et al., 2002) and their blends (Tang, 1986; Shaheen et al., 2001; Dittmer et al., 2000) or combinations of inorganic-organic materials (O`Reagan & Graetzel, 1991; Greenham et al., 1996; Günes et al., 2008; to develop organic solar cells (Güneş & Sariçiftçi, 2007). Mostly, two concepts are considered in organic solar cell researches: first one, (Krebs, 2009a) which is the most successful is using conjugated polymers (Fig. 1) with fullerene derivatives by solution based techniques and second one is cooperating small molecular materials (as donor and acceptor) by thermal evaporation techniques (Deibel & Dyakonov, 2010).

A conventional organic solar cell (Fig. 2) device is based on the following layer sequence: a semi-transparent conductive bottom electrode (indium tin oxide (ITO)) or a thin metal layer), a poly(3,4-ethylenedioxythiophene:poly(styrene sulfonic acid) (PEDOT:PSS) layer facilitating the hole injection and surface smoothness, an organic photoactive layer (most common poly(3- hexylthiophene):[*6,6*]-*phenyl-C61-butyric acid* methyl ester (P3HT:PCBM)) to absorb the light and a metal electrode (Aluminum, Al and Calcium, Ca) with a low work function to collect charges on the top of the device (Brabec et al., 2001a; Brabec et al., 2001b; Padinger et al., 2003). To form a good contact between the active layer and metal layer, an electron transporting layer (i.e. Lithium Fluoride, LiF) is also used (Brabec et al., 2002).

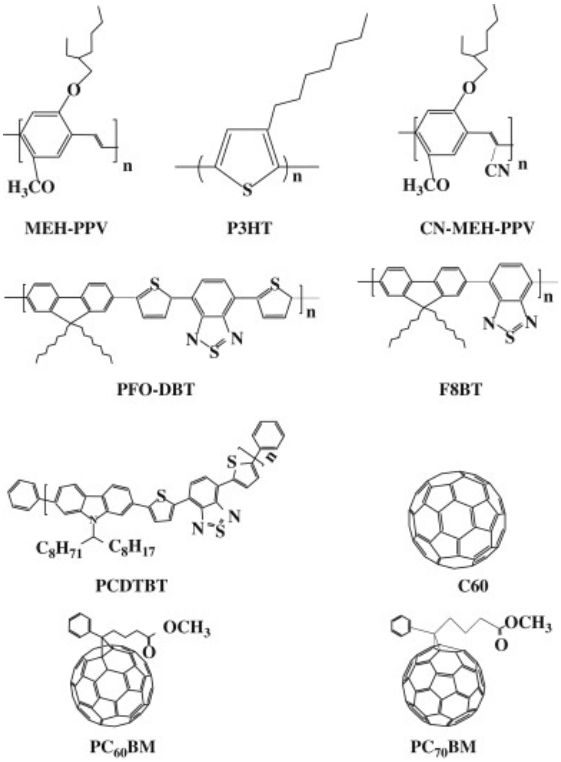

Fig. 1. Example of organic semiconductors used in polymer solar cells. Reprinted from Solar Energy Materials and Solar Cells, 94, Cai, W.; Gong, X. & Cao, Y. Polymer solar cells: Recent development and possible routes for improvement in the performance, 114–127, Copyright (2010), with permission from Elsevier.

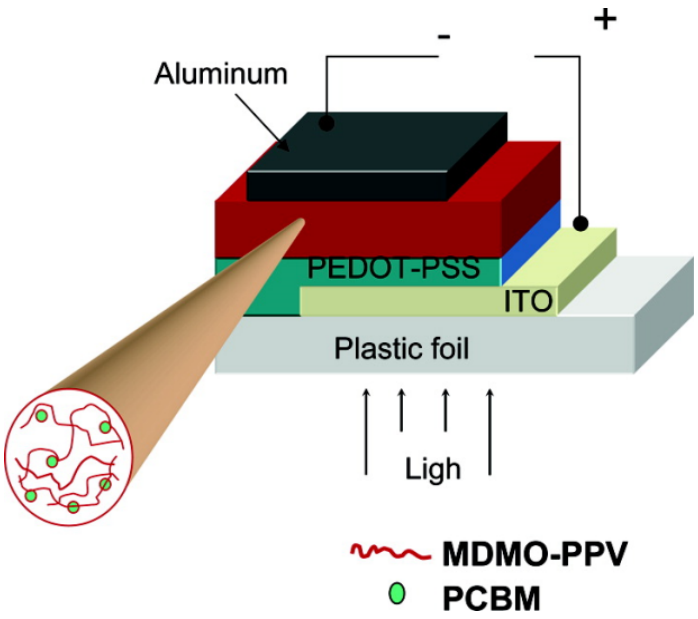

Fig. 2. Bulk heterojunction configuration in organic solar cells (Günes et al., 2007)

ITO is the most commonly used transparent electrode due to its good transparency in the visible range and good electrical conductivity (Zou et al., 2010). However, ITO, which exhibits poor mechanical properties on polymer based substrates, has limited conductivity for fabricating large area solar cells and needs complicated techniques, which tend to increase the cost of the solar cells (Zou et al., 2010). Indium availability is also limited. To alleviate limitations arised from ITO, alternative materials are needed to replace transparent conducting electrode. There are some approaches such as using carbon nanotubes (CNTs) (Rowell et al., 2006; Glatthaar et al., 2005; (Celik) Bedeloglu et al., 2011; Dresselhaus et al., 2001), graphenes (Eda et al., 2008), different conductive polymers (i.e. PEDOT:PSS and its mixtures (Ouyang et al., 2005; Kushto et al., 2005; Huang et al., 2006; Ahlswede et al., 2008; Zhou et al., 2008), metallic grids (Tvingstedt & Inganäs, 2007; Kang et al., 2008), nanowires (Lee et al., 2008) for potential candidates to substitute ITO layer and to perform as hole collecting electrode. In particular, CNTs have a wide variety of application area due to their unique features in terms of thermal, mechanical and electrical properties (Ajayan, 1999; Baughman et al., 2002). A nanotube has a diameter of a few nanometers and from a few nanometers to centimeters in length. Carbon nanotubes can be classified into two groups according to the number of combinations that form their walls: Single-walled nanotubes (SWNTs) and multi-walled nanotubes (MWNTs) (Wang et al., 2009) Recently, CNTs are used in solar cells and can substitute ITO as a transparent electrode in organic solar cells (Rowell et al., 2006; Glatthaar et al., 2005; (Celik) Bedeloglu et al., 2011; Dresselhaus et al., 2001).

In the organic solar cell, the photoactive layer, light absorbing layer, is formed by combination of electron donor (p) and an electron accepting (n) materials (Deibel & Dyakonov, 2010) C_{60}, its derivatives and Perylen pigments are mostly used as electron

accepting materials. Also, phtalocyanines, porphyrins, poly(3- hexylthiophene) (P3HT) and poly[2-methoxy-5-(2'-ethyl-hexyloxy)-1,4-phenylene vinylene] (MEH-PPV) are good donors (Nunzi,*2002).* Most of the time, evaporation step is indispensable in the manufacturing of conventional organic photovoltaic devices, but this process tends to increase the cost of the cell. Besides, ITO-PEDOT:PSS interface (de Jong et al., 2000) and Al top electrode (Do et al., 1994) is known to be quite unstable, which limits the lifetime of organic solar cells. Organic solar cells have low charge transport and a mismatch between exciton diffusion length and organic layer thickness. While the efficient absorption of light is provided by organic film based on P3HT:PCBM having a thickness over 250 nm (Liu et al., 2007a), exciton diffusion length of which surpassing causes exciton recombination, is about 10-20 nm in polymer based and in organic semiconductors (Nunzi, 2002). Although, organic solar cells have lower power conversion efficiency (~5%) than inorganic traditional solar cells (for crystalline silicon based solar cells ~25% in laboratory conditions); their cost and processing parameters are favorable (Deibel & Dyakonov, 2010*).*

In order to avoid the limitations of organic semiconductor and to improve the power conversion efficiency of organic solar cells, several approaches such as optical concepts, different device configurations such as inverted layer architecture, multijunction solar cells, novel materials with lower band gap (Park et al., 2009; Chen et al., 2009; Huo et al., 2009; Coffin et al., 2009), wider absorption ranges, higher dielectric constants and higher charge carrier mobility are some approaches are studied in last few years (Deibel & Dyakonov, 2010). Reversing the nature of charge collection in organic solar cells using a less air sensitive high work function metal (Ag, Au) (de Jong et al., 2000; Do et al., 1994; Liu et al., 2007a; Park et al., 2009; Chen et al., 2009; Huo et al., 2009; Coffin et al., 2009; Wong et al., 2006) as hole collecting electrode at the back contact and a metal oxide (TiO_x, ZnO) as hole blocking barrier and electron selective contact at the ITO interface to block the oxidation (Hau et al., 2008) is a beneficial approach to avoid from low power conversion efficiency, which limited absorption in solar spectrum causes. In particular, non-clorinated solvents are more appropriate for high volume manufacturing with low cost. Besides, active layer can be protected by use of metal oxides (i.e. vanadium oxide and cesium carbonate), which are used as buffer layer of inverted polymer solar cells (Li et al., 1997). However, there is still a trade-off between stability and photovoltaic performance in inverted solar cells (Hsieh et al., 2010).

Organic solar cells have many advantages such as potential to be semi-transparent, manufacture on both large or small areas compatible with mass production and low-cost, production possibility with continuous coating and printing processes on lightweight and flexible substrates (for example textiles), ecological and low-temperature production possibilities (Dennler et al., 2006a; Dennler & Sariciftci, *2005*).

Polymer heterojunction organic solar cells have attracted much attention because of their potential applications in large area, flexible and low-cost devices (Park et al., 2009; Yu et al., 1995; Chang et al., 2009; Dridi et al., 2008; Peet et al., 2009; Oey et al., 2006; Yu et al., 2008). Polymer based thin films on flexible and non-flexible substrates can be achieved by various printing techniques (see Fig. 3) (screen printing, inkjet printing, offset printing, flexo printing and so on), solution based coating techniques (dipping, spin coating, doctor blading, spray coating, slot-die coating and so on), and electrospinning (Krebs, 2009a).

Roll to roll, reel to reel, process is suitable for solar cells, which are on long flexible substrates (polymeric substrates and thin metal foils), and, which can be wound on a roll

(Krebs, 2009a). Various coating and printing techniques including knife-over-edge coating and slot die coating can be used for manufacturing flexible solar cells. The most appropriate processes for flexible photovoltaics should be free from Indium, toxic solvents and chemicals, and should have solution based manufacturing steps (coating and printing techniques), which results an environmentally recyclable product (Hoppe & Sariciftci, 2006). The studies about improving polymer solar cells (Günes et al., 2007; Hoppe & Sariciftci, 2006; Bundgaard & Krebs, 2007; Jørgensen et al., 2008; Thompson & Frechet, 2008; Tromholt et al., 2009) include developments in material properties and manufacturing techniques.

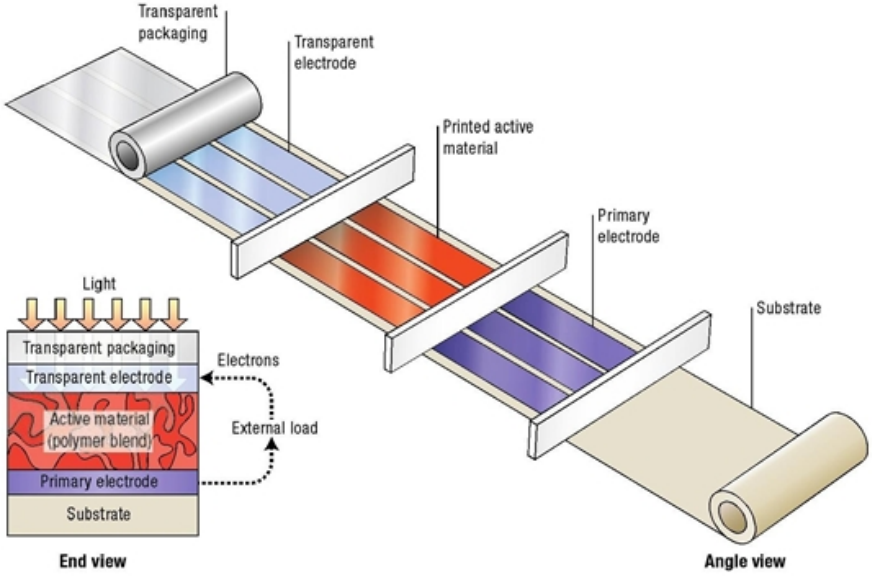

Fig. 3. Schematic description of printing process used for manufacturing of polymer-based photovoltaic cells. Reprinted by permission from Macmillan Publishers Ltd: Nature Photonics, *Gaudiana,* R. & *Brabec,* C. (2008). Organic materials: Fantastic plastic. Vol.2, pp.287- 289, copyright (2008).

2.3 Characterization of organic solar cells

Characterization of organic solar cells performed by measuring efficiencies in the dark and under an illumination intensity of 1000 W/m^2 (global AM1.5 spectrum) at 25^{o}C (IEC 60904-3: 2008, ASTM G-173-03 global) (Green et al., 2010). Generally a solar simulator is used as illumination source for simulating AM1.5 conditions. Air Mass (AM) is a measure of how much atmosphere sunlight must travel through to reach the earth's surface. AM1.5 means that the sun is at an angle about 48^o (Benanti & Venkataraman, 2006). A graph (Fig. 4) on which shows the current-voltage characteristics in the dark and under an illumination, gives significant information about photovoltaic performance and photoelectrical behavior of the cells (Nunzi, 2002).

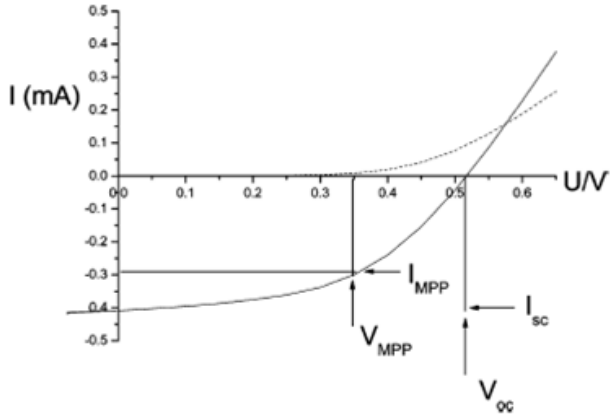

Fig. 4. Current-voltage (I-V) curves of an organic solar cell (dark, - - -; illuminated, -). The characteristic intersections with the abscissa and ordinate are the open circuit voltage (*V*oc) and the short circuit current (*I*sc), respectively. The largest power output (*P*max) is determined by the point where the product of voltage and current is maximized. Division of *P*max by the product of *I*sc and *V*oc yields the fill factor *FF* (Günes et al., 2007).

The overall efficiency of a solar cell can be expressed as follows :

$$\eta = \frac{P_{\max}}{P_{in}} = \frac{I_{sc}\ V_{oc}\ FF}{P_{in}} \tag{1}$$

Here, maximum power point is the point on the I-V curve where maximum power (P_{max}) is produced. The photovoltaic power conversion efficiency (η) of a solar cell is defined as the ratio of power output to power input. I_{sc} is the short-circuit current, which flows through the cell when applied voltage is zero, under illumination. Under an external load, current will always be less than max. current value. V_{oc}, the open-circuit voltage is the voltage when no current is flowing, under illumination. When current flows, voltage will be less than max. voltage value. FF, fill factor is the ratio of max. power output to the external the short-circuit current and open-circuit voltage values. FF is given by following formula:

$$FF = \frac{P_{\max}}{I_{sc}\ V_{oc}} = \frac{I_{mpp}\ V_{mpp}}{I_{sc}\ V_{oc}} \tag{2}$$

where I_{mpp} and V_{mpp} represent the current and the voltage at the maximum power point (P_{max}) in the four quadrant, respectively (Nunzi,*2002;* Benanti & Venkataraman, 2006).
The incident photon to collected electron (IPCE) or external quantum efficiency (EQE) under monochromatic lightning at a wavelength λ includes losses by reflection and transmission (Benanti & Venkataraman, 2006) and gives the ratio of collected charge carriers per incident photons (Dennler et al., 2006a):

$$IPCE = \frac{1240\ I_{sc}}{\lambda\ P_{in}} \tag{3}$$

2.4 Flexible organic solar cells

Solar cells generally developed on rigid substrates like glass and suffer from heavy, fragile and inflexible devices. However, stiff substrates limit usage, storage and transport of photovoltaic devices. Therefore, a big interest from both industrial and academic sides has been observed for research and development of flexible (foldable or rollable) solar cells, recently. Organic solar cells, easy scalable and suitable to roll-to-roll production with low-cost have potential to be used with flexible substrates such as textiles and fibers. Materials used in organic solar cells are also capable of producing lightweight photovoltaics. Polymer based substrates, which are used to replace rigid substrates and which have adequate flexibility are required to have mechanically and chemically stable, while organic solar cell manufacturing processes continue. Optimum substrate should have some features such as resistance to effects of chemical materials, water and air and also, mechanical robustness, low coefficients of thermal expansion, anti-permeability and smooth surface properties and so on.

Polyethylene terephtalate (PET), ITO coated PET, Poly(ethylene naphthalate) (PEN), Polyimide (PI), Kapton and Polyethersulphone (PES) are used as substrates to develop flexible solar cells.

Polyethylene terephtalate (PET) based fibers, which melt about 260^{o}C show good stability to UV light and most of the chemicals and exhibit good mechanical properties including flexibility and comfort ability both in fiber and fabric form (Mather *&* Wilson*, 2006*). However, PET foils are often used as substrate of the flexible photovoltaics (Breeze, et al., 2002; Aernouts et al., 2004; Winther-Jensen & Krebs, 2006; Krebs, 2009b). Manufacturing of photovoltaics using PET substrates is suitable for reel to reel production, which reduces material and production costs. PET foils are preferable materials for solar cells due to their price, mechanical flexibility and easy availability comparing to other substrates. However, use of PET foils is limited because it melts about 140 ^{o}C (Zimmermann et al., 2007; Krebs, 2009a; Krebs, 2009b). Thermocleavable materials are used for the preparation of very stable solar cells (Liu et al., 2004; Krebs & Spanggaard 2005; Krebs & Norrman, 2007; Krebs, 2008; Bjerring et al., 2008; Krebs et al., 2008) but, these materials are required to heat to a temperature of around 200^{o}C to achieve insolubility, which is a limitation to use of PET foils in conventional methods. However, PET substrates can be used with thermocleavable materials thanks to longer processing time (Krebs, 2009b).

Spin coating and screen printing techniques are used to coat highly conductive PEDOT:PSS dispersions onto flexible PET substrates as anode, which also improves an application of a metallic silver(Ag)-grid deposited between foil and electrode (Aernouts et al., 2004). A silk screen printing procedure (Winther-Jensen & Krebs, 2006) can be applied to develop PEDOT electrode with surface resistances down to 20 Ω^{-1} on flexible PET substrates. Researchers obtained 0.7 V open circuit voltage, 1 mA/cm^2 short circuit current and 0.2%, efficiency under simulated sun light (AM1.5 at 1000 W m^{-2}) with an active area of 4.2 cm^2 based on MEH-PPV:PCBM mixture and Al counter electrode.

In recent years, carbon nanotubes have found a wide variety of applications in photovoltaics. Films of SWNT networks can be printed on PET foils to get flexible transparent conducting electrodes. The well dispersed and stable solutions of SWNTs can be produced as electrode of flexible polymer based solar cells with various methods, which are inexpensive, scalable to large areas, and allows for the transfer of the film to a variety of surfaces. Such a flexible photovoltaic device configuration (Rowell et al., 2006) (see Fig. 5) (PET/SWNTs/PEDOT:PSS/P3HT:PCBM/Al) gave 2.5% efficiency of which efficiency is very close to conventional ITO coated glass based rigid solar cells.

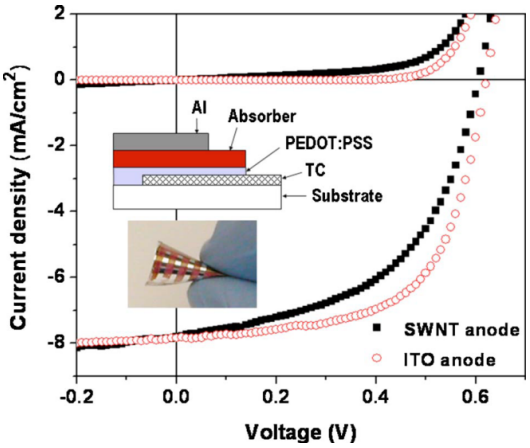

Fig. 5. Current density-voltage characteristics of P3HT:PCBM devices under AM1.5G conditions using ITO on glass (open circles) and flexible SWNTs on PET (solid squares) as the anodes, respectively. Inset: Schematic of device and photograph of the highly flexible cell using SWNTs on PET. Reprinted with permission from Rowell, M.W.; Topinka, M.A.; McGehee, M.D.; Prall, H.J.; Dennler, G.; Sariciftci, N.S.; Hu, L. & Gruner, G. (*2006*). Organic Solar Cells with Carbon Nanotube Network Electrodes. *Applied Physics Letters,* Vol.88, pp. 233506. Copyright 2006, American Institute of Physics.

An inverted layer sequence (see Fig. 6) was used (Zimmermann et al., 2007) in an ITO-free wrap through approach of which device configuration included PET/ AL-Ti/ Absorber (P3HT:PCBM)/ PEDOT:PSS/Au layer sequence. Thermal evaporation, e-beam evaporation and spin coating techniques were used for device fabrication on flexible substrate. Researchers obtained a power conversion efficiency of 1.1% (under 1000W/m² AM 1.5) from the device with additional serial circuitry, which employed top illumination by avoiding the use of ITO.

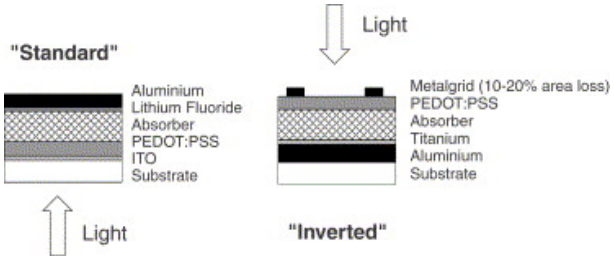

Fig. 6. Comparison of the widely used layer sequence on ITO/PEDOT:PSS electrode (left) and inverted layer sequence (right), where the ITO is replaced by a metal grid for small area devices. Reprinted from Sol. Energy Mater. Sol. Cells, 91, Zimmermann, B.; Glatthaar, M.; Niggemann, M.; Riede, M. K.; Hinsch, A. & Gombert, A., ITO-free wrap through organic solar cells–A module concept for cost- efficient reel-to-reel production., 374- 378, Copyright (2007), with permission from Elsevier.

The commercially available ITO-coated PET foils are used mostly in studies about flexible organic solar cells. PET layer is as polymeric substrate and ITO is the transparent conducting electrode of photovoltaic device.

Researchers (Brabec et al., 1999) performed efficiency and stability studies on large area (6 cm x 6 cm) flexible solar cells based on MDMO-PPV and PCBM materials and compared them with small area devices. Thin films were produced on two different substrates including ITO coated glass substrates and ITO coated PET foils with different active areas. The overall conversion efficiency of the flexible plastic solar cell is calculated with app. 1,2 % and a filling factor FF - 0.35 under monochromatic illumination (488 nm) with 10 mW/cm^2. It is possible to produce organic solar cells on flexible substrates without loosing efficiency, whereas fullerene bulk heterojunctions was still limited by charge transport. Al-Ibrahim et al. (Al-Ibrahim et al., 2005) developed photovoltaic devices based on P3HT and PCBM materials on ITO coated polyester foils with an active cell area of 0.5×0.5 cm^2 with the following photovoltaic device configuration: PET/ITO/PEDOT:PSS/P3HT:PCBM/Al. Device parameters without any special postproduction treatment were obtained as: V_{OC} = 600 mV, I_{SC} = 6.61 mA/cm^2, FF=0.39 and η=1.54% under irradiation with white light (AM1.5, 100mW/cm^2). These results were hopeful for device up-scaling and development of processing technologies for reel to reel production of flexible organic photovoltaic devices.

Different oligothiophene materials are used to develop (Liu et al., 2008) flexible organic photovoltaic devices on ITO-coated PET films. The organic layers (5-formyl-2,2′:5′,2″:5″,2‴-quaterthiophene (4T-CHO), 5-formyl-2,2′:5′, 2″:5″,2‴:5‴,2‴-quinquethiophene (5T-CHO) and 3,4,9,10-perylenetertracarboxylic dianhydride (PTCDA)) were deposited by vacuum deposition. While the PET-ITO/4T-CHO/PTCDA/Al device showed an open circuit voltage (V_{oc}) of 1.56 V and a photoelectric conversion efficiency of 0.77%, the PET-ITO/5T-CHO/PTCDA/Al device exhibited a V_{oc} of 1.70 V and photoelectric conversion efficiency of 0.84%. Stakhira et al. (2008) fabricated an organic solar cell consisting of an ITO/PEDOT:PSS/ pentacene (Pc)/Al multilayer structure on flexible PET substrate coated with conductive ITO layer. PEDOT:PSS/Pc and Al contact were formed by electron beam deposition technique. The photovoltaic effect was measured with open circuit voltage of ~0.5 V, short circuit current of 0.6 lA and fill factor 0.2. Researchers (Blankenburg et al., 2009) used continuous reel-to-reel (R2R) slot die coating process to develop polymer based solar cells on plastic foils with adjustable coating thicknesses. Transparent conducting and photoactive layers were prepared with good reproducibility and promising power conversion efficiencies (0.5–1% (1.7% as maximum value)).

Krebs et al. (2007) fabricated organic solar cells on ITO coated PET substrates. Active layer consisted of MEH-PPV was coated by screen-printing method and an optional layer of fullerene (C_{60}) and the final Al electrode were applied by vacuum coatings. Thirteen individual solar cells with an active area of 7.2 cm^2 were connected in series. In the simple geometry ITO/MEH-PPV/Al the module gave a V_{oc} of 10.5 V, an I_{sc} of 5 A, a FF of 13% and an efficiency (η) of 0.00001% under AM1.5 illumination with an incident light intensity. A geometry (ITO/MEH-PPV/C_{60}/Al) employing a sublimed layer of C_{60} improved *V*oc, *I*sc, FF and η to 3.6V, 178 A, 19% and 0.0002%, respectively. The results of roll-to-roll coated flexible large-area polymer solar-cell modules (eight serially connected stripes), which was performed in 18 different laboratories in Northern America, Europe and Middle East, were presented in another study (Krebs et al., 2009c). In all steps, roll-to-roll processing was employed. A zinc oxide nanoparticle layer, P3HT-PCBM and PEDOT:PSS layers were coated onto ITO coated PET by a modified slot-die coating procedure, respectively. ZnO as buffer layer has high electron mobility compared to titanium oxide (Yip et al., 2008) and so, can be ideal electron selective contact layer in polymer solar cells (Hau et al., 2008). The devices were completed by screen-printing silver paste and lamination of PET protective layer on top. In another study of Krebs (2009c) they prepared polymer solar cell module using all-solution processing on ITO

coated PET substrates. zinc oxide nanoparticles (ZnO-nps) were applied using either knife-over- edge coating or slot-die coating. A mixture of the thermocleavable poly-(3-(2-methylhexan-2-yl)- oxy-carbonyldithiophene)(P3MHOCT) and ZnO-nps was applied by a modified slot-die coating procedure as second layer. The third layer was patterned into stripes and juxtaposed with the ITO layer. The fourth layer comprised screen-printed or slot-die-coated PEDOT:PSS and the fifth and the final layer comprised a screen-printed or slot-die-coated silver electrode. Coating ITO onto the PET substrate by sputtering process in a vacuum, cost of ITO and thermal disadvantage of PET foils (temperatures only up to 140°C) were some implications of the research. Also, efficient inverted polymer solar cell fabricated by roll-to-roll (R2R) process could be obtained in terms of both power conversion efficiency and operational stability. Maximum 1.7% efficiency for the active area of the full module was obtained from eight serially connected cells (Krebs et al., 2009a). They (Krebs et al., 2009b) showed the versatility of the polymer solar cell technology with abstract forms for the active area, a flexible substrate, processing entirely from solution, complete processing in air using commonly available screen printing, and finally, simple mechanical encapsulation using a flexible packaging material and electrical contacting post-production using crimped contacts. Following two different devices were developed:

PET/ITO/ZnO/P3CT/ZnO/PEDOT:PSS/Ag paste/Cold laminated PET with acrylic resin and

PET/ITO/ZnO/P3CT/PCBM/ZnO/PEDOT:PSS/Ag paste/Cold laminated PET with acrylic resin

Poly(ethylene naphthalate) (PEN), has higher glass transition temperature than PET and this provides potential post-treatment of devices (Dennler et al., 2006b). However, shrinkage is seen in the material and so, subsequent processes will be problematic (Krebs, 2009b). PEN substrates (Dennler et al., 2006b) were used to develop flexible solar cells and were coated with ultra-high barrier multilayer coatings (Fig. 7). Shelf lifetime of conjugated polymer:fullerene

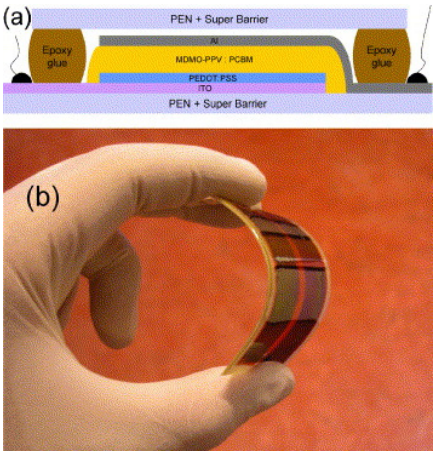

Fig. 7. (a) Cross-sectional view of the conjugated polymer:fullerene solar cells investigated here; (b) picture of a bent device. Reprinted from Thin Solid Films, 511–512, Dennler, G.; Lungenschmied, C.; Neugebauer, H.; Sariciftci, N. *S.*; Latreche, M.; Czeremuszkin, *G.* & Wertheimer, M. R., A new encapsulation solution for flexible organic solar cells, *349*–353, Copyright (2006), with permission from Elsevier.

solar cells fabricated on PEN substrates and encapsulated with flexible, transparent PEN-based ultra-high barrier material entirely fabricated by plasma enhanced chemical vapor deposition (PECVD) was studied. ITO bottom electrodes were sputtered through a mask onto flexible substrates and so, good adhesion and ~60 Ω/square sheet resistance was obtained. The complete device provided a shelf lifetime of more than 3000h. Lungenschmied et al. (2007) also studied interconnected organic solar cell modules on flexible ultrahigh barrier foils (Fig. 8). Flexible solar cell modules had 11 cm^2 total active area and reached 0.5% overall powerconversion efficiency under AM1.5 conditions. ITO bottom electrode was structured by deposition through a shadow mask directly onto substrate and a sheet resistance of approximately 60 Ω/square was obtained. PEDOT:PSS and P3HT: PCBM were coated using the doctor blade technique. Al top electrode was thermally evaporated using a shadow mask.

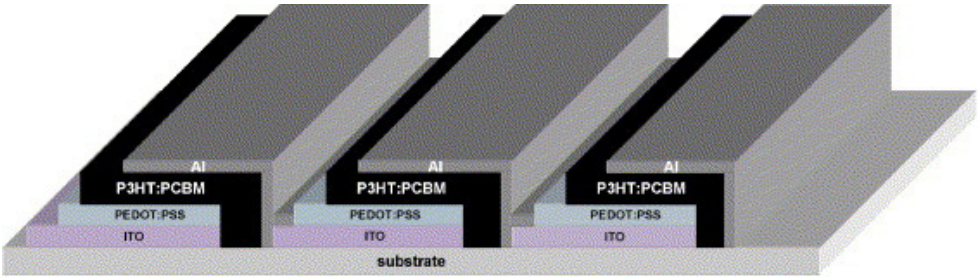

Fig. 8. Serial connection of organic solar cells. Reprinted from Sol. Energy Mater. Sol. Cells, 91, Lungenschmied, C.; Dennler, G.; Neugebauer, H. ; Sariciftci, N. S. ; Glatthaar, M. ; Meyer, T. & Meyer, A., Flexible, long-lived, large-area, organic solar cells, 379–384, Copyright (2007), with permission from Elsevier.

A roll-to-roll process enables fabrication of polymer solar cells with many layers on flexible substrates. Inverted solar cell designs (Krebs, 2009b) can be used on both transparent and non-transparent flexible substrates. Silver nanoparticles on PEN were developed as bottom electrode. ZNO-nps from solution, P3HT-PCBM as active layer and PEDOT:PSS as hole transporting layers were coated, respectively, using slot-die coating. The last electrode was applied by screen printing of a grid structure that allowed for transmission of 80% of the light. The devices were tested under simulated sunlight (1000Wm^{-2}, AM1.5G) and gave 0.3% of power conversion efficiency for the active layer. The illumination of the device is through the top electrode enabling the use of non-transparent substrates. The poor optical transmission in PEDOT:PSS-silver grid electrode caused a decrease in performance.
Polyimide (PI) films, which show high glass transition temperatures, low surface roughnesses, low coefficients of thermal expansion, and high chemical resistance under manufacturing conditions, are suitable for fabrication of flexible electronics. Inverted polymer solar cells were studied on PI substrates (Hsiao et al., 2009). Surface-nickelized polyimide films (NiPI films) as cathodes (back contact electrode) and high-conductivity PEDOT:PSS films as anodes were coated using solution based processes (see Fig. 9). The resulting FF of 0.43 was lower than that of standard devices. However, this ITO-free inverted polymer solar cells exhibited high performance, with the power conversion efficiency reaching 2.4% under AM 1.5 illumination (100$mWcm^{-2}$).

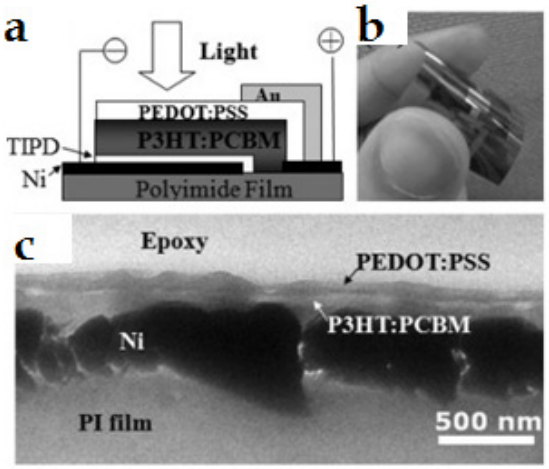

Fig. 9. (a) Architecture of an inverted PSC featuring an inverted sequence on NiPI as the back contact electrode. (b) Optical image of an inverted PSC on NiPI. (c) TEM cross-sectional image of an inverted PSC on NiPI. Scale bars, 500 nm. Reprinted from Org.Electron, 10, Hsiao, Y. S.; Chen, C. P. ; Chao, C. H. & Whang, W. T., All-solution-processed inverted polymer solar cells on granular surface-nickelized polyimide, 551-561, Copyright (2009), with permission from Elsevier.

Kapton®, which was synthesized by polymerizing an aromatic dianhydride with an aromatic diamine, has good chemical and thermal resistance (>400 ºC). Kapton® polyimide films can be used in a variety of electrical and electronic uses such as wire and cable tapes, substrates for printed circuit boards, and magnetic and pressure-sensitive tapes (matweb, 2010). Guillen and Herrero (2003) developed both bottom and top electrodes onto polyimide sheets (Kapton KJ) to be used in applications of lightweight and flexible thin film photovoltaic devices. ITO as the frontal electrical contact and Mo, Cr and Ni layers as the back electrical connections were prepared and then compared with conventional electrodes on glass substrates. ITO deposited polyimide sheets showed similar optical transmittance and higher electrical conductivity than ITO coated glass substrates. Mo, Cr and Ni coated polyimide sheets showed similar structure and electrical conductivity to Mo, Cr and Ni coated glass substrates without bending or adhesion failure.

A commercially available polyimide foil (Kapton), which was overlayed with copper, was used as the substrate of polymer solar cell in a roll-to-roll process that does not involve ITO (Krebs, 2009d). Titanium metal was sputtered onto the kapton/copper layer in the vacuum and both the monolithic substrate and back electrode for the devices were obtained. PEDOT:PSS and the active layer were slot-die coated onto the kapton (25 μm) /Cu/Ti foil, respectively. A front electrode, a protective layer and finally a silver grid was applied by screen printing technique. Vacuum coating step was the current limitation of the device.

Polyethersulphone (PES), which is related to polyetheretherketone and polyetherimide, is used as thermoplastic substrate and has high glass transition temperature (Tg ~223ºC). PES was used as substrate to fabricate small molecule organic solar cells, which have single heterojunction structure, and, which use PEDOT:PSS anodes possessing low sheet resistance (~450 Ω/ℝ). High conductivity PEDOT:PSS layers were prepatterned using photolithographic technique and spin cast onto fully flexible thermoplastic PES-based substrates having %90 optical transmission. Both organic solar cells, which have plastic and

glass based substrates, and, which use a hole transport material, 4,4-bis[*N*-(1-naphthyl)-*N*-phenyl-amino]biphenyl (α-NPD) and C_{60} bilayer structure, exhibited high carrier mobilities and high V_{oc}=0.85V (AM1.5, 97 mW/cm^2) (Kushto et al., 2005).

2.5 Solar cell integrated textiles

Among the photovoltaic technologies, organic solar cells are the most suitable ones to textile structures in terms of favorable features such as flexibility, lightness, cost-effectiveness and usage performance. Studies about photovoltaic textiles consider two main approaches: First, solar cell is formed elsewhere and then, photovoltaic structure is integrated in/onto textiles using various techniques, i.e. patching. Second, solar cell is formed in fiber or textile form. So, it can be used as fiber itself or can form textile structures, which are partly or completely photovoltaic. Shelf lifetime, cost and efficiency of organic solar cells are still important issues for also photovoltaic fibers and textiles to be overcome before commercialization.

Utilizing flexible solar cells with textiles can open many application fields for photovoltaic textiles such as electronic textiles besides powering movable electronic devices. Solar cell integrated bags, jackets and dresses are some of the recent applications of polymer based solar cells. For example, in study of Krebs et al. (2006) incorporation of polymer based organic solar cells into textile structures were performed by two ways: In first one, PET substrate was coated with ITO, MEH-PPV, C_{60} and Al, respectively. Then, device was laminated using PET. In second one, PE layer was laminated onto textile substrate. Then, by applying PEDOT, active material and final electrode, respectively, device was completed. Completed devices were integrated into clothes (Fig. 10).

Fig. 10. An example of patterned polymer solar cells on a PET substrate incorporated into clothing by sewing through the polymer solar cell foil using an ordinary sewing machine. Connections between cells were made with copper wire that could also be sewn into the garment. The solar cells were incorporated into a dress and a belt. Design by Tine Hertz Reprinted from Sol. Energy Mater. Sol. Cells, 90, Krebs F.C.; Biancardo M.; Jensen B.W.; Spanggard H. & Alstrup J., Strategies for incorporation of polymer photovoltaics into garments and textiles, 1058-1067, Copyright (2006), with permission from Elsevier.

2.6 Studies about polymer nanofibers for solar cells

There are several studies about developing conductive polymer nanofibers used to fabricate solar cells. Various methods such as self-assembly (Merlo & Frisbie, 2003), polymerization in nanoporous templates (Martin, 1999), dip-pen nano-lithography (Noy et al., 2002), and electrospinning (Babel et al., 2005; Wutticharoenmongkol et al., 2005; Madhugiri; 2003) techniques are used to produce conductive polymer nanowires and nanofibers. Nanofibers having ultrafine diameters provide some advantages including mechanical performance, very large surface area to volume ration and flexibility to be used in solar cells (Chuangchote et al., 2008a).

Since morphology of the active layer in organic solar cells plays an important role to obtain high power conversion efficiencies, many researchers focus on developing P3HT nanofibers for optimized morphologies (Berson et al., 2007; Li et al., 2008; Moulé & Meerholz, 2008). Nanofibers can be deposited onto both conventional glass-based substrates flexible polymer based substrates, which have low glass transition temperature (Bertho et al., 2009).

A fabrication method (Berson et al., 2007) was presented to produce highly concentrated solutions of P3HT nanofibers and to form highly efficient active layers after mixing these with a molecular acceptor (PCBM), easily. A maximum PCE of 3.6% (AM1.5, 100 $mWcm^{-2}$) has been achieved without any thermal post-treatment with the optimum composition:75 wt% nanofibers and 25 wt% disorganized P3HT. Manufacturing processes were appropriate to be used with flexible substrates at room temperatures. Bertho et al. (Bertho et al., 2009) demonstrated that the fiber content of the P3HT-fiber:PCBM casting solution can be easily controlled by changing the solution temperature. Optimal solar cell efficiency was obtained when the solution temperature was 45 ^{o}C and the fiber content was 42%. Fiber content in the solution effected the photovoltaic performances of cells.

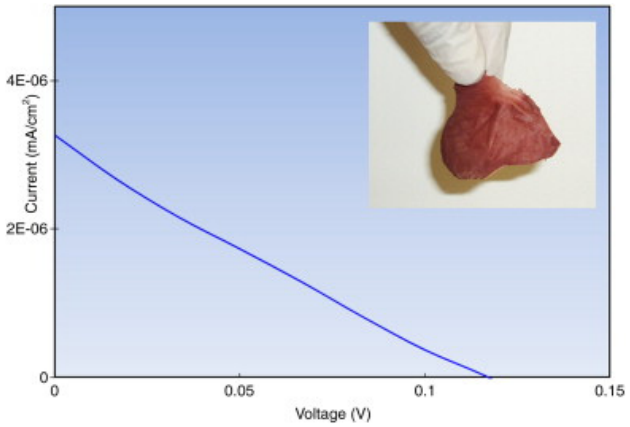

Fig. 11. Jsc–V graph of the P3HT/PCBM based solar cloth measured under 1 Sun conditions. Inset shows a picture of the solar cloth fabricated using electrospinning. Reprinted from *Materials Letters*, 64, Sundarrajan, S.; Murugan, R.; Nair, A. S. & Ramakrishna, S., 2369 -2372., Copyright (2010), with permission from Elsevier.

Electrospinning technique (Chuangchote et al., 2008b) is also used to prepare photoactive layers of polymer-based organic solar cells without thermal post-treatment step. Electrospun MEH-PPV nanofibers were obtained after polyvinylpyrrolidone (PVP) was removed from

as-spun MEH-PPV/PVP fibers. A ribbon-like structure aligned with wrinkled surface in fiber direction was gained. Bulk heterojunction organic solar cells were manufactured by using the electrospun MEH-PPV nanofibers with a suitable acceptor. Chuangchote et al. produced ultrafine MEH-PPV/PVP composite fibers (average diameters ranged from 43 nm to 1.7 mm) by electrospinning of blended polymer solutions in mixed solvent of chlorobenzene and methanol under the various conditions.
Recently, a photovoltaic fabric (Sundarrajan et al., 2010) based on P3HT and PCBM materials were developed. The non-woven organic solar cloth was formed by co-electrospinning of two materials: the core-shell nanofibers as the core and PVP as the shell. The efficiency of the fiber-based solar cloth was obtained as 8.7×10^{-8} due to processing conditions and thickness of structure (Fig. 11-12). However, this is an novel and improvable approach to develop photovoltaic fabrics for smart textiles.

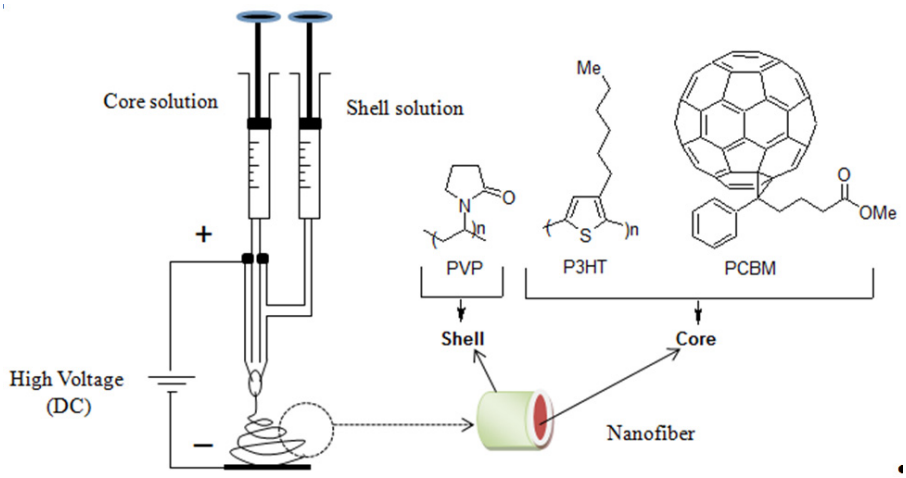

Fig. 12. Schematic diagram of core-shell electrospinning set-up used in this study: direct current voltage at 18 KV, the flow rate of P3HT/PCBM in chloroform/toluene (3:1 ratio, as core) and PVP in chloroform/ethanol (1:1 ratio, shell) was set at 1.3 mL/h and 0.8 mL/h, Respectively. Reprinted from *Materials Letters*, 64, Sundarrajan, S.; Murugan, R.; Nair, A. S. & Ramakrishna, S., 2369 -2372., Copyright (2010), with permission from Elsevier

3. Organic photovoltaic fibers

In recent years, attention on fibrous and flexible optoelectronic structures is increased in both scientific and industrial areas in terms of lightweight, low-cost and large scale production possibilities. Photovoltaic fibers, cost effective and scalable way of solar energy harvesting, work with the principle of solar cell, which produces electricity by converting photons of the sun. Although solar cells made from silicon and other inorganic materials are far more efficient for powering devices than organic solar cells, they are still too expensive to be used in widespread and longterm applications. In studies of fiber-based solar cells, which are incorporated in textiles, organic semiconductors that are naturally flexible and light-weight, are ideal candidates compared to conventional inorganic semiconductors.

For developing optimum photovoltaic textile, choice of the fiber type, which determines UV resistance and maximum processing temperature for photovoltaics and textile production methods (Mather & Wilson, 2006) need to be considered.
In recent years, there are several studies about photovoltaic fibers based on polycrystalline silicon (Kuraseko et al., 2006), dye sensitized solar cells (Fan et al., 2008; Ramier et al., 2008; Toivola et al., 2009) and organic solar cells (Bedeloglu et al., 2009, 2010a, 2010b, 2010c, 2011; Curran et al., 2006; Curran et al., 2008; Curran et al., 2009; Lee et al., 2009; Liu et al., 2007a; Liu et al., 2007b; O'Connor et al., 2008; Zhou et al., 2009; Zou et al., 2010). Protection of liquid electrolyte in DSSCs is problematic causing leakage and loss of performance. However, solid type DSSCs suffer from cracking due to low elongation and bending properties. The organic solar cells based fibers still suffer from low power conversion efficiency and stability. However, organic materials are very suitable to develop flexible photovoltaic fibers with low-cost and in large scale (Bedeloglu et al., 2009; DeCristofano, 2008).
The fiber geometry due to circular cross-section and cylindrical structure brings advantages in real usage conditions. Contrast to planar solar cells, absorption and current generation results in a greater power generation, which can be kept constant during illumination owing to its symmetric structure. A photovoltaic fiber has very thin coatings (about a few hundred nanometers). Therefore, a photovoltaic fabric made from this fiber will be much lighter than that of other thin film technologies or laminated fabric (Li et al., 2010a).
Organic photovoltaic fibers have been produced in different thicknesses and lengths, using different techniques and materials in previous studies. In order to develop fiber based solar cells, mainly solution based coating techniques were applied to develop polymer based electrodes and light absorbing layers. However, deposition techniques in a vacuum were used to develop a photovoltaic fiber formation, too.
Current studies about fiber shaped organic photovoltaics used different substrate materials such as optical fibers (Do et al., 1994), polyimide coated silica fibers (O'Connor et al., 2008), PP fibers and tapes (Bedeloglu et al., 2009, 2010a, 2010b, 2010c, 2011) and stainless steel wires (Lee et al., 2009).
In order to fabricate photovoltaic fiber with low-cost and high production rate, an approach is using a drawing a metal or metalized polymer based fiber core through a melt containing a blend of photosensitive polymer. A conductor can also be applied parallel to the axis of the photoactive fiber core (Shtein & Forrest, 2008).
In optical fiber concept, photovoltaic fiber takes the light and transmitted down the fiber by working as an optical can. The fiber shaped photovoltaics approach can reduce the disadvantage of organic solar cells, which is trade-off between exciton diffusion length and the photoactive film thickness in conjugated polymers based solar cells, by forming the solar cell around the fiber (Li et al., 2010b).

3.1 Device structures

Organic solar cell materials are generally coated around the fibers concentrically in an order in photovoltaic fibers, as in planar solar cells. The Substrate, active layer and conductive electrodes do their own duties. Recent studies about photovoltaic fibers can be classified in two groups: First one is interested with photovoltaic fibers that were illuminated from outside as in photovoltaic textiles, second one is the study of illuminated from inside the photovoltaic fiber (Zou et al., 2010).
For the outside illuminated photovoltaic fibers, different device sequences and manufacturing techniques were used. A fiber-shaped, ITO-free organic solar cell using small molecular

organic compounds was demonstrated by Shtein and co-workers (O'Connor et al., 2008). Light was entered the cell through a semitransparent outer electrode in the fiber-based photovoltaic cell. Concentric thin films of Mg/Mg:Au/Au/CuPc/C_{60}/Alq_3/Mg:Ag/Ag were deposited onto rotated polyimide coated silica fibers having 0.48 mm diameter by thermal evaporation technique in a vacuum (see Fig. 13). The cell exhibited 0.5% power conversion efficiency, which was much less dependent on variations in illumination angle. However, coated fiber length was limited by the experimental deposition chamber geometry.

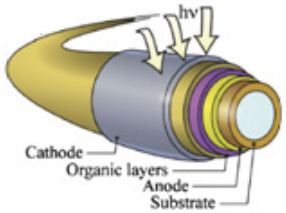

Fig. 13. A flexible polyimide coated silica fiber substrate device, with the layers deposited concentrically around the fiber workers. Reprinted with permission from O'Connor, B.; Pipe, K. P. & Shtein, M. (2008). Fiber based organic photovoltaic devices. *Appl. Phys. Lett.*, vol. 92, pp. 193306-1–193306-3. Copyright 2008, American Institute of Physics.

Bedeloglu et al. developed flexible photovoltaic devices (Bedeloglu et al., 2009, 2010a, 2010b, 2010c, 2011) to manufacture textile based photovoltaic tape and fiber by modifying planar organic solar cell sequence. The non-transparent and non-conductive polymeric materials (PP tapes and fibers) were used as substrate and dip coating and thermal evaporation technique were used to coat active layer and top electrode, respectively. Devices gave moderate efficiencies in photovoltaic tape (PP/Ag/PEDOT:PSS/P3HT:PCBM/LiF/Al) and in photovoltaic fiber (PP/PEDOT:PSS/P3HT:PCBM/LiF/Al) (see Fig. 14). Light entered the photovoltaic structure from the outer semi-transparent cathode (10 nm LiF/Al). Obtained structures that were very flexible and lightweight were hopeful for further studies using textile fibers.

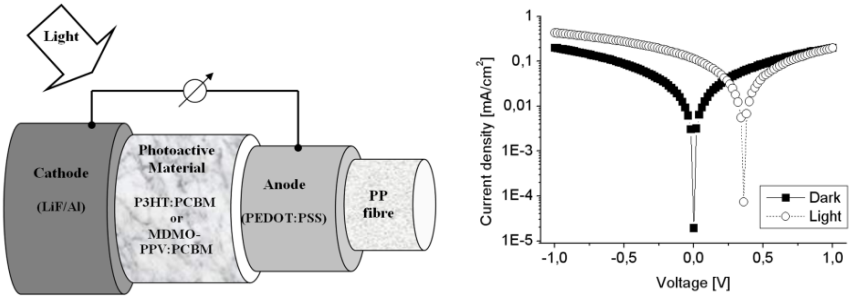

Fig. 14. Schematic drawing of a photovoltaic fiber and I–V curves of P3HT:PCBM -based photovoltaic fibers, lighting through the cathode direction. The final, definitive version of this paper has been published in < Textile Research Journal>, 80/11/July/2010 by <<SAGE Publications Ltd.>>/<<SAGE Publications, Inc.>>, All rights reserved. ©.

Flexible photovoltaic wires based on organic materials can also be produced to be used in a broad range of applications including smart textiles (Lee et al., 2009). In the study, a stainless steel wire used as primary electrode was coated with TiO_x, P3HT and $PC_{61}BM$,

PEDOT·PSS materials as electron transport layer, active layer and hole transport layer, respectively (Fig. 15). Another wire as secondary electrode was wrapped around the coated primary wire with a rotating stage similar to commercial wire winding operations. In the best cell, the short circuit current density was 11.9 mA/cm² resulting 3.87% power conversion efficiency.

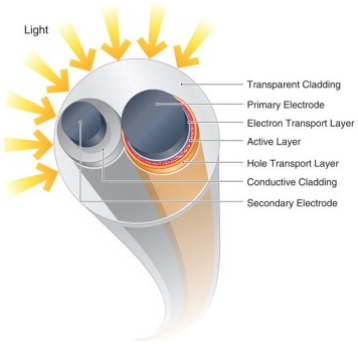

Fig. 15. Schematic of a complete fiber showing the potential for shadowing by the secondary electrode. From Lee, M. R.; Eckert, R. D. ; Forberich, K. ; Dennler, G.; Brabec, C. J. & Gaudiana, R. A. (2009). Solar power wires based on organic photovoltaic materials. *Science*, Vol. 324, pp. 232–235. Reprinted with permission from AAAS.

Many researchers considered photovoltaic fiber design for different function from an optical perspective to capture or trap more light. An optical design was investigated (Curran et al., 2006) to increase the efficiency of photovoltaic device by directing the incident light into the photoactive layer using optical fibers. Prepared fibers are worked up into bundle to confine the light in the device. Polymer based organic solar cell materials are used to develop an optical fiber-based waveguide design (Liu et al., 2007a). P3HT:PCBM is commonly used composite material to form active layer. Carroll and co-workers added top electrode (Al) to only one side of the fiber and tested the photovoltaic fibers under standard illumination at the cleaved end of the fibers. Optical loss into the fiber based solar cell increased as the fiber diameter decreased (See Fig. 16) and increasing efficiency was obtained by the smaller diameter photovoltaic fibers. In their other study (Liu et al., 2007b), performances of the photovoltaic fibers were compared as a function of incident angle of illumination (varied from 0^o – 45^o) on the cleaved face of the fiber. 1/3 of the circumference was coated with thick outer electrode (LiF/Al) due to fibers having small diameter. Photovoltaic performance of the devices was dependent on fiber diameter and the angle of the incidence light onto the cleaved fiber face.

Using an optical fiber having 400 μm in diameter, microconcentrator cell (Curran et al., 2008) was fabricated to develop an efficient method of light capturing for the optical concentration by using a mathematical based model to pinpoint how to concentrate light within the microconcentrator cell. Behaviour of light between the fiber entrance and active semiconductor layer was investigated. The fiber-based photovoltaic cell, which was a solar collector that utilized internal reflector to confine light into an organic absorber, collected nearly 80% of the incoming photons as current, at ~3 kOhms.cm (Zhou et al., 2009). Li et al. (2010) developed a mathematical model that was also supported by experimental results, for light transmission, absorption and loss in fiber-based organic solar cells using ray tracing

and optical path iteration. A patent was developed about photovoltaic devices having fiber structure and their applications (Curran et al., 2009). A tube-based photovoltaic structure was developed to capture optical energy effectively within the absorbing layer without reflective losses at the front and rear surfaces of the devices (Li et al., 2010b). That architecture was enabled that the absorption range of a given polymer (P3HT:PCBM) can be broaden by producing power from band edge absorption.

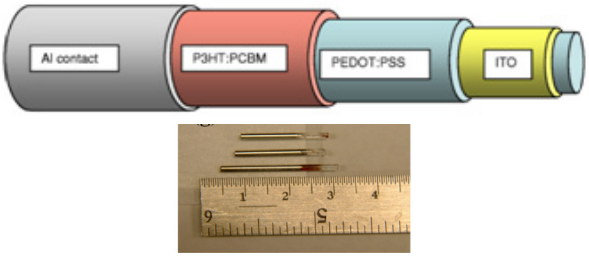

Fig. 16. (a) Schematic diagram showing the device structure (we note that a 0.5nm LiF layer is added below the metal contact but not shown), and (g) optical micrographs of the finished fibers. Reprinted with permission from Liu, J. W.; Namboothiry, M. A. G. & Carroll, D. L. (2007). Fiber-based architectures for organic photovoltaics. *Appl. Phys. Lett.*, Vol. 90, pp. 063501-1–063501-3. Copyright 2007, American Institute of Physics.

4. Conclusions

Polymer solar cells carry various advantages, which are suitable to flexible and fiber-shaped solar cells. However, optimum thickness for photovoltaic coatings and adequate smoothness for the surface of each layer (substrate, photoactive layer and electrodes) are required to obtain higher power conversion efficiencies and to prevent the short-circuiting in the conventional and flexible devices. Suitable coating techniques and materials for developing photovoltaic effect on flexible polymer based textile fibers are also needed not to damage photovoltaic fiber formation in continuous or discontinuous process stages. Many studies still continue for improving stability and efficiency of photovoltaic devices.

Flexible solar cells can expand the applications of photovoltaics into different areas such as textiles, membranes and so on. Photovoltaic fibers can form different textile structures and also can be embedded into fabrics forming many architectural formations for powering portable electronic devices in remote areas. However, optimal photovoltaic fiber architecture and the suitable manufacturing processes to produce it are still in development stage. More studies are required to design and perform for a working photovoltaic fiber.

A viable photovoltaic fiber that is efficient and have resistance to traditional textile manufacturing processes, which are formed from some consecutive dry and wet applications, and, which damage to textile structure, will open new application fields to concepts of smart textiles and smart fabrics.

5. References

Aernouts, T.; Vanlaeke, P.; Geens, W.; Poortmans, J.; Heremans, P.; Borghs, S.; Mertens, R.; Andriessen,R. & Leenders, L. (2004). Printable anodes for flexible organic solar cell modules. *Thin Solid Films,* Vol.22, pp.451-452, ISSN: 0040-6090.

Ajayan, P. M. (1999). Nanotubes from Carbon, *Chem. Rev*. Vol.99, pp.1787- 1800, ISSN: 1520-6890.

Ahlswede, E.; Muhleisen, W.; bin Moh Wahi, M.W.; Hanisch, J. & Powalla, M. (2008). Highly efficient organic solar cells with printable low-cost transparent contacts. *Appl. Phys. Lett.* Vol.92, pp.143307, ISSN: 1077-3118.

Al-Ibrahim, M.; Roth, H.-K.; Zhokhavets, U.; Gobsch, G. & Sensfuss S. (2005) Flexible large area polymer solar cells based on poly(3-hexylthiophene)/fullerene. *Solar Energy Materials and Solar Cells,* Vol.85, No.1, pp. 13-20, ISSN 0927-0248.

Antoniadis, H.; Hsieh, B. R.; Abkowitz, M. A.; Stolka, M., & Jenekhe, S. A. (1994). Photovoltaic and photoconductive properties of aluminum/poly(p-phenylene vinylene) interfaces. *Synthetic Metals*, Vol. 62, pp. 265-271, ISSN: 0379-6779.

Babel, A.; Li, D.; Xia, Y. & Jenekhe, S. A. (2005). Electrospun nanofibers of blends of conjugated polymers: Morphology, optical properties, and field-effect transistors. *Macromolecules,* Vol. 38, pp.4705- 4711, ISSN: 1520-5835.

Baughman, R. H.; Zakhidov, A. A. & de Heer, W. A. (*2002*). Carbon Nanotubes – The Route Towards Applications. *Science,* Vol.297, pp.*787*-792, ISSN: 0036-8075 (print), 1095-9203 (online).

Bedeloglu, A.; Demir, A.; Bozkurt, Y. & Sariciftci, N.S. (2009). A flexible textile structure based on polymeric photovoltaics using transparent cathode. *Synthetic. Metals*, Vol.159, pp.2043–2047, ISSN: 0379-6779.

Bedeloglu, A.; Demir, A.; Bozkurt, Y.& Sariciftci, N.S. (2010a).A Photovoltaic Fibre Design for. Smart Textiles. *Textile Research Journal,* Vol.80, No.11, pp.1065-1074, eISSN: 1746-7748, ISSN: 0040-5175.

Bedeloglu, A.; Koeppe, R.; Demir, A.; Bozkurt, Y. & Sariciftci, N.S. (2010b). Development of energy generating photovoltaic textile structures for smart applications. *Fibers and Polymers,* Vol.11, No.3, pp.378-383, ISSN: 1229-9197 (print version), 1875-0052 (electronic version).

Bedeloglu, A.; Demir, A.; Bozkurt, Y. & Sariciftci, N.S. (2010c). Photovoltaic properties of polymer based organic solar cells adapted for non-transparent substrates. *Renewable Energy,* Vol.35, No.10, pp.2301-2306, ISSN: 0960-1481.

Bedeloglu, A.; Jimenez, P.; Demir,A.; Bozkurt, Y.; Maser, W. K., & Sariciftci, NS. (2011). Photovoltaic textile structure using polyaniline/carbon nanotube composite materials. *The Journal of The Textile Institute,* Vol. 102, No. 10, pp. 857–862, ISSN:1754-2340 (electronic) 0040-5000 (paper).

Beeby, S.P. (2010). Energy Harvesting Materials for Smart Fabrics and Interactive Textiles. *http://gow.epsrc.ac.uk/ViewGrant.aspx?GrantRef=EP/I005323/1*

Benanti, T. L. & Venkataraman, D. (*2006*). Organic Solar Cells: An Overview Focusing on Active Layer Morphology. *Photosynthesis Research,* Vol. 87, pp.73-81, ISSN: 0166-8595 (print version), 1573-5079 (electronic version).

Berson, S.; De Bettignies, R.; Bailly, S. & Guillerez, S. (2007). Poly(3-hexylthiophene) Fibers for Photovoltaic Applications. *Adv. Funct. Mater.* , Vol.17, pp. 1377-1384, Online ISSN: 1616-3028.

Bertho, S.; Oosterbaan, W.; Vrindts, V.; D'Haen, J.; Cleij, T.; Lutsen, L.; Manca, J. & Vanderzande, D. (2009). Controlling the morphology of nanofiber-P3HT:PCBM blends for organic bulk heterojunction solar cells. *Organic Electronics,* Vol. 10, No.7, pp.1248-1251, ISSN: 1566-1199.

Bjerring, M.; Nielsen, J. S.; Siu, A.; Nielsen, N. C. & Krebs, F. C. (2008). An explanation for the high stability of polycarboxythiophenes in photovoltaic devices—A solid-state NMR dipolar recoupling study *Sol. Energy Mater. Sol.Cells.,*Vol. 92,pp. 772– 784, ISSN 0927-0248.

Blankenburg, L.; Schultheis, K.; Schache, H.; Sensfuss, S. & Schrodner, M. (2009). Reel-to-reel wet coating as an efficient up-scaling technique for the production of bulk heterojunction polymer solar cells. *Sol. Energy Mater. Sol. Cells,* Vol.93, pp.476, ISSN: 0927-0248.

Brabec, C.J.; Padinger, F.; Hummelen, JC; Janssen RAJ. & Sariciftci, NS. (1999). Realization of Large Area Flexible Fullerene - Conjugated Polymer Photocells: A Route to Plastic Solar Cells. *Synthetic Metals,* Vol. 102, pp. 861-864, ISSN: 0379-6779.

Brabec, C. J.; Shaheen S. E.; Winder C. & Sariciftci, N. S. (2002). Effect of LiF/metal electrodes on the performance of plastic solar cells. *Appl. Phys. Lett*., Vol.80, pp.1288–1290, Print: ISSN 0003-6951, Online: ISSN 1077-3118.

Brabec, C.; Sariciftci, N. & J. Hummelen, (2001a). Plastic Solar Cells. *Adv. Funct. Mater.* Vol.11, No.1, pp.15-26, Online ISSN: 1616-3028.

Brabec, C.; Shaheen, S.; Fromherz, T.; Padinger, F.; Hummelen, J.; Dhanabalan, A.; Janssen, R. & Sariciftci, N.S. (2001b). Organic Photovoltaic Devices produced from Conjugated Polymer /Methanofullerene Bulk Heterojunctions. *Synth. Met.* Vol.121, pp.1517-1520, ISSN: 0379-6779.

Breeze, A. J.; Salomon, A.; Ginley, D.S.; Gregg, B. A.; Tillmann, H. & Hoerhold, H. H. (2002). Polymer - perylene diimide heterojunction solar cells. *Appl. Phys. Lett.,* Vol. 81, pp.3085–3087, ISSN: 1077-3118.

Bundgaard, E. & Krebs, F. C. (2007). Low band gap polymers for organic photovoltaics. *Sol. Energy Mater. Sol. Cells*, vol. 91, pp.954– 985, ISSN 0927-0248.

Cai, W.; Gong, X. & Cao, Y. (2010). Polymer solar cells: Recent development and possible routes for improvement in the performance. *Solar Energy Materials and Solar Cells,* Vol.94, No.2, pp.114–127, ISSN 0927-0248.

Chang Y T.; Hsu S L.; Su M. H. & Wei K.H. (2009). Intramolecular Donor–Acceptor Regioregular Poly(hexylphenanthrenyl-imidazole thiophene) Exhibits Enhanced Hole Mobility for Heterojunction Solar Cell Applications. *Adv. Mater.,* Vol.21, pp.2093-2097, Online ISSN: 1521-4095.

Chen, H. Y.; Hou, J. H.; Zhang, S. Q.; Liang, Y. Y.; Yang, G. W.; Yang, Y.; Yu, L. P.; Wu, Y. & Li, G. (2009). Polymer solar cells with enhanced open-circuit voltage and efficiency. *Nat. Photonics,*Vol. 3, pp.649-653, ISSN: 1749-4885, EISSN: 1749-4893.

Chuangchote, S.; Sagawa, T. & Yoshikawa, S. (2008a) Fiber-Based Organic Photovoltaic Cells. *Mater. Res. Soc. Symp. Proc*., 1149E, 1149-QQ11-04.

Chuangchote, S.; Sagawa, T. & Yoshikawa S. (2008b). Electrospun Conductive Polymer Nanofibers from Blended Polymer Solution. *Japanese Journal of Applied Physics*, Vol.47, No.1, pp.787-793, *ISSN* (electronic): 1347-4065.

Coffin, R. C.; Peet, J.; Rogers, J. & Bazan, G. C. (2009). Streamlined microwave-assisted preparation of narrow-bandgap conjugated polymers for high-performance bulk heterojunction solar cells. *Nat. Chem.* Vol.1, pp.657 – 661, *ISSN* : 1755-4330; EISSN : 1755-4349.

Coyle, S.& Diamond, D. (2010). Smart nanotextiles: materials and their application. In: *Encyclopedia* of Materials: Science and Technology *Elsevier* pp. 1-5. ISBN 978-0-08-043152-9.

Curran, S.A.; Carroll, D.L. & Dewald, L. (2009). Fiber Photovoltaic Devices and Applications Thereof, Pub.No.: US2009/0301565 A1.

Curran, S.; Gutin, D. & Dewald, J. (2006). The cascade solar cell, *2006 SPIE – The International Society for Optical Engineering,* 10.1117/2.1200608.0324 , pp. 1-2.

Curran, S.; Talla, J.; Dias, S. & Dewald, J. (2008). Microconcentrator photovoltaic cell (the m-C cell): Modeling the optimum method of capturing light in an organic fiber based photovoltaic cell. *J. Appl. Phys.*, Vol. 104, pp. 064305-1–064305-6, *ISSN* (electronic): 1089-7550, *ISSN* (printed): 0021-8979.

De Jong, M. P.; van Ijzendoorn, L. J. & de Voigt, M. J. A. (2000). Stability of the interface between indium-tin-oxide and poly(3,4-ethylenedioxythiophene)/poly(styrenesulfonate) in polymer light-emitting diodes. *Appl. Phys. Lett.* Vol. 77, pp.2255-2257, ISSN: 1077-3118.

DeCristofano, B.S. (2009). Photovoltaic fibers for smart textiles, RTO-MP-SET-150.

Deibel, *C.* & Dyakonov, V. *(*2010). Polymer-fullerene bulk heterojunction solar cells. *Rep. Prog. Phys.* Vol.73, No.096401, pp. 1-39, *ISSN*: 0034-4885.

Dennler, G.; Lungenschmied, C.; Neugebauer, H.; Sariciftci, N. *S.;* Latreche, M.; Czeremuszkin, *G.* & Wertheimer, M. R. (*2006* b). A new encapsulation solution for flexible organic solar cells. *Thin Solid Films,*Vol. 511–512, pp.*349*–353, ISSN: 0040-6090.

Dennler, *G. &* Sariciftci, N.S. (*2005*). Flexible conjugated polymer-based plastic solar cells: From basic to applications. *Proceedings of the IEEE*, Vol.96, No 8, pp.1429- 1439, *ISSN*: 0018-9219.

Dennler, G.; Sariciftci, N.S. & Brabec, C.J. (2006a). Conjugated Polymer-Based Organic Solar Cells, In: *Semiconducting Polymers: Chemistry, Physics and Engineering* Hadziioannou, G., Malliaras, G. G.,Vol.1, pp.455-519, WILEY-VCH Verlag GmbH & Co. KGaA, *ISBN*: 3527295070, Weinheim.

Do, M.; Han, E. M.; Nidome, Y.; Fujihira, M.; Kanno, T.; Yoshida, S.; Maeda, A. & Ikushima, A. J., (1994). Observation of degradation processes of Al electrodes in organic electroluminescence devices by electroluminescence microscopy, atomic force microscopy, scanning electron microscopy, and Auger electron spectroscopy. *J. Appl. Phys.* Vol. 76, pp.5118-5121, *ISSN* (electronic): 1089-7550, *ISSN* (printed): 0021-8979.

Dresselhaus, M.S.; Dresselhaus, G. & Avouris, P. (2001). Carbon nanotubes: Synthesis, structure, properties and applications. Springer, *ISBN*: 3-54041-086-*4,* Berlin.

Dittmer, J. J.; Marseglia, E. A. & Friend, R. H. (2000). Electron Trapping in Dye/ Polymer Blend Photovoltaic Cells. *Adv. Mat.,* Vol. 12, pp.1270-1274, Online ISSN: 1521-4095.

Dridi, C.; Barlier, V.; Chaabane, H.; Davenas, J. & Ouada, H.B. (2008). Investigation of exciton photodissociation, charge transport and photovoltaic response of poly(*N*-vinyl carbazole):TiO_2 nanocomposites for solar cell applications. *Nanotechnology.* Vol.19, pp.375201–375211, ISSN :0957-4484 (Print), 1361-6528 (Online).

Eda, G.; Lin, Y. Y.; Miller, S.; Chen, C. W.; Su, W. F. & Chhowalla, M. (2008). Transparent and Conducting Electrodes for Organic Electronics from Reduced Graphene Oxide. *App Phys. Lett. Vol.92*, pp.*233305*-1–233305-3, ISSN: 1077-3118.

Enfucell (2011). http://www.enfucell.com/products-and-technology.

European PhotoVoltaic Industry Association (EPIA), (2009). Photovoltaic energy, Electricity from sun, http: www.epia.org

European PhotoVoltaic Industry Association (EPIA) (2010). Global Market Outlook for Photovoltaics until 2014, http: www.epia.org

Fan, X.; Chu, Z.; Chen, L.; Zhang, C.; Wang, F.; Tang, Y.; Sun, J. & Zou, D. (2008).Fibrous flexible solid-type dye-sensitized solar cells without transparent conducting oxide, *Appl. Phys. Lett.* Vol.92, pp. 113510-1 - 113510-3, ISSN: 1077-3118.

Glatthaar, M.; Niggemann, M.; Zimmermann, B.; Lewer, P.; Riede, M.; Hinsch, A. and Luther, J. (2005). Organic solar cells using inverted layer sequence. *Thin Solid Films, Vol.* 491, pp.298-300, ISSN: 0040-6090.

Granström, M.; Petritsch, K.; Arias, A.C.; Lux, A.; Andersson, M.R. & Friend, R.H. (1998). Laminated fabrication of polymeric photovoltaic diodes. *Nature,* Vol. 395, pp.257-260, ISSN: 0028-0836, EISSN: 1476-4687.

Green, M. A.; Emery, K.; Hishikawa, Y. & Warta, W. (*2010).* Solar cell efficiency tables *(*version 36*). Prog. Photovolt: Res. Appl*., Vol.*18*, pp.*346*–* 352, Online ISSN: 1099-159X.

Green, M.A. (2005) Third Generation Photovoltaics, Advanced Solar Energy Conversion, Springer-Verlag Berlin Heidelberg, ISSN 1437-0379.

Greenham, N. C.; Peng, X. & Alivisatos, A.P. (1996). Charge separation and transport in conjugated-polymer/semiconductor-nanocrystal composites studied by photoluminescence quenching and photoconductivity. *Phys. Rev. B*, Vol. 54, pp. 17628-17637, ISSN 1098-0121 Print, 1550-235X Online.

Guillen C. & Herrero, J. (2003). Electrical contacts on polyimide substrates for flexible thin film photovoltaic devices. *Thin Solid Films,* Vol.431–432, pp.403-406, ISSN: 0040-6090.

Gunter, J.C.; Hodge, R. C. & Mcgrady, K.A. (2007). Micro-scale fuel cell fibers and textile structures there from, United States Patent Application 20070071975.

Gunes, S.; Marjanovic, N.; Nedeljkovic J. M. &. Sariciftci, N.S. (2008). Photovoltaic characterization of hybrid solar cells using surface modified TiO2 nanoparticles and poly(3-hexyl)thiophene. *Nanotechnology,* Vol.19, pp.424009-1 – 424009-5, ISSN :0957-4484 (Print), 1361-6528 (Online).

Gunes, S.; Neugebauer H. & Sariciftci, N.S. (2007). Conjugated polymer-based organic solar cells, *Chem. Rev.* Vol.107, pp.1324-1338, *ISSN:* 0009-2665.

Gunes, S. &. Sariciftci, N.S. (2007). An Overview Of Organic Solar Cells. *Journal of Engineering and Natural Sciences,* Vol.25, No.1, pp.1-16.

Halls, J.J.M.; Walsh, C.A.; Greenham, N.C.; Marseglia, E.A.; Friends, R.H.; Moratti,S.C. & Holmes, A.B. (1995). *Nature*, Vol. 78, pp.451, ISSN: 0028-0836, EISSN: 1476-4687.

Hau, S. K.; Yip, H. L.; Baek, N. S. ; Zou, J.; O'Malley, K. & Jen, A. (2008). Air-stable inverted flexible polymer solar cells using zinc oxide nanoparticles as an electron selective layer. *Appl. Phys. Lett.*, Vol.92, No.25, pp.253301-1 -253301-3, ISSN: 1077-3118.

Hoppe, H. & Sariciftci, N. S. (2006). Morphology of polymer/fullerene bulk heterojunction solar cells. *J. Mater. Chem*. Vol.16, pp.45– 61, *ISSN:* 0959-9428.

Hsiao, Y. S.; Chen, C. P. ; Chao, C. H. & Whang, W. T. (2009). All-solution-processed inverted polymer solar cells on granular surface-nickelized polyimide. *Org. Electron.* Vol.10, No.4, pp.551-561, *ISSN*: 1566-1199.

Hsieh, C.-H.; Cheng, Y.-J.; Li, P.-J. ; Chen, C.-H. ; Dubosc, M.; Liang, R.-M. & Hsu, C.-S. (2010). Highly Efficient and Stable Inverted Polymer Solar Cells Integrated with a Cross-Linked Fullerene Material as an Interlayer. *Journal of the American Chemical Society*,Vol.132, No.13, pp.4887-4893, *ISSN:* 0002-7863.

Huang, J.; Wang, X.; Kim, Y.; deMello, A.J.; Bradley, D.D.C. & deMello, J.C. (2006). High efficiency flexible ITO-free polymer/fullerene photodiodes. *Phys. Chem. Chem.Phys.*, Vol.8, pp.3904–3908, *ISSN:* 1463-9076.

Huo, L. J.; Hou, J. H.; Chen, H. Y.; Zhang, S. Q.; Jiang, Y.; Chen, T. L. & Yang, Y. (2009). Bandgap and Molecular Level Control of the Low-Bandgap Polymers Based on 3,6-Dithiophen-2-yl-2,5-dihydropyrrolo[3,4-*c*]pyrrole-1,4-dione toward Highly Efficient Polymer Solar Cells, *Macromolecules,* Vol.42, pp.6564–6571, , ISSN: 1520-5835.

Jenekhe, S. A. & Yi, S. (2000). *Efficient photovoltaic cells* from semiconducting polymer heterojunctions. *App. Pyhsics Lett.,* Vol. 77, pp.2635-2637, *ISSN:* 0003-6951.

Jørgensen, M.; Norrman, K. & Krebs, F. C. (2008). Stability/degradation of polymer solar cells. *Sol. Energy Mater. Sol. Cells,* Vol.92, pp.686– 714, ISSN 0927-0248.

Kang, M.-G.; Kim, M.-S.; Kim, J. & Guo, L. J. (2008). Organic solar cells using nanoimprinted transparent metal electrode. *Adv. Mater*. Vol.*20*, pp.*4408*–4413, Online ISSN: 1521-4095.

Krebs, F. C. (2009a). Fabrication and processing of polymer solar cells: a review of printing and coating techniques. *Sol. Eng. Mater. Sol. Cells* 93, 394–412, ISSN 0927-0248.

Krebs, F. C. (2009 b). All solution roll-to-roll processed polymer solar cells free from indium tin-oxide and vacuum coating steps. *Org. Electron.* Vol.10, No.5, pp.761–768, , *ISSN*: 1566-1199.

Krebs, F. C. (2009 c). Polymer solar cell modules prepared using roll-to-roll methods: Knife over-edge coating, slot-die coating and screen printing," Sol. Energy Mater. Sol. Cells 93(4), 465–475, ISSN 0927-0248.

Krebs, F. C. (2009 d). Roll-to-roll fabrication of monolithic large area polymer solar cells free from indium-tin-oxide. *Sol. Energy Mater. Sol. Cells* Vol.93, No.9, pp.1636–1641, ISSN 0927-0248.

Krebs, F. C.; Gevorgyan, S. A. & Alstrup, J. (2009 a). A roll-to-roll process to flexible polymer solar cells: model studies, manufacture and operational stability studies, *J. Mater. Chem.* Vol.19, No.30, pp.5442–5451, *ISSN:* 0959-9428.

Krebs, F. C.; Jorgensen, M.; Norrman, K.; Hagemann, O. , Alstrup, J.; Nielsen, T. D.; Fyenbo, J.; Larsen, K. & Kristensen, J. (2009 b). A complete process for production of flexible large area polymer solar cells entirely using screen printing—First public demonstration. *Sol. Energy Mater. Sol. Cells,* Vol.93, No.4, pp.422–441, ISSN 0927-0248.

Krebs F.C.; Biancardo M.; Jensen B.W.; Spanggard H. & Alstrup J. (2006). Strategies for incorporation of polymer photovoltaics into garments and textiles, *Sol Energy Mater Sol Cells*, Vol.90, pp.1058-1067, ISSN 0927-0248.

Krebs, F.; Spanggard, H.; Kjar, T.; Biancardo, M. & Alstrup, J. (2007).Large Area Plastic Solar Cell Modules. *Mater. Sci. Eng. B,* Vol.138, No.2, pp.106–111, *ISSN:* 0921-5107.

Krebs, F.C.; Gevorgyan, S.A.; Gholamkhass, B.; Holdcroft, S.; Schlenker, C.; Thompson, M.E.; Thompson, B.C.; Olson, D.; Ginley, D.S.; Shaheen, S.E.; Alshareef, H.N.; Murphy, J.W.; Youngblood, W.J.; Heston, N.C.; Reynolds, J.R.; Jia, S.J.; Laird, D.; Tuladhar, S.M.; Dane, J.G.A.; Atienzar, P.; Nelson, J.; Kroonl, J.M.; Wienk, M.M.;.

Janssen, R.A.J.; Tvingstedt, K. ; Zhang, F.L.; Andersson, M.; Inganas, O.; Lira-Cantu, M. ; Bettignies, R.; Guillerez, S.; Aernouts, T.; Cheyns, D.; Lutsen, L.;Zimmermann, B.; Wurfel, U.; Niggemann, M.; Schleiermacher, H.F.; Liska, P.; Gratzel, M.; Lianos, P.; Katz, E.A.; Lohwasser, W. & Jannon, B. (2009c). A round robin study of flexible large-area roll-to-roll processed polymer solar cell modules, *Sol. Energy Mater. Sol. Cells,* Vol.93, pp.1968-1977, ISSN 0927-0248.

Krebs, F. C. & Spanggaard, H. (2005). Significant Improvement of Polymer Solar Cell Stability. *Chem. Mater.,* Vol.17, pp.5235– 5237, *ISSN:* 0897-4756.

Krebs, F. C. & Norrman, K. (2007). Analysis of the failure mechanism for a stable organic *photovoltaic* during 10000 h of testing. *Prog. Photovoltaics: Res. Appl.,* Vol.15, pp.697–712, Online ISSN: 1099-159X.

Krebs, F. C. (2008). *Sol. Energy Mater. Sol. Cells,* Vol. 92, pp.715– 726, ISSN 0927-0248.

Krebs, F. C.; Thomann, Y.; Thomann, R. & Andreasen, J. W. (2008). A *simple nanostructured polymer/ZnO hybrid solar* cell-preparation and operation in air. *Nanotechnology* Vol.19, pp.424013-1 -424013-12. , ISSN :0957-4484 (Print), 1361-6528 (Online).

Kuraseko, H.; Nakamura, T. ; Toda, S. ; Koaizawa, H. ; Jia, H. & Kondo, M. (2006). Development of flexible fiber-type poly-Si solar cell, *IEEE 4th World Conf. Photovolt. Energy Convers*. Vol.2, pp.1380-1383.

Kushto, G.P.; Kim, W. & Kafafi, Z.H. (2005). Flexible organic photovoltaics using conducting polymer electrodes, *Appl. Phys. Lett.,* Vol.86, pp.093502-1 -093502-3, ISSN: 1077-3118.

Lee, J.-Y.; Connor, S. T.; Cui, Y. *&* Peumans P. (*2008*). Solution-Processed Metal Nanowire Mesh Transparent Electrodes. *Nano Lett.* Vol.*8*, pp.689-692, *ISSN* (printed): 1530-6984.

Lee, M. R.; Eckert, R. D. ; Forberich, K. ; Dennler, G.; Brabec, C. J. & Gaudiana, R. A. (2009). Solar power wires based on organic photovoltaic materials. *Science*, Vol. 324, pp. 232–235, ISSN: 0036-8075 (print), 1095-9203 (online).

Li, F.; Tang, H.; Anderegg, J. & Shinar, J. (1997). Fabrication and electroluminescence of double-layered organic light-emitting diodes with the Al_2O_3/Al cathode. *Appl. Phys. Lett*. Vol.70, pp.1233- 1235, ISSN: 1077-3118.

Li, L.; Lu, G. & Yang, X. (2008). Improving performance of polymer photovoltaic devices using an annealing-free approach *via* construction of ordered aggregates in solution, *J. Mater. Chem.* Vol.18, pp.1984-1990, *ISSN:* 0959-9428.

Li, Y.; Nie, W. ; Liu, J.; Partridge, A. & Carroll, D. L. (2010a). The Optics of Organic Photovoltaics: Fiber-Based Devices, *IEEE J. Sel. Top. Quantum Electron*. Vol.99, pp.1-11.

Li ,Y.; Peterson, E.D.; Huang, H.; Wang, M.; Xue, D.; Nie, W.; Zhou, W., & Carroll, D.L. (2010b). Tube-based geometries for organic photovoltaics. *Appl. Phys. Lett.*, Vol. 96, pp.243505-1 -.243505-3, ISSN: 1077-3118.

Lin, Y.Y.; Wang, D.Y.; Yen, H. C.; Chen, H. L.; Chen, C. C.; Chen, C. M.; Tang, C. Y. & Chen, C. W. (2009). Extended red light harvesting in a poly(3-hexylthiophene)/iron disulfide nanocrystal hybrid solar cell. *Nanotechnology,* Vol.20, pp. 405207-1 - 405207-5, ISSN :0957-4484 (Print), 1361-6528 (Online).

Liu, J. W.; Namboothiry, M. A. G. & Carroll, D. L. (2007a). Fiber-based architectures for organic photovoltaics. *Appl. Phys. Lett.*, Vol. 90, pp. 063501-1–063501-3, ISSN: 1077-3118.

Liu, J. W.; Namboothiry, M. A. G. & Carroll, D. L. (2007 b). Optical geometries for fiber-based organic photovoltaics. *Appl. Phys. Lett.*, Vol. 90, pp. 133515-1–133515-3, ISSN: 1077-3118.

Liu, J. S.; Kadnikova, E. N.; Liu, Y. X.; McGehee, M. D. & Fréchet, J. M. J. (2004). Polythiophene containing thermally removable solubilizing groups enhances the interface and the performance of polymer-titania hybrid solar cells. *J. Am. Chem.Soc.* Vol.126, pp. 9486– 9487, *ISSN*: 0002-7863.

Liu, P.; Chen, T.H.; Pan, W.Z.; Huang, M.S.; Deng, W.J.; Mai, Y.L.; Luan, A.B. (2008). Flexible organic photovoltaic devices based on oligothiophene derivatives. *Chinese Chemical Letters.* Vol.19, No.2, pp.207–210, *ISSN*: 1001-8417.

Lungenschmied, C.; Dennler, G.; Neugebauer, H. ; Sariciftci, N. S. ; Glatthaar, M. ; Meyer, T. & Meyer, A. (2007). Flexible, long-lived, large-area, organic solar cells. *Sol. Energy Mater. Sol. Cells, Vol.* 91, No.5, pp.379–384, ISSN 0927-0248.

Madhugiri, S.; Dalton, A.; Gutierrez, J.; Ferraris, J. P. & Balkus, Jr. K. J. (2003). Electrospun MEH-PPV/SBA-15 Composite Nanofibers Using a Dual Syringe Method. *J. Am. Chem.Soc.*, Vol.125, pp.14531-14538, , *ISSN*: 0002-7863.

Martin, C. R. (1994). Nanomaterials: A Membrane-Based Synthetic Approach. *Science,* Vol.266, pp.1961-1966, ISSN: 0036-8075 (print), 1095-9203 (online).

Mather, R. R. & Wilson, J., (2006). Solar textiles: production and distribution of electricity coming from solar radiation. In Mattila, H. (Eds.), Intelligent textiles and clothing, Woodhead Publishing Limited, first ed., ISBN: 1 84569 005 2, England.

Mattila, H. (Eds.), (2006). Intelligent textiles and clothing, Woodhead Publishing Limited, first ed., ISBN: 1 84569 005 2, England.

Matweb, www.matweb.com/search/datasheettext.aspx?matguid=4827771a785e44ed9a0d400dba931354

Merlo, J. A. & Frisbie, C. D. (2003). Field effect conductance of conducting polymer nanofibers. *J. Polym. Sci. Part B: Polym. Phys.,* Vol. 41, pp.2674-2680, *ISSN* (printed): 0887-6266.

Moule, A.J.& Meerholz, K. (2008). Controlling Morphology in Polymer–Fullerene Mixtures, *Adv. Mater.* Vol.20, pp. 240-245, Online ISSN: 1521-4095.

Noy, A.; Miller, A. E. ; Klare, J. E.; Weeks, B. L.; Woods, B. W. & DeYoreo, J. J. (2002). Fabrication and imaging of luminescent nanostructures and nanowires using dip-pen nanolithography. *Nano Lett.* Vol.2, pp. 109–112, *ISSN* (printed): 1530-6984.

Nunzi, J.-M. (2002). Organic photovoltaic materials and devices, *C. R. Physique.* Vol.3, pp.523–542, ISSN: 1631-0705.

O'Connor, B.; Pipe, K. P. & Shtein, M. (2008). Fiber based organic photovoltaic devices. *Appl. Phys. Lett.*, vol. 92, pp. 193306-1–193306-3, ISSN: 1077-3118.

O`Reagan, B. & Graetzel, M. (1991). A low-cost, high-efficiency solar cell based on dye-sensitized colloidal TiO_2 films. *Nature*, Vol. 353, pp. 737- 740, ISSN: 0028-0836, EISSN: 1476-4687.

Oey, C. C.; Djurisic, A.B.; Wang, H.; Man, K. K. Y.; Chan,W. K.; Xie, M.H.; Leung, Y. H.; Pandey, A.; Nunzi, J. M. & Chui, P. C. (2006). Polymer-TiO2 solar cells: TiO2 interconnected network for improved cell performance. *Nanotechnology,* Vol. 17, pp.706- 713, ISSN :0957-4484 (Print), 1361-6528 (Online).

Ouyang, J.; Chu, C.-W.; Chen, F.-C.; Xu, Q.,& Yang, Y. (2005). High-conductivity poly (3,4-ethylenedioxythiophene): poly(styrene sulfonate) film and its application in

polymer optoelectronic devices, *Adv. Funct. Mater*. Vol.15, pp.203-208, Online ISSN: 1616-3028.

Padinger, F.; Rittberger, R. & Sariciftci, N.S. (2003). Effect of postproduction treatment on plastic solar cells. *Adv. Funct. Mater*. Vol.13, pp.1-4, . Online ISSN: 1616-3028.

Park, S. H., Roy, A., Beaupre, S., Cho, S., Coates, N., Moon, J. S., Moses, D., Leclerc, M., Lee, K. & Heeger, A. J. (2009). Bulk heterojunction solar cells with internal quantum efficiency approaching 100%, *Nat. Photonics*,Vol.3, pp.297-302, *ISSN*:1749-4885 (Print).

Peet, J.; Senatore, M. L.; Heeger, A. J. & Bazan, G. C. (2009). The Role of Processing in the Fabrication and Optimization of Plastic Solar Cells. *Adv. Mater. Vol*.21, pp.1521-1527, Online ISSN: 1521-4095.

Pope, M. & Swenberg, C.E. (1999). Electronic Processes in Organic Crystals and Polymers 2nd edn., Oxford University Press, *ISBN*-10: 0195129636, New York.

Ramier, J.; Plummer, C.; Leterrier, Y.; Manson, J.; Eckert, B. & Gaudiana, R. (2008). Mechanical integrity of dye-sensitized photovoltaic fibers, *Renewable Energy*, Vol.33, pp. 314-319, *ISSN*: *0960-1481*.

Rowell, M.W.; Topinka, M.A.; McGehee, M.D.; Prall, H.J.; Dennler, G.; Sariciftci, N.S.; Hu, L. & Gruner, G. (*2006*). Organic Solar Cells with Carbon Nanotube Network Electrodes. *Applied Physics Letters,* Vol.88, pp. 233506.-1 -233506.-3, ISSN: 1077-3118.

Gaudiana, R. & Brabec, C. (2008). Organic materials: Fantastic plastic. *Nature Photonics,* Vol.2, pp.287- 289, , ISSN: 1749-4885, EISSN: 1749-4893.

Schubert, M. B. & Werner, H. J. (2006). Flexible solar cells for clothing. *Materials Today*, Vol.9, No.6, pp. 42-50, *ISSN*: 1369-7021

Shaheen, S.; Brabec, C. J.; Sariciftci, N. S.; Padinger, F.; Fromherz, T. & Hummelen, J. C. (2001). 2.5% Efficient Organic Plastic Solar Cells. *App. Phys. Lett*., Vol. 78, pp.841., ISSN: 1077-3118.

Starner, T. (1996). Human Powered Wearable Computing. *IBM Systems J*, Vol.35, pp. 618-629.

Shtein, M. & Forrest S.R. (2008). Organic devices having a fiber structure, US2008/0025681A1

Stakhira, P.; Cherpak, V. ; Aksimentyeva, O.; Hotra, Z. ; Tsizh B.; Volynyuk, D. & Bordun, I. (*2008*). Properties of flexible heterojunction based on ITO/poly(3,4-ethylenedioxythiophene): poly(styrenesulfonate)/pentacene/Al. *J Non-Cryst Solids,* Vol.354 pp. 4491–4493, *ISSN*: 0022-3093.

Sundarrajan, S.; Murugan,, R.; Nair, A. S. & Ramakrishna, S. (2010). Fabrication of P3HT/PCBM solar cloth by electrospinning technique. *Materials Letters,* Vol.64, No.21, pp.2369-2372, *ISSN*: 0167-577X.

Takagi, T. (1990). A concept of Intelligent Materials. *J. of Intell. Mater. Syst. And Struct*. Vol.1, pp.149, *ISSN*:1045-389X (Print).

Tang, C.W. (1986). Two Layer Organic Photovoltaic Cell. *Appl. Phys. Lett.,* Vol. 48, pp.183-185, ISSN: 1077-3118.

Tani, J.; Takagi, T. & Qiu, J. (1998). Intelligent material systems: Application of functional material. *Appl. Mech. Rev*. Vol.51. *ISSN*: 0003-6900.

Tao, X. (2001). Smart Fibres, Fabrics and Clothing: Fundamentals and Applications, Woodhead Publishing Ltd., *ISBN:* 1 85573 546 6.

Thompson, B. C. & Fréchet, J. M. J. (2008). Organic photovoltaics—Polymer- fullerene composite solar cells. Angew. Chem., Int. Ed.Vol. 47, pp.58– 77, Online *ISSN*: 1521-3773.

Toivola, M. , Ferenets, M.; Lund, P. and Harlin, A. (2009) Photovoltaic fiber. *Thin Solid Films,* Vol.517, No.8, pp.2799-2802, , ISSN: 0040-6090.

Tromholt, T., Gevorgyan, S.A. ; Jorgensen, M.; Krebs, F.C. & Sylvester-Hvid, K. O. (2009). Thermocleavable Materials for Polymer Solar Cells with High Open Circuit Voltage—A Comparative Study. *ACS Appl. Mater. Interfaces*, Vol.1, No.12, pp.2768–2777, *ISSN*:1944-8244 (Print).

Tvingstedt, K. & Inganas, O. (2007). Electrode grids for ITO-free organic photovoltaic devices, *Adv. Mater.,* Vol.19, pp.2893–2897, Online ISSN: 1521-4095.

Wöhrle, D. & Meissner, D. (1991). Organic Solar Cells. *Adv. Mat.,* Vol.3, pp.129- 137, *ISSN*: 1022-6680.

Wang, X.; Li, Q.; Xie, J.; Jin, Z.; Wang, J.; Li, Y.; Jiang, K.; Fan, S. (2009). Fabrication of Ultralong and Electrically Uniform Single-Walled Carbon Nanotubes on Clean Substrates. *Nano Letters* Vol.9, No.9, pp.3137–3141, *ISSN* (printed): 1530-6984.

Winther-Jensen, B. & Krebs, F.C. (2006) High-conductivity large-area semi-transparent electrodes for polymer photovoltaics by silk screen printing and vapour- phase deposition. *Sol. Energy Mater. Sol. Cells,* Vol.90, pp.123–132, ISSN 0927-0248.

Wong, K. W.; Yip, H. L.; Luo. Y.; Wong, K. Y.; Laua, W. M.; Low, K. H.; Chow,H. F.; Gao, Z. Q.; Yeung,W. L. & Chang, C. C. (2006). Blocking reactions between indium-tin oxide and poly (3,4-ethylene dioxythiophene):poly(styrene sulphonate) with a self-assembly monolayer. *Appl. Phys. Lett.,* Vol.80, pp.2788-2790, ISSN: 1077-3118.

Wutticharoenmongkol, P.; Supaphol, P.; Srikhirin, T.; Kerdcharoen, T. & Osotchan, T. (2005). Electrospinning of polystyrene/poly(2-methoxy-5-(2'-ethylhexyloxy)-1, 4-phenylene vinylene) blends. *J. Polym. Sci., B, Polym* . Phys., Vol.43, pp.1881-1891, Online *ISSN*: 1099-0488.

Yilmaz Canli, N.; Gunes, S.; Pivrikas, A.; Fuchsbauer, A.; Sinwel, D.; Sariciftci, N.S.; Yasa O. & Bilgin-Eran, B. (2010). Chiral (S)-5-octyloxy-2-[{4-(2-methylbuthoxy)-phenylimino}-methyl]-phenol liquid crystalline compound as additive into polymer solar cells, *Sol. Energy Mater. Sol. Cells,* Vol.94, pp.1089–1099, ISSN 0927-0248.

Yip, L.; Hau, S. K.; Baek, N. S.; Jen, A. (2008). Self-assembled monolayer modified ZnO/metal bilayer cathodes for polymer/fullerene bulk-heterojunction solar cells. *Appl. Phys. Lett.*, Vol.92, No.19, pp.193313-1 - 193313-3, ISSN: 1077-3118.

Yu, G. & Heeger, A. J. (1995). Charge separation and photovoltaic conversion in polymer composites with internal donor/acceptor heterojunctions. *J. App. Physics,* Vol. 78, pp.4510-4515, *ISSN* (printed): 0021-8979.

Yu, B. Y.; Tsai, A.; Tsai, S. P.; Wong, K. T.; Yang, Y.; Chu, C. W. & Shyue, J. J. (2008). Efficient inverted solar cells using TiO2 nanotube arrays. *Nanotechnology,* Vol.19, pp.255202, ISSN :0957-4484 (Print), 1361-6528 (Online).

Yu, G.; Gao, J.; Hummelen, J. C.; Wudl, F. & Heeger, A. J. (1995). Polymer Photovoltaic Cells: Enhanced Efficiencies via a Network of Internal Donor-Acceptor Heterojunctions. *Science,* Vol.270, pp. *1789*-1791, ISSN: 0036-8075 (print), 1095-9203 (online).

Zhou, Y.; Zhang, F.; Tvingstedt, K.; Barrau, S.; Li, F.; Tian, W. & Inganas, O. (2008). Investigation on polymer anode design for flexible polymer solar cells. *Appl. Phys. Lett.,*Vol. 92, pp.233308-1- .233308-3,ISSN: 1077-3118.

Zhou, W.; Nie, W. ; Li, Y.; Liu, J. & Carroll, D. L. (2009). Fabrication considerations in fiber based organic photovoltaics. Proceedings of SPIE Vol. 7416, pp. 741613-1– 741613-5, ISBN: 9780819477064.

Zimmermann, B.; Glatthaar, M.; Niggemann, M.; Riede, M. K.; Hinsch, A. & Gombert, A. (2007). ITO-free wrap through organic solar cells–A module concept for cost efficient reel-to-reel production. *Sol. Energy Mater. Sol. Cells,* Vol. 91, No.5, pp.374–378, ISSN 0927-0248.

Zou, D.; Wang, D.; Chu, Z.; Lv, Z.; & Fan, X. (2010). Fiber-shaped flexible solar cells. *Coordination Chemistry Reviews*, Vol. 254, pp.1169–1178, ISSN 0010-8545.

Zou, J.; Yip, H.-L.; Hau, S. K. & Jen, A. K.-Y. (2010). Metal grid/conducting polymer hybrid transparent electrode for inverted polymer solar cells. *Applied Physics* Letters, Vol.96, pp.203301-1- 203301-3, ISSN: 1077-3118.

13

Ultrafast Electron and Hole Dynamics in CdSe Quantum Dot Sensitized Solar Cells

Qing Shen[1] and Taro Toyoda[2]
[1]*PRESTO, Japan Science and Technology Agency (JST)*
[2]*The University of Electro-Communications*
Japan

1. Introduction

A potential candidate for next-generation solar cells is dye-sensitized solar cells (DSSCs). Much attention has been directed toward DSSCs employing nanostructured TiO_2 electrodes and organic-ruthenium dye molecules as the light-harvesting media. The high porosity of nanostructured TiO_2 film enables a large concentration of the sensitizing dye molecules to be adsorbed. The attached dye molecules absorb light and inject electrons into the TiO_2 conduction band upon excitation. The electrons are then collected at a back conducting electrode, generating a photocurrent. DSSCs exhibit high photovoltaic conversion efficiencies of about 11% and good long-term stability. In addition, they are relatively simple to assemble and are low-cost (O'Regan & Grätzel, 1991; Grätzel, 2003; Chiba et al., 2006). However, in order to replace conventional Si-based solar cells in practical applications, further effort is needed to improve the efficiency of DSSCs. A great amount of work has been done on controlling the morphology of the TiO_2 electrodes by employing ordered arrays of nanotubes, nanowires, nanorods and inverse opal structures (Adachi et al., 2003; Paulose et al., 2006; Law et al., 2005; Song et al., 2005; Nishimura et al., 2003) in order to improve the electron transport and collection throughout the device. Another important factor in improving the performance of DSSCs is the design of the photosensitizer. The ideal dye photosensitizer for DSSCs should be highly absorbing across the entire solar light spectrum, bind strongly to the TiO_2 surface and inject photoexcited electrons into the TiO_2 conduction band efficiently. Many different dye compounds have been designed and synthesized to fulfill the above requirements. It is likely that the ideal photosensitizer for DSSCs will only be realized by co-adsorption of a few different dyes, for absorption of visible light, near infrared (NIR) light, and/or infrared (IR) light (Polo et al., 2004; Park et al., 2011). However, attempts to sensitize electrodes with multiple dyes have achieved only limited success to date.

Narrow-band-gap semiconductor quantum dots (QDs), such as CdS, CdSe, PbS, and InAs, have also been the subject of considerable interest as promising candidates for replacing the sensitizer dyes in DSSCs (Vogel et al., 1990, 1994; Toyoda et al., 1999, 2003; Peter et al., 2002; Plass et al., 2002; Shen et al., 2004a, 2004b, 2006a, 2006b, 2008a, 2008b, 2010a, 2010b; Yu et al., 2006; Robel et al., 2006; Niitsoo et al., 2006; Diguna, et al., 2007a , 2007b; Kamat, 2008, 2010; Gimenez et. al., 2009; Mora-Sero et al., 2009, 2010). These devices are called QD-sensitized solar cells (QDSCs) (Nozik, 2002, 2008; Kamat, 2008). The use of semiconductor QDs as sensitizers

has some unique advantages over the use of dye molecules in solar cell applications (Nozik, 2002, 2008). First, the energy gaps of the QDs can be tuned by controlling their size, and therefore the absorption spectra of the QDs can be tuned to match the spectral distribution of sunlight. Secondly, semiconductor QDs have large extinction coefficients due to the quantum confinement effect. Thirdly, these QDs have large intrinsic dipole moments, which may lead to rapid charge separation. Finally, semiconductor QDs have potential to generate multiple electron-hole pairs with one single photon absorption (Nozik, 2002; Schaller, 2004), which can improve the maximum theoretical thermodynamic efficiency for photovoltaic devices with a single sensitizer up to ~44% (Hanna et al., 2006). However, at present, the conversion efficiency of QDSCs is still less than 5% (Mora-Seró´, et al., 2010; Zhang, et al., 2011). So, fundamental studies on the mechanism and preparation of QDSCs are still necessary and very important.

In a semiconductor quantum dot-sensitized solar cell (QDSC), as the first step of photosensitization, a photoexcited electron in the QD should rapidly transfer to the conduction band of TiO_2 electrode and a photoexcited hole should transfer to the electrolyte (Scheme 1). Thus charge separation of the photoexcited electrons and holes in the semiconductor QDs and the electron injection process are key factors for the improvement of the photocurrents in the QDSCs. In this sense, the study on the photoexcited carrier dynamics in the QDs is very important for improving the conversion efficiency of the solar cell. To date, the information on the carrier dynamics of semiconductor QDs adsorbed on TiO_2 electrode is limited, although a few studies have been carried out for CdS, CdSe and InP QDs using a transient absorption (TA) technique (Robel et al., 2006, 2007; Tvrdy et al., 2011; Blackburn et al., 2003, 2005). Most of them focused on the electron transfer process and the measurements mostly were carried out in either dispersed colloidal systems or dry electrodes. In recent years, the authors' group has been applying an improved transient grating technique (Katayama et al., 2003) to study the photoexcited carrier dynamics of semiconductor nanomaterials, such as TiO_2 nanoparticles with different crystal structures and CdSe QDs absorbed onto TiO_2 and SnO_2 nanostructured electrodes (Shen et al., 2005, 2006, 2007, 2008, 2010). The improved TG technique is a simple and highly sensitive time-resolved optical technique and has proved to be powerful for measuring various kinds of dynamics, such as population dynamics and excited carrier diffusion. Comparing to the TA technique, the improved TG technique has a higher sensitivity and measurements under lower light intensity are possible (Katayama et al., 2003; Shen et al., 2007, 2010a). This fact is very important for studying the carrier dynamics of QDs used in QDSCs under the conditions of lower light intensity similar to sun light illumination. The improved TG technique is also applicable to samples with rough surfaces, like the samples used in this study.

This chapter will focus on the ultrafast photoexcited electron and hole dynamics in CdSe QD adsorbed TiO_2 electrodes employed in QDSCs characterized by using the improved TG technique. CdSe QDs were adsorbed on TiO_2 nanostructured electrodes with different adsorption methods. The following issues will be discussed:

1. Pump light intensity dependence of the ultrafast electron and hole dynamics in the CdSe QDs adsorbed onto TiO_2 nanostructured electrodes;
2. Separation of the ultrafast electron and hole dynamics in the CdSe QDs adsorbed onto TiO_2 nanostructured electrodes;
3. Electron injection from CdSe QDs to TiO_2 nanostructured electrode;
4. Changes of carrier dynamics in CdSe QDs adsorbed onto TiO_2 electrodes versus adsorption conditions;
5. Effect of surface modification on the ultrafast carrier dynamics and photovoltaic properties of CdSe QD sensitized TiO_2 electrodes.

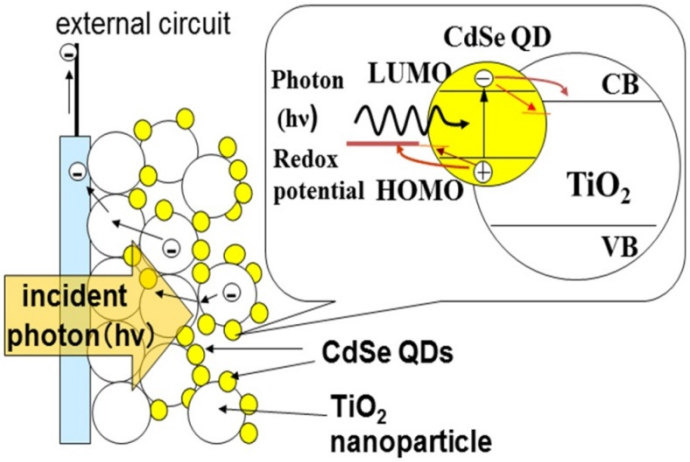

Scheme 1. Electron- hole pairs are generated in semiconductor QDs after light absorption. Then photoexctied electrons in the semiconductor QDs are injected to the conduction band of TiO_2 and/or trapped by surface or interface states. The photoexcited holes are scavenged by reducing species in the electrolyte and/or trapped by surface or interface states. The nanostructured TiO_2 is employed as an electron conductor and electrons transport in TiO_2 to a transparent conductive oxide (TCO) substrate, while the electrolyte is used as a hole transporter and hoels are transported to a counter electrode.

2. Electron and hole dynamics in CdSe QDs adsorbed onto TiO_2 electrodes

2.1 Preparation methods of CdSe QD adsorbed TiO_2 nanostructured electrodes

The method for preparing the TiO_2 electrodes has been reported in a previous paper (Shen et al., 2003). A TiO_2 paste was prepared by mixing 15 nm TiO_2 nanocrystalline particles (Super Titania, Showa Denko; anatase structure) and polyethylene glycol (PEG) (molecular weight (MW): 500,000) in pure water. The resultant paste was then deposited onto transparent conducting substrates (F-doped SnO_2 (FTO), sheet resistance = 10 Ω/sq). The TiO_2 films were then sintered in air at 450 ^oC for 30 min to obtain good necking. The highly porous nanostructure of the TiO_2 films (the pore sizes are of the order of a few tens of nanometers) was confirmed through scanning electron microscopy (SEM) images.

CdSe QDs can be adsorbed onto the TiO_2 nanostructured electrodes by using the following methods:

1. Chemical bath deposition (CBD) method (Hodes et al., 1994; Shen et al., 2008)
   Firstly, for the Se source, an 80 mM sodium selenosulphate (Na_2SeSO_3) solution was prepared by dissolving elemental Se powder in a 200 mM Na_2SO_3 solution. Secondly, 80 mM $CdSO_4$ and 120 mM of the trisodium salt of nitrilotriacetic acid ($N(CH_2COONa)_3$) were mixed with the 80 mM Na_2SeSO_3 solution in a volume ratio of 1:1:1. The TiO_2 films were placed in a glass container filled with the final solution at 10 ^oC in the dark for various times to promote CdSe adsorption.
2. Successive ionic layer adsorption-reaction (SILAR) method (Guijarro et al., 2010a)
   In situ growth of CdSe QDs using the SILAR method was carried out by successive immersion of TiO_2 electrodes in ionic precursor solutions of cadmium and selenium.

Aqueous solutions were employed in all cases. A 0.5 M $(CH_3COO)_2Cd$ (98.0%, Sigma-Aldrich) solution was used as the cadmium source, while a sodium selenosulfate (Na_2SeSO_3) solution was used as the selenium precursor. The sodium selenosulfate solution was prepared by heating under reflux for 1h a mixture of 1.6 g of Se powder, 40 mL of 1 M Na_2SO_3 (98.0%, Alfa Aesar) and 10 mL of 1 M NaOH. The resulting solution was filtered and mixed with 40 mL of 1M CH_3COONa (99.0+%, Fluka) solution, and finally was stored in the dark. The pH of the sodium selenosulfate solution was optimized to improve the QD deposition rate by using 0.25 M H_2SO_4 and/or 0.1 M NaOH stock solutions.

3. Direct adsorption (DA) of previously synthesized QDs (Guijarro et al., 2010b)
   Colloidal dispersions of CdSe QDs capped with trioctylphosphine (TOP) were prepared by a solvothermal route which permits size control. DA of CdSe QDs was achieved by immersion of TiO_2 electrodes in a CH_2Cl_2 (99.6%, Sigma Aldrich) CdSe QD dispersion, using soaking times ranging from 1 h to 1 week.
4. Linker assisted adsorption (LA) of previously synthesized QDs (Guijarro et al., 2010b)
   LA was performed employing p-mercaptobenzoic acid (MBA; 90%, Aldrich), cysteine (97%, Aldrich), and mercaptopropionic acid (MPA; 99%, Aldrich) as molecular wires. First, the linker was anchored to the TiO_2 surface by immersion in saturated toluene solutions of cysteine (5 mM) or MBA (10 mM) for 24 h. Secondly, these electrodes were washed with pure toluene for ½ h to remove the excess of the linker. Finally, the modified electrodes were transferred to a toluene CdSe QD dispersion for 3 days, to ensure QD saturation. The procedure for modification of TiO_2 with MPA has previously been reported (Guijarro et al., 2009).

After the CdSe QD adsorption, the samples were coated with ZnS by alternately dipping them three times in 0.1 M $Zn(CH_2COO)$ and 0.1 M Na_2S aqueous solutions for 1 minute for each dip (Yang et al., 2003; Diguna, et al., 2007a; Shen et al., 2008).

2.2 An improved transient grating (TG) technique

The transient grating (TG) method is a well-established laser spectroscopic technique of four wave mixing (Eichler et al., 1986; Harata et al., 1999). In the TG method, two time-coincident short laser pulses (pump beams) with the same wavelength and intensity intersect with an angle in a sample to generate an optical interference pattern at the intersection. Interaction between the light field and the material results in a spatially periodic modulation of the complex refractive index, which works like a transient diffraction grating for a third laser pulse (probe beam) incident to the photoexcited region. Then, by measuring the time dependence of the diffraction light of the probe beam, dynamics of the transient grating produced in the sample can be monitored. The TG technique is a powerful tool for detecting population dynamics (Rajesh et al., 2002), thermal diffusion (Glorieux et al., 2002), diffusion of photoexcited species (Terazima et al., 2000), energy transfer from photoexcited species to liquids (Miyata et al, 2002), structural or orientational relaxation (Glorieux et al., 2002), the sound velocity of liquids (Ohmor et al., 2001), and so on. Although this technique provides valuable information, it presents some technical difficulties for general researchers (Harata et al., 1999). First, the three beams must overlap on a small spot, typically within a spot diameter of less than 100 μm on a sample, and each beam must be temporally controlled. This is very difficult for pulsed laser beams, especially for those with a pulse width of ~100 femtoseconds. Secondly, since the diffraction of the probe beam, namely the signal, is quite weak, it is difficult to find the diffraction beam during the measurements. Thirdly, for a solid sample, the surface must be optically smooth. It is almost impossible to measure a sample with a rough surface by using the conventional TG technique.

In 2003, Katayama and co-workers (Katayama et al., 2003; Yamaguchi et al., 2003) proposed an improved TG technique (it was also called a lens-free heterodyne TG (LF-HD-TG) or a near field heterodyne TG (NF-HD-TG) technique in some papers), which overcomes the difficulties that exist in the conventional TG technique. The improved TG technique features (1) simple and compact optical equipment and easy optical alignment and (2) high stability of phase due to the short optical path length of the probe and reference beams. This method is thought to be versatile with applicability to many kinds of sample states, namely opaque solids, scattering solids with rough surfaces, transparent solids, and liquids, because it is applicable to transmission and reflection-type measurements. The principle of the improved TG technique has been explained in detail in the previous papers (Katayama et al., 2003; Yamaguchi et al., 2003) and is only described briefly here. Unlike the conventional TG technique, only one pump beam and one probe beam without focusing are needed in the improved TG technique. The pump beam is incident on the transmission grating. Then, the spatial intensity profile of the pump beam is known to have an interference pattern in the vicinity of the other side of the transmission grating, and the interference pattern has a grating spacing that is similar to that of the transmission grating. When a sample is brought near the transmission-grating surface, it can be excited by the optical interference pattern. The refractive index of the sample changes according to the intensity profile of the pump light and the induced refractive index profile functions as a different type of transiently generated grating. When the probe beam is incident in a manner similar to that of the pump beam, it is diffracted both by the transmission grating (called a reference light) and the transiently generated grating (called a signal light). In principle, the two diffractions progress along the same direction; therefore, these two diffractions interfere, which is detected by a detector positioned at a visible diffraction spot of the reference beam.

In the improved TG technique used for studying the ultrafast carrier dynaimcs of semiconductor QDs, the laser source was a titanium/sapphire laser (CPA-2010, Clark-MXR Inc.) with a wavelength of 775 nm, a repetition rate of 1 kHz, and a pulse width of 150 fs. The light was separated into two parts. One of them was used as a probe pulse. The other was used to pump an optical parametric amplifier (OPA) (a TOAPS from Quantronix) to generate light pulses with a wavelength tunable from 290 nm to 3 μm used as pump light in the TG measurement. The probe pulse wavelength was 775 nm.

2.3 Power dependence of carrier dynamics in CdSe QDs adsorbed onto TiO_2 electrodes

As described in depth in previous papers (Katayama et al., 2003; Shen et al., 2005, 2007), the TG signal is directly proportional to the change in the refractive index occurring in the sample ($\Delta n(t)$) upon photoexcitation. In the timescale of these experiments less than 1 ns, assuming Drude's model, the refractive index change, i.e., the TG signal intensity for CdSe QD adsorbed samples, will be a linear function of the concentration of photogenerated carriers (electrons and holes in CdSe QDs, i.e., $N_{e,CdSe}$ and $N_{h,CdSe}$, and injected electrons in TiO_2, i. e., $N_{e,TiO2}$) , as follows (Guijarro et al., 2010a, 2020b):

$$\Delta n(t) = \frac{1}{2n_{0,CdSe}}\left(\frac{-N_{e,CdSe}(t)e^2}{m_{e,CdSe}\omega_p^2\varepsilon_0}\right) + \frac{1}{2n_{0,CdSe}}\left(\frac{-N_{h,CdSe}(t)e^2}{m_{h,CdSe}\omega_p^2\varepsilon_0}\right) + \frac{1}{2n_{0,TiO_2}}\left(\frac{-N_{e,TiO_2}(t)e^2}{m_{e,TiO_2}\omega_p^2\varepsilon_0}\right) \quad (1)$$

where ω_p is the radial probe frequency, e is the elementary charge, ε_0 is free-space permittivity, and $n_{0,CdSe}$ (2.7) and $n_{0,TiO2}$ (2.5) are the refractive indices of CdSe and TiO_2, respectively. The important feature of the TG signal is that both the photoexcited electron

and hole carrier densities contribute to the signal. In principle, the exact contribution on $\Delta n(t)$ by each carrier depends inversely on its carrier effective mass. According to the Drude theory (Kashiski et al., 1989; Kim et al., 2009), it can be considered that only free photoexcited electrons and holes are responsible for the population grating signals. For CdSe, the effective masses of electrons and holes are $0.13m_0$ and $0.44m_0$ (m_0 is the electron rest mass), respectively (Bawendi et al., 1989), so both the photoexcited electron and hole carrier densities in the CdSe QDs contribute to the signal. It is known that the effective mass of electrons for TiO_2 is about 30 m_0, which is about two orders larger than that for CdSe. Therefore, the TG signal due to the injected electrons in TiO_2 (no holes injected into TiO_2) can be ignored (Shen et al., 2005, 2006a, 2007, 2008a, 2010a).

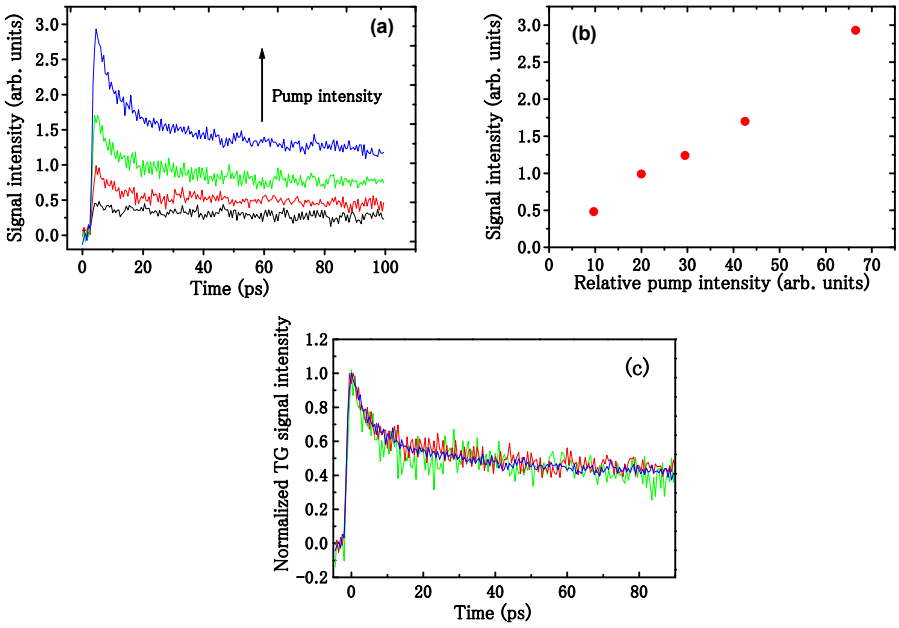

Fig. 1. Dependence of the TG kinetics of CdSe QDs adsorbed onto nanostructured TiO_2 films (CBD method and the CdSe adsorption time was 24 h) on the pump light intensity (a); Dependence of the TG peak intensity on the pump light intensity (b); Normalized TG kinetics measured with different pump light intensities (c) (Shen et al., 2010a).

For a semiconductor material, usually, there are three kinds of photoexcited carrier relaxation dynamics. The first one is a one-body recombination, which is trapping and/or transfer of photoexcited electrons and holes. In this case, the lifetimes of the photoexcited electrons and holes are independent of the pump light intensity. The second one is a two-body recombination, which is a radiative recombination via electron and hole pairs. The third one is a three-body recombination, which is an Auger recombination via two electrons and one hole, or via one electron and two holes. In the latter two cases, the lifetimes of photoexcited electrons and holes are dependent on the pump light intensity. In order to determine what kinds of photoexcited carrier dynamics are reflected in the TG kinetics, we first confirmed many-body recombination processes such as the Auger recombination

process existed or not under our experimental conditions. For this purpose, we measured the dependence of the TG kinetics on the pump intensity (from 2.5 to 16.5 μJ/pulse) for CdSe QD adosrobed TiO_2 electrodes (Figure 1) (Shen et al., 2010a). As shown in Fig. 1, we found that the dependence of the maximum signal intensity on the pump intensity was linear, and that the waveforms of the responses overlapped each other very well when they were normalized at the peak intensity. These results mean that the decay processes measured in the TG kinetics were independent of the pump intensity under our experimental conditions, and many-body recombination processes could be neglected. Therefore, it is reasonable to assume that the decay processes of photoexcited electrons and holes in the CdSe QDs are due to one-body recombination processes such as trapping and transfer under our experimental conditions.

2.4 Separation of the ultrafast electron and hole dynamics in the CdSe QDs adsorbed onto TiO_2 nanostructured electrodes

Figure 2 shows a typical kinetic trace of the TG signal of CdSe QDs adsorbed onto a TiO_2 nanostructured film (prepared by CBD method for 24 h adsorption) measured in air. The vertical axis was plotted on a logarithmic scale. Three decay processes (indicated as A, B, and C in Fig. 2) can be clearly observed. We found that the TG kinetics shown in Fig. 2 could be fitted very well with a double exponential decay plus an offset, as shown in eq. (2):

$$y = A_1 e^{-t/\tau_1} + A_2 e^{-t/\tau_2} + y_0 \tag{2}$$

where A_1, A_2 and y_0 are constants, and τ_1 and τ_2 are the time constants of the two decay processes (A and B in Fig. 2). Here, the constant term y_0 corresponds to the slowest decay process (C in Fig. 2), in which the decay time (in the order of ns) is much larger than the time scale of 100 ps measured in this study. The time constants of the fast (τ_1) and slow (τ_2) decay processes of photoexcited carriers in air are 6.3 ps and 82 ps, respectively (Table 1). As mentioned above, τ_1 and τ_2 are independent of the pump intensity under our experimental conditions, so the three decay processes are mostly due to one-body recombination such as carrier trapping and carrier transfer.

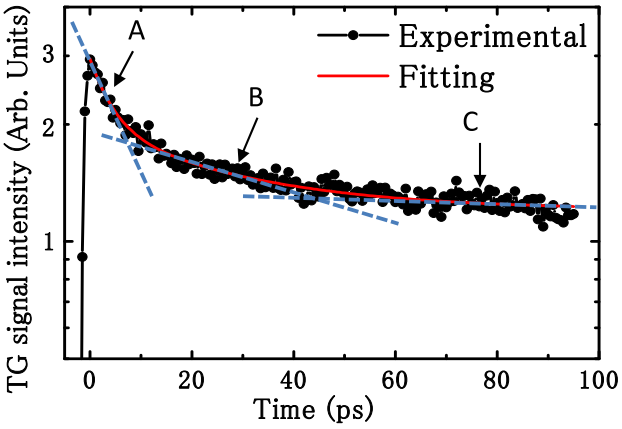

Fig. 2. TG kinetics of CdSe QDs adsorbed onto a nanostructured TiO_2 film measured in air. The vertical axis is plotted on a logarithmic scale. Three decay processes A, B and C can be clearly observed (Shen et al., 2010a).

In order to separate the photoexcited electron dynamics and hole dynamics that make up the TG kinetics, the TG kinetics of the same sample was measured both in air and in a Na_2S aqueous solution (hole acceptor) (1 M) (Shen et al., 2010a). As shown in Fig. 3, a large difference can be clearly observed between the TG responses measured in air and in the Na_2S solution. By normalizing the two TG responses at the signal intensity of 90 ps, we found that they overlapped with each other very well for time periods of longer than 15 ps, but the fast decay process apparently disappeared when the time period was less than 10 ps in the TG kinetics measured in the Na_2S solution (hole acceptor). This great difference can be explained as follows. In air, both hole and electron dynamics in the CdSe QDs could be measured in the TG kinetics. In the Na_2S solution, however, photoexcited holes in the CdSe QDs will transfer quickly to the electrolyte and only electron dynamics should be measured in the TG kinetics. Therefore, the "apparent disappearance" of the fast decay process in the Na_2S solution implies that the hole transfer to S^{2-} ions, which are supposed to be strongly adsorbed onto the CdSe QD surface, can be too fast in these circumstances as indicated by Hodes (Hodes, 2008) and therefore could not be observed under the temporal resolution (about 300 fs) of our TG technique. This observation is particularly important, because the result directly demonstrated that the transfer of holes to sulfur hole acceptors that are strongly adsorbed on the QD surface could approach a few hundreds of fs. An earlier study on the dynamics of photogenerated electron-hole pair separation in surface-space-charge fields at GaAs(100) crystal/oxide interfaces using a reflective electro-optic sampling method

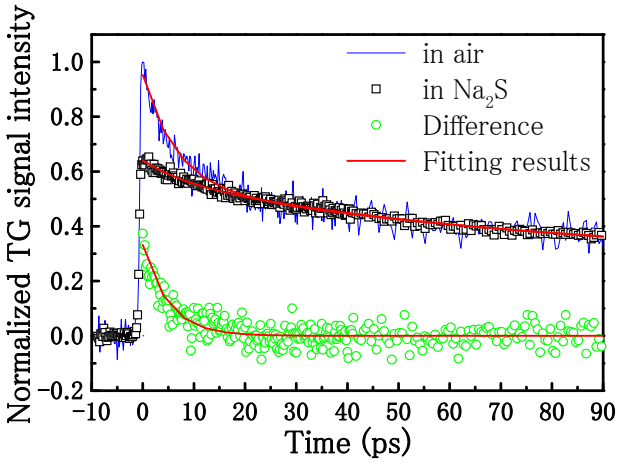

Fig. 3. TG responses of the CdSe QDs adsorbed onto nanostructured TiO_2 films measured in air (-) and in Na_2S solution (□) as well as their "difference response" (○) (Shen et al., 2010a).

showed that the hole carrier transit time was faster than 500 fs (Min et al., 1990). We believe an ultrafast hole transfer time from the QDs to hole acceptors that are strongly adsorbed on the QD surface is a more feasible and reasonable explanation, since photoexcited holes can more easily reach the surface of QDs with diameters of a few nm. The TG response measured in the Na_2S solution, which is considered to only relate to electron dynamics as mentioned above, can be fitted well with eq. (2). As shown in Table 1, besides the slower decay process, a faster decay process with a decay time of 9 ps was also detected in the TG

response measured in the Na_2S solution. Such a faster decay process with a characteristic time of a few picoseconds in the TG response measured in the Na_2S solution was considered to correspond to electron transfer from the QDs in direct contact with the TiO_2 (first layer of deposited QDs) (Guijarro et al., 2010a, 2010b). It is worth noting that the relative intensity A_1 (0.07) measured in the Na_2S solution is much smaller compared to the A_1 (0.39) measured in air and it could be ignored here. The slower relaxation process in the TG response was not influenced by the presence of the Na_2S solution, as shown in Fig. 3. The decay time τ_2 (85 ps) and the relative intensity A_2 (0.31) for the slower decay process in the TG response measured in the Na_2S solution are almost the same as those measured in air (Table 1). The slower electron relaxation mostly corresponds to electron transfer from the CdSe QDs to TiO_2 and trapping at the QD surface states, in which the decay time depends to a great extent on the size of the QDs and the adsorption method that is used (Guijarro et al., 2010a, 2010b; Shen et al., 2006, 2007; Diguna et al., 2007b). The slowest decay process (with a time scale of ns) may mostly result from the non-radiative recombination of photoexcited electrons with defects that exist at the CdSe QD surfaces and at the CdSe/CdSe interfaces.

The difference between the two TG responses measured in air and in Na_2S solution (normalized for the longer time), which was termed the "difference response", is believed to correspond to the photoexcited hole dynamics in the CdSe QDs measured in air. As shown in Fig. 3, the difference response decays very fast and disappears around 10 ps and can be fitted very well with a one-exponential decay function with a decay time of 5 ps (Table 1). Thus, we did well in separating the dynamics of photoexcited electrons and holes in the CdSe QDs and found that the hole dynamics were much faster than those of electrons. Some papers have also reported that the hole relaxation time is much faster than the electron relaxation time in CdS and CdSe QDs (Underwood et al., 2001; Braun et al., 2002). In air, the fast hole decay process with a time scale of about 5 ps can be considered as the trapping of holes by the CdSe QD surface states. This result is in good agreement with the experimental results obtained by a femtosecond fluorescence "up-conversion" technique (Underwood et al., 2001).

Thus, by comparing the TG responses measured in air and in a Na_2S solution (hole acceptor), we succeeded in separating the dynamic characteristics of photoexcited electrons and holes in the CdSe QDs. We found that charge separation in the CdSe QDs occurred over a very fast time scale from a few hundreds of fs in the Na_2S solution via hole transfer to S^{2-} ions to a few ps in air via hole trapping.

TG kinetics	A_1	τ_1 (ps)	A_2	τ_2 (ps)	y_0
In air	0.39± 0.01	6.3±0.4	0.29 ±0.01	82 ±7	0.27± 0.01
In Na_2S	0.07± 0.01	9 ±1	0.31± 0.01	85 ±1	0.25± 0.01
Difference	0.33± 0.01	5.0± 0.3	-	-	-

Table 1. Fitting results of the TG responses of CdSe QDs adsorbed onto nanostructured TiO_2 films measured in air and in Na_2S solution (hole acceptor) as well as their "difference response" as shown in Fig. 3 with a double exponential decay equation (eq. (2)). τ_1 and τ_2 are time constants; A_1, A_2 and y_0 are constants (Shen et al., 2010a).

2.5 Electron injection from CdSe QDs to TiO_2 nanostructured electrode

To investigate the electron transfer rate from CdSe QDs to TiO_2 electrodes, Shen and co-workers measured the TG kinetics of CdSe QDs adsorbed on both nanostructured TiO_2 electrodes and glass substrates under the same deposition conditions (Shen et al., 2008).

Figure 4 shows the TG kintics (pump beam wavelength: 388 nm) of CdSe QDs adsorbed on a TiO_2 nanostructured electrode and on a glass substrate (CBD method). The average diameter of the CdSe QDs was about 5.5 nm for both kinds of substrates. The TG kinetics were fitted to a double exponential decay function (Eq. (3)) using a least-squares fitting method, convoluting with a 1ps Gaussian representing the laser pulse.

$$y = A_1 e^{-t/\tau_1} + A_2 e^{-t/\tau_2} \tag{3}$$

where A_1 and A_2 are constants, and τ_1 and τ_2 are the time constants of the two decay processes, respectively.

The fast decay time constants τ_1 were obtained to be 2.3 ps for both the two kinds of substrates. The slow decay time constants τ_2 were obtained to be approximately 140 ps and 570 ps for the CdSe QDs adsorbed on the TiO_2 electrode and on the glass substrate, respectively. It was found that τ_1 was the same for both kinds of substrates. However, the value of τ_2 for the CdSe QDs adsorbed on the nanostructured TiO_2 electrode was much smaller than that on the glass substrate. Under the experimental conditions (pump intensity < 2 μJ/pulse in this case), the waveforms of the responses overlapped each other very well when they were normalized at the peak intensity, as mentioned above. Therefore, it is reasonable to assume that the two decay processes in the CdSe QDs adsorbed on these two kinds of electrodes were due to one-body recombination, such as trapping, decay into intrinsic states and/or a transfer process. Because the fast decay time constant is independent of the substrates and it is known that hole trapping time is much faster than that of electron relaxation (Underwood et al., 2001; Braun et al., 2002), we believe that the fast decay process with a time scale of 2-3 ps mainly corresponded to a decrease in the photoexcited hole carrier density due to trapping at the CdSe QD surface/interface states or relaxation into the intrinsic QD states, as mentioned earlier.

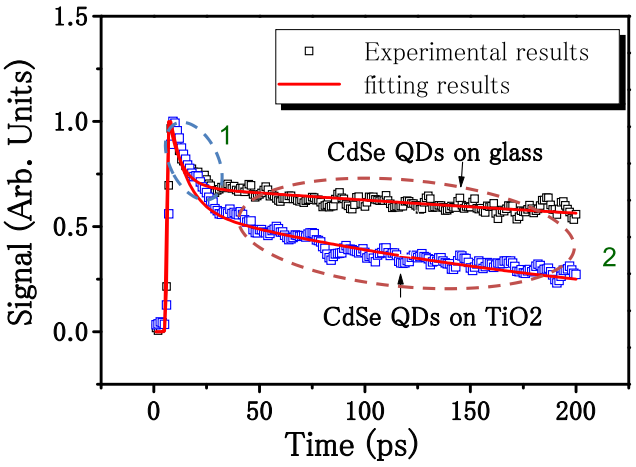

Fig. 4. TG kinetics of the CdSe QDs (average diameter: 5.5 nm) adsorbed on a nanostructured TiO_2 electrode and on a glass substrate under same adsorption conditions (Shen et al., 2008).

This result is in good agreement with the experimental results obtained with a femtosecond fluorescence up-conversion technique and transient absorption measurements (Underwood et al., 2001). The slow decay process was considered to reflect the photoexcited electron relaxation processes. For the glass substrate, no electron transfer from the QDs to the glass substrate could occur. Thus, the slow decay process only corresponded to the relaxation of photoexcited electrons in the CdSe QDs, which was mostly due to trapping at the CdSe QD surfaces. For the nanostructured TiO_2 substrate, the CdSe QDs were adsorbed onto the surfaces of the TiO_2 nanoparticles and electron transfer from the CdSe QDs to the TiO_2 nanoparticles could occur, which had been confirmed by the photocurrent measurements (Shen et al., 2004a, 2004b). As mentioned above, the TG signal due to the change in the refractive index $\Delta n(t)$ of the TiO_2 nanoparticles resulted from the injected free electrons from the CdSe QDs would be very small and can be ignored. Therefore, the slow decay process of the CdSe QDs adsorbed on the nanostructrued TiO_2 film mostly reflected the decrease of the photoexcited electron densities in the CdSe QDs due to both electron trapping at the CdSe QD surfaces/interfaces and electron transfer from the CdSe QDs to the TiO_2 nanoparticles. This is the reason why the τ_2 obtained for the CdSe QDs adsorbed on the nanostructured TiO_2 electrode was much smaller than that obtained for the CdSe QDs adsorbed on the glass substrate. For the CdSe QDs on the nanostructured TiO_2 electrode, the decay rate k_2 ($k_2 = 1/\tau_2$) can be expressed as

$$k_2 = k_r + k_{et} \tag{4}$$

where k_r is the intrinsic decay rate (mostly trapping) in CdSe QDs and k_{et} is the electron-transfer rate from CdSe QDs to TiO_2. The intrinsic decay time of electrons in the CdSe QDs adsorbed on the nanostructured TiO_2 electrode was assumed to be the same as that in the CdSe QDs adsorbed on the glass substrate. In this way, we can estimate the electron transfer rate from the CdSe QDs into the nanostructured TiO_2 electrode to be approximately $5.6 \times 10^9\ s^{-1}$ using the values of τ_2 obtained from the CdSe QDs adsorbed on these two kinds of substrates. This result is very close to the electron transfer rates from CdSe QDs to TiO_2 substrates measured recently using a femtosecond transient absorption (TA) technique by Kamat and co-workers (Robel et al., 2007).

2.6 Changes of carrier dynamics in CdSe QDs adsorbed onto TiO_2 nanostructured electrodes versus adsorption conditions

The photoexcited carrier dynamics of CdSe QDs, including the electron injection rates to the TiO_2 electrodes, depends greatly on the size of the CdSe QDs, the adsorption method (mode of attachment), the adsorption conditons such as adsorption time, and the properties of the TiO_2 electrodes such as crystal structure. In the following, two examples will be introduced.

The first example is the carrier dynamics of CdSe QDs adsorbed onto TiO_2 electrodes with SILAR method (Guijarro et al., 2010a). Figure 5 shows the normalized TG kinetics of CdSe adsorbed TiO_2 electrodes with different SILAR cycles and an example of the fitting result of the TG kinetics with eq. (3) to determine the parameters A_1, A_2, τ_1 and τ_2 shown in Fig. 5. Figure 6 shows the dependence of τ_1 and τ_2 on the number of SILAR cycles. As shown in Fig. 6, τ_1 increases from 2.8 to 6.3 ps and τ_2 increases from 83 to 320 ps upon increasing the number of SILAR cycles from 2 to 9-15. With the SILAR cycle increasing, both the average QD size and the number of QDs increase. Therefore, for a low number of cycles, all the CdSe QDs would be in direct contact with the TiO_2 electrode, favouring electron injection.

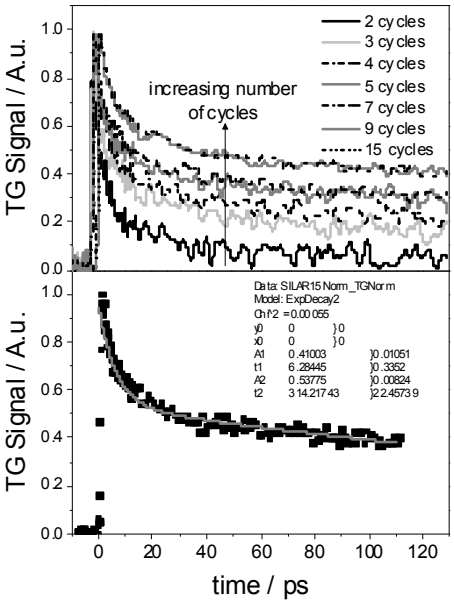

Fig. 5. Transient grating kinetics of CdSe QD adsorbed TiO_2 electrodes with different SILAR cycles (a) and an example of the fitting of the TG kinetics (15 cycles) to a double exponential decay (eq. (3)) (b) (Guijarro et al., 2010a).

However, for a large number of deposition cycles, a large fraction of CdSe QDs would not be in direct contact with the TiO_2 electrode, resulting in an increase in electron injection time. As discussed in depth by Guijarro and co-workers (Guijarro et al., 2010a), in this case, the fast decay component was attributed to direct electron transfer from the first layer of deposited CdSe QDs besides the hole trapping, and the slow one to electron injection into the TiO_2 from CdSe QDs in the outer layers (and trapping at surface and interfacial QD/QD states). For the fast decay component, the increase in QD average sizes resulted from the increase of SILAR cycles likely plays a key role in determining the values of τ_1. The results were in qualitative agreement with those reported by Kamat and co-workers (Robel et al., 2007) showing that electron injection into TiO_2 from CdSe QDs becomes faster as the QD size gets smaller. It was considered to be due to an increase in the driving force as the CdSe conduction band shifts toward higher energies. A plot of τ_1 versus the number of SILAR cycle numbers (Fig. 6(a)) shows approximately a linear dependence. For the slow decay component, the electron relaxation time τ_2 also increases upon increasing the number of SILAR cycles (Fig. 6(b)), which can be explained as follows. The increase in the number of SILAR cycles results in not only an average increase of the CdSe quantum dot size but also an increase in the average distance of the CdSe QDs to the oxide particle. Correspondingly, the concentration of QDs not in direct contact with the TiO_2 would also grow. This leads to an increase in the average time needed for transferring the photoexcited electrons from the QDs to the oxide. Therefore, the values of A_1 and A_2 mainly reflected the relative contribution of the fast electron transfer (from the first QD layer in direct contact with the TiO_2) and the slow one (from the QDs in the outer layers), respectively. A_1 decreases from

0.84 to 0.41 while A_2 increases from 0.22 to 0.54 as the SILAR cycle increases from 2 to 9-15. For a low number of SILAR cycles, A_1 is large, indicating the predominance of electron injection from QDs in direct contact with the TiO_2. As the SILAR cycle increases, A_2 increases because the contribution of the slower electron transfer through CdSe/CdSe interfaces becomes more and more important.

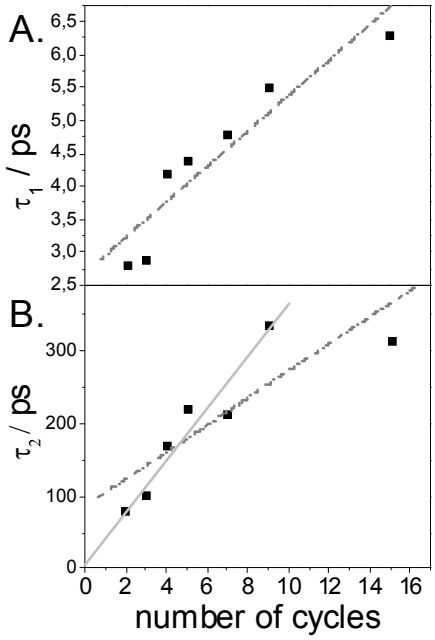

Fig. 6. Dependence of τ_1 (A) and τ_2 (B) on the number of SILAR cycles. Dashed lines correspond to linear fittings including all data, whereas the solid line shows a linear fitting forced to pass through the origin without considering the point corresponding to 15 SILAR cycles (Guijarro et al., 2010a).

The second example is the carrier dynamics of CdSe QDs adsorbed onto TiO_2 electrodes with linker-assisted (LA) method (Guijarro et al., 2010b). Figure 7 shows the TG kinetics for TiO_2 nanostrucuted electrodes modified by linker-adsorbed (using cysteine, p-mercaptobenzoic acid (MBA) and mercaptopropionic acid (MPA)) CdSe QDs (average size: 3.5 nm), together with the TG kinetics of the CdSe QD solution used for the adsorption. The TG kinetics of the LA adsorption samples were not sensitive to adsorption time. It indicates that the specific interaction between the thiol group (-SH) of the three kinds of linkers and the QD leads to homogeneous adsorption, in which all the QDs are adsorbed directly on the TiO_2 surface with no aggregation. As shown in Fig. 7, strong dependence of the decay of the TG kinetics on the linker nature was observed. This result suggests that, not only the length, but also other factors such as the dipole moment, the redox properties or the electronic structure of the linkers may play a role in the carrier dynamics. The TG kinetics of the LA adosprtion samples were fitted very well to eq. (3),

and electron transfer rate constants were calculated according to eq. (4) by assuming that the intrinsic decay rate constant in adsorbed TiO_2 electrodes is the same as that in the CdSe colloidal dispersion (Table 2). The values of the electron transfer rate constant from CdSe to TiO_2 via MPA are in good agreement with the results obtained by Kamat's group (Robel et al., 2007), ranging from 1.0 x 10^9 to 2 x 10^{11} s^{-1}. With respect to the effect of QD size, it was found that the smaller the QD, the faster the electron injection. Very interestingly, a direct correalation between the ultrafast carrier dynamics and the incident photon current conversion efficiency (IPCE) values measured in the absence of electron acceptors in solution for CdSe QDSCs was found. (Guijarro et al., 2010b).

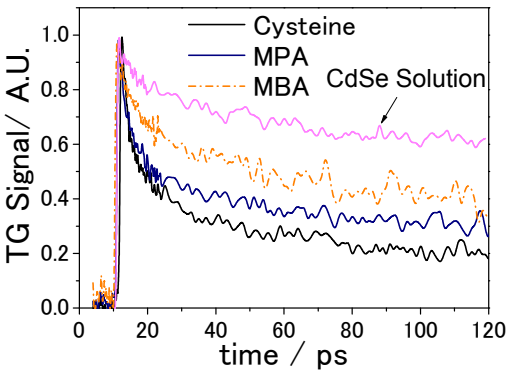

Fig. 7. TG kinetics for CdSe-sensitized TiO_2 electrodes using cysteine, MPA and MBA as linkers. All the curves are normalized to the maximum value. The TG kinetics corresponding to the CdSe solution used for LA adsorption is also given for comparison (Guijarro et al., 2010b).

Sample	A_1	τ_1 (ps)	A_2	τ_2 (ps)	$k_{1,et}$ x 10^{-11} (s^{-1})	$k_{2,et}$ x 10^{-9} (s^{-1})
CdSe solution	0.18 ± 0.01	8.8 ± 0.8	0.77 ± 0.01	506 ± 45		
LA (cysteine)	0.46 ± 0.01	3.9 ± 0.3	0.41 ± 0.01	127 ± 7	1.4 ± 0.3	5.9 ± 0.6
LA (MPA)	0.50 ± 0.01	4.2 ± 0.2	0.46 ± 0.01	204 ± 13	1.2 ± 0.2	2.9 ± 0.5
LA (MBA)	0.38 ± 0.02	7.7 ± 0.3	0.77 ± 0.01	245 ± 24	0.2 ± 0.1	2.1 ± 0.6

Table 2. Fitting parameters of TG kinetics (Fig. 7) of CdSe solution and LA adsorption samples (eq. (3)) and calculated electron transfer rate constants (eq. (4)) (Guijarro et al., 2010b).

2.7 Effect of surface modification on the ultrafast carrier dynamics and photovoltaic properties of CdSe QD sensitized TiO_2 solar cells

As mentioned above, the energy conversion efficiency of QDSCs is still less than 5% at present (Mora-Sero', et al., 2010; Zhang et al., 2011) and more studies are necessary for improving the photovoltaic properties of QDSCs. The poor photovoltaic performance of QDSCs usually results from three kinds of recombination. The first one is the recombination of the injected electrons in TiO_2 electrodes with electrolyte redox species. The second one is

the recombination of photoexcited electrons in the QDs with electrolyte redox species. The third one is the recombination of photoexcited electrons and holes through surface and/or interface defects. To improve the photovoltaic performance, surface passivation should be carried out. In the previous work (Shen et al., 2008; Diguna et al., 2007a), it was found that ZnS surface coating on the CdSe QDs could imporve the photovoltaic properties of CdSe QDSCs significantly. In addition to ZnS, the authors also tried surface mosifications with Zn^{2+} and S^{2-} surface adsorption. The effects of the three kinds of surface modification (ZnS, Zn^{2+}, and S^{2-}) on the photovoltaic performances and ultrafast carrier dynamics of CdSe QDSCs have been investigated.

The three kinds of surface modifications for CdSe QD adsorbed TiO_2 nanostructured electrodes (24 h adsorption at 10 ℃ using CBD method) were carried out as follows: (1) the samples were coated with ZnS by alternately dipping them two times in 0.1 M $Zn(CH_2COO)$ and 0.1 M Na_2S aqueous solutions for 1 minute for each dip; (2) the samples were adsorbed with Zn^{2+} by dipping them in 0.1 M $Zn(CH_2COO)$ for 6 min; (3) the samples were adsorbed with S^{2-} by dipping them in 0.1 M Na_2S for 6 min. For characterization of the photovoltaic performances, solar cells were assembled using a CdSe QD sensitized TiO_2 electrode as the working electrode and a Cu_2S film as the counter electrode (Hodes et al., 1980). Polysulfide electrolyte (1 M S and 1 M Na_2S solution) was used as the regenerative redox couple (Shen et al., 2008b). The active area of the cells was 0.25 cm^2. The photovoltaic characteristics of the solar cells were measured using a solar simulator (Peccell Technologies, Inc.) at one sun (AM1.5, 100 mW/cm^2). For the TG measurements, the pump and the probe wavelengths are 530 nm and 775 nm, respectively.

Figure 8 shows the photocurrent density-photovoltage curves of CdSe QDSCs, in which the QD surfaces were not modified and modified with Zn^{2+}, S^{2-}, and ZnS, respectively. The photovoltaic properties of short circuit current density, open circuit voltage and fill factor (FF) were improved after modifying the surface with ZnS or Zn^{2+}, especially the short circuit current density was improved significantly (Table 3). As a result, the energy conversion efficiencies of the samples with ZnS or Zn^{2+} surface modification increased as many as 3 times compared to the sample without surface modification. The improvement of the photovoltaic performances by means of the ZnS or Zn^{2+} surface modification may be due to (1) the decrease of surface states of TiO_2 and CdSe QDs and (2) the formation of a potential barrier at the CdSe QD/electrolyte and TiO_2/electrolyte interfaces. However, there is little effect of the modification with S^{2-} on the photovoltaic properties. So, maybe Se^{2-} is rich on the CdSe QD surfaces.

Figure 9 shows the TG kinetics of the CdSe QD adsorbed TiO_2 electrodes before and after Zn^{2+} and ZnS surface modification. From the TG kinetics, two decay processes were observed. The fast and slow decay processes were mostly attributed to photoexcited hole trapping and electron transfer dynamics, as discussed earlier. For the sample before and after Zn^{2+} surface modification, the fast decay times were 4.5 and 2 ps, and the slow decay times were 53 ps and 25 ps, respectively. It indicates that the hole and electron relaxation became faster after the surface modification. Similar results were also obtained after the ZnS and S^{2-} surface modifications as shown in Fig. 10. The faster electron transfer due to the surface modification may result from the decrease of the surface trapping states. Further studies on the mechanism of the effects of the surface modifications on the photovoltaic performances and the carrier dynamics are in progress now.

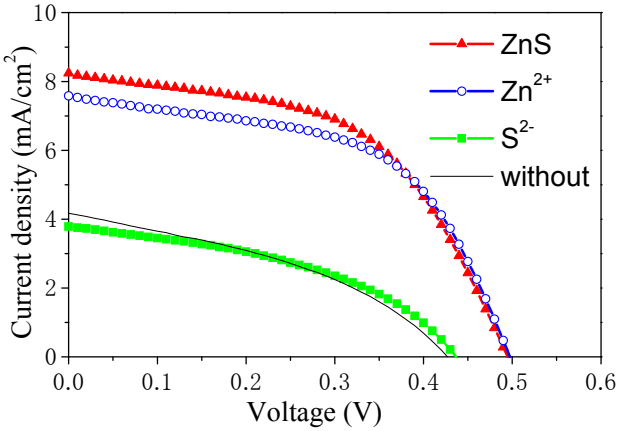

Fig. 8. Photocurrent density-photovoltage characteristics of CdSe QD-sensitized solar cells without and with surface modifications.

Sample	J_{sc} (mA/cm^2)	V_{oc} (V)	FF	η (%)
TiO_2/CdSe	4.2	0.43	0.39	0.69
TiO_2/CdSe/ZnS	8.2	0.49	0.53	2.1
TiO_2/CdSe/Zn^{2+}	7.6	0.50	0.53	2.1
TiO_2/CdSe/S^{2-}	3.8	0.44	0.43	0.82

Table 3. Photovoltaic properties of CdSe QDSCs before and after surface modifications with Zn^{2+}, S^{2-}, and ZnS, respectively. J_{sc} is the short circuit current density, V_{oc} is the open circuit voltage, FF is the fill factor, and η is the energy conversion efficiency.

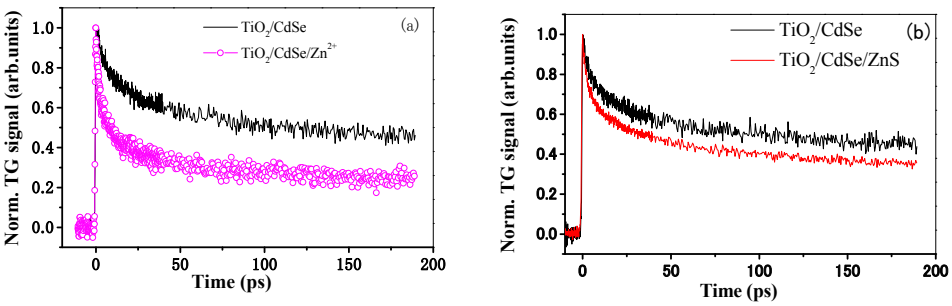

Fig. 9. Transient grating kinetics of CdSe QD adsorbed TiO_2 electrode before and after the surface modification with Zn^{2+} (a) and ZnS (b).

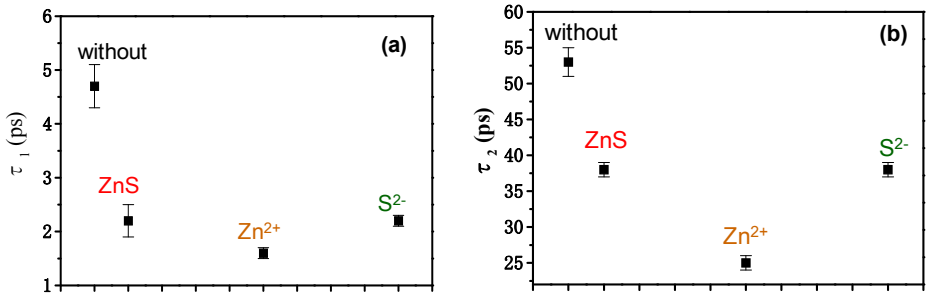

Fig. 10. Fast (τ_1) (a) and slow (τ_2) (b) decay times of the transient grating kinetics for CdSe QD adsorbed TiO_2 electrodes before and after the surface modifications with ZnS, Zn^{2+} and S^{2-}.

3. Conclusion

In summary, the photoexcited carrier dynamics in CdSe QDs adsorbed onto TiO_2 nanostructured electrodes have been characterized by using the improved TG technique. It has been demonstrated that both photoexcited electron and hole dynamics can be detected by using this improved TG technique. By comparing the TG responses measured in air and in a Na_2S solution (hole acceptor), the dynamics of photoexcited electrons and holes in the CdSe QDs has been sucssesfully separated from each other. It was found that charge separation in the CdSe QDs occurred over a very fast time scale from a few hundreds of fs in the Na_2S solution via hole transfer to S^{2-} ions to a few ps in air via hole trapping. On the other hand, the electron dynamics in the CdSe QDs, including trapping and injection to the metal oxide electrodes, depends greatly on the QD size, and adsorption methods (such as CBD, SILAR, DA and LA adsorption methods) and conditons (such as adsorption time and SIALR cycle number). In addition, surface modifications such as ZnS coating and adsorption with Zn^{2+} have been demonstrated to improve the photovoltaic properties and have a great influence on the ultrafast carrier dynamics of CdSe QDSCs. Detailed studies on the correlations between the carrier dynamics and the photovoltaic properties in QDSCs are in progress now.

4. Acknowledgment

Part of this research was supported by JST PRESTO program, Grant in Aid for Scientific Research (No. 21310073) from the Ministry of Education, Sports, Science and Technology of the Japanese Government. The authors would like to thank Dr. Kenji Katayama and Dr. Tsuguo Sawada for their help in the setup of TG equipment and also thank Mr. Yasumasa Ayuzawa for his help in some experiments. The authors are grateful to Prof. Juan Bisquert, Prof. Roberto Go´mez, Mr. Ne´stor Guijarro, Dr. Sixto Gime´nez, and Dr. Iva´n Mora-Sero´ for their collaboration and help in the research.

5. References

Adachi, M.; Murata, Y.; Okada, I.; &Yoshikawa, S. (2003), *J. Electrochem. Soc.*, Vol. 150, G488.
Bawendi, M. G.; Kortan, A. R.; Steigerwals, M.; & Brus, L. E. (1989), *J. Chem. Phys.*, Vol. 91, p. 7282.

Blackburn, J. L.; Selmarten, D. C. & Nozik, A. J. (2003); *J. Phys. Chem. B*, Vol. 107, p. 14154.
Blackburn, J. L.; Selmarten, D. C.; Ellingson, R. J.; Jones, M.; Micic, O. & Nozik, A. J. (2005); *J. Phys. Chem. B*, Vol. 109, p. 2625.
Braun, M.; Link, S.; Burda C.; & El-Sayed, M. A. (2002), *Chem. Phys. Lett.,* Vol. 361, p. 446.
Chiba, Y.; Islam, A.; Watanabe, Y.; Koyama, R.; Koide, N.; & Han, L. (2006), *Jpn. J. Appl. Phys.* Vol. 43, p. L638.
Diguna, L. J.; Shen, Q.; Kobayashi, J.; & Toyoda, T (2007a), *Appl. Phys. Lett.*, Vol. 91, p. 023116.
Diguna, L.J., Shen, Q., Sato, A., Katayama, K., Sawada, T., Toyoda, T. (2007b), *Mater. Sci. Eng. C*, Vol. 27, p. 1514.
Eichler, H.J.; Gunter P. & Pohl, D. W. (1986). *Laser-induced Dynamic Gratings*., Springer, Berlin.
Giménez, S; Mora-Seró, I; Macor, L.; Guijarro, N.; Lala-Villarreal, T.; Gómez, R.; Diguna, L.;Shen, Q.; Toyoda, T; & Bisquert, J (2009), *Nanotechnology*, Vol. 20, p. 295204.
Glorieux, C.; Nelson, K. A.; Hinze, G. & Fayer, M. D. (2002), *J. Chem. Phys.,* Vol. 116, p. 3384.
Gorer, S.; & Hodes, G. (1994), *J. Phys. Chem*., Vol. 98, p. 5338.
Grätzel, M. (2003), *J. Photochem. Photobiol. C: Photochem. Rev*., Vol. 4, p. 145.
Guijarro, N.; Lana-Villarreal, T.; Mora-Sero´, I.; Bisquert, J.; Go´mez, R. (2009), *J. Phys. Chem. C*, Vol. 113, p. 4208.
Guijarro, N.; Lana-Villarreal, T.; Shen, Q.; Toyoda, T.& Gómez, R. (2010a), *J. Phys. Chem. C,* Vol. 114, p. 21928.
Guijarro, N.; Shen, Q.; Giménez, S.; Mora-Seró, I.; Bisquert, J.; Lana-Villarreal, T.; Toyoda, T. & Gómez, R. (2010b), *J. Phys. Chem. C*, Vol. 114, p. 22352.
Hanna, M. C. & Nozik, A. J. (2006), *J. Appl. Phys*., Vol. 100, p. 074510.
Hodes, G; Manassen, J; & Cahen, D. (1980), *J. Electrochem. Soc*., Vol. 127, p. 544.
Hodes, G. (2008), *J. Phys. Chem. C*, Vol. 112, p. 17778.
Kashiski, J. J.; Gomez-Jahn, L. A.; Faran, K. Y.; Gracewski, S. M. & Miller, R. J. D. (1989), *J. Chem. Phys*., Vol. 90, p. 1253.
Kamat , P. V. (2008), *J Phys Chem C*, Vol. 112, p. 18737.
Katayama, K.; Yamaguchi, M.; & Sawada, T. (2003), *Appl. Phys. Lett*., Vol. 82, p. 2775.
Kim, J.; Meuer, C.; Bimberg, D. & Eisenstein, G. (2009), *Appl. Phys. Lett.*, Vol. 94, p. 041112.
Klimov, V. I. (2006), *J. Phys. Chem. B*, Vol. 110, p. 16827.
Law, M.; Greene, L. E.; Johnson, J. C.; Saykally, R. & Yang, P. (2005), *Nat. Mater*., Vol. 7, p. 1133.
Lee, Y-L.; & Lo, Y-S. (2009), *Adv. Func. Mater*., Vol. 19, p. 604.
L. Min, L. & Miller, R. J. D. (1990), *Appl. Phys. Lett.*, Vol. 56, p. 524.
Miyata, R.; Kimura, Y. & Terazima, M. (2002), *Chem. Phys. Lett.,* Vol. 365, p. 406.
Mora-Seró, I; Giménez, S; Fabregat-Santiago, F.; Gómez, R.; Shen, Q.; Toyoda, T; & Bisquert, J. (2009), *Acc. Chem. Res*., Vol. 42, 1848.
Mora-Seró, I & Bisquert, J. (2010), *J Phys Chem Lett*, Vol. 1, p. 3046.
Niitsoo, O.; Sarkar, S. K.; Pejoux, P.; Rühle, S.; Cahen, D.; & Hodes, G., *J. Photochem. Photobiol. A*, Vol. 182, 306.
Nishimura, S.; Abrams, N.; Lewis, B. A.; Halaoui, L. I.; Mallouk, T. E.; Benkstein, K. D.; Lagemaat, J. & Frank, A. K. (2003), *J. Am. Chem. Soc*., Vol. 125, p. 6306.

Nozik, A. J. (2002), *Physica E*, Vol. 14, p. 16827.
Nozik, A. J. (2008), *Chem. Phys. Lett.* , Vol. 457, p. 3.
Nozik, A. J.; Beard, M. C.; Luther, J. M.; Law, M.; Ellingson, R. J. & Johnson, J. C. (2010), *Chem. Rev.*, Vol. 110, p. 6873.
Ohmor, T.; Kimura, Y.; Hirota, N. & Terazima, M. (2001), *Phys. Chem. Chem. Phys.,* Vol. 3, p. 3994.
O'Regan, B.; & Grätzel (1991), *Nature*, Vol. 353, p. 737.
Park, B.-W.; Inoue, T.; Ogomi, Y.; Miyamoto, A; Fujita, S; Pandey, S. S.&Hayase, S. (2011) *Appl. Phys. Express*, Vol. 4, p. 012301.
Paulose, M.; Sharkar, K.; Yoriya, S.; Prakasam, H. E.; Varghese, O. K.; Mor, G. K.; Latempa, T. A.; Fitzgerald, A. & Grimes, C. A. (2006), *J. Phys Chem. B*, Vol. 110, p. 16179.
Peter, L. M.; Riley, D. J.; Tull, E. J. & Wijayanta, K. G. U. (2002), *Chem. Commun.*, Vol. 2002, p. 1030.
Plass, R.; Pelet, S.; Krueger, J.; Gratzel, M. & Bach, U. (2002), *J. Phys. Chem. B*, Vol. 106, p. 7578.
Polo, A. S.; Itokatu, M. K. & Iha, N. Y. M. (2004), *Coord. Chem. Rev.*, Vol. 248, p. 1343.
Rajesh, R. J. & Bisht, P. B. (2002), *Chem. Phys. Lett.,* Vol. 357, p. 420.
Robel, I.; Subramanian, V.; Kuno, M. & Kamat, P. V. (2006), *J. Am. Chem. Soc.*, Vol. 128, p. 2385.
Robel, I.; Kuno, M. & Kamat, P. V. (2007), *J. Am. Chem. Soc.*, Vol. 129, p. 4136.
Schaller, R. D. & Klimov, V. I. (2004), *Phys. Rev. Lett*., Vol. 92., P. 186601.
Shen, Q.; & Toyoda, T (2003), *Thin Solid Films*, Vol. 438-439, p. 167.
Shen, Q.; & Toyoda, T (2004a), *Jpn. J. Appl. Phys*., Vol. 43, p. 2946.
Shen, Q.; Arae, D.; & Toyoda, T. (2004b), *J. Photochem. Photobiol. A*, Vol. 164, p. 75
Shen, Q.; Katayama, K.; Yamaguchi, M.; Sawada, T.& Toyoda, T. (2005), *Thin Solid Films*, Vol. 486, p. 15.
Shen, Q.; Katayama, K.; Sawada, T.; Yamaguchi, M.& Toyoda, T. (2006a), *Jpn. J. Appl. Phys*., Vol. 45, p. 5569.
Shen, Q.; Sato, T.; Hashimoto, M.; Chen, C. C. & Toyoda, T. (2006b), *Thin Solid Films*, Vol. 499, p. 299.
Shen, Q.; Yanai, M.; Katayama, K.; Sawada, T.& Toyoda, T.(2007), *Chem. Phys. Lett.,*Vol. *442*, p. 89.
Shen, Q.; Katayama, K.; Sawada, T.& Toyoda, T. (2008a), *Thin Solid Films*, Vol. 516, p. 5927.
Shen, Q.; Kobayashi, J.; Doguna, L. J.; & Toyoda, T. (2008b), *J. Appl. Phys*., Vol. 103, p. 084304.
Shen, Q.; Ayuzawa, Y.; Katayama, K.; Sawada, T.; & Toyoda, T. (2010a), *Appl. Phys. Lett.*, Vol. 97, p. 263113.
Shen, Q.; Yamada, A.; Tamura, S. & Toyoda, T. (2010b), *Appl. Phys. Lett.*, Vol. 97, p. 23107.
Song, M. Y.; Ahn, Y. R.; Jo, S. M.; Kim, D. Y. & Ahn, J. P. (2005), *Appl. Phys. Lett.*, Vol. 87, p. 113113.
Terazima, M.; Nogami, Y. & Tominaga, T. (2000), *Chem. Phys. Lett.,* Vol. 332, p. 503.
Toyoda, T.; Saikusa, K. & Shen, Q. (1999), *Jpn. J. Appl. Phys*., Vol. 38, p. 3185.
Toyoda, T.; Sato, J. & Shen, Q. (2003), *Rev. Sci. Instrum.* , Vol. 74, p. 297.
Vogel, R.; Pohl, K. & Weller, H. (1990), *Chem. Phys. Lett.*, Vol. 174, p. 241.

Tvrdy, K.; Frantsuzov, P. A.; Kamat, P. V. (2011), *Proceedings of the National Academy of Sciences of the United States of America,* Vol. 108, p. 29.

Vogel, R.; Hoyer, P. & Weller, H. (1994), *J. Phys. Chem*., Vol. 98, p. 3183.

Yamaguchi, M.; Katayama, K.; & Sawada, T. (2003), *Chem. Phys. Lett*., Vol. 377, p. 589.

Underwood, D. F.; Kippeny, T.; & Rosenthal, S. J. (2001), *Eur. Phys, J. D,* Vol. 16, p. 241.

Yan, Y. I.; Li, Y.; Qian, X. F.; Zhu, Z. K. (2003), *Mater. Sci. Eng. B,* Vol. 103, p. 202.

Yang, S. M.; Huang, C. H.; Zhai, J.; Wang, Z. S.; & Liang, L. (2002), *J. Mater. Chem*., Vol. 12, p. 1459.

Yu, P. R.; Zhu, K.; Norman, A. G.; Ferrere, S.; Frank, A. J. & Nozik, A. J. (2006), *J. Phys. Chem. B*, Vol. 110, p. 25451.

Zhang, Q. X.; Guo, X. Z.; Huang, X. M.; Huang, S. Q.; Li, D. M.; Luo, Y. H.; Shen, Q.; Toyoda, T. & Meng, Q. B. (2011), *Phys. Chem. Chem. Phys*., Vol. 13, p. 4659.

14

Transparent Conducting Polymer/Nitride Semiconductor Heterojunction Solar Cells

Nobuyuki Matsuki[1,3], Yoshitaka Nakano[2], Yoshihiro Irokawa[1], Mickael Lozac'h[1] and Masatomo Sumiya[1]
[1]*National Institute for Materials Science, Namiki, Tsukuba, Ibarak,*
[2]*Institute of Science and Technology Research, Chubu University, Matsumoto, Kasugai, Aichi,*
[3]*Department of Electrical and Electronic Engineering, Faculty of Engineering, Gifu University, Yanagido, Gifu, Japan*

1. Introduction

Energy supplies that depend on fossil fuels evoke significant concern about the future depletion of those resources and the emission of carbon dioxide and sulfidizing gas, which are believed to cause environmental problems including climate change and acid precipitation (Solomon et al., 2007). Solar cells, which convert sunlight directly to electric power, are one of the most promising devices for a clean and enduring energy source. The standard energy-weighted power density of sunlight, which is defined as air mass 1.5, is 1kW/m^2 under clear and sunny weather conditions (Myers et al., 2000). The maximum available amount of sunlight is usually lower than the value described above due to the weather and the total hours of sunlight in the region.

Thus, the first important aim for developing a solar cell is to derive the highest possible photovoltaic conversion efficiency from the utilized materials and structure. When a solar cell with a single bandgap, E_g, is exposed to the solar spectrum, a photon with less energy than E_g does not contribute to the cell output. Therefore, a multilayer structure comprising a variety of bandgaps is effective for the collection of photons in a wide range of the solar spectrum.

The current (2010) best research-cell efficiencies of typical solar cells are as follows (Green, 2010): crystalline Si (25.0%), multicrystalline Si (20.4%), crystalline GaAs (26.4%), CuInGaSe (19.4%), CdTe (16.7%), amorphous Si (10.1%), dye-sensitized polymers (10.4%), and organic polymers (5.15%). In addition to these, there have been a number of studies focused on developing "third-generation photovoltaics" with ultra-high conversion efficiencies at a low cost (Green, 2001). More recently, after the discovery of the wide band gap range of 0.65–3.4 eV in $In_xGa_{1-x}N$, this material is considered to be one of the most promising candidates for third-generation photovoltaic cells.

Aiming at developing multijunction solar cells based on III-nitrides, we have focused on the potential of a transparent conductive polymer (TCP) as a UV-transparent window layer for the cell instead of adopting the conventional all-inorganic p-i-n structure. In this chapter, we describe the concept and experimental results of the development of TCP/nitride semiconductor heterojunction solar cells. In addition, prospects for their further development are discussed.

2. Basic concepts

2.1 Background

In 2002, an epochal report on the E_g of InN was published; the E_g, which had been believed to be 2.0 eV for many years, was found to be less than 1.0 eV by photoluminescence characterization (Matsuoka et al., 2002). Subsequent investigations verified that the correct E_g is 0.7 eV (Wu et al., 2003). This fact immediately impelled III-nitride-researchers to consider applying III-nitrides to solar cells because $In_xGa_{1-x}N$, which is the III-nitride compound obtained from InN (E_g = 0.7 eV) and GaN (E_g = 3.4 eV), is a direct transition semiconductor that would widely cover the solar spectrum. Furthermore, the strong Piezo-electric-field that forms in III-nitride semiconductors, which is a critical problem for optical emission devices due to the suppression of carrier recombination (Takeuchi, 1998), will be more advantageous to photovoltaic devices in which carrier separation is necessary. There have been reports on the theoretical predictions of the conversion efficiency of In_xGa_{1-x} N solar cells that suggest that the maximum conversion efficiency of In_xGa_{1-x} N solar cells will reach 35–40% (Hamzaoui, 2005; Zhang, 2008). Experimental results of In_xG_{a1-x} N-based solar cells have been also reported (Chen, 2008; Zheng, 2008; Dahal, 2009; Kuwahara, 2010). Although the potential conversion efficiency of $In_xGa_{1-x}N$ solar cells is promisingly high, the highest one so far obtained through an InGaN/InGaN superlattice structure remains as low as 2.5% (Kuwahara, 2011).

The challenges for the development of high efficiency InGaN solar cells are mainly attributed to the necessity for: (1) a conductive crystalline substrate to grow high quality nitride layers in order to reduce series resistance, (2) a high quality film growth technique to reduce carrier recombination, (3) high-efficiency p-type doping, and (4) a novel cell design that allows absorption in a wide range of the solar spectrum and efficient collection of the photo-generated carrier.

Our research has targeted issues (3) and (4) above by introducing a novel Schottky contact consisting of a transparent conducting polymer/nitride semiconductor heterojunction. In this section, the advantages of the polymer/nitride semiconductor heterojunction are described in comparison with those of a conventional nitride p-n homojunction. In addition, the optical and electrical properties of the transparent conducting polymers are shown.

2.2 Issues with solar cell window layer

Figure 1 shows a schematic structure of the In_xGa_{1-x} N-based solar cell that exhibits 2.5% conversion efficiency (Kuwahara, 2011). Due to the low doping efficiency and activity of Mg in p-type III nitride semiconductors, the In_xGa_{1-x} N-based solar cell requires a highly conductive front layer on top of the p-type layer to collect the photo-generated carriers.

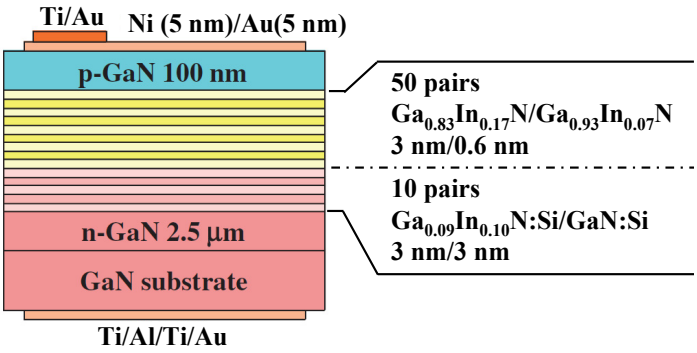

Fig. 1. Schematic of In_xGa_{1-x} N-based solar cell exhibiting 2.5% conversion efficiency (Kuwahara, 2011).

In Figure 1, the electrode on the window side consists of a Ni/Au semitransparent thin film similar to that in the conventional III-nitride-based photoelectric devices. Despite the transparency of the Ni/Au thin-film being as low as 67%, this material is utilized because it forms good ohmic contact with the III-nitride semiconducting layer (Song et al., 2010). With the aim of increasing the transparency of the window-side electrode, indium tin oxide (ITO) was applied to a III-nitride light-emitting diode (LED) (Shim et al, 2001; Chang et al., 2003). In the same study, although the light emitting intensity in the ITO/GaN LED was enhanced compared with that of a Ni/Au/GaN LED under the same current density, the lifetime of the device was significantly shortened due to the heat generated by the high contact resistance between ITO and GaN. Thus, ITO is not a suitable alternative candidate for the metal semitransparent layer unless the contact resistance problem is solved. The low optical transparency and/or the high contact resistance of the front conductive layer are a critical disadvantage for solar cell applications; therefore, new materials that can overcome these issues are highly desirable.

2.3 Conducting polymers as electrodes

Recently, the electronic properties of conducting polymers have been significantly improved and they have been extensively applied in various electric devices (Heeger, 2001).

The study of polymers began with the accidental discovery of vinyl chloride by H. V. Regnault (1835). Thereafter, various kinds of polymers were found and industrialized including ebonite (1851), celluloid (1856), bakelite (1907), polyvinyl chloride (1926), polyethylene (1898; 1933), nylon (1935), etc. Polymers show good electrical insulating properties due to the lack of free electrons; therefore, they have been extensively applied as electrical insulators. However, in 1963, D. E. Weiss and his colleagues discovered that polypyrrole became electrically conductive by doping it with iodine (Bolto et al., 1963). In 1968, H. Shirakawa and his colleagues accidentally discovered a fabrication process for thin-film polyacetylene. In 1975, A. G. MacDiamid noticed the metallic-colored thin-film polyacetylene when he visited Shirakawa's laboratory. Thereafter, collaborative works by A. Heeger, A. G. MacDiamid, and H. Shirakawa began and soon they found a remarkable effect that the electrical conductivity of the polyacetylene thin-film increased over seven

orders of magnitude, from 3.2×10^{-6} to 3.8×10^{2} Ω^{-1} cm^{-1}, with iodine doping (Shirakawa et al., 1977). Since these early studies, various sorts of π-conjugated polymer thin films have been produced and efforts to improve their conductivity have been made.

We briefly describe the origin of conductivity in degenerate π-conjugated polymers below (Heeger, 2001). In degenerate π-conjugated polymers, stable charge-neutral-unpaired-electrons called solitons exist due to defects at the counterturned connection of the molecular chain. When the materials are doped with acceptor ions like I_2, the acceptor ion abstracts an electron from the soliton; then the neutral soliton turns into a positively-charged soliton while I_2 becomes I_3^-. If the density of the positively-charged solitons is low, the positively-charged soliton tends to pair with a neutral soliton to form a polaron. The polaron is mobile along the polymer chain, thus it behaves as a positive charge. However, the mobility of the polaron is quite low due to the effect of Coulomb attraction induced by the counterion (I_3^-). The Coulomb attraction is reduced by increasing the density of the counterions, which block the electric field. Thus, a high doping concentration of up to ~20% is required to gain high conductivity of over 10^2 Ω^{-1} cm^{-1}. Typical conducting polymers that have high conductivity are fabricated based on polyacetylene (PA), polythiophene (PT), polypyrrole (PPy), polyethylenedioxythiophene (PEDOT), and polyaniline (PANI) (Heeger, 2001).

2.4 Transparent conducting polymers as Schottky contacts

Among the various kinds of conducting polymers, we have focused primarily on polyaniline (PANI) and poly(ethylenedioxythiophene)-polystyrene sulfonate (PEDOT:PSS) because of their high conductivity (~1000 Ω^{-1} cm^{-1}) and high optical transparency (>80%) (Lee et al., 2006; Ha, 2004). Conducting polymers with high optical transparency are known as transparent conducting polymers (TCPs). PANI and PEDOT:PSS also have the advantage in a high workfunction of 5.2–5.3 eV (Brown, 1999; Jang, 2008). This workfunction value is comparable to that of Ni (5.1 eV) and Au (5.2 eV). The high workfunction properties of PANI and PEDOT:PSS make them feasible candidates as hole injection layers in polymer light emitting devices (Jang, 2008). If we assume that a heterojunction consists of a metallic layer and an n-type semiconductor, it is expected that electric barrier, or Schottky barrier, will form at the metal-semiconductor interface. The ideal Schottky barrier height, ϕ_B, is given by following equation (Schottky, 1939; Mott, 1939):

$$q\phi_B = q(\phi_m - \chi) \tag{1}$$

where q is the unit electronic charge, ϕ_m is the workfunction of the metallic material, and χ is the electron affinity of the semiconductor. In general, the experimentally observed Schottky barrier is modified due to the influence of image-force surface states of the semiconductor and/or the dipole effect (Tung, 2001; Kampen, 2006). Nevertheless, the ideal Schottky barrier height estimated from Eq. (1) is still useful to evaluate the potential barrier formation. There have been precedential reports on heterojunctions consisting of TCPs and inorganic monocrystalline semiconductors including: sulfonated-PANI/n-type Si (Wang et al., 2007; da Silva et al., 2009), PEDOT:PSS/$SrTiO_3$:Nb (Yamaura et al., 2003), and PEDOT:PSS/ZnO (Nakano et al., 2008). The $(\phi_m - \chi)$ values of these TCP/semiconductor heterojunctions, and those of PEDOT:PSS or AlN with III-nitrides including AlN, GaN and InN, are summarized in Table 1.

TCP material	ϕ_m (eV)	Semiconductor material	χ (eV)	$\phi_m - \chi$ (eV)	References
PANI	5.3[a), b)]	n-type Si	4.05[c), d)]	1.25	a) Brown et al., 1999; b) Jang st al., 2008 c) Wang et al, 2007 d) da Silva et al., 2009 e) Grabowski et al., 2001 f) Wu et al., 1999 g) Wu et al., 2004 h) Yamaura, 2003 i) Nakano et al., 2008
		AlN	0.25[e)]	5.05	
		GaN	3.3[f)]	2.0	
		InN	5.7[g)]	-0.4	
PEDOT:PSS	5.2 [a), b)]	$SrTiO_3$:Nb	4.1[h)]	1.1	
		ZnO	4.3[i)]	0.7	
		AlN	0.25[e)]	4.95	
		GaN	3.3[f)]	1.9	
		InN	5.7[g)]	-0.5	

Table 1. Summary of workfunction barrier height properties of TCP/inorganic semiconductor heterojunction.

The theoretical Schottky barrier height $(\phi_m - \chi)$ is considerably high for AlN and GaN. Thus, it was expected that combinations of these TCPs and III-nitrides would exhibit high-quality Schottky contact properties. When light is irradiated on the Schottky contact, the hole-electron pairs that are photo-generated in the depletion region of the semiconductor are separated due to the strong electric field. As a result, the carriers can be collected as a photocurrent. This suggests that the TCP Schottky contact can be a novel window layer for III-nitride solar cells as an alternative to a p-type layer. Based on this, we began to study transparent conducting polymer/nitride semiconductor heterojunction solar cells.

3. Fabrication processes

3.1 Sample preparation for optical transmittance, workfunction, and conductivity characterizations

Synthetic silica plates (500 μm thick) were utilized as the substrates to prepare samples for characterization to determine their optical transmittance, workfunction, and conductivity. A conductive polymer-dispersed solution of PEDOT:PSS (Clevios PH500, H. C. Starck; without dimethyl sulfoxide dopant) or PANI (ORMECON - Nissan Chemical Industries, Ltd.) was utilized to form the transparent conductive polymer films on the substrate. The same fabrication process was applied to both the PEDOT:PSS and PANI samples. The procedure was as follows:

1. The substrate (2 × 2 cm^2) was cleaned using ethanol and acetone for 5 min each in an ultrasonic cleaning bath at ambient temperature.
2. The cleaned substrate was set in a spin coater (MIKASA Ltd., 1H-D7), and the polymer-dispersed solution were dropped onto the substrate using a dropper.
3. The substrate was spun at a 4000 rpm rotating speed for 30 s.
4. The drop and spin procedures were repeated 4 times in total to obtain a sufficient thickness.
5. The coated sample was baked in air at 130 °C on an electric hotplate for 15 min.

The resulting PEDOT:PSS and PANI film thicknesses were measured using a surface profilometer (Dektak 6M) and were found to be 420 and 170 nm, respectively. In the spin-coat process, we applied the same conditions to both the PEDOT:PSS and PANI samples. Their thicknesses unintentionally differed due to differences in the viscosities of their source solutions.

In order to measure the conductivity, a coplanar electrode was fabricated by adding Ag paste to the TCP/synthetic silica plate sample. The electrode-gap width were both 3.3 mm and the lengths were 10.7 and 11.2 mm, respectively, for the PEDOT:PSS and PANI samples.

3.2 Transparent conducting polymer/nitride semiconductor heterojunction solar cells

We fabricated a TCP/III-nitride heterojunction solar cell structure by employing PEDOT:PSS or PANI for the TCP layer and epitaxial GaN (epi.-GaN) for the III-nitride layer (Matsuki et al, 2009, 2010, 2011). Silicon-doped gallium nitride (GaN) was grown on a sapphire (0001) substrate (sapp (0001)) surface by typical metal-organic vapor-phase epitaxy (MOVPE). Ammonia and trimethylgallium were used as the N and Ga sources, respectively. Nitrogen was used as the carrier gas. An undoped buffer GaN layer with a thickness of 1 μm was deposited, followed by the growth of a 2 μm thick Silicon-doped layer. The carrier concentration and electron mobility of the GaN film was determined to be 6.3×10^{17} cm^{-3} and 360 $cm^2/V{\cdot}s$, respectively, by Hall measurement.

The PEDOT:PSS or PANI thin film was formed on the epi.-GaN surface using the same process described in section 3.1. Then, in order to fabricate isolated cells, the TCP film was divided into several ~3–9 mm^2 square-shaped sections using a scratching tool. Finally, an ohmic contact for the GaN layer was made by soldering indium metal onto the area from which the TCP layer was removed. Figure 2 shows the schematic structure of the fabricated TCP/epi.-GaN heterojunction solar cell.

4. Characterization methods

4.1 Photoemission electron spectroscopy for workfunction determination

The workfunctions of the TCPs were determined using photoemission electron spectroscopy. The photoemission electron yield Y is expressed as follows Kane (1962):

$$Y = \alpha(h\nu - E_t)^n \tag{2}$$

where α is a proportional constant, h is Planck's constant, ν is the frequency, E_t is the threshold energy, and the value of n ranges from 1 to 5/2 depending on the system. For metallic materials, an n value of 2 is recommended, and the E_t is consistent with the

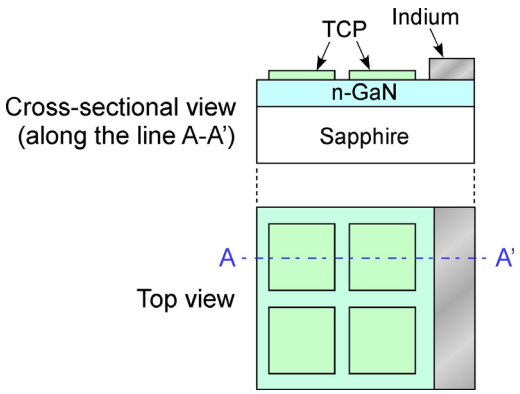

Fig. 2. Schematic of TCP/epi.-GaN sample.

photoelectric workfunction. Thus, if we modify Eq. (2) to the following form (Eq. (2)′), we can determine E_t by extrapolating the linear portion of a $Y^{1/2}$ vs. $h\nu$ plot:

$$Y^{1/2} = \alpha(h\nu - E_t) \,. \tag{2}'$$

We employed a photoemission yield spectrometer (AC-3, Riken Keiki Co., Ltd.) to determine the workfunctions of the TCPs. The sample, which was prepared as described in section 3.1, was installed in the spectrometer and the photoemission yield was measured in air.

4.2 Evaluation of current-voltage characteristics

The diode (rectifying) and photovoltaic characteristics were evaluated using an electronic measurement system consisting of an electrometer and a light source. It is necessary for the diode characterization to cover a wide current range from ~10^{-11} to ~10^{-1} A to estimate the Schottky barrier height (SBH) based on the saturation current of the thermionic emission theory (Crowell, 1965). Thus, for the evaluation of the diode characteristics, we employed a high-precision electrometer with a built-in voltage source (Keithley 6487) and performed the measurement under dark conditions. The sample was put on a measurement stage and probe needles were connected to the indium and TCP parts. A xenon-arc light source (HX-504/Q, Wacom Electric Co., Ltd.) was utilized for the evaluation of the photovoltaic characteristics. The light passed though an AM1.5 filter (Bunko Keiki Co., Ltd) and guided onto the TCP side by an aluminum mirror. The values for the source voltage and measured current were acquired by a computer through a GPIB-USB device (National Instruments Co. ltd.).

4.3 Capacitance measurements

The depletion layer width and built-in potential of the GaN layer in the TCP/GaN heterojunction solar cell were estimated using a capacitance measurement setup. A solartron 1255B frequency response analyzer was utilized for the measurement. The sample was set on a sample stage, which was in a vacuum chamber to avoid any influences from light and humidity.

5. Experimental results and discussion

5.1 Conductivity, transparency, and workfunction of polyaniline and PEDOT:PSS

The electrical conductivity was evaluated using a current-voltage (*I-V*) measurement setup under dark conditions. The conductivities estimated from the result of the *I-V* measurements were 3.4×10^{2} S/cm and 5.7×10^{-1} S/cm for PANI and PEDOT:PSS, respectively.

The optical transmittance was evaluated using a UV-visible-near-infrared spectrophotometer (UV-3150, Shimadzu Co., Ltd.). Figure 3(a) shows the optical transmittance spectra of the PEDOT:PSS and PANI films. Both of the films exhibited transmittance greater than 80% within the wavelength region between 250 and 1500 nm. This is superior to conventional transparent contact materials such as transparent conductive oxides or semi-transparent metals (Kim et al., 2002; Satoh et al., 2007), which exhibit significant drops in transparency particularly near the UV region, as seen in Figure 3.

The workfunctions of the TCPs were estimated using an ultraviolet photoelectron emission spectrometer (AC-3, Riken Keiki Co., Ltd.). Figure 3(b) depicts the photoelectron emission spectra of the PEDOT:PSS and PANI films. The spectra consist of two parts: one with a constant slope and another that linearly increases against the photon energy. The workfunction of PEDOT:PSS and PANI were found to be 5.3 and 5.2 eV, respectively, from Figure 3(b) by assuming that the threshold energy for photoelectron emission is located at the intersection point of the two straight lines that are fitted to the constant-slope and linearly-increasing-slope regions of the plots. These workfunction values show good agreement with those reported previously (Brown et al., 1999; Jang et al., 2008).

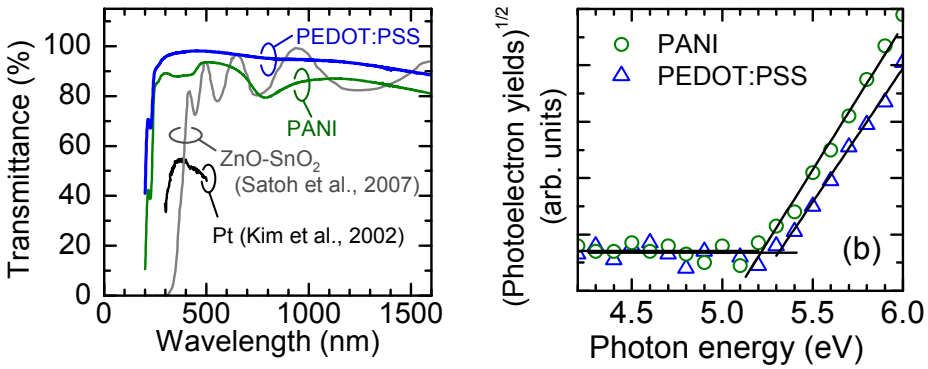

Fig. 3. (a) Optical transmittance spectra of PEDOT:PSS and PANI films. The transmittance spectra of ZnO-SnO_2 (Satoh et al., 2007) and semi-transparent Pt (Kim et al., 2002) thin films are also shown for comparison. (b) Photoelectron emission yield spectra of PEDOT:PSS and PANI films.

5.2 Diode characteristics of transparent conducting polymer/nitride structures

Figure 4(a) shows the current density-voltage (*J-V*) characteristics of the TCP/epi.-GaN samples. The diode ideality factor, *n*, and the SBH, ϕ_B, were evaluated by fitting the theoretical values obtained using the following equation based on the thermionic emission theory (Crowell, 1965):

$$J = A^{*}T^{2}\exp\left(-\frac{\phi_B}{kT}\right)\cdot\left[\exp\left(\frac{qV}{nkT}\right)-1\right] \tag{3}$$

where *q* is the electronic charge, *A** represents the effective Richardson constant, which is defined as $A^{*} \equiv 4\pi m_e^{*}k^2/h^3$ (26.4 A/(cm²·K²) for GaN), *T* is the absolute temperature, *k* is the Boltzmann constant, *V* is the applied bias, *m** is the effective electron mass (0.2 m_e for GaN), and *h* is Planck's constant. The n and ϕ_B values derived using the *J-V* characteristics were 3.0 and 0.90 eV, respectively, for PEDOT:PSS/epi.-GaN, and 1.2 and 0.97 eV, respectively, for PANI/epi.-GaN. The low reverse leakage current, which ranged between 10^{-8} and 10^{-9} A/cm² at a reverse bias voltage of -3 V, indicates that the TCP/epi.-GaN

heterojunctions had a Schottky contact property comparable to that exhibited by conventional metal Schottky contacts.

The depletion width, W_D, in the n-type GaN of the TCP/epi.-GaN heterojunction is expressed by

$$W_D = \sqrt{\frac{2\varepsilon_S\varepsilon_0}{qN_D}\left(V_{Built-in} - V\right)} \tag{4}$$

where ε_S is the relative dielectric constant of GaN and equals 8.9 (Wu, 2009), ε_0 is the vacuum dielectric constant, $V_{built\text{-}in}$ is the built-in voltage formed in GaN, V is the bias voltage, and N_D is the donor concentration. The space charge, Q_{SC}, in the depletion layer is given by $Q_{SC} = qN_DW_D$, thus, the depletion layer capacitance C_D is obtained by

$$C_D = \frac{\left|\partial Q_{SC}\right|}{\partial V} = \sqrt{\frac{q\varepsilon_S\varepsilon_0 N_D}{2(V_{built-in} - V)}}\,. \tag{5}$$

Equation (5) can also be written in the following form:

$$\frac{1}{{C_D}^2} = \frac{2(V_{built-in} - V)}{q\varepsilon_S\varepsilon_0 N_D}\,. \tag{5}'$$

Equation (5)' suggests that if $1/C_D{}^2$ exhibits linear plots against V, $V_{built\text{-}in}$ can be obtained at the V-intercept of extrapolated fit-line of the plots. Figure 4(b) shows the plot of $1/C_D{}^2$ as a function of the applied voltage. The frequencies used for the capacitance measurements were 100 Hz and 1 KHz for the PANI/epi.-GaN and PEDOT:PSS/epi.-GaN heterojunctions, respectively. The frequency for measurement was chosen within a range that was sufficiently lower than the cut-off frequency, which is described in section 5.4. In Figure 4(b), both the data sets are linear and straight lines were successfully fitted to the data. The determined diode characteristics of the TCP/epi.-GaN heterojunction determined from the *J-V* characteristics and capacitance measurements are summarized in Table 2. The observed barrier height was comparable to that obtained by conventional metal Schottky contacts (Tracy et al., 2003). In the case of the conventional metal Schottky contacts, elaborate surface cleaning processes and moderate metal deposition in ultra-high-vacuum conditions are required to attain good Schottky contact with a ϕ_B of more than 1 eV. It is worth noting that the good Schottky contact properties in the TCP/epi.-GaN heterojunction were achieved with convenient spin coating of a water-dispersed TCP solution onto the GaN layer in air at ambient temperature.

The observed ϕ_B of the TCPs were much lower than expected from the energy difference $\phi_m - \chi$. There are various possibilities for the lower barrier heights including the Schottky effect, which is caused by the electronic mirror force, interface dipole effect, surface defects of GaN, inhomogeneous workfunctions in the TCP film, and/or residual contamination (Sze, 1981; Kampen, 2006). However, the major candidates for the modification of the barrier height have been discussed and are still controversial even in conventional metal/semiconductor Schottky heterojunctions (Tung, 2001). Further detailed investigation is required to determine which effects dominate in lowering the barrier in the TCP/epi.-GaN heterojunction.

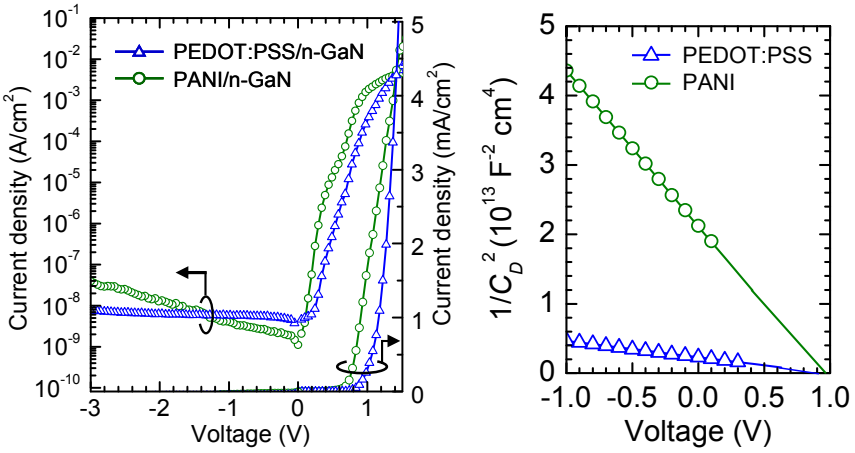

(a) (b)

Fig. 4. (a) *J-V* characteristics and (b) Capacitance-voltage plots of TCP/GaN heterojunction solar cells.

	Polymer thickness (nm)	Schottky contact area (mm²)	*J-V*		*C-V*	
			n	ϕ_B (eV)	W_D (nm)	$V_{Built\text{-}in}$ (V)
PANI	170	7.1	1.2	0.97	39	0.94
PEDOT:PSS	420	3.0	3.0	0.90	40	0.95

Table 2. Diode characteristics of PEDOT:PSS/epi.-GaN (0001) and PANI/epi.-GaN.

5.3 Photovoltaic characteristics of transparent conducting polymer/nitride semiconductor heterojunction solar cells

Figure 5(a) shows the photovoltaic characteristics (*J-V* measurements under AM1.5 light irradiation) of the PANI/epi.-GaN and PEDOT:PSS/epi.-GaN samples. Table 3 represents a summary of the resulting photovoltaic and resistivity characteristics, which include open-circuit voltage (V_{OC}), short-circuit current density (J_{SC}), maximum output power (P_{max}), fill factor (*FF*), shunt resistivity, and series resistivity. Note that the V_{OC} exhibited high values (>0.5 V), which was much higher than the photovoltage observed in metal Schottky contacts on n-type GaN (Zhou et al., 2007) or PEDOT:PSS Schottky contacts on ZnO (Nakano et al., 2008). The superior photovoltages of the TCP/epi.-GaN heterojunctions are attributed to the following advantages conveyed by our process and substance properties: the ambient temperature fabrication resulted in less process damage and GaN exhibits less electron affinity (3.3 eV) than ZnO (4.4 eV) (Wu et al., 1999).

However, the rather small shunt resistivity and large series resistance that are observed, especially in the PANI/epi.-GaN heterojunction solar cell, are clearly due to the

deterioration of V_{OC} and *FF*. The optimization of the deposition process of TCP and introduction of a metal comb-shaped electrode on the TCP layer will improve V_{OC} and *FF*. Figure 5(b) depicts external quantum efficiency of the PANI/epi.-GaN heterojunction solar cell. In order to visualize the capabilities of the photovoltaic device, the transmittance of PANI and the solar light intensity are also plotted as a function of wavelength.

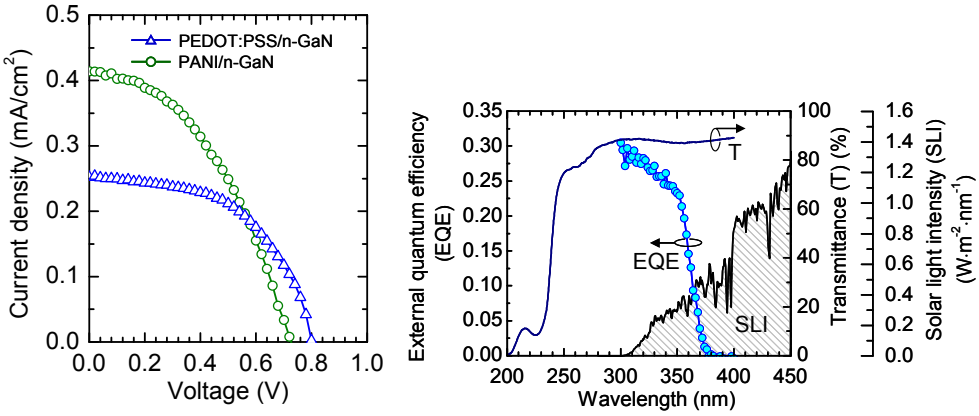

(a) (b)

Fig. 5. (a) Photovoltaic characteristics of PANI/epi.-GaN and PEDOT:PSS/epi.-GaN heterojunction solar cells. (b) External quantum efficiency of PANI/epi.-GaN heterojunction solar cell, transmittance of PANI (T), and solar light intensity (SLI) as a function of wavelength.

	Polymer thickness (nm)	Schottky contact area (mm²)	Photovoltaic characteristics				Resistivity	
			V_{OC} (V)	J_{SC} (mA/cm²)	*FF*	P_{max} (mW/cm²)	R_{sh} (kΩ/cm²)	R_s (Ω/cm²)
PANI	170	7.1	0.73	0.41	0.42	0.13	21.2	310.3
PEDOT:PSS	420	3.0	0.80	0.25	0.54	0.11	36.8	17.4

Table 3. Photovoltaic characteristics of PEDOT:PSS/epi.-GaN and PANI/epi.-GaN.

5.4 Frequency-dependent capacitance and its application to deep-level optical spectroscopy (DLOS)

In this study, we found that the capacitance of the TCP/epi.-GaN heterojunction exhibits significant dependence on the frequency of measurement. Figure 6 shows the capacitance-frequency (*C*–*f*) characteristics of the samples. The characteristics were measured under zero-bias conditions. As seen in the graph, the capacitance is constant at a lower frequency; however, it starts to drop at a specific frequency and then rapidly decreases towards the higher frequencies (cut-off). The frequencies at which the capacitance begins to drop are located at ~20 Hz and ~6 kHz for the PEDOT:PSS/epi.-GaN and PANI/epi.-GaN samples, respectively. It is obvious that the difference in the specific frequencies between the two

samples is due to differences in the intrinsic properties of the TCPs. Conductivity in TCPs is generated by a polaron in the π-conjugated bond; this polarized state causes a Debye-type dielectric dispersion response against an applied alternating electric field (Cole et al., 1941).

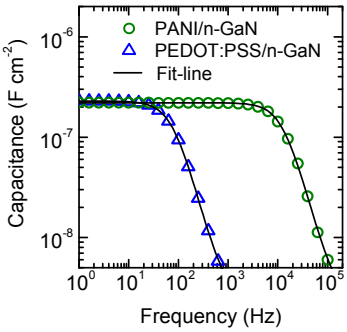

Fig. 6. C-f characteristics of TCP/epi.-GaN heterojunction solar cells.

Referring to a previous study on the frequency-dependent capacitance of PANI film (Mathai et al., 2002), the characteristics can be analyzed by assuming an equivalent circuit consisting of a frequency-independent capacitive element, C_0, in parallel with a resistive element, R, both in series with a constant low-value resistance. Based on this model, the frequency-dependent capacitance of TCP, C_p, is given by the following equation:

$$C_p = C_0 + \frac{1}{(2\pi fR)^2 C_0} \tag{6}$$

where f is the applied bias frequency.
Furthermore, considering that the capacitance of the depletion layer, C_d, is in series with C_P, then the measured total capacitance of the sample, C_{total}, can be expressed by

$$C_{total} = \frac{C_p \cdot C_d}{C_p + C_d}. \tag{7}$$

The solid lines shown in Figure 5 represent the results of the least-square fit of the analytical curve produced based on Equations (6) and (7). The excellent fitting results indicate that the assumed model is adequate. The values of R and C_0, which were derived from the fitting, were 5.3×10^2 Ω and 2.1×10^{-9} F·cm^{-2}, respectively, for PANI/epi.-GaN and 8.4×10^4Ω and 2.3×10^{-9} F·cm^{-2}, respectively, for PEDOT:PSS/epi.-GaN. The large difference in the R values between the two samples is reasonable if we take into account the large difference in the conductivity between PEDOT:PSS (5.7×10^{-1} S/cm) and PANI (3.4×10^2 S/cm).
We describe below that the transparent Schottky contact fabricated by TCP is applicable not only to the photovoltaic device but also to defect density investigation. Nakano et al. applied deep-level optical spectroscopy (DLOS) to the PANI/epi.-GaN samples (Nakano et al., 2010, 2011a, 2011b). DLOS allows the deep-level density in semiconductors to be estimated by detecting the change in capacitance, which is caused by discharging the deep-levels by exciting electrons with monochromatic light. The measurement process was as

follows. The residual electrons in the deep levels were excluded by applying a reverse bias (-2 V) and extending the depletion layer. Then, the bias was removed for 1 second to fill the deep levels with electrons in the dark. After that, the same reverse bias was again applied to form the depletion layer followed by monochromatic light illumination that excites electrons in the deep levels up to the conduction band. The difference in the capacitance between the filled state and post-excited states (discharged) was detected as ΔC. The density of the deep-levels is estimated by $2N_D \Delta C/C_i$, where N_D is the donor concentration and C_i is the initial capacitance that is obtained in the filled state in the dark. Figure 7 shows the resulting DLOS spectra. Interestingly, both the spectra acquired at 1 and 10 kHz bias frequency show no characteristic peaks; however, when the bias frequency was increased to 100 kHz, several peaks appeared in the spectrum. This specific frequency, 100 kHz, corresponds to the point where the total capacitance dropped down to a negligible level compared to the capacitance at 1 and 10 kHz. This means that the C_i became smaller comparable to ΔC, thus, $2N_D \Delta C/C_i$ is effectively enhanced enough to be detectable.

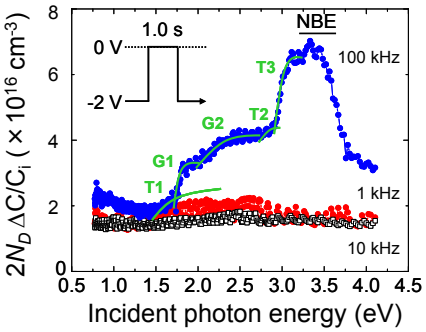

Fig. 7. DLOS spectra of PANI/epi.-GaN heterojunction solar cell.

In Figure 7, five photoemission states are clearly revealed with onsets at ~1.40, ~1.70, ~2.08, ~2.64, and 2.90 eV below the conduction band, which are denoted as T1, G1, G2, T2, and T3, in addition to the near-band-edge (NBE) emissions of GaN at 3.3–3.5 eV. For all the deep levels, electron emission to the conduction band is a dominant process due to their positive photocapacitance transients. The T1, T2, and T3 levels are identical to the deep-level defects that have been commonly reported for GaN, whereas the G1 and G2 levels look like the specific deep levels characteristic of AlGaN/GaN heterointerfaces that were reported recently (Nakano et al., 2008). Using the TCP Schottky contact, we successfully revealed the deep-level states in the near-surface region of the n-GaN layer. These experimental results and further detailed investigations can provide important information on the electronic properties that is needed to improve the performance of the device in optical and electronic fields.

5.5 Future perspective of TCP/nitride semiconductor heterojunction solar cells

In order to increase the output power of TCP/nitride semiconductor heterojunction solar cells, the nitride portion is required to be substituted from GaN to $In_xGa_{1-x}N$. The presumed difficulty in developing the TCP/n-$In_xGa_{1-x}N$ heterojunction is the lowering of the barrier height since the electron affinity significantly increases with an increase of the In content.

One of the most plausible solutions for this issue is to insert a several-tens-nanometer-thick GaN or AIN layer between TCP and n-In_xGa_{1-x} N. With this device structure, it is expected that the barrier height at the TCP/nitride semiconductor interface will be maintained at a high value and an internal electric field should be formed.
The cost of the sapphire substrate will become a high barrier for reducing the production cost of III-nitride based solar cells. Matsuki et al. have shown that high quality GaN can be grown on mica plates (Matsuki et al., 2005), which are inexpensive and flexible. Applying such a novel alternative to sapphire for the epitaxial growth substrate will be effective for developing large area TCP/nitride semiconductor heterojunction solar cells.
TCPs have a high transparency from 250 nm to the visible wavelength region, as described in section 5.1. Thus TCP/nitride semiconductor heterojunction photovoltaic devices also have a high potential for applications in ultraviolet sensors.

6. Conclusion

We have fabricated TCP/nitride semiconductor heterojunction solar cell structures by the spin-coating method using PEDOT:PSS or PANI as the TCP layer and Si-doped GaN as the semiconductor layer. The devices exhibited high quality rectifying properties and have an approximately 1 eV barrier height. Both the PANI/epi.-GaN and PEDOT:PSS/epi.-GaN heterojunction solar cells exhibited ultraviolet-sensitive photovoltaic action. The observed open-circuit voltage was superior to previously reported values for metal/GaN Schottky photo-detectors. A characteristic frequency-dependent behaviour of the interface capacitance was found for the TCP/epi.-GaN solar cells. The *C-f* characteristics were analyzed based on the dielectric dispersion theory and the intrinsic capacitance and resistance were obtained. The considerable reduction of the interface capacitance in the high frequency region allowed for highly-sensitive detection of deep levels in GaN by DLOS measurements.

7. Acknowledgments

The authors wish to acknowledge collaborations and discussions with Professor Michio Kondo, Dr. Takuya Matsui, Dr. Kenji Itaka, Professor Shunro Fuke, and Professor Hideomi Koinuma. This study was partially supported by the New Energy and Industrial Technology Development Organization (NEDO) Project, Research and Development on Innovative Solar Cells.

8. References

Bolto, B. A., McNeill, R., & Weiss, D. E. (1963). Electronic conduction in polymers III. Electronic properties of polypyrrole, *Australian Journal of Chemistry*, Vol. 16, No. 5, (June 1963), pp. 1090-1103, ISSN 0004-9425

Brown, T. M., Kim, J. S., Friend, R. H., Cacialli, F., Daik R., & Feast, W. J. (1999). Built-in field electroabsorption spectroscopy of polymer light-emitting diodes incorporating a doped poly(3,4-ethylene dioxythiophene) hole injection layer, *Applied Physics Letters*, Vol. 75, No. 12, (July 1999), pp. 1679-1681, ISSN 0003-6951

Chang, C. S., Chang, S. J., Su Y. K., Lin, Y. C., Hsu Y. P., Shei, S. C., Chen, S. C., Liu C. H., & Liaw U. H. (2003). InGaN/GaN light-emitting diodes with ITO p-contact layers

prepared by RF sputtering, *Semiconductor Science and Technology*, Vol. 18, No. 4, (February 2003), pp. L21-L23, ISSN 1361-6641

Chen, X., Matthews, K. D., Hao, D., Schaff, W. J., & Eastman, L. F. (2008). Growth, fabrication, and characterization of InGaN solar cells, *Physica Status Solidi (a)*, Vol. 205, No. 5, (July 2003), pp. 1103-1105, ISSN 1862-6300

Crowell, C. R. (1965). The Richardson constant for thermionic emission in Schottky barrier diodes, *Solid-State Electronics*, Vol. 8, No. 4, (April 1965), pp. 395-399, ISSN 0038-1101

Cole, K. S. & Cole, R. H. (1941). Dispersion and absorption in dielectrics I. Alternating current characteristics, *J. Chem. Phys.*, Vol. 9, No. 4, (April 1941), pp. 341-351, ISSN 0021-9606

Dahal, R., Pantha, B., Li. J., Lin, J. Y., & Jiang, H. X. (2009). InGaN/GaN multiple quantum well solar cells with long operating wavelengths, *Applied Physics Letters*, Vol. 94, No. 6, (February 2009), pp. 063505-1-063505-3-1693, ISSN 0003-6951

Grabowski, S. P., Schneider, M., Nienhaus, H., Mönch, W., Dimitrov, R., Ambacher, O., & Stutzmann, M. (2001). Electron affinity of $Al_xG_{a1-x}N(0001)$ surfaces, *Applied Physics Letters,* Vol. 78, No. 17, (April 2001), pp. 2503-2505, ISSN 0003-6951

Green, M. A., Emery, K., Hishikawa, Y., & Warta, W. (2010). Solar cell efficiency tables (version 37). *Progress in Photovoltaics: Research and Applications*, Vol. 19, No. 1, (December 2010), pp. 84-92, ISSN 1099-159X

Green, M. A. (2001). Third generation photovoltaics: Ultra-high conversion efficiency at low cost. *Progress in Photovoltaics: Research and Applications*, Vol. 9, No. 2, (December 2010), pp. 123-125, ISSN 1099-159X

Ha, Y. H., Nikolov, N., Pollack, S. K., Mastrangelo, J., Martin, B. D., & Shashidhar, R. (2004). Towards a transparent, highly conductive poly(3, 4-ethylenedioxythiophene), *Advanced Functional Materials*, Vol. 14, No. 6, (June 2004), pp. 615-622, ISSN 1616-301X

Heeger J. A. (2001). Nobel Lecture: Semiconducting and metallic polymers: The fourth generation of polymeric materials, *Review of Modern Physics*, Vol. 73, No. 3, (July 2001), pp. 681-700, ISSN 0034-6861

Jang J., Ha, J., & Kim, K. (2008). Organic light-emitting diode with polyaniline-poly(styrene sulfonate) as a hole injection layer, *Thin Solid Films*, Vol. 516, No. 10, (August 2007), pp. 3152-3156, ISSN 1616-301X

Kampen, T. U. (2006). Electronic structure of organic interfaces – a case study on perylene derivatives, *Applied Physics A*, Vol. 82, No. 3, (September 2005), pp. 457-470, ISSN 0947-8396

Kane, E. O. (1962). Theory of Photoelectric Emission from Semiconductors, *Physical Review*, Vol. 127, No. 1, (July 1962), pp. 131-141, ISSN 1943-2879

Kim, J. K., Jang, H. W., Jeon, C. M., & Lee, J.-L. (2002). GaN metal–semiconductor–metal ultraviolet photodetector with IrO_2 Schottky contact, *Applied Physics Letters*, Vol. 81, No. 24, (December 2002), pp. 4655-4657, ISSN 0003-6951

Kuwahara, Y., Takahiro F.; Yasuharu, F.; Sugiyama, T.; Iwaya, M.; Takeuchi, T.; Kamiyama, S.; Akasaki, I.; & Amano, H. (2010). Realization of nitride-based solar cell on freestanding GaN substrate, *Applied Physics Express*, Vol. 3, No. 11, (October 2010), pp. 111001-1-111001-3, ISSN 1882-0778

Kuwahara, Y., Takahiro, F., Sugiyama, T., Iida, D., Isobe, Y., Fujiyama, Y., Morita, Y., Iwaya, M., Takeuchi, T., Kamiyama, S., Akasaki, I., & Amano, H. (2011). GaInN-based solar cells using strained-layer GaInN/GaInN superlattice Active Layer on a Freestanding GaN Substrate, *Applied Physics Express*, Vol. 4, No. 2, (January 2011), pp. 021001-1-021001-3, ISSN 1882-0778

Lee, K., Cho, S., Park, S.-H., Heeger, A. J., Lee, C.-W., & Lee, S.-H. (2006). Metallic transport in polyaniline, *Nature*, Vol. 441, (4 May 2006), pp. 65-68, ISSN 0028-0836

Mathai, C. J., Saravanan, S., Anantharaman, M. R., Venkitachalam, S., & Jayalekshmi, S. (2002). Characterization of low dielectric constant polyaniline thin film synthesized by ac plasma polymerization technique, *J. Phys. D: Applied Physics*, Vol. 35, No. 3, (January 2002), pp. 240-245, ISSN 0022-3727

Matsuki, N., Kim, T.-W., Ohta, J., & Fujioka, H. (2005). Heteroepitaxial growth of gallium nitride on muscovite mica plates by pulsed laser deposition, *Solid State Communications*, Vol. 136, No. 6, (August 2005), pp. 338-341, ISSN 0038-1098

Matsuki, N., Irokawa, Y., Matsui, T., Kondo, M., & Sumiya, M. (2009). Photovoltaic Action in Polyaniline/n-GaN Schottky Diodes, *Applied Physics Express*, Vol. 2, No. 9, (August 2009), pp. 092201-1-092201-3, ISSN 1882-0778

Matsuki, N., Irokawa Y., Nakano Y., & Sumiya M. (2010). π-Conjugated polymer/GaN Schottky solar cells, *Solar Energy Materials & Solar Cells*, Vol. 95, No. 9, (May 2010), pp. 284-287, ISSN 0927-0248

Matsuki, N., Irokawa Y., Nakano Y., & Sumiya M. (2011). Heterointerface properties of novel hybrid solar cells consisting of transparent conductive polymers and III-nitride semiconductors, *Journal of Nonlinear Optical Physics & Materials*, Vol. 19, No. 4, (December 2010), pp. 703-711, ISSN 0218-8635

Matsuoka, T., Okamoto, H., Nakano, M., Harima, H., & Kurimoto, E. (2002). Optical bandgap energy of wurtzite InN, *Applied Physics Letters*, Vol. 81, No. 7, (June 2002), pp. 1246-1248, ISSN 0003-6951

Mott, N. F. (1939). The theory of crystal rectifiers, *Proceedings of the Royal Society*, Vol. 171, No. 944, (May 1939), pp. 27-38, ISSN 364–5021

Myers, D. R., Kurtz, S. R., Whitaker, C., & Townsend, T. (2000). Preliminary investigations of outdoor meteorological broadband and spectral conditions for evaluating photovoltaic modules and systems. *Program and Proceedings: NCPV Program Review Meeting 2000*, 16-19 April 2000, Denver, Colorado. BK-520-28064. Golden, CO: National Renewable Energy Laboratory; pp. 69-70; NREL Report No. CP-560-28187

Nakano, M., Makino, T., Tsukazaki, A., Kazunori U., Ohtomo, A., Fukumura, T., Yuji, H., Nishimoto, Y., Akasaka, S., Takamizu, D., Nakahara, K., Tanabe, T., Kamisawa, A., & Kawasaki M. (2007). Mg_xZn_xO-based Schottky photodiode for highly color-selective ultraviolet light detection, *Applied Physics Letters*, Vol. 91, No. 14, (October 2007), pp. 142113-1-142113-3, ISSN 0003-6951

Nakano, M., Makino, T., Tsukazaki, A., Ueno K., Ohtomo, A., Fukumura, T., Yuji H., Akasaka, S., Tamura, K., Nakahara, K., Tanabe, T., Kamisawa, A., & Kawasaki, M. (2008). Transparent polymer Schottky contact for a high performance visible-blind ultraviolet photodiode based on ZnO, *Applied Physics Letters*, Vol. 93, No. 12, (December 2008), pp. 123309-1-123309-3, ISSN 0003-6951

Nakano, Y., Irokawa, Y., & Takeguchi M. (2008). Deep-level optical spectroscopy investigation of band gap states in AlGaN/GaN hetero-interfaces, *Applied Physics Express*, Vol. 1, No. 9, (August 2008), pp. 091101-1-091101-3, ISSN 1882-0778

Nakano, Y., Matsuki, N., Irokawa, Y., & Sumiya, M. (2010). Electrical characterization of n-GaN epilayers using transparent polyaniline Schottky contacts, *Physica Status Solidi C*, Vol. 7, No. 7-8, (April 2010), pp. 2007-2009, ISSN 1610-1634

Nakano, Y., Matsuki, N., Irokawa, Y., & Sumiya, M. (2011a). Deep-level characterization of n-GaN epitaxial layers using transparent conductive polyaniline Schottky contacts, *Japanese Journal of Applied Physics*, Vol. 50, No. 1, (January 2011), pp. 01AD02-1-01AD02-4, ISSN 0021-4922

Nakano, Y., Lozac'h, M., Matsuki, N., Sakoda, K., & Sumiya, M. (2011b). Photocapacitance spectroscopy study of deep-level defects in freestanding n-GaN substrates using transparent conductive polymer Schottky contacts, *Journal of Vacuum Science and Technology B*, Vol. 29, No. 2, (January 2011), pp. 023001-1- 023001-4, ISSN 1071-1023

Satoh, K., Kakehi, Y., Okamoto, A., Murakami, S., Moriwaki, K., & Yotsuya, T. (2007). Electrical and optical properties of Al-doped ZnO–SnO_2 thin films deposited by RF magnetron sputtering, *Thin Solid Films*, Vol. 516, No. 17, (October 2007), pp. 5814-5817, ISSN 1616-301X

Schottky, W. (1939). Zur Halbleitertheorie der Sperrschicht- und Spitzengleichrichter (The semiconductor theory of the barrier layer rectifiers and tip rectifiers), *Zeitschrift für Physik*, Vol. 113, No. 5-6, (May 1939), pp. 367-414, ISSN 0939-7922

Shirakawa, H., Edwin L., MacDiamid, A. G., Chiang, C., & Heeger, A. (1977). Synthesis of electrically conducting organic polymers: halogen derivatives of polyacetylene, (CH), *Journal of the Chemical Society, Chemical Communications*, No. 16, (May 1977), pp. 578-580, ISSN 0022-4936

Shim, K.-H., Paek, M.-C., Lee, B. T., Kim C., & Kang J. Y. (2001). Preferential regrowth of indium–tin oxide (ITO) films deposited on GaN(0001) by rf-magnetron sputter, *Applied Physics A*, Vol. 72, No. 1, (February 2001), pp. 471-474, ISSN 0947-8396

da Silva, W. J., Hümmelgen, I. A., & Mello, R. M. Q. (2009). Sulfonated polyaniline/n-type silicon junctions, *Journal of Material Science: Materials in Electronics*, Vol. 20, No. 2, (February 2009), pp. 123-126, ISSN 0022-2461

Solomon, S., Qin, D., Manning, M., Chen, Z., Marquis, M., Averyt, K., Tignor M. B. M., & Miller Jr., H. L. (Ed.). (2007). *Climate Change 2007, The Physical Science Basis*, Contribution of Working Group I to the Fourth Assessment Report of the IPCC, ISBN 978 0521 88009-1

Song, J. O., Ha, J.-S., & Seong, T.-Y. (2010). Ohmic-contact technology for GaN-based light-emitting diodes: Role of p-type contact, *IEEE Transactions on Electron Devices*, Vol. 57, No. 1, (January 2010), pp. 42-59, ISSN 0018-9383

Sze, S. M. (1981). *Physics of Semiconductor Devices*, Wiley Interscience Publication, ISBN 0-471-05661-8, New York, USA

Takeuchi, T., Wetzel, C., Yamaguchi, S., Sakai, H., Amano, H., & Akasaki I. (1998). Determination of piezoelectric fields in strained GaInN quantum wells using the quantum-confined Stark effect. *Applied Physics Letters*, Vol. 73, No. 12, (July 1998), pp. 1691-1693, ISSN 0003-6951

Tracy, K. M., Hartlieb P. J., Einfeldt, S., Davis, R. F., Hurt, E. H., & Nemanich, R. J. (2003). Electrical and chemical characterization of the Schottky barrier formed between

clean n-GaN (0001) surfaces and Pt, Au, and Ag, *Journal of Applied Physics*, Vol. 94, No. 6, (September 2003), pp. 3939-3948, ISSN 0021-8979

Tung, R. T. (2001). Recent advances in Schottky barrier concepts, *Material Science and Engineering B*, Vol. 35, No. 1-3, (November 2001), pp. 1-138, ISSN 0921-5107

Wang, W. & Schiff, E. A. (2007). Polyaniline on crystalline silicon heterojunction solar cells, *Applied Physics Letters*, Vol. 91, No. 13, (September 2007), pp. 133504-1-133504-3, ISSN 0003-6951

Wu, C.I. & Kahn, A. (1999). Electronic states and effective negative electron affinity at cesiated p-GaN surfaces, *Journal of Applied Physics*, Vol. 86, No. 6, (September 1999), pp. 3209-3212, ISSN 0021-8979

Wu, J., Walukiewicz, W., Shan, W., Yu, K. M., Ager, J. W., Li, S. X., Haller, E. E., Lu, H., & Schaff, W. J. (2003). Temperature dependence of the fundamental band gap of InN, *Journal of Applied Physics*, Vol. 94, No. 7, (July 2003), pp. 4457-1260, ISSN 1089-7550

Wu, J., Walukiewicz. W, Li., S. X., Armitage, R., Ho, J. C., Weber, E., R., Haller, E. E., Lu, H. Schaff, W. J., Barcz, A. & Jakieka R. (2004). Effects of electron concentration on the optical absorption edge of InN, *Applied Physics Letters,* Vol. 84, No. 15, (April 2004), pp. 2805-2807, ISSN 0003-6951

Wu, J. (2009). When group-III nitrides go infrared: New properties and perspectives, *Journal of Applied Physics*, Vol. 106, No. 1, (July 2009), pp. 011101-1-011101-28, ISSN 0021-8979

Yamaguchi, M. (2003). III–V compound multi-junction solar cells: present and future, *Solar Energy Materials & Solar Cells*, Vol. 75, No. 1-2, (April 2003), pp. 261-269, ISSN 0927-0248

Yamaura, J., Muraoka, Y., Yamauchi, T., Muramatsu, T., & Hiroi, Z. (2003). Ultraviolet light selective photodiode based on an organic-inorganic heterostructure, *Applied Physics Letters*, Vol. 83, No. 11, (July 2003), pp. 2097-2099, ISSN 0003-6951

Zheng X., Horng, R.-H., Wuu, D.-S., Chu, M.-T., Liao, W.-Y., Wu, M.-H., Lin, R.-M., & Lu, Y.-C. (2008). *Applied Physics Letters*, Vol. 93, No. 26, (December 1998), pp. 261108-1-261108-3, ISSN 0003-6951

Zhou, Y., Ahyi, C., Tin, C.-C., Williams, J., Park, M., Kim, D.-J., Cheng, A.-J., Wang D., Hanser, A., Edward, A. P., Williams, N. M., & Evans K. (2007). Fabrication and device characteristics of Schottky-type bulk GaN-based ''visible-blind'' ultraviolet photodetectors, *Applied Physics Letters*, Vol. 90, No. 12, (March 2007), pp. 121118-1–121118-3, ISSN 0003-6951

15

High Efficiency Solar Cells via Tuned Superlattice Structures: Beyond 42.2%

AC Varonides
Physics & Electrical Engineering Dept, University of Scranton, Scranton, PA, USA

1. Introduction

Modern PV devices are a direct outcome of solid state devices theory and applications of the last forty years. They are devices made of crystalline structures and basically, when illuminated with solar light, they convert solar photons into electric current. In the following a quick explanation of how this happens is presented. What is a solar cell? What is the basic function behind a cell's operation? Typically, in an illuminated p-n junction, photons are absorbed and electron-hole pairs are generated. These carriers diffuse in opposite directions (separated by the existing electrostatic field at the junction), and within their respective diffusion lengths. Electrons at the p-side diffuse through the junction potential and holes (similarly) get to the opposite directions. Under open-circuit conditions, the voltage across the cell is given by the following formula:

$$V_{oc} = kT \ln(1 + \frac{I_L}{I_o}) \tag{1}$$

Where k is Boltzmann's constant, T (in Kelvin) is the cell temperature, I_L is the light-generated current, and I_o is the p-n junction's reverse saturation current (see below). Cell theory and p-n junctions under a bias are briefly discussed in the next section.

2. Background theory: The p-n junction

Photonic device (solar cells included) operation is based on a p-n junction: two regions of the semiconducting material doped p and n type respectively and brought together in contact form a p-n junction. At thermal equilibrium, the p-n dope bulk semiconducting crystal, in order to keep its equilibrium, develops an internal field and develops its own built-in potential; the latter is total due to p- and n-type carrier migration across the junction.

Donor and acceptor atoms embedded in the lattice of the host material provide electrons and holes (as potential current carriers) that are free to wander in the crystal. In principle these carriers move randomly in the lattice, however, guiding these carriers accordingly could lead to non-zero currents coming off such semiconductors, and therefore to current producing devices. A semiconductor sample doped with donors and acceptors becomes a p-n junction and therefore a device with two regions tending to overlap at their boundary.

If the interface is at (say) x = 0 position, free electrons and free holes diffuse through the interface and inevitably form space charge regions as shown figure 1 below:

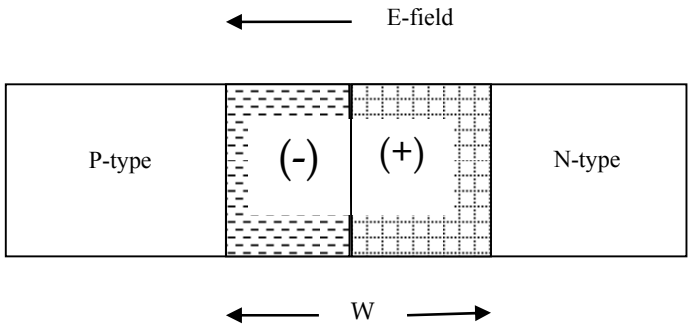

Fig. 1. pn-junction (e.g. of a Si sample) with the depletion W region shown: both sides of the interface are shown, with their space charge distributions respectively.

A static electric field develops at the interface (figure above) emanating from the (+) region and prohibiting respective carriers to further access the PN regions. From basic pn-junction theory, we can solve for the electric field and the potential developed by means of Poisson's equation. If the limits of the depletion region are $-x_p$ and x_n (W = x_p + x_n) respectively, we can derive expressions for both field and potential developed at the junction:

$$E(x) = \frac{qN_d}{\varepsilon}(x - x_n) \qquad 0 < x < x_n \tag{2}$$

$$E(x) = -\frac{qN_a}{\varepsilon}(x + x_p) \qquad -x < x < 0 \tag{3}$$

Where maximum field value is E_{max} = E(at x = 0) = - $(q\ N_d/\varepsilon)\ x_n$; q is the electronic charge, $N_{d,a}$ stands for donor and acceptor atom concentrations (per volume) respectively, ε is the total sample's dielectric constant (or the product of the relative times the free space dielectric constants, e.g. ε_r = 11.7 for Si). Based on expressions (2, 3) and on the fact that potential generated at the junction is the negative integral of the electric field across the depletion region, we can in principle derive the potential V(x) across the junction: it can be shown that V(x) is as follows:

$$V(x) = \frac{qN_a}{2\varepsilon}(x + x_p)^2 \text{ ; In the p-region, and} \tag{4}$$

$$V(x) = -\frac{qN_d}{2\varepsilon}[(x - x_n)^2 - x_n^2] + \frac{qN_a}{2\varepsilon}x_p^2 \text{ ; In the n-region and} \tag{5}$$

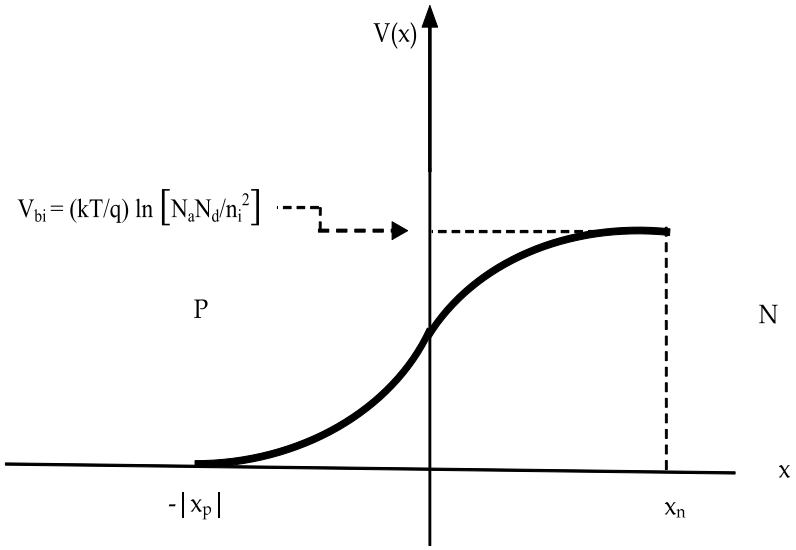

Fig. 2. Potential V as a function of x across the depletion region. Note (a) the two branches of V across both sides of the junction's boundary (x = 0) in accordance with (4) and (5) (b) the built-in voltage V_{bi} at the right edge of the junction [1, 2, 3]. Note also that built-in voltage is normally computed as shown in the inset.

It is a straightforward matter to produce explicit results about widths in the junction area (w, x_n, $-x_p$) in terms of device doping levels and built-in voltage values. The built-in voltage is determined from (4) at $x = x_n$:

$$V_{bi} = V(x = x_n) = \frac{q}{2\varepsilon}(N_a x_n^2 + N_d x_p^2) \tag{6}$$

3. Diode currents

The fundamental current equation for p-n junctions is derived based on considering that the built-in voltage is reduced down to $V_{bi} - V_a$, by the forward bias voltage V_a, helping majority carriers to escape and diffuse in the neighboring regions while, once electrons and holes reach the edges of the depletion region to the p and n regions, they diffuse accordingly according to a decaying exponential law of the type $\exp(x/L_{n,p})$; the latter includes distance x and the diffusion length for electrons and/or holes respectively. Excess minority carriers *diffuse* in both regions according to the following expressions:

$$\delta p(x) = p_{no}(e^{x/Lp} - 1)e^{(x+xn)/Lp} \tag{7}$$

$$\delta n(x) = n_{po}(e^{x/Lp} - 1) \tag{8}$$

Where p_{no} is holes in the n-region, L_p is the diffusion length of holes in the n-region, and where δp represents excess holes in the n-region. Diffusion currents can be calculated by means of the diffusion equation along with suitable boundary conditions:

$$J_p = -qD_p \left. \frac{d\delta p(x)}{dx} \right| \quad (x = x_n) \tag{9}$$

$$Jn = qD_n \left. \frac{d\delta p(x)}{dx} \right| \quad (x = -x_p) \tag{10}$$

Based on the above expressions, current density of the p-n junction due to a forward bias V_a is found to be as follows (see also (1)):

$$J = J_o(e^{Va/Vt} - 1) \tag{11}$$

(Where V_t is the thermal voltage (kT/q))

4. p-n junctions as solar cells

Fundamentally, solar cell modeling correlates incident solar photon flux Φ_{ph} (# of photons cm^{-2} s^1) with generation and recombination carrier rates in the interior of the device. Photo-generated concentrations of diffusing carriers are typically modeled through the diffusion equation (under appropriate boundary conditions):

$$\frac{d^2\delta p_n}{dx^2} - \frac{\delta p_n}{L_p} + \alpha(1-R)\Phi_{ph}e^{-\alpha(x+d)} = 0 \tag{12}$$

Photon-collection efficiency is usually defined as the ratio of total current over solar photo-flux (cm^{-2} s^{-1}):

$$\eta_{col} = \frac{J_p + J_n - J_{rec}}{q\Phi_{ph}} \tag{13}$$

The numerator in (13) is total photo-induced current in the p and n-regions minus recombination current. Boundary conditions include continuity of carrier concentrations at the junction x (j), and the dependence of the first derivative of carrier concentration on recombination velocity s_p, at the edge of the window layer as shown in the figure below:

$$\left(\frac{d\delta p}{dx}\right)_{x=-d} = \frac{s_p}{D_p}(p(-d) - p_{no}) \cong \frac{s_p}{D_p}(p(-d)) \tag{14}$$

Figure-3 shows a generally accepted modeling geometry of a p-n junction solar cell. These two regions are separated by the depletion region (of thickness w): majority electrons from the n-region migrate to the p-region, and majority holes reciprocate from the latter region.

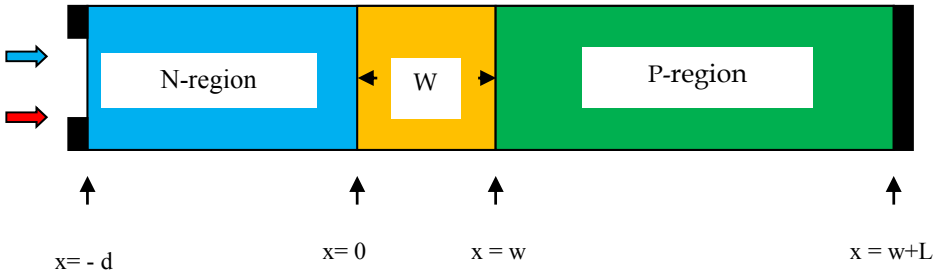

Fig. 3. Typical modeling geometry of a solar cell: w is the depletion width, J is the exact interface, L is the width of the p-region and d is the n-region (window layer). Note that the n-region is the window for solar photons.

Minority holes generated in the window layer (x from –d to 0) are:

$$\delta p_n(x) = C\exp(-x/L_p) + \frac{\alpha\Phi_{ph}(1-R)(L_p^2/D_p)}{1-(\alpha L_p)^2}e^{-\alpha(x+d)} \tag{15}$$

Note that at x = 0: $\delta p_n(0) = \frac{\alpha\Phi_{ph}(1-R)(L_p^2/D_p)}{1-(\alpha L_p)^2}e^{-\alpha(x+d)}$

Maximum hole- current density generated in the n-region is:

$$J_p(x=0) = -qD_p \times \left[\frac{1}{L_p}\left(\frac{\alpha F_{ph}(1-R)(L_p^2/D_p)}{(\alpha L_p)^2-1}\right)\times \left[\tanh(\frac{d}{L_p}) + \frac{\alpha L_p}{\cosh(d/L_p)} + \frac{s_p L_p}{D_p}\times\frac{p(-d)}{\cosh(d/L_p)}\right] + \alpha e^{-\alpha d}\right] \tag{16}$$

The surface recombination velocity s_n at the edge of the p-region is

$$-D_n(\frac{dn}{dx})_{x=L+W} = s_n(n_p - n_{po}) \tag{17}$$

The diffusion equation reads as follows:

$$\frac{d^2 n_p}{dx^2} - \frac{n_p - n_{po}}{L_n} + \alpha(1-R)\Phi_{ph}e^{-\alpha(x+d)} = 0 \tag{18}$$

Solution of (18) is of similar kind with (12) along with boundary conditions (17):

$$\delta n(x) = A\cosh(x/L_n) + B\sinh(x/L_n) + \frac{\alpha\Phi_{ph}(1-R)(L_n^2/D_n)}{1-(\alpha L_n)^2}e^{\alpha(x+d)} \tag{19}$$

The total current out of the cell is the sum of all currents minus recombination components from each region, especially recombination at the w region. Excess carriers in solar cells (as in any photonic device) are minority electrons and holes in the p and n regions respectively. When a cell is illuminated, solar photons excite electron hole pairs in all regions: the p-, n- and depletion regions. The latter may be become of great significance for the following reason: excited electrons and holes do split away from each other due to the existing electrostatic field. This means that these excess carriers will reach the edges of the depletion region in a very short time. Note also that typically, mean diffusion lengths of these carriers are much longer than t he actual width of the depletion area (even in pin devices). This makes the depletion region especially attractive for illumination: electrons and holes will separate from each other quickly, and they will diffuse in the bulk parts of the cell very fast assisted by the electrostatic field. In addition, space availability in the mid-region provides a chance for excess layer s that can be tuned to desired solar photons for subsequent absorption, thus enhancing device performance. This is why multi-layers are used in the intrinsic region (long depletion region in p-n junctions). If tuned quantum wells are grown somewhere in the middle, incident solar illumination will push electrons in the quantum wells and to tunneling or thermionic escape. The notion of additional band gaps integrated in the intrinsic region has been adopted successfully recently. For instance, successful cells with more than one band gaps have been designed and realized, where two or three cells are connected in series forming tandem cells with the advantage of voltage increase. This is possible due to the series connection of the tandem cells. Tandems provide excess voltage but they lack in current, in other words, due to the differences of the layers involved, current matching will be enforced due to the series connection. If these structures can ensure relatively high current outputs, then, along with increased voltage one should expect efficiency improvements. In the next we outline the behavior of a cell in tandem: top cell of AlAs/GaAs and bottom cell of a pin GaAs/Ge/Alloy for long wavelengths.

5. Heterojunction cells

Improved cell design has to include more than one band-gap for larger number of absorbed photons. P-i-n (from now on pin diode) diode designs offer wide intrinsic regions between the p- and n- regions of a p-n junction, where photo-carriers have a great chance to be generated and quickly swept away to the ends of the two-lead diode. This is possible due to the electrostatic field that develops at the depletion region. Illumination of the structure at the intrinsic region or a pin increases the chances of more photo-excited carriers. On the other hand, for a pin diode exposed to solar light and with a thin p-layer, minority electrons from the p-region may cross very fast (τ_n ~ fraction of μs) the junction at the p-i interface and be swept away to the load by the electric field in the mid-region of the cell. More than one band gaps in the mid region may lead to quantum wells where quantum size effects may take over as long as thickness values are in the order of 5 to 8 nm. Superlattice-like structures may be grown in the intrinsic region in order to accommodate both short and long solar wavelengths. It is commonly accepted that thin bulk window layers grown on top of a wide mid-region with quantum wells may offer a two-fold advantage (a) short wavelengths absorbed at the top and longer wavelengths absorbed in the mid region where a superlattice structure is essentially tuned at specific wavelengths. Thus, by growing a superlattice in the middle of a pin region (rather by changing the mid-region into a multi-quantum well (mqw) sequence) one may reach the main objective: to capture more solar

photons with energies higher than the band gap of the host material. The figure below depicts an intrinsic multi-quantum well area, where discrete energy levels cause a widening of the host material's gap (commonly GaAs with gap at 1.42 eV).

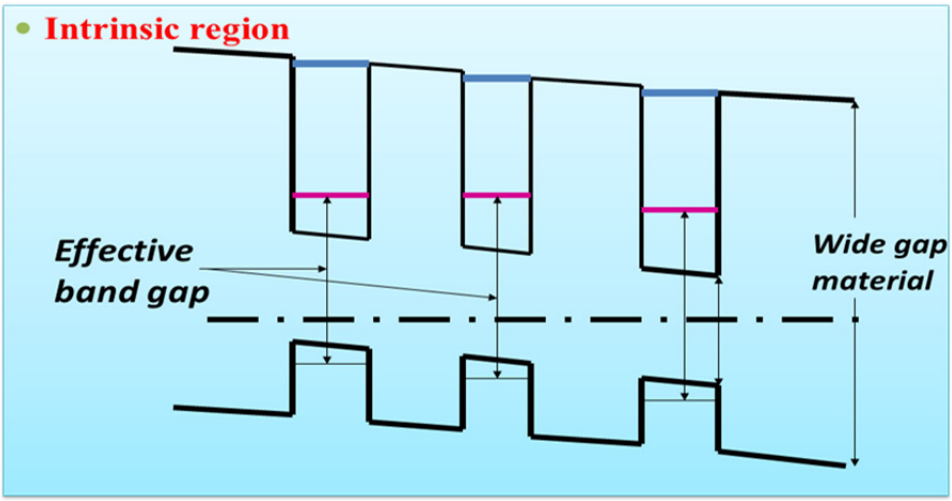

Fig. 4. Detail from a superlattice structure (typically GaAs/alloy and GaAs/Ge (as proposed in this study). The dashed line represents the Fermi level at thermal equilibrium. The optical gap can be tuned to desired energy values.

Figure 5 shows a superlattice covering the mid region of a pin cell:

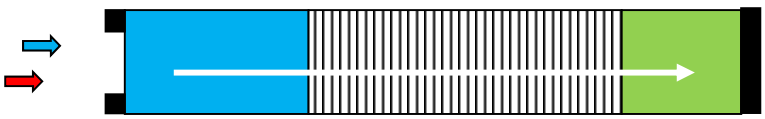

Fig. 5. A p-i-n GaAs/alloy superlattice developed in the mid-region of a pin cell: the middle section depicts: the top layer (blue) is the wide gap alloy (e.g. AlAs) and the bottom layer is GaAs (host material); GaAs is also grown in the superlattice as the low gap medium.

Such a cell design (shown above) is an expanded p-n junction with a wide superlattice mid-region occupying the intrinsic or low doped region between p and n. To reduce cost such a structure can be compromised by inserting a short period tuned superlattice as a small percentage of the device as a total.

6. Top cell (AlAs/GaAs)

Modeling of the top region may be performed in two ways, by considering the equivalent circuit of the device and/or by solving for excess carriers and subsequent electric currents and current densities in the solid state. In this brief outline we are considering the first

approach by starting from the basic illuminated diode equation and adopting standard results regarding maximum power, short circuit current and open-circuit voltage values. Starting from the fundamental solar cell equation, we can derive maximum power conditions:

$$I_m = \frac{\beta V_m}{1+\beta V_m} I_L \tag{20}$$

Where I_m, V_m are maximum current and voltage values, and where $\beta = q\,(kT)^{-1}$.
And

$$V_m = V_{oc} - \frac{1}{\beta}\ln(1+\beta V_m) \tag{21}$$

Efficiency (as power out over power in) is shown to be:

$$\eta = \frac{P_o}{P_{in}} = \frac{I_L V_{oc}}{P_{in}}\left[1 - (\frac{V_m}{V_{oc}})\frac{\ln(\beta V_m)}{\beta V_m}\right] \tag{22}$$

It is clear from (22) that the quantity in brackets is the fill factor (FF) of the device which is found based on maximum voltage values and open circuit voltage:

$$FF = 1 - \frac{\ln(\frac{V_m}{kT})}{(\frac{V_{oc}}{kT})} = 1 - \frac{\ln(\beta V_m)}{\beta V_{oc}} \tag{23}$$

Highly efficient solar cells have been found to have open-circuit voltages within a range from 1 to 1.08V. The table below indicates how open circuit voltage controls maximum voltage (voltage at maximum power point). Assuming short circuit current at 30mA/cm^2, under one-sun (100mW/cm^2), the efficiency is depicted below by Table 1:

V_{oc}(V)	V_m(V)	FF (%)	η (%)
1.02	0.926	0.907	27.75
1.03	0.938	0.906	27.99
1.04	0.948	0.905	28.23
1.05	0.958	0.904	28.50

Table 1. Open circuit and maximum voltages, Fill Factor (FF) and collection efficiency (300 Kelvin). The cell is the top AlAs/GaAs that serves as a window to the solar flux.

It is of advantage to suggest an undoped GaAs-Ge multi-quantum well (MQW) in a standard pin-design, namely, p-intrinsic (MQW)-n geometry that includes lattice-matched GaAs and Ge layers in the intrinsic region of the PV device. This formation could offer the advantage of 1eV absorption (at the appropriate quantum well width), without compromises in device transport properties, such as mobility or conductivity. GaAs-based layers provide (a) high mobility and absorption values and (b) a chance for fine-tuning of the *optical gap* with *specific solar photon wavelength*. Recently, high efficiency cell designs have been proposed where two pn cells are grown in tandem (series connection), where the top

cell is a bulk (e.g. GaAs/AlAs cell) and the bottom is a superlattice-based pin cell optimized at long wavelengths. Such devices offer efficiency increase by acting simultaneously: top unit near 20% and bottom unit near 30% (when they operate on their own) lead to structures (quantum cells) with overall efficiencies in excess of 35% (under one sun and with recombination effects and scattering included). As seen in Figure 5 below, the superlattice approach offers a tool for capturing solar photons at desired wavelengths with the appropriate quantum mechanical tuning. In other words, ground eigen-states in quantum wells match specific wavelengths (corresponding to photons with the same energy);

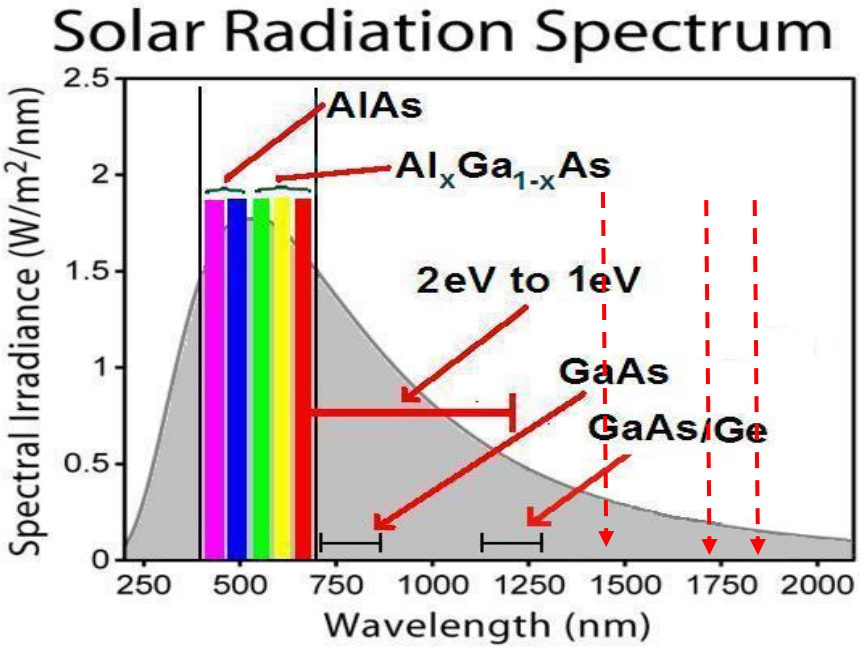

Fig. 6. Regions of the solar spectrum covered by the superlattice cell and the top cell (visible). The superlattice can be tuned at ~1 eV. Dashed arrows indicate region of feasible absorption from the superlattice region

As seen from the figure above, almost full spectrum absorption can be achieved with materials that absorb at desired photon energies. Specifically, visible photons may be absorbed by means of a GaAs/AlAs bulk cell, and IR radiation absorption can be achieved via GaAs (1.42 eV) and Ge (0.67 eV) respectively with superlattice or superlattice sections tuned at desired wavelengths. The n-region of the pin cell can be selected to be Ge in the bulk, ensuring absorption at the tail of the solar spectrum (for Ge: wavelength absorbed at $\lambda = 1.24/0.67 = 1.85$ μm, see last arrow in the figure above). How is the current formed in the superlattice layer? The answer hides in the quantum nature of this region: quantum wells quantized the energy of the captured electrons (and light and heavy holes in the valence band); photo-excited electrons escape thermionically from the wells and form excess current in the conduction band. On the other hand, incident IR photons are expected to be absorbed in the MQW area. Projected excess carrier population (electrons with recombination

included) is of the order of 10^{12} to 10^{13} cm^{-2} per eigen-state. Thermionic current density values have been found to be near order of $30mA/cm^2$ and open-circuit voltage values above 1V, at one sun. Overall (for a composite cell see figure 3) collection efficiency values are initially projected well in excess of 35%, which is a key for immediate improvement to even higher collection efficiency. Total current density is dominated by the lowest of the two sub-cell currents, and open-circuit voltage values are the sum of the two sub-cell V_{oc} values. Total current from the bottom cell is the sum of thermionic and nearest neighbor hopping currents. Preliminary results reach estimates of efficiencies from each of the two (lattice-matched) sub-cells in excess of 21% per cell (predicted synergy of the two sub-cells in excess of 40%). Loss mechanisms at interfaces and quantum wells and their role in overall efficiency determination will also be included. Advantages of the design are:

i. Solar spectrum matching in both visible and IR ranges through layer band gap-matching selection.
ii. Lattice-matching
iii. Increased carrier transport due to GaAs. It is conceivable that even the 40%-plus target of conversion efficiency can be reached with such designs

Heterostructure and (most recently) multijunction solar devices exhibit better performance in transport properties, when compared to bulk solar cells: especially in quantum well devices, photo-excitation causes carrier accumulation in discrete energy levels, with subsequent escape to the conduction band (minus recombination losses) via standard mechanisms such as tunneling, thermal escape or nearest neighbor hopping conduction. Full spectrum absorption and triple junction solar cells have become key factors for high efficiency collection in PV structures of various geometries. Most recently, successful photovoltaic device (PV) designs have shown high efficiency values well above 30%, and efficiency levels in excess of 40% have been reached by means of triple junction metamorphic solar cells and under high sun concentration (good candidate for concentrated PV or CPV). Multijunction solar cells offer a great advantage over their bulk counterparts: by incorporating lattice-matched alloys, one may succeed in designing a device with more than one energy gaps thus increasing the number of absorbed solar photons. During the last decade, various groups have modeled and developed *multijunction* solar cells in order to increase overall collection efficiencies. Emphasis has been given in two types of PV devices (a) lattice-matched solar cells and (b) metamorphic (lattice-mismatched) solar cells. In particular, III-V multijunction solar cells have shown the greatest progress in overall efficiency. The broader impact of this project is a new design proposal for high efficiency solar cells. The target is to exceed 45% collection efficiency for very efficient photovoltaic devices. It is more than clear that once such a cell is realized, the field of concentration photovoltaics (CPV) will benefit greatly: solar cells with (a) record high efficiency values (b) under several hundred suns (Fresnel optics at 500+ suns) and (c) small in size (low area hence less material) is already attracting interest for mass production in many places in the world. In recent years, it has been proposed by us a new design for a high efficiency and lattice-matched solar cell (HESC), where both visible and infrared portions of the solar spectrum are absorbed according to the structure's geometric material arrangement: simultaneous absorption of both short and long wavelengths. In this on-going research enterprise, the synergy between a highly efficient triple junction cell and a highly efficient superlattice or a multi-quantum well region, is presented as a new and innovative way for further efficiency increase. It is well established by now, that triple junction solar cells are exceeding the upper threshold of collection efficiency to ever higher levels, namely

above 38% with latest threshold at 41.1% (Fraunhofer Institute, Germany). Currently, a cell that will operate above the 40% threshold is in target, with ultimate target the efficiency at or near 50%. The cell design is based on a p-i-n bulk device model with three distinct areas, two of which are complete PV-heterostructures on their own; in other words, these two regions could *stand alone* as *two independent solar cell structures with quite acceptable performance* (of the order of 21% and more as it has been demonstrated by our group recently). The power output of the PV composite device is a function of the individual power outputs from each sub-cell in the PV unit. On the other hand, triple junction solar cells seem to lead the way to high efficiency photovoltaics especially in the area of concentrated photovoltaics (CPV), where small cell area and therefore less material (hence lower material costs) may lead to high PV performance. The latter are triple junctions of lattice-matched and non-lattice matched III-V heterostructures with two tunnel junctions between the layers.

7. Suggestions for modeling

Fully develop a theoretical model of PV composite PV devices by first principle calculations and computations based on realistic device parameters; propose a composite PV structure with two major cells: a triple junction and multi-layer tuned cell, with the prospect of high efficiency near 50%. Modeling tools include several established math software packages. Seek for a composite photovoltaic device that combines properties of direct-gap crystalline semiconductors and absorption in the entire spectrum, mainly in the visible and in the infrared (NIR/IR) wavelength ranges, and which is configured as a two-part solar cell: a top triple junction and a multi-layer p-i-n bottom unit tailored to IR infrared wavelengths. The solar spectrum (a 6,000 ^{o}K, see in Figure 5) offers the option of finding suitable band gaps for highest absorption. Material selection shows a blue shift in the absorption via wide gap materials as shown (AlAs). Low gap materials offer wavelength matching in the IR range (note the dashed arrows indicating optical gaps corresponding to various wavelengths. It is of advantage to exploit quantum wells grown on n-type or low-doped substrates.

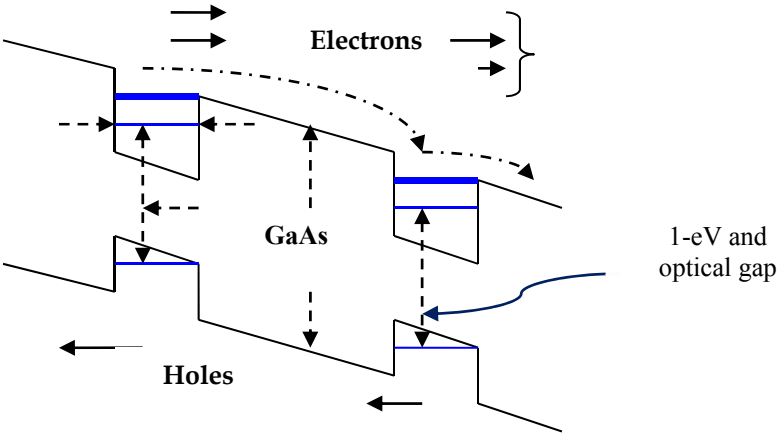

Fig. 7. Tuned quantum wells at 1eV solar photons: shown are energy levels and optical gap increase

Superlattice structures in both cases mentioned above are at the designer's disposal, in the sense that appropriate quantum well geometries may lead to desired solar photons absorption. Enhancement of cell performance can be achieved by replacing the intrinsic region with *tuned* multi-quantum well (MQW) layers, designed for specific wavelengths. Thermionic emission, hopping conduction and tunneling are dominant mechanisms of photo-carrier transport in heterostructures (against losses due to recombination processes). Photo-excited layers thermally escape from quantum wells (minus recombination losses): incident solar photons typically generate 10^{12} to 10^{13} net photo-excited carriers per unit area (cm^2), after recombination effects have been taken into account. This population is expected to migrate to the conduction band assisted by the escape mechanisms named above and the built-in electrostatic field in the p-i-n region.

By selecting suitable geometry of the quantum wells that leads to one or two energy levels in the quantum wells, ground state of electron-hole pairs at 1eV may be formed, and a second state at the very edge of the GaAs layer conduction band (see Fig 2): this event has been shown to act in favor of nearest neighboring hopping electrons from site to site (QW). Thus a three-fold advantage of the superlattice/MQW region is that (1) excess (in addition to carriers from the bulk part of the device) carriers are trapped and thermally escape to the conduction band and (2) nearest neighbor hopping conduction (NNH) becomes a second conduction mechanism and (3) band gaps of other materials may be represented via energy levels in quantum wells. The total current from the intrinsic region will be the sum of the thermionic and the NNH current components (minus recombination losses). Subsequent well width selection may lead to further refinement of solar photon absorption. Near infrared and infrared portions of the solar spectrum can be covered by suitable width selections, with equal amount of modeling effort (from the point of view of computations, it is a mere change of parameters for slightly different optical gaps). It is also interesting to note at this point that quantum well width could be modeled as a random variable, leading to a random distribution of optical gap values (as function of well width) and hence a smeared distribution of optical gap values and absorbed photon wavelengths, for the benefit of the photovoltaic device. Thus, IR photon absorption in the neighborhood of 1eV is feasible. In addition, the superiority of transport properties of the proposed quantum-PV device should be noted compared to its III-N-V "high" efficiency counterpart: our proposed superlattice cell is mainly a GaAs device perturbed by thin Ge layers, and therefore this region exhibits much higher electron mobility. In the absence of tunneling (thick potential barriers) total currents are in essence the sum of (a) bulk currents from the mainly bulk pin device (b) thermionic and (c) hopping current components, due to free electrons in the GaAs conduction band, assisted by the overall electrostatic field in the intrinsic region. Recent modeling and simulation have shown that the top cell retains visible absorption (AlAs/ (Al) GaAs/GaAs at ~21%) or to include a highly efficient triple junction cell (in this proposal, our own choice (InP/GaAs/GaAs at 30% efficiency). The bottom multi-well cell operates at longer wavelengths (1eV or 1,240nm), and therefore the whole of the unit absorbs in both regimes visible and IR respectively. Since germanium and gallium arsenide layers are lattice-matched, it is conceivable that a superlattice would fit in between the p- and n-regions of the device. Advantages of such designs are summarized below:

1. less material to grow
2. small area (exposed to sun-light cell aperture)

3. less complexity in the structure overall
4. reduced scattering of drifting and diffusing carriers
5. reduced carrier trapping and recombination (carriers in MQW region separate from their corresponding holes as being away from the quantum wells)
6. faster growth conditions attainable
7. lower fabrication costs

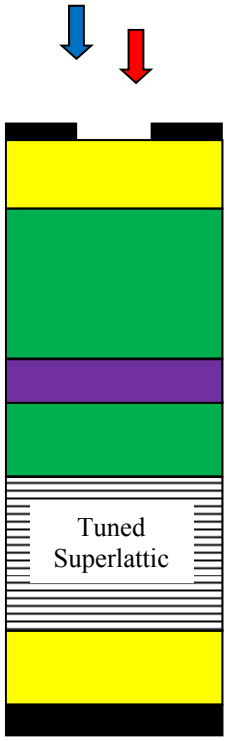

Fig. 8. Proposed cell structure: top cell p-n junction, tunnel junction (TJ) (purple) and p-i-n bottom cell with superlattice in the middle; P region (green), N region (yellow). Top cell is the window facing the sun (anti-reflected coating and surface texturing not shown).

As seen from the figure above, there are several options for further design and optimization (a) top region offers the possibility of another superlattice tuned at selected wavelengths (b) layers and alloys other than GaAs can be used (in the lattice-matched fashion) (c) tuned superlattice (bottom cell) can be split is more than one narrow units tuned at desired solar spectrum peaks (d) cell can be of small area (less material used) or of large area for higher exposure.

8. Some thoughts on concentrated photovoltaics (CPV)

Concentrated light on small solar cells can become of great advantage: a small size cell (~2 mm^2 area) may be placed at the focal point of a Fresnel optical system. Concentrated light causes higher carrier absorption from the bulk of the device and therefore higher

current generation. Currently III-V multijunction cells have shown to have the highest collection efficiency. Efficiency η(%) increases logarithmically with solar power up to about 500 suns (one sun = 100mW/cm²). Currently, it seems that CPV cells show the highest efficiency (consistently above 38%) with latest record efficiencies at 41.1% (Fraunhofer Institute). As it can be seen from equation (11) and the efficiency expression: $\eta(\%) = (V_{oc}\, J_{sc}\, FF)/P_{in}$, the efficiency of a solar cell increases logarithmically with J_{sc}. Such a behavior has been observed, in fact, η(%) increases with increasing current generation (maximum value in the neighborhood of 550 suns).

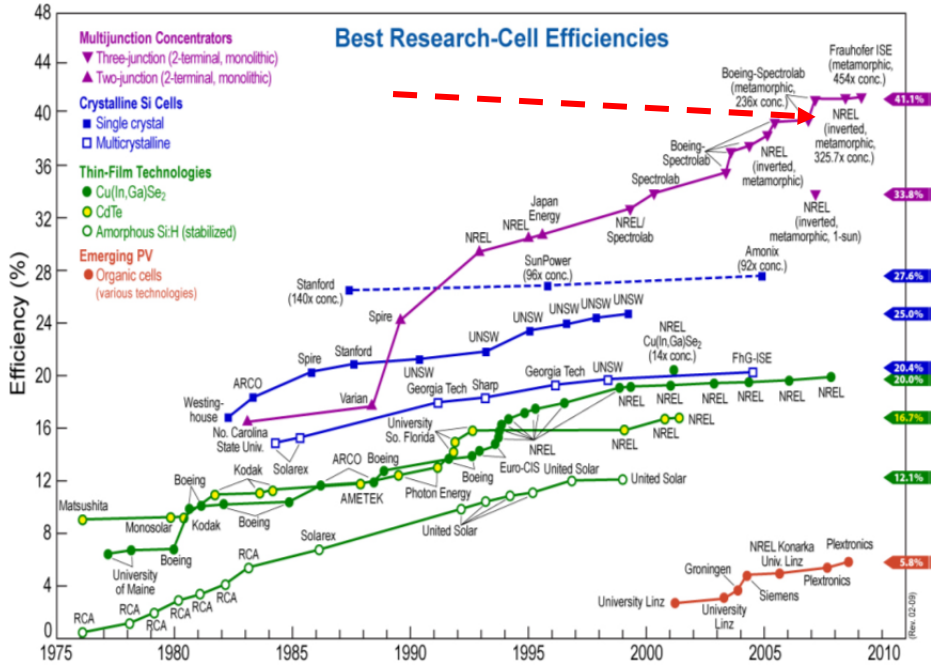

Fig. 9. Current status of cell performance and improvement since the mid seventies. Note that MJ cells have taken the lead in the high efficiency race. Latest (2010) results: 41.1% collection efficiency (Fraunhofer Institute at 454 suns) [© 2009 Spectrolab, Inc. All rights reserved].

As seen from the figure above, multijunction cells, with more than one band gaps, take the lead in current and voltage production (recall that efficiency varies with open-circuit voltage and short-circuit current). CPV systems have given a boost of solar power production globally because they combine (a) highly efficient cells with small exposure area and (b) less costly optical system and components. As of 2009, CPV systems operate at 28 – 30% total efficiency (cell plus optics) and seem to be coming dynamically in the global PV market.

9. Conclusions: The immediate future

Photovoltaics is the child of progress in condensed matter physics, and has matured to the point that solar energy has been competing with fossil fuel energy sources. Small in size

highly efficient solar cells are the answer for our future energy needs. The 40% threshold has already been reached and current research shows that 50% photovoltaics will soon be a reality. It seems that such high conversion will be succeeded by means of small size highly efficient solar cells. By small size we mean from the mm level down to nano-sized PV particles mounted to Fresnel-type optical systems with high solar concentration. Global energy production based on high efficiency PV will solve the energy needs of all nations and will slow down planet pollution. No nuclear waste and zero chance for accidents will guide common sense in immediate future. The concept of tuned superlattices was outlined and its advantages have been presented. Well-understood and lattice-matched materials, such as GaAs/Alloy and Ge, along with improved growth techniques pave the way to high efficiency photovoltaic devices. Integrated circuit techniques are also available for cells of minute size (e.g. 5 mm^2), which is a dramatic reduction of material and hence of cost. Reduced size photovoltaic cells, under high solar concentration (currently from 450 to 500 suns), have opened the avenue for a competitive PV industry in the near future. Concentrated Photovoltaics (CPV-farms) will eventually dominate the world energy production. PV system price range has been steadily reducing from $0.40/KWh (mid-1990's) to mere $0.20/KWh in 2008. Market penetration of the PV industry increases steadily (under 1GW in the US to 6GW by the year 2015). It is expected that the average KWh will be ~10 cents by or before 2015, with a steady GW plant installation. High efficiency solar cells (~50%) and parallel optical system advancement (total system at 30%), will lead to a very strong PV industry, for the benefit of all.

Current modeling of the top structure has indicated top efficiency values in excess of 21% (power out vs. power in) while for the bottom cell preliminary calculations indicate collection efficiency in excess of 25%. The bottom cell is a GaAs-superlattice-Ge structure, where quantum size effects occur. Photo-excited carriers in the middle region are electrons trapped in quantum wells (thin germanium layers sandwiched by gallium arsenide layers). Thin Ge layers (20 nm) are tuned at 1eV. They act as quantum traps and confine electrons in a discrete set of energy levels (one or two at the most). From these traps photo-electrons escape to the conduction band (minus the lost ones). Some advantages of our design over other high-efficiency full-spectrum solar cells are: (a) No excess tunnel junctions are needed to connect the cells (b) The superlattice region includes germanium layers tuned to absorb photons near 1eV (or more, depending on the quantum well thickness) (c) High mobility of carriers in both cells (top, bottom); the latter is a direct advantage over existing III-N-V *high efficiency* competing (nitrogen based) solar cell structures (d) Perfect lattice matching among the layers (e) Parallel carrier transport via (i) tunneling (ii) hopping and (iii) thermionic carrier escape. In the case at hand, tunneling is not a part of the action; instead thermionic emission currents are of importance. Maximum efficiency over 40% is expected via the synergistic action of the two cells.

10. References

[1] SM Sze, High-Speed Semiconductor Devices, John Wiley and Sons, 1990
[2] M Yamaguchi, Solar Energy Materials & Solar Cells 90 (2006) 3068–3077
[3] M Yamaguchi et al, Solar Energy 82, 173 (2008)
[4] R. King, et al, 20th European PVSEC, 2005
[5] K Nishioka, Solar Energy Materials & Solar Cells 90 (2006) 1308–1321, RR King, Nature Photonics, May 2008

[6] Es Yang, Microelectronic Devices, McGraw-Hill, 1988
[7] JF Geisz, S Kurz, MW Wanlass, JS Ward, A Duda, DJ Friedman, JM Olson, WE McMahon, TE Moriarty, and JT Kiehl, Applied Phys. Letters 91, 023502 (2007)
[8] T Kirchartz, Uwe Rau, et al, Appl. Phys Lett. 92, 123502 (2008)
[9] T Mei, Journal of Appl Phys 102, 053708 (2007)
[10] AC Varonides and RA Spalletta, Physica Stat. Sol. 5, No. 2 441 (2008)
[11] GFX Strobl at al, Proc. 7th European Space Power Conference, 9-13 May, Italy, 2005
[12] H. L. Cotal, D. R. Lillington, J. H. Ermer, R. R. King, S.R. Kurtz, D. J. Friedman, J. M. Olson, et al, 28th IEEE PVSC, 2000, p. 955
[13] T Kieliba, S Riepe, W Warta, Journal of Appl. Phys. 100, 093708 (2006)
[14] JF Geisz and DJ Friedman, Semicond. Sci. Technol. 17, 789 (2002)
[15] W Hant, IEEE Trans Electron Devices, VOL ED-26, NO 10, 1573 (1979)
[16] AC Varonides, Physics E 14, 142 (2002)
[17] E Istrate, EH Sargent, Rev Mod Phys, 78, 455 (2006)
[18] H E Runda et al, Nanoscale Res Lett (2006) 1:99
[19] W Li, BE Kardynal, et al, Appl. Phys Lett 93, 153503 (2008)
[20] AC Varonides, Thin Solid Films, Vol. 511-512, July 2006, pp 89-92
[21] BL Stein and ET Yu, Appl. Phys. Lett. 70 (25), 23 June, 1997
[22] AC Varonides, RA Spalletta, WA Berger, WREC-X and Exhibition, 19-25 July 2008, Glasgow, Scotland, UK.
[22] R. King, *Multijunction Cells*, Industry Perspective, Technology Focus, Nature photonics | VOL 2 | MAY 2008 | www.nature.com/naturephotonics
[23] T Kirchartz, BE Pieters, K Taretto, U Rau, Journal of Appl. Physics 104, 094513 (2008)
[24] AC Varonides and RA Spalletta, Thin Solid Films 516, 6729-6733 (2008)
[25] K Jandieri, S D Baranovskii, W Stolz, F Gebhard, W Guter,
[33] M Hermle and A W Bett, J. Phys. D: Appl. Phys. 42 (2009) 155101
[34] R Jones, CPV Summit, Spain, 2009

16

AlSb Compound Semiconductor as Absorber Layer in Thin Film Solar Cells

Rabin Dhakal, Yung Huh, David Galipeau and Xingzhong Yan
Department of Electrical Engineering and Computer Science, Department of Physics, South Dakota State University, Brookings SD 57007, USA

1. Introduction

Since industrial revolution by the end of nineteenth century, the consumption of fossil fuels to drive the economy has grown exponentially causing three primary global problems: depletion of fossil fuels, environmental pollution, and climate change (Andreev and Grilikhes, 1997). The population has quadrupled and our energy demand went up by 16 times in the 20th century exhausting the fossil fuel supply at an alarming rate (Bartlett, 1986; Wesiz, 2004). By the end of 2035, about 739 quadrillion Btu of energy (1 Btu = 0.2930711 W-hr) of energy would be required to sustain current lifestyle of 6.5 billion people worldwide (US energy information administration, 2010). The increasing oil and gas prices, gives us enough region to shift from burning fossil fuels to using clean, safe and environmentally friendly technologies to produce electricity from renewable energy sources such as solar, wind, geothermal, tidal waves etc (Kamat, 2007). Photovoltaic (PV) technologies, which convert solar energy directly into electricity, are playing an ever increasing role in electricity production worldwide. Solar radiation strikes the earth with 1.366 KWm^{-2} of solar irradiance, which amounts to about 120,000 TW of power (Kamat 2007). Total global energy needs could thus be met, if we cover 0.1% of the earth's surface with solar cell module with an area 1 m^2 producing 1KWh per day (Messenger and Ventre, 2004).

There are several primary competing PV technologies, which includes: (a) crystalline (c-Si), (b) thin film (a-Si, CdTe, CIGS), (c) organic and (d) concentrators in the market. Conventional crystalline silicon solar cells, also called first generation solar cells, with efficiency in the range of 15 - 21 %, holds about 85 % of share of the PV market (Carabe and Gandia, 2004). The cost of the electricity generation estimates to about $4/W which is much higher in comparison to $0.33/W for traditional fossil fuels (Noufi and Zweibel, 2006). The reason behind high cost of these solar cells is the use of high grade silicon and high vacuum technology for the production of solar cells. Second generation, thin film solar cells have the lowest per watt installation cost of about $1/W, but their struggle to increase the market share is hindered mainly due to low module efficiency in the range of 8-11% ((Noufi and Zweibel, 2006; Bagnall and Boreland, 2008). Increasing materials cost, with price of Indium more than $700/kg (Metal-pages, n.d.), and requirements for high vacuum processing have kept the cost/efficiency ratio too high to make these technologies the primary player in PV market (Alsema, 2000). Third generation technologies can broadly be divided in two categories: devices achieving high efficiency using novel approaches like concentrating and

tandem solar cells and moderately efficient organic based photovoltaic solar cells (Sean and Ghassan, 2005; Currie et al., 2008). The technology and science for third generation solar cells are still immature and subject of widespread research area in PV.

1.1 Thin film solar cells

Second Generation thin film solar cells (TFSC) are a promising approach for both the terrestrial and space PV application and offer a wide variety of choices in both device design and fabrication. With respect to single crystal silicon technology, the most important factor in determining the cost of production is the cost of 250-300 micron thick Si wafer (Chopra et al., 2004). Thin-film technologies allow for significant reduction in semiconductor thickness because of the capacity of certain materials for absorbing most of the incident sunlight within a few microns of thickness, in comparison to the several hundred microns needed in the crystalline silicon technology (Carabe and Gandia, 2004). In addition, thin-film technology has an enormous potential in cost reduction, based on the easiness to make robust, large-area monolithic modules with a fully automatic fabrication procedure. Rapid progress is thus made with inorganic thin-film PV technologies, both in the laboratory and in industry (Aberle, 2009).

Amorphous silicon based PV modules have been around for more than 20 years Chithik et al. first deposited amorphous silicon from a silane discharge in 1969 (Chittik et al., 1969) but its use in PV was not much progress, until Clarson found out a method to dope it n or p type in 1976 (Clarson, n.d.) Also, it was found that the band gap of amorphous silicon can be modified by changing the hydrogen incorporation during fabrication or by alloying a-Si with Ge or C (Zanzucchi et al., 1977; Tawada et al. 1981). This introduction of a-Si:C:H alloys as p-layer and building a hetero-structure device led to an increase of the open-circuit voltage into the 800 mV range and to an increased short-circuit current due to the "window" effect of the wideband gap p layer increasing efficiency up to 7.1% (Tawada et al. 1981, 1982). Combined with the use of textured substrates to enhance optical absorption by the "light trapping" effect, the first a-Si:H based solar cell with more than 10% conversion efficiency was presented in 1982 (Catalakro et al., 1982). However, there exists two primary reasons due to which a-Si:H has not been able to conquer a significant share of the global PV market. First is the low stable average efficiency of 6% or less of large-area single-junction PV modules due to "Staebler–Wronski effect", i.e. the light-induced degradation of the initial module efficiency to the stabilized module efficiency (Lechner and Schad, 2002; Staebler and Wronski, 1977). Second reason is the manufacturing related issues associated with the processing of large (>1 m^2) substrates, including spatial non-uniformities in the Si film and the transparent conductive oxide (TCO) layer (Poowalla and Bonnet, 2007).

Cadmium Telluride (CdTe) solar cell modules have commercial efficiency up to 10-11% and are very stable compound (Staebler and Wronski, 1977). CdTe has the efficient light absorption and is easy to deposit. In 2001, researches at National Renewable Energy Laboratory (NREL) reported an efficiency of 16.5% for these cells using chemical bath deposition and antireflective coating on the borosilicate glass substrate from $CdSnO_4$ (Wu et al., 2001). Although there has been promising laboratory result and some progress with commercialization of this PV technology in recent years (First Solar, n.d.), it is questionable whether the production and deployment of toxic Cd-based modules is sufficiently benign environmentally to justify their use. Furthermore, Te is a scarce element and hence, even if most of the annual global Te production is used for PV, CdTe PV module production seems limited to levels of a few GW per year (Aberle, 2009).

The CIGS thin film belongs to the multinary Cu-chalcopyrite system, where the bandgap can be modified by varying the Group III (on the Periodic Table) cations among In, Ga, and Al and the anions between Se and S (Rau and Schock, 1999). This imposes significant challenges for the realization of uniform film properties across large-area substrates using high-throughput equipment and thereby affects the yield and cost. Although CIGS technology is a star performer in laboratory, with confirmed efficiencies of up to 19.9% for small cells (Powalla and Bonnet, 2007) however the best commercial modules are presently 11–13% efficient (Green et al. 2008). Also there are issues regarding use of toxic element cadmium and scarcity of indium associated with this technology. Estimates indicate that all known reserves of indium would only be sufficient for the production of a few GW of CIGS PV modules (Aberle, 2009).

This has prompted researchers to look for new sources of well abundant, non toxic and inexpensive materials suitable for thin film technology. Binary and ternary compounds of group III-V and II-VI are of immediate concern when we look for alternatives. AlSb a group III-V binary compound is one of the most suitable alternatives for thin film solar cells fabrication because of its suitable optical and electrical properties (Armantrout et al., 1977). The crystalline AlSb film has theoretical conversion efficiency more than 27% as suggested in literature (Zheng et al., 2009).

1.2 Aluminum antimony thin films

Aluminum Antimony is a binary compound semiconductor material with indirect band gap of 1.62 eV thus ideal for solar spectrum absorption (Chandra et al., 1988). This also has become the material of interest due to relatively easy abundance and low cost of Al and Sb. AlSb single crystal has been fabricated from the Czochralski process but the AlSb thin film was prepared by Johnson et al. by co-evaporation of Al and Sb. They also studied the material properties to find out its donor and acceptor density and energy levels (Johnson, 1965). Francombe et al. observed the strong photovoltaic response in vacuum deposited AlSb for the first time in 1976 (Francombe et al., 1976). Number of research groups around the world prepared thin AlSb thin film and studied its electrical and optical properties by vacuum and non vacuum technique. These include, Leroux et al. deposited AlSb films on number of insulating substrate by MOCVD deposition technique in 1979 (Leroux et al., 1980). Dasilva et al. deposited AlSb film by molecular beam epitaxy and studied its oxidation by Auger and electron loss spectroscopy in 1991 (Dasilva et al., 1991). Similarly, AlSb film was grown by hot wall epitaxy and their electrical and optical properties was studied by Singh and Bedi in 1998 (Singh and Bedi, 1998). Chen et al. prepared the AlSb thin film by dc magnetron sputtering and studied its electrical and optical properties (Chen et al. 2008) in 2007. Gandhi et al. deposited AlSb thin film on by the alternating electrical pulses from the ionic solution of $AlCl_3$ and $SbCl_3$ in EMIC (1-methyl-3-ethylimidazolium chloride) and studied its electrical and optical characters (Gandhi et al. 2008). However, AlSb thin film had never been successfully employed as an absorber material in photovoltaic cells. We, electro-deposited AlSb thin film on the TiO_2 substrate by using the similar technique as Gandhi et al. and had observed some photovoltaic response in 2009 (Dhakal et al., 2009). Al and Sb ions are extremely corrosive and easily react with air and moisture. Thus it becomes very difficult to control the stoichiometry of compound while electroplating. Thus, vacuum deposition techniques become the first choice to prepare AlSb thin films for the solar cell applications. In this work, we fabricated AlSb thin film co-sputtering of Al and Sb target. The film with optimized band-gap was used to fabricate p-n and p-*i*-n device structures. The photovoltaic response of the devices was investigated.

2. Fabrication of AlSb thin films

AlSb film was prepared from dc magnetron sputtering of Al and Sb target (Kurt J. Lesker, Materials Group, PA) simultaneously in a sputtering chamber. Sputtering is a physical vapor deposition process whereby atoms are ejected from a solid target material due to bombardment of the target by plasma, a flow of positive ions and electrons in a quasi-neutral electrical state (Ohring, 2002). Sputtering process begins when the ion impact establishes a train of collision events in the target, leading to the ejection of a matrix atom (Ohring, 2002). The exact processes occurring at the target surface is depends on the energy of the incoming ions. Fig. 1 shows the schematic diagram of sputtering using DC and RF power. DC sputtering is achieved by applying large (~2000) DC voltages to the target (cathode) which establishes a plasma discharge as Ar^+ ions will be attracted to and impact the target. The impact cause sputtering off target atoms to substrates.

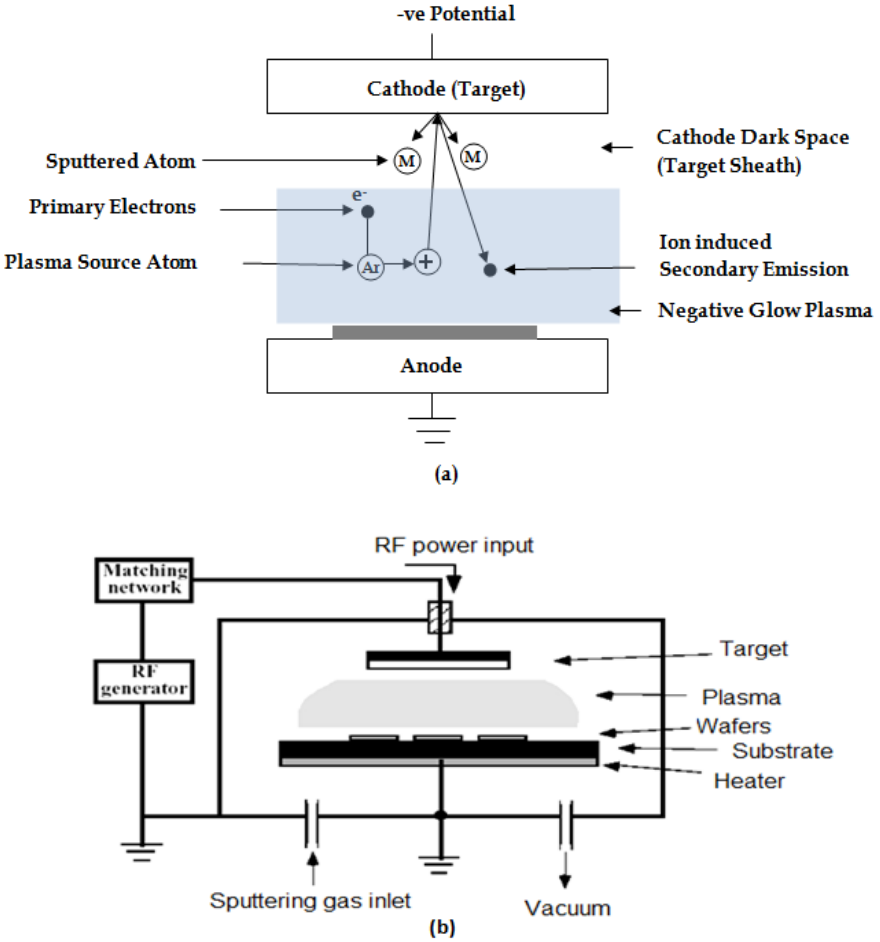

Fig. 1. Schematic Diagrams of (a) DC sputtering and (b) RF sputtering (Ohring, 2002)

In DC sputtering, the target must be electrically conductive otherwise the target surface will charge up with the collection of Ar^+ ions and repel other argon ions, halting the process. RF Sputtering - Radio Frequency (RF) sputtering will allow the sputtering of targets that are electrical insulators (SiO_2, etc). The target attracts Argon ions during one half of the cycle and electrons during the other half cycle. The electrons are more mobile and build up a negative charge called self bias that aids in attracting the Argon ions which does the sputtering. In magnetron sputtering, the plasma density is confined to the target area to increase sputtering yield by using an array of permanent magnets placed behind the sputtering source. The magnets are placed in such a way that one pole is positioned at the central axis of the target, and the second pole is placed in a ring around the outer edge of the target (Ohring, 2002). This configuration creates crossed *E* and *B* fields, where electrons drift perpendicular to both *E* and *B*. If the magnets are arranged in such a way that they create closed drift region, electrons are trapped, and relies on collisions to escape. By trapping the electrons, and thus the ions to keep quasi neutrality of plasma, the probability for ionization is increased by orders of magnitudes. This creates dense plasma, which in turn leads to an increased ion bombardment of the target, giving higher sputtering rates and, therefore, higher deposition rates at the substrate.

We employed dc magnetron sputtering to deposit AlSb thin films. Fig. 2 shows the schematic diagram of Meivac Inc sputtering system. Al and Sb targets were placed in gun 1 and 2 while the third gun was covered by shutter. Both Al and Sb used were purchase from Kurt J. Lesker and is 99.99% pure circular target with diameter of 2.0 inches and thickness of 0.250 inches.

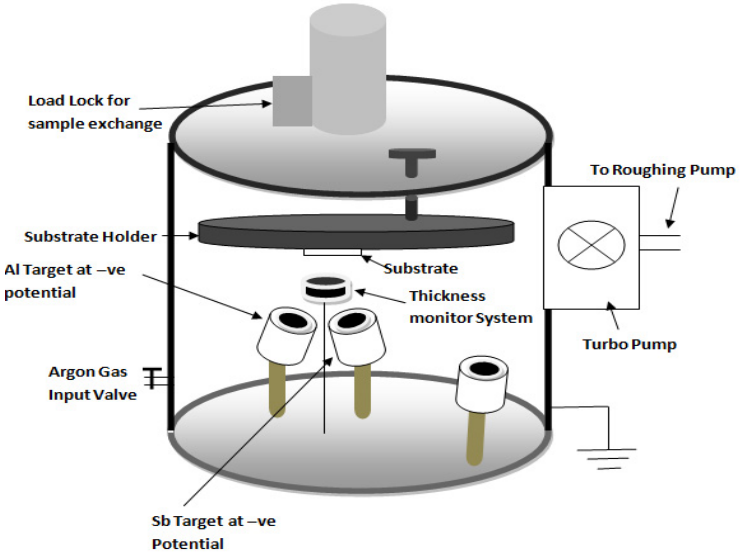

Fig. 2. Schematic diagram of dc magtron sputtering of Al and Sb targets.

Firstly, a separate experiment was conducted to determine the deposition rate of aluminum and antimony and the associated sputtering powers. Al requires more sputtering power than Sb does for depositing the film at same rates. Next Al and Sb was co-sputtered to

produce 1 micron AlSb film in different deposition ratio for Al:Sb. The film was annealed at 200 C in vacuum for 2 hrs and cooled down naturally. Table 1 summarizes the deposition parameters of different AlSb films.

Al: Sb Ratio	Deposition Rate (Å/s)		Sputtering Power (W)		Ar Gas Pressure (mTorr)	Film Thickenss (kÅ)
	Al	Sb	Al	Sb		
1:3	2	6	104	37	20.1	10
2:5	2	5	104	33	20.1	10
3:7	3	7	150	42	20.1	10
1:1	1	1	150	24	20.1	10
7:3	7	3	261	24	20.1	10

Table 1. Deposition Parameters of Different AlSb films.

The film was deposited on glass slides for electrical and optical characterization. The microscopic glass substrate (1 cm x 1 cm) was cleaned using standard substrate cleaning procedure as follows: soaked in a solution of 90% boiling DI and 10% dishwashing liquid for five minutes, followed by soaking in hot DI (nearly boiled) water for five minutes. The substrate was then ultra sonicated, first in Acetone (Fisher Scientific) and then isopropyl alcohol (Fisher Scientific) for 10 minutes each. The substrate was then blown dry with nitrogen.

The morphology of the AlSb film was checked by SEM and was used to validate the grain size and crystalline nature of AlSb particles and shown in Fig. 3.

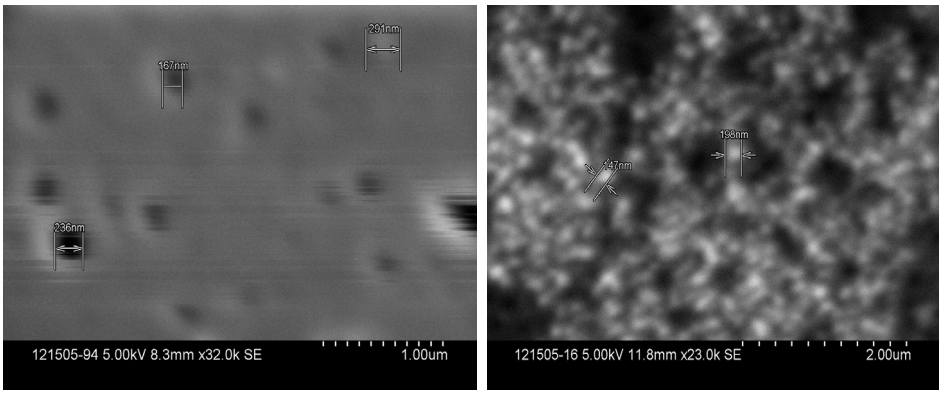

(a) (b)

Fig. 3. SEM images of the AlSb thin film (a) before annealing, and (b) after annealing.

The AlSb grains were found to have been developed after annealing of the film due to proper diffusion and bonding of Al and Sb. Only low magnified image could be produced before annealing the film and holes were seen on the surface. The AlSb microcrystal is formed with an average grain size of 200 nm. Also seen are holes in the film which are primarily the defect area, which could act as the recombination centers. Better quality AlSb film could be produced if proper heating of the substrate is employed during deposition process.

3. Optical characterization of AlSb thin film

The transmittance in the thin film can be expressed as (Baban et al. 2006):

$$T = \frac{I_T}{I_0} = (1 - R1)(1 - R2)(1 - R3)(1 - S)e^{-\alpha d} \quad (1)$$

Where, a is the absorption coefficient antd d is the thickness of the semiconductor film. $R1$, $R2$ and $R3$ are the Fresnel power reflection coefficient and the Fresnel reflection coefficient at semiconductor - substrate and substrate – air interface. S measures the scattering coefficient of the surface.

UV Visible Spectrophotometer (Lambda 850) was used to measure the absorption and transmission data. This system covered the ultraviolet-visible range in 200 – 800 nm. The procedures in the Lambda 850 manual were followed. Figure 4 shows the transmittance spectra of the AlSb thin films. The films have an strong absorption in the visible spectral range up to 550 nm for film with Al:Sb ratio 2:5. Similarly for films with Al:Sb in the ratio of 1:3, 1:1 and 3:7 have strong absorption up to 700 nm. The films were transparent beyond these levels.

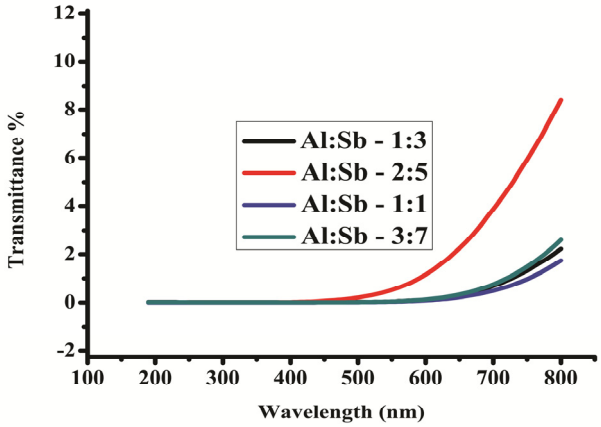

Fig. 4. Transmittance Spectra of AlSb films with different Al:Sb growth ratios.

The film with Al:Sb ratio of 7:3 didn't have a clear transmittance spectra and thus not shown in the figure. This was because the increasing the content of aluminum would make the film metallic thus absorbing most of the light in visible spectrum.

Absorption coefficient of a film can be determined by solving equation 1 for absorption and normalizing the Transmittance in the transparent region as (Baban et al. 2006):

$$\alpha = -\frac{1}{d}\ln\left(T_{normalized}\right) \quad (2)$$

Optical band gap of the film was calculated with the help of transmission spectra and reflectance spectra by famous using Tauc relation (Tauc, 1974)

$$\alpha h\nu = d\left(h\nu - E_g\right)^n \quad (3)$$

Where *Eg* is optical band gap and the constant *n* is 1/2 for direct band gap material and n is 2 for indirect band gap. The value of the optical band gap, *Eg*, can be determined form the intercept of $(\alpha h\nu)^{1/2}$ Vs Photon energy, *hν*, at $(\alpha h\nu)^{1/2} = 0$.

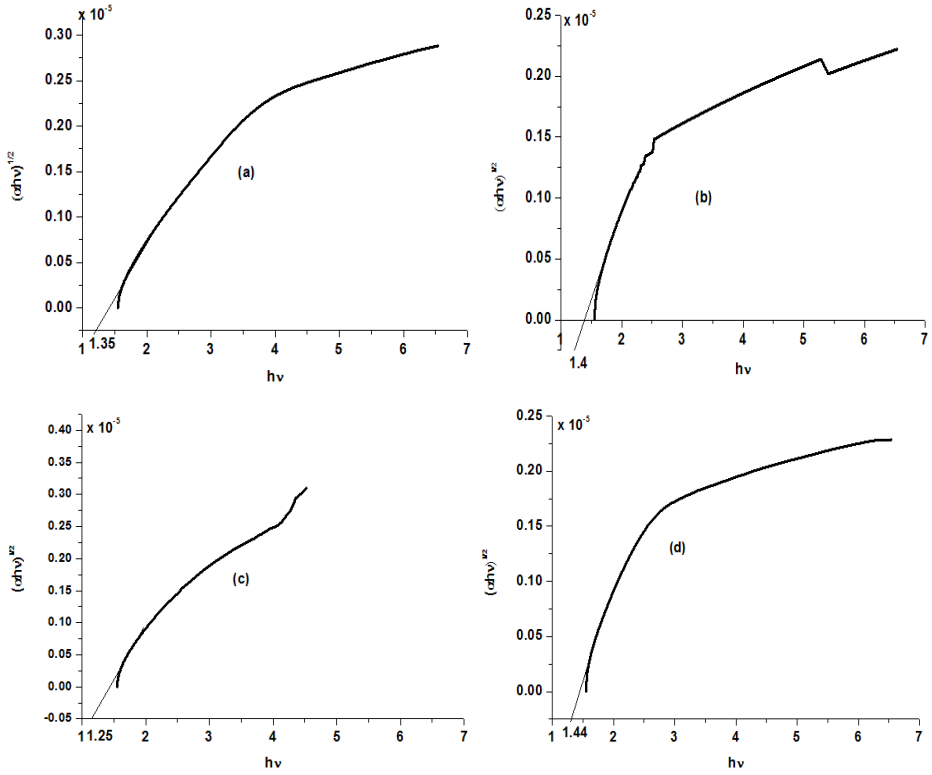

Fig. 5. Bandgap estimation of AlSb semiconductor with Al:Sb growth ratios (a) 1:3, (b) 2:5, (c) 1:1 and (d) 3:7.

The optical absorption coefficient of all the films was calculated from the transmittance spectra and was found in the range of 10^5 cm^{-1} for photon energy range greater than 1.2 eV. Fig. 5 shows the square root of the product of the absorption coefficient and photon energy (*hν*) as a function of the photon energy. The band gap of the film was then estimated by extrapolating the straight line part of the $(\alpha h\nu)^{1/2}$ vs *hν* curve to the intercept of horizontal axis.
This band gap for Al:Sb growth ratio 1:3, 2:5, 1:1 and 3:7 was found out to be 1.35 eV, 1.4 eV, 1.25 eV and 1.44 eV respectively. Since the ideal band gap of AlSb semiconductor is 1.6 eV we have taken the Al:Sb growth ratio to be 3:7 to characterize the film and fabricate the solar cells.

4. Electrical characterization

Material's sheet resistivity, ρ, can be measured using the four point probe method as show in Fig. 6. A high impedance current source is used to supply current (*I*) through the outer two probes and a voltmeter measures the voltage (*V*) across the inner two probes.

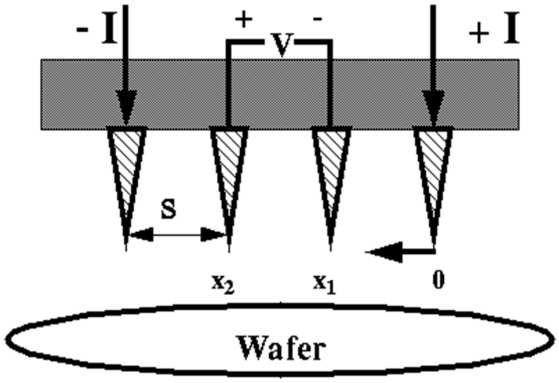

Fig. 6. Schematic diagram of Four point probe configuration.

The sheet resistivity of a thin sheet is given by (Chu et al. 2001):

$$\rho = RCF \frac{V_{measured}}{I_{measured}} \tag{4}$$

Where, RCF is the resistivity correction factor and given by $RCF = \frac{\pi\alpha}{\ln 2}$ The sheet resistance, R_s, could be thus be calculated as $R_s = \rho/d$ and measured in ohms per square. Conductivity (σ) is measured as reciprocal of resistivity and could be related to the activation energy as (Chu et al., 2001):

$$\sigma = \sigma_0 e^{\frac{-\Delta E}{k_b T}} \tag{5}$$

Where, ΔE is the activation energy. This describes the temperature dependence of carrier mobility. The dark conductivity of AlSb film measured as a function of temperature and is shown in Fig. 7.

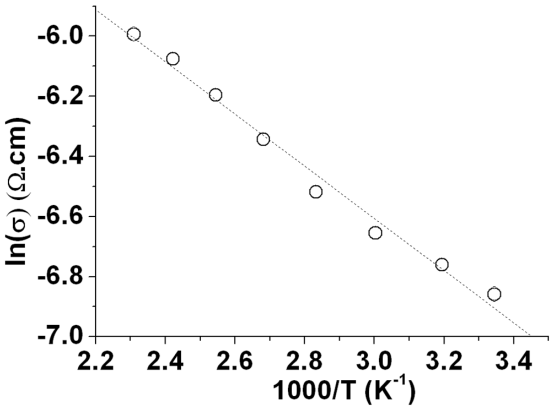

Fig. 7. Temperature dependence of annealed AlSb (3:7) film when heated from 26 - 240 ˚C (dot line for guiding the eyes).

The annealed film shows a linear lnσ vs $1/T$ relationship. The activation energy of the dark conductivity was estimated to be 0.68 eV from the temperature dependence of the conductivity curve for AlSb film. This value is in good agreement with work done by Chen et al. (Chen et al., 2008). This curve also confirms the semiconducting property of the AlSb (3:7) film because the conductivity of the film was seen to be increasing with increasing the excitation.

5. Simulation of solar cell

AMPS 1D beta version (Penn State Univ.) was used to simulate the current voltage characteristics of p-*i*-n junction AlSb solar cells. The physics of solar cell is governed by three equations: Poisson's equation (links free carrier populations, trapped charge populations, and ionized dopant populations to the electrostatic field present in a material system), the continuity equations (keeps track of the conduction band electrons and valence band holes) for free holes and free electrons. AMPS has been used to solve these three coupled non-linear differential equations subject to appropriate boundary conditions. Following simulation parameters was used for the different layers of films.

Contact Interface				
Barrier Height (eV)	0.1 (E_C-E_F)		0.3 (E_F-E_V)	
S_e (cm/s)	1.00×10^8		1.00×10^8	
S_h (cm/s)	1.00×10^8		1.00×10^8	
* S surface recombination velocity of electrons or holes.				
Semiconductor Layers				
	CuSCN	**AlSb**	**ZnO**	**TCO**
Thicknesses, **d** (nm)	100	1000	45	200
Permittivity, $\varepsilon/\varepsilon_0$	10	9.4	10	9
Band gap, E_g (eV)	3.6	1.6	2.4	3.6
Density of electrons on conduction band, N_C (cm^{-3})	1.80×10^{18}	7.80×10^{17}	2.22×10^{18}	2.22×10^{18}
Density of holes on valence band, N_V (cm^{-3})	2.20×10^{19}	1.80×10^{19}	1.80×10^{19}	1.80×10^{19}
Electron mobility, μ_e (cm^2/Vs)	100	80	100	100
Hole mobility, μ_p (cm^2/Vs)	25	420	25	25
Acceptor or donor density, N_A or N_D (cm^{-3})	$N_A = 1\times 10^{18}$	$N_A = 1\times 10^{14}$	$N_D = 1.1\times 10^{18}$	$N_D = 1\times 10^{18}$
Electron affinity, X (eV)			4.5	4.5
* $\varepsilon_0 = 8.85\times10^{-12}$ F/m electric constant; TCO is In_2O_3: SnO_2.				
Gaussian Midgap defect states				
N_{DG}, N_{AG} (cm^{-3})	A = 1×10^{19}	D = 9×10^{10}	A = 1×10^{19}	D = 1×10^{16}
W_G (eV)	0.1	0.1	0.1	0.1
σ_e (cm^2)	1.00×10^{-13}	1.00×10^{-8}	1.00×10^{-16}	1.00×10^{-11}
σ_p (cm^2)	1.00×10^{-13}	1.00×10^{-11}	1.00×10^{-13}	1.00×10^{-14}

* $N_{DG/AG}$ the donor-like or acceptor-like defect density, W_G the energy width of the Gaussian distribution for the defect states, τ carrier lifetime, and σ capture cross section of electrons (σ_e) or holes (σ_p).

Table 2. Parameters of the simulating the IV behavior or p-*i*-n junction solar cells.

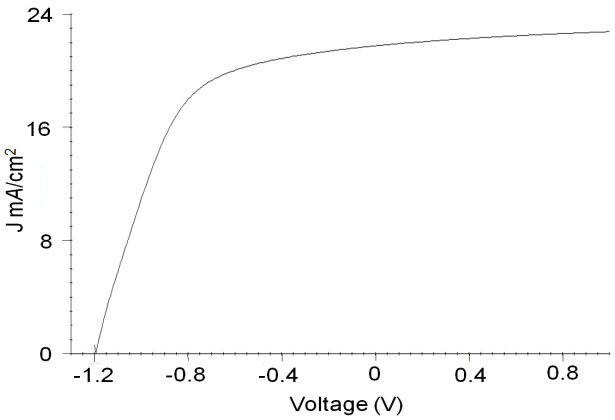

Fig. 8. Current-voltage simulation of AlSb p-i-n junction structure in AMPS 1D software.

Fig. 8 shows the current voltage simulation curve of pin junction solar cell - CuSCN/AlSb/ZnO with AlSb as an intrinsic layer. CuSCN was used as a p layer and ZnO as a n layer. The cell was illuminated under one sun at standard AM 1.5 spectrum.
The simulation result shows that the solar cell has the FF of 55.5% and efficiency of 14.41%. The short circuit current for the cell was observed to be 21.7 mA/cm² and the open circuit voltage was observed to be 1.19 V. AlSb is thus the promising solar cell material for thin film solar cells. The efficiency of the same cell structure could be seen increased up to 19% by doubling the thickness of AlSb layer to 2 micron.

6. Solar cell fabrication

Both p-n and p-*i*-n junction solar cells were designed and fabricated in 1cm x 2 cm substrate with AlSb as a p type and an absorber material respectively. Variety of n type materials including TiO_2 and ZnO were used to check the photovoltaic response of AlSb thin film. Fig. 9 shows the p-n and p-*i*-n based solar cell design with ZnO and TiO_2 are an n-type layer and CuSCN as a p-type layer.

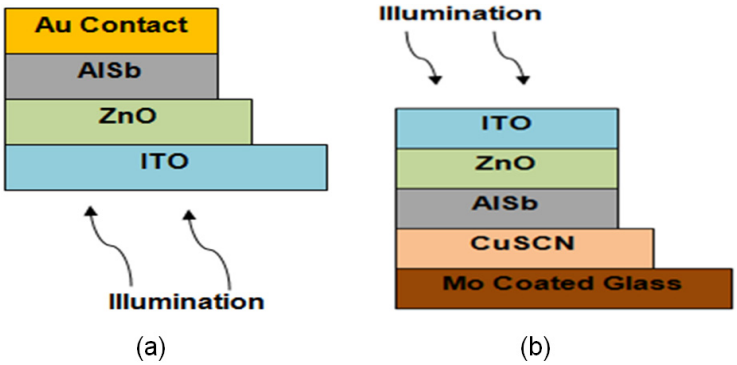

Fig. 9. Solar Cell Design (a) p-n and (b) p-*i*-n structure.

ZnO thin film was prepared by RF sputtering of 99.999% pure ZnO target (Kurt J. Lesker, PA, diameter 2 inches and thickness 0.25 inches). ZnO intrinsic film was deposited by RF power of 100 W at 0.7 Å/s and subsequently annealed in air at 150 ^{0}C. ITO film was also prepared from 99.99% pure ITO target (Kurt J. Lesker, PA, diameter 2 inches and thickness 0.25 inches) on the similar fashion using dc magnetron sputtering. Transparent ITO film was deposited at plasma pressure of 4.5 mTorr. The sputtering power of 20 W yields deposition rate 0.3 Å/s. The film was then annealed at 150 ^{0}C in air for 1 hour. The highly ordered mesoporous TiO_2 was deposited by sol gel technique as described by Tian et al. (Tian et al. 2005). CuSCN thin film was prepared by spin coating the saturated solution of CuSCN in dipropyl sulphide and dried in vacuum oven at 80 ^{0}C (Li et al., 2011). The thickness of all three films ZnO, ITO and TiO_2 film was about 100 nm and the thickness of AlSb layer is ~1 micron. The active layer was annealed.

7. I-V Characterization of solar cell

Current voltage measurement of the solar cells was carried out using Agilent 4155c (Agilent, Santa Clara, CA) semiconductor parameter analyzer equipped with solar cell simulator in SDSU. Fig. 10 shows the experimental set up used for measuring I-V response of the solar cells, where 2 SMUs (source measurement unit) were used. The SMU s could operate as a voltage source (constant sweep voltage) or a current source and it could measure voltage and current at the same time. The SMUs could measure from 10^{-12} A to 1 A and -10 V to 10 V. SMU 1 was set as voltage sweep mode from -1 V to 1 V with steps of 0.01 V, and SMU 2 was set to measure current of the solar cell during IV measurement. IV responses were measured under both dark and illuminated condition. During illumination, the intensity of the simulated light was 100 mW cm^{-2} and calibrated using the NREL calibrated standard cell.

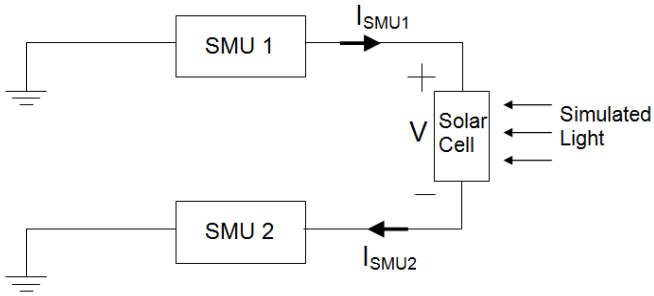

Fig. 10. Experimental set up for measuring IV response of a solar cell.

Table 3 shows the current voltage characteristics of p-n junction solar cells with structures AlSb/TiO_2, AlSb/ZnO. The active cell area was 0.16 cm^2 and fabricated on ITO coated glass surface.

The *V*oc of the best cell with ZnO as an n type layer was found out to be 120 mV and *I*sc to be 76 uA. The *FF* of the cell was calculated to be 0.24 and the efficiency was 0.009%. The cell with TiO_2 as an n layer has even lower V_{OC} and *I*sc. TiO_2 is less suitable n-type layer for making junction with AlSb than ZnO because it is far more conductive than TiO_2. A number of reasons may be attributed for this low efficiency. First, is due to small electric field at the junction between AlSb and the n type material (ZnO or TiO_2). This severely limits the charge

separation at the junction and decreases V_{OC} of the device. A better material needs to be explored to dope AlSb n type to increase the built in field. The field could also be extended using the p-*i*-n structure to design the solar cells.

Cell	V_{OC} (mV)	I_{SC} (mA)	FF	Efficiency %
AlSb/TiO2	80	$12x10^{-3}$	0.23	0.001
AlSb/ZnO	120	$76x10^{-3}$	0.24	0.009

Table 3. Current-voltage characteristics of p-n junction solar cells

Interesting results were obtained with a p-*i*-n junction, CuSCN/AlSb/ZnO. The used cell has an active cell area of this cell was 0.36 cm^2 and fabricated on Mo coated glass surface. Charge was collected from the silver epoxy fingers casted on top of ITO surface and Mo back contact. The cell showed a V_{OC} of ~ 500 mV and a J_{SC} of 1.5 mA/cm^2. With a FF value of 0.5, the efficiency of this cell was calculated to be 0.32%. This observation may be attributed to the more efficient charge separation than that in the p-n junction devices due to a strong build-in field. However, the efficiency of the p-*i*-n junction device is very low in comparison to other available thin film solar cells devices. There are still many unknown factors including the interfaces in the junction. Such a low efficiency could be attributed to the defects along the AlSb interface with both the p- and n-type of layers. Interfaces between AlSb and other layers needed to be optimized for a better performance.

8. Summary

AlSb thin film has been prepared by co-sputtering aluminum and antimony. The deposition rate of Al:Sb was required to be 3:7 to produce the stoichiometric AlSb film with optical band gap of 1.44 eV. After annealing the film at 200 ^{0}C in vacuum for two hours, the film likely formed crystalline structures with a size of ~200 nm and has strong absorption coefficient in the range of 10^5 cm^{-1} in the visible light. p-n and p-*i*-n heterojunction solar cells were designed and fabricated with AlSb as a p-type material and an intrinsic absorber layer. The simulation of the p-i-n junction solar cell with CuSCN/AlSb/ZnO using AMPS at AM1.5 illumination shows efficiency of 14% when setting ~1 μm-thick absorber layer. The p-n junction solar cells were fabricated with different types of n layers shows the photovoltaic responses. The p-*i*-n showed better photovoltaic performance than that of p-n junction cells. All the preliminary results have demonstrated that AlSb is promising photovoltaic material. This work is at the early stage. More experiment is needed for the understanding of the crystallization and properties of the AlSb films and the interface behaviors in the junctions.

9. Acknowledgments

Support for this project was from NSF-EPSCoR Grant No. 0554609, NASA-EPSCoR Grant NNX09AU83A, and the State of South Dakota. Simulation was carried out using AMPS 1D beta version (Penn State University). Dr. Huh appreciates AMES Lab for providing sputtering facility. We appreciate AMPS 1D beta version (Penn State Univ.)

10. References

Aberle, A. G. (2009). Thin Film Solar cells, *Thin Solid Films*, Vol. 517, pp. (4706-4710).

Alsema, E. A. (2000). Energy Pay-back Time and CO_2 Emissions of PV Systems, *Prog. Photovolt. Res. Appl.*, Vol. 8, pp. 17-25.

Andreev, V. M., & Grilikhes, V. A. (1997), *Photovoltaic conversion of concentrated sunlight*, John Wiley and sons, Inc., England.

Armantrout, G. A., Swierkowski, S. P., Sherohman, J. W., &Yee, J. H., 1977, *IEEE Trans. Nucl. Sci.,* NS-24, Vol. 121.

Baban, C., Carman, M., & Rusu, G. I. (2006) Electronic transport and photoconductivity of polycrystalline CdSe thin films, *J. Opto. Elec. and Adv. Materials*, Vol. 8, No. 3, pp. 917-921.

Bagnall, D. M., & Boreland, M. (2008). Photovoltaic Technologies, *Energy Policy*, Vol. 36, No. 12, pp. 4390-4396.

Bartlett, A. A. (1986). Sustained availability: A management program for nonrenewable resources, *Am. J. Phys.*, 54, pp (398-402).

Carabe, J., & Gandia, J. (2004), Thin – film - silicon solar cells, *Optoelectronics Review*, Vol. 12, No. 1, pp. 1-6.

Catalakro, A. (1982). Investigation on High efficiency thin film solar cells, *Proc. of 16th IEEE Photovoltaic Specialist Conf.*, San Diego (CA), pp. 1421-1422.

Chandra, Khare, S., & Upadhaya, H. M. (1988). Photo-electrochemical solar cells using electrodeposited GaAs and AISb semiconductor films, *Bulletin of Material Sciences*, Vol. 10, No. 4, pp. 323-332.

Chen, W., Feng, L., Lei, Z., Zhang, J., Yao, F., Cai, W., Cai, Y.,Li, W.,Wu, L., Li, B., & Zheng, J. (2008). AlSb thin films prepared by DC magnetron sputtering and annealing, *International Journal of Modern Physics B*, *Vol.* 22, No. 14, pp. 2275-2283.

Chittik, R. C., Alexander, J. H., & Sterling, H. E. (1968). The preparation and properties of amorphous Silicon, *Journal of Electrochemical Society*, Vol. 116, No. 1, pp. (77-81).

Chopra, K. L., Paulson, P. D., & Dutta, V. (2004). Thin Film Solar cells: An Overview, *Prog. Photovolt. Res. Appl.*, Vol. 12, pp. (69-92).

Chu, D. P., McGregor, B. M., & Migliorato, P. (2001), Temperature dependence of the ohmic conductivity and activation energy of $Pb_{1+}y(Zr0_{.3}Ti_{0.7})O_3$ thin films, *Appl. Phys. Letter*, Vol. 79, No. 4, pp. 518-520.

Clarson, D. E. (1977). Semiconductor device having a body of amorphous silicon, *US patent* no. 4064521.

Currie, M. J., Mapel, J. K., Heidel, T. D., Goffri, S., & Baldo, M. A. (2008). High-Efficiency Organic Solar Concentrators for Photovoltaics, *Science*, Vol. 321, No. 5886, pp. 226-228.

Dasilva, F. W. O., Raisian, C., Nonaouara, M., & Lassabatere, L. (1991). Auger and electron energy loss spectroscopies study of the oxidation of AlSb(001) thin films grown by molecular beam epitaxy, *Thin Solid Films*, Vol. 200 pp. 33-48.

Dhakal, R., Kafford, J., Logue, B., Roop, M., Galipeau, D., & Yan, X. (2009). Electrodeposited AlSb compound semiconductor for thin film solar cells, *34th IEEE Photovoltaic Specialists Conference (PVSC)*, Philadelphia, pp. 001699 – 001701.

First Solar, n.d. Available from <http://www.firstsolar.com/company_overview.php>

Francombe, M. H., Noreika, A. J., & Zietman, S. A. (1976). Growth and properties of vacuum-deposited films of AlSb, AlAs and AlP, *Thin Solid Films*, Vol. 32, No. 2, pp. 269-272.

Gandhi, T., Raja, K. S., & Mishra, M. (2008). Room temperature Electro-deposition of aluminum antimonide compound semiconductor, *Electrochemica Acta*, Vol. 53, No. 24, pp. 7331-7337.

Green, M. A., Emery, K., Hishikawa, Y., & Warta, W. (2008). Solar Cell Efficiency Tables (Version 32), *Prog.Photovolt:Res.Appl.*Vol. 16, pp. 61–67.

Johnson, J. E. (1965). Aluminum Antimonide Thin Films by co-evaporation of elements, *Journal of Applied Physics*, Vol. 36, pp. 3193-3196.

Kamat, P. V. (2007). Meeting the Clean Energy Demand: Nanostructure Architecture for Solar energy conversion, *J. Phys. Chem. C,* Vol. 111, pp. 2834-2860.

Lechner, P., & Schade, H. (2002). Photovoltaic thin-film technology based on hydrogenated amorphous silicon, *Prog. Photovolt.,* Vol. 10, pp. 85–97.

Leroux, M. (1980). Growth of AlSb on insulating substrates by metal organic chemical vapor depositon, *Journal of crystal growth*, Vol. 48, pp. 367-378.

Li, Y. Yan, M., Jiang, M., Dhakal, R., Thapaliya, P. S., & Yan, X. (2011), Organic inorganic hybrid solar cells made from hyperbranched phthalocyanines, *J of Photonics Energy,* Vol. 1, No. 011115.

Messenger, R. A., & Ventre, J. (2004). *Photovoltaic systems engineering*, CRC Press, pp (2).

Metal Pages, n.d. Available from <http://www.metal-pages.com/metalprices/indium/>

Noufi, R., & Zweibel, K. (2006). High efficiency CdTe and CIGS solar cells, *Photovoltaic Energy Conversion Conference*, pp. 317-320.

Ohring, M. (2002). Material Science of Thin Films, *Academic Press,* pp. 95-273.

Powalla, M., & Bonnet, D. (2007). Thin-Film Solar Cells Based on the Polycrystalline Compound Semiconductors CIS and CdTe, *Advances in OptoElectronics 2007*, article ID 97545, 6 pages.

Rau, U., & Schock, H. W. (1999). Electronic properties of Cu(In,Ga)Se_2 hetero-junction solar cells – recent achievements, current understanding, and future challenges, *Appl. Phys., A Mater. Sci. Process.*, Vol. 69, No. 2, pp. 131–147.

Sean, E., & Ghassan, E. (2005). Organic-Based Photovoltaics: Towards Low Cost Power Generation, *MRS bulletin*, Vol. 30, No. 1, pp. 10-15.

Singh, T., & Bedi, R. D. (1998). Growth and properties of aluminium antimonide films produced by hot wall epitaxy on single-crystal KCl, *Thin Solid Films,* Vol. 312, pp. 111-115.

Staebler, D. L., & Wronski, C. R. (1977). Estimation of the degradation of amorphous silicon solar cells, *Appl. Phys. Lett.,* Vol. 31, pp. 292–294.

Tauc, J. (1974). Amorphous and Liquid Semiconductors, *New-York: Plenum*, pp. (159).

Tawada, Okamoto, Y., H., & Hamakawa, Y. (1981). a-Si:C:H/a-Si:H heterojunction solar cells having more than 7.1% conversion efficiency, *Applied Physics Letters*, Vol. 39, pp. 237-239.

Tawada, Y., Kondo, M., Okamoto, Y., H., & Hamakawa, Y. (1982). Hydrogenated amorphous silicon carbide as a window material for high efficiency a-Si solar cells, *Solar Energy Mater.* Vol. 6, pp. 299-315.

Tian, B., Li, F., Bian, Z., Zhao, D., & Huang, C. (2005). Highly crystallized mesoporous TiO_2 films and their applications in dye sensitized solar cells, *J. Mater. Chem.*, Vol. 15, pp. 2414-2424.

US energy information administration (2010). Available from <http://www.eia.doe.gov/oiaf/ieo/world.html>.

Wesiz, P. B. (2004). *Basic choices and constraints on long-term energy supplies*, Physics Today.

Wu, X. (2001). 16.5% CdS/CdTe polycrystalline thin film solar cell, *Proceedings of 17th European Photovoltaic Solar energy Conference*, Munich, pp. 995-1000.

Zanzucchi, P., Wornski, C. R., & Clarson, D. E. (1977). Optical photoconductivity properties of discharge produced a-Si, *J. Appl. Phys.*, Vol. 48, No. 12, pp. 5227-5236.

Zheng, H., Wu, L. Li, B., Hao, X., He, J., Feng, L. Li, W., Zhang, J., & Cai, Y. (2009). The electrical, optical properties of AlSb polycrystalline thin films deposited by magnetron co-sputtering without annealing, *Chin. Phys. B*, Vol. 19, No. 12, pp. 127204-127207.

17

Photons as Working Body of Solar Engines

V.I. Laptev[1] and H. Khlyap[2]
[1]*Russian New University,*
[2]*Kaiserslautern University,*
[1]*Russian Federation*
[2]*Germany*

1. Introduction

Models of solar cells are constructed using the concepts of band theory and thermodynamic principles. The former have been most extensively used in calculations of the efficiency of solar cells (Luque & Marti, 2003; Badesku et al., 2001; De Vos et al., 1993, 1985; Landsberg & Tonge, 1989, 1980; Leff, 1987). Thermodynamic description is performed by two methods. In one of these, balance equations for energy and entropy fluxes are used, whereas the second (the method of cycles) comes to solutions of balance equations (Landsberg & Leff, 1989; Novikov, 1958; Rubin, 1979; De Vos, 1992).Conditions are sought under which energy exchange between radiation and substance produces as much work as possible. Work is maximum when the process is quasi-static. No equilibrium between substance and radiation is, however, attained in solar cells. We therefore believe that the search for continuous sequences of equilibrium states in solar energy conversion, which is not quasi-static on the whole, and an analysis of these states as separate processes aimed at improving the efficiency of solar cells is a problem of current interest. Examples of such use of the maximum work principle have not been found in the literature on radiant energy conversion (Luque & Marti, 2003; Badesku et al., 2001; De Vos et al., 1993, 1992, 1985; Landsberg & Tonge, 1989, 1980; Leff, 1987; Novikov, 1958; Rubin, 1979).

2. Theory of radiant energy conversion into work

2.1 Using model for converting radiant energy into work

We use the model of solar energy conversion (De Vos, 1985) shown in Fig. 1. The absorber of thermal radiation is blackbody *1* with temperature T_A. The blackbody is situated in the center of spherical cavity *2* with mirror walls and lens *3* used to achieve the highest radiation concentration on the black surface by optical methods. Heat absorber *4* with temperature $T_0<T_A$ is in contact with the blackbody.

The filling of cavity *2* with solar radiation is controlled by moving mirror *5*. If the mirror is in the position shown in Fig. 1, the cavity contains two radiations with temperatures T_A and T_S. If the mirror prevents access by solar radiation, the cavity contains radiation from blackbody *1* only. Radiations in excess of these two are not considered. In this model, solar energy conversion occurs at T_0= 300 and T_S = 5800 K. The temperature of the blackbody is T_A = 320 K.

2.2 Energy exchange between radiation and matter

2.2.1 Energy conversion without work production

It is known that the solar radiation in cavity *2* with volume V has energy $U_S=\sigma V T_S^4$ and entropy $S_s=4\sigma V T_S^3/3$, where σ is the Stefan-Boltzmann constant (Bazarov, 1964). The black body absorbs the radiation and emits radiation with energy $U_A=\sigma V T_A^4$ in cavity *2*. If T_A=320 K, these energies stand in a ratio of $U_S/U_A=(T_S/T_A)^4 \approx 10^6$, while $S_S/S_A=(T_S/T_A)^3 \approx 6x10^3$. As the volumes of radiations are equal, the amount of evolved heat ΔQ is proportional to the difference T_A^4-T_S^4 and is equal to the area under the isochore st on the entropy diagram drawn on the plane formed by the temperature (T) and entropy (S) axes in Fig. 2. The solar energy U_S entering the cavity and heat ΔQ are in ratio:

$$\eta_U = \Delta Q / U_S = (U_S - U_A)/U_S = 1-(T_A/T_S)^4. \quad (1)$$

Our model considers the value η_U as an efficiency of the photon reemission for a black body if the radiation and matter do not perform work in this process.

One should note that the efficiency of the photon absorption can be defined as (Wuerfel, 2005)

$$\eta_{abs} = 1-(\Omega_{emit} / \Omega_{abs})(T_A/T_S)^4,$$

where Ω is a solid angle for the incident or emitted radiation. In our case, the ratio $\Omega_{emit}/\Omega_{abs}$ can be ignored because value of η_U is close to one, for $(T_A/T_S)^4=(320/5800)^4 \approx 10^{-5}$. Thereafter we have to assume that $\eta_U = \eta_{abs.}$ The consequence is that solar energy can be almost completely transmitted to the absorber as heat if no work is done. Then a part of evolved heat ΔQ can be tranformed into work.

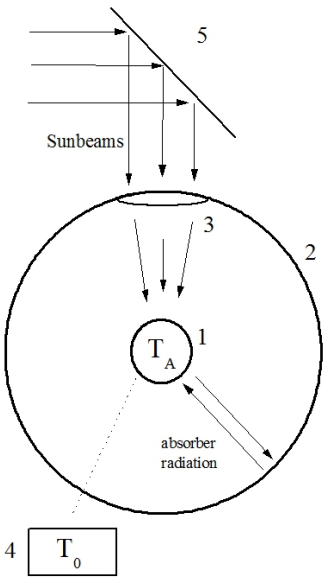

Fig. 1. Model of solar energy conversion from (Landsberg, 1978). Designations: 1. black body, *2*. spherical cavity, *3*. lens, *4*. heat receiver, *5*. movable mirror added by the author.

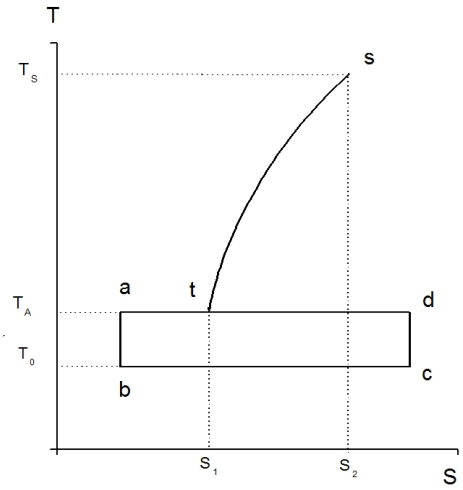

Fig. 2. Entropy diagram showing isochoric cooling of radiation (line st) in the cavity 2. The amount of evolved radiant heat is proportional to the area sts_ts_s. The amount of radiant heat converted into work is proportional to the area abcd. The work is performed by matter in a heat engine during Carnot cycle abcd.

2.2.2 Work production during the Carnot cycles

The absorbed radiant heat is converted into work by Carnot cycles involving matter as a working body. One such cycle is the rectangle abcd in Fig. 2. Work is performed during this cycle with an efficiency of

$$\eta_0 = 1 - T_0/T_A = 0.0625 \quad (2)$$

between the limit temperatures T_0=300 K and T_A=320 K.

It is common to say that the matter is the working body in this cycle. But radiation can be involved in the isothermic process ad in Fig. 2, because the efficiency of a Carnot cycle does not depend on kind and state of the working body. We will not discuss the properties of a matter-radiant working body. Let us simply note that a matter-radiant working body is possible. In this case upper limit of temperature T_A can reach 5800 K. The curve AB on Fig. 3 is the efficiency of this Carnot cycle where the matter cools down and heats up between temperatures T_A, T_0 and radiation has temperature T_A. In this cyclic process the matter and radiation are in equilibrium.

Let us show the absorption of radiation on an entropy diagram (Fig. 4) as an isothermal transfer of radiation from the volume V_2 of the cavity (state s) to the volume V_1 of the black body (state p). One can even reduce the radiation to state p* in Fig. 4. We will not discuss the properties of points p and p* here. Let us simply note that radiation reaches heat equilibrium with the black body (state e) from these points either through the adiabatic process p*e or through the isochoric process pe.

Let us represent the emission of radiation as its transfer from the volume of the black body (state e) to the volume V_2 of the cavity along the isotherm T_A (state t). As the radiation fills the cavity, it performs a work equal to the difference between the evolved and absorbed

heat. The radiation performs a considerable work if it reaches state t* on Fig. 3. Our calculations show that work is performed along the path sp*et* with an efficiency of

$$\eta_C = 1 - T_A/T_S = 0.945 \quad (3)$$

when T_A=320 K. It is important to note that, when radiation returns to its initial state s along the adiabat t*s, it constitutes a Carnot cycle with the same efficiency η_C.

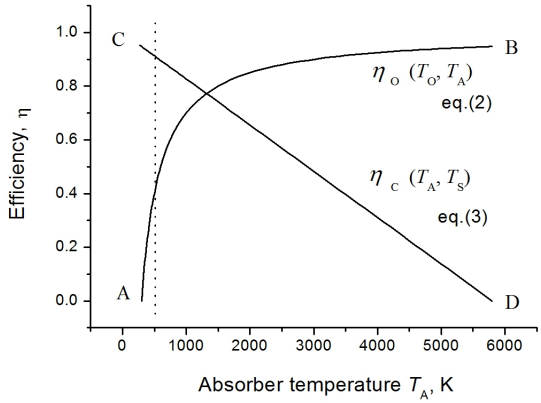

Fig. 3. Efficiencies of Carnot cycles in which the radiation takes place. The efficiency η_0 of work of radiation and matter in a cycle with temperatures limited at T_0 and T_A is shown as curve AB. Line CD shows the efficiency of a cyclic process where work is performed by radiation only.

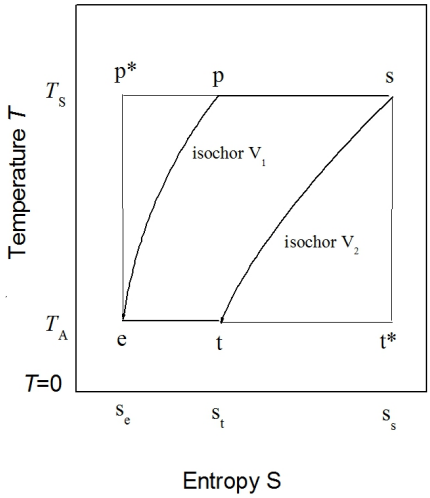

Fig. 4. Entropy diagram showing some thermodynamic cycles for conversion of solar heat into work in cavity 2 with the participation of a black body. Isotherms represent the absorption and emission of radiant energy. Lines pe, p*e correspond to the cooling of radiation in the black body. Line st indicates the temperature and entropy of radiation in cavity.

Fig. 3 compares work efficiencies η_0 and η_C during Carnot cycles described above. Radiation performs work during the Carnot cycle with a greater efficiency than η_0. η_0 and η_C values are calculated from Eqs. (2),(3) as a function of temperature T_A. We see that the efficiency η_C of conversion of heat into work in process with radiation only decreases with increasing temperature of the absorber, but the work efficiency η_0 of matter and radiation increases. Efficiencies are equal to 0.77 at T_A = 1330K.
Fig. 3 is divided in two parts by an isotherm at 500 K. On the left side is the region with temperatures where solar cells are used. The efficiency there of conversion of heat into work can reach value of 0.39 for a Carnot cycle with matter and be above 0.91 during a Carnot cycle with radiation. It is important to note, that other reversible and irrevesible cycles between these limit temperatures have efficiency smaller than efficiencies η_C or η_0.
The efficiency of parallel work done by radiation in the Carnot cycle sp*et*s (Fig. 4) and the matter in the Carnot cycle abcda (Fig. 3) is $\eta_0\eta_C$. It follows from (2) and (3) that

$$\eta_0\,\eta_C = (1-T_0/T_A)(1-T_A/T_S) = 0.0591.$$

After mathematical operations, it takes the form

$$\eta_0\,\eta_C = \eta_0+\eta_C -(1-T_0/T_S)= \eta_0+\eta_C-\eta_{OS},$$

where

$$\eta_{OS} = (1-T_0/T_S) \tag{4}$$

is the efficiency of the Carnot cycle in which the isotherm T_S corresponds to radiation and isotherm T_0, to the matter. Efficiency η_{OS} is independed from an absorber temperature T_A which divides adiabates in two parts. Upper parts of adiabates correspond to the change of radiation temperature, bottom parts to that of matter. It is important that such a Carnot cycle allows us to treat radiant heat absorption and emission as an isothermal and adiabatic processes performed by the matter. Efficiency η_{OS} is limiting for solar-heat engine. It is equal to 0.948 for limit temperatures T_0=300 K and T_S=5800 K. This Carnot cycle is not described in literature.

2.2.3 Work production during unlike Carnot cycles

Solar energy is converted as a result of a combination of different processes. Their mechanisms are mostly unknown. For this reason, one tries to establish the temperature dependence of the limit efficiency of a reversible combined process with the help of balance equations for energy and entropy flows. For solar engine, it takes the form (Landsberg, 1980; 1978)

$$\eta_{AS} = 1 - 4T_A/3T_S + T_A^4/3T_S^4. \tag{5}$$

For example, η_{AS} = 0.926 when T_A=320 K. Fig. 5 compares work efficiencies η_{AS} and η_C during the cycles with radiant working body at the same limit temperatures. η_{AS} and η_C values are calculated from Eqs. (3),(5) as a function of absorber temperature T_A. We see that $\eta_{AS} < \eta_C$, that is not presenting controversy to the Carnot theorem. The efficiencies η_{AS} and η_C of conversion of radiant heat into work decreases with increasing absorber temperature. The maximum difference η_C-η_{AS} is approx. 18% when T_A=3500 K (Landsberg, 1980; 1978).
The maximal value of the efficiency if for a black body at a temperature $T_A < T_S$ were possible to absorb the radiation from the sun without creating entropy is shown in (Wuerfel,

2005). It follows from a balance of absorbed and emitted energy and entropy flows under the condition of reversibility. The efficiency of a reversible process in which radiation and matter perform work is equal to

$$\eta_L = 1-(T_A/T_S)^4 - 4T_0\,[1 - (T_A/T_S)^3]/3T_S. \quad (6)$$

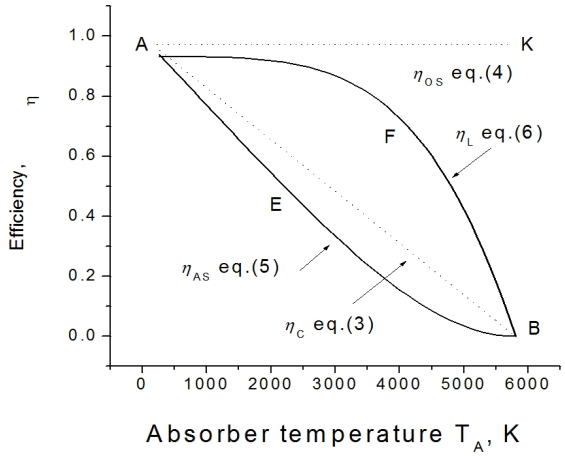

Fig. 5. Consideration of Carnot efficiencies and efficiencies of reversible processes other than the Carnot cycle. Dot lines AB,AK denote Carnot efficiencies η_C and η_{OS} at lower limit temperatures 320 and 300 K respectively. Solid curves AFB and AEB are efficiencies η_L and η_{AS} of non-Carnot engines at the same limit temperatures. Line AK and curve AFB discribe cycles with a radiant-matter working bodies. In the same time line AB and curve AEB describe cycles with radiant working body only.

For example, η_L = 0.931 when T_A=320 K and T_0=300 K. Condition T_0=T_A excludes temperature T_0 from expression (6) which in this case is described by the Eq. (5). It means that the work can be obtained during a cycle with a radiant and matter working bodies. Dependencies (5), (6) are shown in the Fig. 5 by curves AFB and AEB, respectively. Line AB presenting η_C from Eq. (3) and line AK presenting η_{OS} from Eq. (4) are also shown.

3. Elementary and matter-radiant working bodies

Two types of working body are considered:

- Elementary working body – matter or radiation in one cycle;
- Matter-radiant working body – matter and radiation in one cycle.

3.1 Energy conversion without irrevocable losses

According to Carnot theorem, an efficiency of a Carnot engine does not depend on a chemical nature, physical and aggregate states of a working body. The work presents a peculiarity of applying this theorem for solar cells. The statement is that the maximal efficiency of solar cells can be achieved with help of a combined working body only. Let's consider it in detail.

For example, the maximal efficiencies of the solar energy conversion are equal 94.8% at the limit temperatures 300 K and 5800 K (η_{OS} in the Table 1). Under these temperatures the efficiencies of the solar energy conversion can be equal 5.91% ($\eta_O\eta_C$ in Table 1). The one belongs to a Carnot cycle, in which a matter and radiation are found as a combined working body, i.e. matter and radiation as a whole system. The other belongs to 2 cycles running parallel. A matter performs the work with a low efficiency 6.25% (η_O in Table 1), but the radiation performs the work with a high efficiency 94.5% (η_C in Table 1). In these cases matter and radiation are elementary working bodies. The efficiencies of these parallel processes is

$$\eta_0\eta_C = 0.948 * 0.0625 = 0.0591 = 5.91\%.$$

Table 1 shows that a matter performs the work with a low efficiency in solar cells. However, the efficiency of the radiant work at the same absorber temperature is considerably higher. For example, a radiation performs the work with efficiency 92.6% during a non-Carnot cycle (η_{AS} in Table 1), but a matter produces work only with an efficiency 6.25% (η_0 in Table 1) at the absorber temperature 320 K. This difference is caused by various limit temperatures of the cycles (Table 1). The efficiencies of these processes running parallelis smaller than that of $\eta_0\eta_C$:

$$\eta_0\eta_{AS} = 0.926 * 0.0625 = 0.0579 = 5.79\%.$$

However, at the same temperatures the efficiency of solar energy conversion achieves 94.8% (η_{OS} in Table 1), if a work is performed during a cycle with the matter-radiant working body.

Classification of engines	**Efficiency at T_A = 320 K and other parameters of cycles**					
	Cycle	**Working body**	**Limit tempe-ratures,K**	**Symbols**	**Limit, %**	**Calcilated equation**
Carnot engines						
heat	Carnot	Elementary / *matter or radiation*	300-320	η_0	6.25	2
solar	Carnot	elementary	320-5800	η_C	94.5	3
ideal solar-heat	Carnot	matter-radiation / *matter and radiation in one cycle*	300-5800	η_{OS}	94.8	4
non-Carnot engines						
solar	non-Carnot	elementary	320-5800	η_{AS}	92.6	5
solar- heat	non-Carnot	matter-radiation	300-5800	η_L	93.1	6
combined engines						
combined	Carnot, Carnot	elementary	300-320 320-5800	$\eta_0\eta_c$	5.91	2,3
combined	Carnot Carnot	elementary	300-320 300-5800	$\eta_0\eta_{OS}$	5.93	2,4
combined	Carnot, non-Carnot	elementary	300-320 320-5800	$\eta_0\eta_{AS}$	5.79	2,5
combined	Carnot, non-Carnot	elementary	300-320 300-5800	$\eta_0\eta_L$	5.82	2,6

Table 1. Classification and efficiencies of the engines with the elementary and matter-radiant working bodies

A Carnot cycle with the efficiency η_{OS} and the matter-radiant working body has been considered by the author earlier in the chapter, its efficiency is given by eq.4. Further we will call an engine with the matter-radiant working body an ideal solar-heat one. The elementary working bodies perform the work by solar or heat engines. Their properties are listed in Table 1. The advantage of the cyclic processes in comparison with the matter-radiant working body is obvious.

So, the elementary working bodies perform the work with the efficiencies η_0, η_C, η_L and η_{AS}. The matter-radiant working bodies perform the work with the efficiency η_{OS}. According to the Table. 1, one can confirm:

- a Carnot cycle with the matter-radiant working body has a maximally possible efficiency of solar energy conversion. It is equal 94.8% and does not depend on absorber temperature T_A. Engine where work is done during such cycle we will call an ideal solar-heat engine.
- electrical energy can be obtained under operating an ideal heat-solar engine with a very high efficiency and without additional function of low efficiency heat engine.

Therefore, high efficiency solar cells should be designed as solar-heat engine only.

3.2 Energy conversion with irrevocable losses

The absorption of radiation precedes the conversion of solar heat into work. In our model, the black body absorbs solar radiation and generates another radiation with a smaller temperature. Heat is evolved in this process; it is either converted into work or irrevocable lost. In this work the photon absorption in solar cells is divided into processes with and without work production. For the sake of simplicity, let us assume that heat evolved during solar energy reemission is lost with an efficiency of η_U from Eq. (1). The work of the cyclic processes is performed with the efficiencies of η_0, η_C, η_{AS}, η_{OS} and η_L (Tabl. 1). Then the conversion of solar heat with and without work production is performed with the efficiencies, for example, $\eta_C\eta_U$ or $\eta_0\eta_C\eta_U$. These and other combinations of efficiencies are compared in (Laptev, 2008).

It is important to note that the irrevocable energy losses of absorber at temperature 320 K do not cause the researchers' interest in thermodynamic analysis of conversion of solar heat into work. Actually, efficiency of the solar energy reemission as the irrevocable energy losses μ_U is close to 1 for $(T_A/T_S)^4 = (320/5800)^4 \approx 10^{-5}$. So efficiency of the solar energy reemission at 320 K has a small effect on efficiency of solar cell. The Tables 1,2 list efficiencies of the solar cells with and without irrevocable losses calculated in this work. The difference between these values does not exceed 0.01%. Values of $\mu_0\mu_C$ and $\mu_0\mu_C\mu_U$ may serve as examples. It might be seen that irrevocable energy losses are not to be taken into account in the thermodynamic analysis of conversion of solar heat into work. However, the detailed analysis of efficiencies of conversion of solar heat into work enabled us to reveal a correlation between the reversibility of solar energy reemission and efficiency of solar cell. The following parts of the chapter are devoted to this important aspect of conversion of solar heat into work.

3.3 Combinations of reversible and irreversible energy conversion processes

The temperature dependencies of μ_L from Eq. (5) and $\mu_0\mu_U$ from Eqs. (1),(2) are shown by lines LB, CB in Fig. 6. Let us also make use of the fact that every point of the line LB is (by definition) a graphical illustration of the sequence of reversible transitions from one energy state of the system to another, because each reversible process consists of the sequence of reversible transitions only.

Cycle parameters			Efficiency at T_A=320 K			
working body	**cycle**	**Limit temperatures,K**	**Symbols**	**Limit, %**	**eq-tion**	
non-working conversion						
-	reemission	320-5800	η_U	99.99	1	
heat, solar and heat-solar endoreversible engines						
elementary*	Carnot	300-320	$\mu_0\mu_U$	6.25	1, 2	
elementary	Carnot	320-5800	$\mu_C\mu_U$	94.5	1, 3	
elementary	non-Carnot	320-5800	$\mu_{AS}\mu_U$	92.6	1, 5	
matter-radiation**	non-Carnot	300-5800	$\mu_L\mu_U$	93.1	6	
matter-radiation	Carnot	300-5800	$\mu_{OS}\mu_U$	94.8	1, 4	
Combined endoreversible engines						
elementary	Carnot	300-320/320-5800	$\mu_0\mu_C\mu_U$	5.91	1, 2, 3	
elementary	Carnot/non-Carnot	300-320/320-5800	$\mu_0\mu_{AS}\mu_U$	5.79	1, 2, 5	
elementary	Carnot	300-320/300-5800	$\mu_0\mu_{0S}\mu_U$	5.93	1, 2, 4	
elementary	Carnot	300-320/320-5800/300-5800	$\mu_0\mu_C\mu_{0S}\mu_U$	5.60	1, 2, 3, 4	
elementary and matter-radiation	Carnot/non-Carnot	300-320/300-5800/320-5800	$\mu_0\mu_{0S}\mu_{AS}\mu_U$	5.49	1, 2, 4, 5	

* elementary working body – matter or radiation;
** matter-radiant working body – matter and radiation in one cycle.

Table 2. Classification and efficiencies of the engines with solar energy conversion as a irrevocably losses

Based on this statement one can say that every point of the line CB is (by definition) a graphical illustration of the sequence of reversible and irreversible energy transitions. First represent a Carnot cycle abcd in the Fig.2, second represent a process of cooling of radiation running according to the line st. This engine performs the work with the efficiency $\mu_0\mu_U$. The combination of reversible and irreversible processes allows us to call this engine an endoreversible. Engines with the efficiencies μ_L and μ_0 are reversible.

Curves CB и LB in Fig.6 have some dicrepancy because of the entropy production without a work production in endoreversible engine. Indeed reversible energy conversion with the efficiency μ_L or μ_0 occurs without entropy production. The energy conversion with efficiency μ_0 μ_U is accompanied by the entropy production during the solar energy reemissions. The latter ones do not take place in the work production and cause irrevocably losses.

So, the entropy is not performed during a reversible engines. Endoreversible engines perform the entropy. Thus, the author supposes that difference between efficiencies (μ_L- μ_0 μ_U) of these engines is proportional to the quality (or number) of irreversible transitions. In most cases the increase of number of irreversible transitions in conversion of radiant heat into irrevocably losses calls a reduce of the efficiency of engine from μ_L down to μ_0 μ_U.

Then, with help of the Fig. 6 one can find a ratio of reversible and irreversible transitions in a solar cell performing the work with the efficiency $\mu_0\,\mu_U$. For example, let point *a* on Fig. 6 denote the conversion of solar energy with an efficiency of 30%. Let us draw an isotherm running through the point *a*; the intersections of this line with the line LB and the y-axis give us the values $\mu_L = 0.93$ and T_A=430 K. Then, by the lever principle, the fraction of irreversible transitions q_{ir} in point *a* is

$$q_{ir} = (\mu_L\text{-}30)100/\ \mu_L = 68\%.$$

The fraction of irreversible transitions q_{rev} in point *a* will be 100–68=32%.
In other words, when in solar-heat engine (with the efficiency μ_L) 68% energy transitions can be made irreversible then the radiant work production will be ceased. If the reversible transitions (their number is now 32% of the total transitions' number) may form a Carnot cycle with the efficiency μ_0, then one can say that the reduce of number of reversible transitions leads to a cease of radiant work production, makes it possible to continue matter work production and reduces efficiency of engine from 93% down to 30%. The radiant heat evolved under these conditions partially takes a form of irrevocably losses as irreversible non-working transitions.

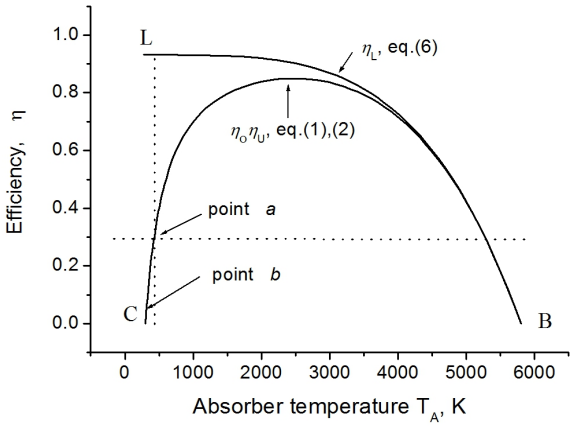

Fig. 6. Efficiency μ_L of solar-heat reversible engine (line LB) as a function of the absorber temperature T_A compared with the efficiency $\mu_0\mu_U$ of an heat endoreversible engine (line CB). Every point of the line LB correspond to 100% reversible transitions in energy conversion without entropy production. Every point of the line CB correspond to 100% irreversible transitions in energy conversion without work production. Every point of the region LBC between lines LB and CB correspond the reversible and irreversible transitions. Their parts can be found according to the lever's law (see text).

Let's consider a case of parallel work of matter and radiation. One could assume the work of radiation should increase an efficiency of solar-heat engine. However, it is not correct. The efficiencies of endoreversible processes whose elements are Carnot cycles with the efficiencies μ_C and μ_0 are shown in Fig. 7 by the CEB and CFB lines. They are situated below the LB line, whose every point is the efficiency μ_L of a reversible process by definition. We can therefore calculate the contributions of the Carnot cycle to the efficiencies $\mu_0\,\mu_U$ and μ_0

μ_C μ_U if the efficiency μ_L (μ-coordinates of line LB points) is taken as one. For example, the efficiency μ_0 μ_U at 320 K (point *b* in Fig.6) is 6.25% (Tabl.2). Let us draw an isotherm running through the point *b*; the intersections of this line with the line LB and the y-axis give us the value μ_L = 0.931. Then, by the lever principle, point *b* corresponds to a fraction

$$q_{ir} = (\mu_L\text{-}0.0625)100/\ \mu_L\text{=}93.3\%$$

of the irreversible transitions and the fraction q_{rev} = 6.7% of the reversible ones in conversion solar energy with the efficiency μ_0 μ_U=6.25%. If matter and radiation produce work with the efficiency μ_0 μ_C μ_U=5.91% at 320 K (Tabl.2), the fraction of irreversible transitions as irrevocably losses is

$$q_{ir} = (\mu_L\text{-}5.91)100/\ \mu_L\text{=}93.6\%.$$

The fraction of irreversible transitions q_{rev} of two Carnot cycles will be equal 100-93.6=6.4%. Thus, when matter and radiation produce work simultaneously in Carnot cycles, only less then 7% of energy transitions in solar energy conversion are working cycles. Remaining 97% of energy transitions in solar energy conversion are non-working processes. So, the efficiency of solar-heat engine sufficiently depends on the reversability of non-working processes, rather than on the efficiencies of the work cycles. Let's explain in more details.

3.4 Reversible and irreversible non-working processes

As it was mentioned above, the reason of descrepancy between curves μ_L, $\mu_0\mu_U$ and $\mu_0\mu_C\mu_U$ at T_A<T_S is entropy production during the processes without work production. Then the μ-coordinates of the points belonging to the plane between line μ_L and the lines $\mu_0\mu_U$, $\mu_0\mu_C\mu_U$ on Fig. 7 are proportional to the shares of the reversible and irreversible transitions without work production. We propose the following method for calculating relative contributions of reversible and irreversible processes without work production.

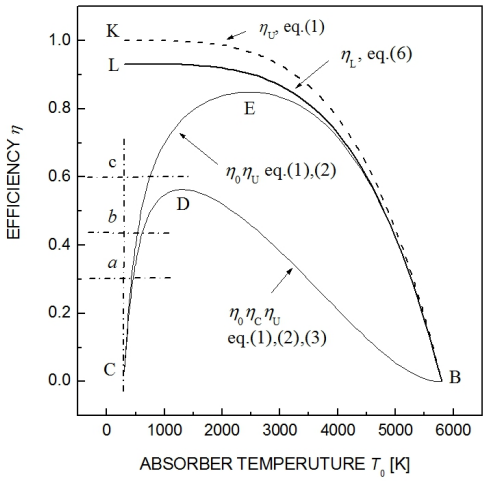

Fig. 7. The comparison of the well-known thermodynamic efficiency limitations of the solar energy conversion with and without entropy production.

The temperature dependencies of μ_L, $\mu_0\mu_U$, $\mu_0\mu_C\mu_U$ derived from Eqs. (1),(2),(3) and(6) are shown by lines LB, CEB and CDB in Fig. 7. Remember that the μ-coordinates of the points belonging to the lines $\mu_0\mu_U$, $\mu_0\mu_C\mu_U$ are proportional to the shares of reversible transitions which are one or two Carnot cycles with the efficiencies μ_0 and μ_C. At the same time remaining 100% irreversible transitions are (form) irreversible processes without work production as irrevocably losses.

The lines CEB and CDB on Fig. 7 are not only the illustration of possible ways of converting solar energy. For example, it is known that the limiting efficiencies of solar cells on the basis of a p,n-transition are 30% (Shockley & Queisser, 1961) and 43% (Werner et al., 1994). at T_A=320 K. They are shown by points *a* and *b* on Fig. 7 and lie above the lines $\mu_0\mu_U$, $\mu_0\mu_C\mu_U$, but below the line μ_L. One can say that processes without work production may be the combination of reversible and irreversible processes running parallel. Then the μ-coordinates of the points above the lines CEB, CDB are proportional to the shares q of reversible and irreversible transitions, which are appearing as processes without work production. According to the lever's principle, fraction of irreversible transitions q_{ir} in conversion of solar energy is

$$q_{ir} = (\mu_L - \mu_0\mu_C\mu_U)100/\mu_L.$$

For example, according to Tabl. 1,2, μ_L=93.1% and $\mu_0\mu_C\mu_U$=5.91% at T_A=320 K. Then q_{ir} = (93.1-5.91)100/93.1=93.7%. The fraction of reversible transitions q_{rev} is 100-93.7=6.3%.

Point *a* in Fig.7 denotes the conversion of solar energy with an efficiency μ=30% at T_A=320 K. It lies above the line $\mu_0\mu_C\mu_U$. Then the value

$$q_{ir} = (\mu_L - \mu)100/(\mu_L - \mu_0\mu_C\mu_U)$$

is a part of irreversible transitions in the conversion of solar energy without work production. In our case it is (93.1-30)100/(93.1-5.91)=70.0%. The fraction of reversible transitions will be equal to 100-70.0=30.0%. Note that there are no reversible transitions of Carnot cycles.

The band theory proposes mechanisms of converting solar energy into work with an efficiency of 43% (Landsberg & Leff, 1989). Let us denote last value by the point *b* on the isotherm in Fig. 7. Then the fraction of irreversible transitions q_{ir} without work production is (93.1-43)100/(93.1-5.91)= 57.5%, and the fraction of reversible transitions q_{rev} without work production will be equal 100-57.5=42.5%. So that, to increase efficiency of endorevesible solar-heat engine from 30 up to 43% at T_A=320 K, it's necessary to reduce a fraction of irreversible transitions without work production from 72.4% down to 57.5%.

As an example of reverse calculations let's find out efficiency of solar-heat engine with 50% irreversible transitions without work production. Denote the value is to be found as x and write down the equation

$$q_{ir} = (93.1-x)100/(93.1-5.91) = 50\%.$$

Solving it reveal that x=49.5%. Note that for q_{ir} = 100% efficiency $\mu_0\mu_C\mu_U$=50% may be achieved only under T_A=700 K (see Fig.7). This temperature is much higher than the temperatures of solar cells' exploitation (the temperatures of solar cells' working conditions) Thus, the author supposes the key for further increase of solar cells' efficiency is in the study and perfecting processes without work production.

3.5 Ideal solar-heat engines

According to the Eqs. (4),(6), there are two efficiency limits of solar energy conversion in reversible processes for a pair of limiting temperatures T_0 and T_S, namely, μ_{OS}, μ_L. In the Fig. 8 are shown their dependencies on absorber temperature T_A. Obviously, under all values of T_A the condition $\mu_{OS} > \mu_L$ is fulfilled. The suggestion can be made that processes can occur whose efficiency is between these limits. By virtue of the second law of thermodynamics, they cannot be reversible.

For instance, radiant energy conversion with the efficiency $\mu_{OS}\mu_U$ is irreversible, because radiation performs an irreversible process with the efficiency μ_U along the line st shown in Fig. 2. We see from Fig. 8 that the $\mu_{OS}\,\mu_U$ values (line AB) at temperatures $T_A << T_S$ are indeed larger than μ_L (line LB) and smaller than μ_{OS} (line AD).

In each point of the line AB the irreversible processes appeare as a sequence of transitions without work production. Because the efficiency $\mu_{OS}\,\mu_U$ of the processes with their participation larger then μ_L, one can suppose that the fraction of irreversible transitions along the line LB is equal to zero, and along the line AB is equal to unity. In the plane between lines AB и LB the fraction of irreversible transitions q_{ir} may be calculated according to the lever principle:

$$q_{ir} = (\mu_{OS}\mu_U - \mu)100/(\mu_{OS}\mu_U - \mu_L).$$

In each point of the line AB the fraction of irreversible transitions q^0_i of total number of irrevesible transitions is

$$q^0_{ir} = (\mu_{OS}\mu_U - \mu_L)100/(\mu_S\mu_U).$$

According to the Tables 1, 2, q^0_{ir}=1.8% at T_A=320 K. The processes consisting of these transitions, do not produce work.

So, along the line AD (Fig. 8) conversion of solar energy is perfomed during a Carnot cycle, along the line AB – during a Carnot cycle and the processes without work production. In the plane between these lines only work is perfomed. The working process is a non-Carnot cycle.

Between the lines AB and LB non-working processes are reversible and irreversible. There the fraction of irrevesible transitions decreases with closing the line LB. Along the line LB all energy transitions (with and without work production) are reversible, i.e. q^0_{ir}=0.

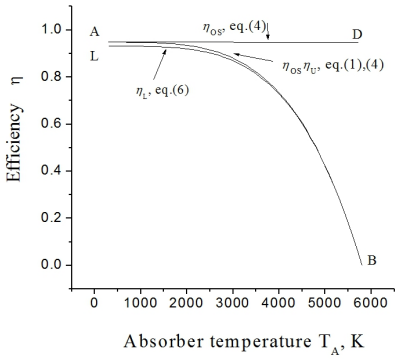

Fig. 8. Comparison of the efficiency $\mu_{OS}\mu_U$ of combinations of reversible working and irreversible non-working processes (the AB line) with the efficiency μ_{OS} of a reversible Carnot working process (the AD line) and the efficiency μ_L of reversible non-Carnot working processes (the LB line). Lines AD и AB coincide at T_A=0 K.

Irreversible processes without work production appear under the line LB. Their fraction increase as we move off the line LB. The previous chapter gives examples of calculating their contributions to solar energy conversion.

The value μ_L is a keyword in separation of solar energy conversion in processes with and without work production. It is referred as Landsberg efficiency (Wuerfel, 2005). According to this tradition, solar-heat engine with the efficiency μ_L are called Landsberg engine. It has a minimal efficiency of all solar-heat engines.

Solar-heat engine with the maximal efficiency μ_{OS} we call ideal solar-heat engine. Then solar-heat engine with the efficiency between μ_{OS} и $\mu_{OS}\mu_U$ may be noted as ideal non-Carnot solar-heat engine, and a solar-heat engine with the efficiency between $\mu_{OS}\mu_U$ and μ_L as an endoreversible solar-heat engine.

Solar-heat engine have cycles with the matter-radiant working body. We will not discuss the properties of the matter-radiant working body here. Let us simply note that all energy transitions in solar-heat engines are performed by the matter-radiant working body (Table 3). In the endoreversible solar-heat engine the matter-radiant working body makes working transitions, their fraction of total number of energy transitions is 100-1.8=98.2% because the processes without work production have only 1.8% energy transitions. Engine with the matter-radiant working body is not produced yet.

Engine	*Efficiency at 320 K*	*contributions of energy transitions, %*		*matter and radiation state*
		working	*non-working*	
Idel Carnot solar-heat	94.80	100	-	equilibrium
Ideal non-Carnot solar-heat	94.79	100	-	equilibrium
Endoreversible solar-heat	93.10-94.79	98.2	1.8	Non-equilibrium
Landsberg reversible	93.10	< 7	>93	equilibrium
Combined endoreversible	<6	< 7	>93	Non-equilibrium

Table 3. Comparison between the engine efficiencies and the contributions of working and non-working transitions

Existent solar cells are endoreversible combined engines with the non-Carnot cycles and elementary working bodies (matter or radiation). The working bodies perform working energy transitions, their fraction (as it is shown in the Table 3) can achieve only 7 % of transitions total number. We cannot overcome this 7% barrier but it doesn't mean that there is no possibility to increase the efficiency of such a machine. According to the Table 3, the non-working transitions are more than 93% from the total number of energy transitions. They can be either irreversible or revesible. If the first are made as the last, the engine efficiency can be increased from 6 up to 93.1%. So the aim of perfection in endoreversible solar-heat engine processes without work production is arisen. In ideal case it is necessary to obtain Landsberg engine.

So, efficiencies of the combined endoreversible engines with the non-Carnot cycles and elementary working bodies (matter or radiation) mostly depend on reversibility of processes without work production, running in the radiation absorber rather than on the work

production processes. It follows that the contribution of reversible processes is smaller than the contribution of irreversible processes in devices that are currently used. According to the maximum work principle, their efficiency can be increased by increasing the fraction of reversible processes in solar energy absorbers. The following approach to solution of this problem can be suggested.

4. Antenna states and processes

Antenna states of atomic particles or their groups are the states between them resulting from the reemission of photons without work production and heat dissipation. Below is shown that a comparison of the efficiencies of the reversible and irreversible photon reemissions occuring in parallel made it clear that it is impossible to attain very high efficiencies in the conversion of solar heat into work without the reversible photon reemissions as antenna process.

4.1 Photon reemissions as non-working processes

Matter and solar radiation are never in equilibrium in solar cells and quasi-static conversion of the solar energy is not achieved. For this reason, the irreversible thermodynamic engines are described using the method of endoreversible thermodynamics of solar energy conversion (Novikov, 1958; Rubin, 1979; De Vos, 1992). Remember that endoreversible engines are irreversible engines where all irreversibilities are restricted to the coupling of engine to the external world. It is assumed that the inner reversible part of an endoreversible engine is a Carnot cycle. We have also considered the non-Carnot cycles and found out that photon absorption in solar cells can be considered as the external reversible part of an endoreversible engine.

The photon absorption in solar cells is separated into processes with and without work production. These processes are sequencies of transitions from one energy state of the system to another. The energy transitions between particle states are called "photon reemission" if they do not take part in performing work and heat dissipation.

The photon reemission is divided into reversible and irreversible processes. These non-working processes are regarded as a continuous series of equilibrium states outside the irreversible or endoreversible engine, are isolate into separate processes, and are used to obtain a higher efficiency of the generally non-quasistatic solar energy conversion. We can consider those equilibrium processes as a base of the „exoreversible“additional device for the irreversible or endoreversible engine.

So, we have called the processes without work production photon reemission. Let us now shown that they play a special role in the conversion of solar heat into work.

4.2 Antenna states of the absorber particles

Let us consider these particle states in a radiant energy absorber, transitions between them result from the absorption of photons. The states of atomic particles or their groups, as well as energy transitions between them, are called "working" if they take part in performing work. It is known that solar energy conversions are not always working processes. The states of atomic particles and the energy transitions between them are said to be "antenna" ones if they take part in the absorption and emission of radiant energy without work production, i.e. in the photon reemission. Carnot cycles are examples of working processes, while cycles described below involving the photon reemission are examples of antenna processes.

It is clear that antenna and working states are equilibrium ones if cycles of the radiant energy conversion are not accompanied by entropy production, i.e. if it takes place along line LB on Fig. 9 with an efficiency μ_L from Eq. (5). Let us take their total amount to be 100%. Now assume that the conversion of radiant energy consists of reversible working processes with an efficiency μ_O from Eq. (2) for matter, with an efficiency μ_{AS} from Eq. (5) for radiation and irreversible with an efficiency μ_U from Eq. (1) for irreversible antenna processes, i.e. that the conversion of radiant energy corresponds to line CEB. In this case, the μ-coordinates of all points belonging to the line CEB divided by μ_L are equal to the fraction of working states, while $1-\mu/\mu_L$ is equal to the fraction of antenna non-equilibrium states.
Fig. 9 shows that the number of antenna non-equilibrium states in solar cells decreases as the efficiency μ grows along lines CE and CF. The isothermal growth of the efficiency μ implies that the total amount of antenna states remains constant, but certain antenna states have become equilibrium states and that reversible transitions that do not generate work have appeared. If the temperature dependence of μ is determined by experiment, Fig. 9 becomes in our opinion an effective tool for interpreting and modeling the paths along which work is performed by solar cells. We can consider Fig. 9 as the reversibility diagram of the conversion of solar heat into work.

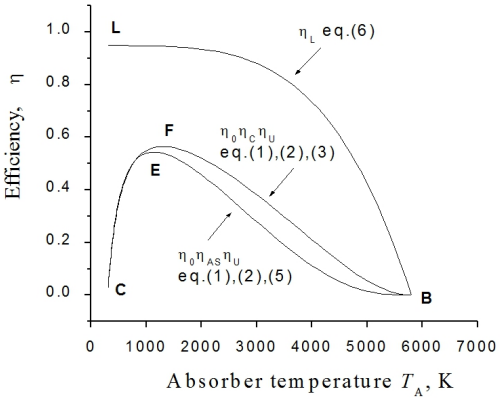

Fig. 9. Comparison of the efficiency μ_L of Landsberg engine (the LB line) with the efficiencies of combined engines (the CEB, CFB lines). A difference between the efficiencies $\eta_0\eta_{AS}\eta_U$ and $\mu_O\mu_C\mu_U$ is that in the first case radiation working cycle is not a Carnot cycle. Lines CEB and CFB are practically coincide at temperatures used for operation of solar cells.

Obviously, knowledge of physical and chemical nature of antenna states of particles is important for revealing optimal schemes for radiant energy conversion. The question about technical realization of antenna states is not subject of this chapter. This is a material science problem. One only should note the model of absorber with antenna states does not contradict to thermodynamic laws and represents a way of solution of following aim: how to separate any given cycle into infinite number of infinitely small arbitrary cycles.

4.3 Antenna processes

The absorption and generation of photons in the abcd (Fig. 2) and spet (Fig. 4) processes is accompanied by the production of work. No work is done in the st process (Fig. 2). This

difference can be used to divide all processes with the absorption and generation of photons into two types. The first type includes processes in which the matter and radiation do work, that is, participate in the working process. The second type includes processes in which the substance absorbs and emits radiant energy without doing work, that is, participates in an antenna process. The spontaneous evening out of the temperatures of the matter and radiation is an example of antenna processes, and radiant energy conversion in a solar cell is a combination of processes of the first and second type.

The highest efficiency of a combination of work and antenna processes is described by the line AB in Fig. 8. If the work is performed during a non-Carnot cycle then efficiency of the work and antenna processes is described by the LB line. The difference between $\eta_{OS}\eta_U$ and η_L is 94.8-93.1=1.7%. For analysis of antenna processes one should choose the temperature dependence of the value η_L because in this case a conversion process is reversible.

The CEB line in Fig.9 shows the efficiency of a combination of work done by matter (in a Carnot cycle with the efficiency η_0), by radiation (in a non-Carnot cycle with the efficiency η_{AS}) and a background antenna process with the efficiency η_U. The η coordinates of the CEB line divided by η_L describe the largest contribution of working processes to the efficiency of solar energy conversion if η_L is taken as one. The contribution of the antenna process is then $1- \eta_0\eta_{AS}\eta_U/\eta_L$.

It follows that the efficiency of conversion higher than $\eta_0\eta_{AS}\eta_U$ (the region between the LB and CEB lines, Fig. 9) can be obtained by perfecting the antenna process only. The efficiency of solar energy conversion is maximum in this case if all antenna processes are reversible. The efficiency is minimum if all antenna processes are irreversible.

The η coordinates of points between the LB and CEB lines are then proportional to the fraction of reversible antenna processes. An irreversible antenna process corresponds to the $1 - \eta/\eta_L$ value. The character of this dependence will not be discussed here. Only note that Fig. 9 can be used to calculate the fractions of work and antenna processes, as well as contributions of reversible and irreversible antenna processes in solar energy conversion if experimental data on the temperature dependence of the solar cell efficiency are available.

So, the antenna processes in Landsberg engine are reversible. When antenna processes are made irreversible, then the efficiency of transformation of radiant energy decreases from η_L=94.8% down to $\eta_0\eta_{AS}\eta_U$=5.79% at T_A=320 K. We have to select the opposite way.

4.4 Photon reemissions as reversible antenna processes

The notion of the reversibility of a process is applicable to any thermodynamic system, although we have not found it applied to quantum systems in physical literature. Let us recall that the transition of a system from equilibrium state 1 to equilibrium state 2 is called reversible (i.e., bi-directional) if one can return from state 2 to state 1 without making any changes in the surrounding environment, i.e. without compensations. The transition of a system from state 1 to state 2 is said to be irreversible if it is impossible to return from state 2 to state 1 without compensations.

Let us consider these particle states in an absorber, transitions between them result from the absorption of photons. The state of radiation will not change if the photon reemissions (121) or (12321) can take place (Fig. 10). These reemission processes will be reversible ones if the equilibrium state of matter is not violated by a photon absorption. According to these definitions, the reemission (123) or (1231) will alter the frequency distribution of photons (Fig. 11). For this reason, such reemission processes are irreversible.

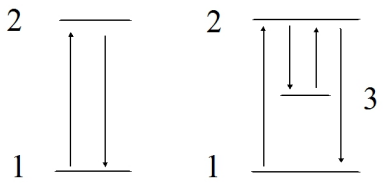

Fig. 10. The reversible reemissions in the systems with 2 and 3 energy levels.

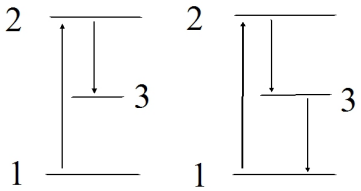

Fig. 11. The irreversible reemissions in the systems with 3 energy levels.

4.5 Photon reemissions as quasi-static process

Every quasi-static process is reversible and infinitely slow. Are the continuous series of the photon reemissions $(121)_n$ and $(12321)_n$ quasi-static processes? For the sake of simplicity, let us approximate the spatial arrangement of particles by a periodic chain of elements that have a length of 2μm (absorber thickness) and that are separated by 2 Å (atomic distance). Use the identity of electronic states 1, 2, 3 in particles **A** and present the sequence of electronic excitations in the particles' chain with help of reemission cycles in the Figs. 10, 11, for example, as follows:

$$\begin{aligned}
&\mathbf{A}_1+h\upsilon_{12}\rightarrow \\
&\quad\rightarrow\mathbf{A}_{1\rightarrow2\rightarrow1}+h\upsilon_{21}\rightarrow \\
&\qquad\rightarrow\mathbf{A}_{1\rightarrow2\rightarrow3\rightarrow1}+h\upsilon_{23}+h\upsilon_{31}\rightarrow \\
&\qquad\qquad\rightarrow\mathbf{A}_{1\rightarrow3\rightarrow1}+h\upsilon_{31}\rightarrow \\
&\qquad\qquad\qquad\rightarrow\mathbf{A}_{1\rightarrow3\rightarrow2\rightarrow1}+h\upsilon_{21}\rightarrow \ldots. \\
&\qquad\qquad\qquad\qquad\rightarrow \mathbf{A}_{1\rightarrow2\rightarrow1}+h\upsilon_{21} \qquad (7)
\end{aligned}$$

In this expression the first particle is excited by the photon with energy $h\upsilon_{21}$ and emits the same photon. This emitted photon excites the second particle, which emits two photons with energies $h\upsilon_{23}$ and $h\upsilon_{31}$. They, in turn, excite the third particle and so on.

The time period during which solar radiation will excite only the first particle in the chain, while subsequent particles are excited only by reemitted photons, is equal to 10^{-4} s if the lifetime of the excited state is ~10^{-8} s. The time needed for the wave to travel down the chain and excite only the last particle is ~10^{-14} s. These time intervals are related to each other as 320 years to one second. Therefore, the energy exchange due to reemission in a chain of particles is an infinitely slow process in comparison with the diffusion of electromagnetic radiation in the chain. Even the multiple repetition of reemission (121) by one particle during ~10^{-6} s is an infinitely slow process, the time taken by such reemission exceeds the lifetime of the excited states by a factor of 100.

The radiant energy conversion may be characterized by the variable ratio of numbers of reversible and irreversible processes. In the chain (7) this ratio depends on (as shown in Figs. 10, 11) the order of states 1, 2, 3 alternation in cycle of each particle **A**. The index of **A** points it out. In general case we do not know either the reemission number, or states number in the cycle of reemission, as well as their alternation. But formally we can make a continuum consisting of all reversible cycles of the chain (7) and photons of reemission. Separate the reversible cycles and photons by brackets and right down the following expression:

$$(\mathbf{A}_{1\to2\to1} + h\upsilon_{21} + \mathbf{A}_{1\to3\to1} + h\upsilon_{31} + \mathbf{A}_{2\to3\to2} + h\upsilon_{32} + ...) +$$

$$\mathbf{A}_{1\to2\to3\to1} + h\upsilon_{23} + h\upsilon_{31} + \mathbf{A}_{1\to3\to2\to1} + h\upsilon_{32} + h\upsilon_{21} \quad (8)$$

The particles with irreversible reemission cycles are out of brackets.
The sequence of particles states in brackets may be thought as infinite one. (Note that if only one particle were in the brackets, then manifold repetition of its cycle might be considered as an infinite sequence of equilibrium states). In the solid absorber one can select a big number (~10^{19}) of chains consisting of these particles. While the quasistatic process is by definition an infinite and continous sequence of equlibrium states, then there is a fundamental possibility to consider local quasistatic processes in the whole irreversible process of radiant energy transformation.
Thus the sequences of photon reemissions of absorber particles in solar cells can take the form of quasi-static processes. Their isolation out from the general process of the conversion of solar energy into work (which is a non-equilibrium process on the whole) does not contradict the laws of thermodynamics.

4.6 Antenna processes and temperature of radiation

Let us call the reemission of solar energy during an antenna process *retranslation*, if the temperature of the radiation remains constant, and *transformation*, if the temperature of the radiation changes. The retranslation of radiation by a black body is, by definition, a reversible process. Transformation can take place both in a reversible and irreversible way. Therefore, the efficiency of the work performed by a solar cell can be improved by increasing the fraction of retranslating and transforming reversible antenna processes as well as working equilibrium states in an absorber.

4.7 Antenna processes and photon cutting

A photon cutting process (Wegh et al., 1999) as photon reemission is an example for an antenna process. It includes the emission of two visible photons for each vacuum ultraviolet photon absorbed. For us important, that materials with introduced luminescent activators ensure the separation of the photon antenna reemissions and the photon work production processes. In our opinion, ultra-high efficiencies can be reached if: firstly, we solve the problem of separating the photon antenna reemissions and the photon work production processes. Secondly, one should know a way of transformation of irreversible photon antenna reemissions into reversible. Let us consider the activator states in an absorber as state 3. A photon cutting process is irreversible in case of the reemissions $(1231)_n$. They can be luminescent. A photon cutting process can be reversible if an activator performs the reemissions $(1231321)_n$. They cannot be luminescent. An absorber with such activators can resemble a black body. Therefore, photon cutting processes can also play a role in transformation of irreversible reemission into reversible. This way is one of many others.

4.8 Antenna processes in plants

Let us leave the discussion of technological matters relating to the manipulation of antenna processes aside for the time being. We will devote a subsequent publication to this subject. Let us only remark here that the conversion of solar energy involving the participation of antenna molecules figures in the description of photosynthesis in biology. Every chlorophyll molecule in plant cells, which is a direct convertor of solar energy, is surrounded by a complex of 250-400 pigment molecules (Raven et al., 1999). The thermodynamic aspects of photosynthesis in plants were studied in (Wuerfel, 2005; Landsberg, 1977), yet the idea of antenna for solar cells was not proposed. We hope that the notions of the antenna and working states of an absorber particles will make it possible to attain very high efficiencies of the radiant energy convertors, especially in those cases when solar radiation is not powerful enough to make solar cells work efficiently yet suffices to drive photosynthesis in plants.

4.9 Conclusion

This leads us to conclude that reemission of radiant energy by absorbent particles can be considered a quasi-static process. We can therefore hope that the concept of an antenna process, which is photon absorption and generation, can be used to find methods for attaining the efficiency of solar energy conversion close to the limiting efficiency without invoking band theory concepts.

5. Thermodynamic scale of the efficiency of chemical action of solar radiation

Radiant energy conversion has a limit efficiency in natural processes. This efficiency is lower in solar, biological and chemical reactors. With the thermodynamic scale of efficiency of chemical action of solar radiation we will be able to compare the efficiency of natural processes and different reactors and estimate their commercial advantages. Such a scale is absent in the well_known thermodynamic descriptions of the solar energy conversion, its storage and transportation to other energy generators (Steinfeld & Palumbo, 2001). Here the thermodynamic scale of the efficiency of chemical action of solar radiation is based on the Carnot theorem.

Chemical changes are linked to chemical potentials. In this work it is shown for the first time that the chemical action of solar radiation **S** on the reactant **R**

$$\mathbf{R} + \mathbf{S} \leftrightarrow \mathbf{P} + \mathbf{M} \tag{9}$$

is so special that the difference of chemical potentials of substances R and P

$$\mu_R - \mu_P = f(T) \tag{10}$$

becomes a function of their temperature even in the idealized reverse process (9), if the chemical potential of solar radiation is accepted to be non-zero. Actually, there are no obstacles to use the function $f(T)$ in thermodynamic calculations of solar chemical reactions, because in (Kondepudi & Prigogin, 1998) it is shown that the non–zero chemical potential of heat radiation does not contradict with the fundamental equation of the thermodynamics. The solar radiation is a black body radiation.

Let us consider a volume with a black body R, transparent walls and a thermostat T as an idealized solar chemical reactor. The chemical action of solar radiation S on the reactant R will be defined by a boundary condition

$$\mu_R - \mu_P = \mu_m - \mu_S = f(T), \tag{11}$$

where μ_m is a chemical potential of heat radiation emitted by product P. Then the calculation of the function $f(T)$ is simply reduced to the definition of a difference $(\mu_m - \mu_S)$, because chemical potential of heat radiation does not depend on chemical composition of the radiator, and the numerical procedure for μ_m and μ_S is known and simple (Laptev, 2008).

The chemical potential as an intensive parameter of the fundamental equation of thermodynamics is defined by differentiation of characteristic functions on number of particles N (Laptev, 2010). The internal energy U as a characteristic function of the photon number

$$U(V,N) = (2.703N\mathrm{k})^{4/3}/(\sigma V)^{1/3}$$

is calculated by the author in (Laptev, 2008, 2010) by a joint solution of two equations: the known characteristic function

$$U(S,V) = \sigma\, V(3S/4\, \sigma\, V)^{4/3}$$

(Bazarov, 1964) and the expression (Couture & Zitoun, 2000; Mazenko, 2000)

$$N = 0.370\, \sigma T^3 V/\mathrm{k} = S/3.602\ \mathrm{k}, \tag{12}$$

where T, S, V are temperature, entropy and volume of heat radiation, σ is the Stephan–Boltzmann constant, k is the Boltzmnn constant. In total differential of $U(V, N)$ the partial derivative

$$(\partial U/\partial N)_V \equiv \mu_{\text{heat radiation}} = 3.602kT \tag{13}$$

introduces a temperature dependence of chemical potential of heat radiation (Laptev, 2008, 2010). The function $U(S, V, N)$ is an exception and is not a characteristic one because of the relationship (12).

The Sun is a total radiator with the temperature T_S = 5800 K. According to (13), the chemical potential of solar radiation is $3.602kT$ = 173.7 kJ/mol. Then the difference $f(T) = \mu_m - \mu_S$ is a function of the matter temperature T_m. For example, $f(T)$ = –165.0 kJ/mol when T_m = 298.15 K, and it is zero when $T_m = T_S$. According to (13), the function $f(T)$ can be presented as proportional to the dimensionless factor:

$$f(T) = \mu_m - \mu_S = -\mu_S\,(1 - T_m/T_S).$$

According to the Carnot theorem, this factor coincides with the efficiency of the Carnot engine $\eta_C(T_m, T_S)$. Then the function

$$f(T)/\ \mu_S = -\eta_c(T_m, T_S) \tag{14}$$

can characterize an efficiency of the idealized Carnot engine-reactor in known limit temperatures T_m and T_S.

In the heat engine there is no process converting heat into work without other changes, i.e. without compensation. The energy accepted by the heat receiver has the function of compensation. If the working body in the heat engine is a heat radiation with the limit temperatures T_m and T_S, then the compensation is presented by the radiation with temperature T_m which is irradiated by the product P at the moment of its formation. We will call this radiation a compensation one in order to make a difference between this radiation and heat radiation of matter.

The efficiency of heat engines with working body consisting of matter and radiation is considered for the first time in (Laptev, 2008, 2010). During the cycle of such an engine–reactor the radiation is cooled from the temperature T_S down to T_m, causing chemical changes in the working body. The working bodies with stored energy or the compensational radiation are exported from the engine at the temperature T_m. The efficiency of this heat engine is the base of the thermodynamic scale of solar radiation chemical action on the working body.

Assume that the reactant R at 298.15 K and solar radiation S with temperature 5800 K are imported in the idealized engine–reactor. The product P, which is saving and transporting stored radiant energy, is exported from the engine at 298.15 K. Limit working temperatures of such an engine are 298.15 K and 5800 K. Then, according to relationships (10), (11), (14), the equation

$$(\mu_m - \mu_S) / \mu_S = -\eta_c (T_m, T_S) \tag{15}$$

defines conditions of maintaining the chemical reaction at steady process at temperature T_m in the idealized Carnot engine–reactor.

According to the Carnot theorem, the way working body receives energy, as well as the nature of the working body do not influence the efficiency of the heat engine. The efficiency remains the same under contact heat exchange between the same limit temperatures. The efficiency of such an idealized engine is

$$\eta_0 (T_m, T_S) = (1 - T_m/T_S). \tag{16}$$

Then the ratio of the values η_C and η_0 from (15), (16)

$$\zeta = \eta_c / \eta_0 = (\mu_P - \mu_R) / [\mu_S (1 - T_m/T_S)]. \tag{17}$$

is a thermodynamic efficiency ζ of chemical action of solar radiation on the working body in the idealized engine–reactor.

We compare efficiencies ζ of the action of solar radiation on water in the working cycle of the idealized engine-reactor if the water at 298.15 K undergoes the following changes:

$$H_2O_{water} + S_{solar\ rad.} = H_2O_{vapor} + M_{heat\ rad.,.vapor}\ ; \tag{18}$$

$$H_2O_{water} + S_{solar\ rad.} = H_{2gas} + \tfrac{1}{2}O_{2gas} + M_{heat\ rad.,}\ H_2 + \tfrac{1}{2}M_{heat\ rad.,}O_2; \tag{19}$$

$$H_2O_{water} + S_{solar\ rad.} = H^+_{gas} + OH^-_{gas} + M_{heat\ rad.,}\ H^+ + M_{heat\ rad.,}\ OH^-. \tag{20}$$

Chemical potentials of pure substances are equal to the Gibbs energies (Yungman & Glushko, 1999). In accordance with (17),

$$\zeta_{(18)} = [-228.61-(-237.25)] / 173.7 / 0.95 = 0.052$$

$$\zeta_{(19)} = \zeta_{(18)} [0 + \tfrac{1}{2}\ 0 - (-228.61)] / 173.7 / 0.95 = 0.052x1.39 = 0.072$$

$$\zeta_{(20)} = \zeta_{(18)} [1517.0 - 129.39 - (-228.61)] / 173.7 / 0.95 = 0.052x\ 9.79 = 0.51$$

So, in the engine–reactor the reaction (20) may serve as the most effective mechanism of conversion of solar energy.

In the real solar chemical reactors the equilibrium between a matter and radiation is not achieved. In this case the driving force of the chemical process in the reactor at the temperature T will be smaller than the difference of Gibbs energies

$$\Delta G_T = (\mu_P - \mu_R) + (\mu_m - \mu_S). \quad (21)$$

For example, water evaporation at 298.15 K under solar irradiation is caused by the difference of the Gibbs energies

$$\Delta G_{298.15} = -228.61 - (-237.25) + (-165.0) = -156.4 \text{ kJ/mol}.$$

At the standard state (without solar irradiation)

$$\Delta G^0_{298.15} = (\mu_P - \mu_R) = -228.61 - (-237.25) = 8.64 \text{ kJ/mol}.$$

The changes of the Gibbs energies calculated above have various signs: $\Delta G_{298.15} < 0$ and $\Delta G^0_{298.15} > 0$. It means that water evaporation at 298.15 K is possible only with participation of solar radiation. The efficiency ζ of the solar vapor engine will not exceed $\zeta_{(18)} = 5.2\%$. There is no commercial advantage because the efficiency of the conventional vapor engines is higher. However, the efficiency of the solar engine may be higher than that of the vapor one if the condition $\Delta G_{298.15} < 0$ and $\Delta G^0_{298.15} > 0$ is fulfilled. The plant cell where photosynthesis takes place is an illustrative example.

If the condition is $\Delta G_{298.15} < 0$ and $\Delta G^0_{298.15} < 0$ the radiant heat exchange replaces the chemical action of solar radiation. If $\Delta G_{298.15} > 0$ and $\Delta G^0_{298.15} > 0$, then neither radiant heat exchange, nor chemical conversion of solar energy cause any chemical changes in the system at this temperature. The processes (19) and (20) are demonstrative. Nevertheless, at the temperatures when ΔG becomes negative, the chemical changes will occur in the reaction mixture. So, in solar engines–reactors there is a lower limit of the temperature T_m. For example, in (Steinfeld & Palumbo, 2001) it is reported that chemical reactors with solar radiation concentrators have the minimum optimal temperature 1150 K.

The functions $\Delta G(T)$ and $\zeta(T)$ describe various features of the chemical conversion of solar energy. As an illustration we consider the case when the phases R and P are in thermodynamic equilibrium. For example, the chemical potentials of the boiling water and the saturated vapor are equal. Then both their difference $(\mu_P - \mu_R)$ and the efficiency ζ of the chemical action of solar radiation are zero, althought it follows from Eq. (21) that $\Delta G(T) < 0$. Without solar irradiation the equation $\Delta G(T) = 0$ determines the condition of the thermodynamic equilibrium, and the function $\zeta(T)$ loses its sense.

The thermodynamic scale of efficiency $\zeta(T)$ of the chemical action of solar radiation presented in this paper is a necessary tool for choice of optimal design of the solar engines_reactors. It is simple for application while its values are calculated from the experimentally obtained data of chemical potentials and temperature. Varying the values of chemical potentials and temperature makes it possible to model (with help of expressions (17), (21)) the properties of the working body, its thermodynamic state and optimal conditions for chemical changes in solar engines and reactors in order to bring commercial advantages of alternative energy sources.

6. Thermodynamic efficiency of the photosynthesis in plant cell

It is known that solar energy for glucose synthesis is transmitted as work (Berg et al., 2010; Lehninger et al., 2008; Voet et al., 2008; Raven et al., 1999). Here it is shown for the first time that there are pigments which reemit solar photons whithout energy conversion in form of heat dissipation and work production. We found that this antenna pigments make 77% of all

pigment molecula in a photosystem. Their existance and participation in energy transfer allow chloroplasts to overcome the efficiency threshold for working pigments as classic heat engine and reach 71% efficiency for light and dark photosynthesis reactions. Formula for efficiency calculation take into account differences of photosynthesis in specific cells. We are also able to find the efficiency of glycolysis, Calvin and Krebs cycles in different organisms.

The Sun supplies plants with energy. Only 0.001 of the solar energy reaching the Earth surface is used for photosynthesis (Nelson & Cox, 2008; Pechurkin, 1988) producing about 1014 kg of green plant mass per year (Odum, 1983). Photosynthesis is thought to be a low–effective process (Ivanov, 2008). The limiting efficiency of green plant is defined to be 5% as a ratio of the absorbed solar energy and energy of photosynthesis products (Odum,1983; Ivanov, 2008). Here is shown that the photosynthesis efficiency is significantly higher (71% instead of 5%) and it is calculated as the Carnot efficiency of the solar engine_reactor with radiation and matter as a single working body.

The photosynthesis takes place in the chloroplasts containing enclosed stroma, a concentrated solution of enzymes. Here occure the dark reactions of the photosynthesis of glucose and other substances from water and carbon dioxide. The chlorophyll traps the solar photon in photosynthesis membranes. The single membrane forms a disklike sac, or a thylakoid. It encloses the lumen, the fluid where the light reactions take place. The thylakoids are forming granum (Voet et al., 2008; Berg et al., 2010). Stacks of grana are immersed into the stroma.

When solar radiation with the temperature T_S is cooled in the thylakoid down to the temperature T_A, the amount of evolved radiant heat is a fraction

$$\eta_U = 1 - (T_A/T_S)^4$$

of the energy of incident solar radiation (Wuerfel, 2005). The value η_U is considered here as an efficiency of radiant heat exchange between the black body and solar radiation (Laptev, 2006).

Tylakoids and grana as objects of intensive radiant heat exchange have a higher temperature than the stroma. Assume the lumen in the tylakoid has the temperature T_A = 300 K and the stroma, inner and outer membranes of the chloroplast have the temperature T_0 = 298 K. The solar radiation temperature T_S equals to 5800 K.

The limiting temperatures T_0, T_A in the chloroplast and temperature T_S of solar radiation allow to imagine a heat engine performing work of synthesis, transport and accumulation of substances. In idealized Carnot case solar radiation performs work in tylakoid with efficiency

$$\eta_C = 1 - T_A/T_S = 0.948,$$

and the matter in the stroma performs work with an efficiency

$$\eta_0 = 1 - T_0/T_A = 0.0067.$$

The efficiency $\eta_0\eta_C$ of these imagined engines is 0.00635.

The product $\eta_0\eta_C$ equals to the sum $\eta_0 + \eta_C - \eta_{0S}$ (Laptev, 2006). Value η_{0S} is the efficiency of Carnot cycle where the isotherm T_S relates to the radiation, and the isotherm T_0 relates to the matter. The values η_{0S} and η_C are practically the same for chosen temperatures and $\eta_{0S}/\eta_0\eta_C$ = 150. It means that the engine where matter and radiation performing work are a single working body has 150 times higher efficiency than the chain of two engines where matter and radiation perform work separately.

It is known (Laptev, 2009) that in the idealized Carnot solar engine–reactor solar radiation S produces at the temperature TA a chemical action on the reagent R

$$\mathbf{R}_{\text{reagent}} + \mathbf{S}_{\text{solar radiation}} \leftrightarrow \mathbf{P}_{\text{product}} + \mathbf{M}_{\text{thermal radiation of product}}$$

with efficiency

$$\zeta = (\mu_P - \mu_R)/[\mu_S/(1 - T_A/T_S)], \tag{22}$$

where μ_P, μ_R are chemical potentials of the substances, μ_S is the chemical potential of solar radiation equal to $3.602kT_S$ = 173.7 kJ/mol. The efficiency of use of water for alternative fuel synthesis is calculated in (Laptev, 2009).

Water is a participant of metabolism. It is produced during the synthesis of adenosine triphosphate (ATP) from the adenosine diphosphate (ADP) and the orthophosphate (P_i)

$$ADP + P_i = ATP + H_2O. \tag{23}$$

Water is consumed during the synthesis of the reduced form of the nicotinamide adenine dinucleotide phosphate (NADPH) from its oxidized form ($NADP^+$)

$$2NADP^+ + 2H_2O = 2NADPH + O_2 + 2H^+_{\text{thylakoid}} \tag{24}$$

and during the glucose synthesis

$$6CO2 + 6H_2O = C_6H_{12}O_6 + 6O_2. \tag{25}$$

Changes of the Gibbs energies or chemical potentials of substances in the reactions (23)–(25) are 30.5, 438 and 2850 kJ/mol, respectively (Voet et al., 2008).

The photosynthesis is an example of joint chemical action of matter and radiation in the cycle of the idealized engine–reactor, when the water molecule undergoes the changes according to the reactions (23)–(25). According to (22), the photosynthesis efficiency ζ_{Ph} in this model is

$$\zeta_{(5)} \times 1/2\zeta_{(6)} \times 1/6\zeta_{(7)} = 71\%.$$

The efficiency ζ_{Ph} is smaller than the Landsberg limiting efficiency

$$\eta_L = \eta_U - 4T_0/3T_S + 4T_0\, T_A^3/3\, T_S^4, \tag{26}$$

known in the solar cell theory (Wuerfel, 2005) as the efficiency of the joint chemical action of the radiation and matter per cycle. ζ_{Ph} and the temperature dependence η_L are shown in Fig. 12 by the point F and the curve LB respectively. They are compared with the temperature dependence of efficiencies $\eta_0\eta_C\eta_U$ (curve CB) and $\eta_{0S}\eta_U$ (curve KB). Value η_U is close to unity because $(T_A/T_S)^4 \sim 10^{-5}$.

We draw in Fig. 12 an isotherm t–t' of η values for T_A = 300 K. It is found that η_{0S} = 94.8% at the interception point K, η_L = 93.2% at the point L and $\eta_0\eta_C\eta_U$ = 0.635% at the point C. The following question arises: which processes give the chloroplasts energy for overcoming the point C and achieving an efficiency ζ_{Ph} = 71% at the point F?

First of all one should note that the conversion of solar energy into heat in grana has an efficiency η_g smaller than η_U of the radiant heat exchange for black bodies. From (26) follows that the efficiency ζ_{Ph} cannot reach the value η_L due to necessary condition $\eta_g < \eta_U$.

Besides in the thylakoid membrane the photon reemissions take place without heat dissipation (Voet et al., 2008; Berg et al., 2010). The efficiency area between the curves *LB* and *CB* relates to photon reemissions or antenna processes. They can be reversible and irreversible. The efficiencies of reversible and irreversible processes are different. Then the point *F* in the isotherm *t*–*t*' is the efficiency of engine with the reversible and irreversible antenna cycles.

The antenna process performs the solar photon energy transfer into reaction centre of the photosystem. Their illustration is given in (Voet et al., 2008; Berg et al., 2010). Every photosystem fixes from 250 to 400 pigments around the reaction center (Raven et al., 1999). In our opinion a single pigment performs reversible or irreversible antenna cycles. The antenna cycles form antenna process. How many pigments make the reversible process in the photosynthetic antenna complex?

One can calculate the fraction of pigments performing the reversible antenna process if the line *L*C in Fig. 12 is supposed to have the value equal unity. In this case the point *F* corresponds to a value $x = \zeta/(\eta_L - \eta_0\eta_C\eta_U) = 0.167$. This means that 76.7% of pigments make the revesible antenna process. 23.3% of remaining pigments make an irreversible energy transfer between the pigments to the reaction centres. The radiant excitation of electron in photosystem occurs as follows:

$$\text{chlorophyll } a + \text{photon} \leftrightarrow \text{chlorophyll } a^{+} + e^{-}. \tag{27}$$

The analogous photon absorption takes place also in the chlorophylls *b*, *c*, *d*, various carotenes and xanthophylls contained in different photosystems (Voet et al., 2008; Berg et al., 2010). The excitation of an electron in the photosystems P680 and P700 are used here as illustrations of the reversible and irreversible antenna processes.

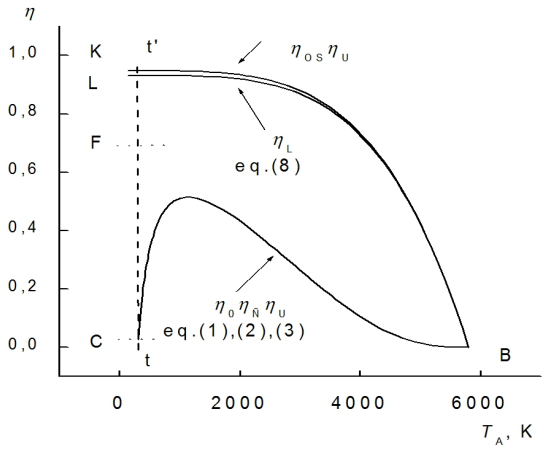

Fig. 12. The curve *CB* is the efficiency of the two Carnot engines (Laptev, 2005). The curve *LB* is the efficiency of the reversible heat engine in which solar radiation performs work in combination with a substance (Wuerfel, 2005). The curve *KB* is the efficiency of the Carnot solar engine_reactor (Laptev, 2006), multiplied by the efficiency η_U of the heat exchange between black bodies. The isotherm *t*–*t*' corresponds to the temperature 300 K. The calculated photosynthesis efficiency is presented by the point *F* in the isotherm.

Schemes of working and antenna cycles are shown in Fig. 13. Working pigment (a) is excited by the photon in the transition 1 → 3. Transition 3 → 2 corresponds to the heat compensation in the chloroplast as engine–reactor. The evolved energy during the transition 2 → 1 is converted into the work of electron transfer or ATP and NADPH synthesis.
When the antenna process passes beside the reaction centre, the photosystems make the reversible reemissions. Fig. 13 presents an interpretation of absorption and emission of photons in antenna cycles. The reemission 2 → 3 → 2 shows a radiant heat exchange. The reemissions 1 → 2 → 1 and 1 → 3 → 1 take place according to (27). Examples are the pigments in chromoplasts.
According to the thermodynamic postulate, the efficiency of reversible process is limited. In our opinion, just the antenna processes in the pigment molecules of the tylakoid membrane allow the photosystems to overcome the forbidden line (for a heat engine efficiency) *CB* in Fig. 12 and to achieve the efficiency $\zeta_{Ph} = 71\%$ in the light and dark photosynthesis reactions.
There are no difficulties in taking into account in (22) the features of the photosynthesis in different cells. The efficiency of glycolyse, Calvin and Krebs cycles in various living structures may be calculated by the substitution of solar radiation chemical potential in the expression (22) by the change of chemical potentials of substances in the chemical reaction.
The cell is considered in biology as a biochemical engine. Chemistry and physics know attempts to present the plant photosynthesis as a working cycle of a solar heat engine (Landsberg, 1977). The physical action of solar radiation on the matter of nonliving systems during antenna and working cycles of the heat engine is described in (Laptev, 2005, 2008). In this article the Carnot theorem has been used for calculation of the thermodynamic efficiency of the photosynthesis in plants; it is found that the efficiency is 71%.

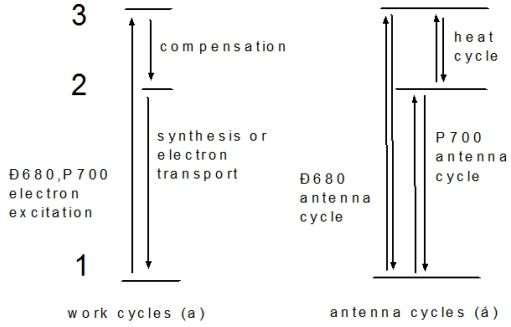

Fig. 13. The interpretation of energy transitions in the work (a) and antenna (b) cycles. Level *1* shows the ground states, levels *2*, *3* present excited states of pigment molecules.

One can hope that the thermodynamic comparison of antenna and working states of pigments in the chloroplast made in this work will open new ways for improving technologies of solar cells and synthesis of alternative energy sources from the plant material.

7. Condensate of thermal radiation

Thermal radiation is a unique thermodynamic system while the expression $dU = TdS - pdV$ for internal energy U, entropy S, and volume V holds the properties of the fundamental

equation of thermodynamics regardless the variation of the photon number (Kondepudi & Prigogin, 1998. Bazarov, 1964). Differential expression $\mathrm{d}p/\mathrm{d}T=S/V$ for pressure p and temperature T is valid for one-component system under phase equilibrium if the pressure does not depend on volume V (Muenster, 1970). Thermal radiation satisfies these conditions but shows no phase equilibrium.

The determinant of the stability of equilibrium radiation is zero (Semenchenko, 1966). While the „zero" determinants are related to the limit of stability, there are no thermodynamic restrictions for phase equilibrium of radiation (Muenster, 1970). However, successful attempts of finding thermal radiation condensate in any form are unknown. This work aims to support enthusiasm of experimental physicists and reports for the first time the phenomenological study of the thermodynamic medium consisting of radiation and condensate.

It is known (Kondepudi & Prigogin, 1998; Bazarov, 1964), that evolution of radiation is impossible without participating matter and it realizes with absorption, emission and scattering of the beams as well as with the gravitational interaction. Transfer of radiation and electron plasma to the equilibrium state is described by the kinetic equation. Some of its solutions are treated as effect of accumulation in low-frequency spectrum of radiation, as Bose-condensation or non-degenerated state of radiation (Kompaneets, 1957; Dreicer, 1964; Weymann, 1965; Zel'dovich & Syunyaev, 1972; Dubinov A.E. 2009). A known hypothesis about Bose-condensation of relic radiation and condensate evaporation has a condition: the rest mass of photon is thought to be non-zero (Kuz'min & Shaposhnikov, 1978). Nevertheless, experiments show that photons have no rest mass (Spavieri & Rodrigues, 2007).

Radiation, matter and condensate may form a total thermal equilibrium. According to the transitivity principle of thermodynamic equilibrium (Kondepudi & Prigogin, 1998; Bazarov, 1964), participating condensate does not destroy the equilibrium between radiation and matter. Suppose that matter is a thermostat for the medium consisting of radiation and condensate. A general condition of thermodynamic equilibrium is an equality to zero of virtual entropy changes δS or virtual changes of the internal energy δU for media (Bazarov, 1964; Muenster, 1970; Semenchenko, 1966). Using indices for describing its properties, we write $S=S_{\mathrm{rad}}+S_{\mathrm{cond}}$, $U=U_{\mathrm{rad}}+U_{\mathrm{cond}}$. The equilibrium conditions $\delta S_{\mathrm{rad}}+\delta S_{\mathrm{cond}}=0$, $\delta U_{\mathrm{rad}}+\delta U_{\mathrm{cond}}=0$ will be completed by the expression $T\delta S=\delta U+p\delta V$, and then we get an equation

$$(1/T_{\mathrm{cond}}-1/T_{\mathrm{rad}})\delta U_{\mathrm{cond}}+(p_{\mathrm{cond}}/T_{\mathrm{cond}})\delta V_{\mathrm{cond}}+(p_{\mathrm{rad}}/T_{\mathrm{rad}})\delta V_{\mathrm{rad}}=0.$$

If $V_{\mathrm{rad}}+V_{\mathrm{cond}}=V=\mathrm{const}$ and $\delta V_{\mathrm{rad}}=-\delta V_{\mathrm{cond}}$, then for any values of variations δU_{cond} and δV_{cond} we find the equilibrium conditions: $T_{\mathrm{rad}}=T_{\mathrm{cond}}=T$ and $p_{\mathrm{rad}}=p_{\mathrm{cond}}=p$. When condensate is absolutely transparent for radiation, it is integrated in condensate, so that $V_{\mathrm{rad}}=V_{\mathrm{cond}}=V$ and $\delta V_{\mathrm{rad}}=\delta V_{\mathrm{cond}}$. Thus, conditions

$$T_{\mathrm{rad}}=T_{\mathrm{cond}},\qquad p_{\mathrm{rad}}=-p_{\mathrm{cond}} \tag{28}$$

are satisfied for any values of variations δU_{cond} and δV_{cond}.

The negative pressure arises in cases, when $U-TS+pV=0$ and $U>TS$. We ascribe these expressions to the condensate and assume the existence of the primary medium, for which the expression $S_0=S_{\mathrm{cond}}+S_{\mathrm{rad}}$ is valid in the same volume. Now we try to answer the question about the medium composition to form the condensate and radiation from indefinitely small local perturbations of entropy S_0 of the medium. Two cases have to be examined.

Suppose that the primary medium is radiation and for this medium $U_{00,\mathrm{rad}}-TS_0+p_{\mathrm{rad}}V=0$. Then the condition $U_{00,\mathrm{rad}}<U_{\mathrm{rad}}+U_{\mathrm{cond}}$ is satisfied for values of p and T necessary for equilibrium. According to this inequality and the Gibbs stability criterion (Muenster, 1970), the medium consisting of the condensate and radiation is stable relatively to primary radiation, i.e. the condensation of primary radiation is a forced process.

In contrary, the equilibrium state of condensate and radiation arises spontaneously from the primary condensate, because $U_{00,\mathrm{cond}}>U_{\mathrm{rad}}+U_{\mathrm{cond}}$, if $U_{00,\mathrm{cond}}-TS_0+p_{\mathrm{cond}}V=0$. However, the condensate has to lower its energy before the moment of the equilibrium appearance to prevent self-evaporation of medium into radiation. Such a process is possible under any infinitely small local perturbations of the entropy S_0. Really, the state of any equilibrium system is defined by the temperature T and external parameters (Kondepudi & Prigogin, 1998; Bazarov, 1964; Muenster, 1970).

While the state of investigated medium is defined by the temperature only, the supposed absence of external forces allows the primary condensate to perform spontaneous adiabatic extension with lowering energy by factor $\Delta U_{\mathrm{cond}}=U_{0,\mathrm{cond}}-U_{00,\mathrm{cond}}=p_{\mathrm{cond}}\Delta V$. When the energy rest will fulfill the condition $U_{0,\mathrm{cond}}=U_{\mathrm{rad}}+U_{\mathrm{cond}}$, the required condition $U_{0,\mathrm{cond}}-TS_0+p_{\mathrm{cond}}V=0$ for arising equilibrium between condensate and radiation will be achieved.

Let's consider the evolution of the condensate being in equilibrium with radiation. Once the medium is appeared, this medium consisting of the equilibrium condensate and radiation can continue the inertial adiabatic extension due to the assumed absence of external forces. When $V_{\mathrm{rad}}\equiv V_{\mathrm{cond}}$, the second law of thermodynamics can be written as $u=Ts-p$, where u and s are densities of energy and entropy, respectively. Fig. 14 plots a curve of radiation extension as a cubic parabola $s_{\mathrm{rad}}=4\sigma T^3/3$, where σ is the Stefan-Boltzmann constant. Despite the fact that the density of entropy of the condensate is unknown, we can show it in Fig.1 as a set of positive numbers $\lambda=Ts$, if each λ_i is ascribed an equilateral hyperbola $s_{\mathrm{cond}}=\lambda_i/T$. Fig.14 illustrates both curves.

We include the cross-section point c_i of the hyperbola cd and the cubic parabola ab in Fig. 14 in the interval $[c_0, c_k]$. Assume the generation of entropy along the line cd outside this interval and the limits of the interval are fixing the boundary of the medium stability. Absence of the entropy generation inside the interval $[c_0, c_k]$ means that the product $2s_i(T_k-T_0)$ is $\int_{T_0}^{T_k} \mathrm{d}T(s_{\mathrm{cond}}+s_{\mathrm{rad}})$. By substituting s we can see that these equalities are valid only at $T_0=T_k=T_i$. So, if the condensate and radiation are in equilibrium, the equality $s_{\mathrm{cond}}=s_{\mathrm{rad}}$ is also valid.

Thus, when the equilibrium state is achieved the medium extension is realized along the cross-section line of the parabola and hyperbolas. Equalities $s_{\mathrm{cond}}=s_{\mathrm{rad}}=4\sigma T^3/3$ are of fundamental character; all other thermodynamic values for the condensate can be derived from these values. For example, we find that $\lambda_i=4\sigma T_i^4/3$. For the condensate $u-Ts+p=0$ is valid. Then, according to (28),

$$u_{\mathrm{cond}}=Ts-p_{\mathrm{cond}}=5\sigma T^4/3. \tag{29}$$

For the equilibrium medium consisting of the condensate and radiation $u_{\mathrm{cond}}=5u_{\mathrm{rad}}/3$ and $u_0=u_{\mathrm{rad}}+u_{\mathrm{cond}}=8\sigma T^4/3=2\lambda$. For the primary condensate before its extension $u_{00}=u_{\mathrm{rad}}+u_{\mathrm{cond}}-p=3\sigma T^4$. For thermal radiation $u_{\mathrm{rad}}=3p$ and the pressure is always positive (Kondepudi & Prigogin, 1998; Bazarov, 1964).

The extension of the medium is an inerial process, so that the positive pressure of radiation p_{rad} lowers, and the negative pressure of the condensate p_{cond} increases according to the condition (1). Matter is extended with the medium. As it is known in cosmological theory (Kondepudi & Prigogin, 1998; Bazarov, 1964), the plasma inertial extension had led to formation of atoms and distortion of the radiation-matter equilibrium. Further local unhomogeneities of matter were appeared as origins of additional radiation and, consequently, matter created a radiation excess in the medium after the equilibrium radiation-matter was disturbed This work supposes that radiation excess may cause equilibrium displacement for the medium, thus radiation and condensate will continue extending inertially in a non-equilibrium process.

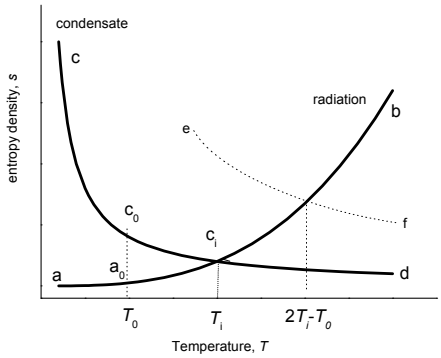

Fig. 14. Schematically plots the density of entropy for radiation (curve *ab*) and for a condensate (curves *cd* and *ef*). The positive pressure of the radiation and negative pressure of condensate are equal by absolute value at the points c_i and e_k at the interceptions of these curves.

We assume that the distortion of the equilibrium radiation-condensate had been occurred at the temperature T_i of the medium at the point c_i in Fig. 14. The radiation will be extended adiabatically along the line c_ia of the cubic parabola without entropy generation. While the condition $V_{rad}=V_{cond}$ is satisfied if the equilibrium is disturbed, the equality $s_{cond}=s_{rad}$ points out directions of the condensate extension without entropy generation. As it is shown in Fig.14, the unchangeable adiabatic isolation is possible if the condensate extends along the isotherm T_i without heat exchange with radiation. Differentiation of the expression $U_{cond}-T_iS_{cond}+p_{cond}V=0$ with T=const and S=const gives that p_{cond} is also constant.

The medium as a whole extends in such a manner that the positive pressure p_{rad} of radiation decreases, and the negative pressure p^*_{cond} remains constant. As radiation cools down, the ratio p^*/p_{rad} lowers, the dominant p^* of the negative pressure arises, and the medium begins to extend with positive acceleration.

The thermodynamics defines energy with precision of additive constant. If we assume this constant to be equal to TS_{cond}, then the equality $u^*_{cond}=U^*_{cond}/V = -p^*_{cond}$, is valid; this equality points out the fixed energy density of the condensate under its expansion after distortion of the medium equilibrium.

The space is transparent for relic radiation which is cooling down continuously under adiabatic extension of the Universe. Assuming existence of the condensate of relic radiation we derive an expression for a fixed energy density of the condensate u^* with the beginning of accelerated extension of the Universe. The adiabatic medium with negative pressure and

a fixed energy density 4 GeV/m³ is supposed to be the origin of the cosmological acceleration. The nature of this phenomenon is unknown (Chernin, 2008; Lukash & Rubakov, 2008; Green, 2004) . What part of this energy can have a relic condensate accounting the identical equation of state $u = -p$ for both media?

The relic condensate according to (29) has the energy density 4 GeV/m³ when the temperature of relic radiation is about 27 K. If the accelerated extension of the cosmological medium arises at $T^* \leq 27$ K, the part of energy of the relic condensate in the total energy of the cosmological medium is $(T^*/27)^4$. According to the Fridman model T^* corresponds to the red shift ≈0.7 (Chernin, 2008) and temperature 4.6 K. Then the relic condensate can have a 0.1% part of the cosmological medium.

As a conclusion one should note that the negative pressure of the condensate of thermal radiation is Pascal-like and isotropic, it is constant from the moment as the equilibrium with radiation was disturbed by the condensate and is equal (by absolute value) to the energy density with precision of additive constant. The condensate of thermal radiation is a physical medium which interacts only with the radiation and this physical medium penetrates the space as a whole. This physical medium cannot be obtained under laboratory conditions because there are always external forces for a thermodynamic system in laboratory. While this paper was finalized the information (Klaers et al., 2009) showed the photon Bose-condensate can be obtained. This condensate has no negative pressure while it is localized in space. It seems very interesting to find in the nature a condensate of thermal radiation with negative pressure. Possible forms of physical medium with negative pressure and their appearance at cosmological observations are widely discussed. The radiation can consist of other particles, then the photon, among them may be also unknown particles. We hope that modelling the medium from the condensate and radiation will be useful for checking the hypotheses and will allow explaining the nature of the substance responsible for accelerated extension of the Universe. The medium from thermal radiation and condensate is the first indication of the existence of physical vacuum as one of the subjects in classical thermodynamics and the complicated structure of the dark energy.

8. Electrical properties of copper clusters in porous silver of silicon solar cells

Technologies for producing electric contacts on the illuminated side of solar cells are based on chemical processes. Silver technologies are widely used for manufacturing crystalline silicon solar cells. The role of small particles in solar cells was described previously (Hitz, 2007; Pillai, 2007; Han, 2007; Johnson, 2007). The introduction of nanoparticles into pores of photon absorbers increases their efficiency. In our experiments copper microclusters were chemically introduced into pores of a silver contact. They changed the electrical properties of the contact: dark current, which is unknown for metals, was detected.

In the experiments, we used 125 x×125-mm commercial crystalline silicon wafers Si<P>/SiN_x (70 nm)/Si<B> with a silver contact on the illuminated side. The silver contact was porous silver strips 10–20 μm thick and 120–130 μm wide on the silicon surface. The diameter of pores in a contact strip reached 1μm. The initial material of the contact was a silver paste (Dupont), which was applied to the silicon surface through a tungsten screen mask. After drying, organic components of the paste were burned out in an inert atmosphere at 820–960° C. Simultaneously, silver was burned in into silicon through a 70-nm-thick silicon nitride layer. After cooling in air, the wafer was immersed in a copper salt

solution under the action of an external potential difference; then, the wafer was washed with distilled water and dried with compressed nitrogen until visible removal of water from the surface of the solar cell (Laptev & Khlyap, 2008).
The crystal structure of the metal phases was studied by grazing incidence X-ray diffraction. A 1-μm-thick copper layer on the silver surface has a face-centered cubic lattice with space group *Fm*3*m*. The morphology of the surface of the solar cell and the contact strips before and after copper deposition was investigated with a KEYENCE-5000 3D optical microscope. Fig. 15 presents the result of computer processing of images of layer-by-layer optical scanning of the surface after copper deposition.

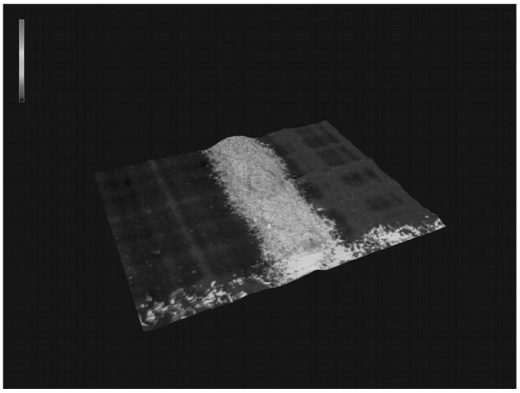

Fig. 15. Contact strip morphology. Scanning area 430 x 580 μm²; magnification 5000x.

The copper deposition onto the silver strips did not change the shape and profile of the contact, which was a regular sequence of bulges and compressions of the contact strip. The differences in height and width reached 5 μm. In some cases, thin copper layers caused slight compression of the contact in height. The profiles of the contacts were studied using computer programs of the optical microscope. It was found that copper layers to 1 μm in thickness on the silver contact could cause a decrease in the strip height by up to 10%.
The chemical composition of the contact and the depth distribution of copper were investigated by energy dispersive X-ray analysis, secondary ion mass spectrometry, and X-ray photoelectron spectroscopy. The amount of copper in silver pores was found to decrease with depth in the contact. Copper was found at the silicon–silver interface. No copper diffusion into silicon was detected.
The resistivity of the contacts was measured at room temperature with a Keithley 236 source-measure unit. Two measuring probes were placed on the contact strips at a distance of 8 mm from each other. A probe was a tungsten needle with a tip diameter of 120 μm. The measurements were made on two samples in a box with black walls and a sunlight simulator. Fig. 16 presents the results of the experiments.
Line *1* is the current–voltage diagram for the initial silver contact strip on the silicon wafer surface. The other lines are the current–voltage diagrams for the contacts after copper deposition. All the lines confirm the metallic conductance of the contact strips. The current–voltage diagrams for the contacts with copper clusters differ by the fact that they do not pass through the origin of coordinates for both forward and reverse currents. A current through a metal in the absence of an external electric field is has not been observed. In our

experiment, the light currents were 450 μA in the contact where copper clusters were only in silver pores and 900 μA in the contact where copper clusters were both in silver pores and on the silver surface.

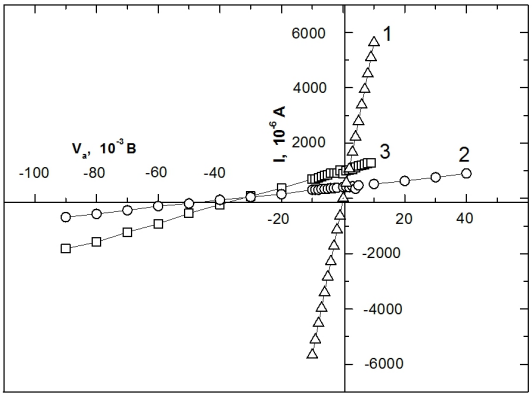

Fig. 16. Electrical properties of (*1*) a silver contact strip, (*2*) a contact strip with copper clusters in silver pores, and (*3*) a strip with a copper layer on the surface and copper clusters in silver pores.

It is worth noting that the electric current in the absence of an external electric field continued to flow through these samples after the sunlight simulator was switched off. The light and dark currents in the contact strips are presented in Fig. 17. It is seen that the generation of charge carriers in the dark at zero applied bias is constant throughout the experiment time. The dark current in the silver contact is caused by the charge carrier generation in the contact itself. The source of dark-current charge carriers are copper clusters in silver pores and on the silver surface.

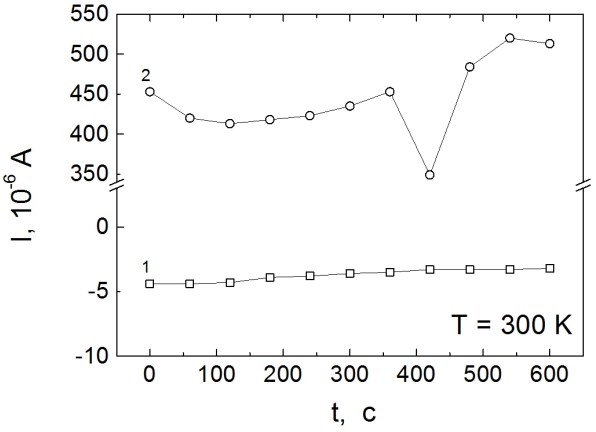

Fig. 17. Time dependence of the (*1*) dark and (*2*) light currents at zero applied bias in contact strips with copper clusters in silver pores.

The current in the silver contact with copper clusters while illuminating the solar cell is caused by the generation of charge carriers in the semiconductor part of the silicon wafer. The number of charge carriers generated in the *p–n* junction is two orders of magnitude larger than the number of charge carriers in copper clusters since the light current is so larger than the dark current (Fig. 17).
The copper deposition onto silver does not lead to the formation of a silver–copper solid solution. The contact of the crystal structures gives rise to an electric potential difference. This is insufficient for generation of current carriers.
However, the contact of the copper and silver crystal structures causes compression of the metal strip and can decrease the metal work function of copper clusters.
We consider that the charge carrier generation in the dark by copper clusters in the contact strip as a component of the solar cell is caused by the deformation of the strip. It is known (Albert & Chudnovsky, 2008), that deformation of metal cluster structures can induce high-temperature superconductivity. Therefore, it is necessary to investigate the behavior of the studied samples in a magnetic field.
Solar energy conversion is widely used in electric power generation. Its efficiency in domestic and industrial plants depends on the quality of components (Slaoui A & Collins, 2007). Discovered in this work, the dark current in the silver contact on the illuminated side of a silicon solar cell generates electricity in amount of up to 5% of the rated value in the absence of sunlight. Therefore, the efficiency of solar energy conversion plants with copper–silver contacts is higher even at the same efficiency of the semiconductor part of the solar cell.

9. Metallic nanocluster contacts for high-effective photovoltaic devices

High efficiency of solar energy conversion is a main challenge of many fields in novel nanotechnologies. Various nanostructures have been proposed early (Pillai et al., 2007; Hun et al., 2007; Johnson et al., 2007; Slaoui & Collins, 2007). However, every active element cannot function without electrodes. Thus, the problem of performing effective contacts is of particular interest.
The unique room-temperature electrical characteristics of the porous metallic nanocluster-based structures deposited by the wet chemical technology on conventional silicon-based solar cells were described in (Laptev & Khlyap, 2008). We have analyzed the current-voltage characteristics of Cu-Ag-metallic nanocluster contact stripes and we have registered for the first time dark currents in metallic structures. Morphological investigations (Laptev & Khlyap, Kozar et al., 2010) demonstrated that copper particles are smaller than 0.1 μm and smaller than the pore diameter in silver.
Electrical measurements were carried out for the nanoclustered Ag/Co-contact stripe (Fig.18, inset) and a metal-insulator-semiconductor (MIS) structure formed by the silicon substrate, SiN_x cove layer, and the nanocluster stripe. Fig. 18 plots experimental room-temperature current-voltage characteristics (IVC) for both cases.
As is seen, the nanocluster metallic contact stripe (function 3 in Fig. 18) demonstrates a current-voltage dependence typical for metals. The MIS-structure (functions 1 and 2 in Fig. 18) shows the IVC with a weak asymmetry at a very low applied voltage; as the external electric field increases, the observed current-voltage dependence transforms in a typical "metallic" IVC. More detailed numerical analysis was carried out under re-building the experimental IVCs in a double-log scale.

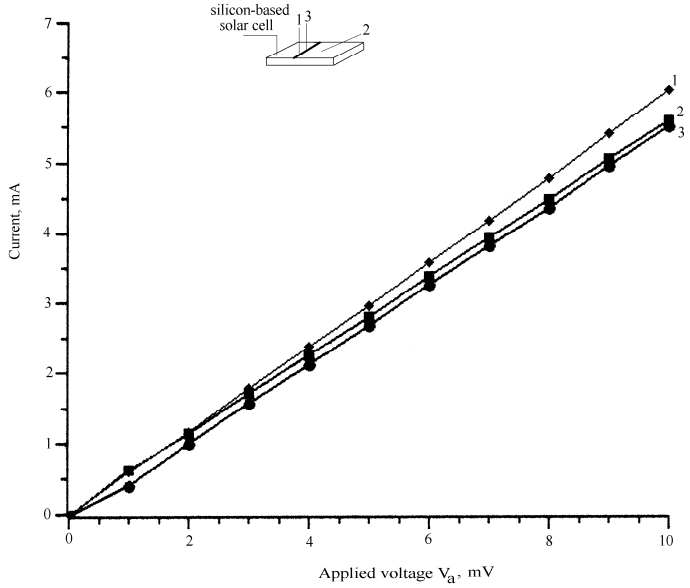

Fig. 18. Room-temperature current-voltage characteristics of the investigated structures <8see text above): functions 1 and 2 are "forward" and "reverse" currents of the MIS-structure (contacts 1-2), and the function 3 is a IVC for the contacts 1-3.

Fig. 19 illustrates a double-log IVCs for the investigated structure. The numerical analysis has shown that both "forward" and 'reverse" currents can be described by the function

$$I = f(V_a)^m,$$

where I is the experimental current (registered under the forward or reverse direction of the applied electric field), and V_a is an applied voltage. The exponential factor *m* changes from 1.7 for the "forward" current at V_a up to 50 mV and then decreases down to ~1.0 as the applied bias increases up to 400 mV; for the "reverse" current the factor *m* is almost constant (~1.0) in the all range of the external electric field.

Thus, these experimental current-voltage characteristics (we have to remember that the investigated structure is a metallic cluster-based quasi-nanowire!) can be described according to the theory (Sze & Ng, 2007) as follows: the first section of forward current

$$I = T_{tun}A_{el}(4\varepsilon/9L^2)(2e/m^*)^{1/2}(V_a)^{3/2}$$

(ballistic mode) and the second one as

$$I = T_{tun}A_{el}(2\varepsilon v_s/L^2)V_a,$$

and the reverse current is

$$I = T_{tun}A_{el}(2\varepsilon v_s/L^2)V_a$$

(velocity saturation mode). Here T_{tun} is a tunneling transparency coefficient of the potential barrier formed by the ultrathin native oxide films, A_{el} and L are the electrical

area and the length of the investigated structure, respectively, ε is the electrical permittivity of the structure, m* is the effective mass of the charge carriers in the metallic Cu-Ag-nanoclucter structure, and v_s is the carrier velocity (Kozar et al., 2010). These experimental data lead to the conclusion that the charge carriers can be ejected from the pores of the Cu-Ag-nanocluster wire in the potential barrier and drift under applied electric field (Sze & Ng, 2007; Peleshchak & Yatsyshyn, 1996; Datta, 2006; Ferry & Goodnick, 2005; Rhoderick, 1978).

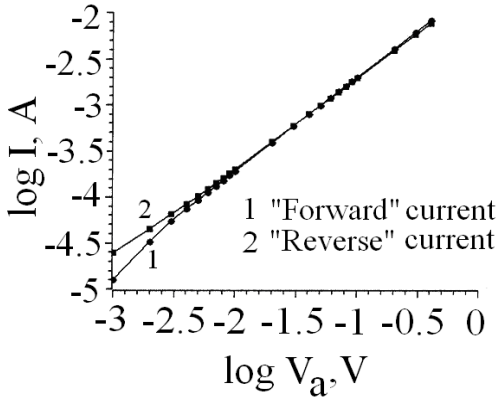

Fig. 19. Experimental room-temperature current-voltage characteristic of the examined structure in double-logarithmic scale.

10. References

Albert J. & Chudnovsky E.M. (2008). Voltage from mechanical stress in type-II superconductors: Depinning of the magnetic flux by moving dislocations, *Appl. Phys. Lett.*, Vol. 93, Issue 4, pp. 042503-1–3, doi:10.1063/1.2960337, 0003-6951(print), 1077-3118 (online).

Badesku V., Landsberg P. T. & De Vos A., Desoete B. (2001). Statistical thermodynamic foundation for photovoltaic and photothermal conversion. IV. Solar cells with larger-than-unity quantum efficiency revisited, *Journal of Applied Physics*, Vol. 89, No.4, (February 2001), pp.2482-2490, ISSN 0021-8979.

Bazarov I.P. (1964).*Thermodynamics*, Pergamon Press, ISBN 978-0080100050, Oxford, Great Britain.

Berg J.M., Tymoczko J.L. & Stryer, L. (2010). *Biochemistry*, Freeman W. H. & Company, ISBN: 1429229365, ISBN-13: 9781429229364, New York, USA.

Chernin A.D. (2008). Dark energy and universal antigravitation. *Phys. Usp.* Vol. 51, No. 3, pp. 253–282, ISSN: 1063-7869(Print), 1468-4780(Online).

Couture L. & Zitoun R. (2000). *Statistical Thermodynamics and Properties of Matter*, Gordon and Breach, ISBN 9789056991951, Amsterdam, Holland.

Curzon F. & Ahlborn B. (1975). Efficency of a Carnot engine at maximum power output, *American Journal of Physics,* Vol. 43, Issue 1, January 1975, pp. 22-24, ISSN 0002-9505.

Datta S. (2006). *Quantum transport: Atom to Transistor*, Cambridge Univ. Press, ISBN 0-521-63145-9, Cambridge, Great Britain.

De Vos A.et al. (1993). Entropy fluxes, endoreversibility, and solar energy conversion, *Journal of Applied Physics,* Vol. 74, No. 6, (June 1993), pp.3631-3637, ISSN 0021-8979.

De Vos A. (1992). *Endoreversible thermodynamics of solar energy conversion*, Oxford Univ. Press, ISBN 978-0198513926, Oxford, Great Britain.

De Vos A. (1985). Efficiency of some heat engine at maximum-power conditions, *Am. J. Phys*., Vol. 53, Issue 6, pp. 570-573, ISSN 0002.9505.

Dreicer H. (1964). Kinetic Theory of an Electron-Photon Gas, *Phys. Fluids*, Vol. 7, No. 5, pp. 732-754, Print: ISSN 1070-6631 Online: ISSN 1089-7666.

Dubinov A.E. (2009). Exact stationary solution of the Kompaneets kinetic equation. Точное стационарное решение кинетического уравнения Компанейца, Technical Physics Letters, Vol.35, No.3, pp.260-262. *Письма в ЖТФ*, том 35, вып.6, С.25-30, ISSN: 0320 - 0116.

Ferry D. & Goodnick S. (2005). *Transport in Nanostructures*, Cambridge Univ. Press, ISBN 0-521-66365-2, Cambridge, Great Britain

Green B. (2004). *The fabric of the cosmos: space, time, and the texture of realiti*. Alfred A. Knoff, ISBN 978-5-397-00001-7, New York, USA.

Han H., Bach U. & Cheng Y., Caruso R.A. 2007. Increased nanopore filling: Effect on monolithic all-solid-state dye-sensitized solar cell. *Applied Physics Letters*, Vol. 90, No.21, (May 2007), pp.213510-1-3, ISSN 0003-6951.

Hitz B. (2007). Mid-IR Fiber Laser Achieves ~10 W, *Photonics Spectra*, Vol. 41, No. 9, pp. 21–23. ISSN: n.d.

Ivanov K.P. (2008). Energy and Life. Энергия и жизнь, *Успехи современной биологии* (*Usp. Sovrem. Biol*), Vol. 128, No. 6, pp. 606–619. ISSN Print: 0042-1324

Johnson D.C., Ballard I.M. & Barnham K.W.J., Connolly J.P., Mazzer M., Bessière A., Calder C., Hill G., Roberts J.S. (2007). Observation of the photon recycling in strain-balanced quantum well solar cell. *Applied Physics Letters*, Vol. 90, No.21, (May 2007), pp.213505-1-3, ISSN 0003-6951.

Klaers J., Schmitt J., & Vewinger F., Weitz M. (2009). Bose–Einstein condensation of photons in an optical microcavity. *Nature*, Vol. 468, pp. 545-548, doi:10.1038/nature09567. ISSN: 0028-0836.

Kompaneets A.S., (1957). The establishment of thermal equilibrium between quanta and electrons, *Soviet Physics - JETP*, Vol. 4, No. 5, pp. 730-740, ISSN: 0038-5646.

Kondepudi D. & Prigogin I. (1998). *Modern Thermodynamics: From Heat Engines to Dissipative Structure*, John Wiley & Sons, Inc., ISBN 5-03-765432-1, New York, USA.

Kozar T. V., Karapuzova N. A. & Laptev G. V., Laptev V. I., Khlyap G. M., Demicheva O. V., Tomishko A. G., Alekseev A. M. (2010). Silicon Solar Cells: Electrical Properties of Copper Nanoclusters Positioned in Micropores of Silver Stripe-Geometry Elements, *Nanotechnologies in Russia*, Vol. 5, № 7-8, p.549-553, DOI: 10.1134/S1995078010070165, ISSN: 1995-0780 (print), ISSN: 1995-0799 (online).

Kuz'min V.A. & Shaposhnikov M.E. (1978). Condensation of photons in the hot universe and longitudinal relict radiation, *JETP Lett*., Vol. 27, No. 11, pp.628-631, ISSN: 0370-274X.

Landsberg, P.T. & Leff, H. (1989). Thermodynamic cycles with nearly universal maximum-work efficiencies. *Journal of Physics A*, Vol. 22, No.18, (September 1989), pp.4019-4026. ISSN 1751-8113(print).

Landsberg P.T. & Tonge G. (1980). Thermodynamic energy conversion efficiency, *Journal of Applied Physics,* Vol. 51, No. 7, (July 1980), pp. R1-R20, ISSN 0021-8979.

Landsberg P.T. (1978). *Thermodynamics and statistical mechanics*. Oxford University Press, ISBN 0-486-66493-7, Oxford, Great Britain.

Landsberg P.T. (1977). A note on the thermodynamics of energy conversion in plants, *Photochemistry and photobiology*, Vol. 26, Issue 3, pp. 313-314, Online ISSN: 1751-1097.

Laptev V.I. (2010). Chemical Potential and Thermodynamic Functions of Thermal Radiation, *Russian Journal of Physical Chemistry A*, Vol. 84, No. 2, pp. 158–162, ISSN 0036-0244.

Laptev V.I. (2009). Thermodynamic Scale of the Efficiency of Chemical Action of Solar Radiation. *Doklady Physical Chemistry,* Vol. 429, Part 2, pp. 243–245, ISSN 0012-5016.

Laptev V.I. (2008). Solar and heat engines: thermodynamic distinguish as a key to the high efficiency solar cells, In: *Solar Cell Research Progress*, Carson J.A. (Ed.), pp. 131–179, Nova Sci. Publ., ISBN 978-1-60456-030-5, New York, USA.

Laptev V.I. & Khlyap H. (2008). High-Effective Solar Energy Conversion: Thermodynamics, Crystallography and Clusters, In: *Solar Cell Research Progress*, Carson J.A. (Ed.), pp. 181–204, Nova Sci. Publ., ISBN 978-1-60456-030-5, New York, USA.

Laptev V.I. (2006). The Special Features of Heat Conversion into Work in Solar Cell Energy Reemission. *Russian Journal of Physical Chemistry,* Vol. 80, No. 7, pp. 1011–1015, ISSN 0036-0244.

Laptev V.I. (2005). Conversion of solar heat into work: A supplement to the actual thermodynamic description, *J.Appl. Phys*., Vol. 98, 124905, DOI: 10.1063/1.2149189, ISSN 0021-8979(print), 1089-7550 (online).

Leff H. (1987). Thermal efficiency at maximum work output: New results for old heat engines. *American Journal of Physics,* Vol. 55, Issue 7, July 1987, pp.602-610, ISSN 0002-9505.

Lehninger A.L., Nelson D.L. & Cox M.M. (2008). *Lehninger Principles of Biochemistry*, 5th ed., Freeman, ISBN: 1572599316, ISBN-13: 9781572599314, New York, USA.

Lukash V.N, Rubakov V.A. (2008). Dark energy: myths and reality. Phys. Usp. Vol. 51, No. 3. pp. 283–289. ISSN: 1063-7869(Print), 1468-4780(Online).

Luque A. & Marti A. (2003). In: *Handbook of Photovoltaic Science and Engineering*, Luque A. & Hegedus S.(Eds.), John Wiley and Sons Ltd., ISBN: 978-0-471-49196-5. pp. 113-151, New York, USA.

Mazenko G.F. (2000). *Equilibrium Statistical Mechanics*, Wiley & Sons, Inc, ISBN 0471328391, New York, USA.

Muenster A. (1970). *Classical Thermodynamics*, Wiley-Interscience, ISBN: 0471624306, ISBN-13: 9780471624301, New York, USA.

Novikov I. (1958). The efficiency of atomic power stations. *Journal of Nuclear Energy,* Vol. 7, No. 1-2, (August 1958), pp.125-128.

Odum E.P. (1983). *Basic Ecology*, CBS College Publ., ISBN: 0030584140, ISBN-13: 9780030584145 New York, USA.

Pechurkin N.S. (1988). *Energiya i zhizn'* (Energy and Life), Nauka, Novosibirsk, Russia.

Peleshchak R.M. & Yatsyshyn V.P. (1996). About effect of inhomogeneous deformation on electron work function of metals, *Physics of Metals and Metallography*, MAIK Nauka Publishers – Springer, vol. 82, No. 3, pp.18-26, ISSN Print: 0031-918X, ISSN Online: 1555-6190.

Pillai S , Catchpole K.R. & Trupke T., Green M.A. (2007). Surface plasmon enhanced silicon solar cells, *Journal of Applied Physics,* Vol. 101, No.9, (May 2007), pp. 093105-1-8, doi:10.1063/1.2734885, ISSN: 0021-8979 (print), 1089-7550 (online)

Raven P.H.; Evert, R.F. & Eichhorn S.E. (1999). *Biology of Plants*. 6nd ed., Worth Publiscers, Inc., ISBN: 1572590416, USA.

Rhoderick E. H., (1978). *Metal-semiconductor contacts*. Clarendon Press, ISBN 0198593236, Oxford, Great Britain.

Rubin M. (1979). Optimal configuration of a class of irreversible heat engines. I. *Physical Review A*, Vol. 19, No. 3, (March 1979), pp.1272-1276. ISSN 1094-1622 (online), 1050-2947 (print).

Semenchenko V.K. (1966). *Selected Chapters of Theoretical Physics,* Education, Moscow

Shockley W.; Queisser H., (1961). Detailed Balance Limit of Efficiency of *p-n* Junction Solar Cells, *J. Appl. Phys.*, , 32, 510-519. ISSN 0021-8979.

Slaoui A. & Collins R.T. (2007). Advanced Inorganic Materials for Photovoltaics. *MRS Bulletin*, Vol. 32, No.3, pp.211-214, ISSN: 0883-7694.

Spavieri G. & Rodrigues M. (2007). Photon mass and quantum effects of the Aharonov-Bohm type, *Phys. Rev. A*, Vol. 75, 05211, ISSN 1050-2947 (print) 1094-1622 (online).

Steinfeld A. & Palumbo R. (2001). *Encyclopedia of Physical Science & Technology*. R.A. Mayers (Editor)Vol. 15, pp. 237–256, Academic Press, ISBN: 0122269152, ISBN-13: 9780122269158, New York.

Sze S.M. & Ng, K.K. (2007). *Physics of semiconductor devices*, J. Wiley & Sons, Inc., ISBN 0-471-14323-5, Hoboken, New Jersey, USA.

Voet D.J., Voet J.G. & Pratt C.W. (2008). *Principles of Biochemistry*, 3d ed., John Wiley & Sons Ltd, ISBN:0470233966, ISBN-13: 9780470233962, New York,USA.

Wegh R.T., Donker, H. & Oskam K.D., Meijerink A. (1999). Visible Quantum Cutting in $LiGdF_4:Eu^{3+}$ Through Downconversion, *Science*, 283, 663-666, *DOI:10.1126/science.283.5402.663*, ISSN 0036-8075 (print), 1095-9203 (online).

Werner J.; Kolodinski S. & Queisser H. (1994). Novel optimization principles and efficiency limits for semiconductor solar cells. *Physical Review Letters,* vol.72, No.24 (June 1994), p.3851-3854. ISSN 0031-9007 (print), 1079-7114 (online)

Weymann R. (1965). Diffusion Approximation for a Photon Gas Interacting with a Plasma via the Compton Effect , *Phys. Fluids*, Vol. 8, No. 11, pp. 2112-2114, Print: ISSN 1070-6631 Online: ISSN 1089-7666.

Wuerfel P. (2005). *Physics of Solar Cells*, WILEY-VCH Verlag GmbH and Co. KGaA, ISBN 978-3527408573, Wienheim, Germany.

Yungman V.S. & Glushko (Eds). (1999). *Thermal Constant of Substances*, 8 volume set, Vol. 1, John Wiley & Sons, ISBN: 0471318558 New York, USA.

Zel'dovich Ya.B. & Syunyaev R.A. (1972). Shock wave structure in the radiation spectrum during bose condensation of photons, *Soviet Physics - JETP*, Vol. 35, No. 1, pp. 81-85, ISSN: 0038-5646.

18

Hybrid Solar Cells Based on Silicon

Hossein Movla[1], Foozieh Sohrabi[1],
Arash Nikniazi[1], Mohammad Soltanpour[3] and Khadije Khalili[2]
[1]*Faculty of Physics, University of Tabriz*
[2]*Research Institute for Applied Physics and Astronomy (RIAPA), University of Tabriz*
[3]*Faculty of Humanities and Social Sciences, University of Tabriz*
Iran

1. Introduction

Human need for renewable energy resources leads to invention of renewable energy sources such as Solar Cells (SCs). Historically, the first SCs were built from inorganic materials. Although the efficiency of such conventional solar cells is high, very expensive materials and energy intensive processing techniques are required. In comparison with the conventional scheme, the hybrid Si-based SC system has advantages such as; (1) Higher charging current and longer timescale, which make the hybrid system have improved performances and be able to full-charge a storage battery with larger capacity during a daytime so as to power the load for a longer time; (2) much more cost effective, which makes the cost for the hybrid PV system reduced by at least 15%(Wu et al., 2005). Thus, hybrid SCs can be a cheap alternative for conventional SCs.

One type of hybrid SCs is a combination of both organic and inorganic materials which combines the unique properties of inorganic semiconductors with the film forming properties of conjugated polymers. Organic materials are inexpensive, easily processable, enabling lightweight devices and their functionality can be tailored by molecular design and chemical synthesis. On the other hand, inorganic semiconductors can be manufactured as nanoparticles and inorganic semiconductor nanoparticles offer the advantage of having high absorption coefficients, size tenability and stability. By varying the size of nanoparticles the bandgap can be tuned therefore the absorption range can be tailored (Günes & Sariciftci, 2008). These kinds of hybrid SCs based on organic-inorganic materials are fabricated by using different concepts such as solid state dye-sensitized SCs and hybrid SCs using Bulk Heterojunction (BHJ) concept such as TiO_x(Hal et al., 2003), ZnO (Beek et al., 2006), CdSe (Alivisatos, 1996; Huynh et al., 2002), Cds (Greenham et al., 1996), PbS (McDonald et al.,2005), and $CuInS_2$.

Another generation of hybrid SCs are silicon-based modules due to the direct bandgap and high efficiency of Si. This system includes SC module consisting of crystalline and amorphous silicon-based SCs. The methods for enhancing the efficiencies in these types of hybrid SCs such as applying textured structures for front and back contacts as well as implementing an intermediate reflecting layer (IRL) between the individual cells of the tandem will be discussed (Meillaud et al., 2011). This chapter brings out an overview of principle and working of hybrid SCs consisting of HJ SCs which is itself devided into two groups, first organic-inorganic

module and second, HJ SCs based on single crystalline, amorphous and microcrystalline Si and SCs in dye-sensitized configuration. Afterward, material characterization of these kinds of SCs will be investigated. Precisely, Crystalline Si thin film SCs and later amorphous and microcrystalline Si SCs and the recent works are discussed.

2. Principle and working of hybrid solar cells

One of the methods to build hybrid SCs is Bulk Hetrojunction (BHJ) SCs, composed of two semiconductors. Excitons created upon photoexcitation are separated into free charge carriers at interfaces between two semiconductors in a composite thin film such as a conjugated polymer and fullerene mixtures. One of these materials of an HJ obviously must be an absorber. The other may be an absorber, too, or it may be a window material; i.e., a wider–gap semiconductor that contributes little or nothing to light absorption but is used to create the HJ and to support carrier transport. Window materials collect holes and electrons, which function as majority-carrier transport layers, and can separate the absorber material from deleterious recombination at contacts. The interface they form with the absorber is also used for exciton dissociation in cells where absorption is by exciton formation. Absorber and window materials may be inorganic semiconductors, organic semiconductors, or mixtures (Fonash, 2010, as cited in Khalili et al. 2010; Sohrabi et al. 2011). For applying HJ structure (HJS) for hybrid SCs, the blends of inorganic nanocrystals with semiconductive polymers as a photovoltaic layer should be employed.

Schematically, the HJ hybrid SCs consist of at least four distinct layers, excluding the substrate, which may be glass. These our layers are anode, cathode, hole transport layer and active layer. Induim tin oxide (ITO) is a popular anodic material due to its transparency and glass substrate coated with ITO is commercially available. A layer of the conductive polymer mixture PEDOT:PSS may be applied between anode and the active layer. The PEDOT:PSS layer serves several functions. It not only serves as a hole transporter and exciton blocker, but it also smoothens out the ITO surface, seals the active layer from oxygen, and keeps the anode material from diffusing into the active layer, which can lead to unwanted trap sites. Next, on the top of the PEDOT:PSS, layer deposited is the active layer. The active layer is responsible for light absorption, exciton generation/dissociation and charge carrier diffusion (Chandrasekaran et al., 2010). The so-called two materials are inserted in active layer namely donor and acceptor. Polymers are the common donors whereas nanoparticles act as common acceptors. On the top of active layer is cathode, typically made of Al, Ca, Ag and Au (Chandrasekaran et al., 2010).

BHJ hybrid SCs attracts much interest due to these features:

a. HJs allow the use of semiconductors that can only be doped either n-type or p-type and yet have attractive properties which may conclude their absorption length, cost, and environmental impact. The existence of concentration gradient of the n-type nanoparticles within the p-type polymer matrix may allow optimization of the topology of the HJ network.
b. HJs allow the exploitation of effective forces.
c. HJs of window-absorber type can be used to form structures that shield carriers from top-surface or back-surface recombination sinks (Fonash , 2010).
d. The affinity steps at HJ interfaces can be used to dissociate excitons into free electrons and holes.
e. HJs can also permit open-circuit voltages that can be larger than the built-in electrostatic potential.

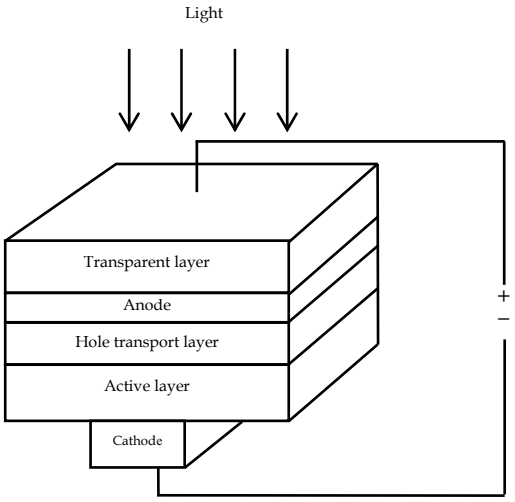

Fig. 1. Structure of HJ hybrid SCs

f. Inorganic semiconductor materials can have high absorption coefficients and photoconductivity as many organic semiconductor materials (Günes & Sariciftci, 2008).

Typically, inorganic semiconductors in macroscopic dimensions, irrespective of their size, will absorb all electromagnetic radiation with energy greater than the bandgap. However, if the particles become smaller than that of the exciton in the bulk semiconductor (typically about 10 nm), their electronic structure has changed. The electronic properties of such small particles will depend not only on the material of which they are composed, but also on their size, the so-called quantum confinement effect (Arici et al., 2004, as cited in Weller, 1993; Steigerwald & Brus, 1990; Alivisatos, 1996; Empedocles & Bawendi, 1999; Murphy & Coffer, 2002; Movla et al. 2010a). The lowest energy of optical transition, among others, will increase significantly due to the quantum confinement with decreasing size of the inorganic clusters. Since the energy levels of the polymers can be tuned by chemical modification of the backbone chain and the energy levels of the nanoparticles can be tuned through the size-dependent quantum confinement effects, blends of the two materials offer the possibility of tailoring optimal conditions for a solar cell, including energy gain from charge transfer for the efficient charge separation and the spectral range of the absorbing light (Arici et al., 2004). Therefore, in order to obtain hybrid polymer SCs with high current and fill factor, both electron and hole mobilities must be optimized and most importantly balanced (Chandrasekaran et al., 2010). However, diffusion of nanoparticles into the polymer matrix takes place with the penetration depth controlled by temperature, swelling of the polymer layer, and not at least by the size and shape of the nanocrystals.

Another module of HJ hybrid SCs consists of crystalline and amorphous silicon-based SCs which is the main discussion in this chapter. The present PV market is dominated by three kinds of Si-based solar cells, that is, single-, multi-crystalline or amorphous Si-based solar cells (for short, marked hereafter as Sc-Si, Mc-Si and a-Si solar cells, respectively). The conventional PV system in general uses Sc-Si or Mc-Si solar cell module as the element for solar energy conversion, which have comparatively higher conversion efficiency. However, it is not only the module efficiency that decides whether a PV system is cost effective but

also the timescale during which the module works efficiently in a daytime of use and the cost the module itself requires. At this point, a-Si solar cell comes with its advantages of broader timescale and lower cost (Wu et al., 2005, as cited in Goetzberger et al., 2003).
The broader timescale merit of a-Si solar cell arises from its high absorption of light with wavelength around 300–800nm, no matter if it is scattered or not, and no matter if it is weak or blazing. The Sc-, Mc- and a-Si solar cells, therefore, reinforce each other in performances, which could be exploited to construct a hybrid PV system with lower cost in view of the well balanced set of system performance (Wu et al., 2005). The last efficiencies reported for c-Si, Mc-Si and a-Si are approximately 25%, 20% and 10%, respectively (Green et al., 2011).
The newest configuration for hybrid SCs is dye-sensitized SC developed by O'Reagan and Graetzel in 1991.This class of cell has reached efficiencies of over 11%. The basic structure of a dye-sensitized SC involves a transparent (wide-band-gap) n-type semiconductor configured optimally in a nanoscale network of columns, touching nanoparticles, or coral-like protrusions. The surface area of the network is covered everywhere with a monolayer of a dye or a coating of quantum dots, which functions as the dye (Fonash, 2010). A monolayer of dye on a flat surface can only harvest a negligibly small fraction of incoming light. In this case it is useful to enlarge this interface between the semiconductor oxide and the dye. As mentioned above, it is achieved by introducing a nanoparticle based electrode construction which enhances the photoactive interface by orders of magnitude (Grätzel, 2004). The dye sensitizer is the absorber. An electrolyte is then used to permeate the resulting coated network structure to set up a conduit between the dye and the anode. The dye absorbs light, producing excitons, which dissociate at the dye-semiconductor interface, resulting in photogenerated electrons for the semiconductor and oxidized dye molecules that must be reduced and thereby regenerated by the electrolyte (Fonash, 2010).

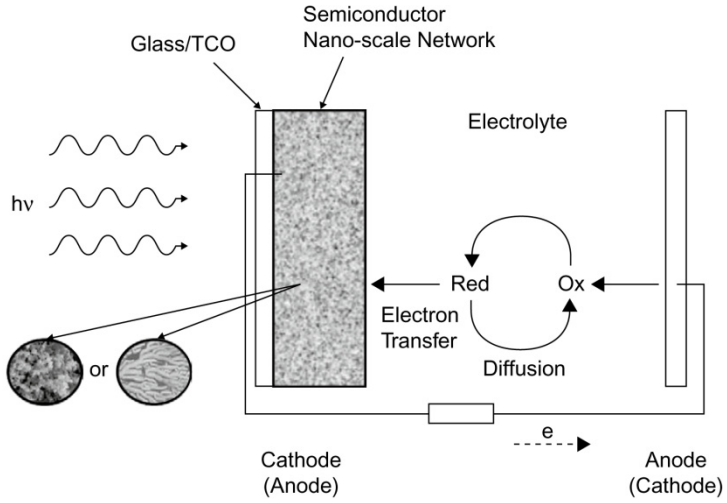

Fig. 2. Schematic of a dye-sensitized SC

A dye-sensitized SC of Graetzel type comprises of several different materials such as nanoporous TiO_2 electrodes, organic or inorganic dyes, inorganic salts and metallic catalysts (Grätzel, 2004, 2005, as cited in Nogueira et al., 2004; Mohammadpour et al., 2010) which

will be discussed more in next section. The dye sensitization of the large band-gap semiconductor electrodes is achieved by covering the internal surfaces of porous TiO_2 electrode with special dye molecules which absorb the incoming photons (Halme, 2002).
Alternatives to the liquid electrolyte in dye-sensitized SCs are a polymer gel electrolyte or solid state dye-sensitized SCs which can contain organic hole conductor materials, inorganic p-type semiconductors or conjugated polymers (Fonash, 2010). The impetus for this effort is the increased practicality of an all-solid-state device and the avoidance of chemical irreversibility originating from ionic discharging and the formation of active species (Fonash, 2010, as cited in Tennakone et al., 2000). And also this method avoids problems such as leakage of liquid electrolyte. In solid state dye-sensitized SCs, the sensitizer dye is regenerated by the electron donation from the hole conductor (Wang et al., 2006). The hole conductor must be able to transfer holes from the sensitizing dye after the dye has injected electrons into the TiO_2. Furthermore, hole conductors have to be deposited within the porous nanocrystalline (nc) layer penetrating into the pores of the nanoparticle and finally it must be transparent in the visible spectrum, or, if it absorbs light, it must be as efficient in electron injection as the dye. (Günes & Sariciftci, 2008)

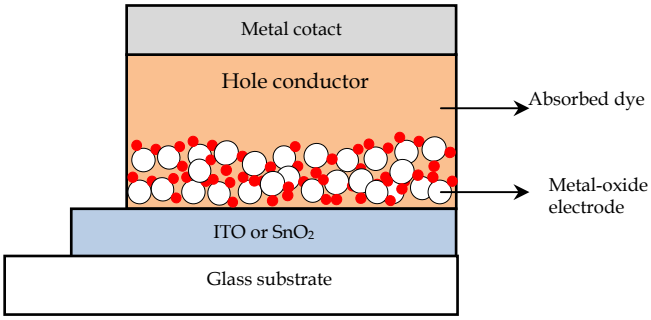

Fig. 3. Schematic of solid state dye-sensitized SC

Other quasi-dye sensitized SCs are nanoparticle sensitized SCs and extremely thin absorber (ETA) SCs. Nanoparticle sensitized SCs are prepared by replacing the dye with inorganic nanoparticles or quantum dots. They can be adsorbed from a colloidal quantum dot solution (Zaban et al., 1998; as cited in Günes et al., 2006; Guenes et al., 2007) or produced in situ (Liu & Kamat, 1993; as cited in Hoyer & Könenkamp, 1995). Inorganic nanocrystals instead of organic dyes could imply tunability of the band-gap and thereby the absorption range. Nanocrystals have large extinction coefficients due to quantum confinement and intrinsic dipole moments, leading to rapid charge separation and are relatively stable inorganic materials (Alivisatos, 1996). To embed the particles into porous TiO_2 films and to use those modified layers as light converting electrodes, the incorporated nanoparticles need to be much smaller than the pore sizes of the nanoporous TiO_2 electrodes (Shen, 2004).
ETA SCs are conceptually close to the solid state dye-sensitized solar cells. In the ETA SCs, an extremely thin layer of a semiconductor such as $CuInS_2$ or CdTe or CuSCN replaces the dye in TiO_2 based SCs. The ETA SCs has the advantage of enhanced light harvesting due to the surface enlargement and multiple scattering. Similar to the solid state dye sensitized Scs, the operation of the ETA SC is also based on a heterojunction with an extremely large interface (Nanu et al., 2005).

3. Material characterization of hybrid solar cells

Relating to the configuration of hybrid SCs like HJ SCs or dye-sensitized SCs, various materials have been suggested by research groups. The BHJ devices were characterized by an interpenetrating network of donor and acceptor materials, providing a large interface area where photo-induced excitons could efficiently dissociate into separated electrons and holes. However, the interpenetrating network cannot be easily formed in the blended mixture. In addition, the organic materials are not good in carrier transport. Thus, the power conversion efficiency is still limited by the low dissociation probability of excitons and the inefficient hopping carrier transport (Huang et al., 2009, as cited in Sirringhaus et al.,1999; Shaw et al.,2008). Semiconductor nanostructures are used to be combined with the organic materials to provide not only a large interface area between organic and inorganic components for exciton dissociation but also fast electron transport in semiconductors. Therefore, many research groups combined organic materials with semiconductor nanostructures to overcome the drawbacks of the organic solar cells. Many inorganic nanowire (NW) had been experimented for this purpose, including CdTe, CdS, CdSe, ZnO, and TiO_2 NWs (Huang et al., 2009, as cited in Kang & Kim, 2006). Totally, BHJ hybrid SCs itself have been demonstrated in various inorganic materials such as CdSe nanodots, nanorods and tetrapods, TiO_2, ZnO, ZnS nanoparticles, $CuInS_2$, $CuInSe_2$, CuPc, CdS, SnS, CIS , PbSe or PbS nanocrystals , HgTe ncs, Si NWs, Si ncs (Chandrasekaran et al., 2010 as cited in Kwong et al.,2004, Arici et al., 2004 Greenham et al., 1996 Qi et al., 2005; Choudhury et al., 2005), etc. which act as acceptors and polymer materials acting as donors are P3HT, PPHT, P3OT, P3BT, P3MeT (Lin et al., 2006), MDMO-PPV, MEH-PPV, MOPPV, etc. (Chandrasekaran et al., 2010). However,CdTe, CdS,and CdSe materials are harmful to the environment, while ZnO and TiO_2 have a bandgap higher than 3eV and so cannot effectively absorb the solar spectrum. To overcome this, SiNWs are suitable for this application because they are environmental friendly and have high absorption coefficient in the infrare dregion (Huang et al., 2009).
J.Haung et al. (2009) reported the fabrication of the SiNW/P3HT:PCBM blend hybrid SCs using the SiNW transfer technique.

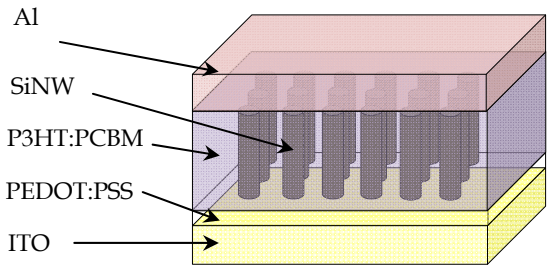

Fig. 4. A schematic of the hybrid SC using SiNWs and P3HT:PCBM blend

Their investigation showed that after introducing the SiNWs, the J_{sc} increases from 7.17 to 11.61 mA/cm² and η increases from 1.21% to 1.91% (Haung et al., 2009). This increase is due to this fact that the NWs act as a direct path for transport of charge without the presence of grain boundaries.(Movla et al., 2010b).

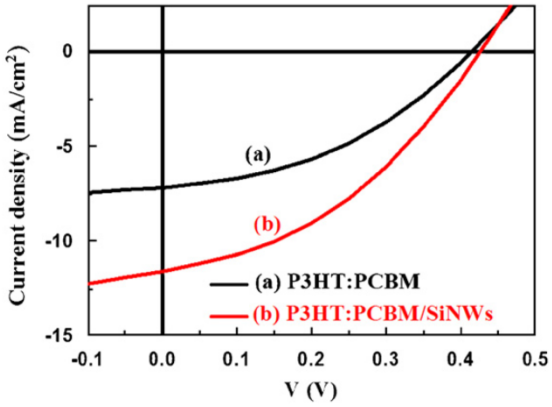

Fig. 5. The current density–voltage characteristics for the SCs with and without the SiNWs under simulated AM1.5 illumination. Reprinted with permission from Solar Energy Materials & Solar Cells Vol.93, Huang, J. et al. Well-aligned single-crystalline silicon nanowire hybrid solar cells on glass, pp. 621–624 © 2009, Elsevier.

More precisely, the results clearly indicate that combination of the SiNWs and P3HT:PCBM blend is an attractive route to obtain high J_{sc} and efficiencies by improving the optical absorption, dissociation of excitons, and the electron transport. Silicon wafer is commercially available and cheap. SiNWs can be fabricated at low temperature from solution processing without any vacuum equipment or high-temperature processing. In addition, this transfer method for SiNWs is simple and fast. It is not a laborious way.This method is suitable for plastic SCs because it can be processed fast, is cheap and simple (Haung et al., 2009).

Similar work was done by G. Kalita et al. (2009) for demonstrating hybrid SCs using Si NWs and polymer incorporating MWNTS. This fabricated device with the structure of Au/P3OT+O-MWNTS/n-Si NWs marked a conversion efficiency of 0.61% (Bredol et al., 2009). Another study was done by C. Y. Liu et al. (2009) about fabricating the hybrid SCs on blends of Si ncs and P3HT (Liu et al., 2009). Also, V. Svrcek et al. (2009), investigated the photoelectric property of BHJ SC based on Si-ncs and P3HT. They came into conclusion that I–V characteristic enhanced when BHJ was introduced into TiO_2 nanotube (nt). The arrangement of Si-ncs/P3HT BHJ within ordered TiO_2 nt perpendicular to the contact facilitated excition separation and charge transfer along nts (Chandrasekaran et al., 2010, as cited in Svrcek et al., 2009).

A new approach for hybrid metal-insulator-semiconductor (MIS) Si solar cells is adopted by the Institute of Fundamental Problems for High Technology, Ukrainian Academy of Sciences. In this technique, the porous silicon layers are created on both sides of single crystal wafers by chemical etching before an improved MIS cell preparation process. The porous Si exhibits unique properties. It works like a sunlight concentrator, light scattering diffuser and reemitter of sunlight as well as an electrical isolator in the multilayer Si structure. The most important advantage of using porous Si in SCs is its band gap which behaves as a direct band gap semiconductor with large quantum efficiency and may be adjusted for optimum sunlight absorption. Employing a specific surface modification, porous Si improves the PV efficiency in UV and NIR regions of solar spectra (Tuzun et al.,

2006, as cited in Tiris et al., 2003). In this approach, due to high quality starting materials and rapid low-temperature (<800 ^{0}C) processing a high minority carrier life time is attainable; this, in turn, gives rise to a high photogenerated current collection. Therefore, the SCs with efficiencies above 15% have been obtained under AM1.5 condition (under 100 mW/cm^2 illumination at 25 ^{0}C) (Tuzun et al., 2006).

Another study was reported by J. Ackermann et al. (2002) about the growth of quaterthiophene (4T), a linear conjugated oligomer of thiophene behaving as a p-type semiconductor, on n-doped GaAs and Si substrates to form hybrid HJ SCs. This study shows that in the case of Si as substrate there is almost defect-free high ordered films with grain sizes of several micrometers up to a film thickness of 250 mm (Ackermann et al., 2002).

K.Yamamoto et al. (2001) investigated a-Si/poly-Si hybrid (stacked) SC paying attention to the stabilized efficiency, since a-Si has photo degradation, while a poly-Si is stable. This tandem cell exhibited a stabilized efficiency of 11.3%. Also, this research group prepared three-stacked cell of a-Si:H/poly-Si/poly-Si(triple), which will be less sensitive to degradation by using the thinner a-Si. This triple cell showed a stabilized efficiency of 12%(Yamamoto et al., 2001) . Their reasons for applying poly-Si are (i) high growth rate (ii) large area and uniform deposition at the same time and (iii) monolithic series interconnection. In addition, for enhancing the absorption, they suggested natural surface texture and a back reflector (See Fig .6.) (Yamamoto et al., 2001).

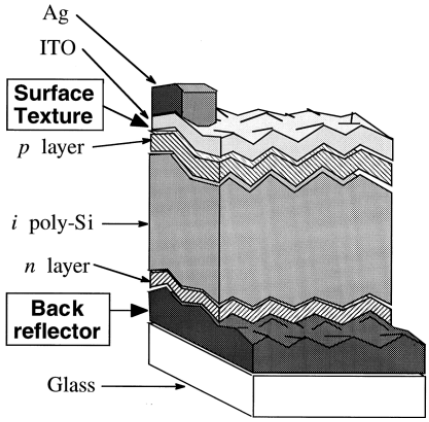

Fig. 6. Schematic view of thin film poly-Si solar cell with natural surface texture and enhanced absorption with back reflector structure. Reprinted with permission from Solar Energy Materials & Solar Cells Vol.93, Huang, J. et al. Well-aligned single-crystalline silicon nanowire hybrid solar cells on glass, pp. 621–624 © 2009, Elsevier.

Apart from BHJ SCs, solid state dye-sensitized SCs can experience various materials. CuI, CuBr, CuSCN, MgO (Tennakone et al.,2001) can be replacements for liquid crystals as inorganic p-type semiconductors. Also, 2,2',7,7'-tetranis(N,N-di-p-methoxyphenyl-amine)9,9'-spirobifluorene (OMETAD) can replace the liquid crystals as organic p-type semiconductor due to their low cost processability (Bach et al.,1995). Poly (3 alkylthiophenes) were used to replace the liquid electrolyte by Sicot et al. (Sicot et al., 1991) and Gebeyehu et al. (Gebeyenha et al.,2002a,2002b) as conjugated polymers although high molecular weight polymers cast from solution, do not penetrate into the pores of the

nanoparticles. A polymeric gel electrolyte is considered as a compromise between liquid electrolytes and hole conductors in quasi solid state dye-sensitized SCs (Günes & Sariciftci,2008, as cited in Nogueira et al.,2004;Murphy,1998; Megahed & Scosati,1995) . A mixture of NaI, ethylene carbonate, propylene carbonate and polyacrylonitrile was reported by Cao et al. [55]. Poly (vinylidenefluoride- co-hexafluoropropylene) (PVDF-HFP) used to solidify 3-methoxypropionitrile (MPN) was utilized by Wang et al. (Wang et al.,2004). The last efficiency for dye-sensitized reported by Sharp Corporation is about 10.4 which stands in lower rank in comparison with crystalline Si showing efficiency of approximately 25% (Green et al., 2011).

3.1 Crystalline silicon thin film solar cells

Silicon is the leading material used in microelectronic technology and shows novel photoelectrochemical properties in electrolyte solutions (Wang et al.,2010). Now and before Si-based cells especially crystalline Si has shown higher efficiencies. The last efficieny reported by UNSW PERL is 25% which exceeds other types of Si-based SCs (Green et al., 2011, Zhao et al., 1998).

Crystalline silicon (c-Si) is an extremely well suited material for terrestrial photovoltaics (PV). It is non-toxic and abundant (25% of the Earth's crust), has excellent electronic, chemical and mechanical properties, forms a simple monoelemental semiconductor that has an almost ideal bandgap (1.1 eV) for terrestrial PV, and gives long-term stable SCs and modules. Furthermore, it is the material of choice in the microelectronics industry, ensuring that a large range of processing equipment exists and is readily available. Given these properties of c-Si, it is not surprising that almost all (>90%) terrestrial PV modules sold today use Si wafer SCs. However, the fabrication of Si wafers is both material and energy intensive. Therefore, there is a need for a less material intensive c-Si technology calling a thin-film technology. Besides cost savings on the materials side, thin-film technologies offer the additional benefits of large-area processing (unit size about 1 m^2) on a supporting material, enabling monolithic construction and cell interconnection. The recent c-Si thin-film PV approaches can broadly be classified as follows: (i) fabrication of thin, long stripes of c-Si material from thick single crystalline Si wafers (''ultrathin slicing''); (ii) growth of c-Si thin-films on native or foreign supporting materials (Aberle, 2006).

Recently photoelectrochemical (PEC) SCs based on 1D single crystalline semiconductor micro/nanostructures have attracted intense attention as they may rival the nanocrystalline dye-sensitized SCs (Wang et al., 2010, as cited in Law et al., 2005; Peng et al., 2008; Baxter & Aydil, 2005; Jiang et al., 2008; Mor et al., 2006; Hwang et al., 2009; Dalchiele et al., 2009; Goodey et al., 2007; Maiolo et al., 2007). Therefore, X.Wang et al. (2010) proposed single crystalline ordered silicon wire/Pt nanoparticle hybrids for solar energy harvesting. In this configuration, wafer-scale Si wire arrays are fabricated by the combination of ultraviolet lithography (UVL) and metal-assisted etching. This method emphasizes that the etching technology forms SiNWs non-contaminated by catalyst material while SiNWs by vapor-liquid-solid (VLS) is generally contaminated by gold (Wang et al., 2010, as cited in Allen et al., 2008). It is found that PtNPs modified Si wire electrochemical PV cell generated significantly enhanced photocurrents and larger fill factors. The overall conversion efficiency of PtNPs modified Si wire PEC solar cell is up to 4.7%. Array of p-type Si wire modified with PtNPs also shows significant improvement for water splitting (Wang et al., 2010).

3.2 Amorphous (protocrystalline) and microcrystalline silicon solar cells

The use of thin-film silicon for SCs is one of the most promising approaches to realize both high performance and low cost due to its low material cost, ease of manufacturing and high efficiency. Microcrystalline silicon (μc) SCs as a family of thin film SCs formed by plasma CVD at low temperature are assumed to have a shorter carrier lifetime than single-crystal cells, and it is common to employ a p–i–n structure including an internal electric field in the same way as an amorphous SC. These cells can be divided into p–i– n and n–i–p types according to the film deposition order, although the window layer of the SC is the p-type layer in both cases. A large difference is that the underlying layer of a p–i–n cell is the transparent p-type electrode, whereas the underlying layer of an n–i–p cell is the n-type back electrode. Light-trapping techniques are a way of increasing the performance of mc-SCs. This is a core technique for cells made from μc-silicon because—unlike a-silicon—it is essentially an indirect absorber with a low absorption coefficient. That is, the thickness of the Si film that forms the active layer in a mc-silicon SC is just a few μm, so it is not able to absorb enough incident light compared with SCs using ordinary crystalline substrates. As a result, it is difficult to obtain a high photoelectric current. Light trapping technology provides a means of extending the optical path of the incident light inside the SC by causing multiple reflections, thereby improving the light absorption in the active layer (Yamamoto et al., 2004). Light trapping in this method of categorizing the SCs according to p-i-n or n-i-p types, can be achieved in two ways: (1) by introducing a highly reflective layer at the back surface to reflect the incident light without absorption loss, and (2) by introducing a textured structure at the back surface of the thin-film Si SC (see Fig.7.) (Komatsu et al.,2002; Yamamoto et al.,2004).

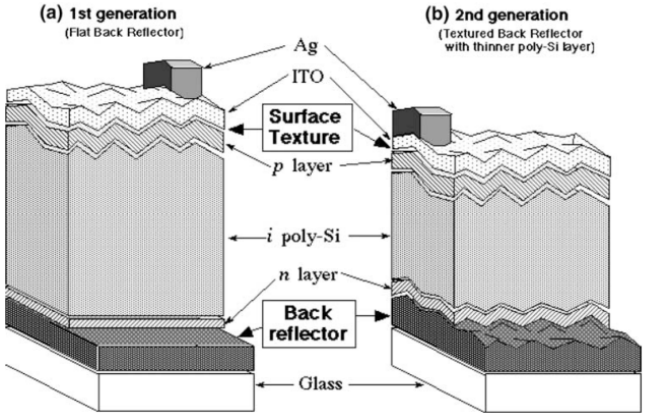

Fig. 7. Cross-sections through light-trapping μc-silicon SC devices: (a) first generation (flat back reflector); (b) second generation (textured back reflector, thinner polycrystalline silicon layer). Reprinted with permission from Solar Energy Vol. 77, Kenji Yamamoto et al., A high efficiency thin film silicon solar cell and module, pp. 939–949 © 2004, Elsevier.

Although the μc-silicon cells formed at low temperature have a potential for high efficiently, their efficiency in single-cell structures is currently only about 10%, which is much lower than that of bulk polycrystalline cells. In order to achieve high efficiencies, Yamamoto et al.(2004) investigated the use of two-and three-stacked (hybrid) structures in which multiple

cells with different light absorption characteristics are stacked together. This approach allows better characteristics to be obtained with existing materials and processes. The advantages of using a layered structure include the following: (1) it is possible to receive light by partitioning it over a wider spectral region, thereby using the light more effectively; (2) it is possible to obtain a higher open-circuit voltage; and (3) it is possible to suppress to some extent the rate of reduction in cell performances caused by photo-degradation phenomena that are observed when using a-silicon based materials. Therefore, they have engaged in thin film amorphous and microcrystalline (a-Si/μc-Si) stacked solar cell (Yamamoto et al., 2004).

The advantage of a high Jsc for our μc-Si Sc as mentioned before was applied to the stacked cell with the combination of a-Si cell to gain stabilized efficiency as the study done by K.Yamamoto et al. (2001) since a-Si has a photo-degradation while a μc-Si cell is stable. They have also prepared three stacked cell of a-Si:H/μc-Si/c-Si (triple), which will be less sensitive to degradation by using the thinner a-Si and they have investigated the stability of a-Si:H/μc-Si/μc-Si (triple) cell, too (Yamamoto et al., 2001, 2004). Some other three stacked Si-based SCs can be named such as a-Si/a-SiGe/a-SiGe(tandem) and a-Si/nc-Si/nc-Si (tandem) SCs. The last efficiency reported for a-Si/a-SiGe/a-SiGe(tandem) is about 10.4% and for a-Si/nc-Si/nc-Si (tandem) is approximately 12.5% (Green et al., 2011).

As a next generation of further high efficiency of SC, the new stacked thin film Si SC is proposed where the transparent inter-layer was inserted between a-Si and μc-Si layer to enhance a partial reflection of light back into the a-Si top cell (see fig.8.). This structure is called as internal light trapping enabling the increase of current of top cell without increasing the thickness of top cell, which leads less photo-degradation of stacked cell (Yamamoto et al., 2004).

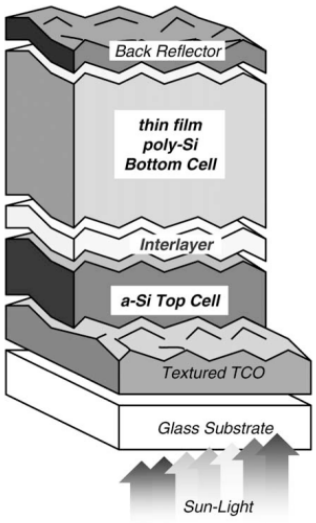

Fig. 8. Schematic view of a-Si/poly-Si (μc-Si) stacked cells with an interlayer. Reprinted with permission from Solar Energy Vol. 77, Kenji Yamamoto et al., A high efficiency thin film silicon solar cell and module, pp. 939–949 © 2004, Elsevier.

By introduction of this interlayer, a partial reflection of light back into the a-Si top cell can be achieved. The reflection effect results from the difference in index of refraction between the interlayer and the surrounding silicon layers. If n is the refractive index and d is the thickness of inter-layer, the product of $\Delta n \times d$ determine the ability of partial reflection. Namely, the light trapping is occurred between the front and back electrode without inter-layer, while with inter-layer, it is also occurred between inter-layer and back electrode. This could reduce the absorption loss of TCO and a-Si:H (see Fig.9.) (Yamamoto et al., 2004).

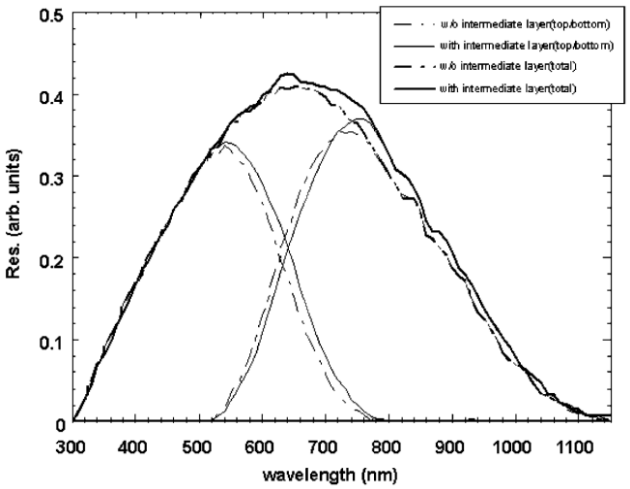

Fig. 9. Spectral-response of the cell with and without interlayer. Bold and normal line shows the spectral-response of the cell with and without inter-layer. Reprinted with permission from Solar Energy Vol. 77, Kenji Yamamoto et al., A high efficiency thin film silicon solar cell and module, pp. 939–949 © 2004, Elsevier.

Some of the advantages of thin film SCs are being characterized to low temperature coefficient, the design flexibility with a variety of voltage and cost potential. Therefore, the thin film Si SCs can be used for the PV systems on the roof of private houses as seen in Fig.10. (Yamamoto et al., 2004).

Another similar work was done by F. Meillaud et al.(2010). They investigated the high efficiency (amorphous/microcrystalline) "micromorph" tandem silicon SCs on glass and plastic substrates. High conversion efficiency for micromorph tandem SCs as mentioned before requires both a dedicated light management, to keep the absorber layers as thin as possible, and optimized growth conditions of the µc-silicon(µc-Si:H) material. Efficient light trapping is achieved in their work by use of textured front and back contacts as well as by implementing an intermediate reflecting layer (IRL)between the individual cells of the tandem.The latest developments of IRLs at IMT Neuchˆatel are: SiOx based for micromorphs on glass and ZnO based IRLs for micromorphs on flexible substrates successfully incorporated in micromorph tandem cells leading to high,matched, current above 13.8mA/cm² for p–i–n tandems. In n–i–p configuration, asymmetric intermediate reflectors (AIRs) were employed to achieve currents of up to 12.5mA/cm² (see fig.11.) (Meillaud et al., 2011).

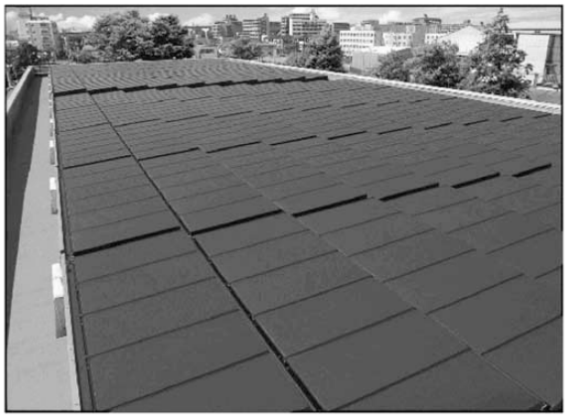

Fig. 10. KW system at the top of the building Osaka (HYBRID modules). Note that modules are installed at low angle (5 degree off from horizontal).

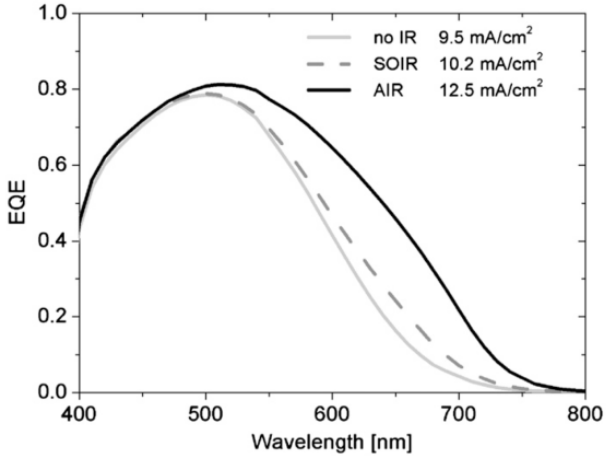

Fig. 11. External quantum efficiency of the top cell in an n–i–p/n–i–p micromorph on flexible substrate (i-layer thickness:200nm). Reprinted with permission from Solar Energy Vol. 95, Meillaud et al., Realization of high efficiency micromorph tandem silicon solar cells on glass and plastic substrates: Issues and potential, pp. 127-130 © 2010, Elsevier.

The last efficiency reported by Oerlikon Solar Lab, Neuchatel for a-Si/μc-Si (thin film cell) is about 11.9% (Green et al., 2011, as cited in Bailat et al., 2010). More precisely talk about tandem cells will be done in following sections.

3.3 Tandem cell

The tandem junction cell is a high-performance silicon solar cell, which is best suited for terrestrial solar power systems. The most distinctive design feature of this device is the use

of only back contacts to eliminate the metal shadowing effects because of lower conversion efficiency and steady-state bias requirement. Here we discuss tandem devices consisting of the a-si:H with other forms of silicon:

3.3.1 Tandem cell with multicrystalline Si

In the tandem cell configuration in 1983, Hamakawa reported the structure that a-Si: H/μc-Si heterojunction cell has been investigated as a bottom cell (Hamakawa et al. 1982). Its advantage is that it does not require high temperature processing for junction formation, and the top a-Si:H cell can be fabricated continuously. A heterojunction cell that is reported in 1994 by Matsuyama consisting of a-Si:H as p-type and μc-Si as n-type, with a 10 pm thick μc-Si film fabricated by solid phase crystallization yielded an efficiency of 8.5%. By using a p-μc-Si: C/n-μc-Si/n-pc-Si heterojunction bottom solar cell a conversion efficiency of 20.3% and good stability can be gained. At least in this type of devices the highest efficiency reported up to now is 20.4% (Green et al., 2011).

3.3.2 Tandem cell with microcrystalline Si

Microcrystalline silicon (μc-Si) has been studied extensively for three decades and has been used for doped layers in a-Si solar cells for over 15 years. Microcrystalline silicon is a complex material consisting of conglomerates of silicon nanocrystallites embedded into amorphous silicon. It can be more easily doped than a-Si:H; but, on the other hand, it is also more sensitive to contaminants than a-Si:H. The nucleation and growth of μc-Si:H are determinant for device quality; a certain amount of amorphous material is needed for the passivation of the nanocrystallites and for the reduction of defect related absorption. During the growth of the layer, the formation of crystallites starts with a nucleation phase after an amorphous incubation phase. During continued layer deposition, clusters of crystallites grow (crystallization phase) until a saturated crystalline fraction is reached. These processes are very much dependent on the deposition conditions. In general, crystalline growth is enhanced by the presence of atomic hydrogen, which chemically interacts with the growing surface.

Much research effort has been put worldwide into the development of both fundamental knowledge and technological skills that are needed to improve thin film silicon multijunction solar cells. The research challenges are:

1. To enhance the network ordering of amorphous semiconductors (leading to protocrystalline networks), mainly for improving the stability;
2. To increase the deposition rate, in particular for microcrystalline silicon;
3. To develop thin doped layers, compatible with the new, fast deposition techniques;
4. To design light-trapping configurations, by utilizing textured surfaces and dielectric mirrors.

The first report on practical microcrystalline cells is given in 1992 by Faraji that reported a thin film silicon solar cell with a μc-Si: H: O i-layer by using VHF PECVD and the first solar cell with a μc-Si: H i-layer was fabricated with 4.6% power efficiency (Meier et al., 1994).

In 1996, Fischer reported that microcrystalline (pc) Si: H p-i-n junctions have an extended infrared response, and are entirely stable under photoexcitation with an efficiency of 7.7% (Fischer et al., 1996). The tandem arrangement of an a-Si: H solar cell with a μc-Si: H solar cell also appears promising a remaining problem of the insufficient deposition rates for the

μc-Si: H layers. In 2002, Meier published a micromorph tandem cell with efficiency of 10.8% in which the bottom cell was deposited at a rate of R_d =0.5 nm/s with the thickness of 2 μm (Meier et al.,2002). At least in this type of devices the highest efficiencies reported to date are 15.4% (tandem cell consisting of microcrystalline silicon cell and amorphous silicon cell) (Yan et al., 2010).

Further development and optimization of a-Si: H/μc-Si: H tandems will remain very important because it is expected that in the near future, its market share can be considerable. For example, in the European Roadmap for PV R&D, it is predicted that in 2020, the European market share for thin film silicon (most probably a-Si: H/μc-Si: H tandems) will be 30%. This shows the importance of thin film multibandgap cells as second-generation solar cells.

4. Conclusions and outlook

Although conventional SCs based on inorganic materials specially Si exhibit high efficiency, very expensive materials and energy intensive processing techniques are required. In comparison with the conventional scheme, the hybrid Si-based SC system has advantages such as; (1) Higher charging current and longer timescale, which make the hybrid system have improved performances and be able to full-charge a storage battery with larger capacity during a daytime so as to power the load for a longer time; (2) much more cost effective, which makes the cost for the hybrid PV system reduced by at least 15% (Wu et al., 2005). Therefore, hybrid SCs can be suitable alternative for conventional SCs. Among hybrid SCs which can be divided into two main groups including HJ hybrid SCs and dye-sensitized hybrid SCs, HJ hybrid SCs based on Si demonstrate the highest efficiency. Thus, the combination of a-Si/μc-Si has been investigated. These configurations of SCs can compensate the imperfection of each other. For example, a-Si has a photo-degradation while a μc-Si cell is stable so the combination is well stabilized. Furthermore, applying textured structures for front and back contacts and implementing an IRL between the individual cells of the tandem will be beneficial to enhancement of the efficiencies in these types of hybrid SCs. Due to recent studies; a-Si/μc-Si (thin film cell) has an efficiency of about 11.9%. Another study is done over three stacked cell of a-Si:H/μc-Si/c-Si (triple), which will be less sensitive to degradation by using the thinner a-Si. The last efficiency reported for a-Si/a-SiGe/a-SiGe(tandem) is about 10.4% and for a-Si/nc-Si/nc-Si (tandem) is approximately 12.5%.

Furthermore, Si based SC systems are being characterized to low temperature coefficient, the design flexibility with a variety of voltage and cost potential, so it can be utilized in large scale. In near future, it will be feasible to see roofs of many private houses constructed by thin film Si solar tiles. Although hybrid SCs are suitable replacements for conventional SCs, these kinds of SCs based on inorganic semiconductor nanoparticles are dependent on the synthesis routes and the reproducibility of such nanoparticle synthesis routes. The surfactant which prevents the particles from further growth is, on the other hand, an insulating layer which blocks the electrical transport between nanoparticles for hybrid SCs son such surfactants should be tailored considering the device requirements. Therefore, there is an increased demand for more studies in the field of hybrid SCs to find solutions to overcome these weak points.

5. Acknowledgment

The authors would like to express their thanks to Prof. Dr. Ali Rostami from Photonic and Nanocrystal Research Lab (PNRL) and School of Engineering Emerging Technologies at the University of Tabriz, for grateful helps to prepare this chapter. The corresponding author would like to acknowledge financial support of Iran Nanotechnology Initiative Council.

6. References

Aberle , A.G. (2006). Fabrication and characterisation of crystalline silicon thin-film materials for solar cells. *Thin Solid Films*, Vol. 511 – 512, pp. 26 – 34.

Ackermann, J.; Videlot ,C. & El Kassmi, A. (2002). Growth of organic semiconductors for hybrid solar cell application, *Thin Solid Films*, Vol. 403 –404 , pp. 157-161

Arici,E.; Serdar Sariciftci, N. & Meissner, D. (2004). Hybrid Solar Cell. *Encyclopedia of Nanoscience and Nanotechnology*, Nalwa, H.S., (Ed.), pp. 929-944, American Scientific Publishers, ISBN: I -58883-059-4

Chandrasekaran, J.; Nithyaprakash, D.; Ajjan, K.B.; Maruthamuthu, M.; Manoharan, D.& Kumar, S. (2011). Hybrid Solar Cell Based on Blending of Organic and Inorganic Materials—An Overview. *Renewable and Sustainable Energy Reviews*, Vol.15, Issue 2, pp. 1228-1238

Eshaghi G. N.; Movla, H.; Sohrabi, F.; Hosseinpour, A.; Rezaei, M. & Babaei, H. (2010). The effects of recombination lifetime on efficiency and J–V characteristics of InxGa1_xN/GaN quantum dot intermediate band solar cell. Physica E, Vol.42, pp. 2353–2357

Fischer, D.; Dubail, S.; Selvan, J. A. A.; Vaucher, N. P.; Platz, R.; Hof, Ch.; Kroll, U.; Meier, J.; Torres, P.; Keppner, H.; Wyrsch, N.; Goetz, M.; Shah, A. and Ufert, K.-D. (1996). The "micromorph" solar cell: extending a-Si:H technology towards thin film crystalline silicon, *Photovoltaic Specialists Conference, 1996., Conference Record of the Twenty Fifth IEEE*, Washington, DC , USA, pp. 1053 – 1056

Fonash, S.J. (2010). *Solar Cell Device Physics* (2nd edition), Academic Press (Elsevier), ISBN 978-0-12-374774-7, United State of America

Green, M.A.; Emery,K.; Hishikawa, Y. & Wilhelm, W. (2011). Solar Cell Efficiency Tables (version 37). *Prog. Photovolt: Res. Appl.*, Vol.19, No.9, pp. 84-92

Günes, S. & Serdar Saiciftci, N. (2008). Hybrid Solar Cells, *Inorganica Chimica Acta*, Vol. 361, pp. 581-588

Hamakawa Y. (1982), *Amorphous Semiconductor, Technologies & Devices*, Elsevier, ISBN: 978-0-44-487977-6, United State of America

Huang, J.; Hsiao, C.; Syu, S.; Chao, J. & Lin, C. (2009). Well-aligned single-crystalline silicon nanowire hybrid solar cells on glass, *Solar Energy Materials & Solar Cells* , Vol.93 , pp. 621-624

Khalili Kh.; Asgari A.; Movla H.; Mottaghizadeh A. & Najafabadi H. A. (2011). Effect of interface recombination on the performance of SWCNT\GaAs heterojunction solar cell. *Procedia Engineering, Physics Procedia,* Vol.8, pp. 275–279

Komatsu, Y.; Koide, N.; Yang, M.; Nakano, T.; Nagano, Y.; Igarashi, K.; Yoshida, K.; Yano, K.; Hayakawa, T.; Taniguchi, H.; Shimizu, M. & Takiguchi, H. (2002). a-Si/mc-Si hybrid solar cell using silicon sheet substrate, *Solar Energy Materials & Solar Cells,* Vol.74, pp. 513–518

Meier, J.; Flückiger R.; Keppner H.; and A. Shah (1994). Complete microcrystalline p-i-n solar cell—Crystalline or amorphous cell behavior?, *Applied Physics Letters,* Vol.65, pp. 860-862

Meier, J.; Dubail, S. ; Golay, S. ; Kroll, U.; Faÿ, S.; Vallat-Sauvain, E.; Feitknecht, L. ; Dubail, J.; Shah, A (2002). Microcrystalline Silicon and the Impact on Micromorph Tandem Solar Cells, *Solar Energy Materials and Solar Cells*, Vol. 74, num. 1-4, pp. 457-467

Meillaud, F; Feltrin, A; Despeisse, M.; Haug, FJ.; Domine, D.; Python, M.; Söderström, T.; Cuony, P.; Boccard, M.; Nicolay, S. & Ballif, C. (2011). Realization of high efficiency micromorph tandem silicon solar cells on glass and plastic substrates: Issues and potential. *Solar Energy Materials & Solar Cells*, Vol.95, No.1, pp. 127-130

Mohammadpour, A. & Shankar, K. (2010). Anodic TiO_2 nanotube arrays with optical wavelength-sized apertures, *Journal of Materials Chemi*stry, Vol. 20, pp. 8474–8477

Movla, H.; Gorji N. E.; Sohrabi, F.; Hosseinpour, A. & Babaei H. (2010). Application of nanostructure materials in solar cells, *Proceeding of The 2th International Conference on Nuclear and Renewable Energy Resources, (NURER 2010)*, Ankara, Turkey 4-7 July, 2010.

Movla, H.; Sohrabi, F.; Fathi J.; Nikniazi A.; Babaei H. & Gorji N. E. (2010). Photocurrent and Surface Recombination Mechanisms in the InxGa1-xN\GaN Different-sized Quantum Dot Solar Cells, *Turkish Journal of Physics*, Vol. 34, pp. 97-106.

Sohrabi, F.; Movla H.; Khalili Kh.; Najafabadi H. A.; Nikniazi A. & Fathi J. (2011). J-V Characteristics of Heterojunction Solar Cell Based on Carbon Nanotube-Silicon, *proceeding of 2nd Iranian Conference on Optics & Laser Engineering*, Malek Ashtar University of Technology, Isfahan, Iran, 19-20 May, 2011.

Tuzun, O.; Oktik, S.; Altindal, S. & Mammadov, T.S. (2006). Electrical characterization of novel Si solar cells, *Thin Solid Films*, Vol. 511– 512, pp. 258-264

Wang, X.; Peng, K-Q.; Wu, X-L. & Lee, S-T. (2010). Single crystalline ordered silicon wire/Pt nanoparticle hybrids for solar energy harvesting. *Electrochemistry Communications*, Vol. 12, pp. 509–512

Wu, L.; Tian ,W. & Jiang, X. (2005). Silicon-based solar cell system with a hybrid PV module, *Solar Energy Materials & Solar Cells*, Vol.87, pp. 637-645

Yamamoto, K.; Yoshimi, M.; Tawada, Y.; Okamoto, Y. & Nakajima, A. (2001). Cost effective and high-performance thin Film Si solar cell towards the 21st century, *Solar Energy Materials & Solar Cells*, Vol.66, pp. 117-125

Yamamoto, K.; Nakajima, A.; Yoshimi, M.; Sawada, T.; Fukuda, S.; Suezaki, T; Ichikawa, M.; Koi, Y.; Goto, M.; Meguro, T.; Matsuda, T.; Kondo, M.; Sasaki, T.; Tawada, Y. (2004). A high efficiency thin film silicon solar cell and module. *Solar Energy*, Vol.77, No.6, pp. 939–949

Yan, B.; Yue, G.; Xu, X.; Yang, J.; and Guha, S. (2010). High efficiency amorphous and nanocrystalline silicon solar cells, Physica Status Solidi A, Vol.207, No. 3, pp.671–677

19

Organic Bulk Heterojunction Solar Cells Based on Poly(*p*-Phenylene-Vinylene) Derivatives

Cigdem Yumusak[1,2] and Daniel A. M. Egbe[2]
[1]*Department of Physics, Faculty of Arts and Sciences, Yildiz Technical University, Davutpasa Campus, Esenler, Istanbul,*
[2]*Linz Institute for Organic Solar Cells (LIOS), Physical Chemistry, Johannes Kepler University of Linz, Linz,*
[1]*Turkey*
[2]*Austria*

1. Introduction

Since the discovery of electrical conductivity in chemically doped polyacetylene (Shirakawa et al., 1977; Chiang et al., 1977; Chiang et al., 1978), enormous progress has been made in the design, synthesis and detailed studies of the properties and applications of π-conjugated polymers (Yu et al., 1998; Skotheim et al., 1998; Hadziioannou et al., 1998). The award of the Nobel prize in Chemistry three decades later in the year 2000 to Alan J. Heeger, Alan G. MacDiarmid and Hideki Shirakawa for the abovementioned discovery and development of semiconducting polymers, was greeted worldwide among researchers as a recognition for the intensified research, which has been going on in the field of organic π-conjugated polymers (Shirakawa, 2001). Such polymers are advantageous compared to inorganic semiconductors due to their low production cost, ease of processability, flexibility as well as tenability of their optical and electronic properties through chemical modifications. These outstanding properties make them attractive candidates as advanced materials in the field of photonics and electronics (Forrest, 2004; Klauk, 2006; Bao & Locklin, 2007; Sun & Dalton, 2008; Moliton, 2006; Hadziioannou & Mallarias, 2007; Shinar & Shinar, 2009; Nalwa, 2008).

Among the most used polymers in optoelectronic devices are the poly(*p*-phenylene-vinylene)s (PPV), polyfluorenes, polythiophenes and their derivatives. The insertion of side-chains in these polymers reduces the rigidity of the backbone, increases their solubility and enables the preparation of films through inexpensive, solution-based methods, such as spin-coating (Akcelrud, 2003). Besides, these ramifications can also be used to tune the photophysical and electrochemical properties of these polymers using a variety of routes.

Solar cells based on solution-processable organic semiconductors have shown a considerable performance increase in recent years, and a lot of progress has been made in the understanding of the elementary processes of photogeneration (Hoppe & Sariciftci, 2004; Mozer & Sariciftci, 2006; Günes et al., 2007). Recently, organic bulk heterojunction solar cells with almost 100% internal quantum yield were presented, resulting in up to almost 8% power conversion efficiency (Park et al., 2009; Green et al., 2010). This device concept has

been shown to be compatible with solution-processing at room temperature, for instance, by high-throughput printing techniques. Processing on flexible substrates is possible, thus allowing for roll-to-roll manufacturing as well as influencing the properties of the finished electronic devices. The recent considerable achievements in terms of power conversion efficiency have been made possible now by more than 15 year long research and development on solution-processed organic solar cells. Nevertheless, in order to let the scientific progress be followed by a commercial success, further improvements in term of efficiency and device lifetime have to be made.
In this chapter, we will briefly introduce the basic working principles of organic solar cells and present an overview of the most often studied PPV-type materials as applied within the photoactive layer.

2. Organic solar cells

2.1 A brief history

The first organic solar cells consisted of a single layer of photoactive material sandwiched between two electrodes of different work functions (Chamberlain, 1983; Wohrle & Meissner, 1991). However, due to the high binding energy of the primary photoexcitations, the separation of the photogenerated charge carriers was so inefficient that far below 1% power conversion efficiency could be achieved.
The next breakthrough was achieved in 1986 by introducing the bilayer heterojunction concept, in which two organic layers with specific electron or hole transporting properties were sandwiched between the electrodes (Tang, 1986). In this organic bilayer solar cell were consisting of a light-absorbing copper phthalocyanine layer in conjunction with an electronegative perylene carboxylic derivative. The differing electron affinities between these two materials created an energy offset at their interface, thereby driving exciton dissociation.
The efficiencies of the first organic solar cells reported in the 1980s were about 1% at best at that time. Primarily, this is due to the fact that absorption of light in organic materials almost always results in the production of a mobile excited state, rather than free electron-hole pairs as produced in inorganic solar cells. This occurs because in organic materials the weak intermolecular forces localize the exciton on the molecules. Since the exciton diffusion lengths in organic materials are usually around 5-15 nm (Haugeneder et al., 1999), much shorter than the device thicknesses, exciton diffusion limits charge-carrier generation in these devices because most of them are lost through recombination. Photogeneration is therefore a function of the available mechanisms for excitons dissociation.
The discovery of ultrafast photoinduced electron transfer (Sariciftci et al., 1992) from a conjugated polymer to buckminsterfullerene (C_{60}) and the consequent enhancement in charge photogeneration provided a molecular approach to achieving higher performances from solution-processed systems. In 1995 the first organic bulk heterojunction organic solar cell was fabricated based on a mixture of soluble *p*-phenylene-vinylene (PPV) derivative with a fullerene acceptor (Yu et al., 1995). In 2001, Shaheen et al. obtained the first truly promising results for bulk heterojunction organic solar cells when mixing the conjugated polymer poly(2-methoxy-5-(3',7'-dimethyl-octyloxy)-*p*-phenylene vinylene) (MDMO-PPV) and methanofullerene [6,6]-phenyl C_{61}-butyric acid methyl ester (PCBM) yielding a power conversion efficiency of 2.5% (Shaheen et al., 2001).

Padinger *et al.* (Padinger et al., 2003) presented a further increase in the power conversion efficiency by using a blend, which is nowadays the best investigated organic solar cell system: a poly(3-hexyl thiophene) donor (P3HT) in conjunction with PCBM. It was shown that annealing at a temperature above the glass transition of the polymer enabled an enhancement of the efficiency from 0.4% to 3.5%.
In the following years, the power conversion efficiency could be increased steadily. This is, to a large fraction, due to the considerable amount of time that has been spent by many laboratories around the world on the optimization of bulk heterojunction solar cells—many of them using P3HT:PCBM—but also by new approaches. Additives have been used in order to allow an increased control of the phase segregation during film formation of a copolymer–fullerene blend (Park et al., 2009; Peet et al., 2007), thus yielding efficiencies of up to 6%. The process additive is a solvent for the fullerene, but not the polymer, thus allowing the PCBM an extended time for self-organization during the drying process. A positive effect by heating the solvent before the film application could also be shown (Bertho et al., 2009). Today, up to 8% power conversion efficiency are reported in this kind of organic solar cells (Park et al., 2009; Green et al., 2010).

2.2 Organic bulk heterojunction solar cells

The sequential process involved in the light into electricity conversion can be summarized by the following steps: First, incident light is absorbed within the photoactive layer leading to the created of a bound electron-hole pairs (singlet excitons); the created excitons start to diffuse within the donor phase leading to charge separation; the separated charge carriers are transported to the corresponding electrodes.

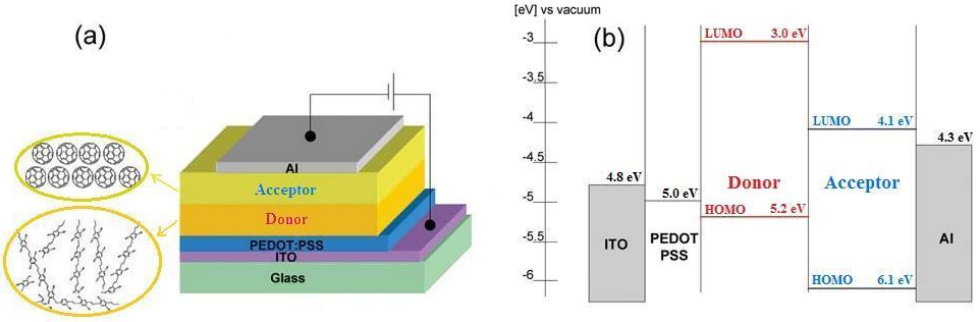

Fig. 1. (a) Schematic device structure and (b) energy diagram for an organic bilayer solar cell

Figure 1 (a) shows the simplest structure of an organic bilayer solar cell appears to be the superposition of donor and acceptor materials on top of each other, providing the interface needed to ensure the charge transfer. The schematic energy diagram of such an organic bilayer solar cell is depicted in Figure 1 (b). The excitons photogenerated in the donor or in the acceptor can diffuse to the interface where they are dissociated. According to the Onsager theory (Onsager, 1938) that can be invoked as a first approximation in organic semiconductors, photoexcited electrons and holes, by virtue of the low dielectric constant intrinsic to conjugated polymers, are coulombically bound. Due to the related exciton binding energy, which with around 0.5 eV is much larger than the thermal energy, the photogenerated excitons are not easily separated. Once excitons have been generated by the

absorption photons, they can diffuse over a length of approximately 5-15 nm (Haugeneder et al., 1999). Since the exciton diffusion lengths in conjugated polymers are less than the photon absorption length, the efficiency of a bilayer cell is limited by the number of photons that can be absorbed within the effective exciton diffusion range at the polymer/electron interface. This limits drastically the photocurrent and hence the overall efficiency of the organic bilayer solar cells. To overcome this limitation, the surface area of the donor/acceptor interface needs to be increased. This can be achieved by creating a mixture of donor and acceptor materials with a nanoscale phase separation resulting in a three-dimensional interpenetrating network: the "bulk heterojunction solar cells" (Figure 2).

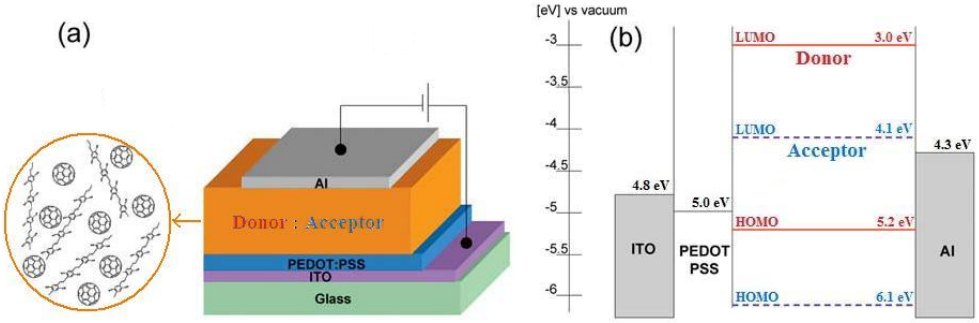

Fig. 2. (a) Schematic device structure and (b) energy diagram for an organic bulk heterojunction solar cell

The discovery of 1-(3-methoxycarbonyl)propyl-1-phenyl[6]C_{61} (PCBM) (Hummelen et al., 1995), a soluble and processable derivative of fullerene C_{60}, allowed the realization of the first organic bulk heterojunction solar cell by blending it with poly(2-methoxy-5-(2'-ethyl-hexoxy)-1,4-phenylene-vinylene) (MEH-PPV) (Yu et. Al., 1995). Figure 2(b) demonstrates the schematic energy diagram of an organic bulk heterojunction solar cell. Contrary to Figure (1b), excitons experience dissociation wherever they are generated within the bulk. Indeed, the next interface between donor and acceptor phases is present within the exciton diffusion length everywhere in the device. After having been generated throughout the bulk, the free carriers have to diffuse and/or be driven to the respective electrodes (Dennler & Sariciftci, 2005).

2.3 Characteristics of bulk heterojunction solar cells

Conjugated polymer thin films sandwiched between two metal electrode are usually described using a metal-insulator-metal (MIM) picture (Parker, 1994). The different operating regimes the MIM device due to externally applied voltages is shown in Figure 3.
As illustrated in Figure 3(a), the vacuum levels (E_{vac}) of the stacked materials shall align themselves (Shottky-Mott model).
Figure 3(a) indicates the energy diagram of a bulk heterojunction solar cell in open circuit condition. The E_{vac} of the different materials are aligned as explained above, and no electrical field is present within the device. Figure 3 (b) represents the short circuit condition. The Fermi levels of the two electrodes align themselves and a built-in field appears in the bulk, resulting in a constant slope for the HOMO and LUMO levels of the donor and acceptor (respectively, HD, LD, HA, and LA) and for the E_{vac}.

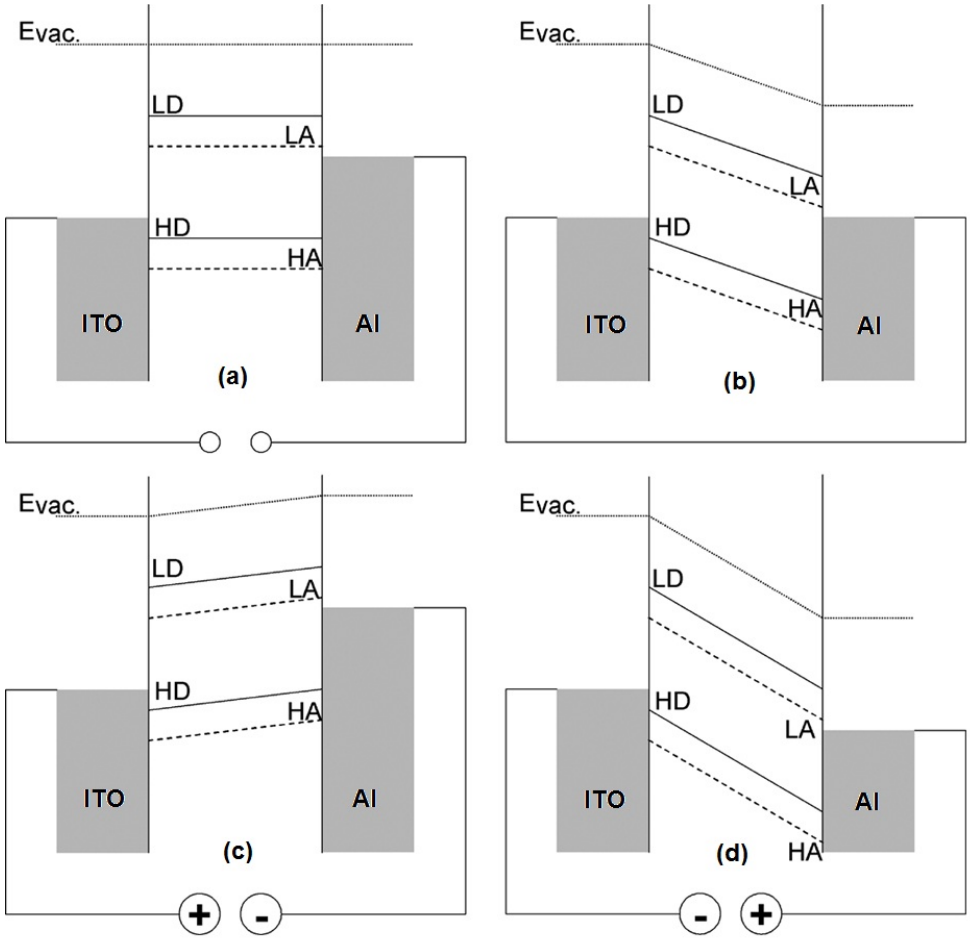

Fig. 3. MIM picture for a polymer diode under different operating modes. (a) open circuit condition, (b) short circuit condition, (c) forward bias, (d) reverse bias.

When polarized in the forward direction (high work function electrode (ITO) connected to (+) and low work function electrode (Al) connected to (-)) as in Figure 3 (c), electrons can be injected from the Al electrode to ITO electrode and holes from ITO electrode to Al electrode. The effective field in the device will ensure the drift of electrons from Al electrode to ITO electrode and hole from ITO electrode to Al electrode. Finally, when the device is polarized in the reverse direction (ITO connected to (-) and Al connected to (+)) (Figure 3 (d), charge injection is hindered by the field present in the device (Dennler & Sariciftci, 2005).

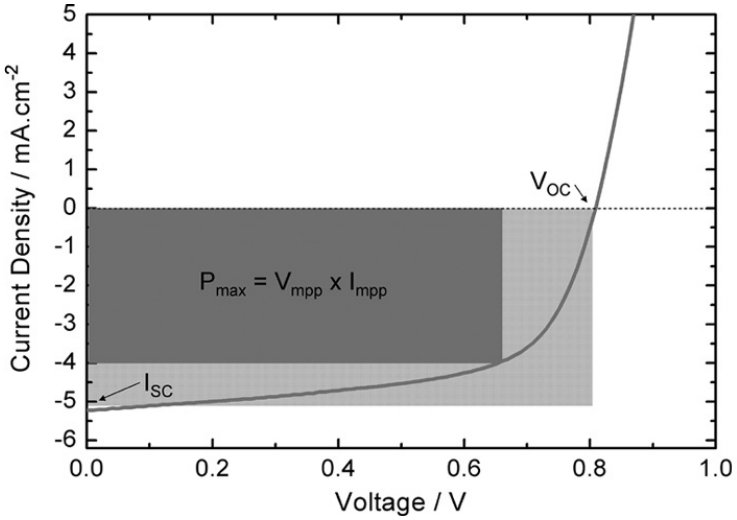

Fig. 4. First and fourth quadrant of a typical *J-V* curve observed for a Glass/ITO/PEDOT:PSS/MDMO-PPV:PCBM(1:4)/Al solar cell. Shown are the short circuit current (I_{SC}), the open circuit voltage (V_{OC}), the current (I_{mpp}) and voltage (V_{mpp}) at the maximum power point (P_{max})

Solar cells are operated between open circuit and short circuit condition (fourth quadrant in the current-voltage characteristics), as shown in Figure 4. In the dark, there is almost no current flowing, until the contacts start to inject heavily at forward bias for voltages larger than the open circuit voltage. Under illumination, the current flows in the opposite direction than the injected currents. The overall efficiency of a solar cell can be expressed by the following formula:

$$\eta = \frac{V_{OC}.I_{SC}.FF}{P_{in}} \tag{1}$$

where V_{OC} is the open circuit voltage, I_{SC} is the short circuit current, and P_{in} is the incident light power. The fill factor (FF) is given by

$$FF = \frac{I_{mpp}.V_{mpp}}{V_{OC}.I_{SC}} \tag{2}$$

where I_{mpp} and V_{mpp} represent the current and voltage at the maximum power point (P_{max}) in the fourth quadrant, respectively (Figure 4).

3. *p*-phenylene-vinylene based conjugated polymers

3.1 Poly(*p*-phenylene-vinylene) and its derivatives

Poly(*p*-phenylene-vinylene)s (PPVs) and its derivatives are one of the most promising classes of conjugated polymers for organic solar cells due to their ease of processability as

well as tunability of their optical and electronic properties through chemical modifications. Since the first report of electroluminescence from PPV, a great research attention has been focused on these types conjugated polymers (Burroughes et al., 1990). This focus was moreover up heaved after the discovery of an ultrafast photoinduced charge transfer from alkoxy-substituted PPV to the buckminsterfullerene (Sariciftci et al., 1992). PPV and its derivatives remain the most popular conjugated polymers for this application and continue to generate considerable interest and much research for photovoltaic applications (Cheng et al., 2009).

The pure PPV is insoluble, intractable, and infusible and therefore difficult to process. Solution processability is desirable as it allows polymeric materials to be solution cast as thin films for various applications. A general methodology to overcome this problem is to develop a synthetic route that involves a solution-processable polymer precursor. First synthetic route for high quality PPV films with high molecular weights was first introduced by Wessling (Figure 5) allowed the synthesis of soluble precursors, which can be processed into thin films prior to thermal conversion to PPV (Wessling & Zimmerman, 1968; Wessling, 1985). A potential drawback of the precursor routes is the limited control over poly-dispersity and molecular weight of the resulting polymer.

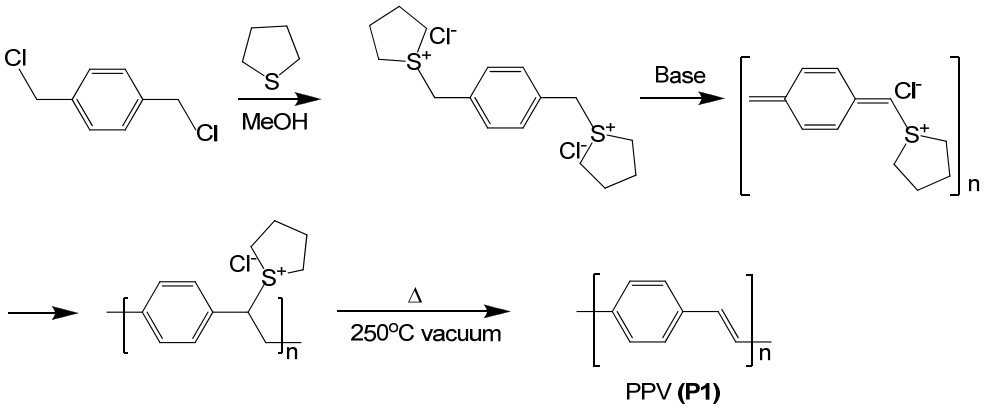

Fig. 5. Synthesis of PPV **(P1)** via the Wessling Route

Some of the drawbacks of this precursor approach include the generation of toxic side products during the solid state elimination process, structural defects arising from incomplete thermal conversion or oxidation, and undefined molecular weights and distribution (Papadimitrakopoulos et al., 1994). By incorporating long alkyl or alkoxy chains into the phenylene ring before polymerization to ensure the solubility, a one step approach can be applied to make processable PPV derivatives which can then be cast into thin films directly without conversion for device fabrication (Braun & Heeger, 1991). To date, the most widely used method for the preparation of PPV derivatives is the Gilch route (Gilch, 1966). A typical Gilch route to the synthesis of a representative solution-processable poly(2-methoxy-5-((2′-ethylhexyl)oxy)-1,4-phenylene-vinylene) (MEH-PPV, **P2**) is represented in Figure 6 (Neef & Ferraris, 2000). By following the same synthetic route, poly(2-methoxy-5-((3′,7′-dimethyloctyl)oxy)-1,4-phenylenevinylene) (MDMO-PPV, **P3**) can also be synthesized

(Figure 7). This route involves mild polymerization conditions, and the molecular weights of the polymers obtained are generally high (Cheng et al., 2009).

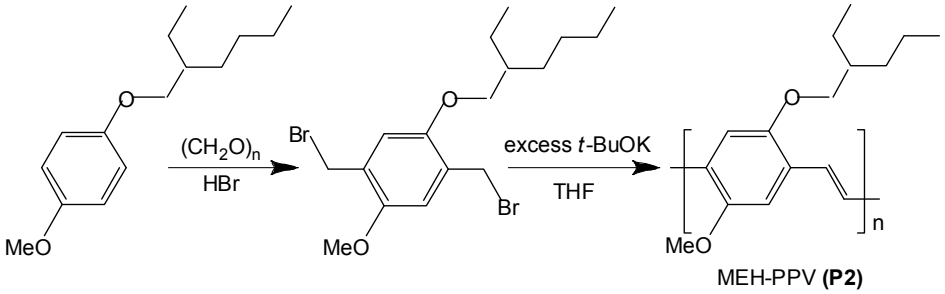

Fig. 6. Synthesis of MEH-PPV (**P2**) via the Gilch Route

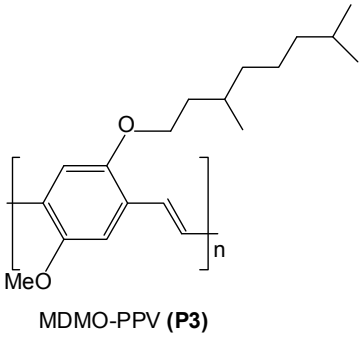

Fig. 7. Chemical structure of MDMO-PPV (**P3**)

Solution-processable PPV derivatives were first reported by Wudl et al. (Wudl et al., 1991; Braun & Heeger, 1991) and by Ohnishi et al. (Doi et al., 1993). The solubility of the materials was achieved by grafting of long alkoxy chains, which cause some conformational mobility of the polymers. Consequently the soluble derivatives have lower glass transition temperatures than pure PPV. Poly[(2,5-dialkoxy-1,4-phenylene)-vinylene]s including long alkoxy side chains are soluble in common organic solvents such as chloroform, toluene, chlorobenzene, dichloromethane, tetrahydrofuran. Fig. 8 shows the chemical structures of PPV and its various alkoxy-substituted derivatives. The solubility increases from left to right, whereby the solubility of the much studied MEH-PPV and MDMO-PPV is enhanced by the branched nature of their side chains (Braun & Heeger, 1991).

PPV derivatives are predominantly hole conducting materials with high-lying LUMO (lowest unoccupied molecular orbital) levels. The unbalanced charge carrier transport properties and the relatively high barrier for electron injection from electrode metals such as aluminium limit the efficiency of the photovoltaic devices.

Several approaches have been explored to improve the electron affinity of PPVs. The insertion of weak electron-withdrawing triple bonds (—C≡C—) within the PPV backbone can be regarded as one of the most original approach of enhancing the electron affinity of PPVs Brizius et al., 2000; Egbe et al., 2001).

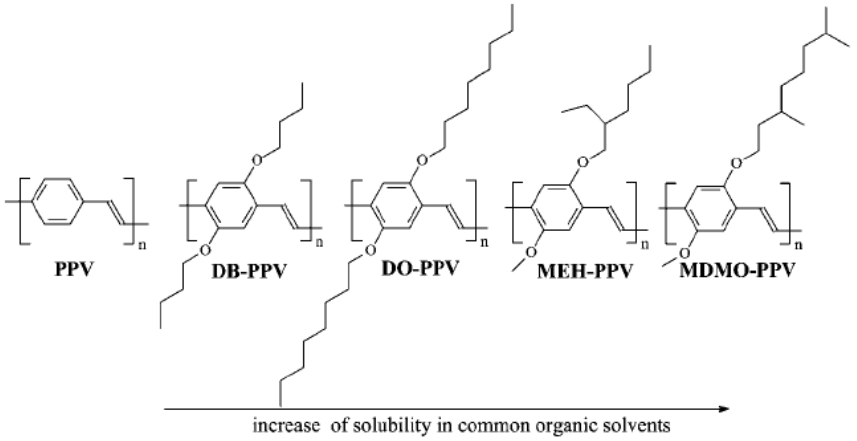

Fig. 8. Chemical structures of PPV and its different alkoxy-substituted derivatives

The substituent on the phenylene ring of PPV allows for the tuning of the band gap. Enhanced electron affinity of substituted PPVs is reflected by higher absorption coefficients, lower-lying HOMO (highest occupied molecular orbital) levels, and higher open circuit voltages from fabricated organic solar cells. The HOMO and LUMO levels of unsubstituted PPV are reported to be ca. -5.1 and -2.7 eV, respectively, with a band gap around 2.4 eV. Introducing two alkoxy groups into the phenylene ring to perturb the molecular orbitals lowers the LUMO to -2.9 eV with an essentially unchanged HOMO level. Hence, the band gap is reduced to 2.2 eV (Alam & Jenekhe, 2002). As a consequence, PPV emits a green-yellow light, while MEH-PPV exhibits a yellow-orange emission. Because PPV derivatives are the earliest conjugated polymers developed for organic electronics application, they were also frequently used as the active materials in organic bilayer solar cells before the concept of bulk heterojunction configuration was widely accepted. For organic bilayer solar cells, PPV and MEH-PPV serve as the electron donor in conjunction with a poly(benzimidazobenzophenanthroline ladder) (BBL, **P4**) as the electron acceptor (Figure 9). The photovoltaic parameters of the bilayer device with the configuration ITO/PPV/**P4**/Al showed a J_{sc} of 2.3 mA/cm^2, a V_{oc} of 1.06 V, an FF of 47%, and power conversion efficiency (PCE) value of 1.4%. In case of using MEH-PPV as the electron donor, the device reached a PCE of 0.8% under the same conditions (Alam & Jenekhe, 2004). The better photovoltaic performance of PPV over MEH-PPV can be accredited to the greater crystallinity and structural order of the PPV main chain compared to alkylated MEH-PPV.

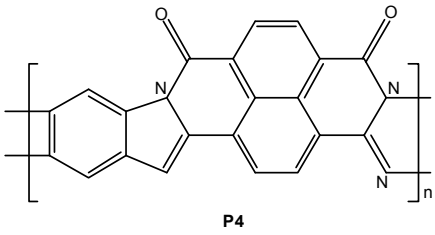

Fig. 9. Chemical structure of BBL **P4**

Soluble MEH-PPV was also combined with PCBM for organic solar cell applications. The organic bilayer solar cell with the configuration ITO/PEDOT:PSS/MEH-PPV/PCBM/Al showed a J_{sc} of 2.1 mA/cm², a V_{oc} of 0.75 V, an FF of 23%, and a PCE value of 0.46% (Zhang et al., 2002). An organic bulk heterojunction solar cell including MEH-PPV/PCBM as the photoactive layer showed better PCE values in the range 1.1-1.3% than bilayer solar cells. Furthermore, by stacking two independent single organic solar cells together with the help of the transparent cathode LiF/Al/Au, the PCE of the multiple-device stacked structure can be dramatically improved to 2.6% (Shrotriya et al., 2006). The devices can be stacked together and connected either in parallel or in series, resulting in doubled J_{sc} or V_{oc}, respectively, compared to those of a single device (Cheng et al., 2009).

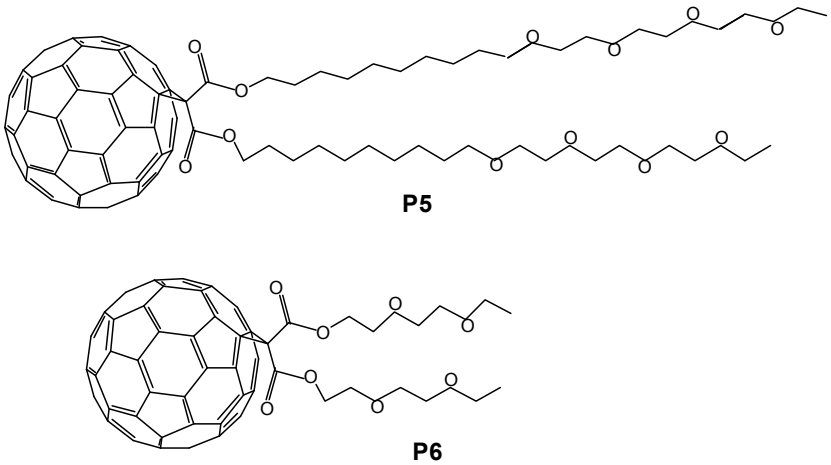

Fig. 10. Chemical structures of C_{60} derivatives **P5** and **P6**

Two alternative soluble methanofullerene derivatives **P5** and **P6** have been developed to serve as electron acceptors and combined with MEH-PPV to produce organic solar cells. The chemical structures of the C_{60} derivatives are shown in Figure 10. Due to a better compatibility of **P5** with MEH-PPV, the MEH-PPV/**P5** system shows a better device PCE of 0.49% than the MEH-PPV/**P6** system, which has a PCE of 0.22% (Li et al., 2002). In addition to C_{60} derivatives, different types of titanium oxide (TiO_2) were blended with MEH-PPV for photovoltaic device applications (Breeze et al., 2001; Song et al., 2005; Wei et al., 2006; Neyshtadt et al., 2008; Shim et al., 2008). However, their device performances were generally low, with PCE values lower than 0.5% (Cheng et al., 2009).

In organic bulk heterojunction solar cells, MDMO-PPV is the most widely used PPV derivative to serve as the electron donor in combination with C_{60} electron acceptor derivatives. Organic solar cells based on combined MDMO-PPV:PCBM (1:4, w/w) were fabricated by Shaheen and co-workers (Shaheen et al., 2001). It was found that when chlorobenzene was used as the casting solvent instead of toluene to deposit the active layer, an optimal morphology with suppressed phase segregation and enhanced microstructure was obtained, resulting in increased charge carrier mobility for both holes and electrons in the active layer. And this device achieved a J_{sc} of 5.23 mA/cm², a V_{oc} of 0.82 V, and a high PCE of 2.5% (Shaheen et al., 2001).

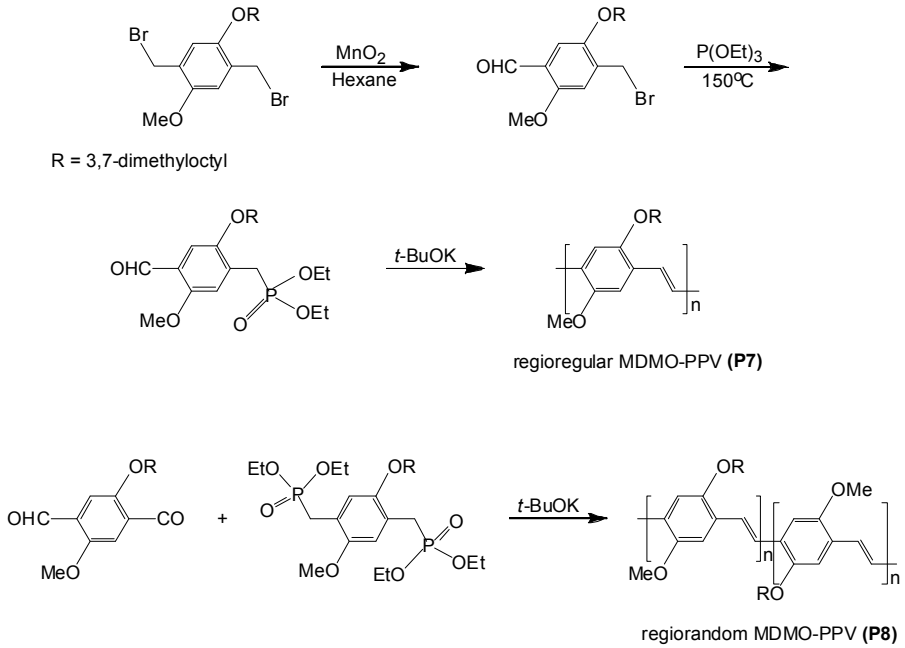

Fig. 11. Synthesis of regioregular and regiorandom MDMO-PPVs (**(P7)** and **(P8)**)

Regioregularity in MDMO-PPV also plays an important role in determining the photovoltaic device performance. A fully regioregular MDMO-PPV (**P7**) by the Wittig-Hornor reaction of a single monomer comprised of aldehyde and phosphonate functionalities was synthesized (Tajima et al., 2008). Regiorandom MDMO-PPV (**P8**), from dialdehyde and diphosphnate monomers, was also prepared for comparison (Figure 11). The device achieved a PCE of 3.1%, a J_{sc} of 6.2 mA/cm^2, a V_{oc} of 0.71 V, and an FF of 70% with regioregular MDMO-PPV (**P7**). This is the highest efficiency reported for the PPV:PCBM system so far. But the device based on regiorandom MDMO-PPV (**P8**)/PCBM only achieved a PCE of 1.7%. It is concluded that higher crystallinity of the polymer for higher hole mobility and better mixing morphology between the polymer and PCBM contribute to the improvement of photovoltaic device performance with regioregular MDMO-PPV (Cheng et al., 2009).

Miscellaneous physics and engineering aspects have been investigated for devices based on the MDMO-PPV/PCBM bulk heterojunction active layer system: photooxidation (Pacios et al., 2006), stacked cells (Kawano et al., 2006), active layer thickness (Lenes et al., 2006), NMR morphology studies (Mens et al., 2008), and insertion of a hole-transporting layer between PEDOT and the active layer (Park et al., 2007). Besides the PCBM organic acceptor, inorganic electron acceptors (van Hal et al., 2003; Beek et al., 2005; Boucle et al., 2007; Sun et al., 2003) such as metal oxides or quantum dots are also under active development and have been combined with MDMO-PPV to prepare hybrid (organic-inorganic) bulk heterojunction solar cells. Optimized photovoltaic devices using blends of MDMO-PPV:ZnO (Beek et al., 2005) or MDMO-PPV:cadmium selenide (Sun et al., 2003) showed moderate PCE values of 1.6% and 1.8%, respectively.

3.2 Cyano-substituted poly(*p*-phenylene-vinylene)s

Cyano-substituted poly(*p*-phenylene-vinylene)s (CN-PPV) with electron deficient cyano groups on the vinyl units are synthesized by Knoevenagel polycondensation polymerization of terephthaldehyde and 1,4-bis(cyanomethyl)benzene in the presence of the base *t*-BuOK (Figure 12). Hence, the LUMO and HOMO levels of PPV derivatives can also be tuned by incorporating electronic substituent into the vinylene bridges (Cheng et al., 2009).

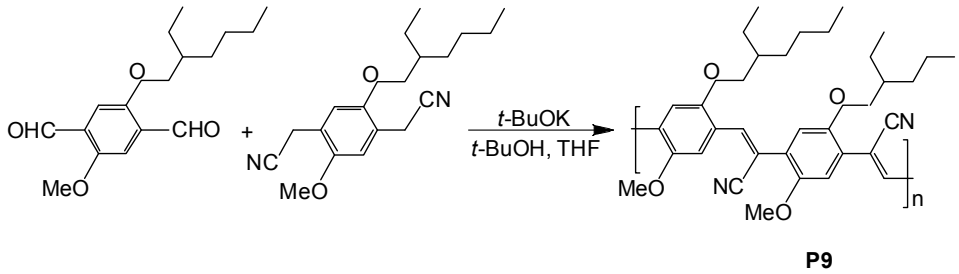

Fig. 12. Synthesis of CN-PPV copolymer **P9** via a Knoevenagel Polycondensation

CN-PPVs show high electron affinity to reduce the barrier to electron injection and good electron-transport properties as a result of the electron-withdrawing effect of the cyano side group and suitable electron acceptors in organic photovoltaic devices (Granström et al., 1998; Halls et al., 1995; Gupta et al., 2007). To effectively reduce the band gap of CN-PPV below 2 eV, electron-rich thiophene units with lower aromaticities have been incorporated into the main chain to form a D-A arrangement. A series of copolymers based on the bis(1-cyano-2-thienylvinylene)pheniylene structures with different alkyl or alkoxy side chains on the thiophene rings were reported by Vanderzande et al. (Colladet et al., 2007) (Figure 13).

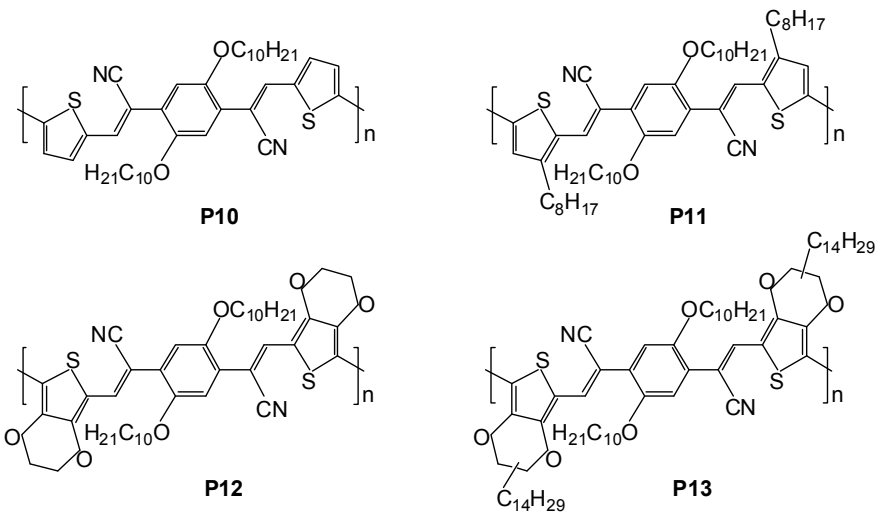

Fig. 13. Chemical structures of **P10-P13**

These monomers were all prepared by Knoevenagel condensations to construct cyanovinylene linkages. The electron-rich nature of thiophene units in these polymers makes them good candidates to serve as electron donors in organic bulk heterojunction solar cells. For example, both **P11**/PCBM- and **P12**/PCBM-based solar cells achieved a PCE of around 0.14%. Optimization of these devices by thermal annealing showed a slight increase of PCE to 0.19%. Reynold et al. also reported synthesizing a range of CN-PPV derivatives (**P14-P17)** containing dioxythiophene moieties in the polymer main chain (Figure 14) (Thompson et al., 2005; Thompson et al., 2006). The best photovoltaic device based on these CN-PPV derivatives with PCBM as the active layer achieved a PCE of 0.4%.

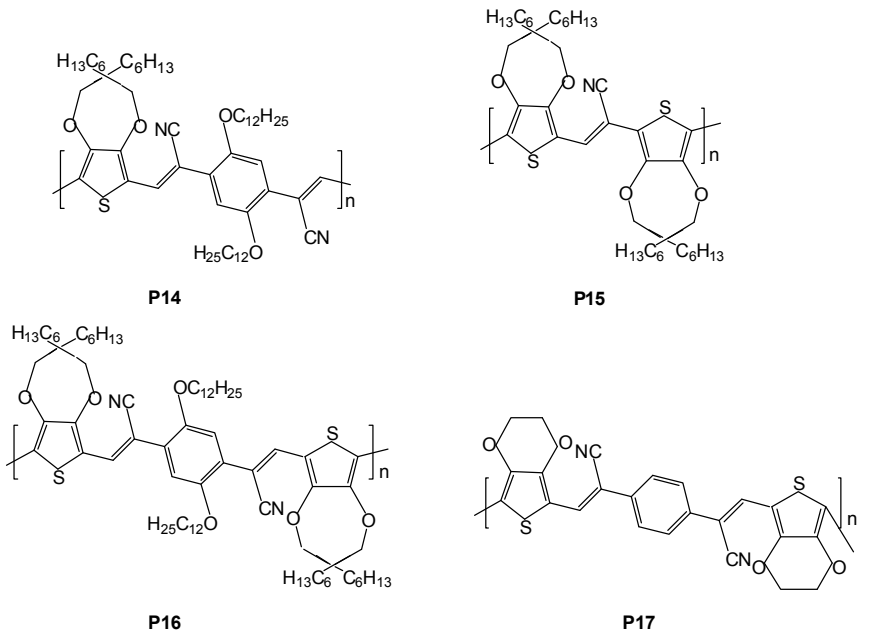

Fig. 14. Chemical structures of **P14-P17**

3.3 Acetylene-substituted poly(*p*-phenylene-vinylene)s

Acetylene-substituted PPV derivatives can be synthesized via the Wittig – Horner Reaction (Figure 15). The coplanar and rigid nature of the acetylene moiety in the polymer chain may have the potential to obtain a higher degree of packing and thus improve the photovoltaic performance of such devices. Having coplanar electron-rich anthracene units and triple bond bridges, **P18** exhibits broader absorption, a lower HOMO level, and a smaller optical band gap of 1.9 eV, compared to MDMO-PPV. A device with the configuration of ITO/PEDOT/**P18**:PCBM (1:2, w/w)/LiF/Al, achieved a PCE value of up to 2% with a high V_{oc} of 0.81 V. Figure 16 shows the chemical structures of a series of acetylene-substituted PPV derivatives synthesized by similar procedures. For polymers **P21** and **P22** (Egbe et al., 2007), the introduction of a thiophene ring into the polymer backbone showed an improvement in the PCE ranging from 1.2% to 1.7%. This is higher than those for **P19** and **P20** (Egbe et al., 2005), based on the same device configuration of ITO/PEDOT/polymer:PCBM (1:3, wt%)/LiF/Al (Cheng et al., 2009).

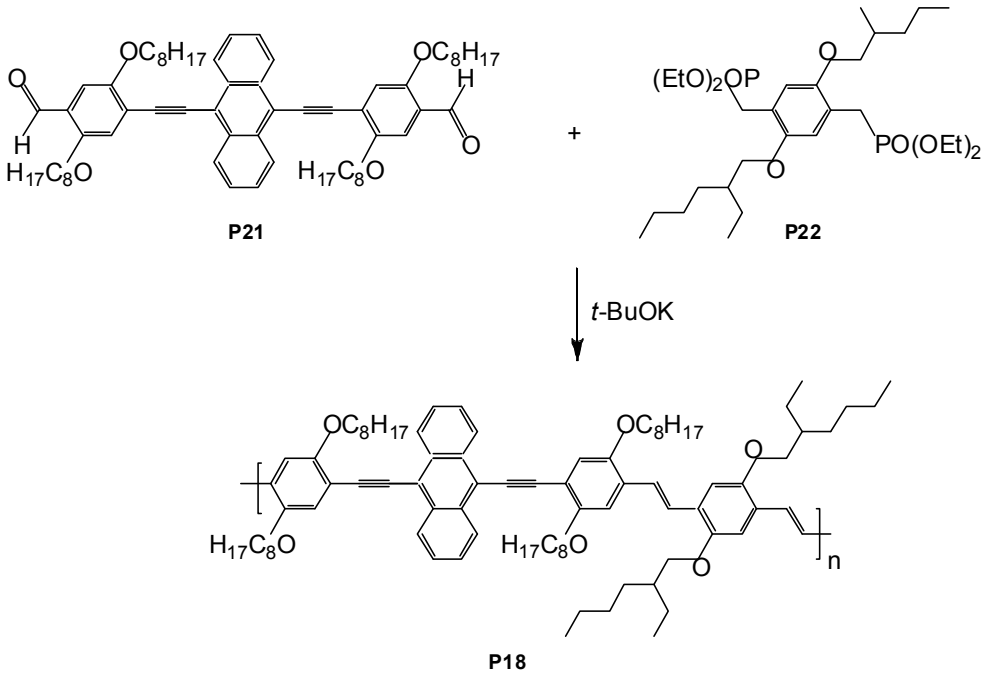

Fig. 15. Synthesis of acetylene-containing **P18** via a Wittig – Horner reaction

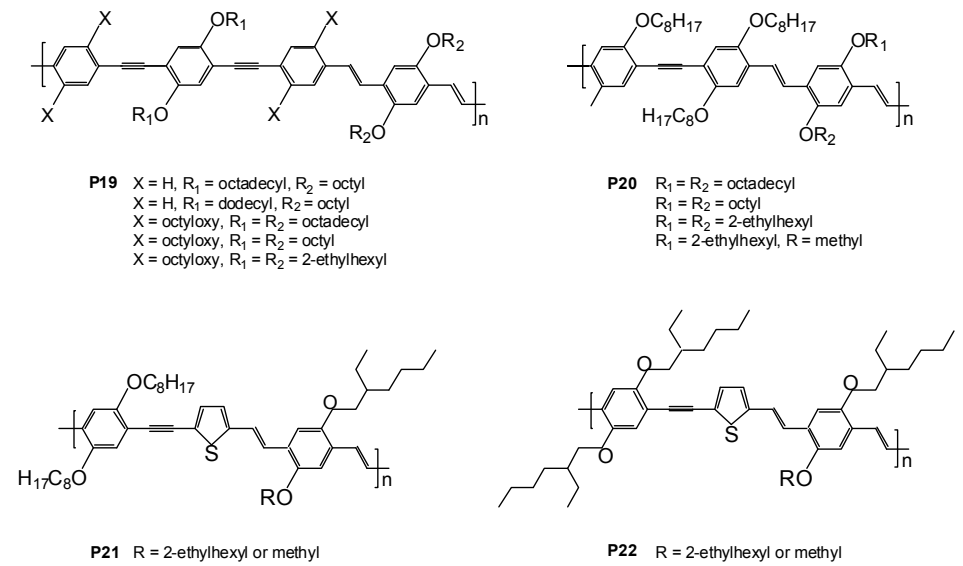

Fig. 16. Chemical structures of acetylene-containing PPV derivatives **P19-P22**

4. Conclusion

The efficiency of organic solar cells is increasing steadily by means of interdisciplinary approach. Extensive efforts are currently carry out by chemists in order to create new low bandgap materials to harvest more photons and increase the power conversion efficiency. Furthermore, processability of conjugated polymers that can be deposited from liquid solutions at low temperature make them suitable for large scale production on flexible substrates at low cost roll-to-roll process. To integrate new advanced device concepts and the nanostructure engineering of the morphology are also important in bringing high efficiency and low cost organic solar cells one step closer to successful commercialization.

5. References

Akcelrud, L. (2003). Electroluminescent polymers. *Prog. Polym. Sci.*, Vol.28, pp.875-962.

Alam, M.M.; Jenekhe, S.A. (2002). Polybenzobisazoles are efficient electron transport materials for improving the performance and stability of polymer light-emitting diodes. *Chem. Mater.*, Vol.14, pp.4775-4780.

Alam, M.M.; Jenekhe, S.A. (2004). Efficient solar cells from layered nanostructures of donor and acceptor conjugated polymers. *Chem. Mater.*, Vol.16, pp.4647-4656.

Bao, Z.; Locklin, J. (2007). Organic Field Effect Transistors., Taylor & Francis, Boca Raton, FL.

Beek, W.J.E.; Wienk, M.M.; Kemerink, M.; Yang, X.; Janssen, R.A.J. (2005). Hybrid zinc oxide conjugated polymer bulk heterojunction solar cells. *J. Phys. Chem. B*, Vol.109, pp.9505-9516.

Bertho, S.; Oosterbaan W.D.; Vrindts, V.; DHaen, J.; Cleij, T.J.; Lutsen, L.; Manca, J.; Vanderzande, D. (2009). Controlling the morphology of nanofiber-P3HT:PCBM blends for organic bulk heterojunction solar cells. *Org. Electron.,* Vol.10, pp.1248-1251.

Boucle´, J.; Ravirajan, P.; Nelson, J. (2007). Hybrid polymer-metal oxide thin films for photovoltaic applications. *J. Mater. Chem.*, Vol.17, pp.3141-3153.

Breeze, A.J.; Schlesinger, Z.; Carter, S.A.; Brock, P. (2001). Charge transport in TiO2/MEH-PPV polymer photovoltaics. *J. Phys. Rev.B*, Vol.64, pp.125205-1 – 125205-9.

Braun, D.; Heeger, A.J. (1991). Visible-light emission from semiconducting polymer diodes. *Appl. Phys. Lett.*, Vol.58, pp.1982.

Burroughes, J.H.; Bradley, D.D.C.; Brown, A.R.; Marks, R.N.; Mackay, K.; Friend, R.H.; Burns, P.L.; Holmes, A.B. (1990). Light-emitting diodes based on conjugated polymers. *Nature,* Vol.*347*, pp.539-541.

Chamberlain, G.A. (1983). Organic solar cells: a review. *Solar Cells,* Vol.8, pp.47-83.

Cheng, Y.J.; Yang, S.H.; Hsu, C.S. (2009). Synthesis of conjugated polymers for organic solar cell applications. *Chem. Rev.*,Vol.109, pp.5868-5923.

Chiang, C.K.; Fischer, C.R.; Park, Y.W.; Heeger, A.J.; Shirakawa, H.; Louis, E.J.; Gau, S.C.; MacDiarmid, A.G. (1977). Electrical conductivity in doped polyacetylene. *Phys. Rev. Lett.*, Vol.39, pp.1098-1101.

Chiang, C.K.; Druy, M.A.; Gau, S.C.; Heeger, A.J.; Louis, E.J.; MacDiarmid, A.G.; Park, Y.W.; Shirakawa, H. (1978). Synthesis og highly conducting films of derivatives of polyacetylene, (CH). *J. Am. Chem. Soc.,* Vol.100, pp.1013-1015.

Colladet, K.; Fourier, S.; Cleij, T.J.; Lutsen, L.; Gelan, J.; Vanderzande, D.; Nguyen, L.H.; Neugebauer, H.; Sariciftci, S.; Aguirre, A.; Janssen, G.; Goovaerts, E. (2007). Low band gap donor-acceptor conjugated polymers toward organic solar cells applications. *Macromolecules*, Vol.40, pp.65-72.

Dennler, G.; Sariciftci, N.S. (2005). Flexible conjugated polymer-based plastic solar cells: from basics to applications. *Proceedings of The IEEE*, Vol.93, pp.1429-1439.

Egbe, D.A.M.; Nguyen, L.H.; Schmidtke, K.; Wild, A.; Sieber, C.; Guenes, S.; Sariciftci, N.S. (2007). Combined effects of conjugation pattern and alkoxy side chains on the photovoltaic properties of thiophene-containing PPE-PPVs. *J. Polym. Sci., Part A: Polym. Chem.*, Vol.45, pp.1619-1631.

Egbe, D.A.M.; Nguyen, L.H.; Hoppe, H.; Mühlbacher, D.; Sariciftci, N.S. (2005). Side chain influence on electrochemical and photovoltaic properties of yne-containing poly(phenylene vinylene)s. *Macromol. Rapid Commun.*, Vol.26, pp.1389-1394.

Forrest, S.R. (2004). The path to ubiquitous and low-cost organic electronic appliances on plastic. *Nature,* Vol.428, pp.911-918.

Gilch, H.G.; Wheelwright, W.L. (1966). Polymerization of α-halogenated p-xylenes with base *J. Polym. Sci., Part A: Polym.Chem.*, Vol.4, pp.1337-1349.

Granström, M.; Petritsch, K.; Arias, A.C.; Lux, A.; Andersson, M.R.; Friend, R.H. (1998). Laminated fabrication of polymeric photovoltaic diodes. *Nature*, Vol.395, pp.257-260.

Green, M.A.; Emery, K.; Hishikawa, Y.; Warta, W. (2010). Solar cell efficiency tables (version 35). *Prog. Photovolt. Res. Appl.,* Vol.18, pp.144-150.

Gunes, S.; Neugebauer, H. Sariciftci, N.S. (2007). Conjugated polymer-based organic solar cells. *Chem. Rev.,* Vol.107, pp.1324-1338.

Gupta, D.; Kabra, D.; Kolishetti, N.; Ramakrishnan, S.; Narayan, K.S. (2007). An efficient bulk-heterojunction photovoltaic cell based on energy transfer in graded-bandgap polymers. *Adv. Funct. Mater.*, Vol.17, pp.226-232.

Hadziioannou, G.; van Hutten, P.F. (2000). Semiconducting polymers : chemistry, physics and engineering, 1st ed., Wiley-VCH, Weinheim, Germany.

Hadziioannou, G.; Mallarias, G.G. (2007). Semiconducting Polymers., Wiley-VCH, Weinheim, Germany.

Halls, J.J.M.; Walsh, C.A.; Greenham, N.C.; Marseglia, E.A.; Friend, R.H.; Moratti, S.C.; Homles, A.B. (1995). Efficient photodiodes from interpenetrating polymer networks. *Nature*, Vol.376, pp.498-500.

Haugeneder, A.; Neges, M.; Kallinger, C.; Spirkl, W.; Lemmer, U.; Feldmann, J.; Scherf, U.; Harth, E.; Gügel, A.; Müllen, K. (1999). Exciton diffusion and dissociation in conjugated polymer/fullerene blends and heterostructures. *Phys. Rev. B.,* Vol.59, pp.15346-15351.

Hoppe, H.; Sariciftci, N.S. (2004). Organic solar cells: an overview. *J. Mater. Res.,* Vol.19, pp.1924-1945.

Hummelen, J.C.; Knight, B.W.; LePeq, F.; Wudl, F.; Yao, J.; Wilkins, C.L. (1995). Preparation and characterization of fulleroid and methanofullerene derivatives. *J. Org. Chem.,* Vol.60, pp.532-538.

Kawano, K.; Ito, N.; Nishimori, T.; Sakai, J. (2006). Open circuit voltage of stacked bulk heterojunction organic solar cells. *Appl. Phys. Lett.*, Vol.88, pp.073514-1 – 073514-3.

Klauk, H. (2006). Organic Electronics., Wiley-VCH, Weinheim, New York.Shirakawa, H.; Louis, E.J.; MacMiarmid, A.G.; Chiang, C.K.; Heeger, A.J. (1977). Synthesis of electrically conducting organic polymers : halogen derivatives of polyacetylene, $(CH)_x$. *J. C. S. Chem. Comm.,* pp.578-580.

Lenes, M.; Koster, L.J.A.; Mihailetchi, V.D.; Blom, P.W.M. (2006). Thickness dependence of the efficiency of polymer : fullerene bulk heterojunction solar cells. *Appl. Phys. Lett.*, Vol.88, pp.243502-1 – 243502-3.

Li, J.; Sun, N.; Guo, Z.X.; Li, C.; Li, Y.; Dai, L.; Zhu, D.; Sun, D.; Cao, Y.; Fan, L. (2002). Photovoltaic devices with methanofullerenes as electron acceptors. *J. Phys. Chem. B*, Vol.106, pp.11509-11514.

Mens, R.; Adriaensens, P.; Lutsen, L.; Swinnen, A.; Bertho, S.; Ruttens, B.; D'Haen, J.; Manca, J.; Cleij, T.; Vanderzande, D.; Gelan, J. (2008). NMR study of the nanomorphology in thin films of polymer blends used in organic PV devices: MDMO-PPV/PCBM. *J. Polym. Sci., Part A: Polym. Chem*., Vol.46, pp.138-145.

Moliton, A. (2006). Optoelectronics of Molecules and Polymers., Springer-Verlag, Berlin, Germany.

Mozer, A.; Sariciftci, N.S. (2006). Conjugated polymer photovoltaic devices and materials. *Chimie*, Vol.9, pp.568-577.

Nalwa, H.S. (2008). Handbook of Organic Electronics and Photonics., American Scientific Publishers, Valencia, CA.

Neef, C.J.; Ferraris, J.P. (2000). MEH-PPV: Improved synthetic procedure and molecular weight control. *Macromolecules*, Vol.33, pp.2311-2314.

Neyshtadt, S.; Kalina, M.; Frey, G.L. (2008). Self-organized semiconducting polymer-incorporated mesostructured titania for photovoltaic applications. *Adv. Mater.*, Vol.20, pp.2541-2546.

Onsager, L. (1938). Initial recombination of ions. *Phys. Rev.,* Vol.54, pp.554-557.

Pacios, R.; Chatten, A.J.; Kawano, K.; Durrant, J.R.; Bradley, D.D.C.; Nelson, J. (2006). Effects of photo-oxidation on the performance of poly[2-methoxy-5-(3 ',7 '-dimethyloctyloxy)-1,4-phenylene vinylene]:[6,6]-phenyl C-61-butyric acid methyl ester solar cells. *Adv. Funct. Mater.*, Vol.16, pp.2117-2126.

Padinger, F.; Rittberger, R.S.; Sariciftci, N.S. (2003). Effects of postproduction treatment on plastic solar cells. *Adv. Funct. Mater.,* Vol.13, pp.85-88.

Park, J.; Han, S.H.; Senthilarasu, S.; Lee, S.H. (2007). Improvement of device performances by thin interlayer in conjugated polymers/methanofullerene plastic solar cell. *Sol. Energy Mater.Sol. Cells*, Vol.91, pp.751-753.

Park, S.H.; Roy, A.; Beaupre, S.; Cho, S.; Coates, N.; Moon, J.S.; Moses, D.; Leclerc, M.; Lee, K.; Heeger, A.J. (2009). Bulk heterojunction solar cells with internal quantum efficiency approaching 100%. *Nat. Photon.,* Vol.3, pp.297-303.

Parker, I.D. (1994). Carrier tunneling and device characteristics in polymer light-emitting diodes. *J. Appl. Phys.*, Vol.75, pp.1656-1666.

Papadimitrakopoulos, F.; Konstadinidis, K.; Miller, T.M.; Opila, R.; Chandross, E.A.; Galvin, M.E. (1994). The Role of Carbonyl Groups in the Photoluminescence of Poly(p-phenylenevinylene). *Chem. Mater.*, Vol.6, pp.1563-1568.

Peet, J.; Kim, J.Y.; Coates, N.E.; Ma, W.L.; Moses, D.; Heeger, A.J.; Bazan, G.C. (2007). Efficiency enhancement in low-bandgap polymer solar cells by processing with alkane dithiols. *Nat. Mater.,* Vol.&, pp.497-500.

Sariciftci, N.S.; Smilowitz, L.; Heeger, A.J.; Wudl, F. (1992). Photoinduced electron-transfer from a conducting polymer to buckminsterfullerenes. *Science,* Vol.258, pp.1474-1476.

Shaheen, S.E.; Brabec, C.J.; Sariciftci, N.S.; Padinger, F.; Fromherz, T.; Hunnelen, J.C. (2001). 2.5% efficient organic plastic solar cells. *Appl. Phys. Lett.*, Vol.78, pp.841-843.

Shim, H.S.; Na, S.I.; Nam, S.H.; Ahn, H.J.; Kim, H.J.; Kim, D.Y.; Kim, W.B. (2008). Efficient photovoltaic device fashioned of highly aligned multilayers of electrospun TiO2 nanowire array with conjugated polymer. *Appl. Phys. Lett.*, Vol.92, pp.183107-1 – 183107-3.

Shinar, R.; Shinar, J. (2009). Organic Electronics in Sensors and Biotechnology., McGraw-Hill, New York.

Shirakawa, H. (2001). Die Entdeckung der Polyacetylenefilme – der Beginn des Zeitalters leitfähiger Polymere (Nobel – Aufsatz). *Angew. Chem.*, Vol.113, pp.2642-2628.

Shrotriya, V.; Wu, E.H.E.; Li, G.; Yao, Y.; Yang, Y. (2006). Efficient light harvesting in multiple-device stacked structure for polymer solar cells. *Appl. Phys. Lett.*, Vol.88, pp.064104-1 – 064104-3.

Song, M.Y.; Kim, K.J.; Kim, D.Y. (2005). Enhancement of photovoltaic characteristics using a PEDOT interlayer in TiO2/MEHPPV heterojunction devices. *Sol. Energy Mater. Sol. Cells*, Vol.85, pp.31-39.

Skotheim, T.J.; Elsenbaumer, R.L.; Reynolds, J.R. (1998). Handbook of Conducting Polymers, 2nd ed., Marcel Dekker, New York.

Sun, B.; Marx, E.; Greenham, N.C. (2003). Photovoltaic devices using blends of branched CdSe nanoparticles and conjugated polymers. *Nano Lett.*, Vol.3, pp.961-963.

Sun, S.S.; Dalton, L. (2008). Introduction to Organic Electronic and Optoelectronic Materials and Devices., Taylor & Francis, Boca Raton, FL.

Tajima, K.; Suzuki, Y.; Hashimoto, K. (2008). Polymer photovoltaic devices using fully regioregular poly[(2-methoxy-5-(3 ',7 '-dimethyloctyloxy))-1,4-phenylenevinylene]. *J. Phys. Chem. C*, Vol.112, pp.8507-8510.

Tang, C.W. (1986). 2-Layer Organic Photovoltaic Cell. *Appl. Phys. Lett.,* Vol.48, pp.183-185.

Thompson, B.C.; Kim, Y.G.; Reynolds, J.R. (2005). Spectral broadening in MEH-PPV : PCBM-based photovoltaic devices via blending with a narrow band gap cyanovinylene-dioxythiophene polymer. *Macromolecules*, Vol.38, pp.5359-5362.

Thompson, B.C.; Kim, Y.G.; McCarley, T.D.; Reynolds, J R. (2006). Soluble narrow band gap and blue propylenedioxythiophene-cyanovinylene polymers as multifunctional materials for photovoltaic and electrochromic applications. *J. Am. Chem. Soc.*, Vol.128, pp.12714-12725.

van Hal, P.A.; Wienk, M.M.; Kroon, J.M.; Verhees, W.J.H.; Slooff, L.H.; van Gennip, W.J.H.; Jonkheijm, P.; Janssen, R.A.J. (2003). Photoinduced electron transfer and photovoltaic response of a MDMO-PPV:TiO2 bulk-heterojunction. *Adv. Mater.*, Vol.15, pp.118-121.

Wei, Q.; Hirota, K.; Tajima, K.; Hashimoto, K. (2006). Design and Synthesis of TiO_2 Nanorod Assemblies and Their Application for Photovoltaic Devices. *Chem. Mater.*, Vol.18, pp.5080-5087.

Wessling, R.A.; Zimmerman, R.G. (1968). U.S. Patent 3401152.

Wessling, R.A. (1985). The polymerization of xylylene bisdialkyl sulfonium salts. *J. Polym. Sci., Polym. Symp.*, Vol.72, pp.55-66.

Wohrle, D.; Meissner, D. (1991). Organic Solar Cells. *Adv. Mater.,* Vol.3, pp.129-138.

Yu, G.; Gao, J.; Hummelen, J.C.; Wudl, F.; Heeger, A.J. (1995). Polymer photovoltaic cells: Enhanced efficiencies via a network of internal donor-acceptor heterojunction. *Science,* Vol.270, pp.1789-1791.

Yu, G.; Wang, J.; McElvain, J.; Heeger, A.J. (1998). Large-area, full-color image sensors made with semiconducting polymers. *Adv. Mater.,* Vol.10, pp.1431-1434.

Zhang, F.L.; Johansson, M.; Andersson, M.R.; Hummelen, J.C.; Inganäs, O. (2002). Polymer photovoltaic cells with conducting polymer anodes. *Adv. Mater.*, Vol.14, pp.662-665.

20

Towards High-Efficiency Organic Solar Cells: Polymers and Devices Development

Enwei Zhu[1], Linyi Bian[1], Jiefeng Hai[1], Weihua Tang[1,*] and Fujun Zhang[2,*]
[1]*Nanjing University of Science and Technology,*
[2]*Beijing Jiaotong University*
People's Republic of China

1. Introduction

The effective conversion of solar energy into electricity has attracted intense scientific interest in solving the rising energy crisis. Organic solar cells (OSCs), a kind of green energy source, show great potential application due to low production costs, mechanical flexibility devices by using simple techniques with low environmental impact and the versatility in organic materials design (Beal, 2010). In the past years, the key parameter, power conversion efficiencies (PCE), is up to 7% under the standard solar spectrum, AM1.5G (Liang et al., 2010). The PCE of solar cells are co-determined by the open circuit voltage (V_{oc}), the fill factor (FF) and the short circuit density (J_{sc}). Researchers have made great efforts in both developing new organic materials with narrow band gap and designing different structural cells for harvesting exciton in the visible light range.

Solution processing of π-conjugated materials (including polymers and oligomers) based OSCs onto flexible plastic substrates represents a potential platform for continuous, large-scale printing of thin-film photovoltaics (Krebs, 2009; Peet, 2009). Rapid development of this technology has led to growing interest in OSCs in academic and industrial laboratories and has been the subject of multiple recent reviews (Cheng, 2009; Dennler, 2009; Krebs, 2009; Tang, 2010). These devices are promising in terms of low-cost power generation, simplicity of fabrication and versatility in structure modification. The structure modification of π-conjugated materials has offered wide possibilities to tune their structural properties (such as rigidity, conjugation length, and molecule-to-molecule interactions) and physical properties (including solubility, molecular weight, band gap and molecular orbital energy levels). This ability to design and synthesize molecules and then integrate them into organic–organic and inorganic–organic composites provides a unique pathway in the design of materials for novel devices. The most common OSCs are fabricated as the bulk-heterojunction (BHJ) devices, where a photoactive layer is casted from a mixture solution of polymeric donors and soluble fullerene-based electron acceptor and sandwiched between two electrodes with different work functions (Yu et al., 1995). When the polymeric donor is excited, the electron promoted to the lowest unoccupied molecular orbital (LUMO) will lower its energy by moving to the LUMO of the acceptor. Under the built-in electric field caused by the contacts, opposite charges in the photoactive layer are separated, with the holes being transported in the donor phase and the electrons in the acceptor. In this way, the blend can be considered as a network of donor–acceptor heterojunctions that allows efficient

charge separation and balanced bipolar transport throughout its whole volume. Remarkably, the power conversion efficiency (PCE, defined as the maximum power produced by a photovoltaic cell divided by the power of incident light) of the OSCs has been pushed to more than 7% from 0.1% after a decade's intensive interdisciplinary research. The current workhorse materials employed for PSCs are regioregular poly(3-hexylthiophene) (P3HT) and [6,6]-phenyl-C61-butyric acid methyl ester (PCBM). This material combination has given the highest reported PCE values of 4%~5% (G. Li, 2005). Theoretically, the PCE of polymer solar cells can be further improved (ca 10%) (Scharber et al., 2006) by implementing new materials (Cheng, 2009; Peet, 2009; Tang, 2010) and exploring new device architecture (Dennler, 2008; Ameri, 2009; Dennler, 2009) after addressing several fundamental issues such as bandgap, interfaces and charge transfer (Li, 2005; Chen, 2008; Cheng, 2009).

In this account, we will update the recent 4 years progress in pursuit of high performance BHJ OSCs with newly developed conjugated polymers, especially narrow bandgap polymers from a viewpoint of material chemists. The correlation of polymer chemical structures with their properties including absorption spectra, band gap, energy levels, mobilities, and photovoltaic performance will be elaborated. The analysis of structure-property relationship will provide insight in rational design of polymer structures and reasonable evaluation of their photovoltaic performance.

2. Fluorene-based conjugated polymers

Fluorene (FL) and its derivatives have been extensively investigated for their application in light-emitting diodes due to its rigid planar molecular structure, excellent hole-transporting properties, good solubility, and exceptional chemical stability.

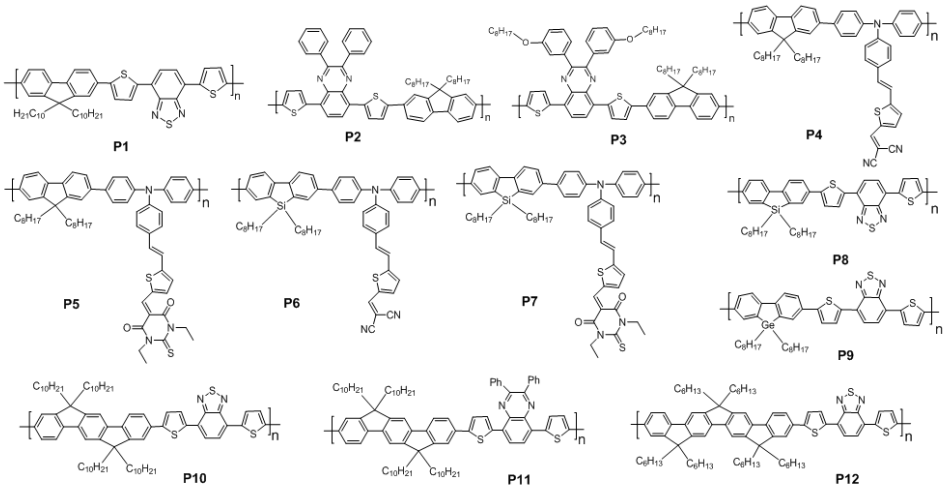

Chart 1. Flourene based narrow band gap polymers.

Along with their low-lying HOMO levels, polyfluorenes (PFs) are expected to achieve higher V_{oc} and J_{sc} in their PSC device, which makes fluorene unit a promising electron-

donating moiety in D-A narrow band gap polymers' design. Besides, feasible dialkylation at 9-position and selective bromination at the 2,7-positions of fluorene allow versatile molecular manipulation to achieve good solubility and extended conjugation *via* typical Suzuki or Stille cross-coupling reactions. By using 4,7-dithien-2-yl-2,1,3-benzothiadiazole (DTBT) as electron accepting unit and didecylated FL as donating unit, Slooff (Slooff et al., 2007) developed **P1** (**P1-12** structure in Chart 1) with extended absorption spectrum ranging from 300 to 800nm. Spin-coated from chloroform solution, the device ITO/PEDOT:PSS/**P1**:PCBM(1:4, w/w)/LiF/Al harvested a extremely high PCE of 4.2% (Table 1). An external quantum efficiency (EQE) of 66% was achieved in the active layer with a film thickness up to 140 nm, and further increasing the film thickness did not increase the efficiency due to limitations in charge generation or collection. For 4.2% PCE device, a maximum EQE of about 75% was calculated, indicating efficient charge collection.

By using quinoxaline as electron accepting unit, **P2** was synthesized with an E_g of 1.95eV (Kitazawa et al., 2009). The device performance is dependent upon the ratio of chloroform(CF)/chlorobenzene(CB) in co-solvent for blend film preparation and a maximal J_{sc} is achieved with CF/CB (2:3 v/v) co-solvent. The optimized device showed 5.5% PCE by inserting 0.1nm LiF layer between BHJ active layer and Al cathode with the structure ITO/PEDOT:PSS/**P2**:PC71BM/LiF/Al. Similarly structured **P3** achieved 3.7% PCE by blending with PC71BM (1:3 w/w) (Gadisa et al., 2007).

Polymer	λ_{max}^{abs} nm	E_g eV	μ_h $cm^2 V^{-1}s^{-1}$	HOMO /LUMO, eV	Polymer: PCBM[b]	J_{sc} mA/cm^2	V_{oc} V	FF	PCE
P1	-	-	-		1:4	7.7	1.0	0.54	4.2
P2	540	1.95	-	-5.37/-	1:4[a]	9.72	0.99	0.57	5.5
P3	542	1.94	-	-6.30/-3.60	1:3	6.00	1.00	0.63	3.7
P4	545	1.87	5.3×10^{-4}	-5.30/-3.43	1:4	9.62	0.99	0.5	4.74
P5	580	1.76	1.2×10^{-3}	-5.26/-3.50	1:4	9.61	0.99	0.46	4.37
P6	541	1.83	1.8×10^{-4}	-5.32/-3.49	1:4[a]	6.69	0.85	0.37	2.50
P7	579	1.74	2.1×10^{-4}	-5.35/-3.61	1:4[a]	6.22	0.90	0.45	3.15
P8	565	1.82	1.0×10^{-3}	-	1:2	9.50	0.90	0.51	5.4
P9	580	1.79	1.1×10^{-4}	-5.58/-3.91	-	6.9	0.79	0.51	2.8
P10	543	1.97	4.2×10^{-3}	-5.47/-3.44	1:3.0	6.10	1.00	0.40	2.44
P11	541	2.00	9.5×10^{-4}	-5.45/-3.36	1:3.5[a]	7.57	1.00	0.40	3.04
P12	531	1.96	9.7×10^{-3}	-5.45/-3.45	1:4.0[a]	10.3	1.04	0.42	4.50

λ_{max}^{abs}: maximum absorption peak in film; E_g: optical band gap; μ_h: hole mobility; J_{sc}: short-circuit current density; V_{oc}: open-circuit voltage; FF: fill factor; PCE: power conversion efficiency; [a]polymer:PC71BM; [b]polymer:PCBM in weight ratio.

Table 1. The optical, electrochemical, hole mobility, and PSC characteristics of **P1-12**

Different from the common linear D-A alternating polymer design, Jen and his coworkers designed a series of novel two-dimensional narrow band gap polymers, whose backbone adopts high hole transporting fluorene-triarylamine copolymer (PFM) and is grafted with malononitrile (**P4**) and diethylthiobarbituric acid (**P5**) through a styrylthiophene π-bridge (Huang et al., 2009). Both of them show two obvious absorption peaks, where the first absorption peaks at ~385 nm are corresponding to the π-π * transition of their conjugated main chains and the others are corresponding to the strong ICT characters of their side chains. Two polymers show narrowed down E_g (<2eV) and present similar HOMO energy

level as that of PFM, while these two polymers exhibit much lowered LUMO levels (-3.43 and -3.50eV for **P4** and **P5**, respectively) than PFM,. The devices with structure of ITO/PEDOT:PSS(40nm)/**P4-5**:PC71BM(1:4 w/w, 85nm)/Ca(10nm)/Al(100nm) exhibit a PCE of 4.74% and 4.37% for **P4** and **P5**, respectively (refer to Table 1). Determined by using space-charge-limited-current (SCLC) method, the hole mobility of these two polymer/P71BM blend films was found to be $5.27\times10^{-4}cm^2V^{-1}s^{-1}$ for **P4** and $1.16\times10^{-3}cm^2V^{-1}s^{-1}$ for **P5**, respectively, which is even higher than that of P3HT with similar device configuration (G. Li, 2005). These two-dimensional polymers are thought to possess better isotropic charge transport ability than linear polymers, which is beneficial for PSC applications. By replacing FL in **P4** and **P5** with silafluorene (2,7-dibenzosilole) unit, similarly structured two-dimensional conjugated polymers **P6** and **P7** were developed (Duan et al., 2010) developed. With an E_g of 1.83 and 1.74eV, **P6** and **P7** OSCs harvest high PCE as 2.5% and 3.51%, respectively, with device configuration ITO/PEDOT:PSS/**P6-7**:PC71BM/Ba/Al. It should be noted that the silofluorene polymers display lower hole transport ability than FL-based **P4** and **P5**.

By alternating silafluorene and DTBT units, copolymer **P8** was synthesized (Boudreault et al., 2007a). With an E_g of 1.82eV, **P8** films presented an absorption spectrum blend covered the range from 350 to 750nm. **P8** device displayed a PCE of 1.6% under AM 1.5 (90 mW/cm^2) illumination with the structure ITO/PEDOT:PSS/**P8**:PCBM(1:4)/Al. By using similar polymer, **P8**:PCBM (1:2 w/w) blend film delivered as high as PCE of 5.4% under AM 1.5 (80 mW/cm^2) (Zhou et al., 2004). By using DTBT as electron accepting unit, Leclerc (Allard et al., 2010) developed germafluorene based polymer **P9** whose device displayed a good PCE of 2.8% with the structure of ITO/PEDOT-PSS/**P9**:PC71BM/LiF(20nm)/Al.

In order to extend π-conjugation of polymer backbone, the ladder-type oligo-*p*-phenylenes (indenofluorene) consisting of several "linearly overlapping" fluorene was developed. Compared to FL unit, indenofluorene presents a broader more intense absorption band. Solubilizing alkyl chains can be easily introduced into this unique molecular backbone, which may provide a better solution processability of the polymers. Zheng (Zheng et al., 2010) reported three alternating D-A copolymers (**P10-12**) combining indenofluorene as the donor and DTBT or 5,8-dithien-2-yl-2,3-diphenyl quinoxaline (DTQX) as the acceptor unit. By spin-coating from chlorobenzene (CB):o-dichlorobenzene(DCB) (4:1 v/v) co-solvent, **P10** with decylated indenofluorene presents good solubility and its device achieved 2.44% PCE with the configuration ITO/PEDOT:PSS/**P10**:PCBM/Cs_2CO_3/Al (Veldman et al., 2008). In comparison with **P10**, **P12** with one more phenylene group in indenofluorene unit presents greatly improved device PCE (3.67%) with the same configuration, due to great improvement of J_{sc}. By blending with PC71BM in 1:4 weight ratio, **P18** OSC showed significantly improved PCE (4.5%). The DTQX-containing **P11** presents a good PCE of 2.32%, which was attributed to broad absorption spectra and high J_{sc}.

3. Carbazole-based conjugated polymers

Structurally analogous to FL, carbazole has been also known as 9-azafluorene. The central fused pyrrole ring makes tricyclic carbazole fully aromatic and electron-rich with its donating nitrogen. The alkyl chains introduced into nitrogen of carbazole improve the solubility. Carbazole derivatives have been widely used as electron-donor materials due to their excellent thermal and photochemical stabilities as well as relatively high charge mobility and good solubility with 9-position alkylation. When two carbazoles fused together

to form indolo[3,2-*b*]carbazole (IC) unit, it exhibits even stronger electron-donating properties, higher hole mobility and better stability than carbazole (Boudreault, 2007b; Li, 2006). With bulky heptadecanyl modified carbazole to improve solubility, Leclerc (Blouin et al., 2007a) developed DTBT-based conjugated poly(N-alkyl-2,7-carbazole) (PC) **P13** (**P13-26** structure in Chart 2), which exhibits excellent thermal stability, relatively high molecular weight and good solubility. Spin-coated from CF solution, **P13**:PCBM(1:4 w/w) OSC delivered a high PCE of 3.6% (Table 2). Such high PCE and excellent stability show its potential application in OSC. By using longer alkyl chain, Hashimoto (Zou et al., 2010) reported a similar PC **P14**, whose device based on **P14**:PCBM (1:3w/w) showed 3.05% PCE, with all photovoltaic parameters similar to those of **P13**. By using 4,7-dithien-2-yl-2,1,3-benzothiadiazoxaline (DTBX) as accepting unit, Leclerc (Blouin et al., 2007b) synthesized **P15**. Due to its symmetrical backbone, **P15** showed good structural organization, which leads to good hole mobility and thus resultant improvement of J_{sc} and FF for its OSC. **P15** based OSC achieved a good PCE of 2.4%.

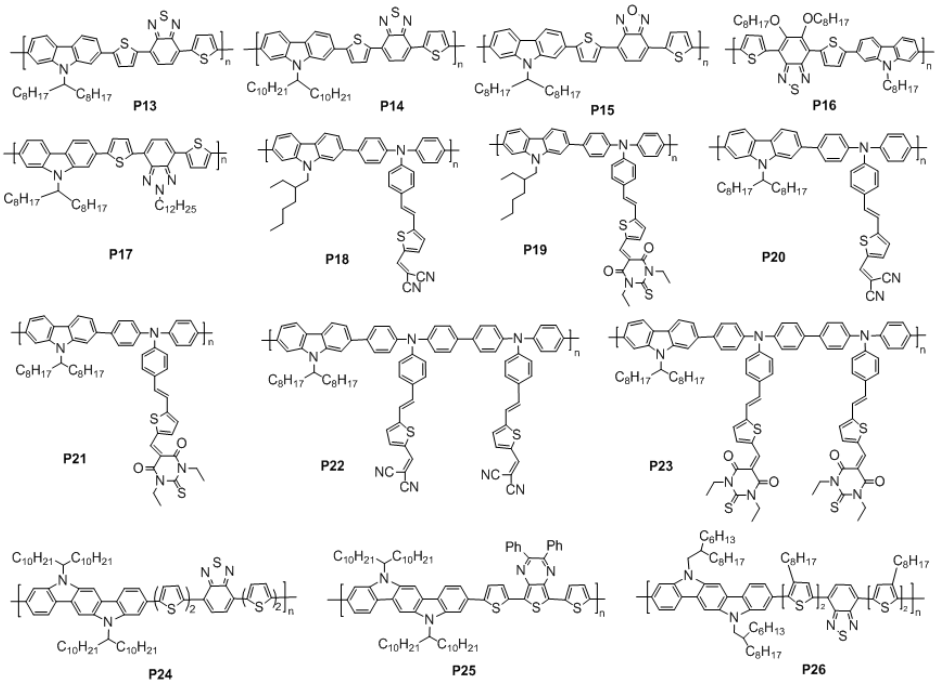

Chart 2. Carbazole based narrow band gap polymers

In order to improve the solubility and close packing of polymer backbone, Zhang (Qin et al., 2009) designed **P16** with planar polymer conformation by introducing two octyloxy chains onto benzothiazole (BT) ring and an octyl chain onto carbazole ring. **P16** showed good solubility at elevated temperature and an E_g of 1.95eV. Spin-coated from DCB mixture solutions with 2.5% 1,8-diiodooctane (DIO), **P16**:PC71BM device showed extremely high

PCE of 5.4% with the structure ITO/PEDOT:PSS/**P16**:PC71BM(1:2.5 w/w)/LiF/Al. By replacing the BT unit with benzotriazole, Cao (Zhang et al., 2010) developed PC **P17**, with an E_g of 2.18eV, which was broader than that of P3HT. The optimized device of **P17** achieved improved PCE from 1.51% to 2.75% by sandwiching a thin layer of PFN between Al cathode and active layer.

On the basis of successful design of two-dimensional PF **P4** and **P5**, Cao [Duan et al., 2010b] developed a series of carbazole-based two-dimensional polymers **P18-23**, with their E_g ranging from 1.7 to 1.9eV. **P18-23** present similar HOMO energy levels as the conjugated backbone while their LUMO levels were mainly determined by narrow band gap side-chains. Among them, **P22** and **P23** exhibited stronger absorption intensity and broader absorption spectra. The photovoltaic performance of **P22** and **P23** devices indicates the 2-ethylhexyl chains had little influence on the V_{oc} of OSC while the bulky heptadecanyl chains on carbazole led to a significant decrease in J_{sc} and FF. In comparison with that of **P4** and **P5**, **P18** devices exhibited excellent PCE of 4.16%. **P18-23** OSCs possessed high V_{oc} (>0.8eV) values, which was relevant with their relatively low HOMO levels. As known, V_{oc} is related to the offset between the HOMO levels of donor materials and the LUMO levels of acceptor materials. The alkyl chains on carbazole unit had important influence on the hole-transporting ability of the resultant polymers: **P18** and **P19** with short side-chains demonstrated hole mobility high as 2.4×10^{-4} and 1.1×10^{-3} $cm^2V^{-1}s^{-1}$, respectively, which are much higher than those of **P20-P23** with bulkier alkyl side-chains. The bulky alkyl chains possibly are thought to result in imbalanced electron transporting and consequently decreased FF of polymer.

Polymer	λ_{max}^{abs} nm	E_g eV	μ_h $cm^2V^{-1}s^{-1}$	HOMO /LUMO, eV	Polymer: PCBM	J_{sc} mA/cm^2	V_{oc} V	FF	PCE
P13	576	1.87	-	-5.50/-3.60	1:4	6.92	0.89	0.63	3.6
P14	551	1.72	-	-5.48/-3.46	1:3	7.66	0.80	0.50	3.05
P15	-	1.87	1×10^{-4}	-5.47/-3.65	1:4	3.70	0.96	0.60	2.4
P16	579	1.95	1×10^{-4}	-5.21/-3.35	1:2.5[a]	9.8	0.81	0.69	5.4
P17	523	2.18	-	-5.54/-3.36	1:2	4.68	0.9	0.65	2.75
P18	548	1.83	2.4×10^{-4}	-5.23/-3.40	1:4[a]	8.94	0.91	0.51	4.16
P19	586	1.74	1.1×10^{-3}	-5.25/-3.51	1:4[a]	8.18	0.92	0.47	3.52
P20	545	1.88	5.3×10^{-5}	-5.29/-3.41	1:4[a]	7.51	0.91	0.44	2.91
P21	575	1.77	1.5×10^{-4}	-5.30/-3.53	1:4[a]	6.23	0.89	0.38	2.09
P22	546	1.83	8.8×10^{-5}	-5.20/-3.37	1:4[a]	7.18	0.83	0.39	2.34
P23	598	1.74	1.6×10^{-4}	-5.24/-3.50	1:4[a]	6.53	0.84	0.40	2.19
P24	551	1.85	-	-5.43/-3.62	1:3	4.83	0.90	0.48	2.07
P25	527	1.91	-	-5.53/-3.54	1:4[a]	7.38	0.80	0.43	2.54
P26	-	-	-	-5.17/3.15	1:2	9.17	0.69	0.57	3.6

Definitions for all parameters are the same as those in Table 1.

Table 2. The optical, electrochemical, hole mobility, and PSC characteristics of **P13-26**

It is widely accepted that the formation of strong intermolecular π-π stacking is necessary to achieve high charge mobility in OSC (Payne, 2004; Mcculloch, 2006). Rigid coplanar fused aromatic rings can efficiently enhance this interaction and hence improve charge mobilities. Indolo[3,2-*b*]carbazole (IC) has large-size fused aromatic ring, making closer packing of

conjugated structure. Hashimoto (Zou et al., 2009) developed narrow band gap (1.90eV) PIC **P24** by alternating IC donating unit and DTBT accepting unit. The optimized **P24** device ITO/PEDOT:PSS/**P24**:PCBM1:3(w/w)/Al demonstrated a PCE of 2.07%. The study reveals that the formation of an interpenetrated network of donors and acceptors inside active layer is critical for obtaining high-performance OSCs. Such interpenetrated networks can be built by tuning device processing parameters such as the ratio of polymer to PCBM in the blend and post-annealing treatment at suitable temperatures. Besides, a simple and effective method to improve the photovoltaic performance of OSCs is to increase the number of unsubstituted thienyl units in D–A copolymers consisting of DTBT as acceptor. The V_{oc} of **P24** is similar with those of some DTBT based narrow band gap polymers with donating units like FL (1.0eV) (Slooff et al., 2007) dibenzosilole (0.9–0.97eV) (Boudreault et al., 2007) or carbazole (0.88 eV) (Blouin et al., 2007) but higher than those of D–A derivatives with donating units such as cyclopenta[2,1-b:3,4-b']dithiophene (0.6eV), dithienosilole (0.44eV) (Liao et al., 2007) or dithieno[3,2-b:2',3'-d] pyrrole(0.52eV) (Zhou et al., 2008). By adopting DTTP as accepting unit, the same group developed **P25**, with an E_g of 1.91 Hashimoto (Zhou et al., 2010a). Spin-coating from CF solution, **P25**:PCBM (1:4, w/w) based OSC contributed a PCE of 1.56% and was further improved to 2.54% by using DCB instead of CF.

By using hexylthiophene moiety in DTBT accepting unit and shorter alkyl chains in IC unit, Movileanu (Lu et al., 2008) developed **P24** analogous PIC **P26**. Long solubilizing side-chains generally resulted in lower charge mobility, balance of the alkyl chains in conjugated polymers was important for charge mobility. **P26** film showed pronounced peak broadening and significant red shift (100nm) in absorption spectra than its solution. **P26** device ITO/PEDOT:PSS/**P26**:PCBM(1:2w/w)/LiF/Al achieved a high PCE of 3.6%.

As discussed above, both PC and PF exhibit relatively low-lying HOMO level and thus high V_{oc} for OSCs via copolymerizing with accepting unit including DTBT, DTTP and DTQX. In contrast with other accepting units, DTBT-containing polymers may maintain deep HOMO and narrow the band gap through reducing LUMO, which results in a high V_{oc}. However, PCs devices generally display low J_{sc} and FF, which was similar to PFs.

4. Thiophene-based conjugated polymers

Polythiophenes (PTs) are considered as the most important conjugated polymers for a broad spectrum of optoelectronic applications such as light-emitting diodes, field-effect transistors, and OSCs due to their excellent optical and electrical properties as well as exceptional thermal and chemical stability (Roncali, 1992).

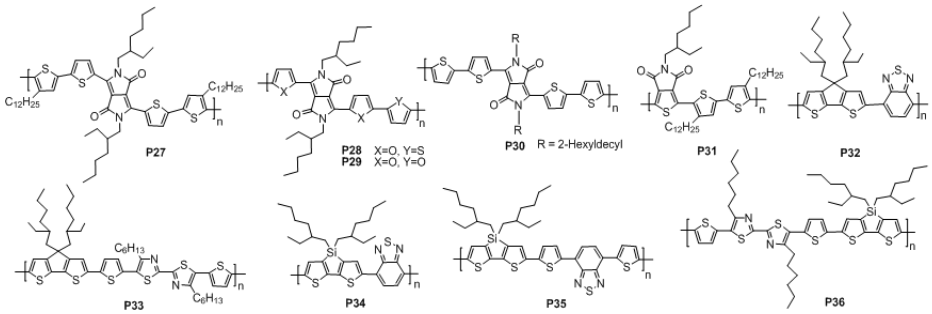

Chart 3. Thiophene-based narrow band gap polymers

By alternating quaterthiophene and diketopyrrolopyrrole (DPP) units, Janssen (Wienk et al., 2008) developed PT **P27** (**P27-36** structure in Chart 3), with an E_g of 1.4eV (Table 3). The absorption spectrum of **P27** in DCB showed stronger red-shift than its solution in CF. Fast evaporation of CF did not allow **P27** to crystallize, which results in poor morphology when spin-coating **P27:**PCBM blend film from CF solution. Certain degree of crystallization could be achieved by heating the film at 130°C. Spin-coated from CF:DCB (4:1 v/v) mixture solution, **P27**:PCBM (1:2 w/w) optimized OSC reached highest PCE of 4%, while OSC achieving only 1.1% PCE using CF as blending solvent and good PCE of 3.2% when prepared from DCB.

Furans have been used as an alternative to thiophenes in organic dyes for dye-sensitized solar cells and have shown very similar optical and electronic properties (R. Li et al., 2009). The first furan-containing DPP-based low band gap polymers **P28-29** were developed (Claire et al., 2010). By spin-coating from CB solution with 1vol% high-boiling-point 1-chloronaphthalene (CN), **P28** device achieved slightly improved PCE from 3.4% to 3.8% with the structure ITO/PEDOT:PSS/**P28**:PCBM(1:3w/w)/LiF/Al, due to optimized blend morphology. The best **P28**:PC71BM (1:3w/w) OSC contributed a PCE of 5.0% with the addition of 9% CN in CB. The device with blend **P29**:PC71BM (1:3 w/w) a PCE of 4.1% with 5% CN addition in CB. The addition of CN led to much finer phase separation between polymer and fullerene to form a fiber-like inter-penetrating morphology at the length scale of 20 nm, which is close to the ideal domain size, assuming an exciton diffusion length of 5-10 nm (Markov et al., 2005; Scully et al., 2006; Shaw et al., 2008). By alternating bithiophene donating unit and DPP accepting unit, Janssen (Johan et al., 2009) developed **P30**, with an E_g of 1.3eV. Terthiophene induced additional planarity, which enhanced packing and charge carrier mobility, as **P30**-based transistors exhibited nearly balanced hole and electron mobilities of 0.04 and 0.01$cm^2V^{-1}s^{-1}$, respectively. The optimized device of **P30**:PCBM (1:2w/w) presented 3.8% PCE by spin-coating from CB solution with a small amount of DIO. The corresponding optimized device of **P30**:PC71BM achieved a PCE of 4.7% by adding 100mg/mL DIO in CF solution, due to low solubility of PC71BM in CF.

Polymer	λ_{max}^{abs} nm	E_g eV	μ_h $cm^2V^{-1}s^{-1}$	HOMO /LUMO, eV	Polymer: PCBM	J_{sc} mA/cm^2	V_{oc} V	FF	PCE
P27	650	1.4	-	-	1:2[a]	11.5	0.61	0.58	4.0
P28	789	1.41	-	-5.40/-3.80	1:3[a]	11.2	0.74	0.60	5.0
P29	767	1.35	-	-5.50/-3.80	1:3[a]	9.1	0.73	0.58	4.1
P30	-	1.36	0.04	-5.17/-3.61	1:2[a]	11.8	0.65	0.60	4.7
P31	572	1.82	1.0×10^{-4}	-5.56/-3.10	1:1.5	8.02	0.95	0.62	4.7
P32	775	1.40	-	-5.30/-3.57	1:3	11.0	0.70	0.47	3.2
P33	560	1.84	-	-5.07/-3.55	1:1	7.70	0.68	0.53	2.79
P34	-	1.45	3×10^{-3}	-5.05/-3.27	1:1[a]	12.7	0.68	0.55	5.1
P35	652	1.53	3.0×10^{-6}	-4.99/-3.17	1:1[a]	9.76	0.60	0.50	2.95
P36	558	1.85	3.1×10^{-4}	-5.18/-3.09	1:1[a]	7.85	0.68	0.54	2.86

Definitions for all parameters are the same as those in Table 1.

Table 3. The optical, electrochemical, hole mobility, and PSC characteristics of **P27-36**

By alternating bithiophene donating unit and thieno[3,4-*c*]pyrrole-4,6-dione (TPD) accepting unit, Wei (Yuan et al., 2010) prepared **P31**, with an E_g of 1.82eV. TPD presented strong electron-withdrawing properties, which were attributed to improvement of intramolecular

interactions and reduction of E_g as well as relatively low HOMO level due to its symmetric, rigidly fused, coplanar structure (Zou et al., 2010). Controlling the active layer thickness of device ITO/PEDOT:PSS/**P31**:PCBM(1:2 w/w)/Al between 90 and 100nm, the best device presented 4.7% PCE, with relatively high V_{oc} (0.95V) attributed to its deep HOMO level.

By alternating cyclopentadithiophene (CPDT) and BT unit, Mühlbacher (Mühlbacher et al., 2006) developed **P32**, which exhibited an E_g of 1.40eV and an absorption spectrum ranged from 300 to 850nm. The device based on **P32**:PCBM obtained a PCE of 3.2%. By incorporating CPDT with bithiazole unit, Lin (K. Li et al., 2009) developed polymer **P33**, with the best device contributed a PCE of 3.04% with the configuration of ITO/PEDOT:PSS/**P33**:PCBM(1:2 w/w)/Ca/Al.

Recently, dithieno-[3,2-b:2′,3′-d]silole-containing polymers have attracted considerable attention due to their potential applications in the field of optoelectronic devices. Many silole-containing polymers have been proven to achieve high V_{oc} by reducing the LUMO levels of polymers (Lu et al., 2008). It is feasible to realize a low-lying HOMO energy level and high V_{oc} simultaneously under the condition of ensuring a sufficient energy level offset (0.3-0.5V) between the LUMO level of silole-containing donor and the LUMO of PCBM. Furthermore, silole-containing polymers applied in OSC have also proved to be effective in improving hole mobility and rendering higher efficiencies compared to CPDT (Wang, 2008; Hou, 2008). By alternating dithieno-[3,2-*b*:2′,3′-*d*]silole and BT unit, Yang (Hou et al., 2008) developed **P34**, with an E_g low 1.45eV. P40 has a broader absorption spectrum ranging from 350-800nm. Its device ITO/PEDOT/PSS/**P34**:PC70BM/Ca/Al achieved an average PCE of 4.7 % for 100 devices, with the OSC showing a PCE of 5.1%. The same group reported DTBT-based silole-containing polymers **P35** (Huo et al., 2009). The device presented 3.43% PCE with the structure of ITO/PEDOT:PSS/**P35**:PCBM/Ca/Al. By alternating dithieno-[3,2-*b*:2′,3′-*d*]silole and dithiazole unit, Li (Zhang et al., 2010) designed **P36**, whose device (ITO/PEDOT:PSS/**P36**:PC71BM(1:2 w/w)/Al) achieved a PCE of 2.86%.

Recently, the polymers containing benzo[1,2-*b*:4,5-*b*′]dithiophene (BDT) have been successfully applied to field-effect transistor (FET) and PSC devices (Huo, 2008; Pan, 2007; Chen, 2009) with a high mobility of 0.15-0.25$cm^2V^{-1}s^{-1}$, owing to the large and planar conjugated structure promoting π-π stacking and thus benefiting charge transport. By incorporating alkoxyl BDT with thieno[3,4-*b*]thiophene, **P37** (**P37-50** structure in Chart 4) was developed, with an E_g 1.62eV (Liang et al., 2009a). Thieno[3,4-*b*]thiophene repeating units contributed to the stability of the quinoidal structure of the backbone narrowing the energy gap of resulting polymer (Sotzing & Lee, 2002). Thieno[3,4-*b*]thiophene with ester substituents in **P37** contributed both good solubility and oxidative stability. The absorption of **P37** coincided with the corresponding maximum photon flux region in solar spectrum. **P37** OSC with the structure of ITO/PEDOT:PSS/**P37**:PCBM(1:1 w/w)/Ca/Al achieved a PCE of 4.76% (Table 4). **P37**:PC71BM presented an improved PCE of 5.30% with the same device structure. The absorption spectra of two devices almost covered the whole visible range. Furthermore, high EQEs were obtained for both **P37**:PCBM and **P37**:PC71BM OSCs. For the former, the maximum EQE was over 60% at 650 nm and was 50% in the range of 550-750 nm; the latter exhibited a higher EQE, almost all over 60% in the range from 400 to 750 nm.

By changing side-chain substituents, **P37** analogous polymers **P38-41** were developed (Liang et al., 2009b). All polymers showed very close between 2.6×10^{-4} and $4.7\times10^{-4}cm^2V^{-1}s^{-1}$ and similar absorption spectra, covering the whole visible region.

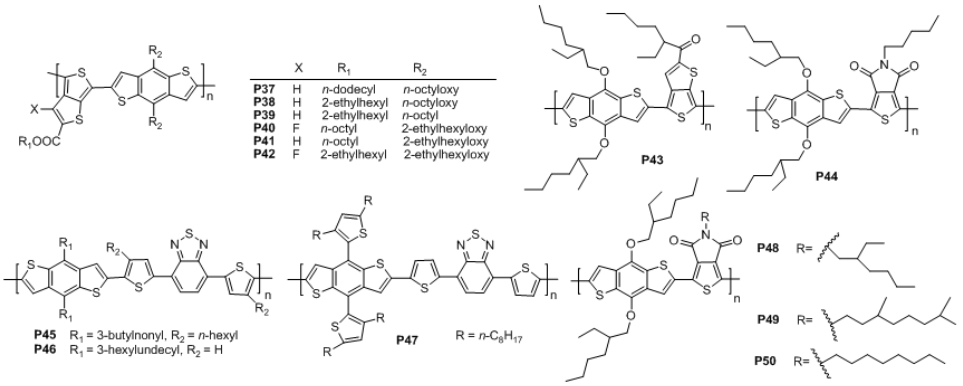

Chart 4. BDT based narrow band gap polymers.

The substitution of octyloxy to octyl group lowered the HOMO energy level of **P38** from -4.94 to -5.04 eV (**P39)**. With electron-withdrawing fluorine in polymer backbone, **P40** had significantly lower HOMO level in comparison to **P41**. The devices based on ITO/PEDOT:PSS/**P38-41**:PCBM (1:1 w/w)/Ca/Al exhibited a PCE of 5.10%, 5.53%, 3.20% and 3.02%,respectively, with active layer spin-coated from DCB solution. By using DCB/DIO (97:3 v/v) mixture solvent, PCE of **P39-P41** can be dramatically improved to 5.85%, 5.90% and 4.10%, respectively. By replacing octyl group in **P40** into 2-ethylhexyl, **P52** was further developed (Liang et al., 2010). Spin-coated from DCB solution, **P51**:PC71BM harvested a PCE of 5.74%, 6.22% and 5.58%, respectively at their D/A weight ratio as 1:1, 1:1.5 and 1:2. The best device contributes PCE as high as 7.4% with the mixture solvent of CB/DIO(97:3 v/v), where uniform morphology of blend film was prepared.

Polymer	λ_{max}^{abs} nm	E_g eV	μ_h $cm^2 V^{-1}s^{-1}$	HOMO/ LUMO, eV	Polymer: PCBM	J_{sc} mA/cm^2	V_{oc} V	FF	PCE
P37	687	1.62	4.5×10^{-4}	-4.90/-3.20	1:1.2[a]	15.0	0.56	0.63	5.30
P38	683	1.59	4.0×10^{-4}	-4.94/-3.22	1:1	12.8	0.60	0.66	5.10
P39	682	1.60	7.1×10^{-4}	-5.04/-3.29	1:1	13.9	0.72	0.58	5.85
P40	682	1.63	7.7×10^{-4}	-5.12/-3.31	1:1	13.0	0.74	0.61	5.90
P41	677	1.62	4.0×10^{-4}	-5.01/-3.24	1:1	10.7	0.66	0.58	4.10
P42	675	1.61	5.8×10^{-4}	-5.15/-3.31	1:1.5[a]	14.5	0.74	0.69	7.4
P43	675	1.61	2×10^{-4}	-5.12/-3.55	1:1.5[a]	14.7	0.7	0.64	6.58
P44	610	1.80	-	-5.56/-3.75	1:2[a]	9.81	0.85	0.66	5.50
P45	595	1.70	1.6×10^{-5}	-5.26/-2.96	1:1	9.70	0.81	0.55	4.31
P46	644	1.70	3.8×10^{-5}	-5.33/-3.17	1:1	7.79	0.83	0.60	3.85
P47	596	1.75	-	-5.31/-3.44	1:2[a]	10.7	0.92	0.58	5.66
P48	608	1.75	-	-5.48/-	1:2	8.1	0.87	0.56	4.0
P49	616	1.70	-	-5.57/-	1:1.5	9.7	0.81	0.67	5.7
P50	627	1.73	-	-5.40/-	1:1.5	11.5	0.85	0.68	6.8

Definitions for all parameters are the same as those in Table 1.

Table 4. The optical, electrochemical, hole mobility, and PSC characteristics of **P37-50**

BDT-containing polymers can finely tune the HOMO level and efficiently narrow the band gap (Pan, 2007; Liang, 2008; Liang, 2009). Besides, alkoxy groups have been proved to be beneficial to reduce the HOMO level of polymer due to its stronger electron-donating property (Liang et al., 2009b). By removal of the oxygen atom on ester group in thieno[3,4-*b*]thiophene unit, ketone-substituted polymer **P43** (Chen et al. 2009) was developed to further reduce the HOMO level. The best OSC based on **P43**:PC71BM showed a high PCE of 6.58%.

By alternating BDT and TPD, Leclerc (Zou et al, 2010) presented polymer **P44**, with an E_g of 1.8eV and HOMO/LUMO energy levels -5.56eV/-3.75eV, respectively. The device ITO/PEDOT:PSS/**P53**:PC71BM/LiF/Al showed a high PCE of 5.5%. By incorporating BDT with DTBT, You (Price et al., 2010) synthesized **P45-46**. Compared with **P45**, **P46** exhibited higher molecular weight while lower hole mobility than other BDT-containing **P37-43**. **P45-46** device showed a PCE of 3.85% and 4.31%, respectively. By introducing thiopene moiety onto BDT, Yang (Huo et al., 2010) synthesized **P45** analogous polymer **P47**, with an E_g of 1.75eV. Spin-coated from DCB, **P47** device (ITO/PEDOT:PSS/**P47**:PC71BM(1:2 w/w)/Ca/Al) contributed the optimized PCE of 5.66% without annealing treatment.

By changing the alky substituent in TPD unit, Frechet (Piliego et al., 2010) synthesized **P44** analogue polymers **P48-50**, with E_g ranging from 1.70 to 1.75 eV and HOMO levels lowered down to -5.4~ -5.57 eV. Spin-coated from CB, **P48-50**:PCBM devices achieved a PCE of 2.8%, 3.9%, 6.4%, respectively. Clearly, the device performance increased as the branch length was decreased in **P48-50**. By spin-coating from CB solution with a small amount of DIO, **P48** and **P49** OSCs achieved improved PCE of 4.0% and 5.7%, respectively (Peet et al., 2008). However, for **P50**, the addition of DIO led to only slight improvements, which was attributed to a high level of order of **P50** in the blend without DIO. It was concluded that alkyl-substituted groups had much impact on the PCE of **P48-50**. The use of DIO is effective in promoting the packing of the polymer by preventing excessive crystallization of PCBM.

Dithieno[3,2-*b*:2′,3′-*d*]pyrrole (DTP) has good planarity and stronger electron-donating ability of nitrogen atoms. Geng (Yue et al. 2009) synthesized BT-based P(DTP)s **P51-52** (Chart 5), with an E_g ~1.43eV. Owing to different alkyl chain, **P52** exhibited stronger absorption in the range of 600-900nm compared to **P51**. **P51-52** devices showed a PCE of 2.06% and 2.8%, respectively with the structure ITO/PEDOT:PSS/**P51-52**:PCBM(1:3 w/w)/LiF/Al, at the optimized blend film thickness of 100 nm for **P51** and 90 nm for **P52**. The device of **P51**-52 delivered a V_{oc} in the range of 0.4-0.54V, leading to relatively low PCE.

By adopting DTP and DTBT units as the donor and acceptor segments, Hashimoto (Zhou et al., 2008) synthesized **P53** with an E_g of 1.46eV, which was the lowest compared with other D-A copolymers based on DTBT acceptor segment with other donor segments such as FL, silafluorene, carbazole, DTS, and CPDT (Slooff, 2007; Blouin, 2007; Moulle, 2008). **P53** device exhibited a PCE of 2.18% and a high J_{sc} of 9.47mA/cm^2, which was attributed to its broad absorption spectrum. However, **P53** device presented a V_{oc} of 0.52V, which is lower than that of the devices based on DTBT-containing D-A copolymers with FL (1V), silafluorene (0.9V) or carbazole (0.9V) as donating unit.

3,6-Dithien-2-yl-2,5-dialkylpyrrolo[3,4-*c*]pyrrole-1,4-dione (DTDPP) emerged as a promising electron acceptor in the design of photovoltaic polymers (Wienk et al., 2008). With DTDPP as accepting unit, Hashimoto (Zhou et al., 2010b) presented **P54**, with an E_g lowed down to 1.13eV. **P54** presented a hole mobility of 0.05cm^{2}V^{-1}s^{-1}, 1-2 orders of magnitude higher than that of other D-A polymers. Spin-coated with mixing solution of CF and DCB (4:1 v/v), **P54** device with structure of ITO/PEDOT:PSS/**P54**:PCBM(or PC71BM)/LiF/Al showed a PCE of 2.34% with PCBM and 2.71% with PC71BM as acceptor in the blend films. The PCE of **P54**

was lower that of P3HT, which was mainly attributed to the lower V_{oc}, resulting from its high-lying HOMO level (-4.90eV). It was expected that the device performance would be improved by further reducing the HOMO and LUMO level.

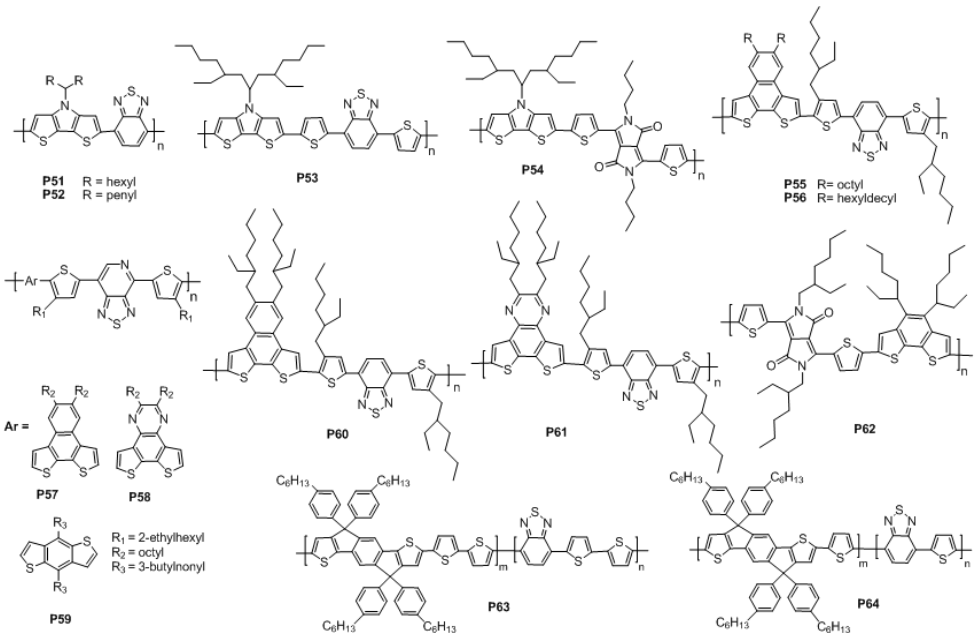

Chart 5. Fused Thiophene based narrow band gap polymers.

Recently, You (H. Zhou, 2010b) proposed a design strategy for narrow band gap polymers by alternating "weak donor" and "strong acceptor" to approach ideal polymers with both low HOMO energy level and small E_g in order to achieve both high V_{oc} and J_{sc} (H. Zhou, 2010e). By alternating DTBT or thiadiazolo[3,4-*c*]pyridine as strong acceptor,with naphtho[2,1-*b*:3,4-*b*′]-dithiophene (NDT), dithieno[3,2-f:2′,3′-*h*]quinoxaline (QDT) or BDT as weak donor, polymers **P55-61** were developed (Yang, 2010; H. Zhou, 2009; H. Zhou, 2010b, 2010c). For NDT-containing **P55-56**, a 4-(2-ethylhexyl)thiophene unit in DTBT was used to reduce the steric hindrance of polymer backbone and hence to achieve near identical E_g and energy levels (H. Zhou, 2010a). It was believed that E_g and energy levels of a conjugated polymer were primarily determined by the molecular structure of conjugated backbone, while the solubilizing alkyl chains should have a negligible impact on these properties and hence a little impact on device's J_{sc} and V_{oc} . However, Yu's study showed variations of length and shape of alkyl chains in NDT had significant influence on device performance: long and branched side-chains would weaken the intermolecular interaction, benefiting for improvement of V_{oc}; while short and straight side-chains would promote the intermolecular interaction, rendering a large J_{sc}. The desirable balance between V_{oc} and J_{sc} could be tuned through adopting suitable short and branched side-chains. **P55-56**:PCBM (1:1,w/w) devices showed a best PCE of 3.0% and 3.36%, respectively.

Polymer	λmax nm	E_g eV	μ_h $cm^2V^{-1}s^{-1}$	HOMO/ LUMO, eV	Polymer: PCBM	J_{sc} mA/cm^2	V_{oc} V	FF	PCE
P51	764	1.42	-	-4.86/-3.07	1:3	11.1	0.43	0.43	2.06
P52	764	1.43	-	-4.81/-3.08	1:3	11.9	0.54	0.44	2.80
P53	697	1.46	-	-5.00/-3.43	1:1	9.47	0.52	0.44	2.18
P54	790	1.13	0.05	-4.90/-3.63	1:2[a]	14.87	0.38	0.48	2.71
P55	547	-	-	-	1:1	10.93	0.59	0.46	3.00
P56	548	-	-	-	1:1	10.67	0.69	0.46	3.36
P57	580	1.53	-	-5.36/-3.42	1:1	14.16	0.71	0.62	6.20
P58	650	1.56	-	-5.50/-3.44	1:1	13.49	0.75	0.55	5.57
P59	675	1.51	-	-5.47/-3.44	1:1	12.78	0.85	0.58	6.32
P60	681	1.61	1.7×10^{-5}	-5.34/-3.29	1:0.8	14.20	0.67	0.54	5.10
P61	647	1.70	7.2×10^{-6}	-5.46/-3.28	1:1.2	11.38	0.83	0.46	4.3
P62	928	1.34	-	-5.21/-3.63	1:2[a]	10.1	0.68	0.63	4.31
P63	520	1.76	7.0×10^{-4}	-5.46/-3.56	1:3[a]	8.7	0.84	0.53	3.9
P64	590	1.70	3.4×10^{-3}	-5.43/-3.66	1:3[a]	10.1	0.80	0.53	4.3

Definitions for all parameters are the same as those in Table 1.

Table 5. The optical, electrochemical, hole mobility, and PSC characteristics of **P51-64**

By replacing BT with a new stronger acceptor, thiadiazolo[3,4-*c*]pyridine, You (H. Zhou, 2010d) developed **P57-59** by adopting NDT, QDT or BnDT as donating unit. **P57-59** exhibit an E_g of 1.53eV, 1.56eV and 1.51eV, respectively, which is noticeably reduced (ca.0.09–0.19eV) compared with the band gaps of their BT counterparts (Price, 2010; H. Zhou, 2010c). The device with ITO/PEDOT:PSS/**P57-59**:PCBM/Ca/Al achieved a PCE of 6.20% for **P57**, 5.57% for **P58**, and 6.32%% for **P59**.By alternating DTBT acceptor with NDT or QDT weak donor, You (H. Zhou, 2010e) developed **P60-61**, with an E_g of **P60-61** of 1.61eV and 1.70eV, respectively. The devices based on **P60-61**:PCBM achieved a PCE of 5.1% and 4.3%, respectively. The donor unit with electron-withdrawing atoms was demonstrated to lead to a lower HOMO level while have little impact on the LUMO level. You thought that future research should be focused on employment of even weaker donors and stronger acceptors via innovative structural modification in order to concurrently achieve a higher V_{oc} and a higher J_{sc}. By alternating DPP and benzo[1,2-*b*:4,5-*b'*]dithiophene, Yang (Huo et al., 2009) synthesized **P62**. Its device with the structure of ITO/PEDOT:PSS/**P62**:PC71BM(1:2 w/w)/Ca/Al achieved improved PCE from 4.31% to 4.45% after device annealing under 110°C for 30 min. **P62** was expected to a very promising candidate for highly efficient OSCs owing to relatively low E_g and suitable HOMO level.

Ladder-type coplanar thiophene-phenylene-thiophene (TPT) structure tends to lead to strong molecular π-π interaction and thus exhibits remarkable hole mobility (Wong et al., 2006). Poly(TPT)s demonstrated an E_g ~2.1eV and hole mobility as high as $10^{-3}cm^2V^{-1}s^{-1}$ (Chan et al., 2008). By alternating TPT donor and DTBT acceptor, Ting (Chen et al., 2008) developed **P63-64**, which exhibited an E_g of 1.76eV and 1.70eV, and absorption band in the range of 350-700nm and 350-730nm, respectively. **P64** displayed a hole mobility up to $3.4\times10^{-3}cm^2V^{-1}s^{-1}$. Both of them showed good solubility at room temperature in organic solvents. Using DCB as blending solvent, the devices ITO/PEDOT:PSS/**P63-64**:PCBM(1:3 w/w)/Ca/Al harvested a PCE of 2.0% and 2.5%, respectively, a little lower than that (3.9% PCE) of P3HT:PCBM(1:1 w/w) device under the same conditions. The optimized device

with **P63-64**:PC71BM (1:3 w/w) showed a PCE of 3.9% for **P63** and 4.3% for **P64**, higher than that of the device based on P3HT:PC71BM (1:1 w/w) (3.4%) under the same conditions.

5. Conclusions

Narrow band gap polymers **P1-P64** developed by alternating donor (ca. fluorene, carbazole and thiophene) and acceptor (ca.benzothiadiazole, quinoxaline and diketopyrrolopyrrole) units in recent 4 years are summarized, with their fullerene blend-based BHJ OSCs contributing PCE over 3%. The design criteria for ideal polymer donors to achieve high efficiency OSCs is: (1) a narrow E_g (1.2-1.9eV) with broad absorption to match solar spectrum; (2) a HOMO energy level ranging from -5.2 to -5.8 eV and a LUMO level ranging from -3.7 to -4.0eV to ensure efficient charge separation while maximizing V_{oc}; and (3) good hole mobility to allow adequate charge transport. Besides, device structure and morphology optimizations of polymer:fullerene blend film have been extensively demonstrated to be crucial for PCE improvement in OSCs. The current endeavors boosted OSCs PCEs up to 7% would encourage further efforts toward a next target of efficiency in excess of 10%.

6. References

Allard, N., Aich, RB., Gendron, D., Boudreault, P-LT., Tessier, C., Alem, S., Tse, S-C., Tao, Y. & Leclerc, M. (2010). Germafluorenes: new heterocycles for plastic electronics. *Macromolecules*, Vol. 43, No. 5, (January 2010), pp. (2328-2333), ISSN: 1520-5835

Ameri, T., Dennler, G., Lungenschmied, C. & Brabec, CJ. (2009). Organic tandem solar cells: a review. *Energ. Environ. Sci.*, Vol. 2, No. 4, (February 2009), pp. 347-363, ISSN: 1754-5692

Beal, RM., Stavrinadis, A., Warner, JH., Smith, JM. & Beal, HE. (2010). The molecular structure of polymer-fullerene composite solar cells and its influence on device performance. *Macromolecules*, Vol. 43, No. 5, (February 2010), pp. 2343-2348, ISSN: 1520-5835

Blouin N, Michaud A. & Leclerc, M. (2007). A low-bandgap poly(2,7-Carbazole) derivative for use in high-performance solar cells. *Adv. Mater.*, Vol.19, No.17, (September 2007), pp. (2295–2300), ISSN: 1521-4095

Blouin, N., Michaud, A., Gendron, D., Wakim, S., Blair, E., Neagu-Plesu, R., Belletete, M., Durocher, G., Tao, Y. & Leclerc, M. (2008). Toward a rational design of poly(2,7-carbazole) derivatives for solar cells. *J. Am. Chem. Soc.*, Vol. 130, No. 2, (December 2007), pp. (732-742), ISSN: 0002-7863

Boudreault, P-LT., Michaud, A. & Leclerc, M. (2007). A new poly(2,7-dibenzosilole) derivative in polymer solar cells. *Macromol. Rapid Commun.*, Vol. 28, No. 22, (November 2007), pp. (2176–2179), ISSN: 1521-3927

Boudreault, P-LT., Wakim, S., Blouin, N., Simard, M., Tessier, C., Tao, Y. & Leclerc, M. (2007). Synthesis, characterization, and application of indolo[3,2-b]carbazole semiconductors. *J. Am. Chem. Soc.*, Vol. 129, No. 29, (June 2007), pp. (9125-9136), ISSN: 0002-7863

Chan, S-H., Chen, C., Chao, T., Ting, C. & Ko, B-T. (2008). Synthesis, characterization, and photovoltaic properties of novel semiconducting polymers with thiophene-phenylene-thiophene (TPT) as coplanar units. *Macromolecules*, Vol. 41, No.15, (June 2008), pp. (5519-5526), ISSN: 1520-5835

Chen, C., Chan, S-H., Chao, T., Ting, C. & Ko, BT. (2008). Low-bandgap poly(thiophene-phenylene-thiophene) derivatives with broaden absorption spectra for use in high-performance bulk-heterojunction polymer solar cells. *J. Am. Chem. Soc.*, Vol. 130, No. 38, (August 2008), pp. (12828–12833), ISSN: 0002-7863

Chen, H., Hou, J., Zhang, S., Liang, Y., Yang, G., Yang, Y., Yu, L., Wu, Y. & Li, G. (2009). Polymer solar cells with enhanced open-circuit voltage and efficiency. *Nat. Photonics*, Vol. 3, No. 11, (November 2009), pp. (649-653), ISSN: 1749-4893

Chen H-Y., Hou, J., Zhang, S., Liang, Y., Yang, G., Yang, Y., Yu, L., Wu, Y. & Li, G. (2009). Polymer solar cells with enhanced open-circuit voltage and efficiency. *Nat. Photonics,* Vol. 3, No.11, (November 2009), pp. (649-653), ISSN: 1749-4885

Cheng, YJ., Yang, SH. & Hsu, CS. (2009). Synthesis of conjugated polymers for organic solar cell applications. *Chem. Rev.*, Vol. 109, No. 11, (September 2009), pp. 5868-5923, ISSN: 1520-6890

Claire, HW., Pierre, MB., Thomas, WH., Olivia, PL. & Fréchet, JMJ. (2010). Incorporation of furan into low band-gap polymers for efficient solar cells. *J. Am. Chem. Soc.*, Vol. 132, No. 44, (October 2010), PP. (15547–15549) ISSN: 0002-7863

Dennler, G. Scharber, MC., Ameri, T., Denk, P., Forberich, K., Waldauf, C. & Brabec, CJ. (2008). Design rules for donors in bulk-heterojunction tandem solar cells - Towards 15% energy-conversion efficiency, *Adv. Mater.,* Vol. 20, No.3, (February 2008), pp. (579-583), ISSN: 1521-4095.

Dennler, G., Scharber, M. C. Brabec, C. J. (2009). Polymer-fullerene bulk-heterojunction solar cells. *Adv. Mater.*, Vol. 21, No. 13, (April 2009), pp. (1323-1338), ISSN: 1521-4095

Duan, C., Cai, W., Huang, F., Zhang, J., Wang, M., Yang, T., Zhong, C., Gong, X. & Cao, Y. (2010). Novel silafluorene-based conjugated polymers with pendant acceptor groups for high performance solar cells. *Macromolecules*, Vol. 43, No. 12, (January 2010), pp. (5262-5268), ISSN: 1520-5835

Duan, C., Chen, K., Huang, F., Yip, H-L., Liu, S., Zhang, J., Jen, AK-Y. & Cao, Y. (2010). Synthesis, characterization, and photovoltaic properties of carbazole-based two-dimensional conjugated polymers with donor-π-bridge-acceptor side chains. *Chem. Mater.,* Vol. 22, No. 23, (November 2010), pp. (6444-6452), ISSN: 1520-5002

Gadisa, A., Mammo ,W., Andersson, LM., Admassie, S., Zhang, F, Andersson, MR. & Inganäs, O. (2007). A new donor–acceptor–donor polyfluorene copolymer with balanced electron and hole mobility. *Adv. Funct. Mater.*, Vol. 17, No.18, (November 2007), pp. (3836–3842), ISSN: 1616-3028

Hou, J., Chen, H-Y., Zhang, S., Li, G. & Yang, Y. (2008). Synthesis, characterization, and photovoltaic properties of a low band gap polymer based on silole-containing polythiophenes and 2,1,3-benzothiadiazole. *J. Am. Chem. Soc.,* Vol. 130, No. 48, (November 2008), pp. (16144-16145), ISSN: 0002-7863

Huang, F., Chen, K-S., Yip, H-L., Hau, SK., Acton, O., Zhang, Y., Luo, J. & Jen, AK-Y. (2009). Developme -nt of new conjugated polymers with donor−π-bridge−acceptor side chains for high performance solar cells. *J. Am. Chem. Soc.*, Vol. 131, No. 39, (September 2009), pp. (13886–13887), ISSN: 0002-7863

Huo, L., Chen, H., Hou, J., Chen, T., Yang, Y. (2009). Low band gap dithieno[3,2-b:2,3-d]silole–con taining polymers, synthesis, characterization and photovoltaic application, *Chem. Commun.*, No. 37, (July 2009) ,PP. (5570–5572), ISSN: 1359-7345

Huo, L., Hou, J., Zhang, S., Chen, H-Y. & Yang, Y. (2010). A polybenzo[1,2-*b*:4,5-*b*′]dithiophene derivative with deep homo level and its application in high-performance polymer solar cells. *Angew. Chem. Int. Ed.*, Vol. 49, No. 8, (February 2010), pp. (1500–1503), ISSN: 1521-3773

Johan, CB., Arjan, PZ., Simon, GJM., Martijn, MW., Mathieu, T., Dago, ML. & Rene, AJJ. (2009). Poly(diketopyrrolopyrrole-terthiophene) for ambipolar logic and photovoltaics. *J. Am. Chem. Soc.*, Vol. 131, No. 46, (September 2009), pp. (16616–16617) ISSN: 0002-7863

Kitazawa, D., Watanabe, N., Yamamoto, S. & Tsukamoto, J. (2009). Quinoxaline-based π-conjugated donor polymer for highly efficient organic thin-film Solar Cells. *Appl. Phys. Lett.*, Vol. 95, No.5, (May 2009), pp. (053701-053703), ISSN: 1077-3188

Krebs, F.C. (2009). Fabrication and processing of polymer solar cells: a review of printing and coating techniques. *Solar Energ. Mater. Solar C.*, Vol. 93, No. 4, (April 2009), pp. 394-412, ISSN: 0927-0248

Li, G., Shrotriya, V., Huang, J. S.; Yao, V. & Moriarty, T. (2005). High-efficiency solution processable polymer photovoltaic cells by self-organization of polymer blends. *Nat. Mater.*, Vol. 4, No. 11, (October 2005), pp. 864-868, ISSN: 1476-4660

Li, K., Huang, J., Hsu, YC., Huang, P., Chu, CW., Lin, J., Ho, KC., Wei, K., Lin, H. (2009). Tunable novel cyclopentadithiophene-based copolymers containing various numbers of bithiazole and thienyl units for organic photovoltaic cell applications. *Macromolecules*, Vol. 42, No. 11, (April 2009), pp. (3681–3693), ISSN: 1520-5835

Li, R., Lv, X., Shi, D., Zhou, D., Cheng, Y., Zhang, G. & Wang, P. (2009). Dye-sensitized solar cells based on organic sensitizers with different conjugated linkers: furan, bifuran, thiophene, bithiophene, selenophene, and biselenophene. *J. Phys. Chem. C*, Vol. 113, No. 17, (April 2009), pp. (7469–7479), ISSN: 1932-7455

Li, Y., Wu, Y. & Ong, BS. (2006). Polyindolo[3,2-*b*]carbazoles: a new class of *p*-channel semiconductor polymers for organic thin-film transistors. *Macromolecules*, Vol. 39, No. 19, (August 2006), pp. (6521-6527), ISSN: 1520-5835

Liang, Y., Wu, Y., Feng, D., Tsai, S-T., Son, H-J., Li, G. & Yu, L. (2009). Development of new semiconducting polymers for high performance solar cells. *J. Am. Chem. Soc.*, Vol. 131, No. 1, (December 2008), pp. (56–57), ISSN: 0002-7863

Liang, Y., Feng, D., Wu, Y., Tsai, S-T., Li, G., Ray, C. & Yu, L. (2009). Highly efficient solar cell polymers developed via fine-tuning of structural and electronic properties. *J. Am. Chem. Soc.*, Vol. 131, No. 22, (May 2009), PP. (7792–7799), ISSN: 0002-7863

Liang, Y., Xu, Z., Xia, J B., Tsai, S-T., Wu, Y., Li, G., Ray, C. & Yu, L. (2010). For the bright future—bulk heterojunction polymer solar cells with power conversion efficiency of 7.4%. *Adv. Mater.*, Vol. 22, No. 20, (May 2010), pp. (E135–E138), ISSN: 1521-4095

Liao, L., Dai, L., Smith, A., Durstock, M., Lu, J., Ding, J. & Tao, Y. (2007). Photovoltaic-active dithienosilole-containing polymers. *Macromolecules*, Vol. 40, No. 26, (November 2007), pp. (9406-9412), ISSN: 1520-5835

Lu, G., Usta, H., Risko, C., Wang, L., Facchetti, A., Ratner, MA. & Marks, TJ. (2008), Synthesis, characterization, and transistor response of semiconducting silole polymers with substantial hole mobility and air stability: experiment and theory. *J. Am. Chem. Soc.*, Vol.130, No. 24, (May 2008), pp. (7670-7685), ISSN: 0002-7863

Lu, J., Liang, F., Drolet, N., Ding, J F., Tao, Y. & Movileanu, R. (2008). Crystalline low band-gap alternating indolocarbazole and benzothiadiazole-cored oligothiophene

copolymer for organic solar cell applications. *Chem. Commun*., Vol. 14, No. 42, (September 2008), pp. (5315–5317), ISSN: 1359-7345

Markov, DE., Amsterdam, E., Blom, PWM., Sieval, AB. & Hummelen, JC. (2005). Accurate measurement of the exciton diffusion length in a conjugated polymer using a heterostructure with a side-chain cross-linked fullerene layer. *J. Phys. Chem. A*, Vol.109, No. 24, (June 2005), pp. (5266–5274), ISSN: 1089-5639

Mcculloch, I., Heeney, M., Bailey, C., Genevicius, K., Macdonald, I., Shkuno,v M., Sparrowe, D., Tierney, S., Wagner, R., Zhang, W., Chabinyc, M., Kline R., McGehee, M., Toney, M. (2006). Liquid-crystalline semiconducting polymers with high charge-carrier mobility. *Nat. Mater.*, Vol. 5, (April 2006), pp. (328-333), ISSN: 1476-4660

Moulle, AJ. ,Tsami, A., Bunnagel, TW., Forster, M. Kronenberg, NM., Scharber, M., Koppe, M., Morana, M., Brabec, CJ., Meerholz, K. & Scherf, U. (2008). Two novel cyclopentadithiophene-based alternating copolymers as potential donor components for high-efficiency bulk-heterojunction-type solar cells. *Chem. Mater.*, Vol. 20, No. 12, (April 2008), pp. (4045-4050), ISSN: 1520-5002

Mühlbacher, D., Scharber, M., Morana, M., Zhu, Z., Waller, D., Gaudiana, R. & Brabec, CJ. (2006). High photovoltaic performance of a low-bandgap polymer. *Adv. Mater.*, Vol. 18, No. 21, (November 2006), pp. (2884–2889), ISSN: 1521-4095

Pan, H., Li, Y., Wu, Y., Liu, P., Ong, BS., Zhu, S. & Xu, G. (2007). Low-temperature, solution-processed, high-mobility polymer semiconductors for thin-film transistors. *J. Am. Chem. Soc.*, Vol. 129, No.14, (March 2007), pp. (4112-4113), ISSN: 0002-7863

Payne, MM., Parkin, SR., Anthony, JE., Kuo, C-C., Jackson, TN. (2005). Organic field-effect transistors from solution-deposited functionalized acenes with mobilities as high as 1cm^2/V.s. *J. Am. Chem. Soc.*, Vol.127, No.14, (December 2004), pp. (4986-4987), ISSN: 0002-7863

Peet, J., Cho, NS., Lee, SK. & Bazan, GC. (2008). Transition from solution to the solid state in polymer solar cells cast from mixed solvents. *Macromolecules*, Vol. 41, No. 22, (October 2008), pp. (8655–8659), ISSN: 1520-5835

Peet, J., Heeger, AJ. & Bazan, GC. (2009). "Plastic" solar cells: self-assembly of bulk heterojunction nanomaterials by spontaneous phase separation. *Acc. Chem. Res.*, Vol. 42, No. 11, (July 2009), pp. 1700-1708, ISSN: 1520-4898

Piliego, C., Holcombe, TW., Douglas, JD., Woo, CH., Beaujuge, PM. & Frechet, JM. (2010). Synthetic control of structural order in n-alkylthieno[3,4-c]pyrrole-4,6-dione-based polymers for efficient solar cells. *J. Am. Chem. Soc.*, Vol. 132, No. 22, (May 2010), pp. (7595–7596), ISSN: 0002-7863

Price, SC., Stuart, AC. & You, W. (2010). Low band gap polymers based on benzo [1,2-b:4,5-b]dithiophene: rational design of polymers leads to high photovoltaic performance. *Macromolecules*, Vol. 43, No. 10, (March 2010), pp. (4609-4612), ISSN: 1520-5835

Qin, R., Li, W., Li, C., Du, C., Veit, C., Schleiermacher, H-F., Andersson, M., Bo, Z., Liu, Z., Inganäs, O., Wuerfel, U. & Zhang, FL. (2009). A planar copolymer for high efficiency polymer solar cells. *J. Am. Chem. Soc.*, Vol. 131, No. 41, (September 2009), pp. (14612–14613), ISSN: 0002-7863

Roncali, J. (1992). Conjugated poly(thiophenes): synthesis, functionalization, and applications. *Chem. Rev.*, Vol. 92, No. 4, (June 1992), pp. (711-738), ISSN: 1520-6890

Scharber, MC., Wuhlbacher, D., Koppe, M., Denk, P., Waldauf, C., Heeger, AJ. & Brabec, CJ. (2006). Design rules for donors in bulk-heterojunction solar cells - Towards 10% energy conversion efficiency, *Adv. Mater.*, Vol. 18, No. 6, (March 2006), pp. (789-794), ISSN: 1521-4095.

Scully, S R. & McGehee, MD. (2006). Effects of optical interference and energy transfer on exciton diffusion length measurements in organic semiconductors. *J. Appl. Phys.*, Vol. 100, (August 2006), pp. (034-907), ISSN: 1089-7550

Shaw, PE., Ruseckas, A. & Samuel, IDW. (2008). Exciton diffusion measurements in poly(3-hexyl thiophene). *Adv. Mater*. Vol. 20, No. 18, (September 2008), pp. (3516–3520), ISSN: 1521-4095

Slooff LH., Veenstra SC., Kroon JM., Moet DJD., Sweelssen J. & Koetse MM. (2007). Determining the internal quantum efficiency of highly efficient polymer solar cells through optical modeling. *Appl. Phys. Lett.*, Vol. 90, No.14, (April 2007), pp. (143506-143508), ISSN: 1077-3188

Sotzing, GA. & Lee, KH. (2002). Poly(thieno[3,4-b]thiophene): A *p*- and *n*-dopable polythiophene exhibiting high optical transparency in the semiconducting state. *Macromolecules*, Vol. 35, No. 19, (August 2002), pp. (7281-7286), ISSN: 1520-5835

Tang, W., Hai, J., Dai,Y., Huang, Z., Lu, B., Yuan, F., Tang, J., Zhang, F. (2010). Recent development of conjugated oligomers for high-efficiency bulk-heterojunction solar cells. Solar Energ. Mater. Solar C., Vol. 94, No. 12, (December 2010), pp. (1963-1979), ISSN: 0927-0248

Veldman, D., Ipek, O., Meskers, SCJ., Sweelssen, J., Koetse, MM., Veenstra, SC., Kroon, JM., Bavel, SS., Loos, J. & Janssen, RAJ. (2008). Compositional and electric field dependence of the dissociation of charge transfer excitons in alternating polyfluorene copolymer/fullerene blends. *J. Am. Chem. Soc.*, Vol. 130, No. 24, (May 2008), pp. (7721–7735), ISSN: 0002-7863

Wang, E., Wang, L., Lan, L., Luo, C., Zhuang, W., Peng, J. & Cao, Y. (2008). High-performance polymer heterojunction solar cells of a polysilafluorene derivative, *Appl. Phys. Lett.*, Vol. 92, No. 3, (January 2008), pp. (303-307), ISSN: 1077-3118

Wienk, MM., Turbiez, M., Gilot, J. & Janssen, RAJ. (2008). Narrow-bandgap diketo-pyrrolo-pyrrole polymer solar cells: the effect of processing on the performance. *Adv. Mater.*, Vol. 20, No. 13, (May 2008), pp. (2556–2560), ISSN: 1521-4095

Wong, KT., Chao, T-C., Chi, L-C., Chu, Y-Y., Balaiah, A., Chiu, S-F., Liu, Y-H., Wang, Y. (2006) Syntheses and structures of novel heteroarene-fused coplanar π-conjugated chromophores, *Org. Lett.*, Vol. 8, No. 22, (September 2006), pp. (5033-5036), ISSN: 1523-7052

Yang, L., Zhou, H. & You, W. (2010). Quantitatively analyzing the influence of side chains on photovoltaic properties of polymer-fullerene solar cells. *J. Phys. Chem. C*, Vol. 114, No. 39, (August 2010), pp. (16793–16800), ISSN: 1932-7455

Yu, G., Gao, J., Hummelen, JC., Wudl, F. & Heeger, AJ. (1995). Polymer photovoltaic cells: enhanced efficiencies via a network of internal donor-acceptor heterojunctions. *Science*, Vol. 270, No. 5243, (December 1995), pp. 1789-1791, ISSN: 1095-9203

Yuan, M-C., Chiu, M-Y., Liu, S-P., Chen, C-M. & Wei, K-H. (2010). A thieno[3,4-c]pyrrole-4,6-dione-based donor-acceptor polymer exhibiting high crystallinity for photovoltaic applications. *Macromolecules*, Vol. 43, No. 17, (Aug, 2010), pp. (6936-6938), ISSN: 1520-5835

Yue, W., Zhao, Y., Shao, S., Tian, H., Xie, Z., Geng, Y. &Wang, F. (2009). Novel NIR-absorbing conjugated polymers for efficient polymer solar cells: effect of alkyl chain length on device performance. *J. Mater. Chem*., Vol. 19, No. 15, (January 2009), pp. (2199-2206), ISSN: 1364-5501

Zhang, L., He, C., Chen, J., Yuan, P., Huang, L., Zhang, C., Cai, W., Liu, Z. & Cao, Y. (2010). Bulk-heterojunction solar cells with benzotriazole-based copolymers as electron donors: largely improved photovoltaic parameters by using PFN/Al bilayer cathode. *Macromolecules*, Vol. 43, No. 23, (November 2010), pp. (9771-9778) ISSN 1520-5835

Zhang, M., Fan, H., Guo, X., He, Y., Zhang, Z., Min, J., Zhang, J., Zhao, G J., Zhan, X. & Li, Y. (2010). Synthesis and photovoltaic properties of bithiazole-based donor−acceptor copolymers. *Macromolecules*, Vol. 43, No 13, (June 2010), pp. (5706-5712), ISSN: 1520-5835

Zheng, Q., Jung, BJ., Sun, J. & Katz, HE. (2010). Ladder-type oligo-*p*-phenylene-containing copolymers with high open-circuit voltages and ambient photovoltaic activity. *J. Am. Chem. Soc*., Vol. 132, No. 15, (October 2009), pp. (5394–5404), ISSN: 0002-7863

Zhou, E., Nakamura, M., Nishizawa, T., Zhang, Y., Wei, Q., Tajima, K., Yang, C. & Hashimoto, K. (2008). Synthesis and photovoltaic properties of a novel low band gap polymer based on n-substituted dithieno[3,2-*b*:2,3-*d*]pyrrole. *Macromolecules*, Vol. 41, No. 22, (October 2008), pp. (8302-8305), ISSN: 1520-5835

Zhou, E., Yamakawa, S., Zhang, Y., Tajima, K., Yang, C. & Hashimoto, K. (2009). Indolo[3,2-*b*] carbazole -based alternating donor–acceptor copolymers: synthesis, properties and photovoltaic application. *J. Mater. Chem*., Vol. 19, No. 41, (August 2009), pp. (7730–7737), ISSN: 1364-5501

Zhou, E., Wei, Q., Yamakawa, S., Zhang, Y., Tajima, K., Yang, C. & Hashimoto, K. (2010). Diketopyrrolopyrrole-based semiconducting polymer for photovoltaic device with photocurrent response wavelengths up to 1.1 μm. *Macromolecules*, Vol. 43, No. 2, (December 2009), pp. (821-826), ISSN: 1520-5835

Zhou, E., Cong, J., Yamakawa, S., Wei, Q., Nakamura, M., Tajima, K., Yang, C. & Hashimoto, K. (2010). Synthesis of thieno[3,4-b]pyrazine-based and 2,1,3-benzothiadiazole-based donor–a cceptor copolymers and their application in photovoltaic devices. *Macromolecules*, Vol. 43, No. 6, (February 2010), pp. (2873 -2879), ISSN: 1520-5835

Zhou, H., Yang, L., Xiao, S., Liu, S. & You, W. (2010). Donor−acceptor polymers incorporating alkylated dithienylbenzothiadiazole for bulk heterojunction solar cells: pronounced effect of positioning alkyl chains, *Macromolecules*, Vol. 43, No. 2, (December 2009), pp. (811–820), ISSN: 1520-5835

Zhou, H., Yang, L., Stoneking, S. & You, W. (2010). A weak donor-strong acceptor strategy to design ideal polymers for organic solar cells. *ACS Appl. Mater. Interfaces*, Vol. 2, No. 5, (May 2010), pp. (1377-1383), ISSN: 1944-8252

Zhou, H., Yang, L. & You, W. (2010). Quantitatively analyzing the influence of side chains on photovoltaic properties of polymer−fullerene solar cell, *J. Phys. Chem. C*, Vol. 114, No. 39, (September 2010), pp. (16793–16800), ISSN: 1932-7455

Zhou, H., Yang, L., Price, SC., Knight, KJ. & You, W. (2010). Enhanced photovoltaic performance of low-bandgap polymers with deep LUMO levels. *Angew. Chem. Int. Ed.*, Vol. 49, No. 43, (October 2010), pp. (7992–7995), ISSN: 1521-3773

Zhou, H., Yang, L., Liu, S. & You, W. (2010). A tale of current and voltage: interplay of band gap and energy levels of conjugated polymers in bulk heterojunction solar cells. *Macromoleccules,* Vol. 43, No. 24, (November 2010), pp. (10390–10396), ISSN: 1520-5835

Zhou, Q., Hou, Q., Zheng, L., Deng, X., Yu, G. & Cao, Y. (2004). Fluorene-based low band-gap copolymers for high performance photovoltaic devices. *Appl. Phys. Lett.*, Vol. 84 , No. 10, (January 2004), pp. (1653-1655), ISSN: 1077-3188

Zou, Y., Najari, A., Berrouard, P., Beaupre, S., Aich, BR., Tao, Y. & Leclerc, M. (2010). A thieno[3,4-*c*]pyrrole-4,6-dione-based copolymer for efficient solar cells. *J. Am. Chem. Soc.*, Vol. 132, No. 15, (August 2010), pp. (5330-5331), ISSN: 0002-7863

21

Conjugated Polymers for Organic Solar Cells

Qun Ye and Chunyan Chi
Department of Chemistry, National University of Singapore, Singapore

1. Introduction

Energy shortage has become a worldwide issue in the 21st century (Lior, 2008). The urge to look for renewable energy to replace fossil fuel has driven substantial research effort into the energy sector (Hottel, 1989). The solar energy has enormous potential to take the place due to its vast energy stock and availability worldwide (Balzani et al., 2008). Conventional solar energy conversion device is based on silicon technology. However, wide use of silicon based solar cell technology is limited by its high power conversion cost (Wöhrle & Meissner, 1991). To address this issue, solution-processing based organic solar cell has been developed to replace Si-solar cell (Tang, 1986). Compared with conventional Si-based solar cell, conjugated polymer based solar cell (PSC) has several important advantages: 1) solution processability by spin-coating, ink-jet printing and roll-to-roll processing to reduce manufacturing cost; 2) tunable physical properties; and 3) mechanical flexibility for PSC application on curved surfaces (Sariciftci, 2004).

During the last decade, the power conversion efficiency (PCE) of organic based solar cell has increased from *ca.* 1% (Tang, 1986) to more than 7% (H. –Y. Chen et al., 2009) with the bulk heterojunction (BHJ) concept being developed and applied. During the pursuit of high efficiency, the importance of the structure-property relationship of the conjugated polymer used in the solar cell has been disclosed (J. Chen & Cao, 2009). It might be helpful to systematically summarize this structure-property relationship to guide polymer design and further improvement of the power conversion efficiency of PSCs in the future.

This chapter will be organized as follows. Firstly, we will discuss about the general criteria for a conjugated polymer to behave as an efficient sunlight absorbing agent. Secondly, we will summarize the properties of common monomer building blocks involved for construction of solar cell polymers. Only representative polymers based on the common building blocks will be discussed due to the space limit. More quality reviews and texts are directed to interested readers (C. Li, 2010; Günes et al., 2007; Sun & Sariciftci, 2005; Cheng et al., 2009).

2. Criteria for an efficient BHJ solar cell polymer

For a conjugated polymer to suit in organic photovoltaic bulk heterojunction solar cell, it should possess favorable physical and chemical properties in order to achieve reasonable device efficiency. Key words are: large absorption coefficient; low band gap; high charge mobility; favorable blend morphology; environmental stability; suitable HOMO/LUMO level and solubility.

2.1 Large absorption coefficient

For polymers used in solar cells, a large absorption coefficient in the film state is a prerequisite for a successful application since the preliminary physics regarding photovoltaic phenomenon is photon absorption. The acceptor component of the BHJ blend, usually $PC_{60}BM$ or $PC_{70}BM$, absorbs inefficiently longer than 400 nm (Kim et al., 2007). It is thus the responsibility for the polymer to capture the photons above 400 nm. Means to increase the solar absorption of the photoactive layer include: 1) increasing the thickness of the photoactive layer; 2) increasing the absorption coefficient; and 3) matching the polymer absorption with the solar spectrum. The first strategy is rather limited due to the fact that the charge-carrier mobilities for polymeric semiconductors can be as low as $10^{-4}cm^2/Vs$ (Sariciftci, 2004). Series resistance of the device increases significantly upon increasing the photoactive layer thickness and this makes devices with thick active layer hardly operational. The short-circuit current (J_{sc}) may drop as well because of the low mobility of charge carriers. With the limitation to further increase the thickness, large absorption coefficient (10^5 to 10^6) in the film state is preferred in order to achieve photocurrent >10 mA/cm^2 (Sariciftci, 2004). By lowering the band gap, absorption of the polymer can be broadened to longer wavelength and photons of λ > 800nm can be captured as well.

2.2 Low band gap to absorb at long wavelength

The solar irradiation spectrum at sea level is shown in Fig 1 (Wenham & Watt, 1994). The photon energy spreads from 300 nm to > 1000 nm. However, for a typical conjugated polymer with energy gap E_g~2.0 eV, it can only absorb photon with wavelength up to *ca.* 600 nm (blue line in Fig 1) and maximum 25% of the total solar energy. By increasing the absorption onset to 1000 nm (E_g=~1.2 eV) (red line in Fig 1), approximately 70 to 80% of the solar energy will be covered and theoretically speaking an increase of efficiency by a factor of two or three can be achieved. A controversy regarding low band gap polymer is that once a polymer absorbs at longer wavelength, there will be one absorption hollow at the shorter wavelength range, leading to a decreased incident photon to electron conversion efficiency at that range. One approach to address this issue is to fabricate a tandem solar cell with both large band gap polymer and narrow band gap polymer utilized simultaneously for solar photon capture (Kim et al., 2007).

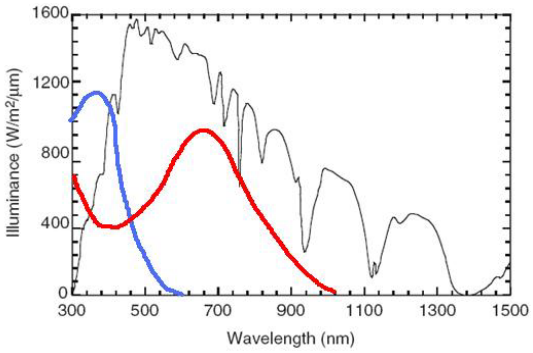

Fig. 1. Reference solar irradiation spectrum of AM1.5 illumination (black line). Blue line: typical absorption spectrum of a large band gap polymer; Red line: typical absorption spectrum of a narrow band gap polymer.

2.3 High charge carrier mobility

Charge transport properties are critical parameters for efficient photovoltaic cells. Higher charge carrier mobility of the polymer increases the diffusion length of electrons and holes generated during photovoltaic process and at the same time reduces the photocurrent loss by recombination in the active layer, hence improving the charge transfer efficiency from the polymer donor to the PCBM acceptor (G. Li et al., 2005). This charge transport property of the photoactive layer is reflected by charge transporting behavior of both the donor polymer and the PCBM acceptor. The electron transport property of pure PCBM thin film has been reported in details and is known to be satisfactory for high photovoltaic performance (~10^{-3} $cm^2V^{-1}s^{-1}$) (Mihailetchi et al., 2003). However, the mobility of the free charge carriers in thin polymer films is normally in the order of 10^{-3} to 10^{-11} $cm^2V^{-1}s^{-1}$, which limits the PCE of many reported devices (Mihailetchi et al., 2006). Therefore, it is promising to increase the efficiency by improving the charge carrier property of the polymer part, since there is huge space to improve if we compare this average value with the mobility value of some novel polymer organic field effect transistor materials (Ong et al., 2004; Fong et al., 2008).

2.4 Favorable blend morphology with fullerene derivatives

The idea that morphology of the photoactive layer can greatly influence the device performance has been widely accepted and verified by literature reports (Arias, 2002; Peet et al., 2007). However, it is still a 'state-of-art' to control the morphology of specific polymer/PCBM blend. Even though several techniques (Shaheen et al., 2001) have been reported to effectively optimize the morphology of the active layer, precise prediction on the morphology can hardly been done. It is more based on trial-and-error philosophy and theory to explain the structure-morphology relationship is still in infancy. Nevertheless, several reliable and efficient methods have been developed in laboratories to improve the morphology as well as the performance of the solar cell devices.

The first strategy is to control the solvent evaporation process by altering the choice of solvent, concentration of the solution and the spinning rate (Zhang et al., 2006). The slow evaporation process assists in self-organization of the polymer chains into a more ordered structure, which results in an enhanced conjugation length and a bathochromic shift of the absorption spectrum to longer wavelength region. It is reported (Peet. et al., 2007) that chlorobenzene is superior to toluene or xylene as the solvent to dissolve polymer/PCBM blend during the film casting process. The PCBM molecule has a better solubility in chlorobenzene and therefore the tendency of PCBM molecule to form clusters is suppressed in chlorobenzene. The undesired clustering of PCBM molecules will decrease the charge carrier mobility of electrons because of the large hopping boundary between segregated grains.

The second strategy is to apply thermal annealing after film casting process. This processing technique is also widely used for organic field effect transistor materials. The choice of annealing temperature and duration is essential to control the morphology. At controlled annealing condition, the polymer and PCBM in the blend network tend to diffuse and form better mixed network favorable for charge separation and diffusion in the photoactive layer (Hoppe & Sariciftci, 2006).

2.5 Stability

The air stability of the solar cell device, as it is important for the commercialization, has attracted more and more attention from many research groups worldwide. Even though

industry pays more attention to the cost rather than the durability of the solar cell device, a shelf lifetime of several years as well as a reasonably long operation lifetime are requested to compete with Si-based solar cells. The air instability of solar cell devices is mainly caused by polymer degradation in air, oxidation on low work function electrode, and the degradation of the morphology of the photoactive layer.

For a conjugated polymer to achieve such a long lasting lifetime, it should have intrinsic stability towards oxygen oxidation which requires the HOMO energy level below the air oxidation threshold (*ca.* -5.27 eV) (de Leeuw et al., 1997). Device engineering can also provide the extrinsic stability by sophisticated protection of the conjugated polymer from air and humidity.

2.6 Desired HOMO/LUMO energy level

The Highest Occupied Molecular Orbital (HOMO) and Lowest Unoccupied Molecular Orbital (LUMO) of the polymer should be carefully tuned for several considerations. First of all, the HOMO energy level of a material, which describes the accessibility of the material molecule to be oxidized, reflects the air stability of the material. The oxidation threshold of air is -5.2 eV ~-5.3 eV against vacuum level. Therefore, the HOMO level cannot be more positive than this value to provide the air stability to the polymer. Secondly, the maximum open circuit voltage (V_{oc}) is correlated to the difference between the LUMO energy level of PCBM and the polymer's HOMO energy level based on experimental evidence (Brabec et al., 2001; Scharber et al., 2006). Therefore, in order to achieve high V_{oc} in the device, HOMO level should be reasonably low.

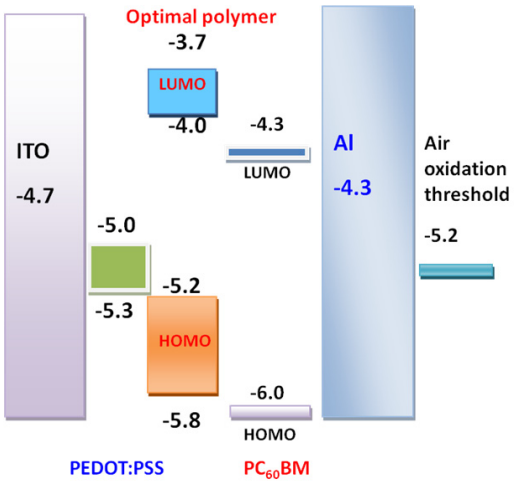

Fig. 2. Optimal HOMO/LUMO energy level of optical polymer used in BHJ solar cell with $PC_{60}BM$ as acceptor (Blouin et al., 2008)

To ensure efficient electron transfer from the polymer donor to the PCBM acceptor in the BHJ blend, the LUMO energy level of the polymer material must be positioned above the LUMO energy level of the acceptor by at least 0.2-0.3 eV. Based on these factors, as shown in Fig 2, the ideal polymer HOMO level should range from -5.2 eV to -5.8 eV against vacuum

level due to the compromise of stability, band gap and open circuit voltage. The ideal polymer LUMO level should range from -3.7 eV to -4.0 eV against vacuum level to assist electron injection from polymer to acceptor.

2.7 Solubility

Polymer prepared for solar cell application should possess reasonable solubility so that it can be analyzed by solution based characterization methods such as NMR spectroscopy. Meanwhile, polymer with poor solubility will be found inappropriate for solution processing and device performance is normally low due to unfavorable microscopic morphology of the thin film formed by spin coating. Aliphatic chains attached to the polymer backbone are essential to ensure solubility of the polymer. However, it should be noted that aliphatic chains, being electronically inactive, will dilute the conjugated part of the polymer and hence, reduce the effective mass of the polymer.

Some rules of thumb regarding the use of alkyl chains include that: 1) longer chain is better than shorter chain to solubilize polymer; 2) branched chain is better than linear chain to solubilize polymer; and 3) the more rigid or planar the polymer backbone is, the more or longer alkyl chains are needed.

3. Common building blocks for BHJ solar cell polymers

Common monomer building blocks to construct conjugated polymer for solar cells have been summarized in Chart 1. They are categorized by number of rings and way of linkage. Due to the space limit, we will only discuss monomers that are commonly encountered in the literature and the property of their representative polymers. Some important building blocks, even though not commonly used for PSC polymer, are also included for comparison.

3.1 Ethylene (double bond)

Ethylene (double bond) is a commonly adopted spacer or bridge in conjugated polymers. Common chemical methods to introduce double bond to the polymer include: Wittig-Horner reaction; Wessling sulfonium precursor method (Wessling, 1985); Gilch route (Gilch & Wheelwright, 1966) and palladium catalyzed coupling reactions.

By utilizing Wittig reaction, fully regioregular and regiorandom poly[(2-methoxy-5- ((3′,7′-dimethyloctyl)oxy)-1,4-phenylenevinylene] (MDMO-PPV, P1 and P2) were synthesized following the route shown in Scheme 1 (Tajima et al., 2008). The device study on these two polymers showed that the regioregular MDMO-PPV-based device had a PCE of 3.1%, which was much higher than 1.7% out of regiorandom MDMO-PPV. The higher crystallinity of the regioregular MDMO-PPV polymer and better mixing morphology with PCBM were ascribed to the improved PCE for regioregular MDMO-PPV. This study highlighted the importance of regioregularity of PPV-based polymer to achieve good solar cell performance.

3.2 Acetylene (triple bond)

Polyacetylene was the first discovered conducting conjugated polymer and inspired a lot of scientific interest in the research of conjugated polymers (Shirakawa et al., 1977). The synthetic chemistry of acetylene-containing polymers has been intensively reviewed by Liu *et al*.(Liu et al., 2009). In polymers designed for solar cell, acetylene is normally introduced to the polymer backbone via Sonogashira cross coupling reaction.

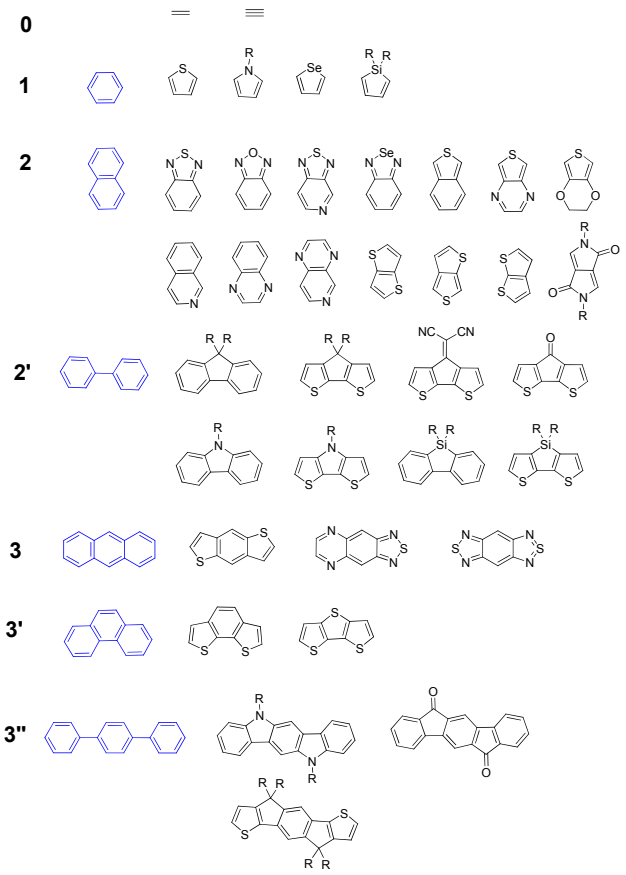

Chart 1. Common monomer building blocks used for construction of solar cell polymers

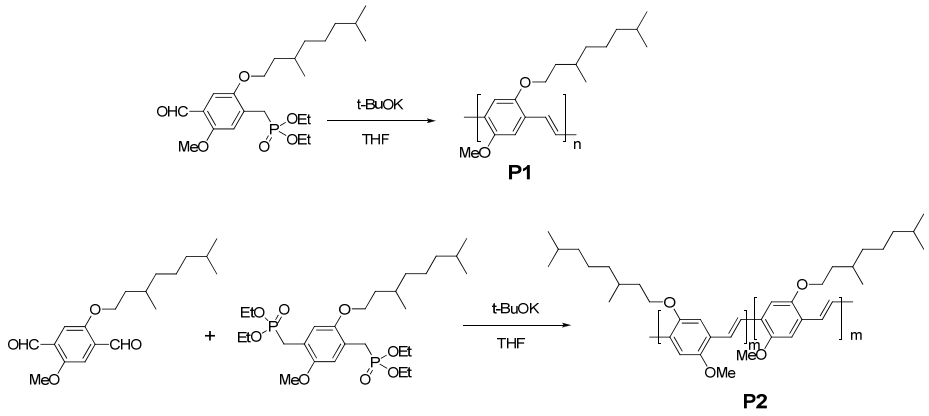

Scheme 1. synthesis of regioregular and regiorandom MDMO-PPV

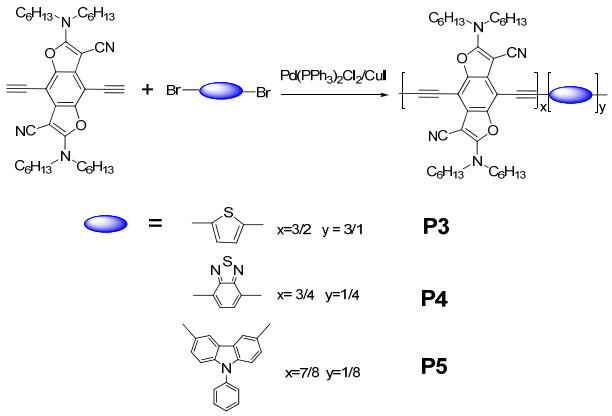

Scheme 2. Synthetic route of acetylene-containing polymers P3, P4 and P5

Benzodifuran moiety was copolymerized with thiophene, electron withdrawing benzothiadiazole and electron donating 9-phenylcarbazole, respectively, to form P3, P4 and P5 as shown in Scheme 2 (H. Li et al., 2010). The ratio of x/y is estimated from the integration of relevant peaks in their NMR spectra. The fraction of benzodifuran is more than 50% due to the self-coupling of diacetylene monomer. All three polymers absorbed beyond 600 nm in the film state and had a LUMO level above -4.0 eV. The high structural order of these three polymers was evidenced by power XRD study, as two reflection peaks, one at $2\theta = 4.95^{o}$–5.5^{o} and the other at $2\theta = 19.95^{o}$ – 21.75^{o}, were well observed. The highest PCE $\eta = 0.59\%$ was obtained based on P3/PCBM (1:4, *w/w*) blend.

Another category of acetylene containing polymer designed for PSC is π-conjugated organoplatinum polyyne polymers (Baek et al., 2008). The platinum-C_{sp} bond extends the conjugation of the polymer as a result of the fact that the *d*-orbital of the Pt can overlap with the *p*-orbital of the alkyne. This kind of Pt-C bond can be chemically accessible by a Sonogashira-type dehydrohalogenation between alkyne and platinum chloride precursor. Examples of this type of polymer and their synthetic routes are shown in Scheme 3 (Wong et al., 2007).

In order to tune the energy gap <2.0 eV, internal D-A function was introduced between electron rich Pt-ethyne groups. This effective band gap control strategy rendered P6 UV-vis absorption maximum at 548 nm and an optical band gap of 1.85 eV. This absorption behavior was proved to occur via the charge transfer excited state but not the triplet state of the polymer by photolumiscence lifetime study and PL temperature dependence study. The electrochemical HOMO and LUMO energy level were measured to be -5.37 eV and -3.14 eV, respectively. The best P6/PCBM (1:4, *w/w*) BHJ solar cell gave the open circuit voltage V_{oc}= 0.82 V, the short-circuit current density J_{sc}=15.43 mA, fill factor *FF*=0.39 and power conversion efficiency η =4.93%.

For polymers P7-P10 (Wong et al., 2007), the electron withdrawing moiety was replaced by bithiazole heterocycles. Nonyl chains were attached to the bithiazole to assist solvation of the polymer. By extending the conjugation (m: 0→3) along the polymer backbone, the band gaps of P7-P10 decreased from 2.40 eV to 2.06 eV. The power conversion efficiency (polymer/PCBM=1:4, *w/w*) was found significantly improved from ~0.2% to ~2.5% as the number of thiophene bridge increased from 0 to 3, most likely due to the improved charge carrier mobility of the active layer.

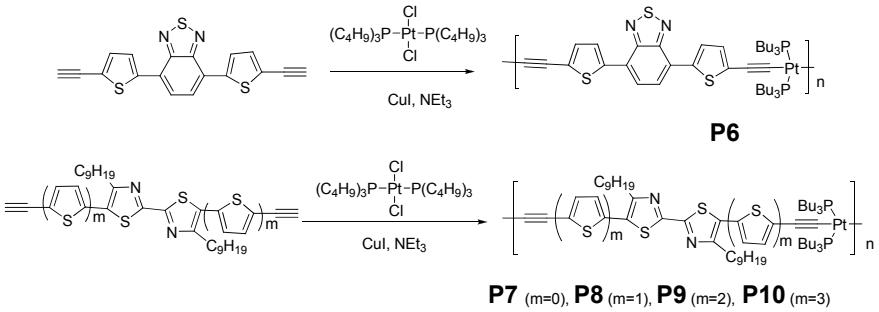

Scheme 3. Synthesis of organoplatinum polyyne polymers: P6, P7-P10

3.3 Phenylene (benzene)

Benzene ring is the most fundamental building block for polymer solar cell materials. A lot of chemistry and reaction carried out in this research area are rooted back to the reactivity of benzene ring. Benzene can be polymerized by direct linkage at the 1,4-position to form poly(*para*-phenylene) (Chart 2). Poly(*para*-phenylene) without any substituents has a linear rod-like structure and poor solubility in common organic solvents which limits its application as organic electronics. One strategy to increase the solubility is to introduce alkyl or alkoxyl chain on the backbone. However, the planarity of the poly(*para*-phenylene) will be disturbed due to the steric effect of the R group attached (Chart 2, P12) and therefore the effective conjugation between adjacent benzene rings will be sacrificed. To address this issue, bridges can be introduced between benzene rings, e.g., double bond in poly(phenylvinylene) (PPV)(Chart 2, P13).

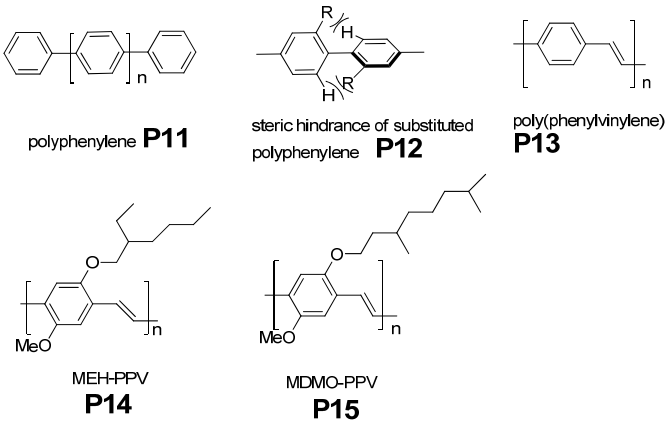

Chart 2. Structures of polyphenylene and its derivatives

PPV and its derivatives have been intensively studied in organic electronics research for OLED and PSC materials due to their excellent conducting and photoluminescent properties (Burroughes et al., 1990). Poly[2-methoxy-5-((2′-ethylhexyl)oxy)-1,4- phenylenevinylene] (MEH-PPV, P14) was utilized to fabricate bilayer solar cell with C_{60} in the early days and it was reported that photoinduced electron transferred from electron donating MEH-PPV onto

Buckminsterfullerene, C_{60}, on a picosecond time scale (Sariciftci et al., 1992). This experiment explained one fundamental physical phenomenon present in organic photovoltaic cells and the concept developed by this study significantly inspired later research on organic solar cells.

Another derivative of PPV, poly[(2-methoxy-5-(3′,7′-dimethyloctyl)oxy)-1,4-phenylene vinylene] (MDMO-PPV, Chart 2) is also widely studied for solar cells and still being used nowadays. The combination of MDMO-PPV and PCBM is used in BHJ solar cell and efficiency up to 3.1% has been reported (Tajima et al., 2008). However, the relatively low hole mobility of MDMO-PPV (5 x 10^{-11} $cm^2V^{-1}s^{-1}$) (Blom et al., 1997) is reported to limit the charge transport inside the photoactive layer. Most PPV polymers have band gap greater than 2.0 eV and have maximum absorption around 500 nm. Furthermore, PPV materials are not stable in air and vulnerable to oxygen attack. Structural defects generated either during synthesis or by oxidation will substantially degrade the performance of the device. All these factors limit the application of PPV polymers in solar cells.

3.4 Thiophene

Thiophene has become one of the most commonly used building blocks in organic electronics due to its excellent optical and electrical properties as well as exceptional thermal and chemical stability (Fichou, 1999). Its homopolymer, polythiophene (PT), was first reported in 1980s as a 1D-linear conjugated system (Yamamoto et al., 1980; Lin & Dudek, 1980). Substitution by solubilizing moieties is adopted to increase the solubility of polythiophenes. The band gap of the polythiophene can also be tuned at the same time by inductive and/or mesomeric effect from the heteroatom containing substitution.

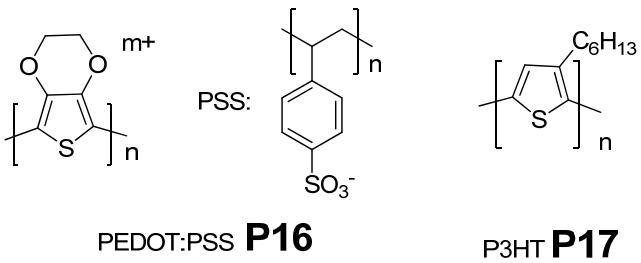

PEDOT:PSS **P16** P3HT **P17**

Chart 3. Chemical structures of PEDOT:PSS and P3HT

Two frequently encountered thiophene-based conjugated polymers in literature are poly (3,4-ethylenedioxythiophene) poly(styrenesulfonate) (PEDOT-PSS, Chart 3) in conducting and hole transport layers for organic light emitting diodes (OLEDs) and PSCs and regioregular poly(3-hexylthiophene) (P3HT, Chart 3) as a hole transporting material in organic field effect transistors (OFETs) and PSCs.

As in PPV polymer, regioregularity is essential for the thiophene unit to conjugate effectively on the same plane since in regioregular form, steric consequence of the substitution is minimized, resulting in longer effective conjugation length and a lower band gap. As shown in Chart 4, three different regioisomers, head-to-head (HH), head-to-tail (HT) and tail-to-tail (TT) can be formed when two 3-alkyl thiophene units are linked via 2,5-position. Presence of HH and TT linkage in polythiophene will cause plane bending and generate structural disorder, which consequently weaken the intermolecular interaction.

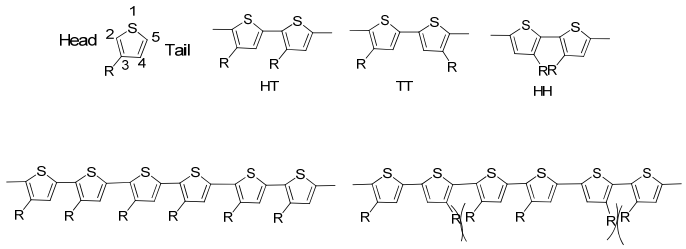

Chart 4. 3-substituted thiophene dimer isomers, regioregular P3HT and regioirregular P3HT

Regioregular P3HT was first synthesized by McCullough's group via a Grignard metathesis method (McCullough & Lowe, 1992, 1993). Polymerization with a Ni(0) catalyst yielded a highly regioregular (>99% HT) PT polymer (M_n=20000-35000, PDI=1.2-1.4). The mechanism of this Ni coupling reaction was proposed and justified to be a 'living' chain growth mechanism (Miyakoshi et al., 2005). Regioregular P3HT has been treated as a standard polymer for solar cell devices and commonly used for device testing and comparison. It represents the 'state of art' in the field of PSCs and efficiency up to ~5% has been reported based on P3HT/PCBM device (Ma et al., 2005).

3.5 Silole

Siloles or silacyclopentadienes, are a group of five-membered silacyclics with 4 accessible substitution positions on the butadiene and another 2 positions on the silicon atom. Compared with many other 5-membered heterocyclopentadiene, such as thiophene, furan or pyrrole, the silole (silacyclopentadiene) ring has the smallest HOMO-LUMO band gap and the lowest lying LUMO level due to the σ* to π* conjugation arising from interaction between the σ* orbital of two exocyclic bonds on silicon and the π* orbital of the butadiene moiety. The small band gap and lowest LUMO energy level render silole outstanding optoelectronic properties such as high PL efficiency and excellent electron mobility (Chen & Cao, 2007).

Random and alternating silole-containing copolymers P18 (Chart 5) (F. Wang et al., 2005) were synthesized via Suzuki coupling reaction from fluorene and 2,5-dithienyl-silole. The band gap of this series of polymer could be tuned from 2.95 eV to 2.08 eV by varying the silole content from 1% to 50% in the polyfluorene chain. The decrease of the band gap was found mainly due to the decrease of LUMO energy level while the HOMO of this series of polymer remained unchanged at ~ -5.7 eV. For the alternating copolymer, field effect charge mobility was measured to be 4.5×10^{-5} $cm^2V^{-1}s^{-1}$ and the best PCE value was reported to be 2.01% using a P18(m=1)/PCBM (1:4, *w/w*) blend as active layer.

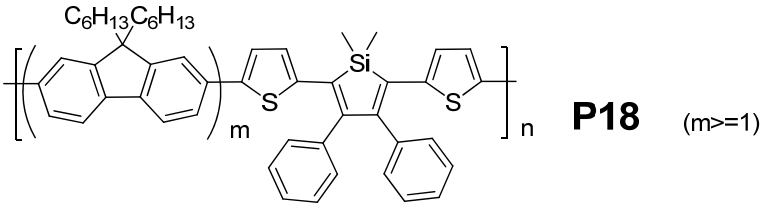

Chart 5. Chemical structure of silole containing polymer P18

3.6 Benzothiadiazole/ Aza-benzothiadiazole/ Se-benzothiadiazole

2,1,3-benzothiadiazole (BT, Chart 6) is an electron deficient heterocycle that has been incorporated with electron donating species to construct low band gap polymer donor for BHJ polymer solar cell. The electron withdrawing ability of BT can be further increased by replacing one carbon atom with sp^2-hybridized N atom (Chart 6). The sulfur atom in the BT unit can also be replaced to selenium, by doing so the band gap is further decreased.

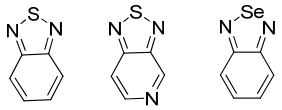

Chart 6. Structure of BT, aza-BT and Se-BT

A variety of low band gap polymers containing BT have been synthesized and tested for PSC performance (P19-P23) (Zhang et al., 2006; E. Zhou et al., 2008; Svensson et al., 2003; Slooff et al., 2007; Q. Zhou et al., 2004; Blouin et al., 2007). The electron donating moiety in the low band gap polymer varies from carbazole, fluorene, dibenzosilole, bridged thiophene-phenylene-thiophene, and dithienopyrrole. This type of polymer has a band gap <2.0 eV and gives moderate to good PCE value ranging from ~1% to ~5%, rendering a promising direction for the research of PSC donor material.

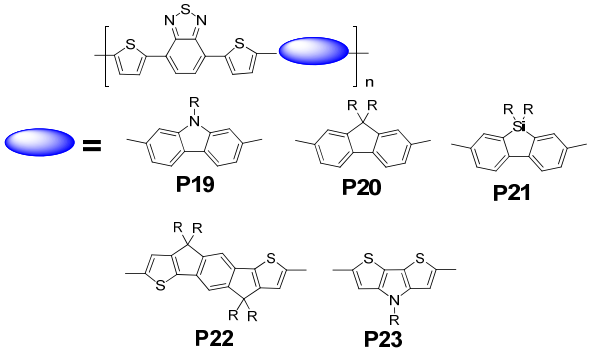

Chart 7. Benzothiadiazole containing low band gap polymers P19-P23

3.7 Isothianaphthene/ Thienopyrazine

The first example of poly(isothianaphthene) is reported by Wudl *et al.* in 1984 (Wudl et al., 1984) as shown in Scheme 4. Poly(isothianaphthene) has a greater tendency to adopt the quinoid structure due to the stabilization of the benzenoid ring formation (Chart 8). The quinoid structure adoption reduces the band gap of poly(isothianaphthene) to *ca.* 1.0 eV, which is about half that of polythiophene (~2.0 eV) (Kobayashi et al., 1984).

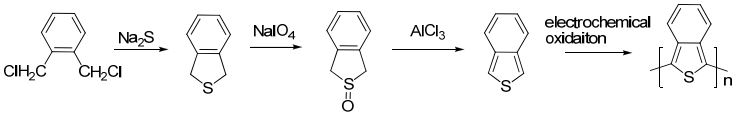

Scheme 4. Synthesis of poly (isothianaphthene)

Poly(thianaphthene) adopts a non-planar conjugation due to the steric hinderance present between benzo-H and thiophene-S atoms as shown in Chart 8. To increase the effective π-conjugation, one C-H can be replaced by sp^2-hybridized nitrogen to release the steric strain. As evidenced by X-ray structure analysis of 2,5-di(2-thienyl) pyridino[c]thiophene (Chart 8) (Ferraris et al., 1994), the torsional angle between the pyridinothiophene moiety and the thiophene unit on the N side is only 3.5°, while it is 39° on the other side. To further release the steric strain, the CH groups on both sides of the isothianaphthene can be replaced by N atom. Due to its effective conjugation and electron withdrawing nature, thieno[3,4-b]pyrazine is proposed as another type of electron withdrawing building block for the construction of low band gap polymers. In necessity of solubility, substituted thieno[3,4-b]pyrazines can be synthesized by condensation of 3,4-diaminothiophene with substituted 1,2-diones.

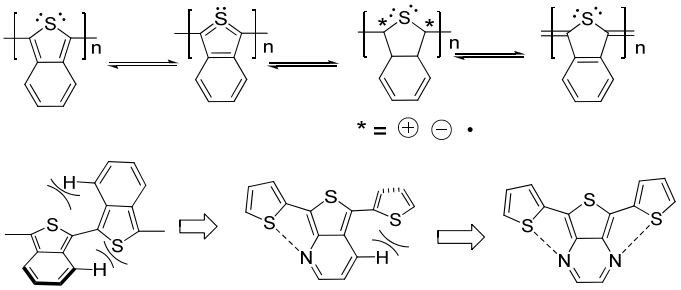

Chart 8. Resonance structure of poly(isothianaphthene) and demonstration of steric strains

The thienopyrazine unit is commonly linked to two thiophene rings at each side and coupled with electron donating moiety, such as fluorene to construct low band gap polymer (P24, P25, and P26) (Zhang et al., 2005, 2006; Mammo et al., 2007). P24 was reported to suffer from low solubility and low molecular weight. The polymerization yield was only 5% owing to the poor solubility in chloroform. The best PCE based on P24/PCBM(1:6, *w/w*) was obtained as η= 0.96%. To address the solubility issue, alkyl and alkoxyl chains were attached to the thienopyrazine moiety and another two low band gap polymers P25 and P26 were synthesized by copolymerization between thienopyrazine and fluorene. The addition of side chains did not change the band gap and HOMO/LUMO energy level as evidenced from absorption spectra and cyclic voltammetry measurement. These two polymers had almost identical absorption and HOMO/LUMO values. The best PCE value obtained for P25 was 1.4% while for P26 the optimal PCE value was 2.2%.

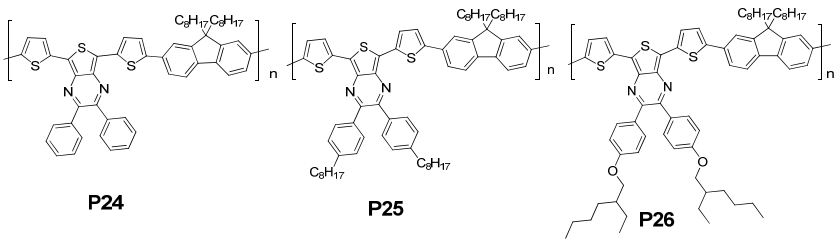

Chart 9. Chemical structures of thienopyrazine containing polymers P24, P25 and P26

3.8 Thieno[3,4-b]thiophene / Thieno[3,2-b]thiophene/ Thieno[2,3-b]thiophene

Annulations of two thiophene rings generates 4 isomers (Chart 10), namely, thieno[3,4-b] thiophene, thieno[3,2-b]thiophene, thieno[2,3-b] thiophene and thieno[3,4-c]thiophene. The first three isomers have been synthesized and isolated. Thieno[3,4-c]thiophene is predicted to be kinetically unstable and not isolated yet (Rutherford et al., 1992).

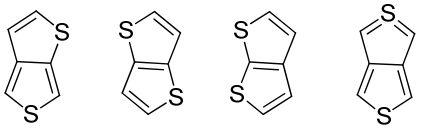

Chart 10. Isomer structure of thienothiophenes; from left to right: thieno[3,4-b]thiophene, thieno[3,2-b]thiophene, thieno[2,3-b]thiophene and thieno[3,4-c]thiophene

Thieno[2,3-b] thiophene, thieno[3,2-b]thiophene and thieno[3,4-b]thiophene are useful building blocks in preparing conjugated polymer for organic electronics applications due to their planarity and electron richness. Compared with thiophene, thienothiophene has a larger π-conjugated system. Therefore, it is introduced to the polymer backbone in the hope that it can facilitate interchain π-stacking to increase the structural order and improve the charge carrier mobility.

An efficient polymer donor P27 copolymerized by thieno[3,4-b]thiophene and benzodithiophene has been reported (Liang et al., 2009). Three dodecyl chains were used in each repeating unit to assist solvation of the polymer. BHJ solar cell fabricated using P27/PCBM(1:1 *w/w*) gave an excellent PCE of 4.76%, with V_{oc} = 0.58V, J_{sc} = 12.5 mA/cm^2 and *FF* = 0.654. A further improvement of the PCE to 5.3% was obtained by utilizing $PC_{70}BM$ as the electron acceptor in the active layer. This high PCE value was ascribed to several factors including well tuned band gap (1.6 eV), proper HOMO/LUMO energy levels, balanced carrier mobility (P27 μ_h=4.5x10^{-4}cm^{2}V^{-1}s^{-1}), favorable morphology of the active layer and thieno-thiophene's ability of stabilizing the quinoid structure along the polymer backbone to enhance the planarity of the polymer.

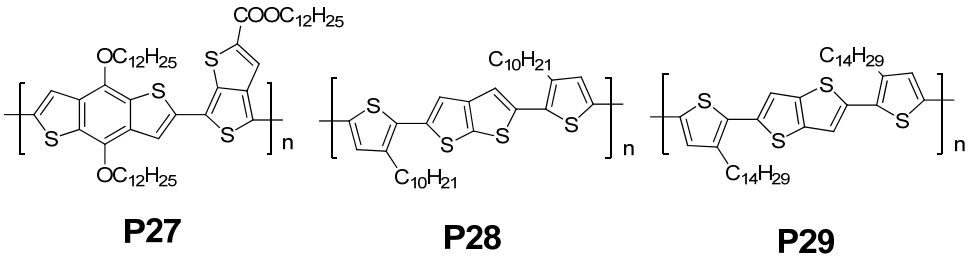

P27 **P28** **P29**

Chart 11. Chemical structures of thienothiophene containing polymer P27, P28 and P29

Liquid-crystalline semiconductor polymers P28 and P29 were prepared by copolymerization of thienothiophene and thieno[2,3-b]thiophene, respectively, with 4,4'-dialkylbithiophene unit (McCulloch et al., 2006; Heeney et al., 2005). P28 had good field effect charge mobility of μ_h = 0.15 cm^{2}V^{-1}s^{-1}. However, its relatively large band gap (absorption maximum λ_{max} = 470 nm) limited its application as efficient solar cell material. For P29, the absorption maximum was red shifted to 547 nm and the field effect charge mobility was increased to

μ_h = ~0.7 $cm^2V^{-1}s^{-1}$. The improved mobility was suggested due to the improved control of crystallization. The PSC device fabricated from P29/$PC_{70}BM$(1:4 *w/w*) blend achieved an optimized PCE η= 2.3% in nitrogen atmosphere. The high lying HOMO energy level (-5.1eV) of P29, which is above the air oxidation threshold (-5.2 eV), makes the polymer relatively unstable in air.

3.9 Diketopyrrolopyrrole (DPP)

The DPP moiety has been utilized for construction of low band gap polymer for BHJ solar cells due to its electron deficient nature, planarity of the core and ability to accept H-bonding. D-A type low band gap polymers based on DDP have been synthesized by varying the electron donating part of the polymer (P30, P31, P32) (Wienk et al., 2008; Bronstein et al., 2011).

By combining electron rich quarterthiophene with electron deficient DDP unit, a low band gap polymer (1.4 eV in film state) P30 was obtained. P30 showed a good solubility in chloroform and tended to aggregate in dichlorobenzene (DCB). Device based on P30/$PC_{60}BM$ (1:2, *w/w*) BHJ thin film prepared from solution in $CHCl_3$/DCB (4:1 *v/v*) gave a PCE of 3.2%. By utilizing $PC_{70}BM$ as the acceptor in the active layer, an improved PCE of 4.0% was achieved under the same condition.

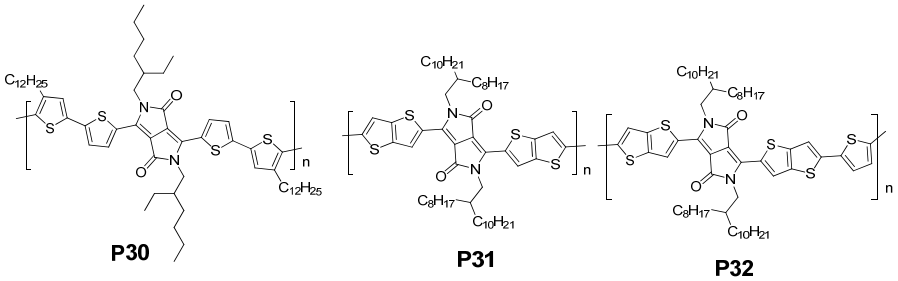

Chart 12. Chemical structures of DPP-containing polymers P30, P31 and P32

By replacing the thiophene unit with larger thieno[2,3-b] thiophene, P31 and P32 were prepared. Long branched chains have been incorporated at the DDP unit to assist solvation. Both polymers had band gap of ~1.4 eV and absorbed beyond 800 nm in the film state. Ambipolar charge transport behavior was found for both of the polymers. P31 had a high hole mobility of 0.04 $cm^2V^{-1}s^{-1}$ and good PCE of 3.0% based on P31/$PC_{70}BM$ (1:2 *w/w*) thin film prepared from $CHCl_3$/DCB (4:1 *v/v*) solution. By modifying the backbone with one more thiophene unit introduced to the repeating unit, P32 showed an even higher hole mobility of *ca.* 2 $cm^2V^{-1}s^{-1}$ and the BHJ solar cell device fabricated under the same condition as that of P31 showed an improved efficiency up to 5.4%.

3.10 Fluorene/ cylcopenta[2,1-b:3,4-b'] dithiophene/ silafluorene/ dithieno[3,2-b:2',3'-d] silole

Fluorene based polymers have been widely explored as organic electronic material in the field of OLED, OFET and PSC due to their high photoluminescence quantum yield, high thermal and chemical stability, good film-forming properties and good charge transport properties. Polyfluorene, however, has a band gap of ~3.0eV, which limits its application in

solar cell. Therefore, fluorene is normally copolymerized with electron withdrawing moieties to construct polymers with band gap <2.0 eV so as to extend sunlight harvesting to longer wavelength. Although some solar cell polymers have been prepared by copolymerization of fluorene and electron-rich moieties, such as thienothiophene and pentacene, their absorption behaviors and wide band gaps are found to account for the moderate to poor performance (Schulz et al., 2009; Okamoto et al., 2008). Palladium catalyzed cross coupling reaction is normally adopted for the polymerization due to the ease of halogenation at the 2,7-position of fluorene unit. Alkynation at the 9-position of the fluorene assists solvation for the D-A type polymer, whereas necessary, alkynation on the electron deficient counterpart is also required. Fluorene copolymers prepared from electron deficient benzothiadiazole and thienopyrazine have been discussed previously.

By replacing two benzene rings of fluorene with thiophene, cylcopenta[2,1-b:3,4-b′] dithiophene can be obtained as another novel building block to construct D-A type low band gap polymer. Alkynation at the bridge sp^3-carbon renders solubility for the polymer. Cyclopenta[2,1-b:3,4-b′]dithiophene based polymer P33 has been synthesized with a low band gap of *ca.* 1.4 eV (Mühlbacher et al., 2006). It was utilized by Kim *et al.* (Kim et al., 2007) to fabricate an efficient tandem solar cell. This brilliant and excellent work addressed the issue that while most low band gap polymers absorb at wavelength longer than 700 nm, there is a hollow at shorter wavelength and the lack of sufficient absorption at the hollow will drag the power conversion efficiency. In this case, P33 had an absorption maximum at *ca.* 800nm and a hollow at *ca.* 450nm. Kim et al. fabricated a tandem BHJ solar cell by utilizing P3HT (λ_{max} =~ 550nm) to absorb at the hollow of P33 and low band gap polymer P33 to absorb light at the NIR region. Tandem solar cell device (Al/TiOx/P3HT:PC_{70}BM/PEDOT:PSS/TiOx/P33:PCBM/PEDOT:PSS/ITO/glass) based on P3HT and P33 gave a typical performance parameter of J_{sc} = 7.8 mA/cm², V_{oc} = 1.24 V, *FF* =0.67 and PCE= 6.5%, which was among the highest values reported.

Silafluorene and dithieno[3,2-b:2′,3′-d]silole are two interesting electron rich moieties that are structurally analogous to fluorene. Low band gap polymer P34 was synthesized by copolymerization of 2,7-silafluorene and dithienyl-benzothiadiazole (E. Wang et al., 2008). Field effect charge mobility of P34 was found to be ~1x10^{-3} $cm^2V^{-1}s^{-1}$. High efficiency up to 5.4% with V_{oc} = 0.9 V, J_{sc} = 9.5 mA/cm², *FF* = 0.51 was obtained by using P34/PCBM(1:2 *w/w*) as active layer. Polymer P35 was synthesized by Stille coupling between dithieno[3,2-b:2′,3′-d]silole and benzothiadiazole (Hou et al., 2008). The optical band gap of P35 was found to be 1.45 eV, which was similar to that of P33. Hole transport mobility of the polymer was determined to be 3 x 10^{-3} $cm^2V^{-1}s^{-1}$, about 3 times higher than that of P33. The best device based on P35 gave a PCE of 5.1% with J_{sc} = 12.7 mA/cm², V_{oc}=0.68 V and *FF* = 0.55.

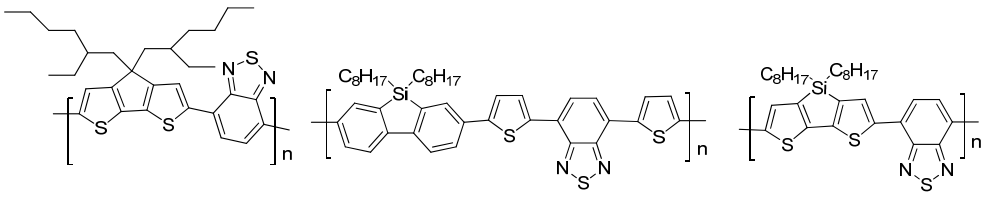

P33 **P34** **P35**

Chart 13. Structures of low band gap polymers P33, P34 and P35

4. Conclusion

In this chapter, main effort has been directed to disclose the structure-property relationship for solar cell polymers. The requirements and criteria for an efficient polymer donor in BHJ solar cell have been discussed with representative examples. Key factors are: absorption efficiency, solubility, stability (thermal-, photo-), low band gap, HOMO/LUMO energy level, charge carrier mobility and morphology. In order to achieve high power conversion efficiency, a good balance among these factors should be met. On the other hand, choice of acceptor counterpart and device engineering for the BHJ device also play important roles for power conversion efficiency improvement. Nowadays choice of donor/acceptor combination and device fabrication is still 'a state of art' but more and more rules of thumb have been pointed out. Provided that if BHJ concept still prevails for the next 10 years or longer, newer device design is also urgently required. Tandem solar cell device reported is one example to address the efficiency issue from this point of view. But no matter what kind of new changes will be brought out, the photon flux capture material, which is conjugated polymer in PSC, will still be the core of the device.

5. Acknowledgment

This work was financially supported by National University of Singapore under MOE AcRF FRC Grant No. R-143-000-412-112 and R-143-000-444-112.

6. References

Arias, A. C., Corcoran, N., Banach, M., Friend, R. H., MacKenzie, J. D. & Huck, W. T. S. (2002). Vertically segregated polymer-blend photovoltaic thin-film structures through surface-mediated solution processing. *Applied Physics Letters*, Vol. 80, No. 10, (March 2002), pp. 1695-1697, ISSN 1077-3118

Baek, N. S., Hau, S. K., Yip, H. L., Acton, O., Chen, K. -S. & Jen, A. K. -Y. (2008). High performance amorphous metallated π-conjugated polymers for field-effect transistors and polymer solar cells. *Chemistry of Materials*, Vol.20, No.18, (September 2008), pp. 5734-5736, ISSN 1520-5002

Balzani, V., Credi, A. & Venturi, M. (2008). Photochemical conversion of solar energy. *ChemSusChem*, Vol.1, No.1-2, (February 2008), pp.26-58, ISSN 1864-5631

Blom, P. W. M., de Jong, M. J. M., & van Munster, M. G. (1997). Electric-field and temperature dependence of the hole mobility in poly(*p*-phenylene vinylene). *Physical Review B*, Vol.55, No.2, (January 1997), pp. R656-R659 ISSN 1550-235X

Blouin, N., Michaud, A., & Leclerc, M. (2007). A low-bandgap poly(2,7-carbazole) derivative for use in high-performance solar cells. *Advanced Materials*, Vol.19, No.17, (September 2007), pp. 2295-2300, ISSN 1521-4095

Blouin, N., Michaud, A., Gendron, D., Wakim, S., Blair, E., Plesu, R. N., Neagu-Plesu, R., Belletête, M., Durocher, G., Tao, Y. & Leclerc, M. (2008). Towards a rational design of poly(2,7-carbazole) derivatives for solar cells. *Journal of the American Chemical Society*, Vol.130, No.2, (January 2008), pp. 732-742, ISSN 1520-5126

Brabec, C. J., Cravino, A., Meissner, D., Sariciftci, N. S., Fromherz, T., Rispens, M. T., Sanchez, L. & Hummelen, J. C. (2001). Origin of the open circuit voltage of plastic solar cells. *Advanced Functional Materials*, Vol. 11, No.5, (October 2001), pp. 374-380, ISSN 1616-3028

Bronstein, H., Chen, Z., Ashraf, R. S., Zhang, W., Du, J., Durrant, J. R., Tuladhar, P. S., Song, K., Watkins, S. E., Geerts, Y., Wienk, M. M., Janssen, R. A. J., Anthopoulos, T., Sirringhaus, H., Heeney, M. & McCulloch, I. (2011). Thieno[3,2-b]thiophene-diketopyrrolopyrrole-Containing polymers for high-performance organic field-effect transistors and organic photovoltaic devices. *Journal of the American Chemical Society*, Vol.133, No.10, (March 2011), pp. 3272-3275, ISSN 1520-5126

Burroughes, J. H., Bradley, D. D. C., Brown, A. R., Marks, R. N., Mackay, K., Friend, R. H., Burns, P. L. & Holmes, A. B. (1990). Light-emitting diodes based on conjugated polymers. *Nature*, Vol.347, No.6293, (October 1990), pp. 539-541, ISSN 1476-4687

Chen, H. -Y., Hou, J., Zhang, S., Liang, Y., Yang, G., Yang, Y., Yu, L., Wu, Y. & Li, G. (2009). Polymer solar cells with enhanced open-circuit voltage and efficiency. *Nature Photonics*, Vol.3, No.11, (November 2009), pp. 649-653, ISSN 1749-4885

Chen, J. & Cao, Y. (2007). Silole-containing polymers: chemistry and optoelectronic properties. *Macromolecular Rapid Communications*, Vol.28, No.17, (September 2007), pp. 1714-1742, ISSN 1521-3927

Chen J. & Cao Y. (2009). Development of novel conjugated donor polymers for high-efficiency bulk-heterojunction photovoltaic devices. *Accounts of Chemical Research*, Vol.42, No.11, (November 2009), pp. 1709-1718, ISSN 1520-4898

Cheng, Y. J., Yang, S. H. & Hsu, C. S. (2009). Synthesis of conjugated polymers for organic solar cell applications. *Chemical Reviews*, Vol.109, No.11, (November 2009), pp. 5868-5923, ISSN 1520-6890

de Leeuw, D. M., Simenon, M. M. J., Brown, A. R. & Einerhard, R. E. F. (1997). Stability of n-type doped conducting polymers and consequences for polymeric microelectronic devices. *Synthetic Metals*, Vol.87, No.1, (February 1997), pp. 53-59, ISSN 0379-6779

Ferraris, J. P., Bravo, A., Kim, W. & Hrncir, D. C. (1994). Reduction of steric interactions in thiophene-pyridino[c]thiophene copolymers. *Journal of Chemical Society Chemical Communications*, Vol.1994, No.8, (April 1994), pp. 991-992, ISSN 0022-4936

Fichou, D. (Ed.). (1999). *Handbook of Oligo- and Polythiophenes,* Wiley-VCH Verlag GmbH, ISBN 3527294457, Weinheim

Fong, H. H., Pozdin, V. A., Amassian, A., Malliaras, G. G., Smilgies, D. -M., He, M., Gasper, S., Zhang, F. & Sorensen, M. (2008). Tetrathienoacene copolymers as high mobility, soluble organic semiconductors. *Journal of the American Chemical Society*, Vol.130, No.40, (October 2008), pp.13202-13203, ISSN 1520-5126

Gilch, H. & Wheelwright, W. (1966). Polymerization of α-halogenated *p*-xylenes with base. *Journal of Polymer Science Part A: Polymer Chemistry*, Vol.4, No.6, (March 2003), pp.1337-1349, ISSN 1099-0518

Günes, S., Neugebauer, H. & Sariciftci, N. S. (2007). Conjugated polymer-based organic solar cells. *Chemical Reviews*, Vol.107, No.4, (April 2007), pp. 1324-1338, ISSN 1520-6890

Heeney, M., Bailey, C., Genevicius, K., Shkunov, M., Sparrowe, D., Tierney, S. & McCulloch, I. (2005). Stable polythiophene semiconductors incorporating thieno[2,3-b]thiophene. *Journal of the American Chemical Society*, Vol.127, No.4, (February 2005), pp. 1078-1079, ISSN 1520-5126

Hoppe, H. & Sariciftci, N. S. (2006). Morphology of polymer/fullerene bulk heterojunction solar cells. *Journal of Materials Chemistry*, Vol.16, No.1, (January 2006), pp. 45-61, ISSN 1364-5501

Hottel, H. (1989). Fifty years of solar energy research supported by the Cabot Fund. *Solar Energy*, Vol.43, No.2, (1989), pp. 107-128, ISSN 0038-092X

Hou, J., Chen, H.-Y., Zhang, S., Li, G. & Yang, Y. (2008). Synthesis, characterization, and photovoltaic properties of a low band gap polymer based on silole-containing polythiophenes and 2,1,3-benzothiadiazole. *Journal of the American Chemical Society*, Vol. 130, No.48, (December 2008), pp. 16144-16145, ISSN 1520-5126

Kim, J. Y., Lee, K., Coates, N. E., Moses, D., Nguyen, T.-Q., Dante, M. & Heeger, A. J. (2007). Efficient tandem polymer solar cells fabricated by all-solution processing. *Science*, Vol.317, No.5835, (July 2007), pp. 222-225, ISSN 1095-9203

Kobayashi, M., Chen, J., Chung, T.-C., Moraes, F., Heeger, A. J. & Wudl, F. (1984). Synthesis and properties of chemically coupled poly(thiophene). *Synthetic Metals*, Vol.9, No.1, (January 1984), pp. 77-86, ISSN 0379-6779

Liang, Y., Wu, Y., Feng, D., Tsai, S.-T., Son, H, -J., Li, G. & Yu, L. (2009). Development of new semiconducting polymers for high performance solar cells. *Journal of the American Chemical Society*, Vol.131, No.1, (January 2009), pp. 56-57, ISSN 1520-5126

Li, C., Liu, M., Pschirer, N. G., Baumgarten, M. & Müllen, K. (2010). Polyphenylene-based materials for organic photovoltaics. *Chemical Reviews*, Vol.110, No.11, (November 2010), pp. 6817-6855, ISSN 1520-6890

Li, G., Shrotriya, V., Huang, J., Yao, Y., Mariarty, T., Emery, K. & Yang, Y. (2005). High-efficiency solution processable polymer photovoltaic cells by self- organization of polymer blends. *Nature Materials*, Vol.4, No.11, (November 2005), pp. 864-868, ISSN 1476-4660

Li, H., Jiang, P., Yi, C., Li, C., Liu, S., Tan, S., Zhao, B., Braun, J., Meier, W., Wandlowski, T. & Decurtins, S. (2010). Benzodifuran-based π-conjugated copolymers for bulk heterojunction solar cells. *Macromolecules*, Vol.43, No.19, (October 2010), pp. 8058-8062, ISSN 1520-5835

Lin, J. W. P. & Dudek, L. P. (1980). Synthesis and properties of poly(2,5-thienylene). *Journal of Polymer Science Polymer Chemistry Edition*, Vol.18, No.9, (September 1980), pp.2869-2873, ISSN 1099-0518

Lior, N. (2008). Energy resources and use: The present situation and possible paths to the future. *Energy*, Vol.33, No.6, (June 2008), pp. 842-857, ISSN 0360-5442

Liu, J., Lam, J. W. Y. & Tang, B. (2009). Acetylenic polymers: syntheses, structures, and functions. *Chemical Reviews*, Vol.109, No.11, (November 2009), pp.5799-5867, ISSN 1520-6890

Ma, W., Yang, C., Gong, X., Lee, K. & Heeger, A. J. (2005) Thermally stable, efficient polymer solar cells with nanoscale control of the interpenetrating network morphology.

Advanced Functional Materials, Vol.15, No.10, (October 2005), pp. 1617-1622, ISSN 1616-3028

McCulloch, I., Heeney, M., Bailey, C., Genevicius, K., Macdonald, I., Shkunov, M., Sparrowe, D., Tierney, S., Wagner, R., Zhang, W., Chabinyc, M. L., Kline, R. J., Mcgehee, M. D. & Toney, M. F. (2006). Liquid-crystalline semiconducting polymers with high charge-carrier mobility. *Nature Materials*, Vol.6, No.4, (April 2006), pp. 328-333, ISSN 1476-4660

McCullough, R. D. & Lowe, R. D. (1992). Enhanced electrical conductivity in regioselectively synthesized poly(3-alkylthiophenes). *Journal of Chemical Society Chemical Communications*,Vol.70, No.1, (January 1992), pp. 70-72, ISSN 0022-4936

McCullough, R. D. & Lowe, R. D. (1993). Design, synthesis, and control of conducting polymer architectures: structurally homogeneous poly(3-alkylthiophenes). *The Journal of Organic Chemistry*, Vol.58, No.4, (February 1993), pp. 904-912, ISSN 1520-6904

Mihailetchi, V. D., Duren, J. K. J., Blom, P. W. M., Hummelen, J. C., Janssen, R. A. J., Kroon, J. M., Rispens, M. T., Verhees, W. J. H. & Wienk, M. M. (2003). Electron transport in a methallofullerene. *Advanced Functional Materials*, Vol. 13, No.1, (January 2003), pp. 43-46, ISSN 1616-3028

Mihailetchi, V. D., Xie, H., Boer, B., Popescu, L. M., Hummelen, J. C. & Blom, P. W. M. (2006). Origin of the enhanced performance in poly(3-hexylthiophene): [6,6]-phenyl C_{61}-butyric acid methyl ester solar cells upon slow drying of the active layer. *Applied Physics Letters*, Vol.89, No.1, (July 2006), pp. 012107, ISSN 1077-3118

Mammo W., Admassie, S., Gadisa, A., Zhang, F., Inganäs, O. & Andersson, M. R. (2007). New low band gap alternating polyfluorene copolymer-based photovoltaic cells. *Solar Energy Materials and Solar Cells*, Vol.91, No.11, (July 2007), pp. 1010-1018, ISSN 0927-0248

Miyakoshi, R., Yokoyama, A. & Yokozawa, T. (2005). Catalyst-transfer polycondensation. Mechanism of Ni-Catalyzed chain-growth polymerization leading to well-defined poly(3-hexylthiophene). *Journal of the American Chemical Society*, Vol.127, No.49, (December 2005), pp. 17542-17547, ISSN 1520-5126

Mühlbacher, D., Scharber, M., Morana, M., Zhu, Z., Waller, D., Gaudiana, R. & Brabec, C. (2006). High photovoltaic performance of a low-bandgap polymer. *Advanced Materials*, Vol.18, No.21, (November 2006), pp. 2884-2889, ISSN 1521-4095

Okamoto, T., Jiang, Y., Qu, F., Mayer, A. C., Parmer, J. E., McGehee, M. D. & Bao, Z. (2008). Synthesis and characterization of pentacene- and anthradithiophene-fluorene conjugated copolymers synthesized by Suzuki reactions. *Macromolecules*, Vol.41, No.19, (October 2008), pp. 6977-6980, ISSN 1520-5835

Ong, B. S., Wu, Y., Liu, P. & Gardner, S. (2004). High performance semiconducting polythiophenes for organic thin-film transistors. *Journal of the American Chemical Society*, Vol.126, No.11, (March 2004), pp. 3378-3379, ISSN 1520-5126

Peet, J., Kim, J. Y., Coates, N. E., Ma, W. L., Moses, D., Heeger, A. J. & Bazan, G. C. (2007). Efficiency enhancement in low-bandgap polymer solar cells by processing with alkane dithiols. *Nature Materials*, Vol.6, No.7, (July 2007), pp. 497-500, ISSN 1476-4660

Rutherford, D. R., Stille, J. K., Elliott, C. M. & Reichert, V. R. (1992). Poly(2,5-ethynylene thiophenediylethynylenes), related heteroaromatic analogs, and poly(thieno[3,2-b]thiophenes): synthesis and thermal and electrical properties. *Macromolecules*, Vol.25, No.9, (April 1992), pp. 2294-2306, ISSN 1520-5835

Sariciftci, N. S. (2004). Plastic photovoltaic devices. *Materials Today*, Vol.7, No.9, (September 2004), pp. 36-40, ISSN 1369-7021

Sariciftci, N. S., Smilowitz, L., Heeger, A. J. & Wudl, F. (1992). Photoinduced electron transfer from a conducting polymer to buckminsterfullerene. *Science*, Vol.258, No.5087, (November 1992), pp. 1474-1476, ISSN 1095-9203

Scharber, M. C., Mühlbacher, D., Koppe, M., Denk, P., Waldauf, C., Heeger, A. J. & Brabec, C. J. (2006). Design rules for donors in bulk-heterojunction solar cells- towards 10% energy-conversion efficiency. *Advanced Materials*, Vol. 18, No.6, (March 2006), pp. 789-794, ISSN 1521-4095

Schulz, G. L., Chen, X. & Holdcroft, S. (2009). High band gap poly(9,9-dihexylfluorene- alt-bithiophene) blended with [6,6]-phenyl C_{61} butyric acid methyl ester for use in efficient photovoltaic devices. *Applied Physics Letters*, Vol.94, No.2, (January 2009), pp. 023302, ISSN 1077-3118

Shaheen, S. E., Brabec, C. J. & Sariciftci, N. S. (2001). 2.5% efficient organic plastic solar cells. *Applied Physics Letters*, Vol.78, No.6, (February 2001), pp. 841-843, ISSN 1077-3118

Shirakawa, H., Louis, E. J., MacDiarmid, A. G., Chiang, C. K., & Heeger, A. J. (1977). Synthesis of electrically conducting organic polymers: halogen derivatives of polyacetylene, $(CH)_x$. *Journal of Chemical Society Chemical Communications*., Vol.1977, No.16, (August 1977), pp. 578-580, ISSN 0022-4936

Slooff, L. H., Veenstra, S. C., Kroon, J. M., Moet, D. J. D., Sweelssen, J., Koetse, M. M. (2007). Determining the internal quantum efficiency of highly efficient polymer solar cells through optical modeling. *Applied Physics Letters*, Vol.90, No.14, (April 2007), pp. 143506, ISSN 1077-3118

Sun, S. S. & Sariciftci, N. S. (Eds.). (March 29 2005). *Organic Photovoltaics: Mechanisms, Materials, and Devices*, CRC press, ISBN 9780824759636, Florida, USA

Svensson, M., Zhang, F., Veenstra, S. C., Verhees, W. J. H., Hummelen, J. C., Kroon, J. M., Inganäs, O., & Andersson, M. R. (2003). High-performance polymer solar cells of an alternating polyfuorene copolymer and a fullerene derivative. *Advanced Materials*, Vol.15, No.12, (June 2003), pp. 988-991, ISSN 1521-4095

Tajima, K., Suzuki, Y. & Hashimoto, K. (2008). Polymer Photovoltaic Devices Using Fully Regioregular Poly[(2-methoxy-5- (3′,7′-dimethyloctyloxy))-1,4- phenylenevinylene]. *Journal of Physiccal Chemistry C,* Vol.112, No.23, (June 2008), pp. 8507-8510, ISSN 1932-7455

Tang, C.W. (1986). Two-layer organic photovoltaic cell. *Applied Physics Letters*, Vol.48, No.2, (January 1986), pp. 183-185, ISSN 1077-3118

Wang, E., Wang, L., Lan, L., Luo, C., Zhuang, W., Peng, J. & Cao, Y. (2008). High performance polymer heterojunction solar cells of a polysilafluorene derivative. *Applied Physics Letters*, Vol.92, No.3, (January 2008), pp. 033307, ISSN 1077-3118

Wang, F., Luo, J., Yang, K., Chen, J., Huang, F. & Cao, Y. (2005). Conjugated fluorene and silole copolymers: synthesis, characterization, electronic transition, light emission, photovoltaic cell, and field effect hole mobility. *Macromolecules*, Vol.38, No.6, (March 2005), pp. 2253-2260, ISSN 1520-5835

Wenham, S. R., & Watt, M. E. (1994). *Applied Photovoltaics,*Bridge Printery, ISBN 0867589094, Syndney

Wessling, R. A. (1985). The polymerization of xylylene bisdialkyl sulfonium salts. *Journal of Polymer Science: Polymer Symposia,* Vol.72, No.1, (March 2007), pp. 55-66, ISSN 1936-0959

Wienk, M. M., Turbiez, M., Gilot, J. & Janssen, R. A. J. (2008). Narrow-bandgap diketo-pyrrolo-pyrrole polymer solar cells: The effect of processing on the performance. *Advanced Materials*, Vol.20, No.13, (July 2008), pp. 2556-2560, ISSN 1521-4095

Wöhrle, D. & Meissner, D. (1991). Organic solar cells. *Advanced Materials*, Vol.3, No.3, (March 1991), pp. 129-138, ISSN 1521-4095

Wong, W. –Y., Wang, X. –Z., He Z., Chan, K. –K., Djurišić, A. B., Cheung, K. –Y., Yip, C. –T., Ng, A. M. –C., Xi, Y. Y., Mak, C. S. K. & Chan, W. –K. (2007). Tuning the absorption, charge transport properties, and solar cell efficiency with the number of thienyl rings in platinum-containing poly(aryleneethynylene)s. *Journal of the American Chemical Society*, Vol.129, No.46, (November 2007), pp. 14372-14380, ISSN 1520-5126

Wong, W. -Y., Wang, X. –Z., He, Z., Djurišić, A. B., Yip, C.-T, Cheung, K. –Y., Wang, H., Mak, C. S. K. & Chan, W. –K. (2007). Metallated conjugated polymers as a new avenue towards high-efficiency polymer solar cells. *Nature Materials*, Vol.6, No.7, (July 2007), pp. 521-527, ISSN 1476-4660

Wudl, F., Kobayashi, M. & Heeger, A. J. (1984). Poly(isothianaphthene). *The Journal of Organic Chemistry*, Vol.49, No.18, (September 1984), pp. 3382-3384, ISSN 1520-6904

Yamamoto, T., Sanechika, K. & Yamamoto, A. (1980) Preparation of thermostable and electric-conducting poly(2,5-thienylene). *Journal of Polymer Science: Polymer Letters Edition*, Vol.18, No.1, (January 1980), pp. 9-12, ISSN 1543-0472

Zhang, F., Mammo, W., Andersson, L. M., Admassie, S., Andersson, M. R. & Inganäs, O. (2006). Low-bandgap alternating fluorene copolymer/methanofullerene heterojunctions in efficient near-infrared polymer solar cells. *Advanced Materials*, Vol.18, No.16, (August 2006), pp. 2169-2173, ISSN 1521-4095

Zhang, F., Jespersen, K. G., Björström, C., Svensson, M., Adderson, M. R., Sundström, V., Magnusson, K., Moons, E., Yartsev, A. & Inganäs, O. (2006). Influence of solvent mixing on the morphology and performance of solar cells based on polyfluorene copolymer/fullerene blends. *Advanced Functional Materials*, Vol.16, No.5, (March 2006), pp. 667-674, ISSN 1616-3028

Zhang, F., Perzon, E., Wang, X., Mammo, W., Andersson, M. R. & Inganäs, O. (2005). Polymer solar cells based on a low-bandgap fluorene copolymer and a fullerene derivative with photocurrent extended to 850nm. *Advanced Functional Materials*, Vol.15, No.5, (May 2005), pp. 745-750, ISSN 1616-3028

Zhou, E., Nakamura, M., Nishizawa, T., Zhang, Y., Wei, Q., Tajima, K., Yang, C. & Hashimoto, K. (2008). Synthesis and photovoltaic properties of a novel low band gap polymer based on N-substituted dithieno[3,2-b:2′,3′-d]pyrrole. *Macromolecules*, Vol.41, No.22, (November 2008), pp. 8302-8305, ISSN 1520-5835

Zhou, Q., Hou, Q., Zheng, L., Deng, X., Yu, G. & Cao, Y. (2004). Fluorene-based low band-gap copolymers for high performance photovoltaic devices. *Applied Physics Letters*, Vol.84, No.10, (March 2004), pp. 1653, ISSN 1077-3118

22

Optical Absorption and Photocurrent Spectra of CdSe Quantum Dots Adsorbed on Nanocrystalline TiO_2 Electrode Together with Photovoltaic Properties

Taro Toyoda and Qing Shen
The University of Electro-Communications
Japan

1. Introduction

There is a great deal of interest in the technological applications of titanium dioxide (TiO_2) to dye-sensitized solar cells (DSCs) made from nanostructured TiO_2 electrodes because of their high photovoltaic conversion efficiency, which exceeds 10% (Chiba et al., 2006). Since the initial pioneering work on DSCs (O'Regan & Grätzel, 1991), they have often been proposed as a sustainable energy source. In DSCs, the applications of organic dye molecules as a photosensitizer, nanostructured TiO_2 as an electron transport layer, and an iodine redox couple for hole transport dramatically improve the light harvesting efficiency. With Ru-based organic dyes adsorbed on nanostructured TiO_2 electrodes, the large surface area enables more efficient absorption of the solar light energy. The main undertaking for those developing next-generation solar cells is to improve the photovoltaic conversion efficiency, together with the long time stability. Nowadays, there exists an intense effort aimed at developing third-generation solar cells. One of a promising approach is to replace the organic dyes by inorganic substances with strong optical absorption characteristics and longer stability over time. Recently, as an alternative to organic dyes, semiconductor quantum dots (QDs) have been studied for their light harvesting capability (Niitsoo et al., 2006; Diguna et al., 2007; Mora-Seró, 2009). The enormous potential of science and technology on nanoscale to impact on industrial output has been recognized all over the world. One emerging area of nanoscience being at the interface of chemistry, physics, biology and materials science is the field of semiconductor QDs, whose unique properties have attracted great attention by researchers during the last two decades. Different strategies for the synthesis of semiconductor QDs have been developed, so that their composition, size, shape, and surface protection can be controlled nowadays with an exceptionally high degree. The surface chemistry of semiconductor QDs is another key parameter, in many respects determining their properties related to their assembly. Semiconductor QDs exhibit attractive characteristics as sensitizers due to their tunable bandgap (or HOMO-LUMO gap) by size control (Yu et al., 2003), which can be used to match the absorption spectrum to the spectral distribution of solar light. Moreover, semiconductor QDs possess higher extinction coefficients than conventional metal-organic

dyes, and larger intrinsic dipole moments leading to rapid charge separation (Underwood et al., 2001). The demonstration of multiple exciton generation (MEG) by impact ionization has fostered an interest in colloidal semiconductor QDs (Schaller et al, 2006; Trinh et al., 2008). One of the most attractive configurations to exploit these fascinating properties of semiconductor QDs is the quantum dot-sensitized solar cell (QDSC) (Nozik, 2002; Klimov, 2006). The efficient formation of more than one photoinduced electron-hole pair (exciton) upon the absorption of a single photon is a process not only of a great current scientific interest but is potentially important for optoelectronic devices that directly convert solar radiant energy into electricity. The demonstration of MEG by impact ionization in colloidal semiconductor QDs could push the thermodynamic photovoltaic conversion efficiency limit of solar cells up to 44% (Klimov, 2006) from the current 31% of the Shockley-Queisser detailed balance limit (Shockley & Queisser, 1961). The optimization of QDSCs can benefit from the intensive effort carried out with DSC. Although the photovoltaic conversion efficiencies of QDSCs lag behind those of DSCs and the use of semiconductor QDs as light absorbers requires the development of new strategies in order to push the performance of QDSCs, QDSCs have attracted significant attention among researchers as promising third-generation photovoltaic devices.

In this chapter, we describe the performance of QDSCs based on CdSe QD sensitizer on nanostructured TiO_2 electrode with a pre-adsorbed layer of CdS QDs (termed combined CdS/CdSe QDs) proposed by Niitsoo et al (Niitsoo et al, 2006) and developed by other groups (Lee & Lo, 2009; Sudhagar et al., 2009). They showed that a pre-adsorbed layer of CdS prior to CdSe adsorption improved the QDSC's performance. Hence it is interesting and useful to investigate the detailed function of combined CdS/CdSe QDs sensitizer on performance of QDSCs, together with the basic studies of optical absorption and photocurrent characteristics. Information regarding the optical absorption properties is initially necessary in order to investigate the electronic states of combined CdS/CdSe QDs for future photovoltaic cell applications. However, few accurate studies of the optical absorption properties of combined CdS/CdSe QDs adsorbed on nanostructured TiO_2 electrodes have been carried out. The main reason for this is the difficulty in using the conventional transmission method because of strong light scattering by the highly porous structure of the nanostructured TiO_2 electrodes. However, scattering effects can be minimized by employing the photothermal (PT) technique. In general, an optically excited solid relaxes to thermal equilibrium by the emission of photons (radiative processes) or phonons (nonradiative processes). In the PT technique, the signal detected is directly proportional to the thermal energy (heat production) induced by the absorbed photons through nonradiative processes (emission of phonons). Heat production by nonradiative processes has been detected by several methods (Tam, 1986). The PT signal is less sensitive to light scattering effects than conventional spectroscopy signals, and the ability of the PT technique to produce optical absorption spectra from strongly scattering media has been demonstrated, in particular using photoacoustic (PA) method which is a PT technique (Inoue et al., 2006; Toyoda et al., 2009). Thus, the PT technique is a useful technique for studying the optical absorption spectra of the strongly scattering and/or opaque samples with which we are dealing in our investigations. PA method detects the acoustic energy produced by heat generation through nonradiative processes in materials (Rosencwaig & Gersho, 1977). The PA cell, which is a small gas-tight enclosure with a sensitive acoustic microphone built in one wall, monitors the temperature changes in the sample produced by absorbed photons through nonradiative processes. Periodic temperature changes in the

sample surface by modulated light by PT effect cause periodic pressure changes in the enclosed gas, which creates acoustic waves. The intensities of the acoustic waves are converted to an electrical signal by the microphone. The PA method can be applied to evaluate the optical absorption properties of combined CdS/CdSe QDs adsorbed on nanostructured TiO_2 electrodes. In order to investigate the subsequent photosensitization of combined CdS/CdSe QDs adsorbed on nanostructured TiO_2 electrodes after optical absorption, photoelectrochemical current measurements were carried out and the incident photon-to-current conversion efficiency (IPCE, namely the quantum efficiency of photocurrent) was evaluated. Also, photovoltaic properties were characterized by solar simulator under the illumination of one sun intensity (AM 1.5: 100 mW/cm^2).

2. Experimental procedure

Experimental sections are divided into three sections, 1) sample preparations on TiO_2 electrodes and CdS/CdSe quantum dots, 2) optical absorption measurements by photoacoustic technique, and 3) photoelectrochemical current (incident photon to current conversion efficiency) and photovoltaic measurements.

2.1 Sample preparation

The method for the preparation of nanostructured TiO_2 electrodes has been reported in a previous paper (Shen & Toyoda, 2003). A TiO_2 paste was prepared by mixing 15 nm TiO_2 nanocrystalline particles (Super Titanai, Showa Denko; anatase type structure) and polyethylene glycol (molecular weight: 500,000) in pure water. The resultant paste was then deposited onto transparent conducting substrates [F-doped SnO_2 (FTO), sheet resistance: 10 μΩ/sq]. The TiO_2 electrodes were then sintered in air at 450 ^oC for 30 min to obtain good necking and to sublimate polyethylene glycol. The highly porous nanostructure of the films (the pore sizes were on the order of a few tens of nanometers) was confirmed from scanning electron microscopy (SEM) images. The thicknesses of the films were measured and found to be ~ 5 μm by examining the cross sectional SEM images.

At first, CdS QDs were adsorbed onto nanostructured TiO_2 electrodes (pre-adsorbed layer) from the common NH_3 bath with a solution composition of 20 mM $CdCl_2$, 66 mM NH_4Cl, 140 mM thiourea, and 0.23 M ammonia to obtain a final pH ~9.5 (Niitsoo et al., 2006; Jayakrishnan et al., 1996). The TiO_2 electrodes were immersed in a container filled with the final solution. The adsorption was carried out at room temperature in the dark for 40 min.

The CdSe QDs were prepared by using a chemical bath deposition (CBD) technique (Shen & Toyoda, 2004; Shen et al., 2004; Gorer & Hodes, 1994). First, for the Se source, an 80 mM sodium selenosulphate (Na_2SeSO_3) solution was prepared by dissolving elemental Se powder in a 200 mM Na_2SO_3 solution. Second, an 80 mM $CdSO_4$ and 120 mM of a trisodium salt of nitrilotriacetic acid [$N(CH_2COONa)_3$] were mixed with the 80 mM Na_2SeSO_3 solution in a volume ratio of 1: 1: 1. TiO_2 electrodes adsorbed with CdS QDs were placed in a glass container filled with the final solution at 10 ^oC in the dark for various times (from 2 to 24 h) to promote CdSe QDs adsorption. To investigate the role of pre-adsorbed layer of CdS QDs, the CdSe QDs only were adsorbed directly on nanostructured TiO_2 electrodes with the same sample preparation conditions as mentioned above.

After the adsorption of CdSe QDs, the samples were coated with ZnS for surface passivation of the QDs by successive ionic layer adsorption and reaction (SILAR) for three times in 0.1

M Zn(CH_2COO) and 0.1 M Na_2S aqueous solution for 1 min for each dip (Yang et al., 2002; Shen et al., 2008). In reference (Shen et al., 2008), we showed that the short-circuit-current density (J_{sc}), open-circuit voltage (Voc), and photovoltaic conversion efficiency (η) were enhanced by the ZnS coating, except for fill factor (FF). Although we applied the scanning electron microscopy (SEM) observation for visual investigation, we could not observe the difference of the morphologies with and without the ZnS coating up to 50,000 magnifications, indicating that the ZnS is coated with several atomic layers. In the future, we are going to observe the morphology of the ZnS coating layer by applying the transmission electron microscopy (TEM). To our knowledge, there are few reports in which ZnS coating has been applied to CdSe QD-sensitized solar cells, although ZnS-capped CdSe QDs dispersed in solution have been used for strong photoluminescence applications (Hines & Sionnet, 1996).

2.2 Optical absorption measurements

The optical absorption properties of nanostructured TiO_2 electrodes adsorbed with combined CdS/CdSe QDs were investigated using PA spectroscopy. The scattering effects in the optical absorption of nanostructured TiO_2 electrodes adsorbed with combined CdS/CdSe QDs can be minimized by employing the PA method. Figure 1 shows the schematic diagram of a photoacoustic spectrometer. Typical gas-microphone method was applied in the PA spectroscopic investigation (Rosencwaig & Gersho, 1977). The PA cell was composed of an aluminum cylinder with a small channel at the periphery in which a microphone (electret condenser type) was inserted (Shen &Toyoda, 2004). The inside volume of the cell was approximately 0.5 cm^3. The cell was suspended by four rubber bands

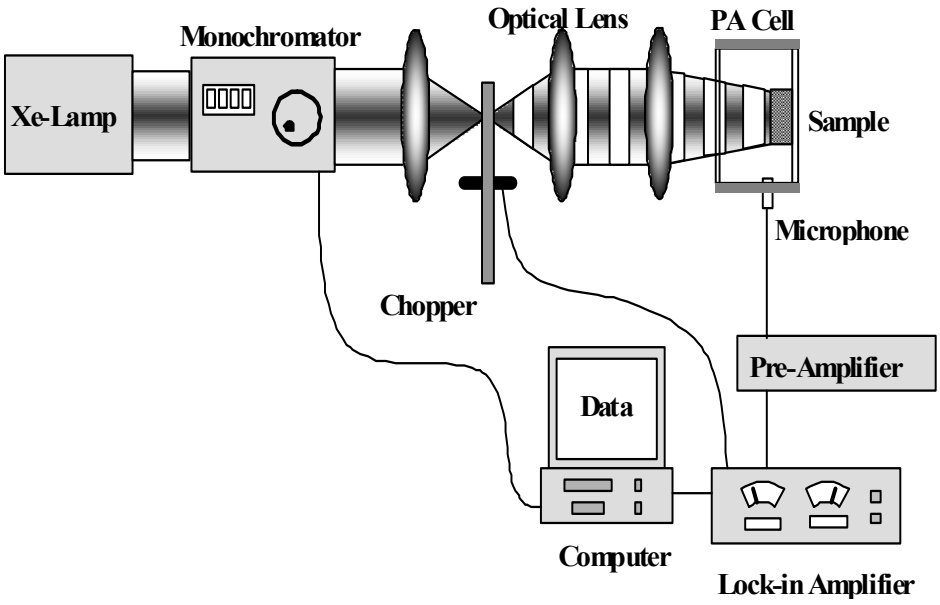

Fig. 1. Schematic diagram of a photoacoustic spectrometer, composed with light source, monochrometer, mechanical chopper, cell, preamplifier, lock-in amplifier, etc.

to prevent interference from external vibration. The cell window made of quartz was highly transparent throughout the observed wavelength range, and the sample holder could be easily removed from the cell to maintain the optical configuration. A 300 W xenon lamp was used as the light source. Monochromatic light through a monochromator was modulated at 33 Hz using a mechanical chopper and was focused within the PA cell. Light was focused on the sample over an impinging area of 0.20 cm^3. Modulation frequency of 33 Hz was determined to exclude the saturation effect of the spectrum. In this case (modulation frequency: 33 Hz), the optical absorption length is longer than the thermal diffusion length, indicating that the PA signal intensity is proportional to the optical absorption coefficient (no saturation effect) (Rosencwaig & Gersho, 1977). The PA signal was monitored by first passing the microphone output through a preamplifier and then into a lock-in amplifier. The data were averaged to improve the signal-to-noise ratio (S/N). The spectra were taken at room temperature in the wavelength range of 250 - 800 nm. The PA spectra were obtained by the normalization to the PA signal intensity of carbon black sheet that was proportional to the light intensity only. A UV cut filter was used for the measurements in the wavelength range of 600 - 800 nm to avoid the mixing of second harmonic light. The conditions for all the PA measurements (optical configuration, path-length, irradiation area, excitation light intensity etc.) were fixed as far as possible to compare each of the PA signals and spectra directly.

2.3 Photoelectrochemical current and photovoltaic measurements

Photocurrent measurements were performed in a sandwich structure cell (i.e., in the two-electrode configuration) with Cu_2S film on brass as the counter electrode (termed the Cu_2S counterelectrode). The applied electrolyte was polysulfide solution (1 M Na_2S + 1 M S). It is well known that the electrocatalytic activity of Pt with a polysulfide electrolyte is not satisfactory for photovoltaic cell applications and alternative counter electrode materials with higher activity such as Cu_2S and CoS have been reported (Hodes et al., 1980). The higher electro-catalytic activities of these materials are due to a reduction in the charge transfer resistance between the redox couple and the counterelectrode (Giménez et al. 2009). The Cu_2S counterelectrodes were prepared by immersing brass in HCl solution at 70°C for 5 min and subsequently dipping it into polysulfide solution for 10 min, resulting in a porous Cu_2S electrode (Hodes et al., 1980). The cells were prepared by sealing the Cu_2S counter-electrode and the nanostructured TiO_2 electrode adsorbed with combined CdS/CdSe QDs, using a silicone spacer (~ 50 μm) after the introduction of polysulfide electrolyte. The IPCE value was evaluated from the short-circuit photocurrent with a zero-shunt meter using the same apparatus and conditions as those used for the PA measurements. The incident light intensity was measured by an optical power-meter. The spectra were taken at room temperature in the wavelength of 250 – 800 nm. The conditions for all the measurements (optical configuration, path-length, irradiation area, excitation light intensity etc.) were fixed as far as possible to compare the IPCE values and spectra directly. Photovoltaic properties were characterized under a one sun illumination (AM 1.5: 100 mW/cm^2) using a solar simulator by the measurements of photocurrent versus photovoltage to investigate J_{sc}, V_{oc}, FF, and η.

3. Results and discussion

Figure 2 shows the PA spectra of the nanostructured TiO_2 electrodes adsorbed with combined CdS/CdSe QDs for different adsorption times, together with that adsorbed with CdS QDs only. The pre-adsorption times for CdS QDs were fixed at 40 min (average diameter: ~ 4.2 nm).

The spectra were normalized to the photon energy of 4.0 eV. With increasing adsorption time, the red-shift of optical absorption at the shoulder point (indicated by arrows) can be clearly observed, implying the growth of CdSe QDs. Also, the comparison between the adsorption of CdSe QDs on the nanostructured TiO_2 electrodes with and without a pre-adsorbed CdS QD layer was carried out to evaluate the difference in PA spectra. For that, Figure 3 shows the PA spectra of the nanostructured TiO_2 electrodes adsorbed with CdSe QDs without a pre-adsorbed CdS QD layer for different adsorption times. The spectra are also normalized to the photon energy of 4.0 eV. As the PA spectra below the CdSe QDs adsorption time of 8 h agree with that of pure nanostructured TiO_2 electrode within the experimental accuracy, the CdSe QDs average size is very small less than 1 nm or no adsorption. Optical absorption in the visible light region due to the adsorbed CdSe QDs can be also observed both in Figs. 2 and 3. With increasing adsorption time, the red-shift of optical absorption at the shoulder point (indicated by arrows) can be clearly observed in Fig.3, also implying the growth of CdSe QDs. The exponential slopes at the fundamental absorption edges in combined CdS/CdSe QDs adsorbed on nanostructured TiO_2 electrodes in Fig. 2 are higher than those of CdSe QDs adsorbed on nanostructured TiO_2 electrodes without a pre-adsorbed CdS QD layer in Fig. 3, indicating that the uniformity of the average sizes or crystal quality of CdSe QDs in the former is better than that of the latter. Relative to the band-gap energy of 1.73 eV for bulk CdSe, the shoulder points in PA spectra of the nanostructured TiO_2 electrodes adsorbed with CdSe QDs shown in Figs. 2 and 3 exhibit blue-shifts, which is indicative of the quantum confinement effect. This fact implies that the radii of the CdSe QDs are smaller than the Bohr radius of bulk CdSe (~5.6 nm). We assume that the photon energy at the shoulder point corresponds to the lowest excitation energy of the CdSe QDs (Shen & Toyoda, 2004). The average diameter of the CdSe QDs for each adsorption time both in combined CdS/CdSe and CdSe without a preadsorbed CdS layer adsorbed on nanostructured TiO_2 electrodes can be estimated with the effective mass approximation (Shen et al., 2008; Bawendi et al., 1989). The dependence of the average diameter on the adsorption time is shown in Fig. 4, both of combined CdS/CdSe (●) and CdSe without apre-adsorbed CdS layer (○). It can be observed that the CdSe QDs on the nanostructured TiO_2 electrodes with a pre-adsorbed CdS QD layer grow rapidly during the initial adsorption process (less than 2 h adsorption). After a certain time, the crystal growth rate is slowed down, which is similar to the reference reported (Toyoda et al., 2007). When the adsorption time is sufficiently long (in this case ~ 24 h), the average diameter of CdSe QDs becomes constant at about 7.1 nm. On the other hand, it can be observed that the CdSe QDs adsorbed on the nanostructured TiO_2 electrodes without a pre-adsorbed CdS layer show very slow growth or no growth during the initial adsorption process (less than 8 hours) due to the fact that the PA spectra below the CdSe adsorption time below 8 hours agree with that of the pure nanostructured TiO_2 electrode within the experimental accuracy. Therefore, the crystal growth rate of CdSe QDs adsorbed on TiO_2 electrode with a pre-adsorbed CdS QD layer is faster than that of CdSe QDs adsorbed on the TiO_2 electrodes without a pre-adsorbed CdS QD layer. There are several possibilities for the faster crystal growth rate of CdSe QDs adsorbed on the nanostructured TiO_2 electrode with a pre-adsorbed CdS QD layer. First, it is possible that the active CdSe QDs form from the excess Cd remaining after CdS adsorption directly on the nanostructured TiO_2 electrode (Niitsoo et al., 2006). This is suggested that CdS QDs act as seed layer for subsequent CdSe growth (Sudhager et al., 2009). Second one is the passivation effect of CdS QDs on the nanostrctured TiO_2 surface to reduce defects or dislocations. Third, CdSe QDs are grown on the assembly of CdS QDs, indicating the growth on the similar crystal structure (or close lattice constant) different from the growth on TiO_2.

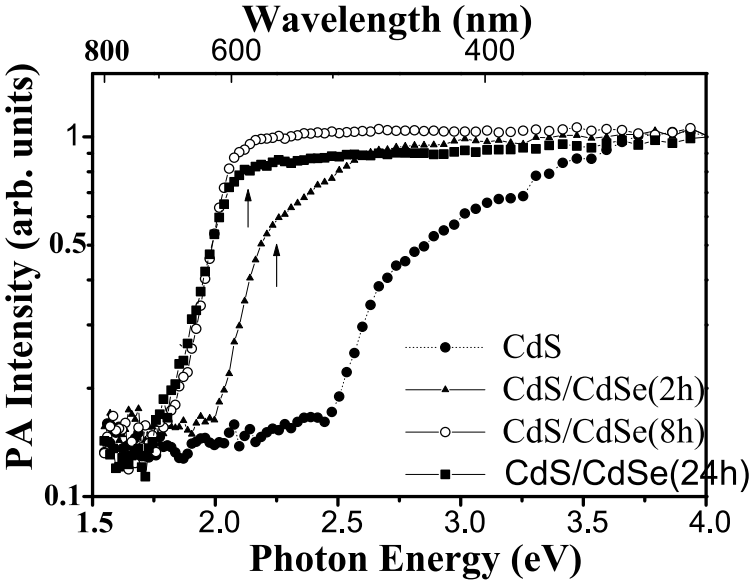

Fig. 2. Photoacoustic spectra of nanostructured TiO_2 electrodes adsorbed with combined CdS/CdSe quantum dots for different adsorption times together with that adsorbed wth CdS quantum dots only (modulation frequency: 33 Hz).

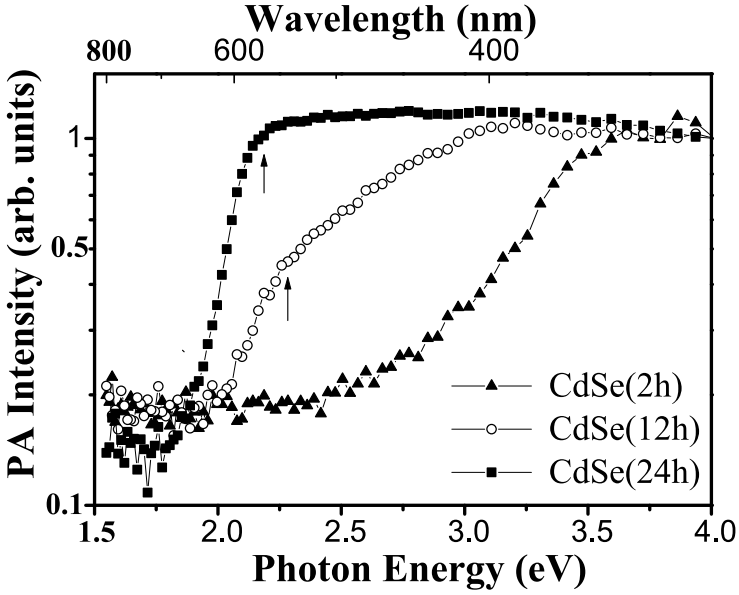

Fig. 3. Photoacoustic spectra of nanostructured TiO_2 electrodes adsorbed with CdSe quantum dots without a preadsorbed CdS quantum dot layer for different adsorption times (modulation frequency: 33 Hz).

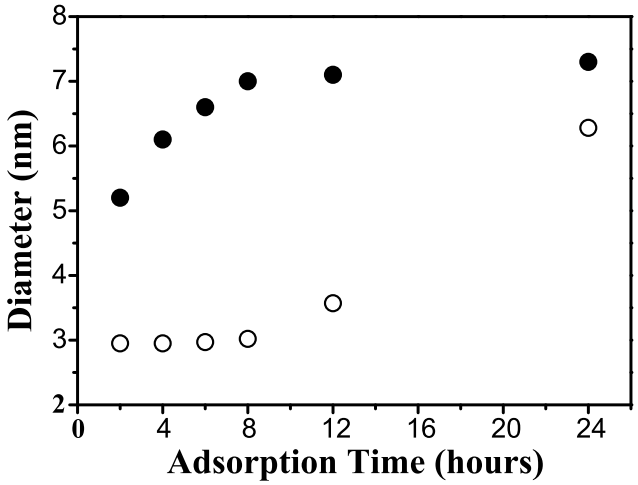

Fig. 4. Dependence of the average diameter on the adsorption time, both of combined CdS/CdSe (●) and CdSe without a preadsorbed CdS layer (○).

Figure 5 shows the IPCE spectra of the nanostructured TiO_2 electrodes adsorbed with combined CdS/CdSe QDs for different adsorption times, together with that adsorbed with CdS QDs only. The pre-adsorption time of CdS QD layer is fixed at 40 min. Photoelectrochemical current in the visible light region due to the adsorbed CdSe QDs can be observed, indicating the photosensitization by combined CdS/CdSe QDs. With increasing adsorption time, the red-shift of photoelectrochemical current can be clearly observed, implying the growth of CdSe QDs. The IPCE peak value increases with the increase of adsorption time up to 8 hours (~ 75%), then decreases until 24 h adsorption owing to the increase of recombination centers or interface states, together with the decrease of energy difference between LUMO in CdSe QDs and the bottom of conduction band of TiO_2. Also, the comparison between the adsorption of CdSe QDs on the TiO_2 electrodes with and without a pre-adsorbed CdS QD layer was carried out to evaluate the difference in IPCE spectra. For that, Figure 5 shows the IPCE spectra of the nanostructured TiO_2 electrodes adsorbed with CdSe QDs without a pre-adsorbed layer of CdS QD layer for different adsorption times. Photoelectrochemical current in the visible light region due to the adsorbed CdSe QDs can be observed in Fig. 6, also indicating the photosensitization by CdSe QDs. With increasing adsorption time, the red-shift of photoelectrochemical current can be clearly observed, implying the growth of CdSe QDs. However, the appearance of the spectrum in Fig. 6 is different from that of combined CdS/CdSe QDs, namely in the reduction of maximum IPCE value (~ 60%) and the adsorption time dependence of the spectrum shape. Also, the IPCE spectra below the CdSe QDs adsorption time of 8 h agree with that of pure nanostructured TiO_2 electrode within the experimental accuracy, indicating that the CdSe QDs adsorbed on the nanostructured TiO_2 electrode without a pre-adsorbed CdS layer show very slow growth or no growth similar to the results of PA characterization in Fig. 3. These results demonstrate that the spectral response of IPCE is enhanced upon combined CdS/CdSe sensitization rather than single CdSe QDs sensitization, indicating the possibility of the reduction in recombination centers and interface states owing to the possibilities of active CdSe QDs by the excess Cd remaining after CdS adsorption and passivation effect of CdS QDs on the nanostructured TiO_2 surface.

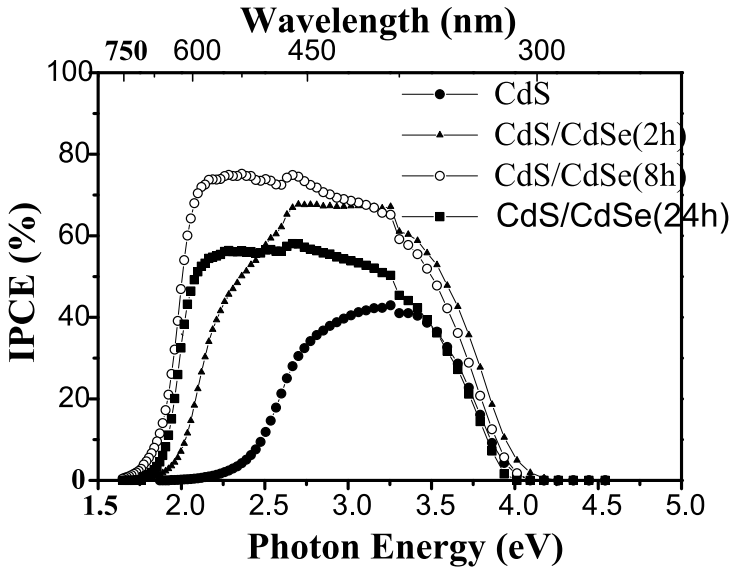

Fig. 5. IPCE spectra of nanostructured TiO_2 electrodes adsorbed with CdS/CdSe quantum dots for different adsorption times together with that adsorbed with CdS quantum dots only.

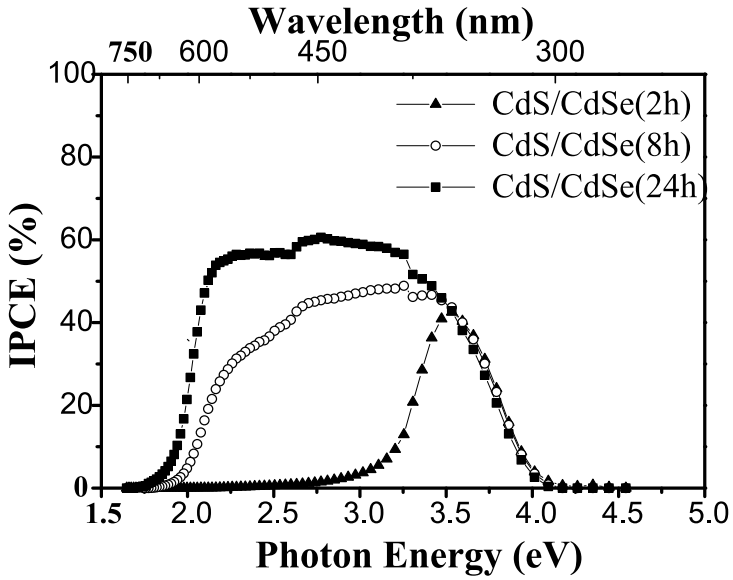

Fig. 6. IPCE spectra of nanostructured TiO_2 electrodes adsorbed with CdSe quantum dots without a preadsorbed CdS QD layer for different adsorption times.

The photocurrent-voltage cureves of (a) combined CdS/CdSe QD- and (b) CdSe QD-sensitized solar cells are shown in Fig. 7 (a) and (b), respectively, for different adsorption times, together with that obtained with cells adsorbed with CdS only. However, the

appearance of the current-voltage curves of combined CdS/CdSe QD-sensitized solar cells is different from those of CdSe QD-sensitized solar cells. Figure 8 and 9 illustrates the photovoltaic parameters ((a) J_{sc}; (b) V_{oc}; (c) FF; (d) η) of combined CdS/CdSe QD-sensitized (●) and CdSe QD-sensitized (○) solar cells as a function of CdSe QDs adsorption times.

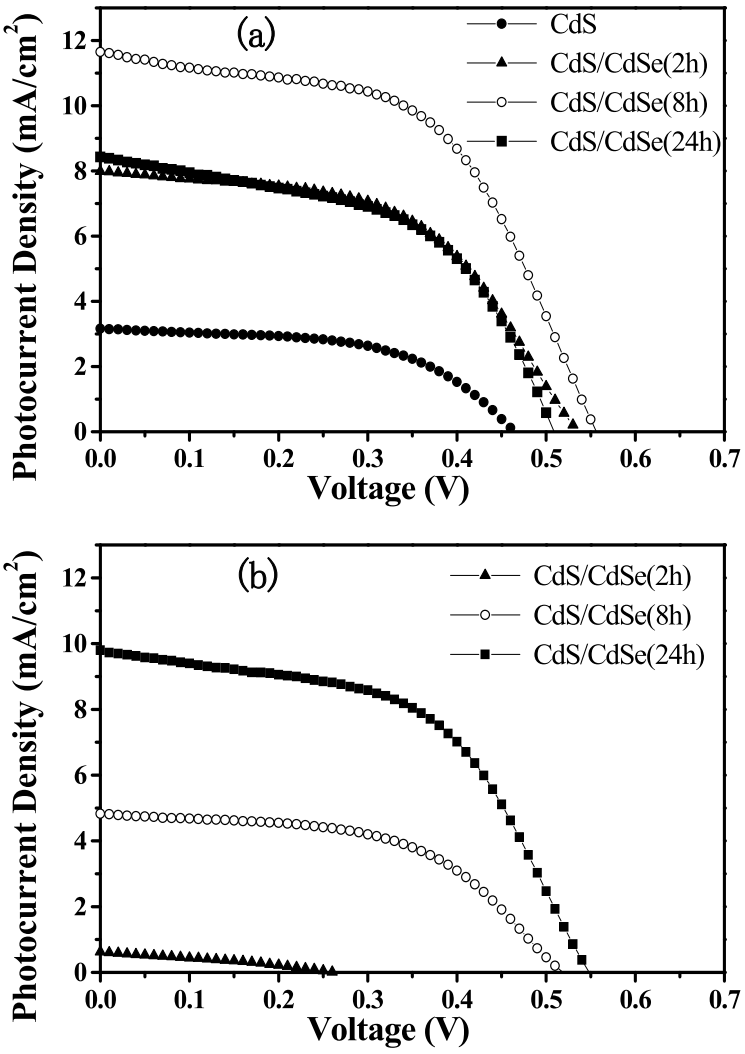

Fig. 7. Photocurrent-voltage curves of (a) combined CdS/CdSe quantm dot- and (b) CdSe quantum dot-sensitized solar cells for different adsorption times together with that adsorbed with CdS quantum dots only.

We observe that the parameter of J_{sc} in combined CdS/CdSe QD-sensitized solar cells increases with the increase of CdSe QDs adsorption times up to 8 h. On the other hand, V_{oc} and FF are independent of adsorption times. The performance of solar cells improved with

an increase in adsorption time up to 8 h due, mainly, not only to the increase of the amount of CdSe QDs but the improvement in crystal quality and decrease of interface states. However, the increase in adsorption times after more than 8 h leads to deterioration in J_{sc} and V_{oc}. High adsorption time of CdSe QDs might cause an increase in recombination centers, poor penetration of CdSe QDs, and the decrease of energy difference between LUMO in CdSe QDs and the bottom of conduction band of TiO_2. Therefore, η of the combined CdS/CdSe QD-sensitized solar cell shows a maximum of 3.5% at 8 h adsorption times. On the other hand, J_{sc} and η below the CdSe QDs adsorption time of 8 h without a pre-adsorbed CdS layer show very small values close to zero, indicating the very small amount of CdSe QDs adsorption similar to the results of PA and IPCE characterization. We can observe that J_{sc}, V_{oc}, FF, and η in

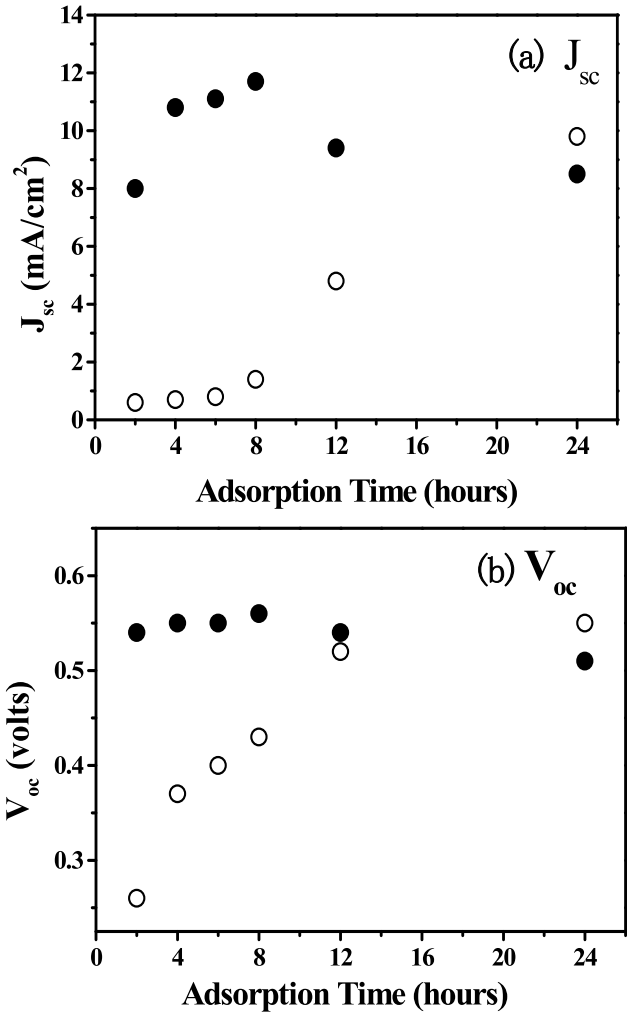

Fig. 8. Dependence of the photovoltaic parameters ((a) J_{sc} and (b) V_{oc}) on the adsorption time, both of combined CdS/CdSe (●) and CdSe without a preadsorbed CdS QD layer (○).

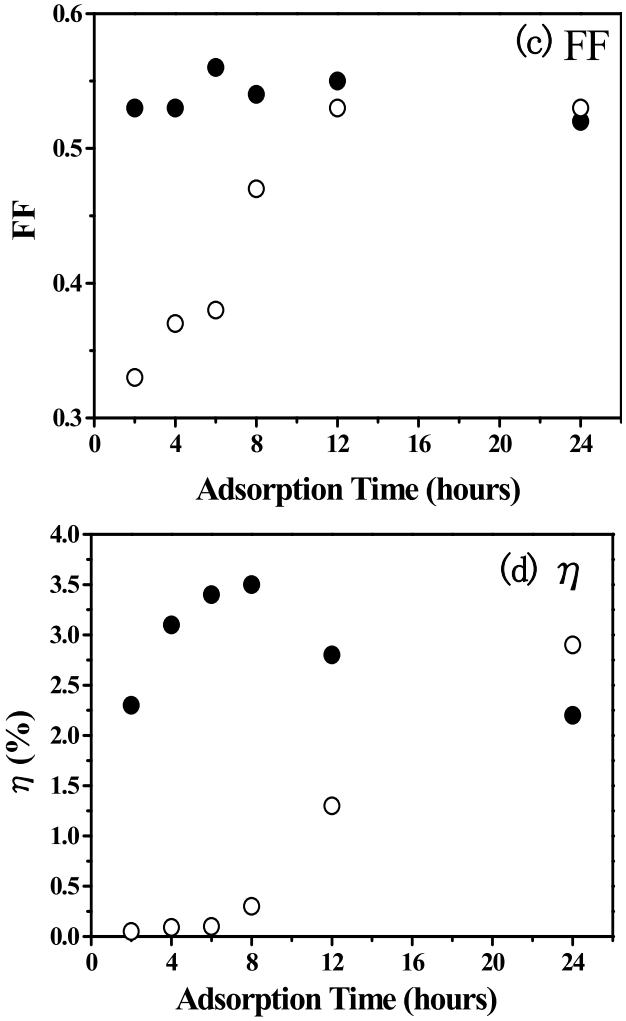

Fig. 9. Dependence of the photovoltaic parameters((c) FF and (d) η) on the adsorption time, both of combined CdS/CdSe (●) and CdSe without a preadsorbed CdS QD layer (○).

CdSe QD-sensitized solar cells without a pre-adsorbed CdS QD layer increase with the increase of adsorption times up to 24 h, indicating the difference of the crystal growth and the formation of recombination centers in combined CdS/CdSe and CdSe QDs.

Figure 9 shows the preliminary ultrafast photoexcited carrier dynamics characterization of combined CdS/CdSe and CdSe without a pre-adsorbed CdS layer (average diameters of both CdSe QDs are ~ 6 nm) using a improved transient grating (TG) technique (Katayama et al., 2003; Yamaguchi et al., 2003; Shen et al., 2010). TG signal is proportional to the change in the refractive index of the sample due to photoexcited carriers (electrons and holes). TG method is a powerful time-resolved optical technique for the measurements of various kinds of dynamics, such as carrier population dynamics, excited carrier diffusion, thermal

diffusion, acoustic velocity and so on. Improved TG technique features very simple and compact optical setup, and is applicable for samples with rough surfaces. Comparing with transient absorption (TA) technique, improved TG method has higher sensitivity sue to its zero background in TG signals, which avoids the nonlinear effect and sample damage. Figure 9 shows that the hole and electron relaxation times of nanostructured TiO_2 electrodes adsorbed with combined CdS/CdSe QDs are faster about twice than those with CdSe QDs without a pre-adsorve CdS layer, indicating the decreases in recombination centers.

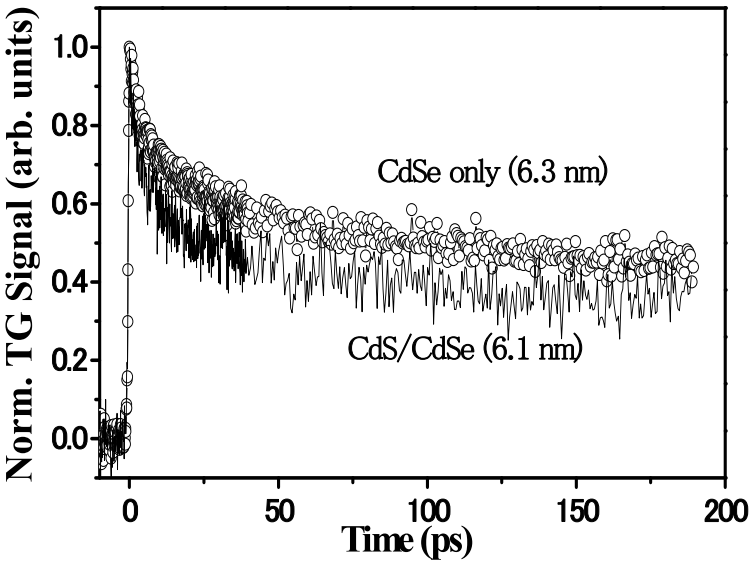

Fig. 10. Ultrafast carrier dynamics of combined CdS/CdSe and CdS without preadsorbed CdS quantum dots layer with a transient grating (TG) technique.

4. Conclusion

We have described the performance of quantum dot-sensitized solar cells (QDSCs) based on CdSe QD sensitizer on a pre-adsorbed CdS layer (combined CdS/CdSe QDs) together with the basic studies of optical absorption and photoelectrochemical current characteristics. It can be observed from optical absorption measurements using photoacoustic (PA) spectroscopy that the CdSe QDs on the nanostructured TiO_2 electrodes with a pre-adsorbed CdS layer grow more rapidly during the initial adsorption process than those without a pre-adsorbed CdS layer. Photoelectrochemical current in the visible light region due to the adsorbed CdSe QDs can be observed, indicating the photosensitization by combined CdS/CdSe QDs. The maximum IPCE value (~ 75%) of the CdSe QDs on the nanostructured TiO_2 electrodes with a pre-adsorbed CdS QD layer is 30% greater than that without a pre-adsorbed CdS layer. It indicates the possibilities of a decrease in recombination centers, interface states, and inverse transfer rate that is suggested by the preliminary ultrafast photoexcited carrier carrier dynamics characterization owing to the possibilities of active CdSe QDs by the excess Cd remaining after CdS adsorption and passivation effect of CdS QDs on the nanostructured TiO_2 surface. The short-circuit current (J_{sc}) in combined CdS/CdSe QD-sensitized solar cells shows

maxima with the increase of CdSe QDs adsorption times between 2 h and 24 h, also indicating the decrease of recombination centers, interface states, and the increase in quasi Fermi level. The open-circuit voltage (V_{oc}) and fill factor (FF) are independent of adsorption times. The photovoltaic conversion efficiency (η) of the combined CdS/CdSe QD-sensitized solar cell shows a maximum value of 3.5%.

5. References

Bawendi, M. G.; Kortan, A. R.; Steigerwals, M.; & Brus, L. E. (1989), *J. Chem. Phys*., Vol. 91, p. 7282.

Chiba, Y.; Islam, A.; Watanabe, Y.; Koyama, R.; Koide, N.; & Han, L. (2006), *Jpn. J. Appl. Phys*.Vol. 43, p. L638.

Diguna, L. J.; Shen, Q.; Kobayashi, J.; & Toyoda, T (2007), *Appl. Phys. Lett*., Vol. 91, p. 023116.

Giménez, S; Mora-Seró, I; Macor, L.; Guijarro, N.; Lala-Villarreal, T.; Gómez, R.; Diguna, L.;Shen, Q.; Toyoda, T; & Bisquert, J (2009), *Nanotechnology*, Vol. 20, p. 295204.

Gorer, S.; & Hodes, G. (1994), *J. Phys. Chem*., Vol. 98, p. 5338.

Hines, M. A.; & Sionnet, P. G. (1996), *J. Phys. Chem*., Vol. 100, p. 468.

Hodes, G; Manassen, J; & Cahen, D. (1980), *J. Electrochem. Soc*., Vol. 127, p. 544.

Inoue, Y.; Toyoda, T; & Morimoto, J (2006), *Jpn. J. Appl. Phys*., Vol. 45, p. 4604.

Jayakrishnan, R.; Nair, J. P.; Kuruvilla, B. A.; & Pandy, R. K. (1996) *Semicond. Sci. Tech*., Vol. 11, p. 116.

Katayama, K.; Yamaguchi, M.; & Sawada, T. (2003), *Appl. Phys. Lett*., Vol. 82, p. 2775.

Klimov, V. I. (2006), *J. Phys. Chem. B*, Vol. 110, p. 16827.

Lee, Y-L.; & Lo, Y-S. (2009), *Adv. Func. Mater*., Vol. 19, p. 604.

Mora-Seró, I; Giménez, S; Fabregat-Santiago, F.; Gómez, R.; Shen, Q.; Toyoda, T; & Bisquert, J. (2009), *Acc. Chem. Res*., Vol. 42, 1848.

Niitsoo, O.; Sarkar, S. K.; Pejoux, P.; Rühle, S.; Cahen, D.; & Hodes, G., *J. Photochem. Photobiol. A*, Vol. 182, 306.

Nozik, A. J. (2002), *Physica E*, Vol. 14, p. 16827.

O'Regan, B.; & Grätzel (1991), *Nature*, Vol. 353, p. 737.

Rosencwaig, A. & Gersho, A. (1977), *J. Appl. Phys*., Vol. 47, p. 64.

Schaller, R. D.; Sykora, M.; Pietryga, J. M.; & Klimov, V. I. (2006), *Nono Lett*., Vol. 6. P. 424.

Shen, Q.; & Toyoda, T (2004), *Jpn. J. Appl. Phys*., Vol. 43, p. 2946.

Shen, Q.; Arae, D.; & Toyoda, T. (2004), *J. Photochem. Photobiol. A*, Vol. 164, p. 75

Shen, Q.; Kobayashi, J.; Doguna, L. J.; & Toyoda, T. (2008), *J. Appl. Phys*., Vol. 103, p. 084304.

Shen, Q.; Ayuzawa, Y.; Katayama, K.; Sawada, T.; & Toyoda, T. (2010), Appl. Phys. Lett., Vol. 97, p. 263113.

Shockley, W.; & Queisser, H. J. (1961), *J. Appl. Phys*., Vol. 32, p. 510.

Sudhager, P.; Jung, J. H.; Park, S; Lee, Y-G.; Sathyamamoorthy, R.; Kang, Y. S.; & Ahn, H.(2009), *Electrochem. Commun*., Vol. 11, p. 2220.

Tam, A. C. (1986), *Rev. Mod. Phys*., Vol. 58, p. 381.

Toyoda, T.; Uehata, T.; Suganuma, R.; Tamura, S; Sato, A; Yamamoto, K.; Shen, Q. & Kobayashi, N. (2007), *Jpn. J. Appl. Phys*., Vol. 46, p. 4616.

Toyoda, T; Tsugawa, S.; & Shen, Q. (2009), *J. Appl. Phys*., Vol. 105, p. 034314.

Trinh, M. T.; Houtepen, A. J.; Schints, J. M; Hanrath, T.; Piris, J.; Knulst, W.; Goossens, P. L. M.; & Siebbeles, L. D. A. (2008), *Nano Lett*, Vol. 8, p. 1713

Yamaguchi, M.; Katayama, K.; & Sawada, T. (2003), *Chem. Phys. Lett*., Vol. 377, p. 589.

Underwood, D. F.; Kippeny, T.; & Rosenthal, S. J. (2001), Eur. Phys, J. D, Vol. 16, p. 241.

Yang, S. M.; Huang, C. H.; Zhai, J.; Wang, Z. S.; & Liang, L. (2002), J. Mater. Chem., Vol. 12,p. 1459.

23

Investigation of Lattice Defects in GaAsN Grown by Chemical Beam Epitaxy Using Deep Level Transient Spectroscopy

Boussairi Bouzazi[1], Hidetoshi Suzuki[2], Nobuaki Kijima[1], Yoshio Ohshita[1] and Masafumi Yamaguchi[1]
[1]*Toyota Technological Institute*
[2]*Myazaki University*
Japan

1. Introduction

With only 3 % of N and 9 % of In, InGaAsN with a band gap of 1.04 eV was obtained and could be lattice matched to GaAs and Ge. This dilute nitride semiconductor has been selected as a promising candidate for high efficiency multijunction tandem solar cells (Geisz and Friedman, 2002). However, the diffusion length of minority carriers and the mobility are still lower than of that in GaAs or InGaAs and showed a considerable degradation with increasing the N concentration. These electrical properties are insufficient to insure the current matching in the multijunction solar cell structure AlInGaP/GaAs/InGaAsN/Ge (Friedman et al., 1998). An obvious reason of such degradation is the high density of N-related lattice defects that can be formed during growth to compensate for the tensile strain caused by the small atomic size of N compared with that of arsenic (As) and to the large miscibility of the gap between GaAs and GaN. These defect centers are expected to act as active recombination and/or scattering centers in the forbidden gap of the alloy (Zhang & Wei, 2001). However, no experimental evidence has yet been reported. On the other hand, the conductivity of undoped *p*-type InGaAsN or GaAsN and their high background doping (Friedman et al., 1998; Kurtz et al., 1999; Moto et al., 2000; Krispin et al., 2000) prevent the design of wide depletion region single junction solar cell and the fabrication of intrinsic layer to overcome the short minority carrier lifetime. This serious problem was expected in the first stage to the density of unintentional carbon in the film (Friedman et al., 1998; Kurtz et al., 1999; Moto et al., 2000). However, the carrier density in some InGaAsN semiconductors was found to be higher than that of carbon (Kurtz et al., 2002). Furthermore, the high density of hydrogen (up to 10^{20} cm^{-3}) and the strong interaction between N and H in InGaAsN to form N-H related complex were confirmed to be the main cause of high background doping in InGaAsN films (Li et al., 1999; Janotti et al., 2002, 2003; Kurtz et al., 2001, 2003; Nishimura et al., 2007). In addition, N-H complex was found theoretically to bind strongly to gallium vacancies (V_{Ga}) to form N-H-V_{Ga} with a formation energy of 2 eV less than that of isolated V_{Ga} (Janotti et al., 2003). These predictions were supported experimentally using positron annihilation spectroscopy results (Toivonen et al., 2003).

On the other hand, similar electrical properties were obtained in InGaAsN grown by metal-organic chemical vapor deposition (MOCVD) and molecular beam epitaxy (MBE) despite the large difference in the density of residual impurities, which excludes them as a main cause of low mobilities and short minority carrier lifetimes. For that, lattice defects, essentially related to the N atom, were expected to be the main reason of such degradation. Several theoretical and experimental studies have investigated carrier traps in InGaAsN films. Theoretically, using the first principles pseudo-potential method in local density approximation, four N-related defects were proposed: $(As_{Ga}\text{-}N_{As})_{nn}$, $(V_{Ga}\text{-}N_{As})_{nn}$, $(N\text{-}N)_{As}$, and $(N\text{-}As)_{As}$ (Zhang & Wei, 2001). While the two first structures were supposed to have lower formation probabilities, the two split interstitials $(N\text{-}N)_{As}$, and $(N\text{-}As)_{As}$ were suggested to compensate the tensile strain in the film and to create two electron traps at around 0.42 and 0.66 eV below the conduction band minimum (CBM) of InGaAsN with a band gap of 1.04 eV, respectively (Zhang & Wei, 2001). Experimentally, the ion beam analysis provided a quantitative evidence of existence of N-related interstitial defects in GaAsN (Spruytte et al., 2001; Ahlgren et al., 2002; Jock, 2009). Furthermore, several carrier traps were observed in GaAsN and InGaAsN using deep level transient spectroscopy (DLTS). A deep level (E2/H1), acting as both an electron and a hole trap at 0.36 eV below the CBM, was observed (Krispin et al., 2001). Other electron traps in GaAsN grown by MBE were recorded: A2 at 0.29 eV and B1 at 0.27 eV below the CBM of the alloy (Krispin et al., 2003). In addition, a well known electron trap at 0.2 ~ 0.3 eV and 0.3 ~ 0.4 eV below the CBM of *p*-type and *n*-type GaAsN grown by MOCVD were observed, respectively (Johnston et al., 2006). Although the importance of these results as a basic knowledge about lattice defects in GaAsN and InGaAsN, no recombination center was yet experimentally proved and characterized. Furthermore, the main cause of high background doping in p-type films was not completely revealed.

Chemical beam epitaxy (CBE) has been deployed (Yamaguchi et al., 1994; Lee et al., 2005) to grow (In)GaAsN in order to overcome the disadvantages of MOCVD and MBE. It combines the use of metal-organic gas sources and the beam nature of MBE. (In)GaAsN films were grown under low pressure and low temperature to reduce the density of residual impurities and to avoid the compositional fluctuation of N, respectively. Furthermore, a chemical N compound source was used to avoid the damage of N species from N_2 plasma source in MBE. Although we obtained high quality GaAsN films gown by CBE, the diffusion length of minority carriers is still short (Bouzazi et al., 2010). This indicates that the electrical properties of GaAsN and InGaAsN films are independent of growth method and the problem may be caused by the lattice defects caused by N. Therefore, it is necessary to investigate these defects and their impact on the electrical properties of the film. For that, this chapter summarizes our recent results concerning lattice defects in GaAsN grown by CBE. Three defect centers were newly obtained and characterized. The first one is an active non-radiative *N*-related recombination center which expected to be the main cause of short minority carrier lifetime. The second lattice defect is a N-related acceptor like-state which greatly contributes in the background doping of p-type films. The last one is a shallow radiative recombination center acceptor-like state.

2. Deep level transient spectroscopy

To characterize lattice defects in a semiconductor, several techniques were used during the second half of the last century. Between these methods, we cite the thermally stimulated

current (TSC) (Leonard & Grossweiner, 1958; Bube, 1960), the admittance spectroscopy (Losee, 1974), the increase or decay curves of photoconductivity (Rose, 1951; Devore, 1959), the optically stimulated conductivity (Lambe, 1955; Bube, 1956), and the analysis of space-charge-limited currents as function of applied voltage (Smith & Rose, 1955; Rose, 1955; Lampert, 1956). The basic concept of using the change of capacitance under bias conditions by the filling and emptying of deep levels was already anticipated fifty years ago (Williams, 1966). The thermally stimulated capacitance (TSCAP), which gives the temperature dependence of junction capacitance (Sah et al., 1978; Sah & Walker, 1973), was used. By dressing the properties of all these techniques, D. V. Lang found that they lacked the sensitivity, the speed, the depth range of recorded trap, and the spectroscopic nature to make them practical for doing spectroscopy on non-radiative centers. For that, in 1974, he proposed DLTS as a characterization method of lattice defects that can overcome the disadvantages of the other methods (Lang, 1974). DLTS is based on the analysis of the change of capacitance due to a change in bias condition at different temperatures. It can be applied to Schottky contacts and *p*-*n* junctions. DLTS has advantages over TSC due to its better immunity to noise and surface channel leakage currents. It can distinguish between majority and minority carrier traps, unlike TSC, and has a strong advantage over admittance spectroscopy, which is limited to majority-carrier traps. Comparing with TSCAP, DLTS has much greater range of observable trap depths and improved sensitivity. Despite the success of optical techniques such as photoluminescence to characterize superficial levels, they are rarely used in the study of non-radiative deep levels. Furthermore, such experiences must be done in the infrared domain. However, sensors are less sensitive than in the visible domain. Thus, we need a technique, which can separate between minority and majority traps and evaluate their concentrations, their energies, and their capture cross sections.

2.1 Fundamental concept of DLTS

2.1.1 Capacitance transient

To fully understand DLTS, it is worth to have a basic knowledge of capacitance transients arising from the SCR of Schottky contacts or p^+-n/n^+-p asymmetric junctions. If a pulse voltage is applied to one of these device structures that is originally reverse-biased, the SCR width decreases and the trap centers are filled with carriers (majority or minority depending on the structure). When the junction is returned to reverse bias condition, the traps that remains occupied with carriers are emptied by thermal emission and results in a transient decay. The capacitance transients provide information about these defect centers. Here, we restrain our description to a p^+-n junction where the p-side is more much heavily doped than the n-side, which gives the SCR almost in the low doped side.

The causes of change in capacitance depend on the nature of applied voltage. In case of reverse biased voltage, the junction capacitance, due to the change in SCR width, is dominant. However, when the applied voltage is forward biased, the diffusion capacitance, due to the contribution of minority carrier density, is dominant. The basic equation governing the capacitance transient in the p^+-n junction is expressed by

$$C(t) = A\sqrt{\frac{\varepsilon\varepsilon_0 e\, N_D}{2(V_R + V_b)}}\left[1 - \frac{N_T}{2N_D}\exp\left(-\frac{t}{\tau}\right)\right] = C_0\left[1 - \frac{N_T}{2N_D}\exp\left(-\frac{t}{\tau}\right)\right] \quad (1)$$

where A is the contact area, V_b is the built-in potential, $\varepsilon\varepsilon_0$ is the permittivity of the semiconductor material, and e is the elementary charge of an electron. C_0, N_T, N_D, and τ

denote the junction capacitance at reverse bias, the density of filled traps under steady state conditions, the ionized donor concentration, and the time constant that gives the emission rate, respectively. The change in capacitance after the recharging of traps is given by

$$\Delta C = C_0\sqrt{1-\frac{N_T}{N_D}} \tag{2}$$

In most cases of using transient capacitance, the trap centers form only a small fraction of the SCR impurity density, i.e., $N_T << N_D$. Hence, using a first-order expansion of Eq. (2) gives

$$\left|\Delta C\right| = C_0\left|1-N_T/2N_D\right| \cong C_0 N_T/2N_D \tag{3}$$

Thus, the trap concentration calculates from the capacitance change ΔC is expressed by

$$N_T = 2\frac{\Delta C}{C_0}N_D \tag{4}$$

Note that Eq. (3) assumes that $N_T << N_D$ and the traps are filled throughout the total depletion width. To be more accurate, N_T should be adjusted to N_{Tadj} according to [30]

$$N_{Tadj} = 2\frac{\Delta C}{C_0}N_D\frac{W_R^2}{L_1^2-L_2^2} \tag{5}$$

where W_R is the total SCR at reverse bias voltage V_R, $L_1 = W_R - \lambda$, $L_2 = W_p - \lambda$, and

$$\lambda = \left(\frac{2\varepsilon\varepsilon_0}{e^2N_D}(E_F-E_T)\right)^{1/2} \tag{6}$$

where W_p, E_F, and E_T denote the SCR at V_p, the Fermi level, and the trap energy level.

2.1.2 Thermal emission of carriers from deep levels

The emission rates for electrons and holes are given, respectively by

$$e_n = \sigma_n v_{thn} N_c \exp\left(-\frac{E_{CBM}-E_T}{kT}\right) \tag{7}$$

$$e_p = \sigma_p v_{thp} N_v \exp\left(-\frac{E_T-E_{VBM}}{KT}\right) \tag{8}$$

where σ_n, N_c, and v_{thn} are the thermal capture cross section, the density of states, and the thermal velocity of holes, respectively. σ_p, N_v, and v_{thp} are the same parameters for holes. E_{CBM}, E_{VBM}, and E_T are the energy levels of the conduction band minimum, the valence band maximum, and the trap, respectively.

2.2 Other DLTS related techniques

The isothermal capacitance transient spectroscopy (ICTS) and the double carrier pulse DLTS (DC-DLTS) are two DLTS related methods. They are used to obtain the density profiling of lattice defects and to check whether they act as recombination centers or not, respectively.

2.2.1 Isothermal capacitance transient spectroscopy

ICTS is used to analyze the profiling of lattice defects in the SCR of the semiconductor. It can be done through three different methods. The first one is obtained by fixing V_R and varying V_p to build difference of transients among the SCR of the device. The second method is evaluated by measuring at constant V_p and varying V_R. The last option is obtained by varying V_R and V_p, where the profiling analysis is also possible without building difference of transients. Using the first method, the medium trap density $\overline{N}_T(x_{ij})$ at a point x_{ij} is given by

$$\overline{N}_T(x_{ij}) = \frac{2\,N_D(\varepsilon\varepsilon_0)^2 A^2}{C_R^3}\frac{\Delta C_{ij}}{(L_{Pi}^2 - L_{Pj}^2)} \tag{9}$$

where ΔC_{ij} is the amplitude difference of the two capacitance transients.

2.2.2 Double carrier pulse DLTS

DC-DLTS is used in asymmetric n^+-p or p^+-n junctions (Khan et al., 2005). It aims to check whether a trap is a recombination center or not. As shown in Fig. 1, two pulsed biases are applied to the sample, in turn, to inject majority and minority carriers to an electron trap. At the initial state, the junction is under reverse bias, and the energy level E_T of the trap is higher than the Fermi level (E_{Fn}).When the first pulse voltage is applied to the sample, E_{Fn} is higher than E_T, which allows the trap to capture electrons. During the second reverse biased pulse, with a duration t_{ip}, holes are injected to the SCR from the p–side of the junction. After the junction pulse is turned off, electrons and holes are thermally emitted. The amount of trapped carriers can be observed as a change in the DLTS peak height of the trap. If the trap captures both electrons and holes, the DLTS maximum of the corresponding level decreases compared with that in conventional DLTS. Such a decrease is explained by the electron–hole (e–h) recombination process, which indicates that the level is a recombination center.

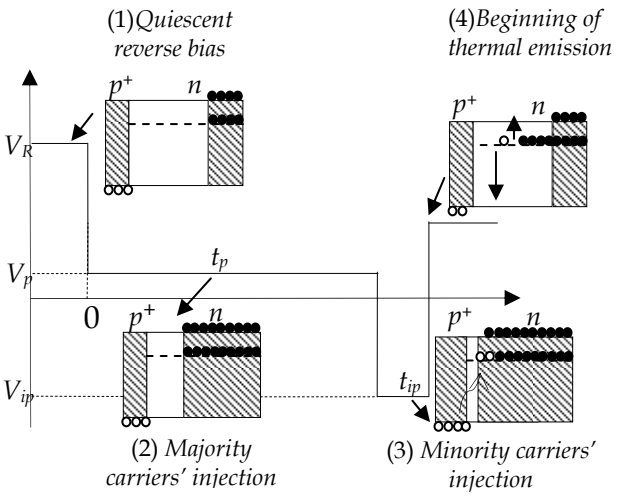

Fig. 1. Basic concept of capture and thermal emission processes from an electron trap located at an energy level E_T in p^+-n junction. A saturating injection pulse is applied to the reverse biased junction to fill the trap with holes.

To formulate the recombination process, we consider the same notation in § 2.1.2, with assuming that $n \approx N_D$. The relationship between the total density of recombination centers and that only occupied by electrons in the n-side of the junction can be expressed by

$$\frac{dn_T}{dt} = -e_p n_T(t) + \langle p \rangle c_p [N_T - n_T(t)] - N_D c_n n_T(t) + e_n [N_T - n_T(t)] \tag{10}$$

where $\langle p \rangle$ is the average of injected holes. As a solution of Eq. (10), we have

$$\frac{dn_T}{dt} = n_T(t_{ip}) = n_T(\infty) + [n_T(0) - n_T(\infty)] \exp(-\frac{t_{ip}}{\tau}) \tag{11}$$

where $n_T(\infty) = (\langle p \rangle c_p + e_n)/(\tau^{-1} N_T)$, $\tau^{-1} = \langle p \rangle c_p + N_D c_n + e_n + e_p$), and t_{ip} is the width of the injected pulse. Considering the I_{DLTS} and $I_{DC\text{-}DLTS}$ the peak heights of the recombination center in conventional and DC-DLTS, respectively. Equation (11) can be rewritten properly as

$$\frac{n_T(t_{ip})}{N_T} = \frac{(I_{DLTS} - I_{DCDLTS})}{I_{DCDLTS}} = \langle p \rangle \sigma_p v_{thp} t_{ip} \tag{12}$$

Similarly for hole trap in the *p*-side of a n^+-*p* junction, which acts as recombination center, we obtain

$$\frac{n_T(t_{ip})}{N_T} = \frac{(I_{DLTS} - I_{DCDLTS})}{I_{DCDLTS}} = \langle n \rangle \sigma_n v_{thn} t_{ip} \tag{13}$$

where $\langle n \rangle$ is the average of injected electrons.

3. Experimental procedure

All GaAsN films were grown by CBE on high conductive *n*- or *p*-type GaAs 2° off toward [010] substrate using Triethylgallium ($(C_2H_5)_3Ga$, TEGa), Trisdimethylaminoarsenic ($[(CH_3)_2N]_3As$, TDMAAs), and Monomethylhydrazine ($CH_3N_2H_3$, MMHy) as Ga, As, and N sources, respectively. The flow rates TEGa = 0.1 sccm and TDMAAs = 1.0 sccm were considered as conventional values. The growth temperatures of 420 °C and 460 °C were used for *p*-type and *n*-type GaAsN, respectively. Concerning the doping, *p*-type GaAsN films are unintentionally doped. The n-type alloys were obtained using a silane (SiH_4) source or by growing the films under lower MMHy and high growth temperature.

Three different device structures are used in this study: (*i*) *n*- and *p*-type GaAsN schottky contacts, (*ii*) n^+-GaAs/*p*-GaAsN/*p*-GaAs, and (*iii*) *n*-GaAsN/p^+-GaAs hetro-junctions. The *N* concentration in all GaAsN layers was evaluated using XRD method. Aluminum (*Al*) dots with a diameter of 0.5/1 *mm* were evaporated under vacuum on the surface of each sample. Alloys of *Au-Ge* (88:12 %) and *Au-Zn* (95:05 %) were deposited at the bottom of *n*-type and *p*-type GaAs substrates for each device, respectively. Some samples were treated by post-thermal annealing under N_2 liquid gas and using GaAs cap layers to avoid As evaporation from the surface. The temperature and the time of annealing will be announced depending on the purpose of making annealing. The background doping and the doping profile in the extended depletion region under reverse bias condition were evaluated using the capacitance-voltage (C-V) method. The leakage current in all used samples ranged from 0.3

*n*A to 10 μA for a maximum reverse bias voltage of -4 V. A digital DLTS system *Bio-Rad DL8000* was used for DLTS and C-V measurements. The activation energy E_t and the capture cross section $\sigma_{n,p}$ were determined from the slope and the intercept values of the Arrhenius plot, respectively.

4. Lattice defects in GaAsN grown by CBE

In this section, the distribution of electron and hole traps in the depletion region of GaAsN grown by CBE will be dressed using DLTS and related methods.

4.1 Electron traps in GaAsN grown by CBE

4.1.1 DLTS spectra and properties of a N-related electron trap

The DLTS spectrum of Fig. 2(a) shows an electron trap (*E*2) at 0.69 eV below the CBM of GaAs. After rapid thermal annealing at 720°C for 2 min, *E*2 disappears completely whereas a new electron trap (*E*3) appears at 0.34 eV below the CBM. From the Arrhenius plots of Fig. 2(d), the capture cross sections of *E*2 and *E*3 are calculated to be σ_{E2} = 8.1 × 10^{-15} cm² and σ_{E3} = 7.5 × 10^{-18} cm², respectively. Based on previous results about native defects in *n*-type GaAs, *E*2 and *E*3 are independent of *N* and considered to be identical to *EL*2 and *EL*3, respectively (Reddy et al., 1996). In order to focus only on *N*-related lattice defects, these two energy levels will be excluded from the DLTS spectra of *N*–containing *n*-type GaAsN. The addition

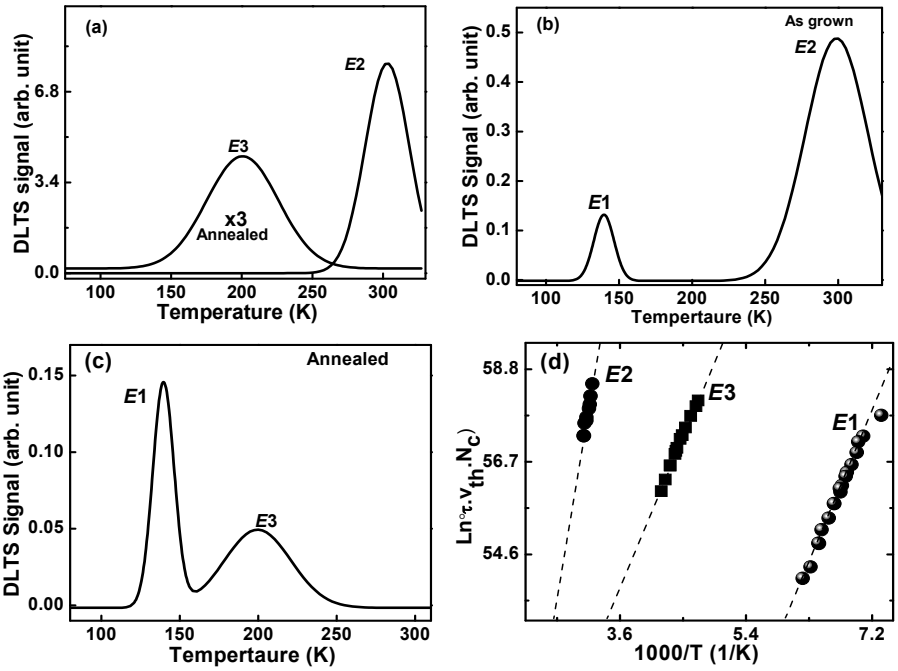

Fig. 2. DLTS spectra of (a) *N* free as grown and annealed GaAs, (b) as grown n-type $GaAs_{0.998}N_{0.002}$, (c) annealed n-type $GaAs_{0.998}N_{0.002}$, and (d) Arrhenius plots of DLTS spectra.

of a small atomic fraction of *N* to GaAs leads to the record of a new electron trap (*E*1), at an average activation energy 0.3 eV below the CBM of GaAsN. The DLTS spectra of as grown and annealed *n*-type $GaAs_{0.998}N_{0.002}$ are given in Figs. 2. (b) and (c), respectively. The activation energies (E_{E1}) and the capture cross sections (σ_{E1}) of *E*1 for *N* varying GaAsN samples are given Fig. 3 (a) and (b), respectively. The fluctuation of E_{E1} from one sample to another can be explained by the effect of Poole–Frenkel emission, where the thermal emission from *E*1 is affected by the electric field (Johnston and Kurtz, 2006). As illustrated in Fig. 3(c), with increasing the filling pulse duration, the DLTS peak height of *E*1 saturates

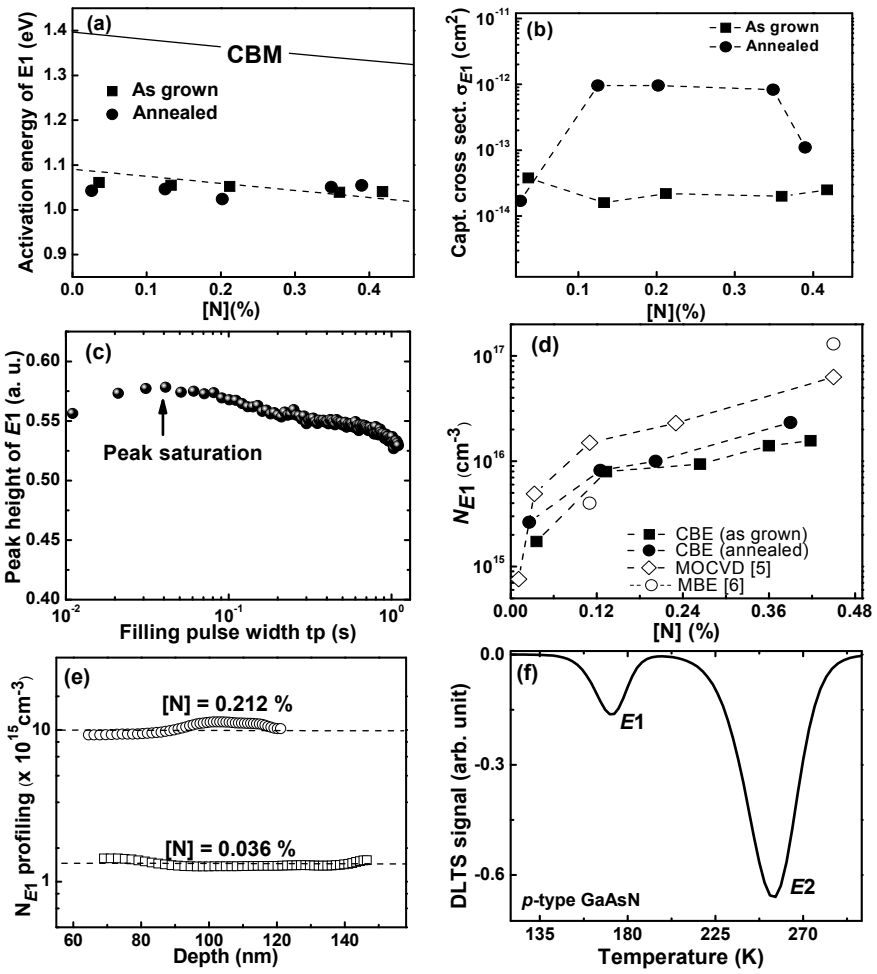

Fig. 3. Nitrogen dependence of (a) thermal activation energy, (b) capture cross section, and (d) adjusted density of *E*1 in as grown and annealed GaAsN samples. The large capture cross section is confirmed with (c) the filling pulse width dependence of the DLTS peak height of *E*1. (e) Density profiling of *E*1 in the bulk of GaAsN films, and (f) DLTS spectrum of undoped *p*-type GaAsN grown by CBE.

rapidly. This behavior is explained by the large value of σ_{E1}, compared with that of *E*2, *E*3, and other native defects in GaAs. The adjusted densities of *E*1 (N_{E1}) in as grown and annealed samples are plotted in Fig. 3(d). N_{E1} increases considerably with increasing [*N*] in the film and persists to post thermal annealing. This indicates that *E*1 is a *N*-related and a stable electron trap.

The defect center *E*1 was not observed previously in *N* free GaAs grown by CBE despite the existence of *N* species in the chemical composition of the As source. This can be explained through three possible scenarios. First, the absence of tensile strain in GaAs prevents the formation of *E*1. Second, the *N* atom in the atomic structure of *E*1 comes from the *N* source. Finally, the *N* atom comes from the *N* and *As* compound sources and in presence of tensile strain *E*1 can be formed. The tensile strain was reported in most theoretical and experimental studies. As given in Fig. 3(e) and using the ICTS, this idea is supported by the uniform distribution of N_{E1} in the bulk of GaAsN. This indicates that *E*1 is formed during growth to compensate for the tensile strain in the GaAsN films caused by the small atomic size of N compared with that of As.

Furthermore, the properties of *E*1 are identical to that of the famous electron traps reported by Johnston et Kurtz (Johnston and Kurtz, 2006) and Krispin et al. (Krispin et al., 2003) in MOCVD and MBE grown *n*–type GaAsN, respectively. As illustrated in Fig. 3(d), the densities of these traps are approximately similar to N_{E1} despite the large difference in the density of residual impurities between the three growth methods. Therefore, the atomic structure of *E*1 may be free from impurities. Furthermore, by carrying out DLTS measurements for minority carriers in undoped *p*-type film, *E*1 was also observed. This indicates clearly that *E*1 is independent of doping atoms (see Fig. 3(f)).

4.1.2 Nature of the electron trap E1

Two methods are used to verify whether *E*1 is a recombination center or not. The first method is indirect, in which the activation energy of deep levels is correlated with that of the reverse bias current in the depletion region of *n*-type GaAsN Schottky junction and n^+-GaAs/*p*-GaAsN heterojunction. These two device structures are selected because the current is due mainly to electrons. The second method is direct, in which DC-DLTS is used to show the behavior of the electron traps in simultaneous injection of majority and minority carriers in the depletion region.

4.1.2.1 Origin of reverse bias current in GaAsN

The temperature dependence of the reverse bias current in the depletion region of *n*-type GaAsN Schottky junction and n^+-GaAs/*p*-GaAsN is shown in Fig. 4(a) for reverse bias voltages of 0.5 and -0.5 V, respectively. At lower temperature, the dark current changes slowly in the two structures, then fellows an Arrhenius type behavior. As shown in Fig. 4(b), the same result is obtained by applying reverse bias voltages of 1 and -1 V. Under these conditions, the reverse bias current $I_d(T)$ can be expressed by

$$I_d(T) = I_\infty \exp(-\frac{\Delta E}{kT}) \tag{14}$$

where I_∞, ΔE, *k*, and *T* denote the limit of the high-temperature current, the thermal activation energy of the reverse bias current, the Boltzmann constant, and the temperature, respectively. The I-V characteristics deviate in the two samples from the thermionic emission. This is

explained by the fact that supplying the *p*-*n* junction under reverse bias conditions decreases the product of excess carriers to less than the square of intrinsic carriers. Hence, the Shockley-Read-Hall (SRH) generation mechanism is activated to increase the product of excess carriers to assure the balance of charge. The generated carriers are swept to the transition regions by the electric field in the depletion region. Therefore, an SRH center, with a thermal activation energy arround 0.3 eV, is the origin of the dark current in the SCR of GaAsN. The thermal activation energies are measured with respect to majority and minority carriers in *n*-type GaAsN schottky junction and n^+-GaAs/*p*-GaAsN heterojunction, respectively. This corresponds to the conduction band in the two structures. By correlating the conduction mechanism and DLTS measurements, the thermal activation energy of the reverse bias current and the activation energy of the *N*-related electron trap *E*1 are typically identical. Therefore, *E*1 is responsible for the generation/recombination current in the depletion region of GaAsN grown by CBE.

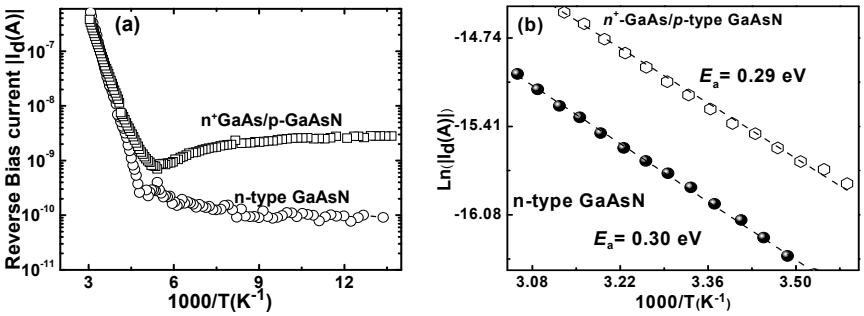

Fig. 4. Temperature dependence of dark current under reverse bias voltages of (a) 0.5 and -0.5V and (b) 1 and -1V in *n*-type GaAsN schottky junction and the n^+-GaAs/*p*-GaAsN heterojunction, respectively.

4.1.2.2 DC-DLTS measurements

DC-DLTS is used to confirm the recombination nature of *E*1 and to characterize the recombination process via this defect center. An unintentionally doped *n*–type GaAsN layer (~ 1 μm) was grown on a *p*–type GaAs by CBE. This structure is not commonly used for DLTS measurements. However, the absence of a *p*-type doping source prevented us to obtaining a p^+-*n* junction. Here, the *p*-type substrate is used as source of minority carriers. As shown in Fig. 5(a), the DC-DLTS spectrum is compared with that of the conventional DLTS. A decrease in the peak height of *E*1 is observed by varying the voltage of the second injected pulse and also confirmed by varying its duration. The obvious reason for such reduction is the mechanism of *e*-*h* recombination at the energy level *E*1 in the forbidden gap of GaAsN. Hence, *E*1 is reconfirmed to act as a *N*-related recombination center. To verify the non-radiative recombination process, the temperature dependence of σ_{E1} is obtained by varying the emission rate window e_{rw} from 0.5 - 50 s^{-1}. The value of σ_{E1} is obtained from the fitting of the Arrhenius plots for each e_{rw}. As shown in Fig. 5(b), the natural logarithmic of σ_{E1} shows a linear increase with the reciprocal of the temperature. It can be expressed as

$$\ln(\sigma_{E1}) = -E_{cap,e}/kT + \ln(\sigma_{\infty}) \tag{15}$$

where $E_{cap,e}$ = 0.13 ± 0.02 eV, *k*, *T*, and σ_{∞} = 1.38 x 10^{-9} cm^2 denote the barrier height for the capture of electron, the Boltzmann constant, the temperature, and the capture cross section of

electrons at an infinite temperature, respectively. At room temperature, σ_{E1}(300 K) is evaluated to ~ 8.89 × 10^{-12} cm^2. Such a value is large enough to shorten the lifetime of electrons in *p*-type GaAsN. This indicates that *E*1 is a strongly active recombination center at room temperature and the *e-h* recombination process is non-radiative. In addition, from the temperature dependence of σ_{E1}, the true energy depth of *E*1 can be obtained by subtracting the barrier height for electron capture from the thermal activation energy obtained from the Arrhenius plot. The recombination center *E*1 is localized at E_a (*E*1) = 0.20 ± 0.02 eV from the CBM of GaAsN. Furthermore, the average capture cross section of holes σ_p, at a temperature of T = 175 K, is estimated using Eq. 12 to be σ_p(175 K) ~ 5.01 × 10^{-18} cm^2. The physical parameters of *E*1 can be summarized in a configuration coordinate diagram (CCD), in which the energy state of *E*1 is described as a function of lattice configuration (Q). As shown in Fig. 5(c), the CCD of *E*1 can be presented in three different branches: (*i*)[0, f.e + f.h]: the charge state of *E*1 is neutral, with a free electron and a free hole, (*ii*)[-, t.e + f.h]: the electron is trapped and the hole remains free, (*iii*)[0]: the free hole is captured at the crossed point B and recombined with the already-trapped electron. *E*1 losses its charge and becomes neutral. As the recombination process is non-radiative, the lattice relaxation occurs with the emission of multi-phonon. The energy of multi-phonon emission can be evaluated as function of N concentration according to

$$E_{phonon}(N) = E_g(N) - (E_a(E1) - E_{cap,e}) \tag{16}$$

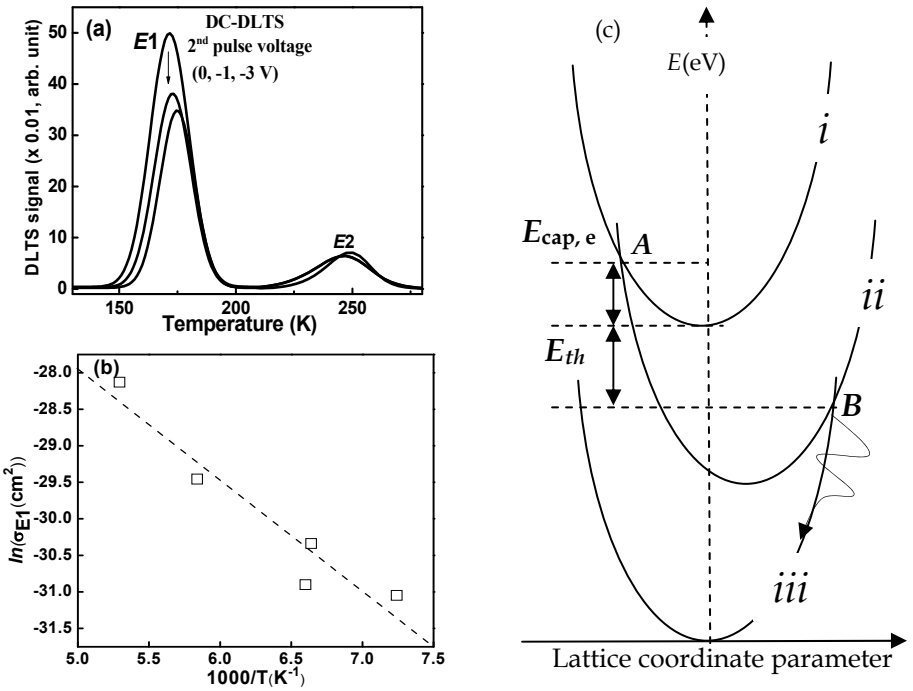

Fig. 5. (a) Reduction of peak height of *E*1 under minority carrier injection spectra, (b) temperature dependence of σ_{E1} for electrons, and (c) Configuration-coordinate-diagram showing the different charge states of E1 as function of lattice coordinate parameter.

4.1.3 Possible origin of the N-related recombination center E1

It is worth remembering that the atomic structure of *E*1 may be free from impurities and doping atoms owing to the difference in the density of residual impurities in GaAsN grown with MOCVD, MBE, and CBE. Furthermore, the uniform distribution of N_{E1} in the bulk of GaAsN indicates that *E*1 is formed during growth to compensate for the tensile strain caused by the small atomic size of N compared with that of As. Therefore, the origin of *E*1 has high probability to depend only on the atoms of the alloy (N, As, Ga). To confirm these expectations, the origin of *E*1 is investigated qualitatively by considering the results of two different experiments: (*i*) the dependence of N_{E1} to the As source flow rate and (*ii*) the effect of H implantation on the distribution of lattice defects in *n*-type GaAsN.

4.1.3.1 Dependence of N_{E1} to As source flow rates

The objective of this experiment is to clarify whether the density of *E*1 is sensitive to the As atom or not. The MMHy was supplied to 9.0 sccm and the TDMAAs was varied between and 0.7 and 1.5 sccm. As shown in Fig. 6. (a), increasing TDMMAs drops the *N* concentration in the film and tends to saturate for a flow rate higher than 1 sccm. For two emission rate e_{rw} = {100, 10} s^{-1} and filling pulse t_p = {0.1, 5} ms values, the DLTS spectra are normalized on the junction capacitance to exclude the effect of various carrier densities in the samples. The same *N*-related recombination center *E*1 was observed in all samples. The TDMAAs flow rate dependence of the DLTS peak height of *E*1 for two settings of measurement parameters is given in Fig. 6(b). A peaking behavior at approximately TDMAAs = 0.9 sccm was obtained. As N_{E1} is uniformly distributed in GaAsN films, the incorporation of *N* atom at the growth surface affects both the incorporation of N_{As} and the formation of *E*1. If *E*1 depends only on *N* atom, the decrease of [*N*] with increasing TDMMAs flow rate results in monotonically dropping of N_{E1}. However, the peaking behavior of N_{E1} indicates the sensitivity of *E*1 to As atom, either than *N*.

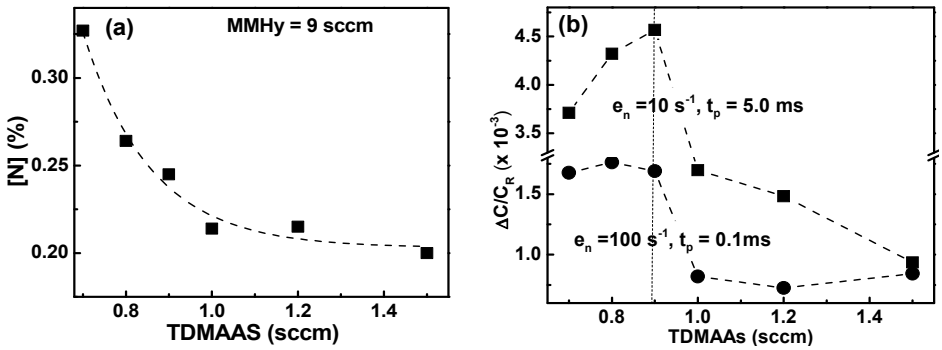

Fig. 6. TDMAAs flow rate dependence of (a) N concentration under supplied MMHy and (b) normalized DLTS peak height of E1 for two settings of measurement parameters.

4.1.3.2 Effect of H implantation on lattice defects in GaAsN

GaAsN films were treated by H implantation. This experiment was used because H bounds strongly to *N* in GaAsN films to form *N-H* complexes (Suzuki et al., 2008; Amore & Filippone, 2005). H ions with multi-energy from 10 to 48 keV were implanted into GaAsN layers with peaks concentration of 5×10^{18} ($GaAsN_{HD1}$) and 1×10^{19} atom/cm^3 ($GaAsN_{HD2}$),

respectively. The depth of implantation was thought to be distributed between 110 and 410 *nm* from the surface of GaAsN by calculating the *SRIM* 2003 simulation code (Ziegler, 1985). After implantation, the samples were treated by post thermal annealing at 500 °C for 10 min under N_2 gas and GaAs cap layers. As plotted in Fig. 7(a) and (b), the crystal quality of GaAsN films after implantation was controlled using XRD curves and C-V measurements. DLTS spectra of implanted samples are shown in Fig. 7(c). After implantation, *E*1 was not observed; however, two new lattice defects appeared. The signature and the density of these traps are summarized in Table 1. The thermal emission from them is plotted as an Arrhenius plot in Fig. 7(d).

GaAsN	Traps	E_a(eV)	σ(cm²)	$N_{t\text{-}adj}$(cm^{-3})	Possible origin
As grown	E1	E_{CM}-0.331	5.18 ×10^{-15}	3.37 ×10^{17}	$(N\text{-}As)_{As}$
Implanted	EP1	E_{CM}-0.414	8.20 ×10^{-13}	5.88 × 10^{17}	EL5 in GaAs
	HP1	E_{VM}-0.105	5.42 ×10^{-18}	1.84 × 10^{16}	N-H-V_{Ga}

Table 1. Summary of E_a, σ, adjusted $N_{t\text{-}adj}$, and possible origin of defects in as grown and implanted GaAsN samples.

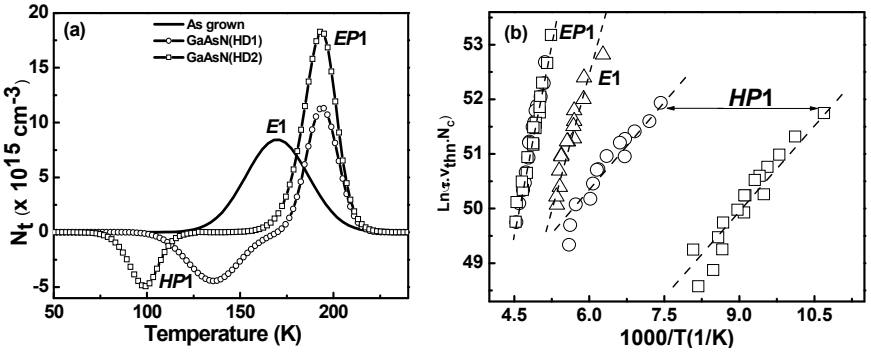

Fig. 7. (a)DLTS spectra of as grown and implanted GaAsN and (b) their Arrhenius plots.

The new electron trap (*EP*1) is located approximately 0.41 eV below the CBM of GaAsN. Its properties are identical to that of the native defect *EL*5 in GaAs (Reddy, 1996). Its atomic structure was discussed in many publications, where the common result indicated that *EL*5 is a complex defect free from impurities and dominated by As interstitials, such V_{Ga}-As_i or As_{Ga}-V_{Ga} (Deenapanray et al., 2000; Yakimova et al., 1993). The second new defect is a hole trap (*HP*1) at approximately an average activation energy 0.11 eV above the VBM of GaAsN. Compared with majority carrier traps in GaAs grown with various techniques, no similar hole trap to *HP*1 was reported. However, in *p*-type GaAsN grown by CBE with around the same *N* concentration, E_{HP1} and σ_{HP1} are identical to that of the hole trap *HC*2 in *p*-type GaAsN grown by CBE (bouzazi et al., 2011). This defect was confirmed recently to be an acceptor state in GaAsN films (see § 4.2.3) and to be related to the N-H bond. While the H impurity was provided by implantation, the N atom can originate through two possibilities: First; examining XRD results, the N atom can originate from its ideal site. However, [N] in as grown is much higher than that in implanted samples (~10^{19} cm^{-3}). It is also much higher than N_{HP1}. Second, N atom can be originated from the complete dissociation of *E*1, since the

ratio N_{E1}/N_{HP1} is less than 2. If *E*1 is the split interstitial $(N\text{-}N)_{As}$, N_{HP1} must be at least equals to that of *E*1 and one N atom remains free. This expectation is disapproved by DLTS measurements, where N_{HP1} is largely less than N_{E1}. This means that *E*1 contains only one N atom in its atomic structure. Considering the results of last sub-section, *E*1 may be the split interstitial $(N\text{-}As)_{As}$ formed from one *N* and one *As* in a single *As* site. This result is supported by the theoretical calculation (Zhang et al., 2001).

4.1.4 Effect of E1 on minority carrier lifetime in GaAsN

The effect of *E*1 on the electrical properties of GaAsN can be evaluated through the calculation of minority carrier lifetime using the SRH model for generation–recombination (Hall, 1952; Shockley & Read, 1952). Such parameter has been estimated to be less than 0.2 ns as a result of the calculation according to

$$\tau_{E1} = \left(v_{thn}\sigma_{E1}N_{E1}\right)^{-1} < 0.2\ ns \tag{17}$$

Therefore, E1 is considered to be the main cause of short minority carrier in GaAsN. It is required to investigate the formation mechanism of this defect in order to decrease its density and to recover the minority carrier lifetime in GaAs.

4.2 Hole traps in GaAsN grown by CBE

4.2.1 DLTS spectra and properties of hole traps in GaAsN

Here, we only focus on the hole traps that coexist in all *p*-type GaAsN based Schottky junctions and n^+-GaAs/*p*-GaAsN heterojunction. The difference between these two structures is the temperature range in which the DLTS measurements can be carried out due to the freeze-out of carriers. The DLTS spectrum of *p*-type GaAsN in the heterojunction is shown in Fig. 8(a). Three hole traps *H*0, *H*2, and *H*5 are observed at 0.052, 0.185, and 0.662 eV above the VBM of GaAsN. Their peak temperatures are 35, 130, and 300 K, respectively. The thermal dependence of emission from the hole traps is plotted as an Arrhenius plot in Fig. 8(b). The activation energy, capture cross section, and density are given in Table 2.

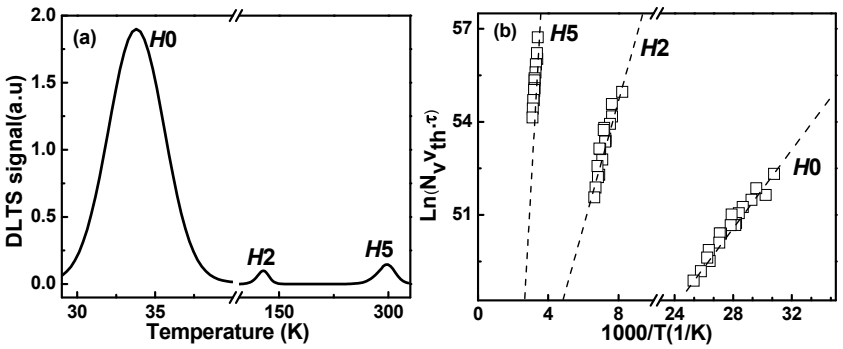

Fig. 8. (a) DLTS spectra of p-type GaAsN grown by CBE and (b) their Arrhenius plots.

The hole traps *H*2 and *H*5 were also observed in Schottky junctions and coexist in all samples. *H*2 is a N-related acceptor-like state and was proved to be in good relationship with high background doping in GaAsN films. These properties will be discussed later. The

hole trap *H*5 presents the same properties as *H*3 and *HA*5 (Li et al., 2001; Katsuhata et al., 1978). It is proposed to be the double donor state ($^{+}/^{++}$) of *EL*2 (Bouzazi et al., 2010). The hole trap *H*0 cannot be observed in Schottky junctions owing to the freeze-out effect.

Traps	E_t (eV)	σ_p(cm^2)	$N_{t\text{-}adj}$(cm^{-3})
*H*0	0.052	2.16×10^{-14}	4.64×10^{16}
*H*2	0.185	3.87×10^{-17}	4.52×10^{15}
*H*5	0.662	6.16×10^{-14}	6.24×10^{15}

Table 2. Summary of E_t, σ_p, and adjusted $N_{t\text{-}adj}$ of *H*0, *H*2, and *H*5.

4.2.2 Radiative shallow recombination center H0

DC-DLTS measurements were carried out to confirm whether there is a recombination center among the hole traps or not. As shown in Figs. 9(a) and (b), the DC-DLTS signal is compared to that of conventional DLTS. A decrease in the DLTS peak height of *H*0 is observed and confirmed by varying the voltage and the duration of the injected pulse.

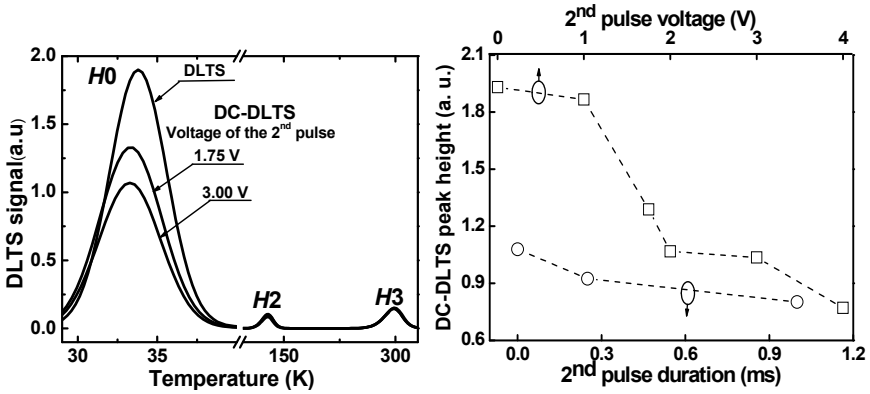

Fig. 9. (a)DC-DLTS spectra of p-type GaAsN for various second pulse voltage and (b) *H*0 DC-DLTS peak height dependence of second pulse voltage and duration.

The shallow hole trap H0 is observed and reported for the first time owing to the temperature range it was recorded, which cannot be reached with standard DLTS systems. Second, its capture cross section is large enough to capture majority carriers and minority carriers. The reduction in the peak height of H0 is explained by the electron hole-recombination. This implies that H0 is a shallow recombination center in p-type GaAsN grown by CBE and can also play the role of an acceptor state. To verify whether the recombination process via H0 is radiative or not, the temperature dependence of the capture cross section of electrons is obtained by varying the emission rate e_{rw} from 1 to 50 s^{-1}. As shown in Fig. 10(a), the peak temperature of H0 shifts to high temperatures with increasing e_{rw}. The value of σ_{H0} is obtained from the fitting of the Arrhenius plots for each e_{rw}. It is important to note that the fitting errors of activation energy and capture cross section are relatively large owing to the instability of temperature in the range of measurements. As shown in Fig. 10(b), the capture cross section of *H*0 does not exhibit an Arrhenius behavior, which excludes the non-radiative recombination process. Its shallow energy level suggests

that *H*0 plays the role of an intermediate center in the recombination process, with the exception that the recombination is quite often radiative.

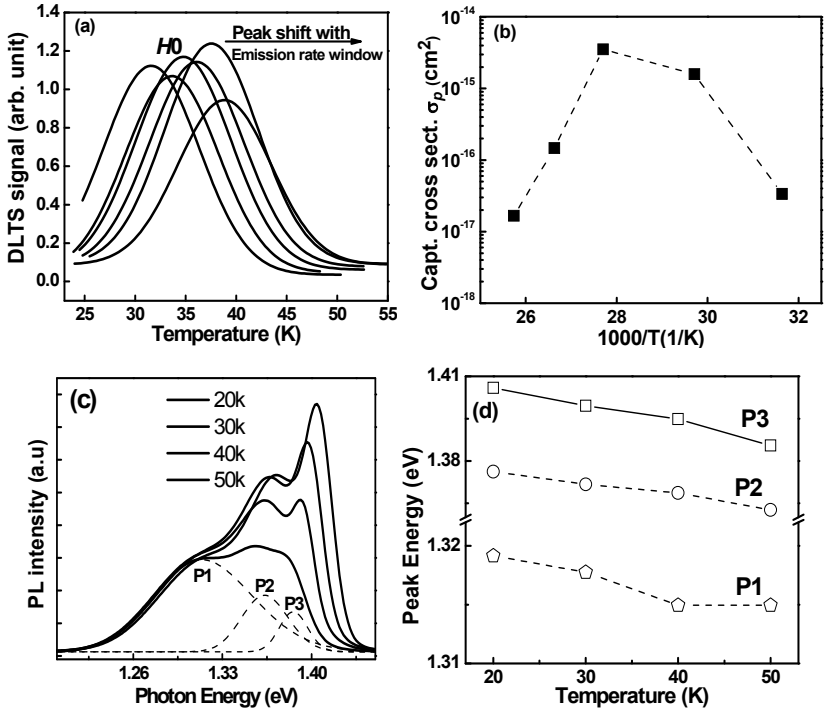

Fig. 10. (a) Emission rate window dependence of *H*0 peak, (b) temperature dependence of capture cross section and activation energy of *H*0, (c) *PL* spectra of p-type GaAsN at 20 to 50 K, and (d) temperature dependence of the peaks *P*1, *P*2, and *P*3 obtained from the fitting of PL spectra.

Furthermore, the capture cross section of electrons can be estimated using Eq. 13 and by the reduction of the peak height of *H*0, which follows from the injection of minority carriers. By varying the injected pulse voltage at fixed duration, the average capture cross section of electrons σ_n, at a temperature T = 35 K, is estimated to be $\sigma_n \sim 3.64 \times 10^{-16}$ cm^2. However, by varying the width of the injected pulse at fixed pulse voltage, it is estimated, at the same temperature, to be $\sigma_n \sim 3.05 \times 10^{-16}$ cm^2. These two values are nearly identical and indicate that the capture cross section of electrons and holes of *H*0 are approximately the same. To identify this radiative recombination, photoluminescence (*PL*) measurements were carried out at low temperature on the same GaAsN sample. The PL spectra at 20, 30, 40, and 50K are shown in Fig. 10 (c). Three different peaks *P*1, *P*2, and *P*3 can be distinguished from PL spectra fitting. The temperature dependence of their energies is plotted in Fig. 10 (d). The three peaks were sufficiently discussed in many N-varying GaAsN samples and they are proposed to be: (*i*) *P*1 is the result of band-to-band transition, (*ii*) *P*2 is caused by free exciton or related to shallow energy level, and (*iii*) *P*3 originates from the transition between a neutral donor and a neutral acceptor pair (DAP) (Inagaki et al., 2011). Therefore, the peak *P*2

is suggested to be in relation with *H*0. The band diagram of such recombination is shown in Fig. 11, where the transition occurs between H0 and the CBM and/or a donor-like defect (E_t). The transition between free electrons in the CBM and charged *H*0 is called free-to-charged bound transition.

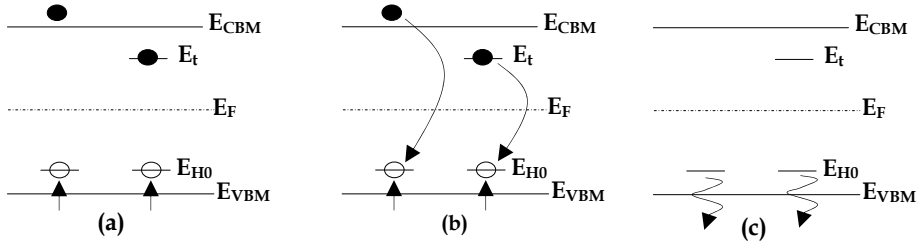

Fig. 11. Band diagram of radiative recombination through *H*0, where the transition occurs between *H*0 and the CBM and/or a donor-like defect (E_t).

Concerning the origin of the acceptor–like hole trap H0, more experiments are required to discuss it. However, considering its density and the distribution of shallow acceptors in GaAs, it can be suggested that *H*0 is a carbon-related acceptor, where the reported ionization energy from *PL* and Hall Effect measurements is 0.026 eV and its density in the 10^{-15} cm^{-3} range (Baldereschi & Lipari, 1974).

4.2.3 Deep N-H related acceptor state H2

The ionized acceptor density (N_A) is found to be in good linear dependence with N concentration in *p*-type GaAsN samples (see Fig. 12 (a)). As given in Figs. 12(b) and (c), the junction capacitance (C_j) showed a *N*-related sigmoid behavior with temperature in the range 70 to 100 K. This behavior has not yet been observed in GaAs and *n*-type GaAsN grown by CBE. It was recorded at 20 K in silicon *p*-*n* junction and explained by the ionization of a shallow energy level (Katsuhata, 1978; 1983). Hence, the N dependence of N_A and C_j is explained by the thermal ionization of a *N*-related acceptor-like state. The thermal ionization energy of this energy level was estimated in the temperature range 70 to 100 K to be between 0.1 and 0.2 eV. It is in conformity with the theoretical calculations, which suggested the existence of a N-related hole trap acceptor-like defect with an activation energy within 0.03 and 0.18eV above the VBM of GaAsN (Janotti et al., 2003; Suzuki et al., 2008). Experimentally, a deep acceptor level, A2, was confirmed in CBE grown undoped GaAsN with ionization energies of E_{A1} = 130 ± 20 meV (Suzuki et al., 2008). On the other hand, the properties of *H*2 in N-varying GaAsN schottky junctions are cited below: The peak temperature of *H*2 is within the temperature range of increase of C_j. This means that the electric field at this temperature range fellows the same behavior of C_j and depends on N concentration. Hence, the emission of carriers from the charged traps is affect by the Poole-Frenkel emission (Johnston and Kurtz, 2006). This is confirmed by the fluctuation of E_{H2} from one sample to another depending on N concentration (see Table 3). However, the average of E_{H2} is within the energy range of the acceptor level obtained from theoretical prediction and identical to E_{A2} (Suzuki et al., 2008; Janotti et al., 2003). Furthermore, as given in Fig. 12 (d), $N_{H2\text{-}adj}$ is in linear dependence with *N* concentration. Therefore, *H*2 is proved to be the N-related hole trap acceptor-like state, which thermal ionization increased C_j and

drops the depletion region width. The contribution of *H*2 in the background doping of p-type GaAsN films grown by CBE can be evaluated from the ratio between the real $N_{H2\text{-}Cj}$ calculated from the change of C_j and N_A at room temperature (Bouzazi et al., 2010). As shown in Fig. 12 (*e*) and (*f*), This ratio comes closer to the unit for a N concentration greater than 0.2%. Thus, *H*2 is the main cause of the high background doping in *p*-type GaAsN.

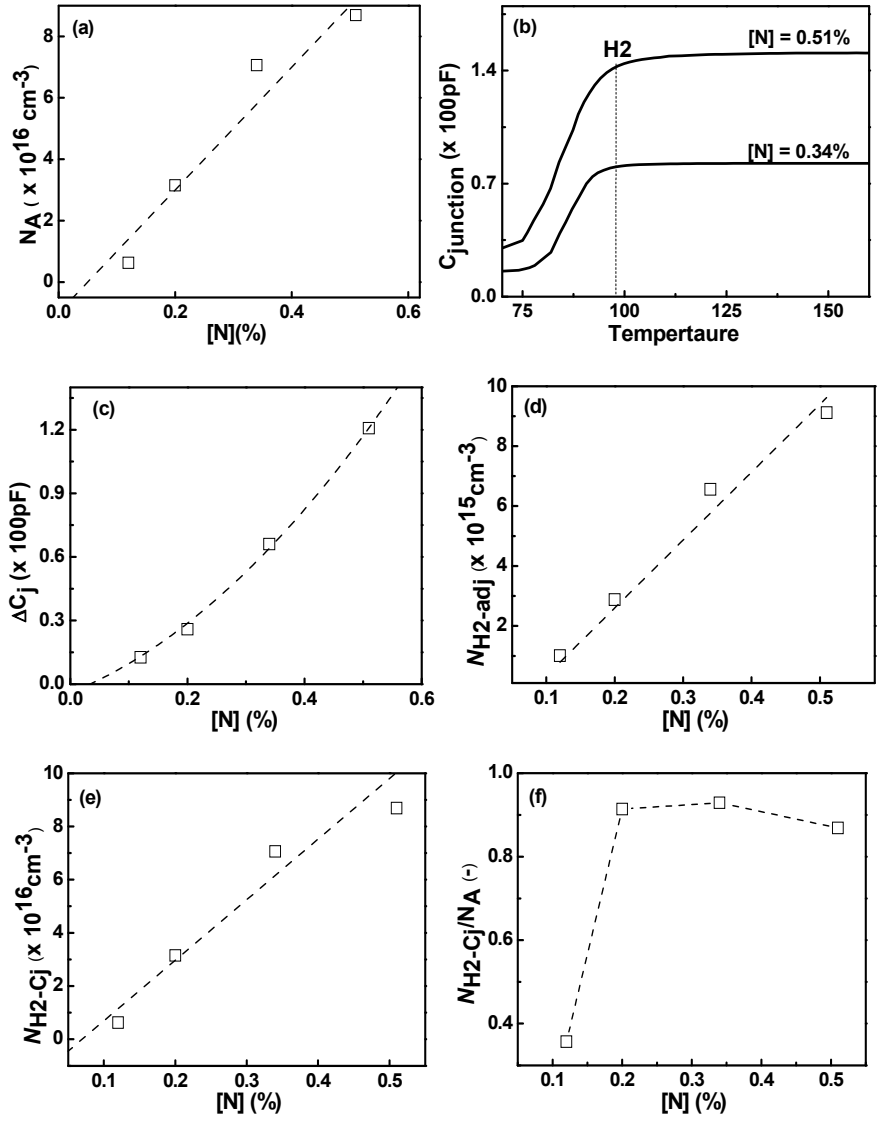

Fig. 12. N dependence of (a) N_A, (c) amplitude of C_j after thermal ionization of *H*2, and (d) $N_{H2\text{-}adj}$. (b) Sigmoid increase of C_j between 70 and 100 K for two different GaAsN samples. *N* dependence of (e) $N_{H2\text{-}Cj}$ and (f) $N_{H2\text{-}Cj}$ /N_A.

To investigate the origin of *H*2, it is worth remembering some previous results about carrier concentration and the density of residual impurities in undoped GaAsN grown by CBE, obtained using Hall Effect, Fourier transform infra-red (FTIR), and second ion mass spectroscopy (SIMS) measurements. On one hand, under lower Ga flow rates (TEGa), N_A and N_{H2} sowed a rapid saturation with [*N*], despite the increase of [*N*] (see Fig. 13 (a)). This means that the atomic structure of *H*2 depends on other atoms, either than *N*. In addition, the densities of *C* and *O* was found to be less than free hole concentration, which excludes these two atoms from the origin of *H*2. On the other hand, using SIMS measurements, the ratio $[H]_{TEGa = 0.02}/[H]_{TEGa = 0.1}$ was evaluated to be ~0.6 (Sato et al., 2008). Furthermore, the free hole concentration at room temperature showed a linear increase with the density of *N-H* bonds (Nishimura et al., 2006). This means that N_A depends strongly on [*H*] and the saturation of N_A under lower TEGa can be explained by the desorption of *H* from the growth surface, since the growth rate in our films was found to be in linear dependence with TEGa. Hence, the structure of *H*2 is related to the N-H bond. However, the *N-H* bond may not be the exact structure of *H*2 because the slope of the linear relationship between N_A and [*N-H*] increased with increasing growth temperature ($T_G \in [400, 430]$ °C). This indicates that N_A is determined by both the number of *N–H* and another unknown defect, which concentration increased with increasing T_G. The binding energy of this unknown defect can be determined from Arrhenius plot. Furthermore, the formation energy of $(N\text{-}H\text{-}V_{Ga})^{-2}$ was found to be lower than $(N\text{-}V_{Ga})^{-3}$, $(H\text{-}V_{Ga})^{-2}$, and isolated V_{Ga}^{-3} (Janotti et al., 2003). This means that the unknown defect may be V_{Ga}. These predictions were experimentally supported using positron annihilation spectroscopy results (Toivonen et al., 2003). Hence, H2 may be related to the $N\text{-}H\text{-}V_{Ga}$ structure.

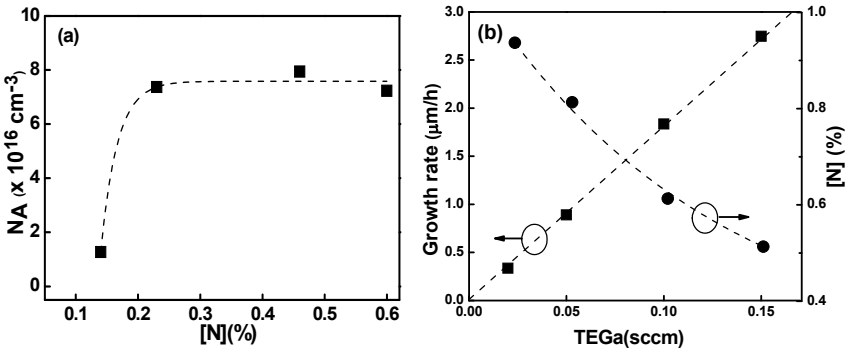

Fig. 13. N dependence of (a) N_A and (b) TEGa flow rate dependence of growth rate and N concentration at a growth temperature of 420 °C.

[N](%)	E_{H2} (eV)	σ_{H2}(cm²)	$N_{H2\text{-}adj}$(cm^{-3})	E_{max} (V/cm)	$N_{H2\text{-}Cj}$(cm^{-3})	$N_{H2\text{-}Cj}/N_A$
0.12	0.210	2.8×10^{-14}	2.64×10^{15}	6.2×10^{4}	2.23×10^{15}	0.36
0.20	0.150	6.3×10^{-16}	3.08×10^{15}	1.4×10^{5}	2.88×10^{16}	0.91
0.34	0.138	6.3×10^{-16}	5.20×10^{15}	2.1×10^{5}	6.56×10^{16}	0.93
0.51	0.103	1.3×10^{-17}	9.12×10^{15}	2.3×10^{5}	7.55×10^{16}	0.87

Table 3. Summary of E_{H2}, σ_{H2}, $N_{H2\text{-}adj}$, E_{max}, $N_{H2\text{-}est}$, and the ratio $N_{H2\text{-}Cj}/N_A$ for CBE grown undoped *p*-type GaAsN Schottky junctions.

5. Conclusion

Three defect centers, related to the optoelectronic properties of GaAsN, were identified and characterized using DLTS and some related methods:

- The first defect is a N-related non-radiative recombination center (*E*1), located approximately 0.33 eV below the CBM of GaAsN grown by CBE. *E*1 is a stable defect and exhibits a large capture cross section at room temperature. Its activation energy comes closer to the midgap by increasing the N concentration in the film, which increases the recombination rates of carriers. In addition, the density profiling of E1 was found to be uniformly distributed, which may indicates that this defect was formed during growth to compensate for the tensile strain caused by N. Using the SRH model for generation-recombination, the lifetime of electrons to *E*1 was evaluated to be ~0.2 ns. Therefore, *E*1 is suggested to be the main cause of poor minority carrier lifetime in GaAsN films. Its origin was suggested to be the split interstitial formed from one N and one As in a single arsenic site.
- The second defect is a radiative shallow hole trap acceptor-like state (*H*0), at 0.052 eV above the VBM of GaAsN. it was observed and reported for the first time in GaAs and GaAsN films. The radiative recombination process through *H*0 is confirmed to be a free-to-charged bound transition. This defect may be in relationship with carrier density and the optical properties of the film.
- The last defect is a N-related hole trap acceptor-like state (*H*2) located approximately 0.15 eV above the VBM of GaAsN. It was newly observed in GaAsN films. *H*2 was proved to have a good relationship with the carrier density and to be the main origin of high background doping in GaAsN films, essentially for relatively high *N* concentration. *H*2 is strongly suggested to be related with N-H bond. Its formation limits the junction depth and minimizes the contribution of the depletion region in the quantum efficiency of GaAsN based solar cells.

In conclusion, the results obtained in this study are very useful for scientific understanding of defects in III-V-N materials and to improve GaAsN and InGaAsN qualities for realizing high efficiency multi-junction solar cells.

6. Acknowledgment

Part of this work was supported by the New Energy Development Organization (NEDO) under the Ministry of Economy, Trade and Industry, Japan.

7. References

Ahlgren, T.; Vainonen-Ahlgren, E.; Likonen, J.; Li, W. & Pessa, M. (2002). Concentration of interstitial and substitutional nitrogen in GaN_xAs_{1-x}. Applied Physics Letters, Vol. 80, pp. 2314-2316.

Amore, B. A. & Filippone, F. (2005). Theory of Nitrogen-Hydrogen Complexes in N-containing III-V Alloys, chapter 13, Dilute Nitride Semiconductors, Henidi, M. Elsevier Ltd, UK.

Baldereschi, A. & Lipari, N. O. (1974). Cubic contributions to the spherical model of shallow acceptor states. Physical Review B, Vol.9, pp. 1525-1539.

Bouzazi, B.; Nishimura, K.; Suzuki H.; Kojima, N.; Ohshita, Y. & Yamaguchi M. (2010). Properties of Chemical Beam Epitaxy grown $GaAs_{0.995}N_{0.005}$ Homo-junction Solar Cell, Current Applied Physics, Vol.10, pp. 188-190.

Bouzazi, B.; Suzuki, H.; Kojima, N.; Ohshita, Y. & Yamaguchi, M. (2011). Japanese Journal of Applied Physics, Vol.49, pp. 121001-121006.

Bube, R. H. (1956). Comparison of Surface-Excited and Volume-Excited Photoconduction in Cadmium Sulfide Crystals. Physical Review, Vol.101, pp. 1668-1676.

Bube, R. H. (1960). Photoconductivity of Solids. John Wiley & Sons, Inc., New York, pp. 292-299.

Deenapanray, P. N. K.; Tan, H. H. & Jagadish, C. (2000). Investigation of deep levels in rapid thermally annealed SiO_2-capped n-GaAs grown by metal-organic chemical vapor deposition. Applied Physics Letters, Vol.77, pp. 696-698.

DeVore, H. B. (1959). Gains, response times, and trap distributions in powder photoconductors. RCA Review, Vol. 20, pp. 79-91.

Friedman, D. J.; Geisz, J. F.; Kurtz, S. R.; & Olson, J. M. (1998). 1-eV Solar Cells with GaInNAs Active Layer. Journal of Crystal Growth, Vol.195, pp. 409-415.

Geisz, J. F.; Friedman, D. J.; Olson, J. M.; Kurtz, S. & Keyes, B. M. (1998). Photocurrent of 1 eV GaInNAs lattice-matched to GaAs. Journal of Crystal Growth, Vol.195, pp. 401-408.

Geisz, J. F. & Friedman, D. J. (2002). III–N–V Semiconductors for Solar Photovoltaic Applications. Semiconductor Science and Technology, Vol.17, No.8, pp. 769-777.

Hall, R. N. (1952). Electron-Hole Recombination in Germanium. Physical Review, Vol. 87, pp. 387-387.

Inagaki, M.; Suzuki, H.; Suzuki, A.; Mutaguchi, K.; Fukuyama, A.; Kojima, N.; Ohshita, Y. & Yamagichi, M. (2011). Shallow Carrier Trap Levels in GaAsN Investigated by Photoluminescene. Japanese Journal of Applied Physics, Vol.50, 4, pp. 04DP141-144.

Janotti, A.; Zhang, S. B.; Wei, S. H. & Van de Walle, C. G. (2002). Effects of hydrogen on the electronic properties of dilute GaAsN alloys. Physical Review Letters, Vol.89, pp. 6403-6406.

Janotti, A.; Wei, S. H.; Zhang, S. B. & Kurtz, S. (2003). Interactions between nitrogen, hydrogen, and gallium vacancies in $GaAs_{1-x}N_x$ alloys. Physical Review B, Vol.67, pp. 161201-161204.

Jock, M. R. (2009). Effect of N Interstitials on the Electronic Properties of GaAsN Alloy Films. Thesis, the University of Michigan, 2009.

Johnston, S. W. & Kurtz, S. R. (2006). Comparison of a dominant electron trap in *n*-type and *p*-type GaNAs using deep-level transient spectroscopy. Journal of Vacuum Science & Technology, A24 (4), pp. 1252-1257.

Katsuhata, M.; Koura, K. & Yoshida S. (1978). Temperature Dependence of Capacitance of Silicon p-n Step Junctions. Japanese Journal of applied physics, Vol.17, pp. 2063-2064.

Katsuhata, M.; Yamagata, S., Miyayama, Y.; Hariu, T. & Shibata, Y. (1983). P-n Junction Capacitance Thermometers. Japanese Journal of Applied Physics, Vol.22, pp. 878-881.

Krispin, P.; Spruytte, S. G.; Harris, J. S. & Ploog, K. H. (2000). Electrical depth profile of p-type GaAs/Ga(As, N)/GaAs hetero-structures determined by capacitance–voltage measurements. Journal of Applied Physics, Vol.88, pp. 4153- 4158.

Krispin P.; Gambin V.; Harris J. S. & Ploog K. H. (2003). Nitrogen-related electron traps in Ga(As,N) layers (< 3% N). Journal of Applied Physics, Vol.93, pp. 6095-6099.

Krispin, P.; Spruytte, S. G.; Harris, J. S. & Ploog, K. H. (2001). Origin and annealing of deep-level defects in p-type GaAs/Ga(As,N)/GaAs hetero-structures grown by molecular beam epitaxy. Journal of Applied Physics, Vol.89, pp. 6294-6301.

Kurtz, S.; Allerman, A. A.; Jones, E. D.; Gee, J. M.; Banas, J. J. & Hammons, B. E. (1999). InGaAsN solar cells with 1.0 eV band gap, lattice matched to GaAs. Applied Physics Letters Vol.74, pp. 729-731.

Kurtz, S.; Webb, J.; Gedvilas, L.; Friedman, D.; Geisz, J.; Olson, J.; King, R., Joslin, D. & Karam, N. (2001). Structural changes during annealing of GaInAsN. Applied Physics Letters, Vol.78, pp. 748-750.

Kurtz, S.; Reedy, R.; Barber, G. D.; Geisz, J. F.; Friedman, D. J.; McMahon, W. E. & Olson, J. M. (2002) Incorporation of nitrogen into GaAsN grown by MOCVD using different precursors. Journal of Crystal Growth, Vol.234, pp. 318-322.

Kurtz, S. R.; Geisz, J. F.; Keyes, B. M.; Metzger, W. K.; Friedman, D. J.; Olson, J. M.; King, R. R. & Karam, N. H. (2003). Effect of growth rate and gallium source on GaAsN. Applied Physics Letters, Vol.82, pp. 2634-2636.

Lambe, J. (1955). Recombination Processes in Cadmium Sulfide. Physical Review, Vol.98, pp. 985-992.

Lampert, M. A. (1956). Simplified Theory of Space-Charge-Limited Currents in an Insulator with Traps, Physical Review, Vol.103, pp. 1648-1656.

Lang, D. V. (1974). Deep-level transient spectroscopy: A new method to characterize traps in semiconductors. Journal of applied Physics, Vol.45, pp.3023-3032.

Lee, H. S.; Nishimura, K.; Yagi, Y.; Tachibana, M.; Ekins-Daukes, N. J.; Ohshita, Y.; Kojima, N.; Yamaguchi, M. (2005). Chemical beam epitaxy of InGaAsN films for multi-junction tandem solar cells. Journal of Crystal Growth, Vol.275, pp. 1127-1130.

Leonard, I. & Grossweiner, A. (1953). A Note on the Analysis of First-Order Glow Curves. Journal of Applied Physics, Vol.24, pp. 1306-1307.

Li, J. Z.; Lin, J. Y.; Jiang, H. X.; Geisz, J. F. & Kurtz, S. R. (1999). Persistent photoconductivity in $Ga_{1-x}In_xN_yAs_{1-y}$. Applied Physics Letters, Vol.75, pp. 1899-1901.

Li, W.; Pessa, M.; Ahlgren, T.; & Dekker, J. (2001). Origin of improved luminescence efficiency after annealing of Ga(In)NAs materials grown by molecular-beam epitaxy. Applied Physics Letters, Vol.79, pp. 1094-1096.

Losee, D. L. (1974). Admittance spectroscopy of deep impurity levels: ZnTe Schottky barriers. Applied Physics Letters, Vol.21, pp. 54-56.

Moto, A.; Takahashi, M. & Takagishi, S. (2000). Hydrogen and carbon incorporation in GaInNAs. Journal of Crystal Growth, Vol.221, pp. 485-490.

Nishimura, K.; Suzuki, H.; Saito, K.; Ohshita, Y.; Kojima, N. & Yamaguchi, M. (2007). Electrical properties of GaAsN film grown by chemical beam epitaxy. Physica B, Vol.401, pp. 343-346.

Reddy, C. V.; Fung, S. & Beling, C. D. (1996). Nature of the bulk defects in GaAs through high-temperature quenching studies. Physical Review B, 54, pp. 11290-11297.

Rose, A. (1951). An outline of some photoconductive processes. RCA Review., Vol.12, pp. 362-414.

Rose, A. (1955). Space-Charge-Limited Currents in Solids. Physical Review, Vol.97, pp. 1538-1544.

Saito K.; Nishimura K.; Suzuki H.; Kojima N.; Ohshita Y. & Yamaguchi, M. (2008). Hydrogen reduction in GaAsN thin films by flow rate modulated chemical beam epitaxy. Thin Solid Films, Vol.516, pp. 3517-3520.

Sah, C. T.; Chan, W. W.; Fu, H. S. & Walker, J. W. (1972). Thermally Stimulated Capacitance (TSCAP) in p-n Junctions. Applied Physics Letters, Vol.20, pp. 193-195

Sah, C. T. & Walker, J. W. (1973). Thermally stimulated capacitance for shallow majority-carrier traps in the edge region of semiconductor junctions. Applied Physics Letters, Vol.22, pp. 384-385.

Shockley, W. & Read. W.T. (1952). Statistics of the Recombinations of Holes and Electrons. Physical Review, Vol. 87, pp. 835-842.

Smith, R. W. & Rose, A. (1955). Space-Charge-Limited Currents in Single Crystals of Cadmium Sulfide. Physical Review, Vol.97, pp. 1531-1537.

Spruytte, S. G.; Coldren, C. W.; Harris, J. S.; Wampler, W.; Ploog, K. & Larson, M. C. (2001). Incorporation of nitrogen in nitride-arsenides: Origin of improved luminescence efficiency after anneal. Journal of Applied Physics, Vol.89, pp. 4401-4406.

Suzuki, H.; Nishimura, K.; Saito, K.; Hashiguchi, T.; Ohshita, Y.; Kojima, N. & Yamaguchi, M. (2008). Effects of Residual Carbon and Hydrogen Atoms on Electrical Property of GaAsN Films Grown by Chemical Beam Epitaxy. Japanese Journal of Applied Physics, Vol.47, pp. 6910-6913.

Toivonen, J.; Hakkarainen, T.; Sopanen, M.; Lipsanen, H.; Oila, J. & Saarinen, K. (2003). Observation of defect complexes containing Ga vacancies in GaAsN. Applied Physics Letters, Vol.82, pp. 40-43.

Williams, R. (1966). Determination of Deep Centers in Conducting Gallium Arsenide. Journal of Applied Physics, Vol.37, pp. 3411-3416.

Yakimova, R.; Paskova, T. & Hardalov, Ch. (1993). Behavior of an EL5-like defect in metalorganic vapor-phase epitaxial GaAs:Sb. Journal of Applied Physics, Vol.74, pp. 6170-6173.

Yamaguchi, M.; Warabisako, T.; Sugiura, H. (1994). Chemical beam epitaxy as a breakthrough technology for photovoltaic solar energy applications. Journal of Crystal Growth, Vol.136, pp.29-36.

Zhang, S. B. & Wei, S. H. (2001). Nitrogen Solubility and Induced Defect Complexes in Epitaxial GaAs:N. Physical Review Letters, Vol.86, pp. 1789-1792.

Ziegler, J. F.; Biersack J. P. & U. Littmark. (1985). The Stopping and Ion Range of Ions in Solids. Pergamon, New York, Vol. 1; SRIM program for PCs available from J. F. Zieglerand: www.srim.org.